

THE CATHOLIC UNIVERSITY OF AMERICA

Time Effects in Relation to Crushing in Sand

A DISSERTATION

Submitted to the Faculty of the

Department of Civil Engineering

School of Engineering

Of The Catholic University of America

In Partial Fulfillment of the Requirements

For the Degree

Doctor of Philosophy

©

Copyright

All Rights Reserved

By

Hamid Karimpour

Washington, D.C.

2012

Time Effects in Relation to Crushing in Sand

Hamid Karimpour, Ph.D.

Director: Poul V. Lade, Ph.D.

Time effects have frequently been reported in granular materials, and differ from those observed in clays. Recent studies suggest that particle crushing and static fatigue may be at the root of observed time-dependent behavior in granular material. This study has focused on time effects associated with crushing. Several series of time-dependent triaxial compression tests were performed on dense Virginia Beach sand to explore time-dependent behaviors of granular materials. Furthermore, to exhibit the relation between the static fatigue phenomenon and breakage of individual particles, two series of single particle tests on glass beads were carried out. Although results of single particle tests showed a considerable amount of scatter, the static fatigue phenomenon was clearly observed and beads fractured after some time under stresses smaller than their short-term strength. The stress-strain behavior was not noticeably affected after aging under isotropic compression stresses, while it was slightly influenced under K_0 stress states.

Time effects were negligible under low confining stresses. However, under high confining pressures, a delay was observed at the beginning of time-dependent phases in the initiation of creep deformations or stress relaxation depending on the prior shearing strain rate; the slower the shearing strain rate was, the longer the delays were. Moreover, time effects were more pronounced at higher deviator stresses. Experimental results after two months suggested that there is no end to creep deformations and stress relaxation.

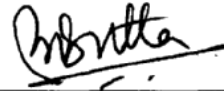
Additional loading at the end of time-dependent phases indicated that there were no structuration effects for dense Virginia Beach sand. Stress drop experiments followed by time dependent phases showed that greater time effects were observed when the initial stress level was closer to the yield surface.

Sieve analyses performed after each experiment showed that particle breakage increased with the energy input. Therefore, a significant amount of particle crushing was observed during creep, while negligible crushing was detected during stress relaxation. Specimens sheared for longer periods of time experienced larger amounts of particle crushing and vice-versa. All the aforementioned observations were adequately explained by the static fatigue phenomenon and the proposed mechanistic picture for time effects in granular materials.

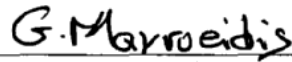
This dissertation by Hamid Karimpour fulfills the dissertation requirement for the doctoral degree in Civil Engineering approved by Poul V. Lade, Ph.D., as Director and by Biprodas Dutta, Ph.D., and George P. Mavroeidis, Ph.D. as Readers.



Poul V. Lade, Ph.D., Director



Biprodas Dutta, Ph.D., Reader



George P. Mavroeidis, Ph.D., Reader

Dedication

I would heartily like to dedicate my PhD dissertation, my most important achievement so far, to my mother and father who simply devoted their lives to their children by their unconditional and continuous love and support.

Table of Contents

Table of Contents	iv
List of Illustrations	x
List of Tables	xxviii
Acknowledgments	xxix
1. Introduction	1
1.1. Time Effects	1
1.1.1. Strain Rate Effects	1
1.1.2. Creep	1
1.1.3. Stress Relaxation	6
1.1.4. Structuration or Aging	6
1.2. Perspective of the Research	8
2. Previous Investigations	11
2.1. Time-Dependent Behavior of Granular Material	11
2.1.1. Effects of Aging Time on Behavior of Granular Material	12
2.1.2. Experimental Studies of Creep in Granular Media	24
2.1.3. Experimental Studies of Stress Relaxation in Granular Media	38
2.1.4. Strain Rate Dependency in Sands	46
2.1.5. Proposed Mechanisms for Time Effects in Granular Geomaterial	56
2.2. High Pressure Testing and Particle Crushing in Sands	62

2.2.1. One-Dimensional Compression	66
Experiments on Granular Material	
2.2.2. Triaxial and Other Types of	70
Experiments on Granular Material	
2.3. Static Fatigue	80
2.3.1. Mechanism of Static Fatigue	82
2.3.2. Speed of Static Fatigue	89
2.4. Effect of Water on Geomaterial Properties	105
2.5. Constitutive Models Incorporating	122
Time Effects or Particle Crushing Effects	
2.5.1. Empirical Models	122
2.5.2. Rheological Models	131
2.5.3. General Constitutive Models Incorporating Time-Effects	139
2.5.4. Constitutive Models Incorporating Particle Crushing	144
3. Experimental Program	157
3.1. Materials	157
3.1.1. Glass Beads Tested	157
3.1.2. Sand Tested	157
3.2. Apparatuses, Specimen Preparation and Measurements	161
3.2.1. Apparatuses	161
3.2.2. Triaxial Specimen Preparation and Measurements	167
3.2.3. Membrane Leakage	168
3.2.4. Volume Change Error Correction	173
3.3. Single Glass Bead Tests	174

3.4. Isotropic Compression–Drained	175
Triaxial Compression Tests	
3.4.1. Effect of Confining Pressure	175
3.4.2. Effect of Initial Axial Strain Rates	177
3.4.3. Effect of Isotropic Aging	178
3.5. K_0 Stress State Compression-	178
Drained Triaxial Compression Tests	
3.6. Creep Tests	179
3.6.1. Effect of Initial Shearing Rate on Subsequent Creep	179
3.6.2. Effect of Soil Gradation Curve on Subsequent Creep	181
3.6.3. 1-Day Creep Curve	181
3.6.4. Long Term Creep	182
3.7. Stress Relaxation Tests	182
3.7.1. Effect of Initial Shearing Rate	182
on Subsequent Stress Relaxation	
3.7.2. 1-Day Stress Relaxation Curve	184
3.7.3. Long Term Stress Relaxation	185
3.8. Mixed Creep-Stress Relaxation Tests	186
3.8.1. Tests with Creep, then Stress Relaxation	186
3.8.2. Tests with Stress Relaxation, then Creep	188
3.8.3. Combined Creep-Stress Relaxation	188
3.8.4. Multiple 1-Day Creep-Shear-Stress Relaxation	191
3.9. Stress Drop- Creep Tests	191
3.9.1. Stress Drop-Creep	191

3.9.2. Multiple Stress Drop-Creep-Shear	192
3.10. Stress Drop- Relaxation Tests	192
3.10.1. Stress Drop-Stress Relaxation	192
3.10.2. Multiple Stress Drop-Stress Relaxation-Shear	193
3.11. Sieve Analyses and Characterizations of Crushing	193
3.11.1. Methods That Assume a Specific Grain Size	194
3.11.2. Methods That Consider Changes in the Whole Grain Size Distribution Curve	195
4. Isotropic and K_0 Stress States Compression-Drained Triaxial Experiments, and Single Glass Bead Tests	199
4.1. Effect of Confining Pressure	199
4.2. Effect of Initial Shearing Strain Rate	213
4.3. Effect of Aging under Isotropic Stresses	222
4.4. Effect of Aging under K_0 Stress States	227
4.5. Single Glass Bead Tests	239
5. Creep Experiments	250
5.1. Effect of Initial Shearing Rate on Subsequent Creep	250
5.2. Effect of Soil Gradation Curve on Subsequent Creep	261
5.3. 1-Day Creep Curve	273
5.4. Long Term Creep	284
5.5. Mechanism of Creep Behavior	287
6. Stress Relaxation Experiments	289
6.1. Effect of Initial Shearing Rate on Subsequent Stress Relaxation	289
6.2. 1-Day Stress Relaxation Curve	315

6.3. Long Term Stress Relaxation	324
6.4. Comparison between 1-Day Creep and Stress Relaxation	327
6.5. Mechanism of Stress Relaxation Behavior	330
7. Creep-Stress Relaxation Experiments	332
7.1. Starting Creep-Ending Stress Relaxation	332
7.2. Starting Stress Relaxation-Ending Creep	336
7.3. Combined Creep-Stress Relaxation	343
7.4. Multiple 1-Day Creep-Shear-Stress Relaxation	352
8. Stress Drop-Creep and Stress Drop-Stress Relaxation	359
8.1. Stress Drop-Creep Tests	360
8.1.1. Stress Drop-Creep	360
8.1.2. Multiple Stress Drop-Creep	363
8.2. Stress Drop-Stress Relaxation Tests	370
8.2.1. Stress Drop-Stress Relaxation	370
8.2.2. Multiple Stress Drop-Stress Relaxation	375
9. Sieve Analyses	385
9.1. Particle Crushing During Isotropic Compression	385
9.2. Particle Crushing During Triaxial Compression	389
9.2.1. Effect of Confining Pressure	389
9.2.2. Effect of Shearing Strain Rate	392
9.3. Particle Crushing During Creep	392
10. Summary and Conclusions	402
10.1. Single Particle Strength Tests	402
10.2. Triaxial Compression Tests	403

10.3. Isotropic Compression and K_0 Aging Tests	405
10.4. Creep Tests	405
10.5. Stress Relaxation Tests	407
10.6. Creep-Stress Relaxation Tests	408
10.7. Stress Drop-Creep and Stress Drop-Stress Relaxation Tests	410
10.8. Sieve Analyses	411
10.9. Overall Observations	412
10.10. The Hypothesis of Creep and Stress Relaxation Behavior	413
Appendices	416
A: Stress-Strain Data for Tests presented	416
B: Sieving Data for Tests Presented	529
Bibliography	537

List of Illustrations

Figure 1.1: Schematic strain rate effect on stress-strain behavior for clays	2
Figure 1.2: Schematic creep effect	4
Figure 1.3: Typical result of a constant stress creep test performed in a triaxial apparatus:	4
(a) strain-time, (b) log (strain rate)-log(time)	
Figure 1.4: Typical result of a consolidation test performed in an oedometer apparatus: (a)	5
strain-log(time), (b) log (strain rate)-log(time)	
Figure 1.5: Schematic stress relaxation effect	7
Figure 1.6: Structuration effect during creep	7
Figure 2.1: Effect of consolidation time on stress-strain behavior of Ham River sand	13
Figure 2.2: Change in stiffness versus consolidation time	14
Figure 2.3: Change in penetration resistance versus aging time	16
Figure 2.4: Structuration effect due to creep	16
Figure 2.5: Variation of applied stress and settlement with logarithm of time for primary treatment plant	21
Figure 2.6: Variation of applied stress and settlement with logarithm of time for second treatment plant	23
Figure 2.7: Variation of volumetric creep strain versus confining pressure	26
Figure 2.8: Pile creep settlement versus (a) time, and (b) logarithm of time	28

Figure 2.9: Creep settlement versus logarithm of time for dry and saturated specimens	30
Figure 2.10: Change in the orientation of plastic strain increments with the logarithm of time under confining pressures of (a) 196 kPa, and (b) 392 kPa	32
Figure 2.11: Deviator creep strain versus logarithm of time for $p' = 600$ kPa and $q = 800$ kPa	34
Figure 2.12: Volumetric creep strain versus logarithm of time for $p' = 600$ kPa and $q = 800$ kPa	34
Figure 2.13: Change in a grain assembly due to a sustained load	36
Figure 2.14: (a) Stress-strain and (b) volume change behavior during three stages of creep at 500, 700 and 900 kPa of deviator stress on crushed coral sand	37
Figure 2.15: Axial creep strain versus logarithm of time for different stress drop-creep tests	39
Figure 2.16: Log-log graph of variation of delay time with strain rate	40
Figure 2.17: Variation of normalized stress relaxation with logarithm of time for Monterey sand	40
Figure 2.18: Variation of deviator stress with logarithm of time for frozen Ottawa sand under $\sigma_3 = 200$ kPa	43
Figure 2.19: (a) Stress-strain and (b) volume change behavior during three stages of stress relaxation at 500, 700 and 900 kPa of deviator stress on crushed coral sand	44

Figure 2.20: Effect of initial strain rate on consequent relaxation tests at deviator stresses of 500, 700 and 900 kPa: (a) stress-strain; (b) volume change	45
Figure 2.21: Stress relaxation versus logarithm of time for different stress drop-relaxation tests	47
Figure 2.22: Effect of strain rate on undrained behavior and instability line for Cambria sand	50
Figure 2.23: Rate dependency of stress-strain behavior of a sand postulated by Matsushita et al. (1999)	52
Figure 2.24: Basic viscous behavior of geomaterials due to strain rate change proposed by Tatsuoka (2007)	52
Figure 2.25: Rate dependency of (a) stress-strain behavior, and (b) volume change behavior for crushed coral sand	57
Figure 2.26: Effect of strain rate change from 1.70 to 0.00665 %/min and vice versa on (a) stress-strain, and (b) volume change of crushed coral sand	58
Figure 2.27: Comparison of 1-day creep and 1000 min stress relaxation curves of crushed coral sand	60
Figure 2.28: Comparison of 1-day creep and 1-day stress relaxation curves of Antelope Valley sand	61
Figure 2.29: Mechanistic picture of time effect in granular material assembly: (a) initial loading, (b) creep condition, (c) relaxation condition	63
Figure 2.30: Various modes of grain crushing: (a) fracture, (b) attrition, (c) abrasion	65
Figure 2.31: Variation of maximum principal stress ratio due to change in confining pressure	72

Figure 2.32: Grain size distribution curve after ring shear tests on Dog's Bay sand presented in (a) semi-logarithmic, axes and (b) double logarithmic axes	79
Figure 2.33: Variation of mobilized friction angle with shear strain in ring shear tests on Dog's Bay sand	81
Figure 2.34: Effect of time on strength of concrete specimens	83
Figure 2.35: One-dimensional model of sharp crack with nonlinear crack-tip bond	83
Figure 2.36: Three-stage fracture process in soil particle loaded in compression	88
Figure 2.37: Fracture process in soil particle involving tensile stresses near crack tips	88
Figure 2.38: Deviator stress and microfracturing events versus axial strain for Westerly granite in (a) uniaxial test, and (b) triaxial under confining pressure of 4 kilo bars	90
Figure 2.39: Variation of fracture time with the level of the constant stress	92
Figure 2.40: Variation of time-to-failure of soda-lime glass rods in bending with temperature	94
Figure 2.41: Effect of variation of the environment temperature on the crack growth of (a) soda-lime silicate, and (b) silica glass submerged in water	96
Figure 2.42: Variation of mean fracture time with temperature	96
Figure 2.43: Effect of the loading rate on the fracture stress of abraded soda-lime-silica glass specimens submerged in water	99

Figure 2.44: Strength at 0.82 second load duration with respect to variation of pH for specimens submerged in HCl, NaOH, and buffer solutions	100
Figure 2.45: Effect of pH of the environment on the crack propagation speed	101
Figure 2.46: Variation of the slope of crack velocity- K_I (stress intensity factor) curves as a function of pH of the environment	101
Figure 2.47: Two-dimensional model of water-induced bond rupture in silica glass	103
Figure 2.48: Schematic representation of chemical reactions at crack-tip between (a) water and quartz, and (b) hydroxyl and quartz in alkaline solution	103
Figure 2.49: Change in frequency of microfracturing events with time. Water is introduced at $t=600$ seconds	104
Figure 2.50: Variation of drained maximum principal stress ratio with confining pressure at different moisture conditions	110
Figure 2.51: Variation of initial tangent modulus with logarithm of confining pressure at different moisture conditions	111
Figure 2.52: Effect of introducing water on the creep behavior of oven-dried Antioch sand specimens	113
Figure 2.53: Variation of volumetric strain of saturated to dry specimens with logarithm of confining pressure	114
Figure 2.54: Variation of ratio of deviator stress of saturated to dry specimens with the logarithm of confining pressure	114
Figure 2.55: Change in degree of particle crushing with confining pressure for dry and saturated specimens	116

Figure 2.56: Variation of amount of particle crushing with one-dimensional pressure for different levels of presence of water	117
Figure 2.57: Schematic plot of force-displacement for single particle crushing test and definition of first peak load and the maximum peak load	119
Figure 2.58: Comparison of probability of survival for particle crushing under dry and wet conditions for (a) silica, and (b) feldspar and mica	120
Figure 2.59: One-dimensional consolidation test for (a) dry, and (b) wet specimens	121
Figure 2.60: Stress-strain behavior in one-dimensional consolidation test under dry and wet conditions	123
Figure 2.61: Compressibility and geological history of young and aged normally consolidated clay	129
Figure 2.62: Graphical definition of instant time line, reference time line, limit time line and positive and negative time lines in stress-strain space	130
Figure 2.63: Schematic explanation of three basic material models: (a) Hookean spring; (b) Newtonian dashpot; and (c) Saint Vernant's slider	132
Figure 2.64: Response of the Maxwell Model: (a) creep; (b) relaxation	134
Figure 2.65: Response of the Kelvin-Voigt Model: (a) creep; (b) relaxation	136
Figure 2.66: Reaction of Bingham model: (a) creep; (b) relaxation; (C) constant rate of strain	136

Figure 2.67: Definition of static and dynamic yield surfaced together with potential surface for current stress point, P , in overstress theory	142
Figure 2.68: Overstress theory for creep in a (a) non-hardening material (b) hardening material	142
Figure 2.69: Illustration of M_c , M_f and M lines and different stress paths in p' - q space	147
Figure 2.70: Stress-strain and volume change behavior related to triaxial compression stress paths of (a) AB , (b) CD , and (c) EF	147
Figure 2.71: A family of yield (potential) surfaces in the p' - q space	149
Figure 2.72: Predictions of drained stress-strain behavior of Toyoura sand by the proposed model by Yao et al. (2008)	149
Figure 2.73: Predictions of undrained stress-strain behavior of Toyoura sand by the proposed model by Yao et al. (2008)	150
Figure 2.74: Impact of particle crushing on the location of critical state line	151
Figure 2.75: Definition of the new critical state line	154
Figure 2.76: Plastic potential surface in p' - q space	156
Figure 3.1: Various grading curves used in the experimental program	158
Figure 3.2: Grain distribution curve for particles finer than $75\ \mu\text{m}$	160
Figure 3.3: Principal cross section of the triaxial cell used in the experimental program	163
Figure 3.4: Pressures acting on a specimen during cell pressure increase	164

Figure 3.5: Actual stress path during increasing confining pressure and correction of the deviator stress	166
Figure 3.6: Volume change response of three triaxial tests with different time-to-failures before installation of spiral tubing	170
Figure 3.7: Volume change response of three triaxial tests with different time-to-failures after installation of spiral tubing	172
Figure 3.8: Schematic stress-strain path for creep-relaxation experiments	187
Figure 3.9: Schematic stress-strain path for relaxation-creep experiments	189
Figure 3.10: Schematic stress-strain path for combined creep-relaxation experiments	190
Figure 3.11: Definition of parameters of Hardin's particle breakage index	197
Figure 4.1: Effect of confining pressures equal to and lower than 250 kPa on (a) stress-strain, and (b) volumetric behavior of Virginia Beach sand	200
Figure 4.2: Effect of confining pressures higher than 250 kPa on (a) stress-strain, and (b) volumetric behavior of Virginia Beach sand	201
Figure 4.3: Principal stress ratio versus axial strain under confining pressures ranging from 25 kPa to 14000 kPa for Virginia Beach sand	202
Figure 4.4: Appearance of specimens after 22% axial strain under confining pressures of (a) 250 kPa, and (b) 14000 kPa	204
Figure 4.5: Variation of (a) normalized initial tangent modulus, and (b) maximum principal stress ratio and its corresponding axial strain with normalized confining pressure	206

Figure 4.6: Variation of measured friction angle with logarithm of normalized confining pressure	209
Figure 4.7: Effect of confining pressure on evolution of grain size distribution curve	211
Figure 4.8: Hardin's breakage factor versus energy input	212
Figure 4.9: Effect of shearing strain rate on stress-strain and volumetric behavior under confining pressure of 250 kPa	214
Figure 4.10: Effect of shearing strain rate on stress-strain and volumetric behavior under confining pressure of 8000 kPa	215
Figure 4.11: Effect of shearing strain rate on evolution of grain size distribution curve under confining pressure of 250 kPa	218
Figure 4.12: Effect of shearing strain rate on evolution of grain size distribution curve under confining pressure of 8000 kPa	219
Figure 4.13: Variation of Hardin's breakage factor with respect to energy input	221
Figure 4.14: Effect of isotropic aging on (a) stress-strain, and (b) volumetric behavior of Virginia Beach sand	223
Figure 4.15: Variation of stiffness ratio and maximum friction angle with isotropic consolidation time	225
Figure 4.16: Grain size distribution curve for specimens sheared after various isotropic aging times	226
Figure 4.17: (a) Stress-strain, and (b) volume change behavior during K_0 stress states compression, aging and shearing	230
Figure 4.18: (a) Stress-strain, and (b) volumetric behavior during K_0 stress states compression and aging	231
Figure 4.19: (a) Stress-strain, and (b) volumetric behavior during shearing	233

Figure 4.20: Variation of stiffness ratio with consolidation time under K_0 stress states	234
Figure 4.21: Appearance of specimens aged under K_0 stress states at end of shearing	234
Figure 4.22: Variation of friction angle at axial strain of 7.5%, and axial and volumetric creep during aging under K_0 stress states with respect to aging time	236
Figure 4.23: Grain size distribution curve for specimens sheared after various aging times under K_0 stress states	237
Figure 4.24: Variation of Hardin's breakage factor with respect to energy input for specimens sheared after various aging times under K_0 stress states	238
Figure 4.25: Definition of point load test and spherical coordinates of r and θ	241
Figure 4.26: "Stress-strain" relations for different size soda lime glass beads tested in compression	243
Figure 4.27: Curve fitting to evaluate exponent of n in Equation (2-2)	244
Figure 4.28: Survival probability versus (a) crushing stress, and (b) normalized stress	246
Figure 4.29: Curve fitting to obtain Weibull modulus, m	247
Figure 4.30: Relation between sustained stress and time-to-fracture for different size soda lime glass beads tested in compression	249
Figure 5.1: Effect of the shearing strain rate on the subsequent creep behavior under $\sigma'_3=250$ kPa: (a) Stress-strain curve; (b) volume change curve	252

Figure 5.2: Effect of the initial shearing strain rate on the variation of (a) axial and (b) volumetric creep strains with time	253
Figure 5.3: Effect of the initial shearing strain rate on the crushing of the particles	255
Figure 5.4: Effect of the shearing strain rate on the subsequent creep behavior under $\sigma'_3=8000$ kPa: (a) Stress-strain curve; (b) volume change curve	257
Figure 5.5: Effect of initial shearing strain rate on variation of (a) axial, and (b) volumetric creep strains with time	258
Figure 5.6: Effect of initial shearing strain rate on crushing of particles	260
Figure 5.7: Relationship between Hardin's breakage factor and the amount of energy input for creep tests initially sheared at different strain rates	262
Figure 5.8: Effect of the grain size distribution curve on the subsequent creep behavior under $\sigma'_3=8000$ kPa: (a) Stress-strain curve; (b) volume change curve	263
Figure 5.9: Variation of the initial tangent modulus with (a) uniformity and (b) curvature coefficients	265
Figure 5.10: Effect of the grain distribution curve on the variation of (a) axial and (b) volumetric creep strains with time	266
Figure 5.11: Schematic variation of minimum void ratio for the mixture of large and fine spherical particles	269
Figure 5.12: Comparison of grain size distribution curves before and after creep tests	272
Figure 5.13: 1-day creep curve for Virginia Beach sand under $\sigma'_3=8000$ kPa	274

Figure 5.14: Effect of the deviator stress level on the (a) axial, and (b) volumetric creep strains with time	276
Figure 5.15: (a) Stress-strain, and (b) volume change curves for the multiple 1-day creep test on Virginia Beach sand	278
Figure 5.16: Variation of (a) axial, and (b) volumetric creep strains of the multiple 1-day creep test with time	280
Figure 5.17: Evolution of grain size distribution curve for the 1-day creep tests	281
Figure 5.18: The relationship between the axial and volumetric creep strains, and Hardin's	282
breakage factor for the 1-day creep tests	
Figure 5.19: The relationship between the energy input and Hardin's breakage factor for the 1-day creep tests	283
Figure 5.20: (a) Stress-strain, and (b) volume change curves for the 2-month creep test on Virginia Beach sand	285
Figure 5.21: Variation of axial and volumetric creep strains of the 2-month creep test with time	286
Figure 6.1: Effect of shearing strain rate on subsequent stress relaxation under $\sigma'_3=250$ kPa: (a)	291
stress-strain curves; (b) volume change curves	
Figure 6.2: Effect of initial shearing strain rate on variation of stress relaxation	292
Figure 6.3: Effect of initial shearing strain rate on crushing of particles	293
Figure 6.4: Effect of shearing strain rate on subsequent stress relaxation under $\sigma'_3=8000$ kPa:	295
(a) Stress-strain curves; (b) volume change curves	

Figure 6.5: Effect of initial shearing strain rate on variation stress relaxation: (a) deviator stress relaxation, and (b) actual deviator stresses	296
Figure 6.6: Effect of initial shearing strain rate on crushing of particles	299
Figure 6.7: Development of axial strain during stress relaxation due to expansion of load cell	300
Figure 6.8: Comparison of drained stress relaxation experiments with and without correction of axial strains	301
Figure 6.9: Comparison of stress relaxation magnitudes in experiments with and without correction of axial strains	303
Figure 6.10: Comparison of volumetric strains during stress relaxation for experiments with and without correction of axial strains	305
Figure 6.11: Effect of shearing strain rate on subsequent undrained stress relaxation under $\sigma'_3=8000$ kPa: (a) stress-strain curves; (b) volume change curves	306
Figure 6.12: Comparison of stress relaxation magnitudes in drained and undrained experiments both with correction of axial strain	308
Figure 6.13: Comparison of normalized stress relaxation magnitudes in drained and undrained experiments, with and without correction of axial strains	310
Figure 6.14: Comparison of volumetric strain response during drained stress relaxation with pore pressure generation during equivalent undrained test	311
Figure 6.15: Grain size distribution curves at the end of drained and undrained stress relaxation tests, with and without correction of axial strain	313

Figure 6.16: Relationship between Hardin's breakage factor and the amount of energy input for stress relaxation tests shown in Fig. 6.15	314
Figure 6.17: 1-day stress relaxation curve for Virginia Beach sand under $\sigma'_3=8000$ kPa	316
Figure 6.18: Effect of deviator stress level on magnitudes of stress relaxation	318
Figure 6.19: (a) Stress-strain, and (b) volume change curves for multiple 1-day stress relaxation test on Virginia Beach sand	320
Figure 6.20: Variation of magnitudes of stress relaxation at different deviator stress levels for multiple 1-day stress relaxation tests with time	321
Figure 6.21: Evolution of grain size distribution curve for 1-day stress relaxation tests	323
Figure 6.22: Relationship between energy input and Hardin's breakage factor for 1-day stress relaxation tests	325
Figure 6.23: (a) Stress-strain, and (b) volume change curves for 2-month creep test on Virginia Beach sand	326
Figure 6.24: Variation of deviator stress in the 2-month stress relaxation test with time.	328
Figure 6.25: Comparison between 1-day creep and 1-day stress relaxation curves	329
Figure 7.1: (a) Stress-strain behavior, and (b) volumetric response for experiments starting with creep and ending with stress relaxation	333

Figure 7.2: (a) Variation of axial and volumetric creep strains during creep phase; (b) variation of deviator stress during stress relaxation phase	335
Figure 7.3: Grain size distribution curve for experiments starting with creep and ending with stress relaxation	337
Figure 7.4: Energy input versus Hardin's breakage factor for experiments starting with creep and ending with stress relaxation	338
Figure 7.5: (a) Stress-strain behavior, and (b) volumetric response for experiments starting with stress relaxation and ending with creep	340
Figure 7.6: (a) Variation of deviator stress during stress relaxation phase, (b) variation of axial, and (c) volumetric creep strains during creep phase	342
Figure 7.7: Grain size distribution curve for experiments starting with stress relaxation and ending with creep	344
Figure 7.8: Energy input versus Hardin's breakage factor for experiments starting with stress relaxation and ending with creep	345
Figure 7.9: (a) Stress-strain behavior, and (b) volumetric response for combined creep-stress relaxation experiments	347
Figure 7.10: Time-dependent phase of combined creep-stress relaxation shown initially from the same points on reference stress-strain curve	350
Figure 7.11: (a) Variation of deviator stress, (b) axial and (c) volumetric creep strains during time dependent phase of combined creep-stress relaxation tests	351
Figure 7.12: (a) Stress-strain behavior, and (b) volumetric response for multiple 1-day creep-stress relaxation experiment	353

Figure 7.13: (a) Variation of axial and volumetric strains during first and second creep phases, and (b) variation of deviator stress during first and second stress relaxation phases for multiple 1-day creep-stress relaxation experiment	355
Figure 7.14: Grain size distribution curve for combined creep-stress relaxation experiments and multiple 1-day creep-stress relaxation test	357
Figure 7.15: Energy input versus Hardin's breakage factor for combined creep-stress relaxation experiments and multiple 1-day creep-stress relaxation test	358
Figure 8.1: (a) Stress-strain behavior, and (b) volumetric response for stress drop- 1- week creep experiments	361
Figure 8.2: Variation of (a) axial, and (b) volumetric strains during creep	362
Figure 8.3: Stress-strain behavior, and (b) volumetric response for multiple stress drop-creep experiments	364
Figure 8.4: Variation of axial and volumetric creep strains during (a) first, (b) second, and (c) third creep phase of multiple stress drop-creep experiments	366
Figure 8.5: Grain size distribution curves for stress drop-creep experiments	369
Figure 8.6: Variation of Hardin's breakage actor with the energy input for stress drop-creep experiments	371
Figure 8.7: (a) Stress-strain behavior, and (b) volumetric response for stress drop- 1- week stress relaxation experiments	373
Figure 8.8: Variation of volume change with time for stress drop- 1- week stress relaxation experiments	374

Figure 8.9: Variation of deviator stress level with creep time for multiple stress drop- 1-week stress relaxation experiments	376
Figure 8.10: Stress-strain behavior, and (b) volumetric response for multiple stress drop-stress relaxation experiments	377
Figure 8.11: Variation of the deviator stress level during (a) first, (b) second, and (c) third stress relaxation phase for multiple stress drop-creep experiments	379
Figure 8.12: Grain size distribution curve for stress drop-stress relaxation experiments	383
Figure 8.13: Variation of Hardin's breakage factor with the energy input for stress drop-stress relaxation experiments	384
Figure 9.1: Grain size distribution curves for isotropic compression tests	386
Figure 9.2: Hardin's breakage factor versus energy input for isotropic compression tests	387
Figure 9.3: Hardin's breakage factor versus confining pressure for isotropic compression tests	388
Figure 9.4: Grain size distribution curves for triaxial compression tests under different confining pressures	390
Figure 9.5: Hardin's breakage factor versus energy input for triaxial compression tests under different confining pressures	391
Figure 9.6: Hardin's breakage factor versus energy input for triaxial compression tests under confining pressure of 8000 kPa	393
Figure 9.7: Grain size distribution curves for creep experiments under confining pressure of 8000 kPa	395
Figure 9.8: Grain size distribution curves for creep experiments under confining pressure of 250 kPa	396

Figure 9.9: Hardin's breakage factor versus energy input for creep experiments under confining pressure of 250 and 8000 kPa	397
Figure 9.10: Grain size distribution curves for creep experiments under confining pressure of 8000 kPa	398
Figure 9.11: Hardin's breakage factor versus energy input for creep experiments under confining pressure of 8000 kPa	399
Figure 9.12: Hardin's breakage factor versus energy input for creep-relaxation experiments under confining pressure of 8000 kPa	401

List of Tables

Table 2.1: Effect of different parameters on viscous behavior of geomaterial	55
Table 2.2: Comparison of deviator stress of various types of sand under dry and saturated conditions	111
Table 3.1: Properties of Virginia Beach sand	158
Table 4.1: Initial stiffnesses, maximum friction angles, and axial and volumetric strains at failure	225
Table 4.2: Energy input and Hardin's breakage factor for specimens aged under isotropic stress state	228
Table 4.3: Energy input and Hardin's breakage factor for specimens aged under K_0 stress states	237
Table 5.1: Change in void ratio, axial and volumetric strains at the end of isotropic compression	268
Table 7.1: Stress-strain points and energy input at the beginning and end of time-dependent phases	348
Table 8.1: Details of multiple stress drop-creep experiments	367
Table 8.2: Hardin's breakage factor and energy input for stress drop-stress relaxation experiments	383

Acknowledgments

I owe my deepest gratitude to my supervisor, Professor Poul Lade, whose encouragement, guidance and support from the very beginning to the end made accomplishment of this study in the best way possible.

I would like to express my sincere regards to my beloved wife, Golnaz, who joined me in a tough time with her genuine supports and without any expectations.

I also thank Nina Maria Rodriguez for proofreading my dissertation and all of those who helped me in any respect during the completion of this study.

1. Introduction

This experimental study is dedicated to the investigation and exploration of time effects in relation to crushing in granular materials, and to proposing a mechanism that throws further light on these phenomena. Time effects considered in this study are basically defined as strain rate effects, creep, stress relaxation and structuration or aging.

1.1. Time Effects

1.1.1. Strain Rate Effects

Shearing strain rate applied to soil specimens has been shown to have an influence on soil behavior specifically in undrained cases where even small tendencies of volume change result in generation of high pore pressures. Fig. 1.1 schematically shows that three different constant shearing strain rates produce different stress-strain curves for clays.

It has been observed that the friction angle, maximum deviator stress and axial strain-to-failure are the most significant parameters that may vary with strain rate.

1.1.2. Creep

When a soil element is loaded to a certain stress level and then the stress level is kept constant, the deformation which occurs with time is considered as creep.

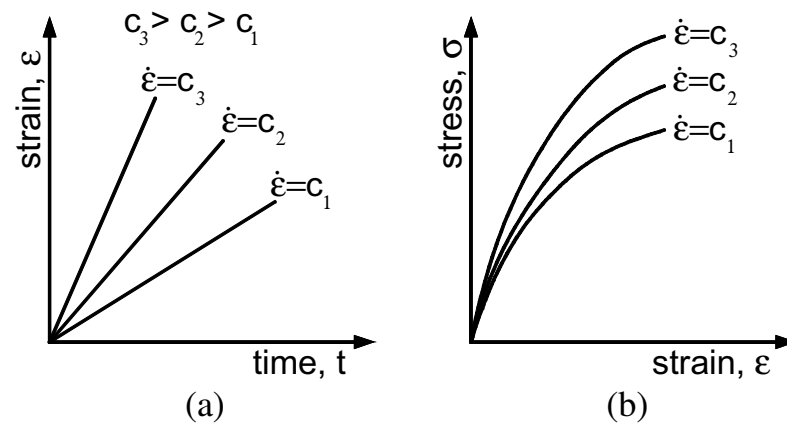


Figure 1.1. Schematic strain rate effect on stress-strain behavior for clays.

A schematic creep effect is shown in Figure 1.2(a). As seen, the specimen is loaded to point *A* where the stress level is kept constant. Fig. 1.2(b) and Fig. 1.2(c) illustrate the schematic variation of stress and strain with respect to time during creep, respectively. From point *A* to *B*, the stress is constant, while the strain increases at a slowing rate with time.

Creep tests in a triaxial apparatus can be performed in drained or undrained conditions. The difference between these conditions is that changes of strain in drained creep tests are purely correlated to creep phenomenon, while in the undrained case due to changes in pore pressure and subsequently effective stress, measured strains are combinations of both plastic and creep strains. It is noted that constant stress creep tests performed in a triaxial apparatus may exhibit three stages of primary, secondary and tertiary (acceleration) creep. Fig. 1.3(a) demonstrates these three stages on a strain-time diagram. In the primary stage, strain rate decreases with time, while it is constant in the second stage. Strain rate starts increasing in the tertiary stage and the specimen usually ends in creep rupture (Fig. 1.3-b).

However, there is some confusion between these creep stages and consolidation stages in oedometer test since the diagram of strain-time from creep tests is similar to strain-log(time) resulting from consolidation tests as shown in Fig. 1.4. Detailed comparison and differences between these two has been presented by Augustesen et al. (2004). However, by comparison of Fig. 1.3(b) and Fig. 1.4(b), it is observed that the

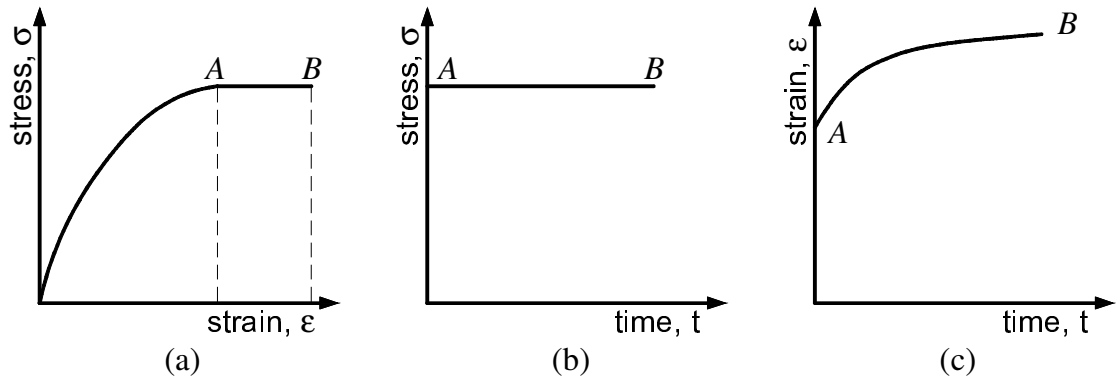


Figure 1.2. Schematic creep effect.

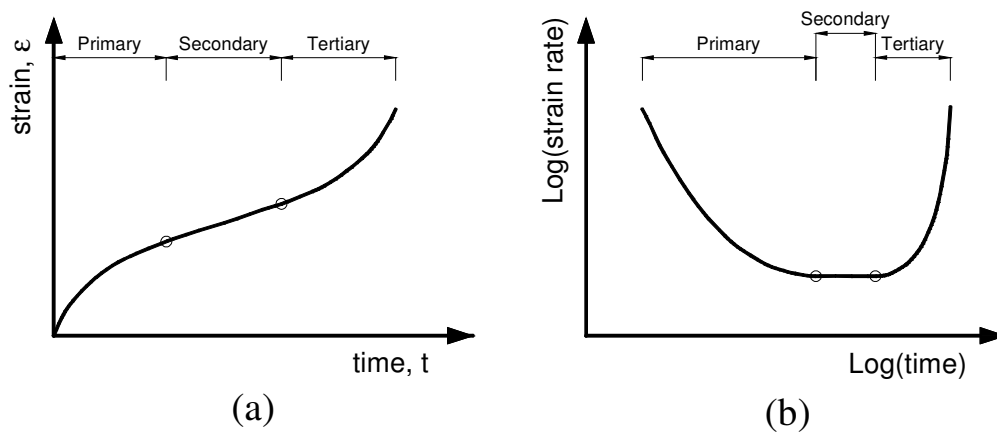


Figure 1.3. Typical result of a constant stress creep test performed in a triaxial apparatus: (a) strain-time, (b) log (strain rate)-log(time).

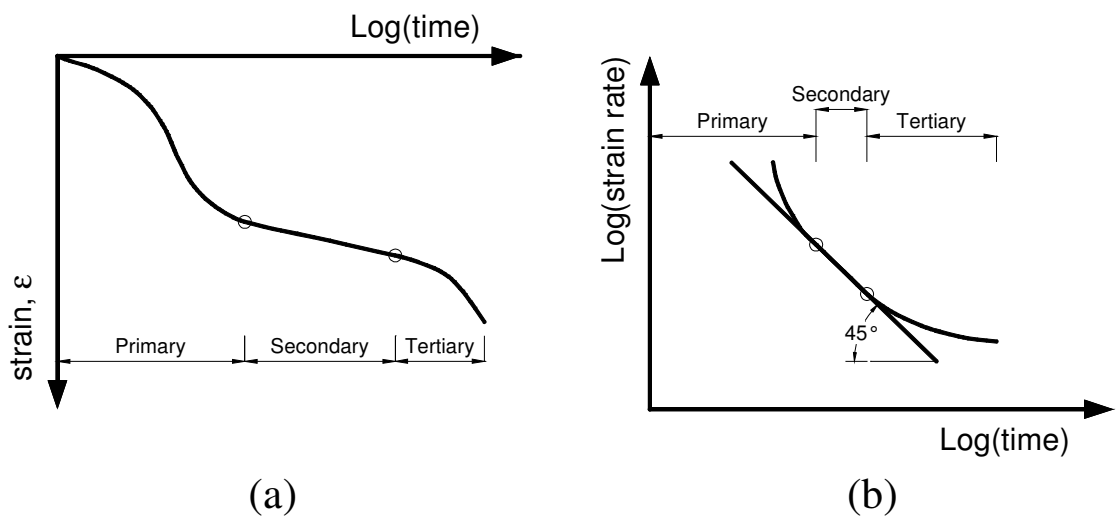


Figure 1.4. Typical result of a consolidation test performed in an oedometer apparatus: (a) strain-log(time), (b) log (strain rate)-log(time).

logarithm of strain rate in creep test decreases first, becomes constant and then increases, whereas strain rate in a consolidation test keeps decreasing the entire time.

1.1.3. Stress Relaxation

By loading a soil element to a specific stress level and keeping the applied strain constant, changes in stress value is referred to as stress relaxation (Fig. 1.5(a)). The variation of strain and stress with time during a stress relaxation test are shown in Fig. 1.5(b) and Fig. 1.5(c), respectively. As seen, during stress relaxation, strain is kept constant, whereas the stress level decreases at a slowing rate. This may be characterized with good approximation as a linear relation on a stress-log(time) diagram.

1.1.4. Structuration or Aging

Structuration is a complicated phenomenon which is explained as gaining strength with time. This extra strength needs to be overcome in order to have further deformation. Many researchers have proposed different ideas as the mechanism behind structuration; however, no clear conclusion has been drawn as will be discussed later. The structuration phenomenon is schematically shown in Fig. 1.6 where the specimen has been loaded to *A*, undergone creep to *B* and been reloaded. The stress-strain curve may merge the original curve at *C* without considering structuration. However, an extra resistance is observed and the curve reaches point *D*. Once this extra gained strength (during creep) is overcome, the curve may join the original curve to reach point *E*, or it may exhibit a permanent off-set as loading continues.

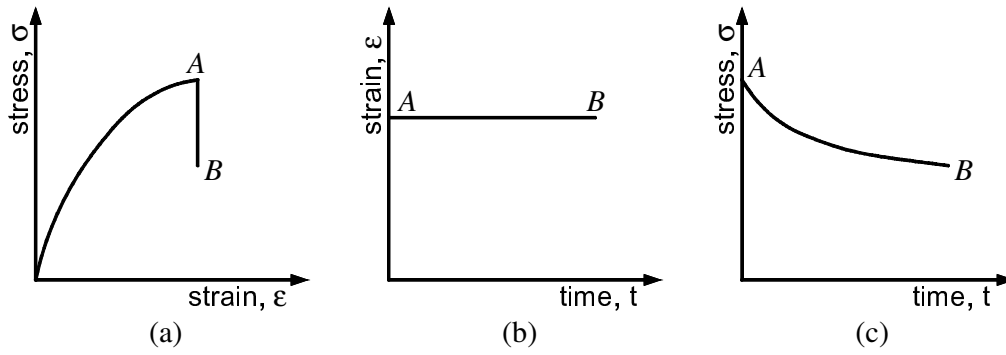


Figure 1.5. Schematic stress relaxation effect.

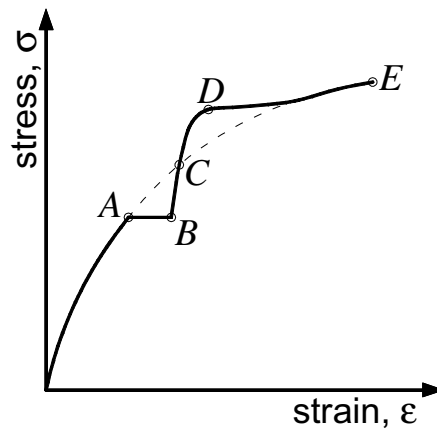


Figure 1.6. Structuration effect during creep.

1.2. Perspective of the Research

The recent studies of time effects suggest that one of the important issues responsible for the observed time-dependent behavior in granular materials may be crushing of particles. Although particle crushing has been investigated by many researchers individually, this issue has not been considered in connection with time effects. Since studies of time-dependent behavior of granular materials have been limited to low confining pressures where no significant breakage is observed in regular sands, some studies have been conducted at low confining pressures on softer materials such as crushed coral sand to illustrate the relation between particle crushing and time effects. However, particle crushing has not been quantitatively explored due to the friability of such materials. It has also been postulated that static fatigue is of the root of breakage of particles and consequently time effects. This phenomenon may be greatly influenced by environmental parameters such as the presence of water.

Accordingly, in a comprehensive experimental program, several series of time-dependent (creep, stress relaxation, etc) triaxial compression tests on a quartz (Virginia Beach) sand under a wide range of confining pressures have been conducted. In addition, a series of single particle strength tests on glass beads have been performed to broaden the existing knowledge of time effects in granular materials. This requires a complete investigation on the previous works by other researchers. In Chapter 2, previous investigations on the time-dependent behavior of granular materials is presented in different categories of: effects of aging time, experimental studies of creep, stress

relaxation and rate dependency, and proposed mechanisms of time effects. In addition, previous studies of high pressure testing and particle crushing of geomaterials are illustrated for one-dimensional, triaxial and other experiments. The mechanism of static fatigue is also discussed in detail to show crucial parameters that influence the progress of this phenomenon. Studies on impact of presence of water as an important factor on behavior of geomaterials are presented. Moreover, a brief description of empirical, rheological and general constitutive models incorporating time-dependent behavior of materials together with constitutive models considering the effects of particle crushing is addressed.

Chapter 3 represents a complete description of the experimental program that includes introducing materials tested, apparatuses used, specimen preparation and measurements, details of experiments, corrections made, and methods of sieve analyses utilized. The remaining chapters of this study are dedicated to the explanation of individual series of experiments performed in the experimental program. In this regard, isotropic and K_0 consolidated drained triaxial tests, and single glass bead experiments are described in Chapter 4 where effects of confining pressure, initial shearing strain rate, and isotropic and K_0 aging are studied, and results and sieve analyses are discussed. In the next chapter, creep experiments are explained and effects of initial shearing strain rate and soil gradation on the consequent creep deformation are investigated. Then, along with presenting 1-day creep curves and long term creep behavior, sieve analyses results are exhibited. A similar outline is used to explain stress relaxation experiments in Chapter 6. This is followed by presentation of creep-stress relaxation experiments and sieve

analyses data in Chapter 7. Included in this chapter are consecutive and concurrent creep-stress relaxation experiments performed on Virginia Beach sand. The last series of experiments are stress drop-creep and stress drop-stress relaxation tests which are fully explained in Chapter 8. The general sieve analyses is elucidated in Chapter 9 where the variation of particle crushing with respect to energy input during isotropic compression, triaxial compression and creep experiments are compared. Finally, a summary of the presented data and conclusions on the performed analyses are drawn into attention in Chapter 10. The appendices contain the digitized data from all experiments and sieve analyses data performed for this study.

2. Previous Investigations

Review of previous studies of time effects in sands provides an insight on the design of the experimental program, as well as the way the results should be interpreted. In this regard, different aspects involved in the current research have been studied and categorized in the following subsections: (1) time-dependent behavior of granular material, (2) high pressure testing and particle crushing in sands, (3) static fatigue, (4) effect of water on geomaterial properties, and (5) constitutive models incorporating time effects or particle crushing. Each part is discussed and depending on its relevance to the research, the related studies in the literature are explained in detail.

2.1. Time-Dependent Behavior of Granular Material

Time-dependent soil behavior has been widely reported by many researchers in the literature. This phenomenon may result in changing soil properties over time (often called aging or structuration), and it includes creep, relaxation and rate dependency. For example, it has been shown that freshly deposited or densified sands gain stiffness, strength or cone penetration resistance over time (Mitchell and Solymar, 1984; Charlie et al., 1992; Thomann and Hryciw, 1992). Also, a hypothesis has been proposed that with time natural sands can develop a structure which is similar to that of sensitive clays. In other words, in case of disturbance, sands may lose a significant portion of their strength and with time they gain strength back. Likewise, in the case of driven and jacked piles, not bored piles, it has been commonly observed (York et al., 1994; Chow et al., 1997, 1998; Bowman, 2002; Bowman and Soga, 2005) that the bearing capacity continues to

increase, even months after installation. This phenomenon is referred to as pile “set up.” It was reported that the increase is caused by an increase in the lateral resistance of the pile rather than by its tip resistance. Augustesen et al. (2004) have extensively reviewed the investigations presented in the literature concerning time effects in soils and this article will be referred to for more information. Moreover, it is emphasized that the word “time” is connected to processes in which the soil skeleton exhibits an apparent viscous behavior; thus, consolidation cannot be considered in this content since it involves dissipation of pore water pressure as well. It also does not include dynamic effects in which inertial forces are incorporated. To have a better understanding of time effects, related studies are presented.

2.1.1. Effects of Aging Time on Behavior of Granular Material

Daramola (1980) studied the effect of consolidation age on the stiffness of Ham River sand. He carried out four drained triaxial tests at the confining pressure of 400 kPa. The first specimen was sheared right after consolidation; however, three other specimens were consolidated for 10, 30 and 152 days before they were sheared. The stress-strain behavior is illustrated in Fig. 2.1 showing that as the consolidation time became longer, a stiffer response was observed. To throw further light on this phenomenon, Daramola (1980) plotted the ratio of the secant modulus (calculated from points of 10% and 50% of the maximum stress difference) of the aged specimens to fresh specimen with respect to age of consolidation as shown in Fig. 2.2. It can be observed that almost every log cycle of time shows 50% increase in the secant modulus. However, no mechanism was suggested to explain this phenomenon.

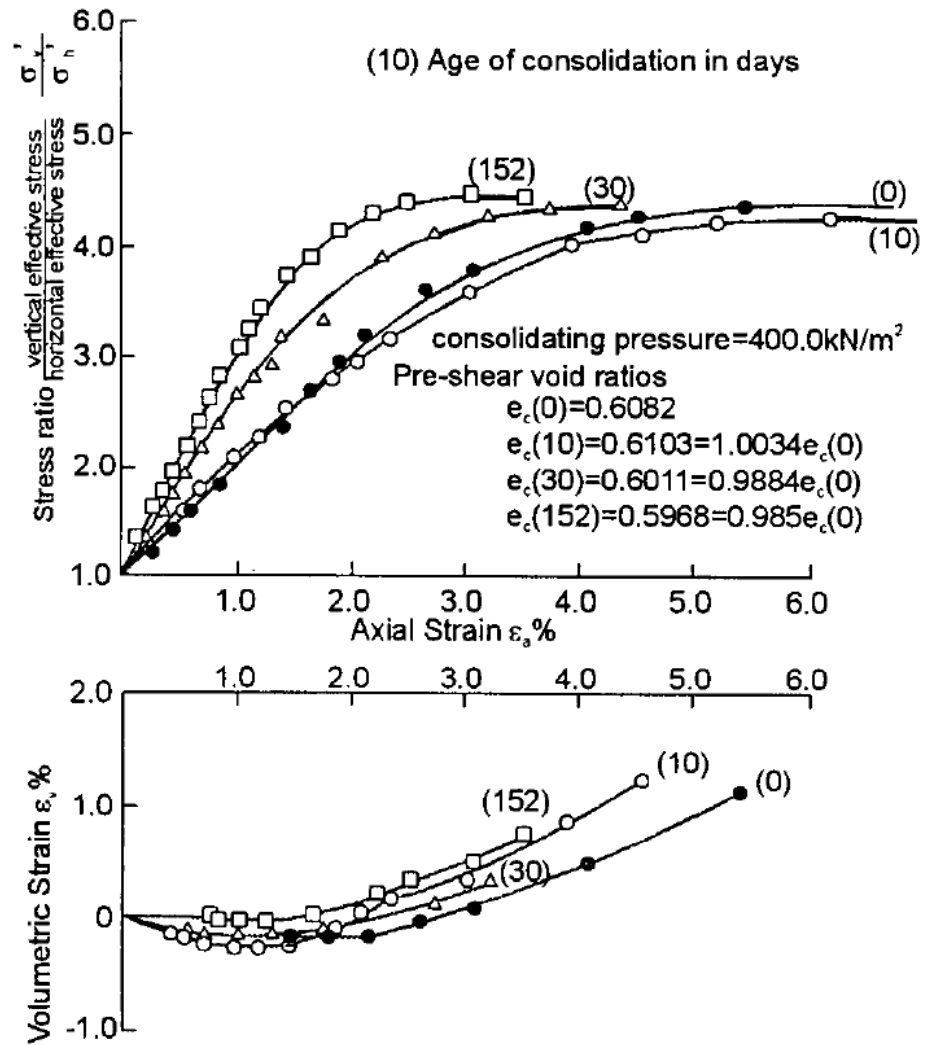


Figure 2.1. Effect of consolidation time on stress-strain behavior of Ham River sand

(after Daramola 1980).

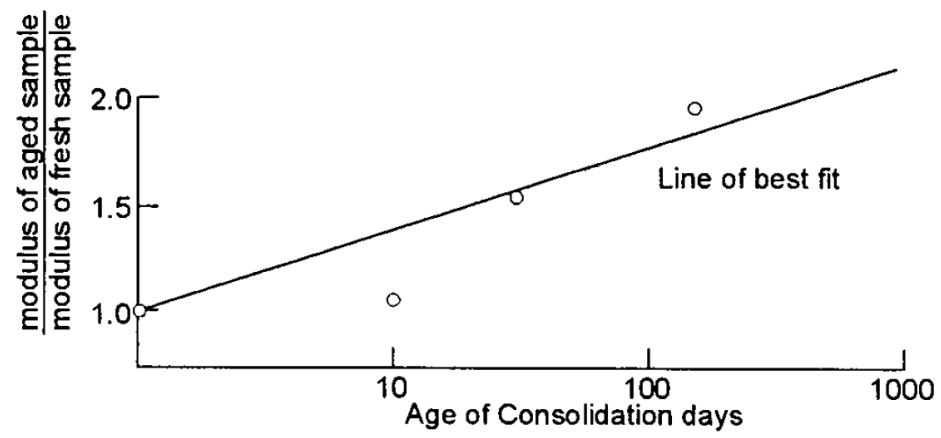


Figure 2.2. Change in stiffness versus consolidation time (after Daramola 1980).

Similarly, Joshi et al. (1995) used Beaufort Sea sand to study the effect of aging on the penetration resistance of a 10 mm diameter penetrometer. The specimens were made in cylindrical PVC cells, held under vertical pressure of 100 kPa and aged for 2 years. As it can be seen in Fig. 2.3, the penetration resistance kept increasing over the course of two years.

On the other hand, Al-Sanad and Ismael (1996) by performing direct shear tests on well graded silty sand with 20% calcium carbonate indicated that the friction angle of the specimens increased with time as they aged under vertical stress. In their research, specimens were built at a relative density of 60% and then aged under the vertical stress of 2 kPa up to 6 months. The following equation was suggested to predict the increase in friction angle with aging time:

$$\phi_t = \phi_i + \frac{3.81t}{2.82 + t} \quad (2-1)$$

where ϕ_i is the friction angle for specimens without aging and t is time in months.

Furthermore, Lagioia (1998) studied the effect of apparent preconsolidation of carbonate sand specimens in confined conditions. Similar to the behavior of normally consolidated clays as explained by Bjerrum (1967), Lagioia (1998) observed that when a specimen creeps at a constant effective stress, upon continuation of loading, it shows an extra strength which needs to be overcome. Fig. 2.4 demonstrates an example of this work in which the specimen was loaded at the load rate of 100 kPa/hr to point *I*, crept at

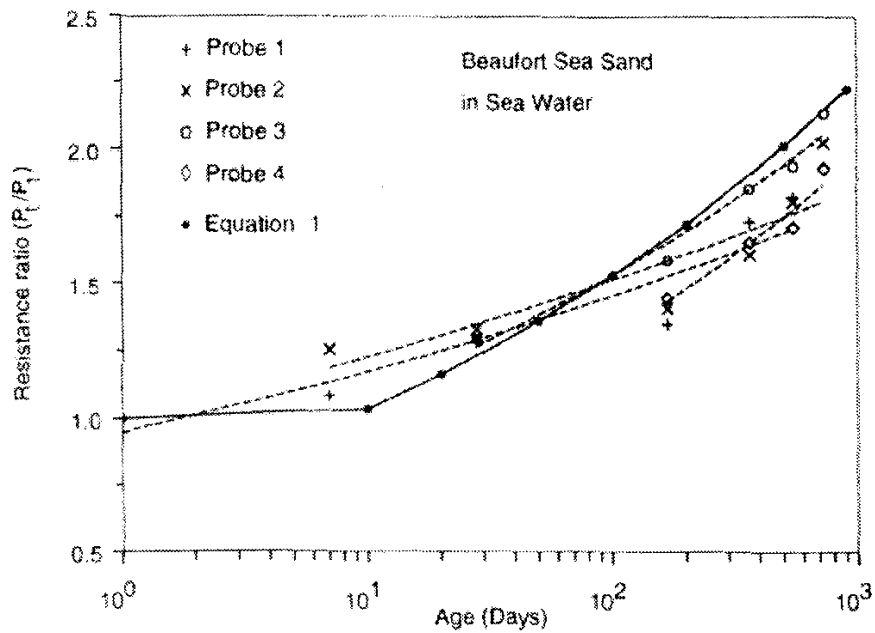


Figure 2.3. Change in penetration resistance versus aging time (after Joshi et al. 1995).

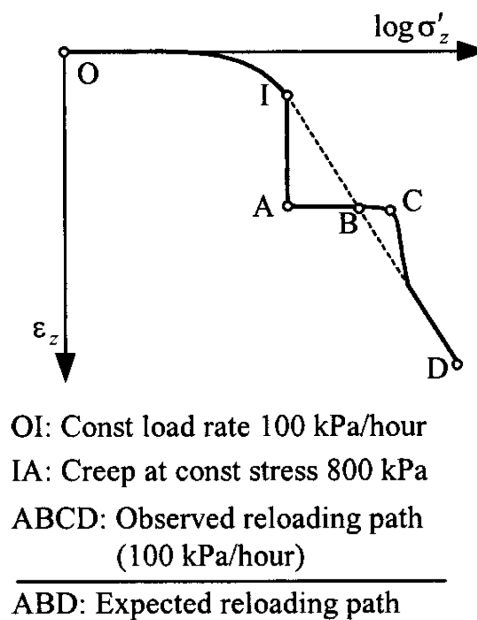


Figure 2.4. Structuration effect due to creep (after Lagioia 1998).

800 kPa to point *A* for a day and sheared to point *D*. If structuration effects had not been present, the stress-strain curve should have rejoined the compression curve at *B*. However, an extra resistance was observed and the curve reached point *C*. After rising to this extra gained strength, it joined back to the original curve and reached point *D*. It was suggested that some complex interparticle cementation was the reason for the observed phenomenon.

Komornik et al. (1972) reported a continuous settlement of piles installed through soft soils on a partially cemented sand for many months after the structural load had been applied. Moreover, Hannink (1994) monitored the settlement of 10 buildings ranging from 12 to 41 stories in Rotterdam, The Netherlands for time periods varying from 2 to 30 years. He observed a settlement of about 130 mm for a period of 19 years in the case of a 110 m high rise, a medical faculty, founded on a group of 18 m piles installed on a sandy soil overlaying overconsolidated loam. Only 35% of this settlement occurred after the construction. Sweeney and Lambson (1991) expressed that the long term settlements of storage tanks may greatly exceed the settlement associated with the initial filling settlement. They simulated the long term behavior of the foundation of storage tanks with a one dimensional drained cyclic loading problem during which they observed settlement growth with number of cycles. The laboratory results were in agreement with the observed field data. However, they did not explain the mechanism behind such behavior and they mentioned that this time-dependent settlement is the major uncertainty in granular materials and specifically for dense sands.

Mitchell and Solymar (1984) considered the strength gain in freshly deposited or densified sands involved with the Jebba Hydroelectric dam project on the Niger River in Nigeria. The alluvial sand base required in-place densification so that liquefaction could be prevented and settlements could be minimized. Consequently, the potential for cracking of the overlying clay core and clay blanket was minimized. Two densification methods of vibrocompaction for the upper 25 m and blasting for levels below 25 m and up to 40 m of the foundation of the dam were used. It was reported that the densification methods initially (for the first few days) reduced the penetration resistance as the soil was disturbed during this ground treatment. However, after some time, the soil started to gain strength to a point higher than the original value. It was noted that this strength gain was not due to dissipation of the generated pore pressure since the soil was permeable enough to dissipate extra pore pressures within a few minutes of densification.

It was mentioned that the formation of silica gel films at the grain contact points, as a cement agent, would be the best explanation for this unusual phenomenon. This idea stemmed from a research project by Denisov and Reltov (1961) who reported that the displacement force of a sand particle from a silica plate doubled after being exposed to air for 20 hrs and tripled after 14 days submerged in water. As another possible mechanism, it was also suggested that the compressibility of micro gaseous bubbles, coming from the explosion, may have caused this phenomenon. However, similar initial reductions and strength gains were reported in connection with vibrocompaction and hydraulic fill methods in which no explosion occurred. This study was followed by Dowding and Hryciw (1986) who performed a series of laboratory blast-densification

tests on saturated clean fine silica Evanston beach sand. They measured the effectiveness of densification in terms of surface settlements and increase in cone-penetration resistance. The cone penetration resistance increased over a period of 1-15 days after blast densification, while generated pore pressures had been totally dissipated in a minute. By comparing the blast densification results with controlled tests with no blasting which showed a slight increase in cone resistance, they proposed that dissipation of gasses which had been dissolved into water due to explosion may be the cause of strength increase with time.

Mesri et al. (1990) analyzed a comprehensive set of data on strength gain in clean sands and concluded that aging phenomena are related to secondary compression. They related the increase in stiffness and effective horizontal stress during aging to “enhanced macrointerlocking of sand grains and microinterlocking of grain surface roughness” due to continual rearrangement of grains. They also found the hypothesis of cementing-bond between particles somewhat irrational to be the main cause of aging. Their conclusion was in agreement with Schmertmann (1987) who presented a discussion on Mitchell and Solymar (1984) and claimed that time-dependent gain in horizontal stress and purely frictional increase in stiffness and strength with time due to grain reorientations during secondary compression is the reason for increase in cone penetration. Later, Schmertmann (1991) postulated that in addition to the aforementioned ideas, arching effects due to non-uniform distribution of stresses in granular materials may contribute to observations of some of the measured increases in penetration resistance with time. Non-uniformity of stress is explained based on the concept of load chains stated by Drescher

and De Josselin De Jong (1972), Kuhn (1987) and Santamarina (2003), suggesting the existence of stiffer zones that transmit higher stresses in comparison to weaker regions in granular media.

Crawford and Morrison (1996) presented case histories illustrating long term settlements of structures built in the Fraser River delta in Canada. The soils in the delta were found to be more than 200 m thick over bedrock. Preloading is the major method used to improve the soil properties and to reduce possible settlements after construction of structures. The most detailed case history and data belonged to construction and operation of a 2-staged waste water treatment plant. Before building the primary treatment plant a 6 m layer of sand was dredged from the river and placed above the construction area for 1 year. The thickness was then increased to 9.1 m and the sand layer stayed for 9 months. Fig. 2.5 shows the variation of applied stress and measured settlement with respect to the logarithm of time during the two preloading steps, construction and operation up to 22 years for the primary treatment plant.

As seen, the settlement-log(time) became linear with the slope of 0.42 m/cycle after approximately 20 days of the first step of preloading. Moreover, an analogous observation was made after construction of the structure was ended, where the rate of settlement became 0.25 m/cycle and continued for the next 19 years.

On the other hand, to amend the properties of the existing soil in the construction site of the secondary treatment plant a similar preloading method was used. A 13 m layer

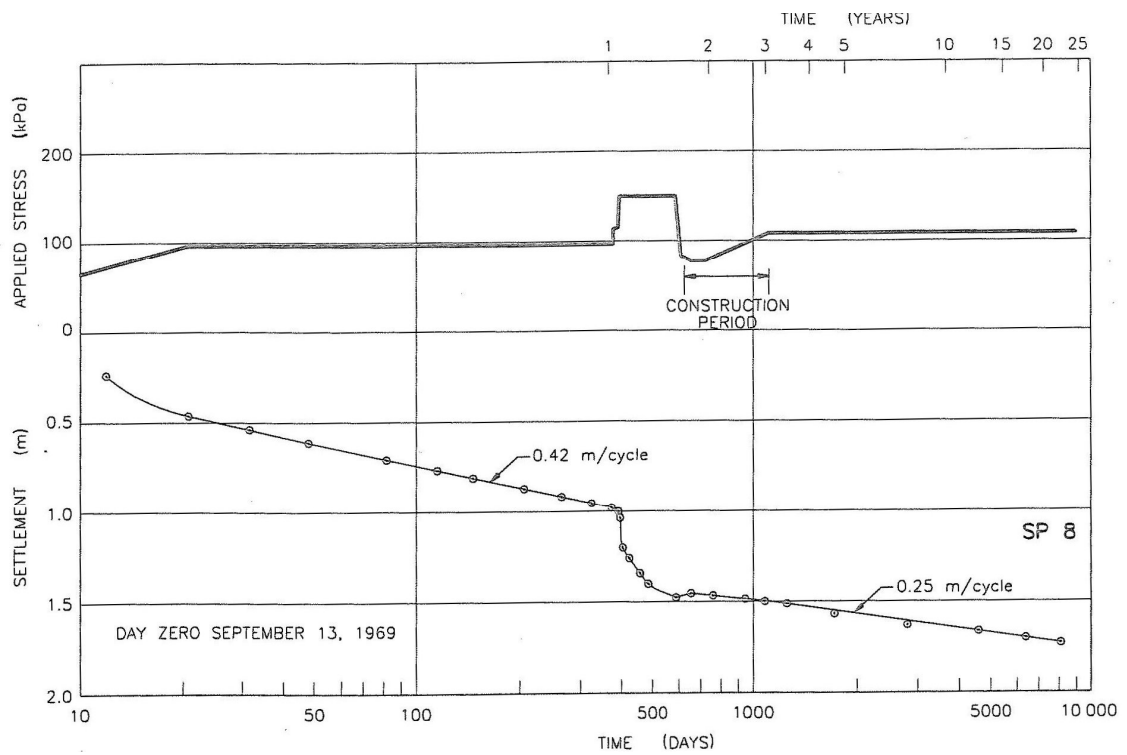


Figure 2.5. Variation of applied stress and settlement with logarithm of time for primary treatment plant (after Crawford and Morrison 1996).

of sand was built by dredging approximately 540000 m³ sand from the Fraser River. This embankment was remained for 250 days and construction of the structure started afterwards.

The variation of settlement and applied stress with the logarithm of time is exhibited in Fig. 2.6 during preloading step and preconstruction excavation. It is observed that a short time after preloading was finished the settlement curve showed a linear variation with logarithm of time (0.75 m/cycle). Crawford and Morrison (1996) stated that this behavior is similar to the secondary phase of a consolidation process. However, no explanation was made on why sand exhibits such a behavior.

Baxter and Mitchell (2004) designed a series of experiments under controlled conditions to investigate mechanisms that are responsible for aging effects in sands. Each test consisted of a cylindrical specimen with diameter of 14.5 cm and height of 16.5 cm which aged for 118 days under a vertical stress of 100 kPa. In their tests, changes in small strain shear modulus, electrical conductivity, minicone penetration resistance, and chemical and mineralogical properties within specimens were measured. Two different sands at two relative densities of 40% and 80% were chosen. They were tested at temperatures of either 25 or 40°C and in three different pore fluids of distilled water, ethylene glycol and CO₂ saturated water. The latter was used to model the condition that occurs after blasting densification. Results indicated that the electrical conductivity increased in specimens saturated with distilled water and ethylene glycol, whereas a decrease was observed in specimens saturated with carbon dioxide-water. In the former,

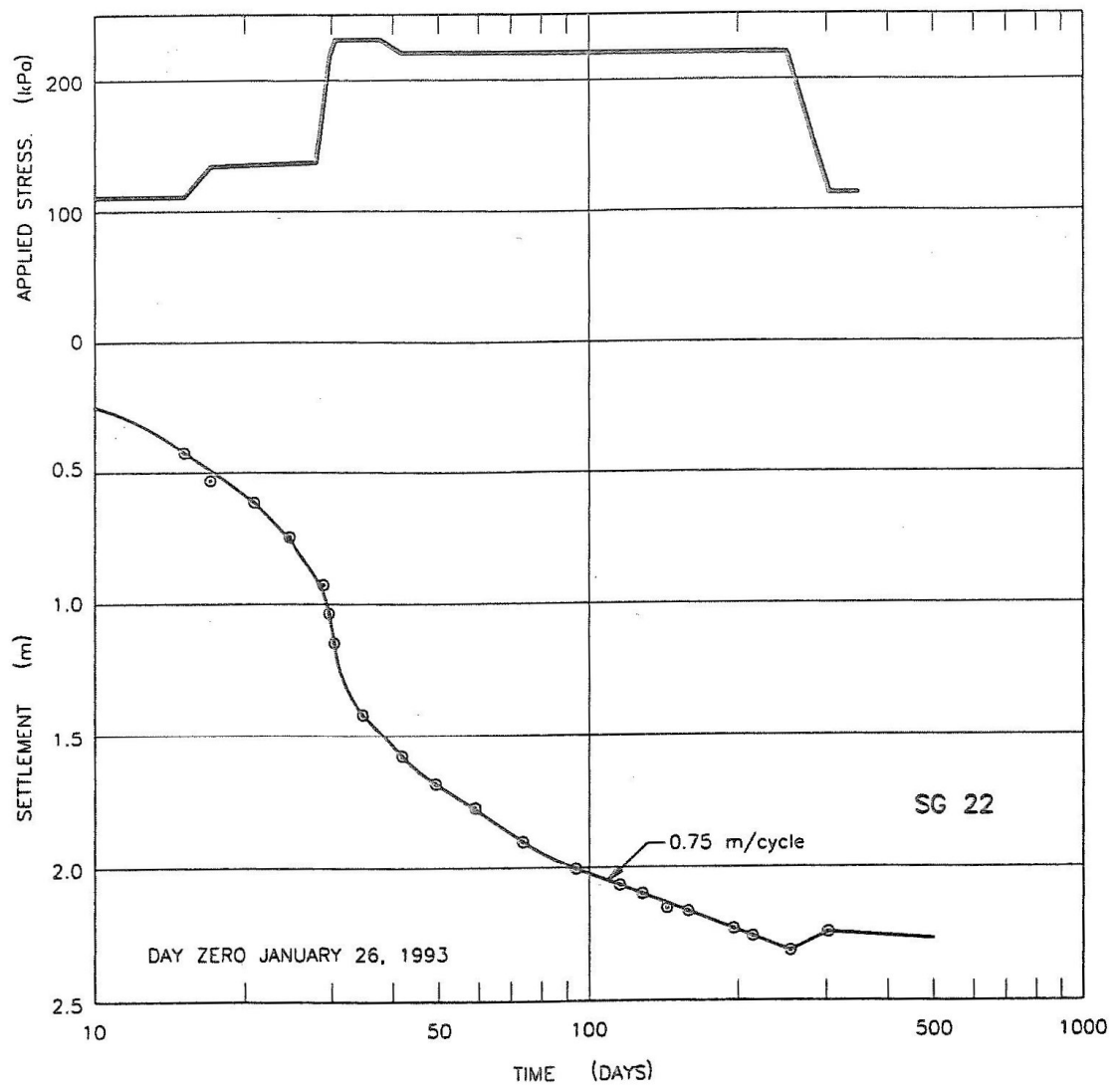


Figure 2.6. Variation of applied stress and settlement with logarithm of time for second treatment plant (after Crawford and Morrison 1996).

this observation suggests a persistent dissolution of minerals into the pore liquid. However, in the latter, it indicates some precipitation of carbonate material from the pore liquid on the particles during the tests. Precipitation on or between contacts was also checked by means of scanning electron microscopy and no evidence was detected in any tests. Moreover, a majority of the specimens experienced a slight increase in the measured small strain shear modulus, while surprisingly no increase was observed for minicone penetration resistance. According to the recorded results, Baxter and Mitchell (2004) stated that it not probable that that dissolution and precipitation cause the observed increase in the penetration resistance in field after blast densification. They concluded that simplifications and idealizations that are considered in experimental studies in comparison to the nature avoid the observation of aging phenomena in laboratory studies.

2.1.2. Experimental Studies of Creep in Granular Media

Murayama et al. (1984) investigated the creep behavior of Toyoura sand by performing a series of triaxial compression creep tests under low confining pressures. It was noticed that there was a critical deviator stress beyond which specimens may fail if they undergo creep. The effect of confining pressure on this critical deviator stress was studied and no dependency was captured. However, the confining pressures employed were in the range of 0.9 to 1.7 kg/cm². Therefore, a considerable time effect could not be expected. They then utilized a rheological model previously proposed by Murayama (1983) to model the observed creep behavior. It was shown that this complicated model, consisting of many springs, dashpots and sliders, can precisely simulate the creep

behavior of sands. According to this model, the creep behavior can be uniquely expressed as a function of the ratio of the stress difference to the mean effective stress. Furthermore, time to creep failure can be estimated from the minimum creep strain rate. However, these relations are found difficult to apply. A discussion on rheological models is given in Section 2.5.2.

Mejia et al. (1988) performed one dimensional creep tests at low confining pressures on loose Ottawa and Brenda Mine Tailing sands. They reported small values of creep strain as a result of sliding and rolling of the grains while the vertical effective stress was not high enough to break the soil particles. It was also noted that creep strains, after a high initial strain rate in the first few seconds, merge to a linear relation on the diagram of strain versus the logarithm of time.

Isotropic creep tests were performed by Colliat-Dangus et al. (1988) on Hostun Silica sand and calcareous sand at low and high pressures. It was reported that creep in sand is a continuous phenomenon with a decreasing rate. The essence of this study is shown in Fig. 2.7 where volumetric creep is plotted versus the creep confining pressure. They specified a “creep stress” above which creep strains are significant, and it is about 0.8 MPa and 5-6 MPa for calcareous sand and Hostun sand, respectively. Similar to Mejia et al. (1988), they reported a linear relationship between creep strain and the logarithm of time for both low and high confining pressures. Furthermore, sieve analyses of the specimens after the tests clearly exhibited increasing effect of time on the amount of particle crushing.

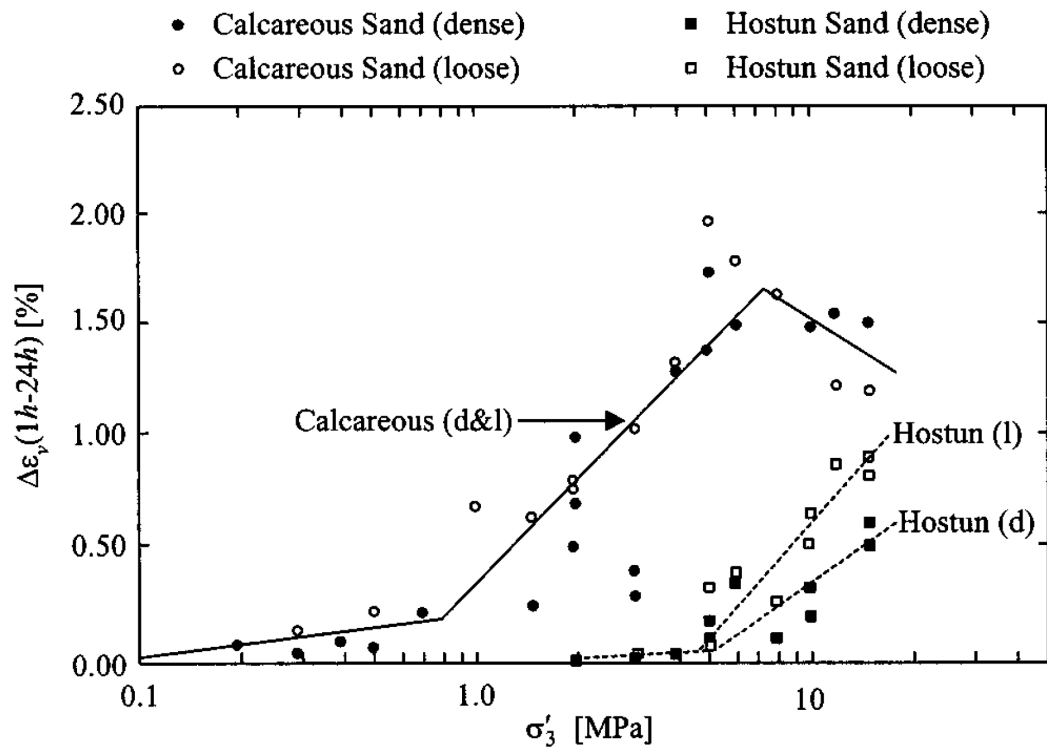


Figure 2.7. Variation of volumetric creep strain versus confining pressure (after Colliat-Dangus et al. 1988).

A series of centrifuge pile creep tests on uniform angular fine silica sand with mean grain diameter of 0.2 mm, together with some one-dimensional creep tests, were performed by Leung et al. (1996). During pile penetration, they observed that the penetration resistance consisted of 41% from the sides and 59% from the tip and it increased with depth. A constant load was held for 45,000 seconds and the settlement of the pile was recorded with time. It was seen that once the load was applied, the pile quickly settled 0.6 mm and the settlement continued gradually afterwards. The rate of settlement decreased on the settlement-time diagram. This suggested that at some time settlement would stop. However, as it can be seen in Fig. 2.8, the pile settled linearly with the logarithm of time. In other words, the settlement did not stop and it continued with time. They also studied the effects of saturation, density and pile shape on creep behavior of piles in sand and it was stated that creep behavior in sand is not affected by water through excess pore pressure dissipation, water-induced chemical reaction, viscosity or other moisture related effects.

Moreover, the creep behavior of granular materials was shown to be dependent on the density of the sand; the looser the sand, the greater the amount of creep. The studies also showed that the creep behavior did not undergo a significant change due to pile shape as long as the cross-sectional area remained the same. Unlike pile penetration during which the ground surface heaves, the ground surface was settling during creep. This implies that, creep behavior is connected to contraction and not dilation. During the creep, the resistance at the lower part of the pile and the tip decreased with time. This was

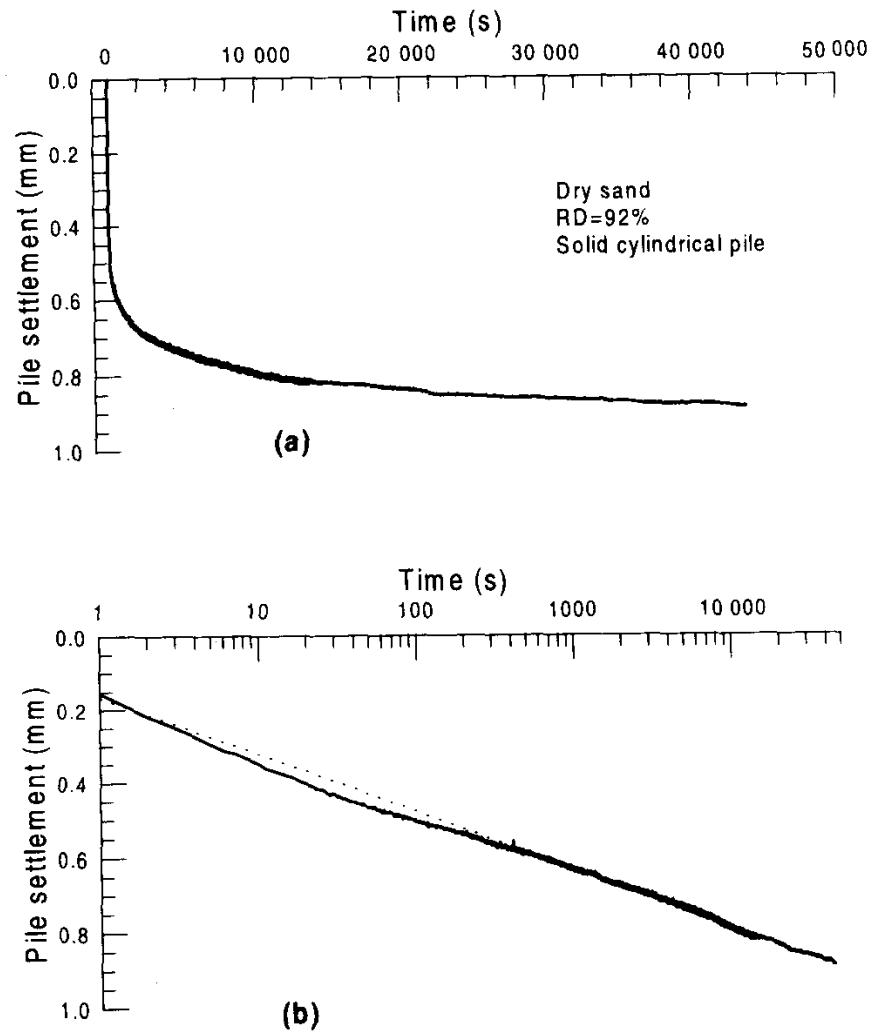


Figure 2.8. Pile creep settlement versus (a) time, and (b) logarithm of time (after Leung et al. 1996).

accompanied by an increase in the side resistance. This may be explained by a stress relaxation phenomenon around the pile tip. To support the aforementioned findings regarding creep behavior in sand, they carried out a series of one-dimensional creep compression tests. Kuhn and Mitchell (1993) made the same observation and claimed that water does not change the sliding behavior between soil grains. Similarly, it was seen that there is no difference between dry and saturated creep behavior of sand in one-dimensional compression tests. Analogous to the creep behavior in pile tests, an almost linear relation between settlement and the logarithm of time was obtained as shown in Fig. 2.9.

The soil specimens were examined before and after running each test and it was seen that asperities (protrusions) of particles had been broken off, and the uniform soil had transformed to a mixture of more rounded particles, smaller particles and fines. Some smooth breakage surfaces were also detected on larger grains when they were observed under a microscope. The authors believed that particle breakage increases with the time of loading and it “is not an instantaneous or quick process.” They claimed that the settlement of piles in granular material is due to progressive particle breakage and not sliding; therefore, inter-particle contact forces play a much more important role than the interlocking of particles in the creep behavior of pile tests.

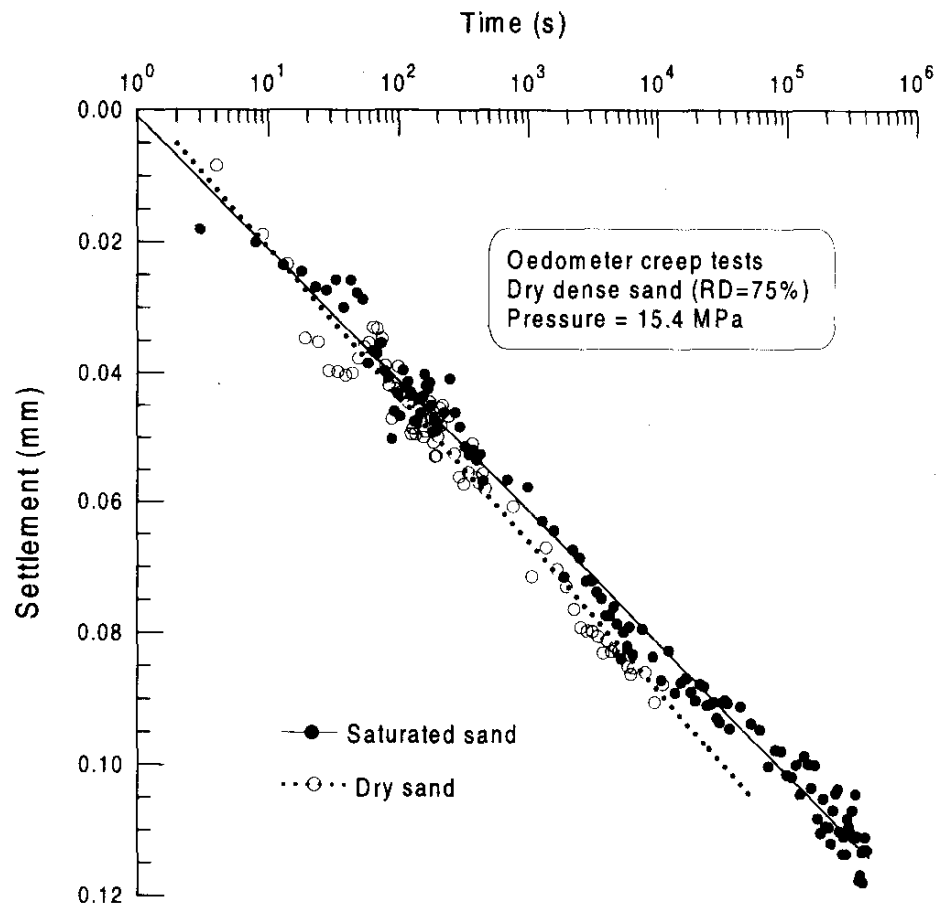


Figure 2.9. Creep settlement versus logarithm of time for dry and saturated specimens (after Leung et al. 1996).

Drained creep behavior of Antelope Valley sand was experimentally studied by Lade and Liu (1998) using a triaxial testing apparatus at a constant controlled temperature. The following issues were investigated in the testing program: (a) stress-strain behavior at different constant confining pressures and constant strain rates (b) effect of various strain rates (c) creep behavior at different stress levels from different paths at constant confining pressure and (d) creep behavior at the same stress levels from different stress paths. According to their test results, it was found that during creep at a constant stress level, the yield surface increased in size and moved out with respect to the stress origin. This was based on the observation of elastic strains when further loading was applied after the creep process was interrupted after a certain amount of time. In the creep experiments, they observed an almost linear relation between the axial and volumetric strains with the logarithm of elapsed creep time. Moreover, to throw further light on the direction of the potential surface and after deducting elastic components from the total measured strain increments, plastic and creep strain increment vectors were superimposed on a triaxial plane together with applied stress paths. It was observed that the direction of plastic strain increment and time-dependent strain increment vectors were essentially the same, suggesting that an identical potential surface may be used for both plastic and time-dependent behavior of this sand in a time-dependent constitutive model. They also carried out the same analyses on plastic and creep strain increments of tests performed on dense fine silica and loose Sacramento River sands. These analyses confirmed the aforementioned observed behavior. Further investigation on the change in potential surface during creep was done by plotting the angle of plastic strain increment vectors versus the logarithm of elapsed creep time as shown in Fig. 2.10.

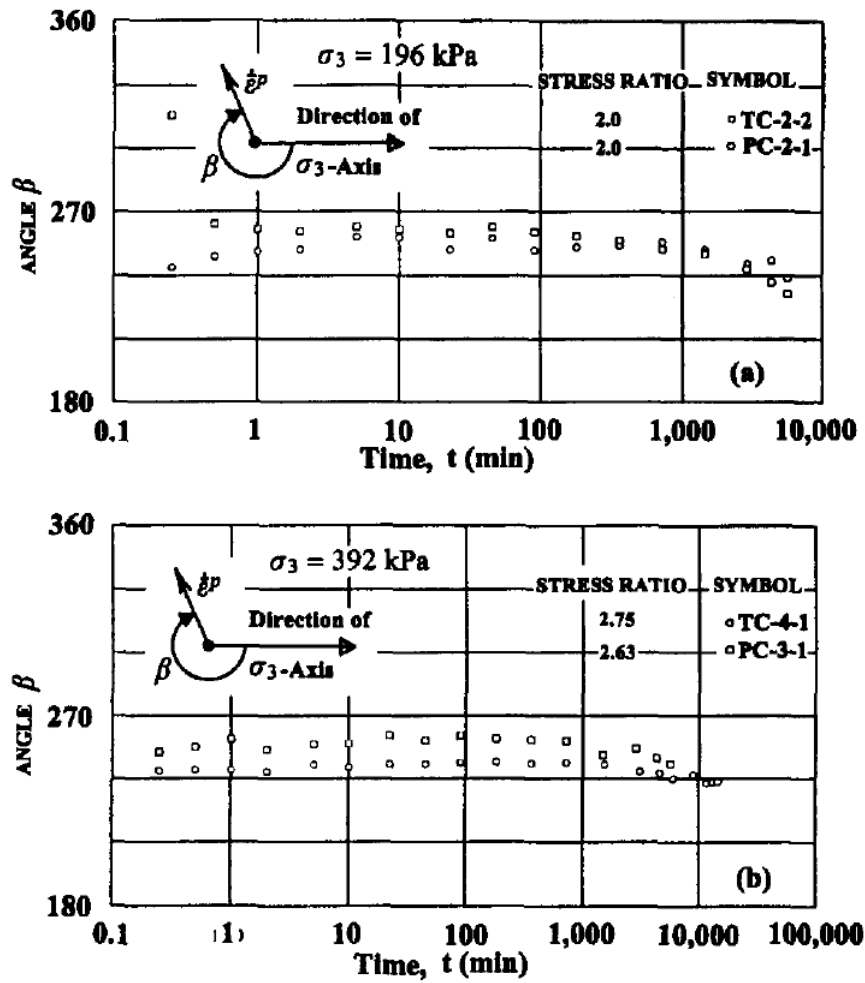


Figure 2.10. Change in the orientation of plastic strain increments with logarithm of time under confining pressures of (a) 196 kPa, and (b) 392 kPa (after Lade and Liu 1998).

It can be observed that these vectors tend to rotate toward the origin which implies the disposition to be less contractive. This indeed proposed that the potential surface moved outward as was the case for the yield surface during creep. A mechanistic picture which can explain the plastic sliding and creep at grain contacts was then schematically presented along the contact of two grains.

Bowman and Soga (2003) studied the microscopic aspects of the time-dependency issue utilizing three types of granular material, namely Leighton Buzzard clean silica sand (E), Montpelier Beach sand (MP) and glass beads (GB). They carried out 24 creep tests using a triaxial testing device for the period of 21.6 hrs at $p' = 600$ kPa and $q = 800$ kPa with a back pressure of 350 kPa. Since GB was less susceptible to crushing at these stress levels than the other two types of sand, a more dilatant behavior was observed during shearing of this material and only the contact asperities may have experienced yielding. Therefore, during creep tests, GB showed more volumetric dilatant creep than type E, while MP displayed contractive creep. Fig. 2.11 and Fig. 2.12 display the creep behavior of the tested materials. At different time periods of the creep tests, resin was injected into the specimen to be able to keep track of particle orientation. Two measures were employed to investigate probable change in the orientation and rearrangement of grains: Fisher distribution analysis and distribution of free path between particles. It was found that particles were aligned perpendicular to the major force direction, but as time passed, the grains rotated in such a way as to make a stronger structure. It was noted that this rotation of grains could be accompanied by the yielding of

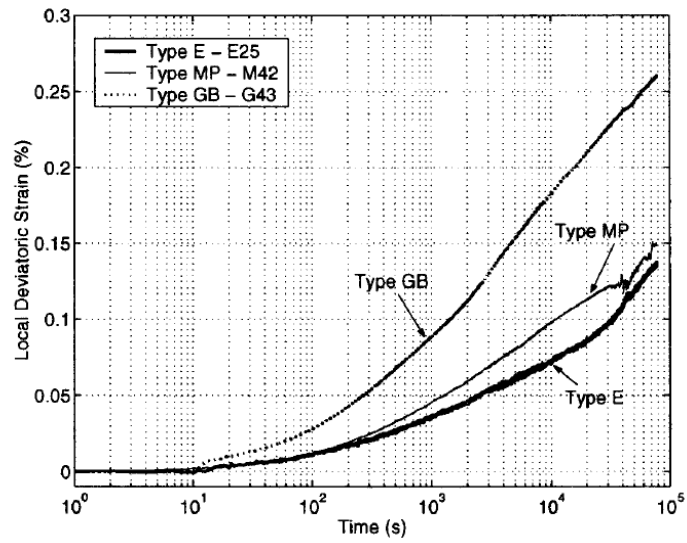


Figure 2.11. Deviator creep strain versus logarithm of time for $p' = 600$ kPa and $q = 800$ kPa (after Bowman and Soga 2003).

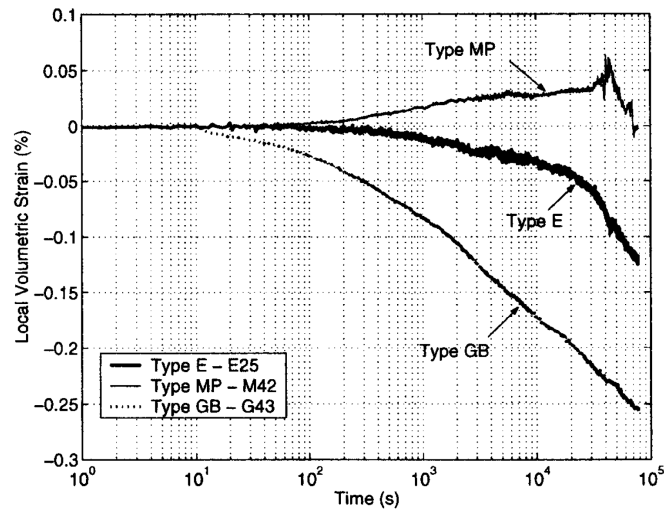


Figure 2.12. Volumetric creep strain versus logarithm of time for $p' = 600$ kPa and $q = 800$ kPa (after Bowman and Soga 2003).

particle asperities. However, in the new structure, aligned particles may buckle, group together at some points and open up in some other regions. Fig. 2.13 schematically illustrates the mechanism which was observed by Bowman and Soga (2003) during creep of sand type E in the dense state.

Augustesen et al. (2004) presented a state of the art study of one-dimensional and triaxial time-dependent effects in both clays and sands. They mentioned that the behavior of granular materials at low confining pressure may be qualitatively compared to that of overconsolidated clays. In comparison, the behavior of granular materials at high confining pressures, which is distinguished from low confining pressures by means of the “critical pressure”, is analogous to the behavior of normally consolidated clays. This “critical pressure,” which in turn is based on the mineralogical composition and density of the soil, can be interpreted as being the same as the “creep stress” previously suggested by Colliat-Dangus et al. (1988). In the first case, rearrangement of particles due to sliding and rolling is the mechanism behind measured deformations, while in the latter case, continuous crushing of grains and rearrangement of grains are at the root of the measured deformations.

Several series of creep and stress drop-creep triaxial tests sand were performed by Lade et al. (2009) in order to explore creep effects in crushed coral sand. It was observed that the specimens exhibited a contractive behavior during creep. Upon further loading after creep, structuration effects were detected. In other words, an extra strength was observed and it was required to be overcome for further plastic straining to occur, as seen in Fig. 2.14.

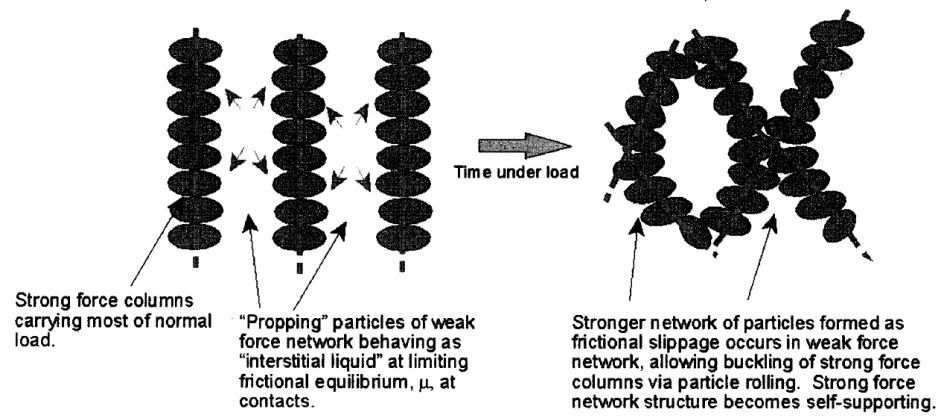


Figure 2.13. Change in a grain assembly due to a sustained load (after Bowman and Soga 2003).

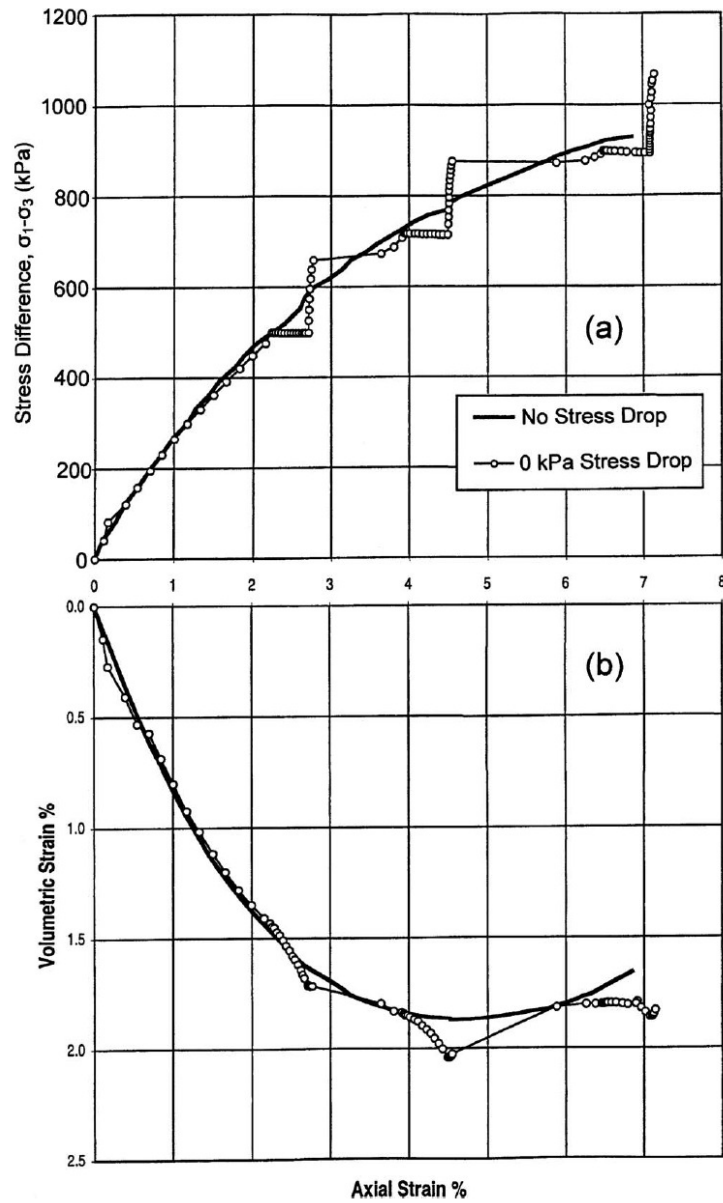


Figure 2.14. (a) Stress-strain and (b) volume change behavior during three stages of creep at 500, 700 and 900 kPa of deviator stress on crushed coral sand (after Lade et al. 2009).

Four different magnitudes of stress drops were employed and these were followed by 1-day creep and further loading at each of three levels of deviator stress. The creep deformation after each individual stress drop test is illustrated in Fig. 2.15. As it can be seen, tests with higher stress drop produced larger delays in initiation of creep deformation as well as smaller creep strains.

2.1.3. Experimental Studies of Stress Relaxation in Granular Media

Only few investigations have been performed on stress relaxation in granular materials. Lacerda and Houston (1973) carried out stress relaxation experiments on several types of clay and quartz sand. Their results showed that once deformation is stopped, there is a delay time, t_0 , before which stress relaxation initiates. They showed that there is an inverse linear relationship between the logarithm of this delay time and the logarithm of the strain rate prior to the initiation of stress relaxation for both clays and the quartz sand. The log-log plot in Fig. 2.16 illustrates this dependence for the materials tested.

Two strain rates were used to shear the specimens of the quartz sand before they were allowed to relax. As Fig. 2.17 implies, the higher strain rates are associated with very small delay times, whereas at very low shearing strain rates a long time is needed for the stress relaxation to begin. It is also observed that change in strain rate does not affect the slope of the stress relaxation curves. Previously, Murayama and Shibata (1961), Vialov and Skibitsky (1961) and Saada (1962) had reported such a behavior for clays. In

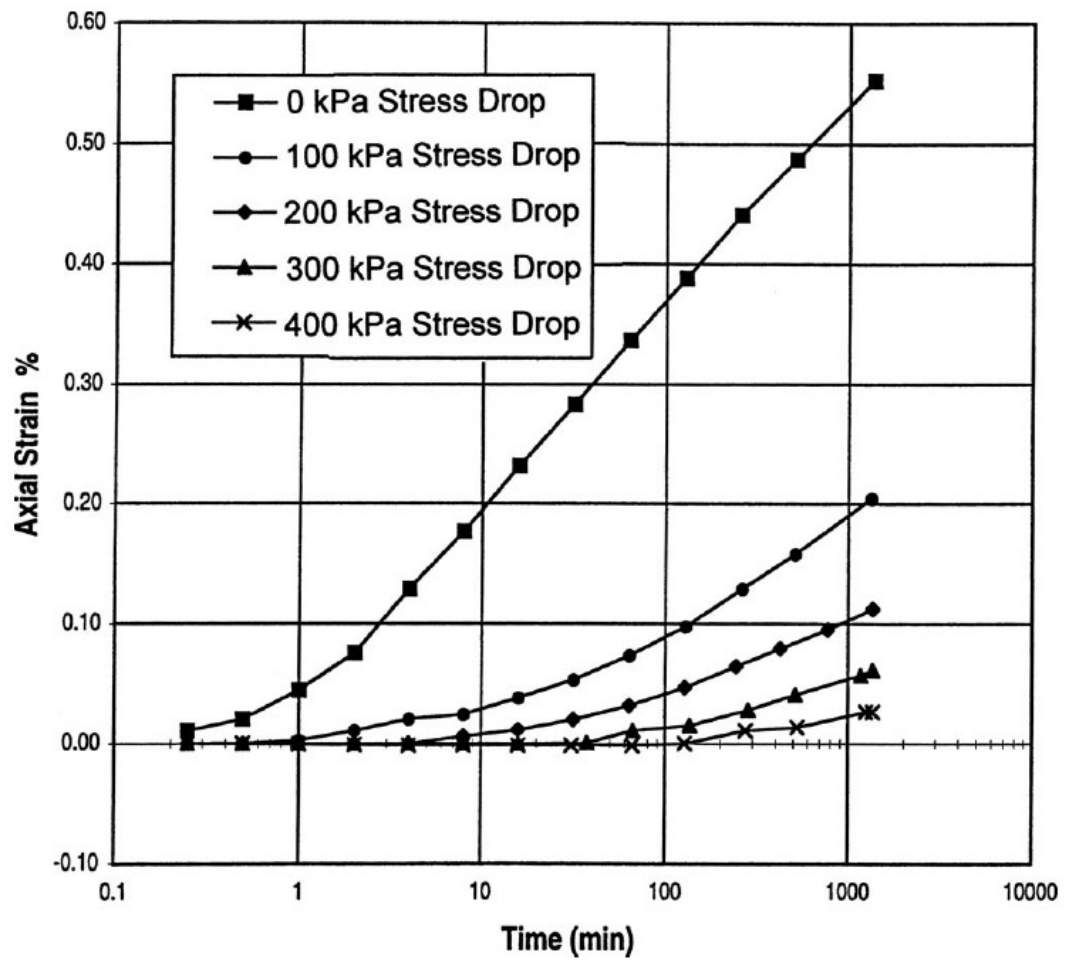


Figure 2.15. Axial creep strain versus logarithm of time for different stress drop-creep tests (after Lade et al. 2009).

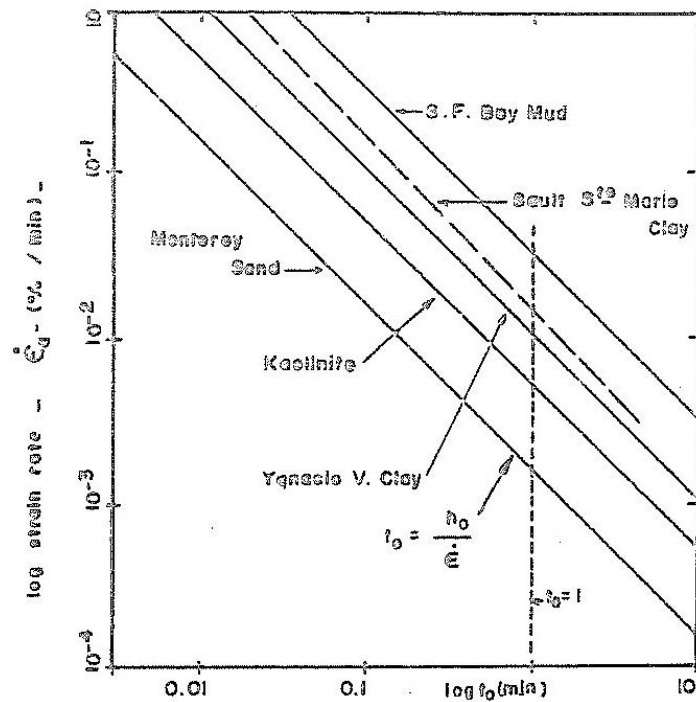


Figure 2.16. Log-log graph of variation of delay time with strain rate (Lacerda and Houston 1973).

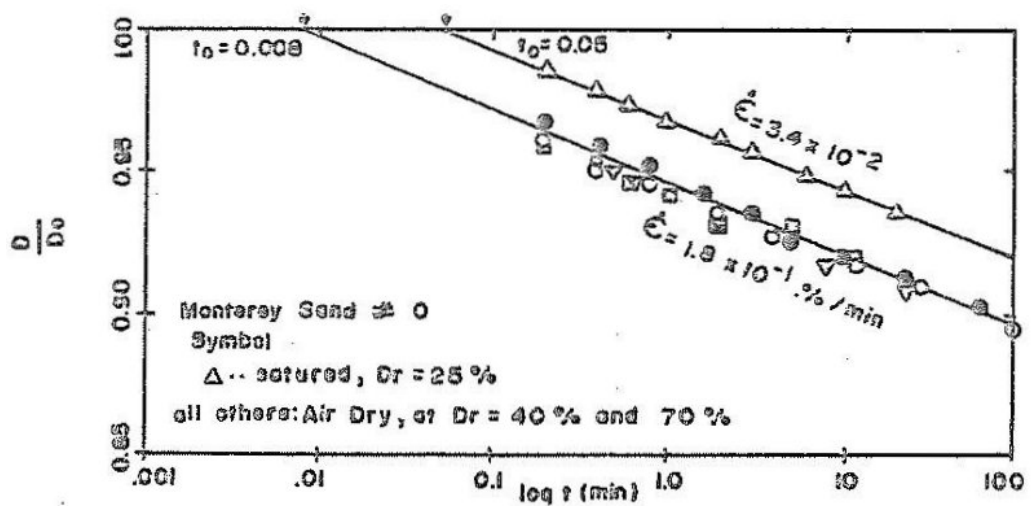


Figure 2.17. Variation of normalized stress relaxation with logarithm of time for Monterey sand (after Lacerda and Houston 1973)

fact, Murayama and Shibata (1961) mentioned that there is a limiting value for stress relaxation, while others did not observe an ending level for stress relaxation.

It was mentioned that the stress relaxation behavior is only affected by the stress level prior to the initiation of stress relaxation and the strain rate with which the specimens had been sheared. However, no dependency was observed on the confining pressure in the range of pressures used ($0.8\text{--}4.0\text{ kg/cm}^2$) in their experimental program. A similar approach was considered for specimens consolidated anisotropically and no measurable difference was captured. They also performed several undrained stress relaxation experiments. The results showed that the amount of generated pore pressure during stress relaxation is small to negligible and this observation was supported by Lo's (1969) hypothesis according to which pore pressure generation is only connected to the amount of applied strain. This was in accordance with the report by Murayama and Shibata (1961) for clays. They also presented a rheological model, explained later, to predict the relaxation behavior of soils.

Ladanyi and Benyamina (1995) stated that it is possible to obtain time-dependent properties of soils from both stress relaxation and creep experiments. Since the structure of soils changes during creep ("due to increasing distortion, sometimes associated with dilatancy"), it could be easier to attain these properties from stress relaxation during which the material structure stays unchanged and only the internal stresses redistribute. Therefore, they carried out a series of stress relaxation experiments on frozen Ottawa sand with the goal of estimating creep parameters of this sand from the relaxation experiments. Based on the experimental results, they concluded that the logarithm of

stress relaxation varies linearly with the logarithm of elapsed relaxation time. However, the slope of this line may vary with the amount of strain at which the stress relaxation is initiated. They have classified these different responses into pre-failure and post-failure regions. In other words, the stress relaxation response in the pre-failure strain region is dissimilar to that achieved in the post-failure strain region. For the range of confining pressures used (100-300 kPa), they concluded that confining stress has no influence on the stress relaxation behavior for frozen Ottawa sand. As a case in point, the variation of stress relaxation with respect to time under confining stress of 200 kPa is plotted in Fig. 2.18.

Lade et al. (2010) performed a series of stress-drop-relaxation tests. These tests were conducted in conjunction with their previous study on creep, strain rate and stress drop-creep effects in crushed coral sand (Lade et al. 2009). Significant amounts of relaxation were seen at different levels of deviator stresses. Analogous to the creep tests (Lade et al. 2009), close observation of the volumetric strain showed contraction during relaxation. Additional loading after each stress relaxation was accompanied by structuration effects. Fig. 2.19 illustrates a 1000 min relaxation test at different deviator stress levels.

Effects of initial loading rate on stress relaxation were also investigated and it was found that higher strain rates resulted in a slightly higher amounts of stress relaxation and larger contraction, independent of whether the specimen was contracting or dilating during primary loading, as shown in Fig. 2.20.

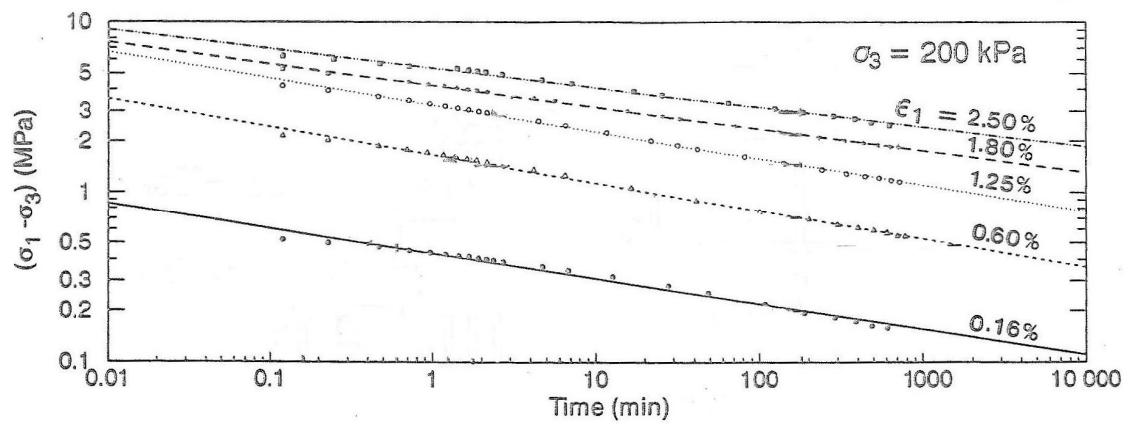


Figure 2.18. Variation of deviator stress with logarithm of time for frozen Ottawa sand under $\sigma_3=200$ kPa (after Ladanyi and Benyamina 1995).

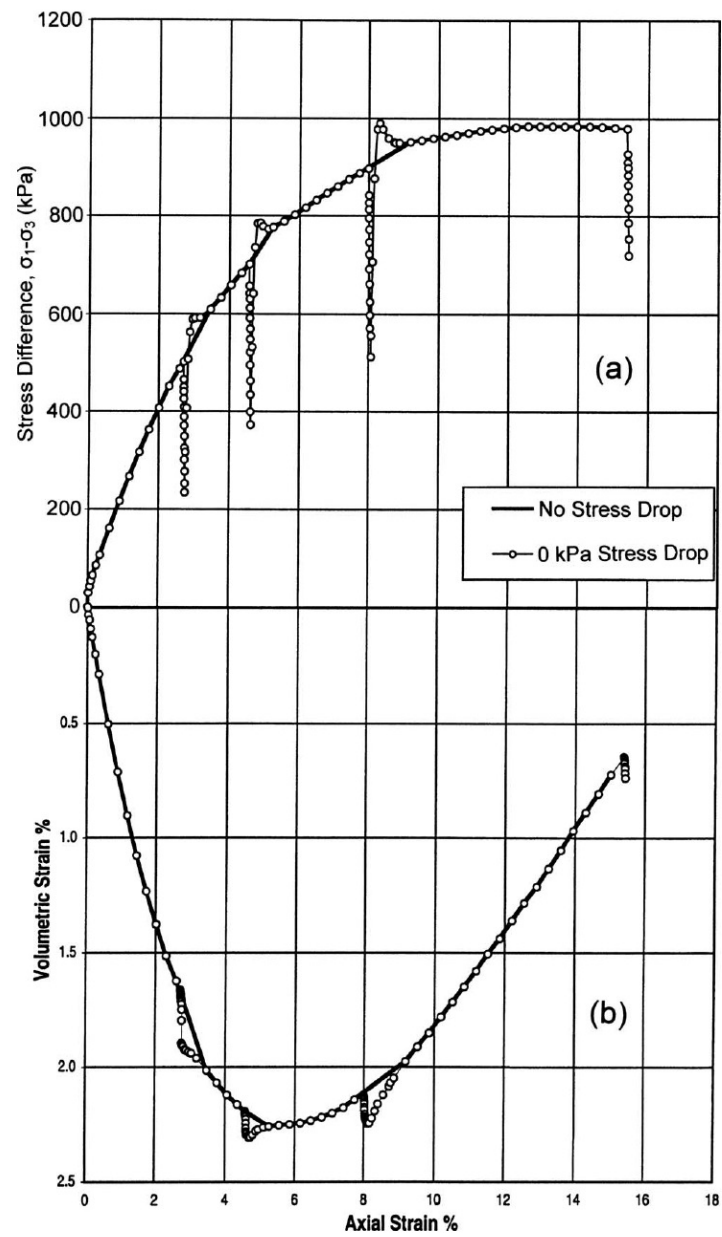


Figure 2.19. (a) Stress-strain and (b) volume change behavior during three stages of stress relaxation at 500, 700 and 900 kPa of deviator stress on crushed coral sand (after Lade et al. 2010).

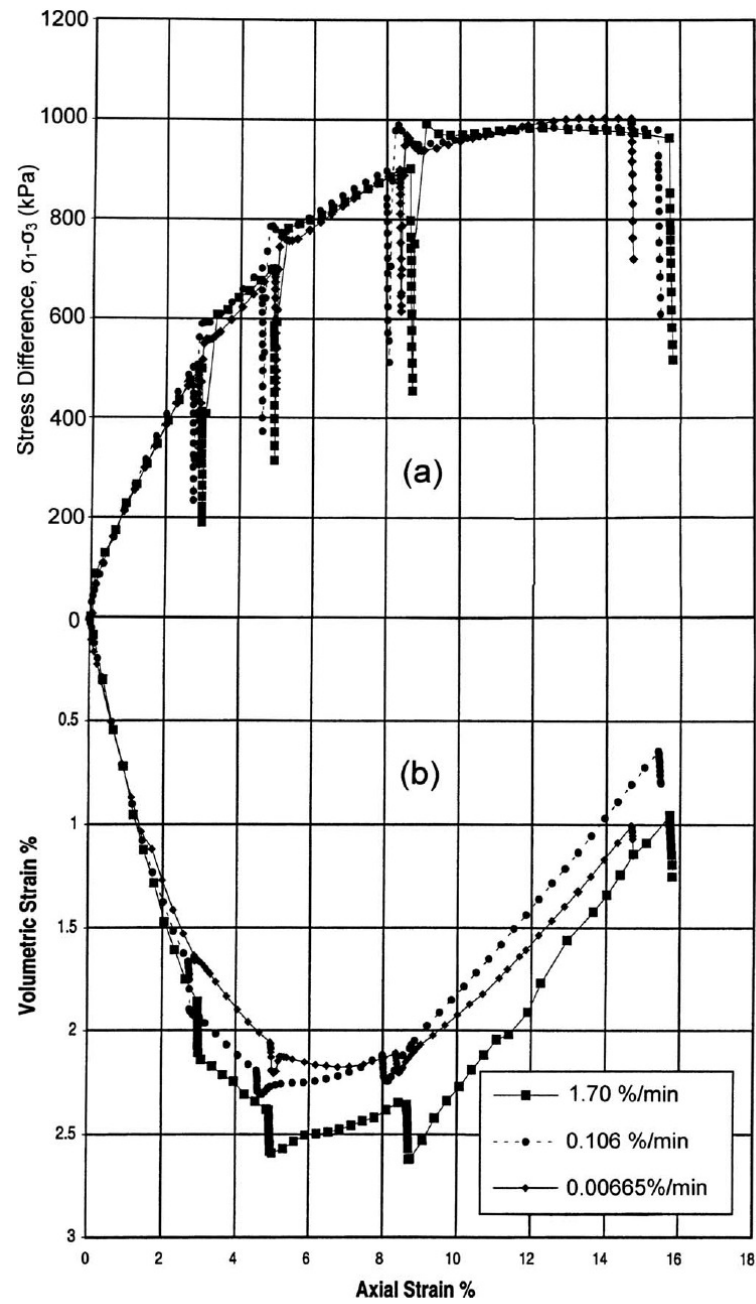


Figure 2.20. Effect of initial strain rate on consequent relaxation tests at deviator stresses of 500, 700 and 900 kPa: (a) stress-strain; (b) volume change (after Lade et al. 2010).

Analysis of stress drop-relaxation experiments showed that the amount of stress relaxation was directly related to the stress level at which relaxation is initiated. In other words, increasing the stress drop to a lower stress level results in smaller amounts of stress relaxation. Fig. 2.21 illustrates the relaxation stress dependency on initial stress level. It shows that larger stress drops bring increasing delays in initiation of stress relaxation. This postponement was also seen for stress drop-creep tests carried out by Lade et al. (2009).

2.1.4. Strain Rate Dependency in Sands

The first experimental study of the strain rate effects was conducted by Casagrande and Shannon (1948) using a triaxial testing apparatus and low confining pressures on dense sand. It was reported that the initial modulus of deformation was not affected by strain rate. However, a decrease in time-to-failure from 2100 to 0.3 seconds (increasing strain rate) resulted in a 10 % increase in strength. In a similar study, Seed and Lundgren (1954) examined drained and undrained behavior of dense sand at confining pressures up to 2 kg/cm^2 with time-to-failures varying from 0.02 to 900 seconds. They stated that the soil strength and initial modulus increased 15 to 20 % for fast drained tests, and these increases were related to the sand approaching undrained conditions and generation of negative pore pressures due to dilation. Rate dependency of undrained sand was investigated at low confining pressures with the strain rate changing from 2 to 8000 %/min by Nash and Dixon (1961).

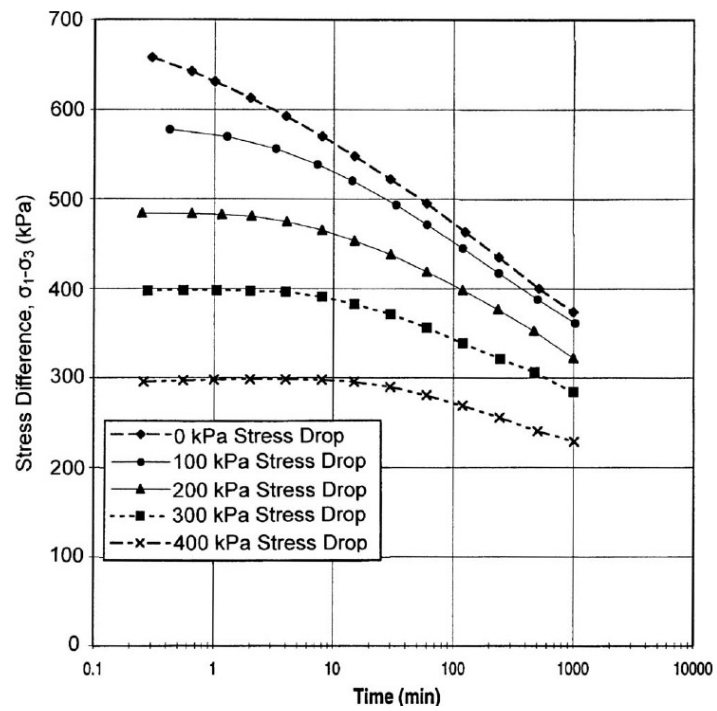


Figure 2.21. Stress relaxation versus logarithm of time for different stress drop-relaxation tests (after Lade et al. 2010).

Nash and Dixon (1961) discovered that lower strain rates culminated in reduction of maximum stress ratio and lower initial modulus. The mechanism of this phenomenon was believed to be related to the time given for the rearrangement and crushing of the particles. Thus, the specimens sheared at higher strain rates were less contractive. Consequently, pore pressure generations were lower and deviator stresses were higher.

The aforementioned results seemed to be somewhat contradictory. Therefore, Whitman and Healy (1962) performed a series of drained and undrained triaxial tests on loose and dense sand specimens at low confining pressures with time-to-failures ranging from 0.005 to 300 seconds. They realized that under drained conditions, the strength had a direct relationship with the strain rate. That is, the highest strain rate resulted in 10 % higher strength. On the other hand, in the undrained case, no dependency was captured. Drained and undrained rate dependency of strength and initial modulus of sand for confining pressures of 1.0 to 15 kg/cm² were examined by Lee et al. (1969). They changed the strain rate from 0.018 to 15000 %/min. It was found that an increase in the strain rate in the drained case under high confining pressures resulted in the increase of soil strength up to 20 %.

Yamamuro and Lade (1993) performed a series of drained and undrained triaxial tests to elucidate effects of strain rate on the instability of granular soils at high confining pressures. The strain rate was changed from 0.0042 to 0.740 %/min while the confining pressure was held constant during all tests at 34.0 MPa. It was observed that higher strain rates produced higher deviator stresses. They connected this rate dependency to the particle crushing and rearrangement of particles at high confining pressures. It was

mentioned that less time was available for tests at higher strain rate; therefore, lower amounts of particles crushed; consequently, lower particle rearrangement and less pore pressure generation occurred. This is analogous to the mechanism proposed by Nash and Dixon (1961). Interestingly, although the maximum deviator stress was changed by the variation of strain rate, the instability line (a line from the origin to the maximum deviator stress point on the $p' - q$ diagram) was not affected as shown in Fig. 2.22.

For drained tests, the same type of behavior was observed, i.e. a higher friction angle was achieved at a higher strain rate. This was in accordance with the findings of Casagrande and Shannon (1948), Seed and Lundgren (1954), Whitman and Healy (1962) and Lee et al. (1969). However, the degree of dependency of strength on the strain rate was found to be much less pronounced for drained conditions than for undrained conditions, since even a small tendency of volume change results in a large pore pressure change under undrained conditions.

Matsushita et al. (1999) carried out plane strain and triaxial tests to investigate time effects on the prepeak deformation properties of Hostun and Toyoura sands. In their tests, two different approaches were employed: constant shear strain rate and stepwise changing shear strain rate. They found that increasing the initial shear strain rate up to 500 times did not have a considerable impact on the stress-strain behavior of the tested material and essentially the same curve was captured. However, if the shear strain rate changes during loading, depending on an increase or decrease in the rate, a temporary overshoot or undershoot occurred, and after undergoing some strains, the curve gradually

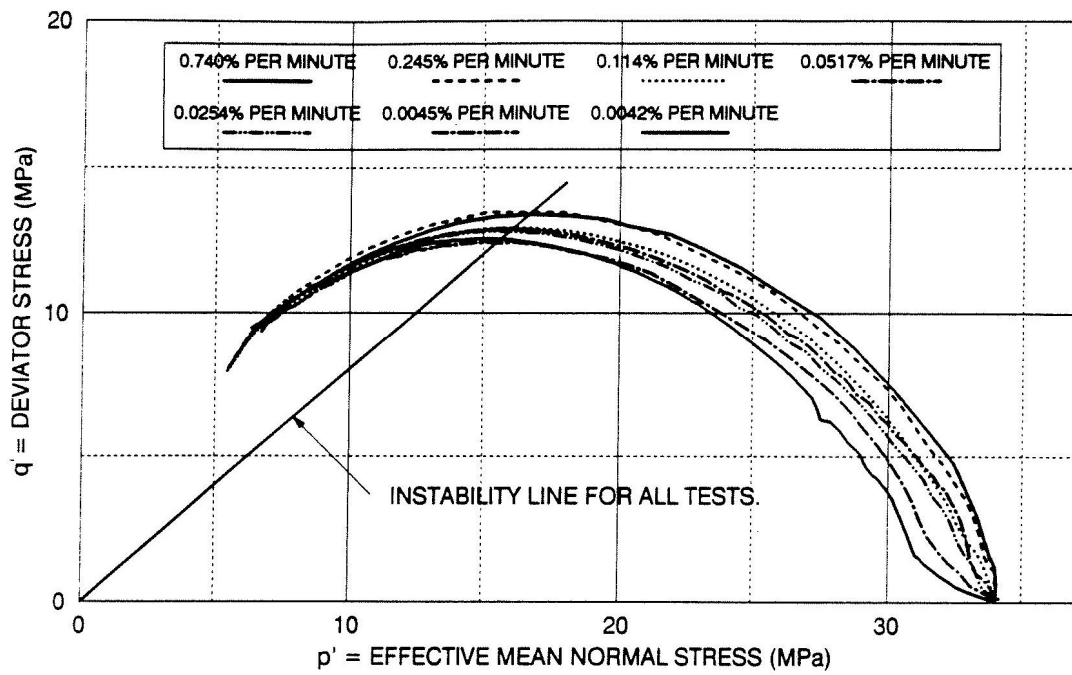


Figure 2.22. Effect of strain rate on undrained behavior and instability line for Cambria sand (after Yamamuro and Lade 1993).

rejoined the overall stress-strain curve which was captured in constant shear rate tests. These effects are schematically shown in Fig. 2.23. They also observed a significant amount of stress relaxation once the loading stopped in triaxial tests. Analogous observations were made by Yamamuro and Lade (1993). They studied strain rate effects at elevated confining pressures on Cambria sand in drained and undrained condition. Their stress-strain relations were found to be independent of the axial strain rate. Santucci de Magistris and Tatsouka (1999) and Tatsouka et al. (2000) have also confirmed the same type of behavior in granular materials.

Tatsouka (2007) and Tatsouka et al. (2008) thoroughly studied the mathematical expression of various viscosity types of soils. They categorized the viscous behavior of geomaterials into four groups of: *Isotach*, *Combined*, *TESRA* (Temporary Effects of Strain Rate and strain Acceleration) and *Positive & Negative*. These types of viscous behavior are schematically displayed in Fig. 2.24.

The first group, *Isotach*, is defined as materials whose stress-strain behavior is a function of irreversible strain, ϵ^{ir} , and its rate, $\dot{\epsilon}^{ir}$. In other words, higher strain rate results in higher shear strength and in the case of change in strain rate, the stress-strain curve joins the one that would be obtained if the specimen had been sheared with that rate in the first place. This means that there is a unique stress-strain-strain rate relation for a specific type of soil. This type of behavior has been reported by different investigators usually in materials with cohesion such as sedimentary soft rocks (Hayano et al., 2001), cemented well-graded gravel compacted at optimum water content (Kongsukprasert and

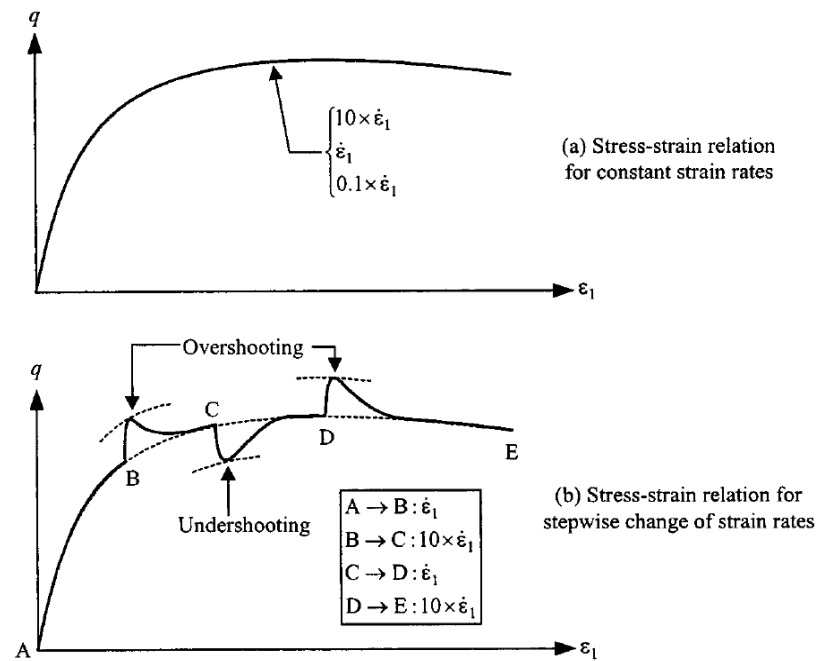


Figure 2.23. Rate dependency of stress-strain behavior of a sand postulated by Matsushita et al. (1999)

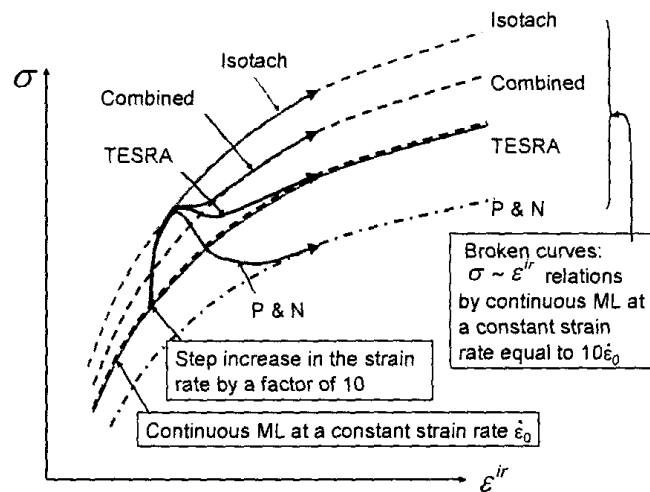


Figure 2.24. Basic viscous behavior of geomaterials due to strain rate change proposed by Tatsuoka (2007)

Tatsuoka, 2005), clays (Sorensen et al., 2007), bituminous materials (di Benedetto et al., 2005) and well graded angular gravelly soils (Anh Dan et al., 2006). Sheahan and Kaliakin (1999) termed this behavior in which creep, relaxation and rate dependency follow the same basic mechanism to be in accordance with the “Correspondence Principle.” In fact, Leroueil and Marques (1996) have suggested that for these materials, creep and relaxation properties can be achieved using a constant rate of strain test and vice versa. In the other three types of behavior, not only the irreversible strain, ϵ^{ir} , and its rate, $\dot{\epsilon}^{ir}$, but also the behavior is a function of strain history.

In the *Combined* behavior, the generated viscous stress increment at the moment of increase in strain rate, defined as $\Delta\sigma^V$, decays partially and a residual value remains if shearing continues at the new rate. However, $\Delta\sigma^V$ clears out totally for *TESRA* behavior; that is, the stress-strain curve follows the original curve and there is no change in strength although it is being sheared at a higher strain rate. The latter type is also referred to as *Non-Isotach* and has been reported elsewhere by Lagioia (1998) for creep tests on carbonate sands, and by Matsushita et al. (1999) for a series of plane strain and triaxial tests at various shearing rates. It should be noted that *Combined* behavior is, in fact, a combination of *Isotach* and *TESRA*. *TESRA* behavior has been reported in poorly graded relatively angular and stiff-particle sands (Kiyota and Tatsuoka, 2006). However, the *Combined* type was observed in undrained tests on some clays (Tatsuoka et al., 2002).

The last category is *Positive and Negative* behavior in which $\Delta\sigma^V$ after a complete decay, reaches a negative value. As it can be seen, even though the shearing

strain rate has increased, the stress-strain relation continues at a lower level of stress, representing lower strength. This type of behavior was recorded in different types of poorly graded granular materials with rounded and stiff particles (Enomoto et al., 2007a and b; Tatsuoka, 2007). Table 2.1 briefly describes how different materials follow different types of behavior.

Tatsuoka et al. (2008) proposed two simultaneous mechanisms by which the time-dependent soil behavior may be controlled, and whichever dominates over the other, the general behavior follows that one. *Mechanism a* describes the general interparticle behavior as *Isotach* because it is logical that an increase in shear displacement rate at interparticle contact points makes a stiffer and stronger load-displacement behavior. According to this mechanism, and independent of material type, all geomaterials demonstrate increases in stiffness and strength as a result of increasing strain rate. On the other hand, *Mechanism b* considers (contractive) creep deformation at the contact plane which becomes more pronounced when the strain rate decreases. Therefore, the interparticle contacts have more time to become stable; as a result, the material exhibits higher strength subsequent to decrease in strain rate. It is obvious that the latter mechanism depends on the material type. Consequently, the general behavior is based on the trade off between these two mechanisms. Tatsuoka et al. (2008) also presented some mathematical functions which, in addition to the aforementioned viscous type behaviors, can simulate the transition among them for geomaterials.

Table 2.1. Effect of different parameters on viscous behavior of geomaterial (after Tatsuoka et al. 2008).

Bound	Unbound		
<i>Isotach</i> (pre-peak) → <i>TESRA</i> (post-peak)	Grading Shape	Well-graded	Poorly graded
	Angular	<i>Isotach</i> (or Combined)→ <i>TESRA</i>	<i>TESRA</i> → <i>P & N</i>
	Round	<i>TESRA</i> → <i>P & N</i>	<i>P & N</i> → <i>P & N</i> with instability

Lade et al. (2009) examined the rate dependency behavior of crushed coral sand by performing a series of drained triaxial compression tests. Five different strain rates, corresponding to a 256-times change from minimum to maximum rate, were used to study the effect of strain rate. Except the volumetric strain change of the test with the minimum rate, which was slightly different from others, essentially no difference was observed among stress-strain behavior of specimens sheared at various strain rates. Fig. 2.25 exhibits the observed stress-strain behavior dependency on strain rate for crushed coral sand. The same observation was made by Matsushita et al. (1999). Employing very high, but constant shearing rates during drained triaxial tests, Abrantes and Yamamuro (2002) also found that, for the strain rates below the range where inertia factors have to be taken into account, sands demonstrate very little or no dependency on the strain rate.

Furthermore, Lade et al. (2009) considered strain rate jump tests in their study where the rate was changed instantaneously 256 times from 0.00665 to 1.70 %/min and vice versa. The results are shown in Fig. 2.26, and it can be seen that increases and decreases in strain rate have only temporary overshoot and undershoot effects on the stress-strain behavior, as discussed by Tatsuoka et al. (2000).

2.1.5. Proposed Mechanisms for Time Effects in Granular Geomaterial

Mitchell (2008) comprehensively addressed investigations in the literature which had reported aging phenomena in sands. In contrast to what was stated by Mitchell and Solymar (1984) who related aging of sands to chemical reactions and silica gel formation

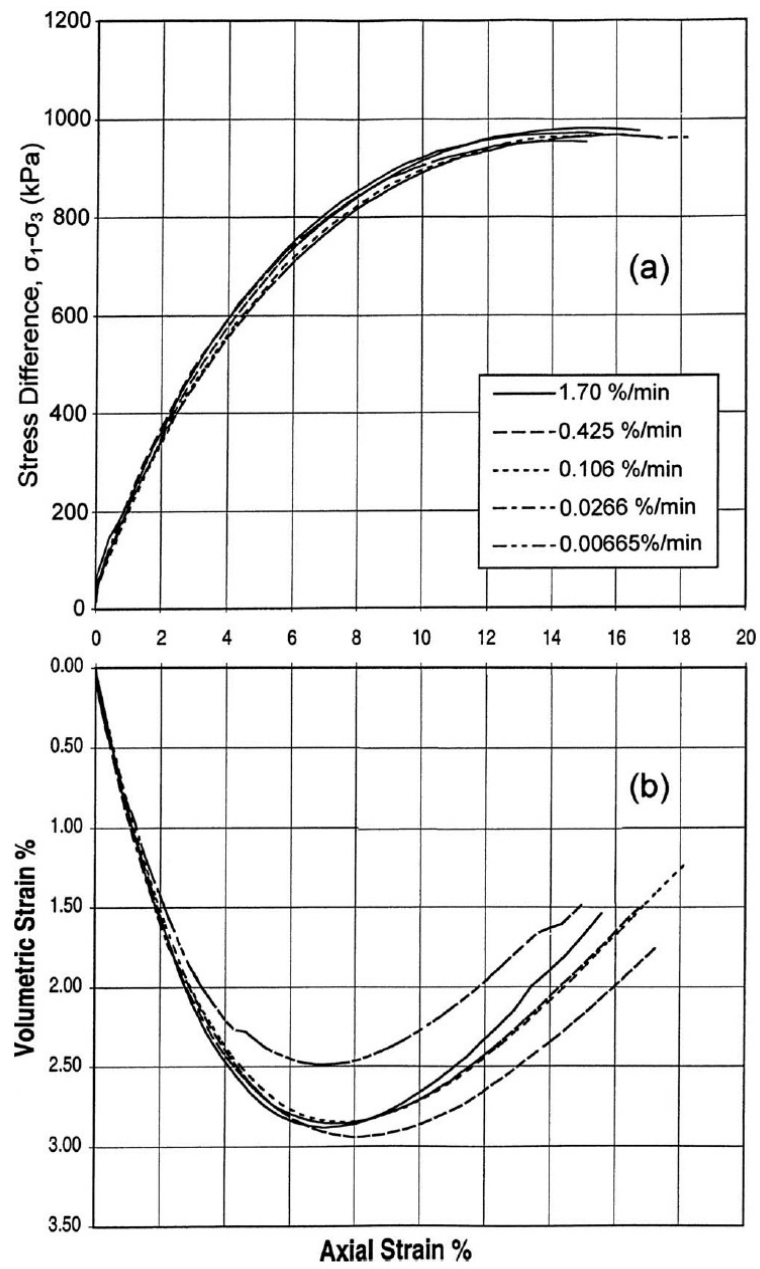


Figure 2.25. Rate dependency of (a) stress-strain behavior, and (b) volume change behavior for crushed coral sand (after Lade et al. 2009).

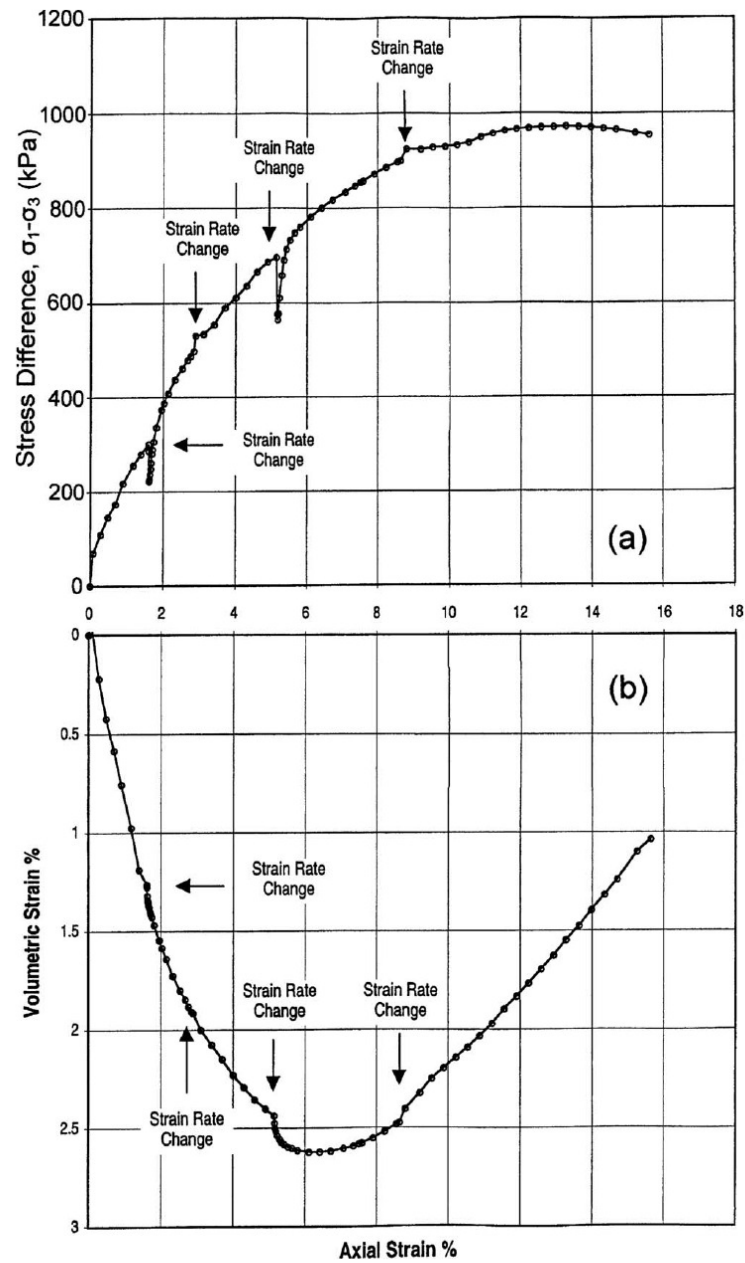


Figure 2.26. Effect of strain rate change from 1.70 to 0.00665 %/min and vice versa on (a) stress-strain, and (b) volume change of crushed coral sand (after Lade et al. 2009).

at particle contact points, Mitchell (2008) suggested another hypothesis for time-dependent behavior of sand. In this hypothesis, time effects are connected with particle rearrangements as well as interparticle stress adjustment and redistribution among grains, and this coincides with a small volumetric contraction as the principal root of aging phenomena. He mentioned that sand type and its initial state and the applied stress state can have considerable effects depending on the type of the measured property. It was also stated that micro-biological processes have been reported in the literature as the cause of aging. In general, any combination of the three aforementioned causes can control aging phenomena.

On the other hand, as previously done for Antelope Valley sand by Lade (2007), Lade et al. (2010) superimposed the creep and relaxation stress-strain curves. Fig. 2.27 and Fig. 2.28 show that 1-day stress relaxation and 1-day creep curves do not coincide, suggesting that granular materials do not follow isotach behavior, as do clays.

In this regard, Lade et al. (2009, 2010) proposed a new mechanism involving grain crushing to explain the time effect in granular material. This mechanism is based on grain assemblies with force chains exposed to boundary conditions corresponding to creep and relaxation. According to this mechanistic picture, when a grain crushes and the stress level is kept constant, the grain assembly needs to adjust its structure to match the boundary conditions. Therefore, creep deformation is observed and it reduces with time as the breakage of grains decreases. Alternatively, if the strain is held constant, the soil structure is no longer able to sustain the stress level due to movement of broken particles;

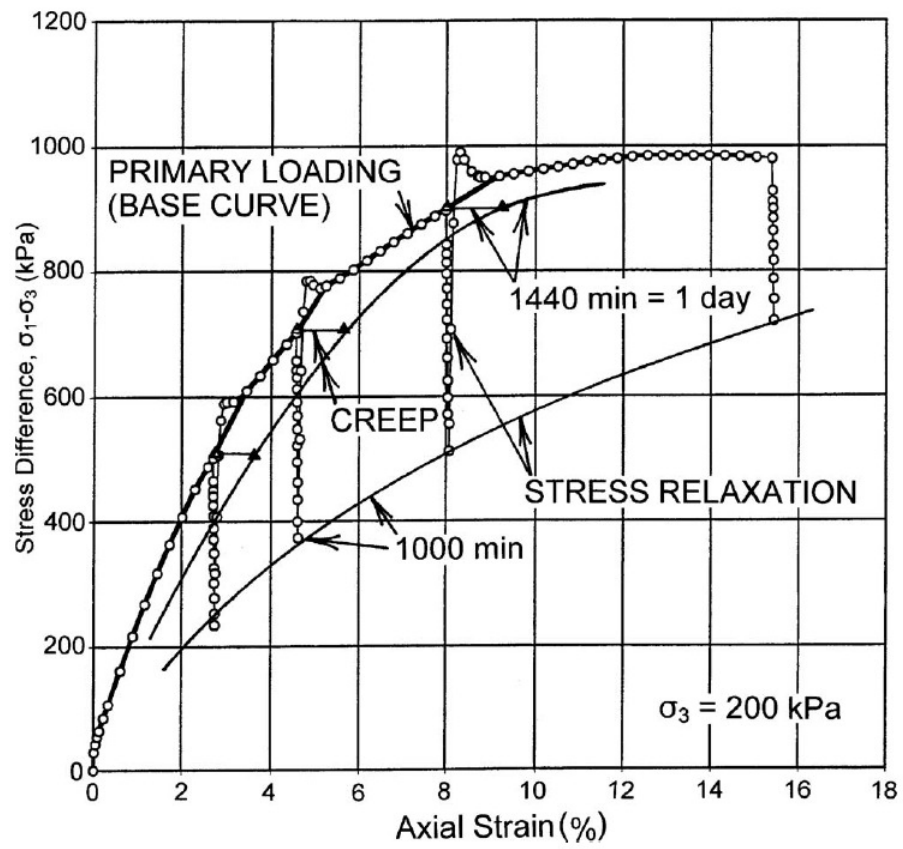


Figure 2.27. Comparison of 1-day creep and 1000 min stress relaxation curves of crushed coral sand (after Lade et al. 2010).

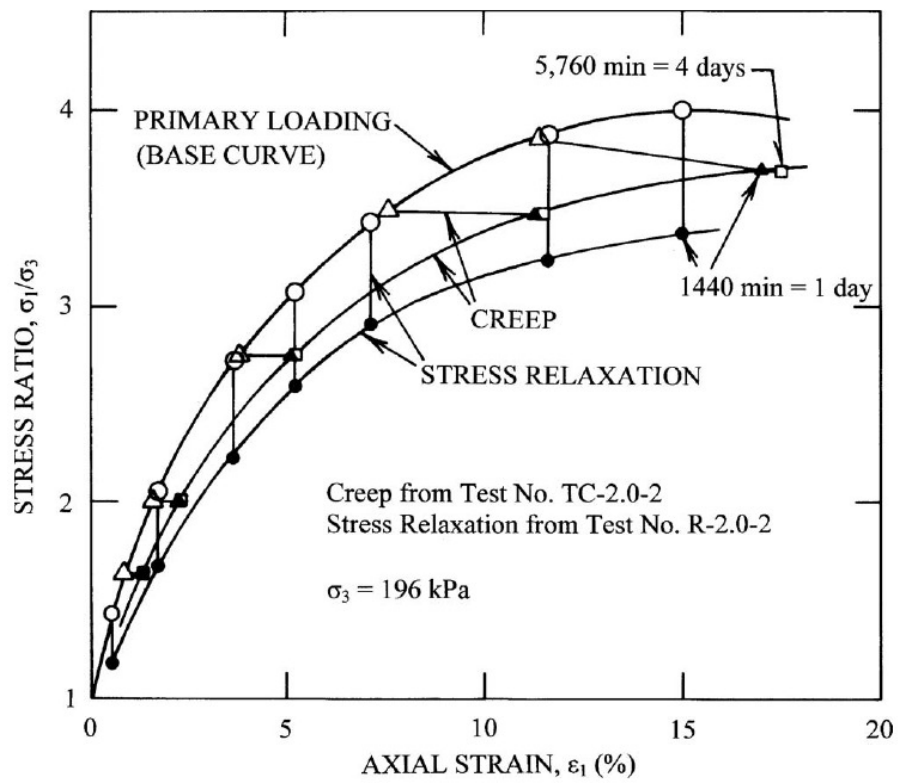


Figure 2.28. Comparison of 1-day creep and 1-day stress relaxation curves of Antelope Valley sand (after Lade 2007).

thus, new force chains are shaped and this is accompanied by the reduction of stress level. This mechanistic picture for time effects in granular material is illustrated in Fig. 2.29. However, they stated that although the crushing was visible in two previous studies, sieve analysis could not be employed to demonstrate grain crushing due to the friability of the tested materials. As a result, no quantitative measure was present to throw further light on the effect of particle breakage and time effects, and further experiments on sands with stronger grains were suggested.

2.2. High Pressure Testing and Particle Crushing in Sands

In warm tropical seas, deep deposits of biogenic skeletal sediments are observed, which are highly crushable. Also, exposed granitic materials subjected to severe weathering are easy to crush. Fundamental components of rockfill dams such as drains and filters, which may be located at the bases of dams and experience very high pressures, are made with granular materials. It is widely known that the change in hydraulic conductivity is greatly influenced by particle crushing. Hazen (1911) has proposed a formula for finding permeability based on grain size, which has been extensively used both in practice and in research (Taylor, 1948). Therefore, the study of particle breakage is of importance, and the change in grading due to grain crushing may culminate in irrecoverable problems.

The stress levels encountered in regular geotechnical structures may not be sufficient to cause crushing of many common types of sand. However, this is not the case for many other engineering projects. For example, Allen et al. (1957) reported the

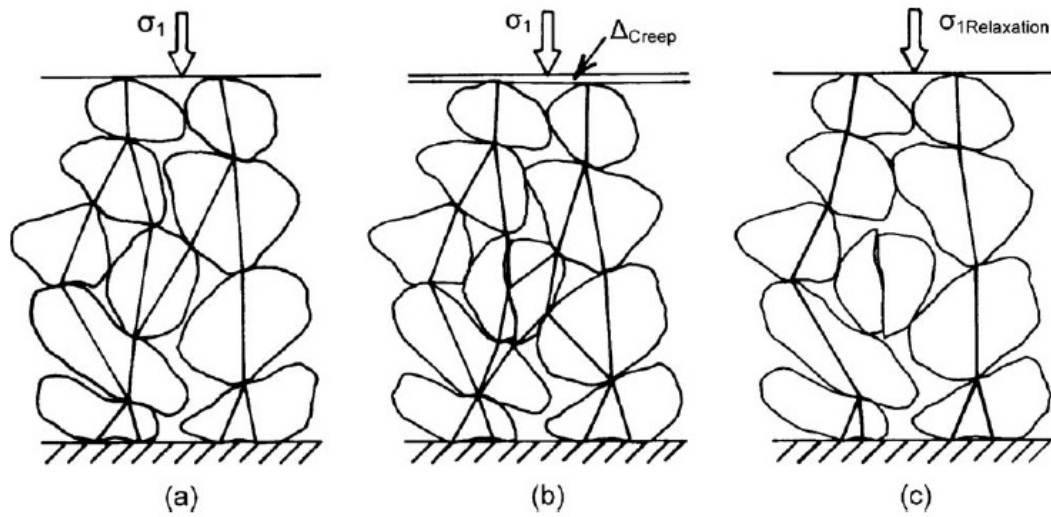


Figure 2.29. Mechanistic picture of time effect in granular material assembly: (a) initial loading, (b) creep condition, (c) relaxation condition (after Lade et al. 2009).

crushing of grains due to even small projectiles. Furthermore, Caudle et al. (1967) and Henrych (1979) showed that stresses over 138 MPa can be experienced around large projectiles and around explosion sites. Other examples of high stresses can be found around explosively inserted anchors, during deep well drilling in the petroleum industry, near tips of relatively long piles (15–30 m) and around deep tunnels.

According to Ramamurthy (1969), particle crushing depending on the breakage type is categorized in the three following groups, which are displayed in Fig. 2.30.

- a) Fracture: A grain particle splits into two or more smaller pieces when it undergoes a stress higher than the grain tensile strength, which usually occurs at high confining pressures for strong grains such as silica.
- b) Attrition: The main part of the grain remains intact, but many smaller particles detach from the body. This is usually the case for breakage of the sharp angles of the grain.
- c) Abrasion: Only the asperities of the grain break and the grain seems intact. This type of breakage happens due to the sliding of grains at low confining pressures.

In the following, studies of particle crushing and high pressure testing of granular materials are presented according to the type of test employed.

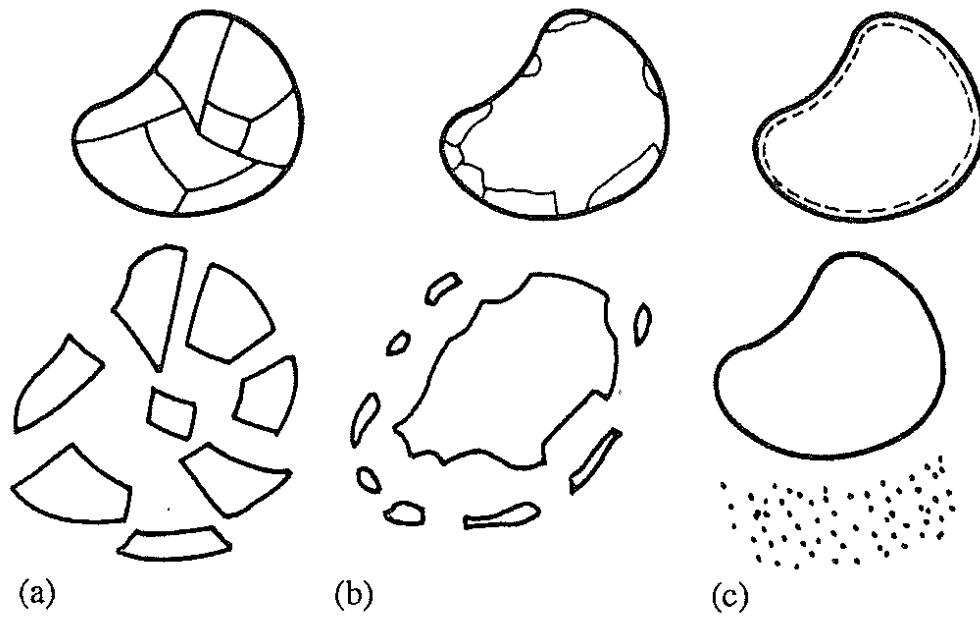


Figure 2.30. Various modes of grain crushing: (a) fracture, (b) attrition, (c) abrasion
(after Daouadji and Hicher 2010).

2.2.1. One-Dimensional Compression Experiments on Granular Material

After performing compression tests on sand specimens extracted from deeply buried oil-field sediments, Blackwelder (1923) stated that even at stresses much higher than 7 MPa particle crushing is not considerable. Similarly, Terzaghi (1925) studied particle crushing up to stresses about 8.5 MPa and concluded that this phenomenon is insignificant in natural sands at such stresses and higher stresses are not commonly reached. Botset and Reed (1935) reported an investigation on sand specimens subjected to stresses as high as 23.6 MPa and observed no volume change due to crushing at high stresses. They concluded that particle crushing is not a substantial issue in sands. However, these findings were different from observations made by Terzaghi and Peck (1948). They published a series of one-dimensional compression tests on sand with vertical stresses up to 96.5 MPa which clearly showed particle breakage. The phenomenon was presented as the main cause of compressibility in sands at high confining pressures.

The study on crushing of particles was continued by de Souza (1958). He performed several high pressure compression tests up to 138 MPa on three types of materials namely, very angular quartz grains, uniform and rounded grain Ottawa sand and New England beach sand. He found that there is a break point on the e - $\log P$ curve where the compression index changes. It was seen that the amount of particle breakage increases dramatically for stresses beyond this point. de Souza stated that the location of this point changes based on the soil's initial density, angularity and grain size; the higher the density, the lower the angularity and the lower the median grain size are, the higher the

stress at the break point will be. Moreover, it was noticed that particle crushing is a progressive phenomenon. That is, when stress is applied slower, the particles crush more extensively.

Roberts and de Souza (1958) also observed considerably more particle crushing and greater compressibility for angular sands compared to rounded sands even at moderately low pressures. However, they mentioned that this difference diminishes as the pressure increases. Harremoes (1959) studied the influence of mineralogy on particle crushing. He tested a variety of sands namely, Hawaiian Beach sand, Ottawa sand, pure dolomite sand, pure feldspar and pure quartz sand under stresses as high as 138 MPa. Oddly, he noted that change in mineralogy does not affect the break point stress. However, he observed that higher unsmooth surfaces resulted in a greater crushing for stresses higher than the breakage point stress. Later, tests performed by Roberts (1964) on the same sands up to stresses of 268 MPa confirmed the results observed by Harremoes (1959) and de Souza (1958).

Hendron (1963) carried out one-dimensional compression tests on different types of sands up to 2.7 MPa pressure. He found that higher relative density and lower angularity result in a higher break-point stress. This is in accordance to what was observed by de Souza (1958), Harremoes (1959) and Roberts (1964). However, in contrast with their findings, he noted that higher median grain size results in a higher stress at the break-point.

DeBeer (1963) implemented one-dimensional compression tests on uniform sands to investigate particle breakage in granular materials. He found that for pressures lower than 9.8 MPa, particle crushing could be ignored. Particle crushing then became dominant at stress levels around 15 MPa, while it started progressively decreasing after reaching 34 MPa. This trend finally decreased dramatically above 98 MPa.

Hagerty et al. (1993) performed a series of one-dimensional compression tests with vertical stresses up to 689 MPa on six types of material namely, Ottawa sand, Black Beauty and four types of soda lime glass to throw further light on the effects of initial density, median grain size, particle mineralogy and angularity. The first series of tests showed that the value of break-point stress increases with initial density and more crushing was seen in looser specimens. The hypothesis behind this is that the smaller number of contacts per unit of cross-sectional area exists in the looser specimens compared to the dense ones. It was observed that larger particles underwent higher amounts of crushing. This also confirms the results presented by other researchers (e.g. de Souza 1958, Hendron 1963 and Roberts 1964). Analogous to the effect of density, they postulated that because the coordination number of specimens with larger particles is lower for specimens with smaller particles, higher interparticle stresses would be expected. Furthermore, more crushing occurred in angular particles in comparison to more rounded grains since in the former greater eccentric loading was probable. This was accompanied by a lower break-point stress. Interestingly, one type of soda lime glass whose Moh's hardness was about 5.5 exhibited considerably lower amount of crushing than Ottawa sand, having very similar grading and grain shape, and with Moh's hardness

of 7. Hagerty et al. (1993) stated that when the voids are filled with crushed material, the number of contact points increases and the average stress level drops. Therefore, at higher stresses, fewer particles break and progressively, less additional crushing occurs. This explains the ending part of the e -log P diagram at very high stresses where another break-point seems to exist from which crushing continues at a declining rate and the media behaves as pseudo elastic solids.

Another aspect of high pressure testing of granular material was studied by Yamamuro et al. (1996) who performed one-dimensional compression tests on three sands, namely, quartz, gypsum and Cambria sands under vertical pressures up to 800 MPa. Similar to the findings by Vesic and Clough (1968), it was observed that the effect of initial void ratio vanished at elevated stresses. Depending on the hardness of the grains, the K_0 -value may become constant or increase at high stresses. Furthermore, it was realized that the K_0 -value continues to increase during creep at high pressures. Sands with softer grains experience greater increase in K_0 -value than sands with harder particles.

From another point of view, Valdes and Caban (2006) measured the hydraulic conductivity changes while different sands were subjected to serious particle crushing. By testing six types of sands, they found that the hydraulic conductivity was considerably affected by the amount of fines produced by crushing. As mentioned by Lee and Farhoomand (1967), Valdes and Caban (2006) observed that the hydraulic conductivity change is of importance for designing filters of earth dams, for cone penetration data analysis and for oil production operation.

2.2.2. Triaxial and Other Types of Experiments on Granular Material

Kjaernsli and Sande (1963) studied the effect of grain shape on the amount of crushing utilizing a triaxial compression apparatus. They noted that at a given stress level, breakage is more pronounced in angular, rough-surfaced grains than smooth and round grains.

A similar study was carried out by Hall and Gordon (1963) on gravelly soil with particle sizes of up to 75 mm. In addition to presenting more crushing during shearing of the specimens than during isotropic compression, their results showed that poorly graded granular soil experienced more crushing than well-graded soil, at a same level of stress.

Marsal (1967) performed a series of high pressure triaxial compression tests with the confining pressures varying from 0.3 kg/cm^2 to 25 kg/cm^2 on three types of material. The diameter and height of the specimens were 113 and 250 cm, respectively. Specimens were made as dense as possible with the maximum grain size of 20 cm. To avoid puncturing and probable leaks, the membrane consisted of two layers of 3 mm and 6 mm-rubber membranes filled with 5 cm of fine sand and a layer of cardboard as an interface between the rockfill material and the inner membrane. The high confining pressure of the cell was provided by using constant level tanks which were consistently compensated according to the dilation and contraction of the specimens. These tanks were located on different elevations on near hills.

For the first material which consisted of well graded basaltic rockfill ranging from 0.6 mm to 200 mm with the initial void ratio of 0.3, it was found that increasing the

confining pressure from 5 kg/cm^2 to 25 kg/cm^2 resulted in decreasing the principal stress ratio from 6.1 to 4.2. In other words, the internal friction angle at failure dropped from 45.9° to 38.0° . Also, the strain-to-failure increased with confining pressure from 8% to 15%. Another material tested was well graded Granitic Gneiss with a wider range of particles, from smaller than 0.1 mm and up to 200 mm and with initial void ratio of 0.32. The same trend was observed; the principal stress ratio decreased from 4.0 to 3.3 as the confining pressure increased from 5 kg/cm^2 to 25 kg/cm^2 . This change is equal to a reduction of friction angle from 36.9° to 32.3° , and corresponds to an increase of strain-to-failure from 8% to 16%. On the other hand, the third material was the same as the second type but with a more uniform grain distribution, with particles varying from 40 mm to 200 mm and an initial void ratio of 0.62. In general, as it can be seen in Fig. 2.31, the principal stress ratio decreases linearly with the confining pressure in a log-log diagram. Moreover, some other triaxial tests were performed on the above mentioned materials in dry state with confining pressures of 0.4 kg/cm^2 and 0.9 kg/cm^2 . Interestingly, it was clearly observed that for the same material in dry condition, higher principal stress ratios were obtained compared to the values extracted from the extrapolation of the linear relation between principal stress ratio and confining pressure for the wet material, as shown in Fig. 2.31. This may suggest a weakening effect of water on the properties of geomaterials. Marsal (1967) also studied the breakage of particles and introduced a particle breakage parameter, B . This parameter is defined as the sum of the positive portion of differences in percentage retained, which could be positive or

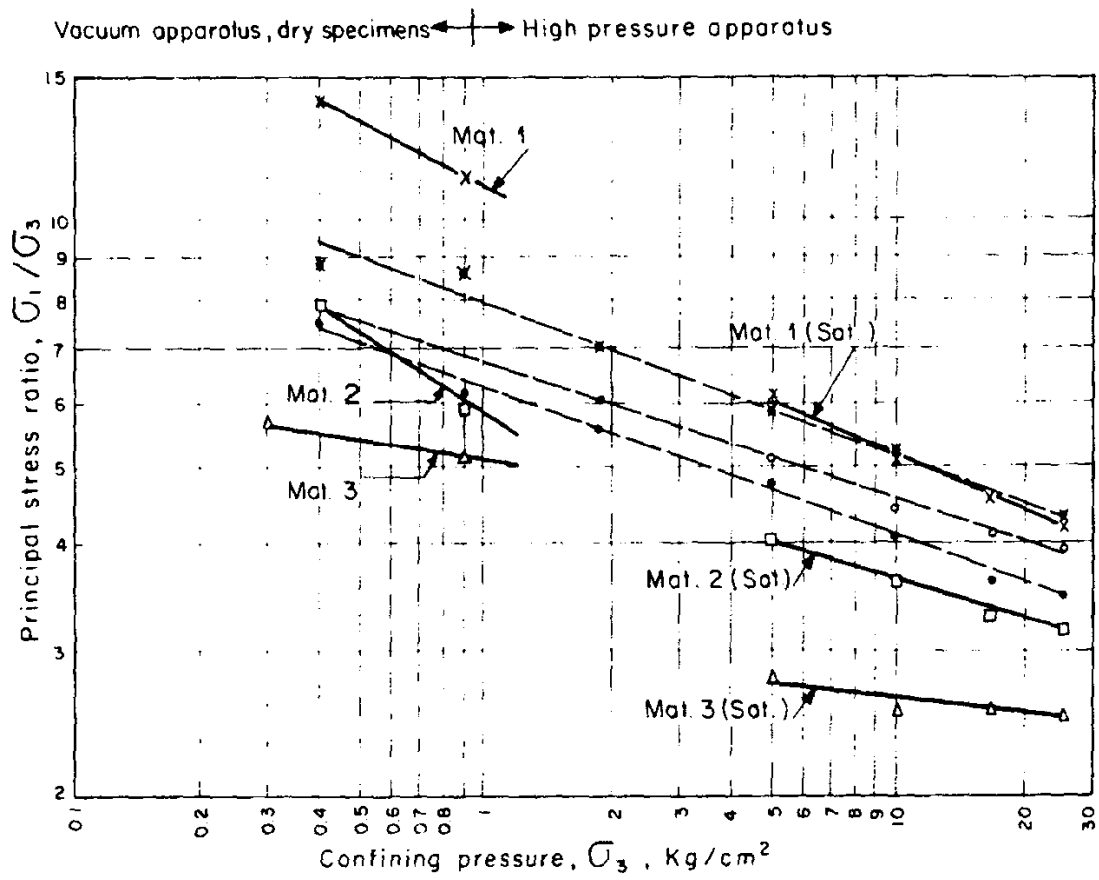


Figure 2.31. Variation of the maximum principal stress ratio due to change in confining pressure (after Marsal 1967).

negative, in each size after crushing. It was shown that confining pressure did not have any effect on the particle crushing for material type 1; however, for materials 2 and 3 crushing increased almost linearly with confining pressure. He stated that for material 1, micro-fissures present in the soil grains from blasting and from the crushing process before testing is the main cause of particle breakage which happens at relatively low confining pressures and does not change at higher stresses. However, for the second and third materials, which were essentially composed of the same minerals, the difference in breakage was due to the initial gradation and void ratio as particle breakage was expected to be more pronounced during contraction than during dilation. Furthermore, Marsal (1967) showed that the higher the breakage factor gets, the lower the principal stress ratio at failure will be. This also makes sense because when crushing happens, the specimen tends to contract as the new small particles fill the available voids.

Lee and Farhoomand (1967) studied the compressibility and crushing of granular soil in high pressure anisotropic triaxial compression tests on crushed granitic gravel with 100% relative density. With the interest on study of the crushing effects on the filter and drain design, they adopted D_{15i}/D_{15a} to quantify the amount of crushing. This ratio corresponds to the grain size at 15% on the grading curve before the test to the same value after the test. They found that the hypothesis suggested by Rutledge (1947) for clays (volume change is a unique function of major principal stress and independent of shear stress or minor principal stress on the soil element) could be applied to this type of soil as the curves of major principal stress versus volumetric strain for all different stress paths coincide. However, no unique relationship was identified between the amount of

crushing and the major principal stress. Similar to other studies (e.g. de Souza, 1958; Hall and Gordon, 1963), Lee and Farhoomand observed that uniform coarse soils compress more than uniform fine soils and well graded soils with the same maximum grain size. Also, it was seen that angular grains undergo more breakage than rounded grains. On account of the fact that the cracking sound was clearly audible from the cell and continued while they were waiting to take the final readings, they mentioned that crushing is a time-dependent phenomenon. It was observed that compression and particle crushing continues to increase at a decreasing rate for an unknown period of time.

Another extensive study was performed by Vesic and Clough (1968) in which the behavior of granular materials under high stresses was investigated. Over 150 triaxial tests were performed on Chattahoochee River sand at confining pressures of up to 633 kg/cm². It was observed that for confining pressures higher than 150 kg/cm² the initial density of the specimen had no effect on the shearing results because at the end of isotropic consolidation they reached the same void ratio. They concluded that at low confining pressures a very low amount of crushing occurs and high friction angles are attained; however, as the confining pressure increases, more particle crushing occurs, so lower friction angles were achieved until a specific stress level was reached. This stress level was defined as the “Breakdown Stress” at which the curvature of the strength envelope for all initial void ratios disappears and a constant friction angle is measured. Subsequently, particle breakage and shearing displacement in the slip plane become the mechanism of further shearing.

Miura and Yamanouchi (1977) studied the particle breakage of quartz sand at high pressure and its effects on the shear strength. They employed grain surface area to quantify particle breakage and found that it was a function of plastic work. Later, Miura and O-Hara (1979) investigated the particle crushing of decomposed granite soil by performing several low confining pressure triaxial tests. The soil particles were so weak that even at low pressures considerable amount of crushing was observed. It was reported that with the increase of confining pressure particle crushing caused significant reduction of the maximum principal stress ratio. Similar to quartz sand at high confining pressures, there was a direct relationship between the maximum principal stress ratio (or shear strength) and particle crushing. Therefore, they concluded that for friable types of soil, particle crushing at low confining stress was markedly the same as this phenomenon under high confining pressures for soils with stronger particles.

The behavior of clean Sacramento River sand was investigated at high pressures by Lee and Seed (1967) and Seed and Lee (1967). They performed a series of triaxial tests with consolidation pressures ranging from 1.0 kg/cm^2 to 140 kg/cm^2 . Lee (1977) noticed that for the specimens consolidated at pressures higher than 60 kg/cm^2 adhesion bonds can form. This was observed after opening the chamber and removing the membrane. The specimens maintained their shape and a considerable effort was required to break them apart even after oven drying (removing all probable capillary effects of moisture). The following explanation was suggested as the mechanism of this phenomenon: capillary forces of small amounts of moisture present at contact points; cold welding at contact points; and silica solution and redeposition at asperity contacts.

Hardin (1985) studied the influence of different factors on crushing of granular materials and found that particle-size distribution, state of effective stress and effective stress path, void ratio, particle hardness and presence of water have an impact on the amount of crushing. Coop and Lee (1995) also showed that saturated specimens of Dog's Bay sand, a carbonate sand, experienced greater amount of particle breakage in comparison to dry specimens.

The significance of particle crushing in granular material was studied by Lade et al. (1996), who performed drained and undrained triaxial tests on Cambria sand under confining pressures up to 68.9 MPa. Different methods together with a new proposed method were then used to quantify the particle breakage of the tested specimens after sieving. The effect of effective stress path was also studied to see whether the amount of particle crushing was affected by comparing drained and undrained test results. It was found that the stress path followed in drained or undrained shearing did not have an impact on particle crushing as long as the same effective mean normal stress was reached. In addition, particle breakage factors were plotted versus the total energy input to each specimen and a unique relationship between these two quantities was found. This may be helpful in estimation of particle crushing based on input energy, which can be determined from numerical analyses.

Nakata et al. (1999) performed several single grain crushing tests together with triaxial compression tests with embedded marked particles to investigate the particle crushing phenomenon individually and in a soil matrix. The material tested was well distributed Aio beach sand composed of 68.7% quartz, 31.3% Orthoclase and plagioclase

feldspar with grain sizes ranging from 0.85 mm to 2 mm. It was stated that during single particle crushing tests, quartz grains split into two or three pieces. However, both kinds of feldspar were shattered into many smaller pieces which was due to a larger number of incipient flaws compared to those in quartz grains. First, the results of single particle crushing tests were analyzed utilizing the probability of survival considering both initial fracture and peak stresses. It was seen that the probability of survival was considerably higher for quartz grains. The Weibull (1951) equation, which will be explained later, was then used to normalize the test results. In order to investigate the particle crushing phenomenon in the soil matrix, several grains were colored and embedded in triaxial specimens undergoing isotropic compression and shear at the confining pressure of 2.94 MPa, 4.91 MPa and 9.81 MPa. For confining pressures of 2.94 MPa, isotropic compression caused no noticeable crushing of the grains, while all types of breakage (defined by Ramamurthy, 1969) were detected for grains in specimens consolidated to a confining pressure of 9.81 MPa. However, abrasion was not studied in single particle crushing tests.

On the other hand, shearing produced more severe crushing than isotropic compression because while a specimen is being sheared, strong force chains transmit the major principal stress, which causes higher amounts of grain crushing. For the purpose of better comparison, the probability of survival of the embedded particles was also calculated. Then, using a simple method based on the stress path, the average acting stresses on particles were found. This allowed determination of the probability of survival for single particles. As the coordination numbers were different in these two types of

tests, some discrepancies were expected. However, a good agreement was observed between grain crushing in single particle tests and in triaxial tests. Moreover, for the change in grading of the triaxial specimens, a new particle breakage factor, B_f , was proposed. This was simply defined as the percentage of particles smaller than the initial minimum grain size after the test. It was shown that there was a good fit between the diagram of B_f versus average stress on particles for triaxial tests, and the diagram of survival probability versus initial breakage stress for single particle breakage tests. Furthermore, Nakata et al. (1999) studied the evolution of the plastic yield surface due to particle crushing using the modified Cam-Clay model. They reported that, independent of stress path, all stress points on a yield surface result in the same amount of crushing. In other words, particle crushing is a function of the yield surface and independent of the stress path. Consequently, they plotted B_f versus mean effective stress and suggested that based on this diagram the mean effective stress at which particle crushing is initiated could be estimated together with a mean effective stress which is required for crushing of all particles to produce particles smaller than the minimum initial grain size.

Coop et al. (2004) studied particle breakage by performing ring shear tests on Dog's Bay sand. The ring shear test was used to prove that the particle crushing continues with increase in strains even after reaching critical state conditions where the constant-volume state is observed in triaxial tests. Test results are shown in Fig. 2.32 (a) indicating that observing no volume change in critical state is because of counteracting compressive and dilative components of volumetric strain due to particle breakage and particle

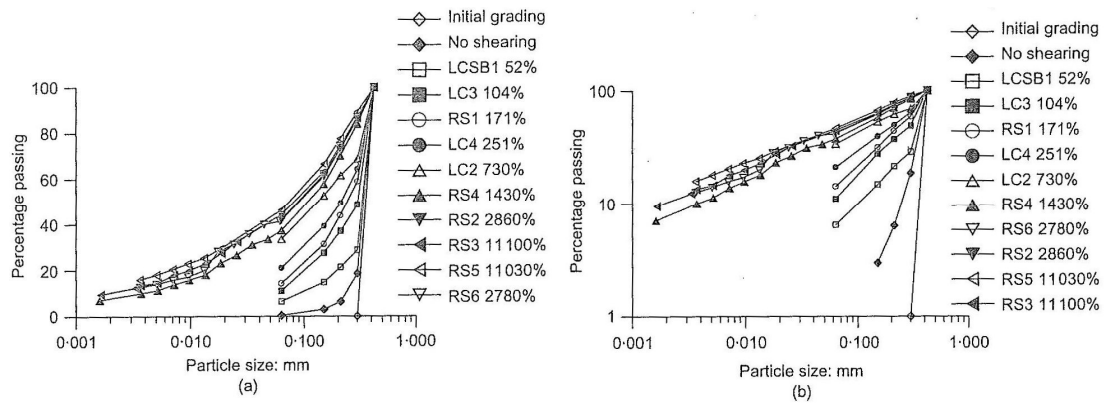


Figure 2.32. Grain size distribution curve after ring shear tests on Dog's Bay sand presented in (a) semi-logarithmic, axes and (b) double logarithmic axes (after Coop et al. 2004).

rearrangement, respectively. This implies that the assumption of reaching a stable grading at the critical state used by Been and Jefferies (1985) in the framework of their state parameter for sand was not correct. As observed in Fig. 2.32 (b), using a double logarithmic graph results in a linear particle distribution curve. This means that particle breakage follows a fractal distribution as identified by McDowell and Bolton (1998) as well. Moreover, Coop et al. (2004) stated that although the particle crushing is continued at very high shear strains, the mobilized friction angle remains unaffected at these strains as illustrated in Fig. 2.33.

In conclusion, from the previous studies, it is implied that increases in grain size, uniformity, angularity, confining pressure, shear stress and decreases in individual particle strength, hardness and coordination number give rise to particle breakage and consequently, compression of granular materials. Furthermore, as discussed later in detail, water may have a significant weakening impact on soil particles depending on the mineral constituents and physical condition of the particles.

2.3. Static Fatigue

Static fatigue is a time-dependent phenomenon that results in fracture of brittle materials such as quartz, feldspar, concrete, rock, glasses, ceramics and other similar materials. It has been observed by many researchers (Lawn, 1993; Lemaitre and Chaboche, 1994; Suresh, 1998; Callister, 2005) that sustained static stresses in brittle materials, even at considerably smaller values than their short-term strength, may ultimately lead to fracture. Specifically, Orowan (1944) suggested that if a stress about

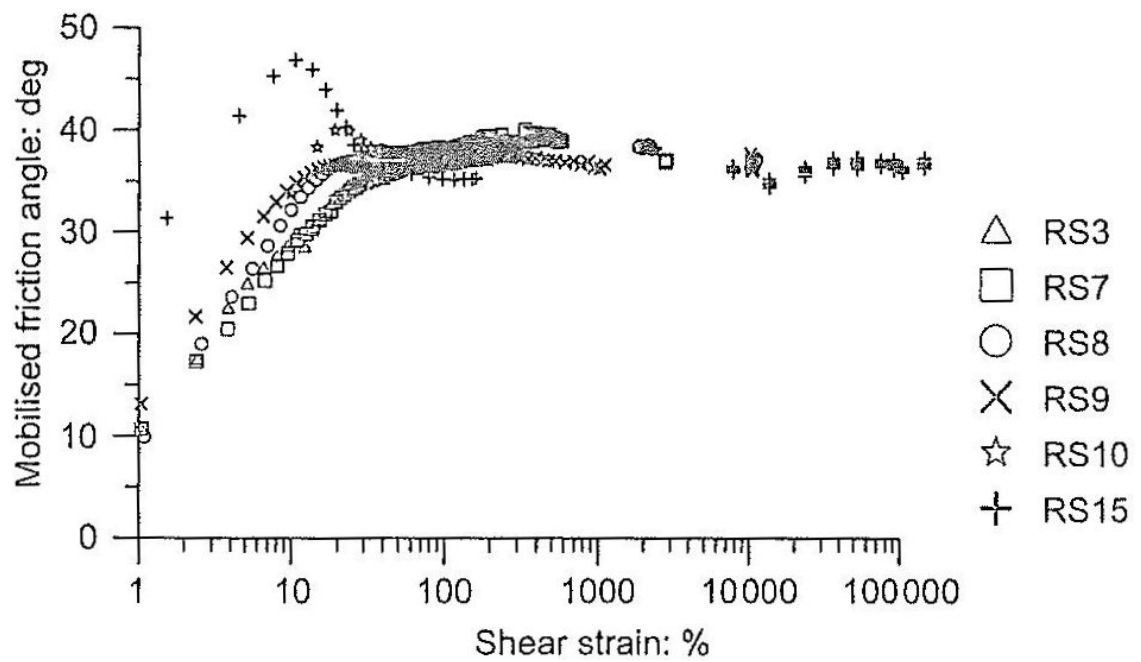


Figure 2.33. Variation of mobilized friction angle with shear strain in ring shear tests on Dog's Bay sand (after Coop et al. 2004).

one third of the short-time breaking stress of a brittle material is sustained for a number of weeks, it would be sufficient to result in fracture. However, Griggs et al. (1960) stated that at some temperature and confining pressure, most brittle materials such as rocks will become ductile. In other words, they will undergo significant amount of inelastic strain before fracture.

Fig. 2.34 illustrates the general stress-strain-time behavior of brittle solids that demonstrate static fatigue (Rüsch, 1960). It can be seen that holding the stress lower than the short-term fracture stress eventually leads to fracture provided that the stress is larger than some limiting stress that may be characterized as a percentage of the short-term fracture strength. This means that for stresses higher than this limiting value, the time-to-fracture decreases with increasing stress level.

2.3.1. Mechanism of Static Fatigue

The reason for fracture in static fatigue is crack propagation through the brittle media while deformation prior to fracture is not noticeable. At the atomic level breakage of bonds occurs when a crack grows. In fact, atomic bonds act as groups of nonlinear elastic springs which snap when they are subjected to an increase of the distance between atoms. This model is schematically shown for a sharp crack at the atomic level in Fig. 2.35.

Initiation of the crack has root in the existence of internal and surface microcracks which provide potential points of nucleation and further spread of major cracks. During

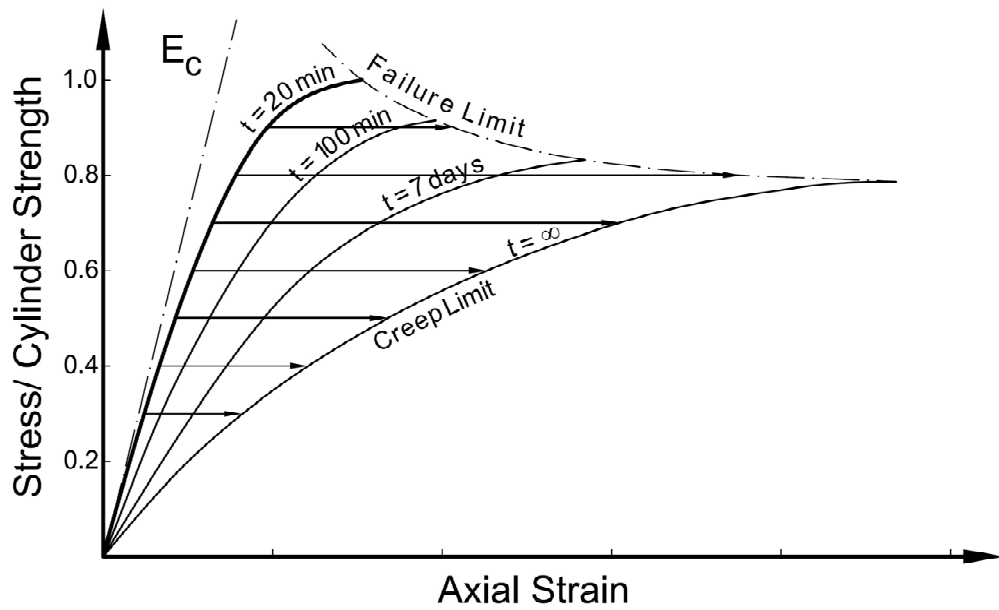


Figure 2.34. Effect of time on strength of concrete specimens (after Rüsch 1960).

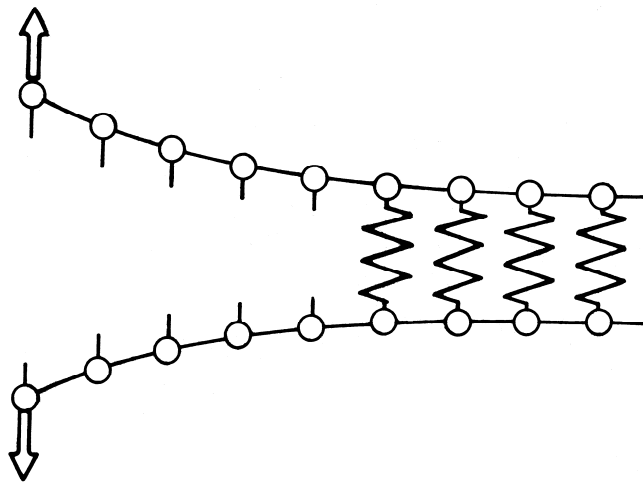


Figure 2.35. One-dimensional model of sharp crack with nonlinear crack-tip bond
(after Lawn 1993).

the process of forming rock materials, a huge number of microcracks and flaws are created. Pores and gas bubbles may also be found in any type of rock. For example, in the formation of igneous rocks, when the magma cools down from very high temperatures, residual stresses are generated at the interfaces between components with dissimilar thermal expansion coefficients and elastic properties. These stresses result in the creation of a distribution of microcracks and flaws. In a similar manner, during the formation of metamorphic rocks, microcracks are created when high temperature and pressure on the original material are diminished by emerging and exposure to chemical and mechanical weathering at the ground surface. In sedimentary rocks, a large number of microcracks exist between grains and cementing agent. In addition to the inherent defects in rocks, imposed cracks are also considerable. Rockfill is formed by blasting of solid rock and the high input energy may produce very angular particles with a large number of surface cracks created by the stress waves, especially by the tensile stress trough following the initial compressive wave from the blast.

Other than internal flaws, surface cracks may exist in brittle material. These cracks play an important role in static fatigue since the environmental aspects such as the presence of humidity or water have great influence on the speed of crack propagation, as explained later. According to Suresh (1998), three main reasons that surface cracks can be created are: (1) stationary normal loading, which results in elastic indentation and tensile stresses parallel to the surface outside the actual contact, (2) partial slip and complete sliding at the particle contacts, which leads to non-uniform shear stress

distribution and tearing parallel to the surface, and (3) rolling of particles, which results in varying normal and shear stresses underneath the contact point.

According to Wiederhorn (1975), strength of brittle materials is a function of load duration, loading rate, temperature and environment. Also, a large number of microcracks, flaws and defects in these materials greatly affect their strength. Weibull (1939) suggested that strengths of brittle materials are a statistical phenomenon. The strengths vary with size and can be calculated for specimens with the same shape as:

$$\sigma_{1ult} = \sigma_{2ult} \cdot \left(\frac{V_2}{V_1} \right)^{1/n} \quad (2-2)$$

in which σ_{1ult} is the strength of a particle with volume V_1 and σ_{2ult} is the strength of a particle with similar shape and volume V_2 . Jaeger and Cook (1969) reported that the value of the exponent n is in the order of 6-18 for different types of coal. This relation indicates that smaller particles fracture at higher stresses compared to larger particles given that there is a higher probability to enclose fewer critically oriented microcracks. Furthermore, Weibull (1951) proposed a relation that correlates the survival probability of a particle of volume V_0 , $P_s(V_0)$, to normalized stress σ/σ_0 as follows:

$$P_s(V_0) = \exp \left[- \left(\frac{\sigma}{\sigma_0} \right)^m \right] \quad (2-3)$$

where σ is the applied stress, σ_0 is a stress level where 36.8% of particles survive and m is the Weibull modulus. In accordance with experimental results of single particle crushing, $P_s(V_0)$ is defined as:

$$P_s = \frac{\text{number of particles crushed at } \sigma \geq \sigma^*}{\text{total number of particles tested}} \quad (2-4)$$

in which σ is the crushing stress and σ^* is the stress at which the probability of survival is calculated. Nakata et al. (1999) normalized the results of single sand particle crushing tests using Equation (2-3) and found the values of m equal to 4.2 and 1.8 for quartz and feldspar particles, respectively. Ashbey and Jones (1986) reported that the value of m is about 5 for brick, pottery and cement while this value is about 10 for engineering ceramics. It is noted that Equation (2-2) is a special case of Equation (2-3) where $P_s = 1/e = 0.368 = 36.8\%$.

Close inspection of the atomic bonds reveals that the required force for breakage of atomic bonds is considerably larger than the observed strengths. Griffith (1924) explained this issue by assuming the occurrence of stress concentrations at the tips of defects of the material. In his model, he stated that brittle materials behave elastically up to the point where the stress concentration at an atomic bond surpasses the necessary breakage force of the bond. This results in the breakage of the adjacent bonds and final fracture of the specimen. However, Scholz (1968a) observed thousands of microfractures at stress levels much lower than the fracture stress in compression experiments on rocks. This was contrary to Griffith's theory. Therefore, Scholz (1968a) proposed that not only

do the existence of cracks and defects produce stress concentrations leading to microfracturing, but also inhomogeneity of materials results in fluctuation of local stresses with respect to the applied stress. For instance, rocks are polycrystalline aggregates composed of many anisotropic phases. Therefore, applying uniform stress leads to fluctuation of stress through the medium. Adding the effect of the existing pores and cracks generates a higher degree of non-uniformity of stress.

Scholz (1972) broke more than 200 specimens of single-crystal quartz in uniaxial compression to investigate static fatigue. In a similar manner to other researchers, he suggested that static fatigue is due to stress corrosion cracking which is caused by hydration of Si-O bonds. This had been previously found for fused silica by Schoening (1960) and le Roux (1965).

In a fracture process, brittle solids undergo three main stages when subjected to shear loading as shown in Fig. 2.36 (after van Mier 2009). In the first stage, stress concentrations at the microscopic crack tips cause microcracks to grow in size which is shown schematically in Fig. 2.37. When loading is continued, the second stage starts and microcracks join each other and create larger cracks. Although this stage is physically stable, i.e. still additional load can be tolerated, it supplies the basis for the third stage at which eventually catastrophic fracture of the specimen happens. The third stage consists of structural instability and complete fracture of the specimen due to propagation of the larger cracks at an accelerating rate together with very little accompanying plastic

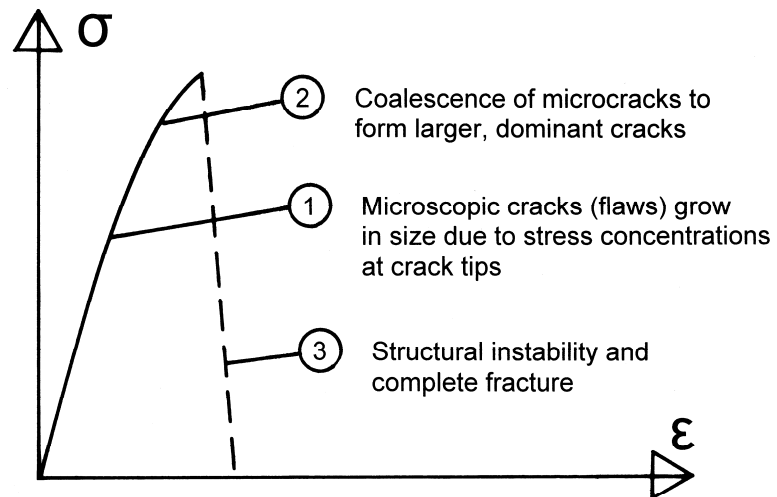


Figure 2.36. Three-stage fracture process in soil particle loaded in compression
(after Van Mier 2009).

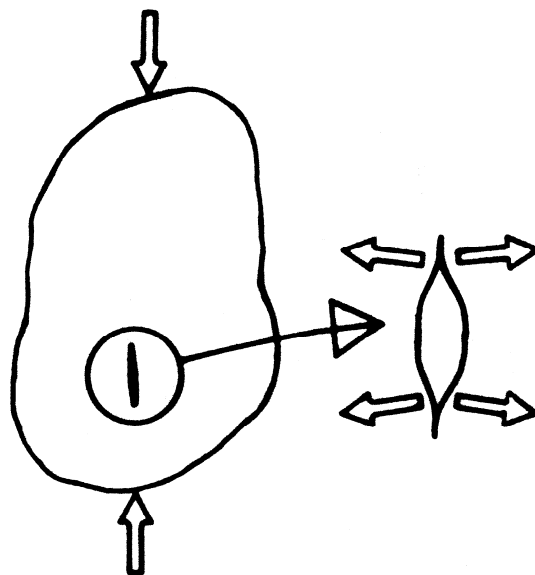


Figure 2.37. Fracture process in soil particle involving tensile stresses near crack tips.

deformation. In fact, stress corrosion causes crack growth at the sharp ends of cracks. It is mainly the strength of atomic bonds at the crack tip which essentially determines the fracture resistance.

2.3.2. Speed of Static Fatigue

Time-to-failure is defined as the time required for growth of an initial crack to a critical size. Environmental and mechanical factors greatly control the speed with which fractures propagate in brittle solids. Consequently, these factors have impact on static fatigue. Obert and Duval (1942) were the first to suggest that if cracks and microfractures propagate in brittle materials, each event may be captured by the radiation of the corresponding elastic wave. Later, Scholz (1968a) used a more sophisticated method to detect microfracture signals in a series of uniaxial and triaxial tests on various rocks. Fig. 2.38 (a) and (b) show the frequency of microfractures and deviator stress versus the axial strain for uniaxial and triaxial experiments on Westerly granite, respectively. As it can be seen, the frequency of microfracture events in brittle rocks increases as the specimen approaches its total fracture point. In the following sub-sections, the effective factors are explained in detail.

Stress Level Effect

It is obvious that stress magnitude has influence on the time-to-fracture. Higher tensile stresses cause higher propagation rate of the microcracks which results in lower time-to-fracture. Similar to the relation previously mentioned by Weibull (1939),

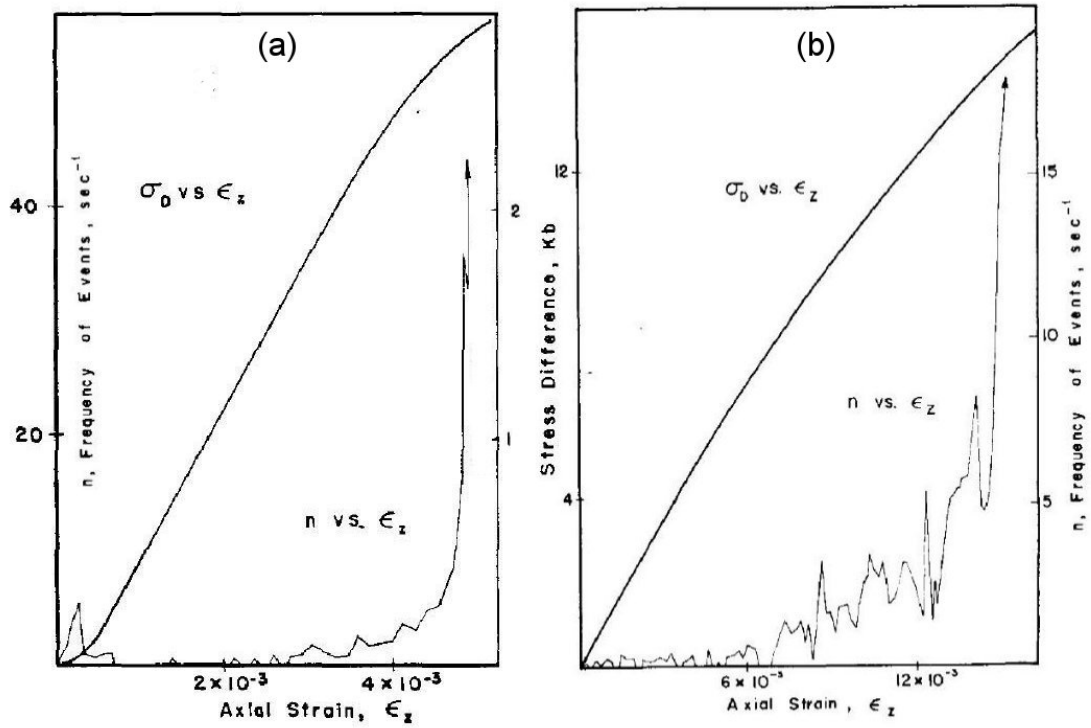


Figure 2.38. Deviator stress and microfracturing events versus axial strain for Westerly granite in (a) uniaxial test, and (b) triaxial under confining pressure of 4 kilo bars (after Scholz 1968a).

Charles (1958a) suggested a relation between tensile strength of glass specimens and time-to-fracture as follows:

$$\sigma_{1ult} = \sigma_{2ult} \cdot \left(\frac{t_2}{t_1} \right)^{1/r} \quad (2-5)$$

in which σ_{1ult} is the strength of a particle with time-to-fracture t_1 and σ_{2ult} is the strength of a particle with time-to-fracture t_2 . Typical values of $r=16$ for glass, $r=98$ for Carrara marble and $r=8$ for Pennant sandstone have been reported (Charles, 1958a; Cruden, 1974). It should be noted that considerable amounts of scatter can be observed in brittle fracture test results on single particles since there is no control of the amount of defects. However, when it is integrated over a large number of particles, like a triaxial specimen consisting of millions of particles, the time-dependent behavior is predicted to be very systematic and follow a distinct pattern. Although Scholz (1972) performed the tests in a controlled experimental condition on highly homogenous single-crystal quartz, results indicated inconsistency in the fracture time. Fig. 2.39 shows these results and as it can be observed, there is a wide range of fracture times corresponding to each constant stress level. Error bars and diamonds show the mean and median fracture time at each stress level respectively, while dots illustrate the fracture time of each individual specimen.

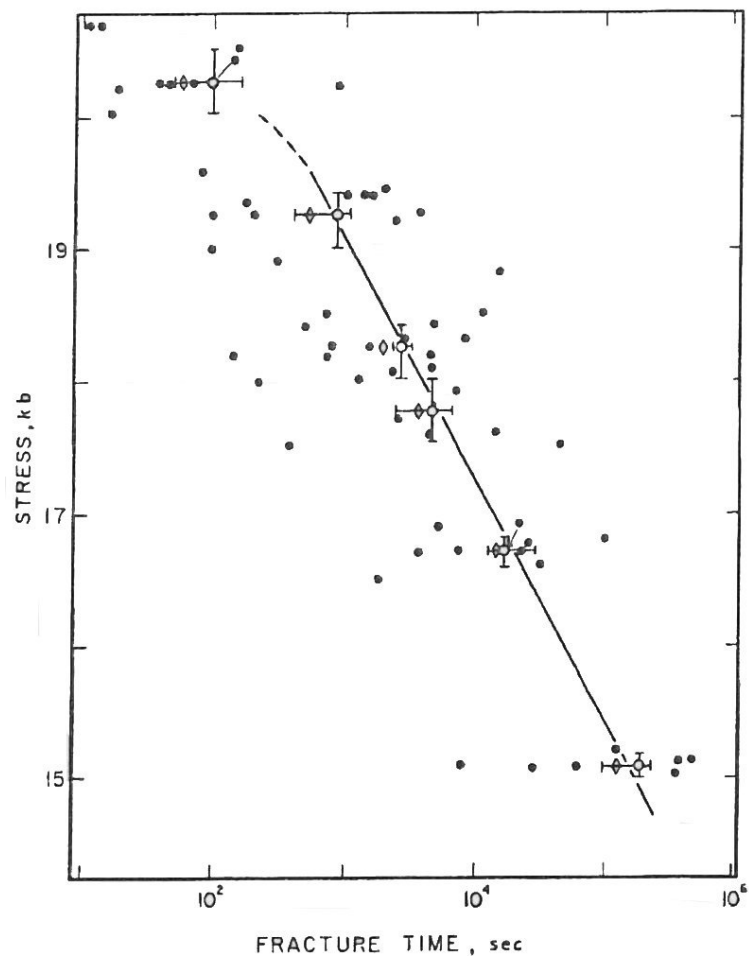


Figure 2.39. Variation of fracture time with the level of the constant stress (after Scholz 1972).

Many other researchers (e.g. Schmitz and Metcalf, 1966; Mould and Southwick, 1959; Glathart and Preston, 1946) used the following exponential equation at a constant temperature to estimate the mean fracture time, $\langle t \rangle$, according to the level of the constant stress:

$$\langle t \rangle_T = a \cdot e^{b(S^* - \sigma)} \quad (2-6)$$

In which S^* is the “no corrosion” strength or short-term strength ($t \rightarrow 0$), σ is the constant stress level, and a and b are material constants. It is seen that there is a linear relationship between the constant stress level and logarithm of mean fracture time. This equation does not stand for low values of $\sigma < 0.4S^*$ since there might be no initiation for microfracturing and crack propagation.

Temperature Effect

It has been reported that the temperature of the environment has a significant impact on static fatigue such that at temperatures as low as -196°C , no static fatigue was detected (Kropschot and Mikesell, 1957). However, at higher temperatures it was found that temperature dependency of static fatigue obeys the Arrhenius type equation as explained below. The activation energy, i.e. energy that has to be overcome for a chemical reaction to occur, has been mentioned to be between 18 and 25 kcal/mol for glass (Charles, 1958b; Charles 1961; Wiederhorn and Bolz, 1970). Charles (1959) performed several bending fracture tests on soda-lime glass rods with environment temperatures ranging from -50 to 150°C . Fig. 2.40 demonstrates the experimental results.

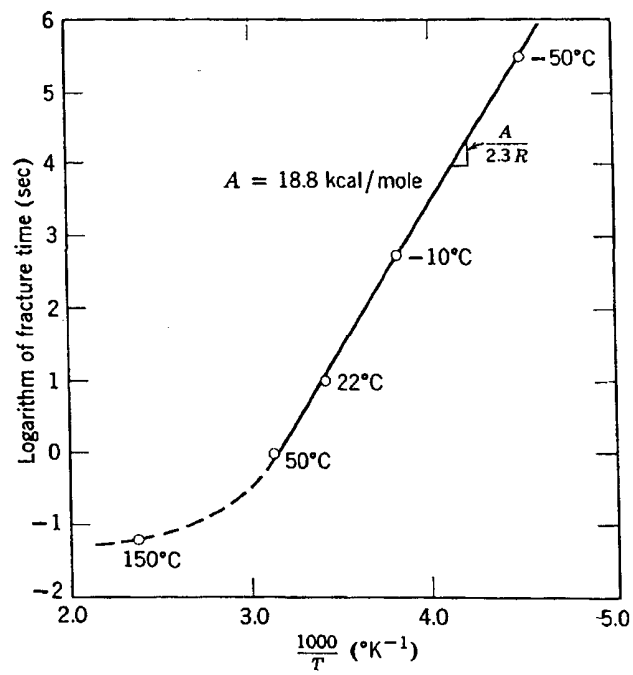


Figure 2.40. Variation of time-to-failure of soda-lime glass rods in bending with temperature (after Charles 1959)

As it can be seen, the logarithm of fracture time is decreased linearly with increase in temperature from -50 to 50°C. It is noted that the x-axis of this diagram is the temperature of the environment in a reverse order. According to Charles (1959), above this temperature corrosion holds the control of crack growth and the magnitude of the applied stress would have less pronounced effect on the static fatigue process.

Wiederhorn and Bolz (1970) studied the stress corrosion and static fatigue of different types of glass at a wide range of environmental temperatures. They noticed that increase in temperature has an enhancing effect on the velocity of cracks at a constant stress. Fig. 2.41 illustrates the same temperature curves for the variation of crack velocity at different stress levels for soda-lime silicate and silica glasses. It can be observed that, at a constant stress level, increase in temperature boosts the crack velocity. The increase in crack velocity was found to be a function of the glass composition since compared to silica glass, soda-lime silicate glass underwent a much higher increase in crack velocity for the same increase in temperature.

Similar to the observation of Wiederhorn and Bolz (1970), Scholz (1972) performed uniaxial compression experiments on quartz at two temperatures of 25 and 50 °C. Fig. 2.42 illustrates that an increase in temperature considerably enhances static fatigue and reduces the mean fracture time. The activation energy of 24 ± 6 kcal/mole was calculated for these experiments.

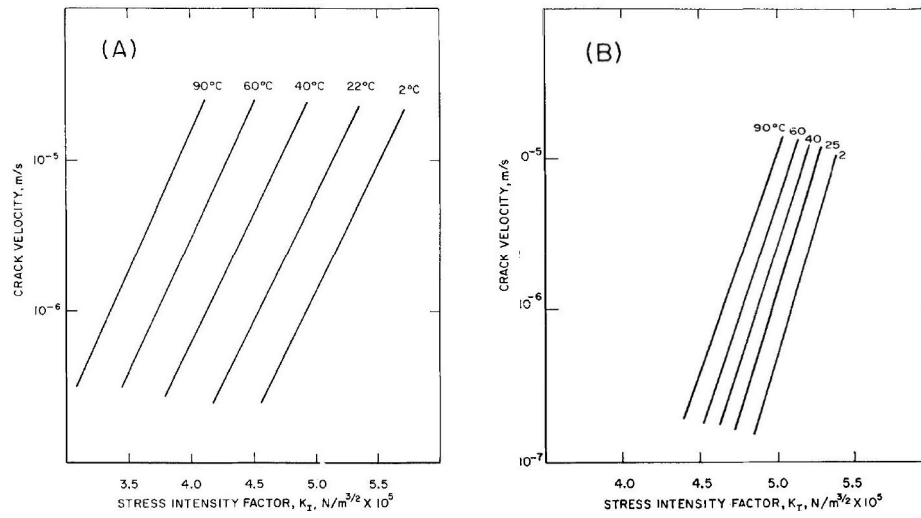


Figure 2.41. Effect of variation of the environment temperature on the crack growth of (a) soda-lime silicate, and (b) silica glass submerged in water (after Wiederhorn and Bolz 1970).

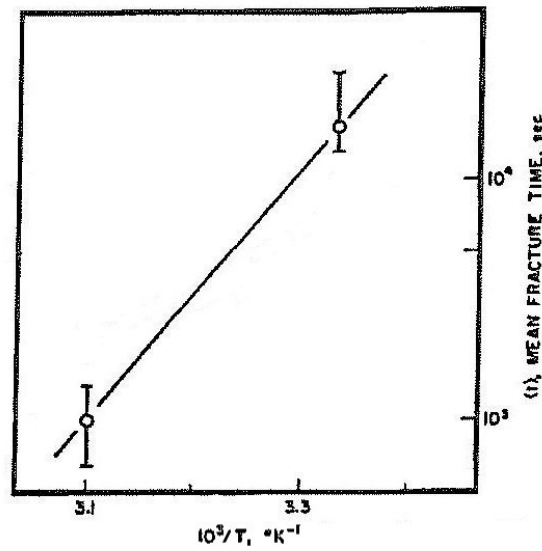


Figure 2.42. Variation of mean fracture time with temperature (after Scholz 1972).

Charles (1959) and le Roux (1965) investigated the dependency of static fatigue on the environment temperature. They proposed the following Arrhenius equation that shows the dependency of the mean fracture time on the temperature of the environment at a constant stress level:

$$\langle t \rangle_{\sigma} = c \cdot e^{u/RT} \quad (2-7)$$

where u is the activation energy for the corrosion reaction, R is Boltzmann's constant, T is the absolute temperature and c is a constant which depends on the environment and the material. However, in a study on the creep of rocks, Scholz (1968b) combined Equations (2-6) and (2-7) to predict the mean fracture time as a function of temperature and applied stress level as follows:

$$\langle t \rangle = (1/\beta) \cdot \exp\left[\frac{u}{RT} + b \cdot (S^* - \sigma)\right] \quad (2-8)$$

in which β is a constant.

Environmental Effect

It has been widely reported that the environment to which surface cracks are exposed plays an important role in the speed of crack growth during the second stage of the fracture process. It was stated that static fatigue only occurs in the presence of water (Baker and Preston, 1946a). This was confirmed during studies of static fatigue of glass in vacuum or in a dry nitrogen environment since not only was the strength found to be independent of the loading rate, but also static fatigue was not captured in the absence of

water (Baker and Preston, 1946b; Gurney and Pearson, 1949). However, the strength of glass, submerged in water, was shown to be a function of the loading rate as indicated in Fig 2.43. This, in turn, proves that crack growth causes the fracture of brittle materials.

Mould (1961) conducted a series of tests on soda-lime-silicate glass in various aqueous and organic environments. Based on the experimental results, as shown in Fig. 2.44, he reported that there is a direct relationship between the pH of the environment and the strength of glass. No significant effect was captured in the middle range of pH; however, for high values of pH, strength was considerably increased. In contrast, very low pH values resulted in lower strengths for glass. Wiederhorn (1975) confirmed that presence of chemical components as well as the pH of the surrounding environment may be a basis for accelerating the speed of stress corrosion. He explained that this is due to chemical reactions and ion exchange of the crack-tip solution.

In addition, Wiederhorn and Johnson (1973) performed crack growth experiments on three types of glass composition with pH of the environment ranging from 0.8 to 14.8. Fig. 2.45 illustrates the variation of crack growth velocity with stress intensity factor, K_I (a factor that shows the concentration of stress at the crack-tip) for different values of pH for silica glass. It is observed that the increase in pH results in a lower slope on the crack propagation curves. A better understanding can be achieved from Fig. 2.46, where the slopes of crack propagation curves have been plotted against pH of the environment.

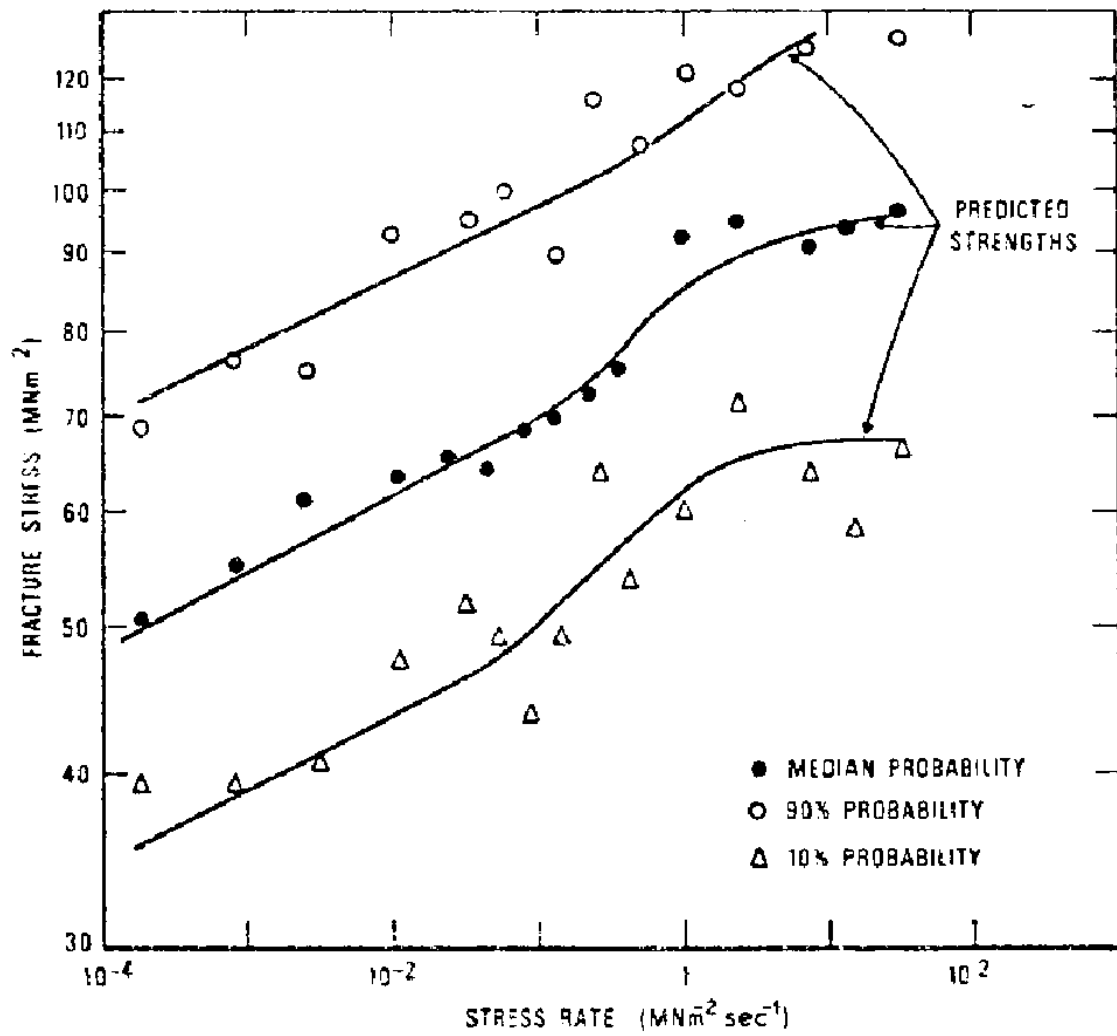


Figure 2.43. Effect of the loading rate on the fracture stress of abraded soda-lime-silica glass specimens submerged in water (after Evans and Johnson 1975).

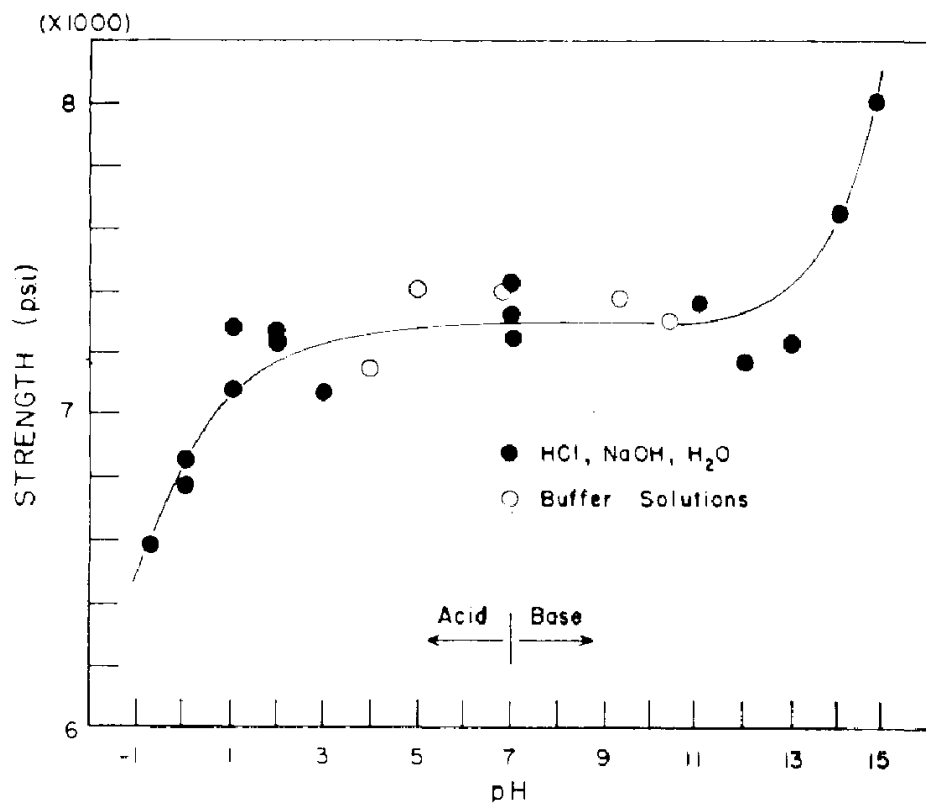


Figure 2.44. Strength at 0.82 second load duration with respect to variation of pH for specimens submerged in HCl, NaOH, and buffer solutions (after Mould 1961).

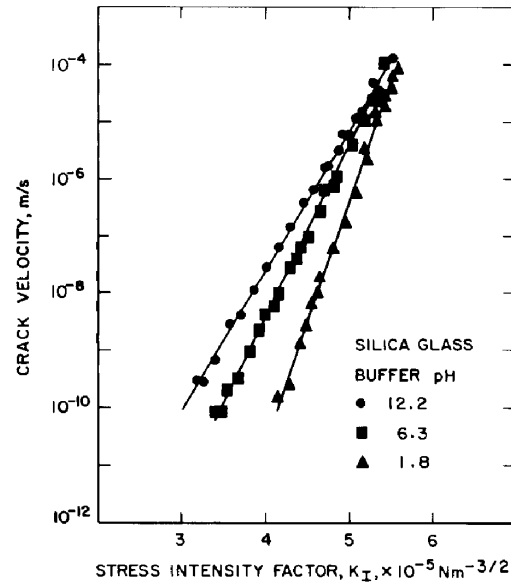


Figure 2.45. Effect of pH of the environment on the crack propagation speed (after Wiederhorn and Johnson 1973).

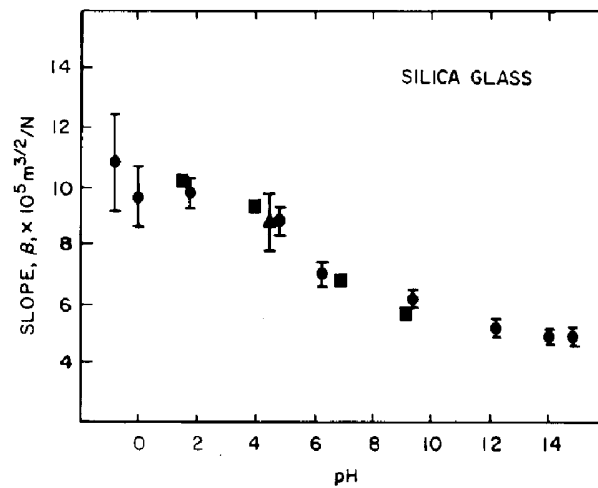


Figure 2.46. Variation of the slope of crack velocity- K_I (stress intensity factor) curves as a function of pH of the environment (after Wiederhorn and Johnson 1973).

It has been found that the existence of water or its vapor close to crack tips results in weakening and ease in tensile failure of atomic bonds due to a chemical reaction of water molecules with silica atoms. In other words, the presence of water at the crack tips may have an unzipping effect on atomic bonds as displayed in Fig. 2.47. The suggested chemical reactions happening at crack tips can be seen in Fig. 2.48 (a) for water and quartz, and in Fig. 2.48 (b) for hydroxyl and quartz in alkaline solution (Michalske and Freiman, 1981, 1983; Gong and Du, 2000). Therefore, this would have an impact on the crack propagation speed through the brittle media.

Scholz (1972) stated that stress level, presence of water (i.e. water concentration when dealing with vapor and water partial pressure in saturated conditions) in and temperature are the most significant parameters in controlling this phenomenon and presented a relation from which the mean fracture time of specimens tested can be predicted. It was also suggested that brittle creep of rocks and time-dependent earthquakes may stem from static fatigue. Test results indicated that fracture time for dry specimens was 2 to 3 times greater than submerged ones at the same experimental condition (e.g. same stress level and temperature). As a case in point, Fig. 2.49 illustrates the frequency of microfractures for a specimen at 25 °C and a stress of 18.25 MPa versus time and the effect of introducing water. It is seen that as soon as water is introduced, the number of microfractures jumps rapidly more than 40 times.

Observation of the effect of water on the enhancement of static fatigue led to the establishment of a new relation in which the mean fracture time is a function of water concentration, environment temperature and magnitude of the applied stresses:

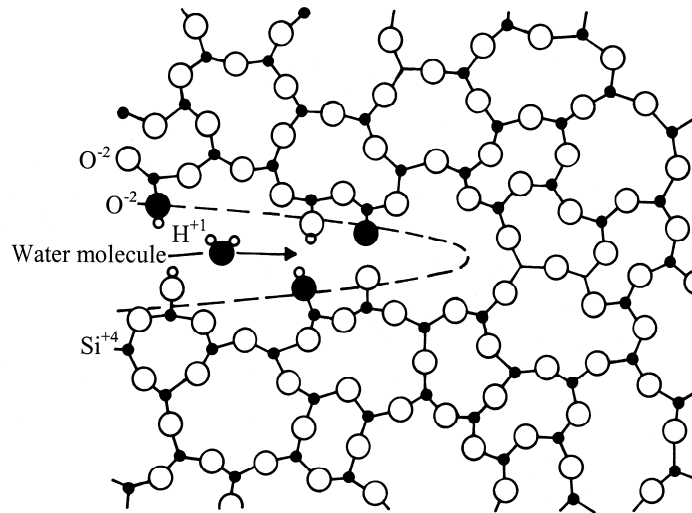


Figure 2.47. Two-dimensional model of water-induced bond rupture in silica glass
(after Lawn 1993).

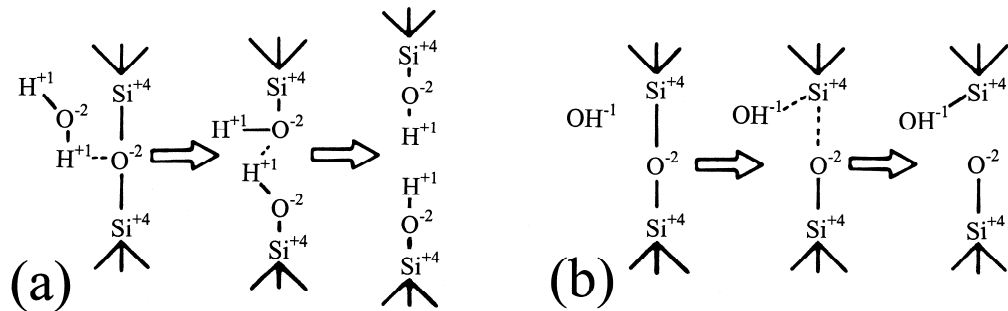


Figure 2.48. Schematic representation of chemical reactions at crack-tip between (a) water and quartz, and (b) hydroxyl and quartz in alkaline solution (after Michalske and Freiman 1981 and Gong and Du 2000).

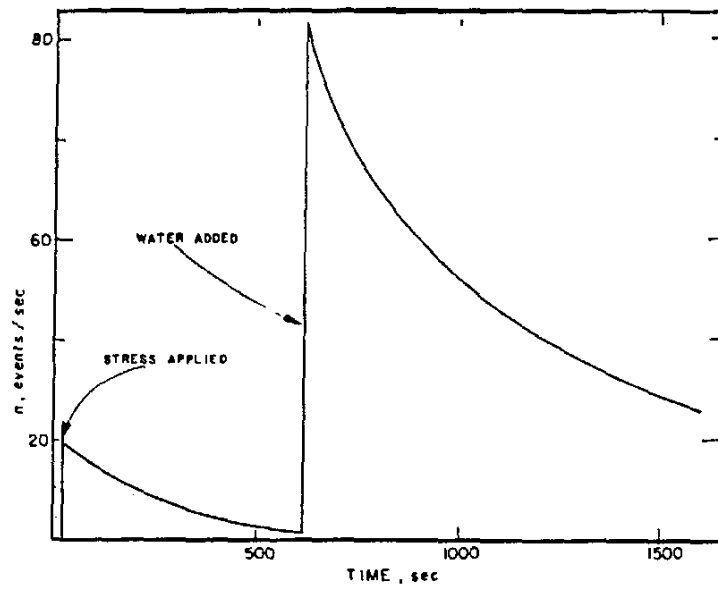


Figure 2.49. Change in frequency of microfracturing events with time. Water is introduced at $t=600$ seconds (after Scholz 1972).

$$\langle t \rangle = t_0 \cdot C_{H_2O}^{-\alpha} \cdot \exp\left(\frac{u}{RT} - k\sigma\right) \quad (2-9)$$

where t_0 , α , u (activation energy), and k are material constants while C_{H_2O} , R , T and σ are water concentration, Boltzmann's constant, environment temperature and applied stress, respectively. C_{H_2O} was replaced with P_{H_2O} , the partial pressure of water, when specimens were submerged in water.

2.4. Effect of Water on Geomaterial Properties

The effect of water on different properties of material has been a controversial issue in geotechnical engineering. Although studies by Rutledge (1947) and Nash (1953) showed that the degree of saturation has no effect on critical void ratio and strength in granular material, Bishop and Eldin (1953) recorded a consistently higher internal friction angle for dry triaxial specimens in comparison to saturated ones in drained tests at a confining pressure of 5 psi. It was stated that the difference was about 5° and 2° for dense and loose sand, respectively. Performing large scale triaxial tests on natural talus rock debris, Zeller and Wullimann (1957) reported that specimens with only 5% water content show 10% to 30% lower strengths than dry specimens and concluded that the lubrication feature of water at particle contact points is the key for this reduction of strength. In another study, Oldecop and Alonso (2007) studied the influence of water on the time-dependency of rockfill material and observed that the settlement of rockfill dams with time can be very well explained in terms of the water-enhanced static fatigue.

However, within Materials Engineering, it is known that the physiochemical properties of the surrounding environment of brittle materials like glass have an important influence on the surface energy, α , expressed in J/m^2 or N/m . Surface energy quantifies the excess energy of a surface of a material in comparison to the bulk. In other words, surface energy can be described as the extra energy required to keep a surface of a material from changing. This means that the surface is less demanding to absorb energy than the bulk; otherwise, there would be a tendency for new surfaces to be created as it is the case in sublimation phenomenon. Fischer-Cripps (1997) has suggested that the minimum critical load to failure can best explain the amount of fracture surface energy. For liquids, this energy is the same as the surface tension and it is measured by the contact angle of a drop of a liquid with a surface. The smaller this angle is, the lower the surface energy will be. This issue is of importance in industry for the purpose of filling holes with penetrants. Better penetrants are recognized as having lower surface tension (surface energy) to be able to seep into gaps and cracks. An alternative method of measuring surface energy for a liquid is by stretching the external layer of a drop of that liquid. This increases the surface area by A and the surface energy density by $\alpha \cdot \delta A$. Therefore, measurement of applied energy and increase of the area would enter into the calculation of surface energy.

However, neither of the aforementioned methods can be applied to solids. In the former method, the material needs to be as a liquid, while in the latter method stretching of the solid involves elastic energy of the bulk. Therefore, for solids measurement of surface energy is performed at high temperatures where the solid can freely deform

(avoiding elastic energy to be developed) with a change in surface area by applying a constant uniaxial tension (change in the volume is considered to be zero). Considering a cylindrical rod with the length of l and radius of r pulled with an axial tension of σ under an equilibrium condition, the surface energy is calculated as follows:

$$\alpha = \frac{\sigma \cdot l}{\pi \cdot r \cdot (l - 2r)} \quad (2-10)$$

In this regard, Orowan (1955) suggested a relation that predicts the failure strength of brittle materials with pre-existing cracks as follows:

$$\sigma = \sqrt{E \cdot \alpha / 2c} \quad (2-11)$$

where σ is the tensile strength of an ideal brittle material, E is the young modulus, c is the depth of surface cracks. Orowan (1944) measured the surface energy of mica in vacuum and air as 4500 and 375 erg/cm², respectively (1 erg=10⁻⁷ J). Applying these values to Equation (2-11) reveals the importance of the environment on the strength of brittle material as it results in 3.5 times higher tensile strength in vacuum than in air. According to the chemical similarity between mica and glass, a similar ratio can be expected. Experimental studies of Schurkow (1932) confirmed that silica glass fibers broken in air showed 3.5-4.5 times lower strength than in vacuum. Orowan (1944) mentioned that adsorbed films of air and moisture penetrating into the cracks are responsible for this reduction in strength.

It can be seen that only surface energy changes with variation in the environmental condition of the brittle material. Also, Hammond and Ravits (1963)

experimentally studied the variation of tensile strength of silica rods surrounded by different types of vapors and found that Orowan's equation can be clearly applied to silica and its strength reduction when it is exposed to water. They postulated that the strength of fused silica is the highest in vacuum and the lowest in water vapor.

Terzaghi (1960) provided an explanation regarding the increase in crushing of rocks in the presence of water. He mentioned that water has a softening effect on mineral bonds. This is similar to the reduction of rock strength caused by saturation. This hypothesis was followed by an extensive case study in which Sowers et al. (1965) presented the results of the settlements of eleven earth dams which settled between 0.25 to 1.0 percent of their initial height after reservoir filling. In addition, their experiments on broken rocks showed that introducing water increases the rate and amount of crushing and subsequent compression. They postulated that the idea of Terzaghi (1960) does not sufficiently explain the impact of water on rocks and mentioned that addition of water into the microfissures in highly stressed contact points results in increase in the stress level and local fracture of grains. In a similar study, Høiestøl et al. (1965) monitored the settlement of Venemo Rockfill Dam in Norway and realized that the settlement of a dam from a few millimeters per week increased to 15 mm per week right after reservoir filling; this was also confirmed by using a 1-ft diameter consolidometer to perform experiments on the same type of material.

Lee et al. (1967) studied the effect of moisture on the strength of Antioch Sand (very similar to Sacramento River Sand) and realized that the presence of moisture can considerably impact the strength of granular materials. An extensive number of tests over

a wide range of confining pressures was performed on oven dried, air dried and saturated specimens. According to the test results, both strength and stiffness of oven dried specimens were higher than saturated specimens while the air dried specimens had an intermediate value. This is shown in Fig. 2.50 and Fig. 2.51 where the maximum principal stress ratio and the initial tangent modulus versus confining pressure are presented for these three types of specimen.

Sieve analyses of specimens after the tests showed that saturated specimens experienced more crushing than oven dried specimens for the same type of tests. This was in accordance with dry specimens exhibiting higher rates of dilatancy. These observations all confirmed that water has a significant effect on weakening the particles, and this results in more particle crushing and drop in shear strength and stiffness of Antioch Sand. The same tests were performed on various types of sands and similar results were attained, except for Ottawa sand which showed no dependency on presence of water. These results have been summarized in Table 2.2. It was proposed that the mechanism by which water affects stiffnesses and strengths consisted of water absorption by the very thin clayey films which separate and have a weakening effect on the behavior of the sand.

To throw further light on the effect of presence of water on the behavior of granular materials, Lee et al. performed additional creep tests during which the stress level of oven dried and air dried specimens were kept constant for a specific amount of time and then water was introduced into the specimen. In these tests, confining pressures

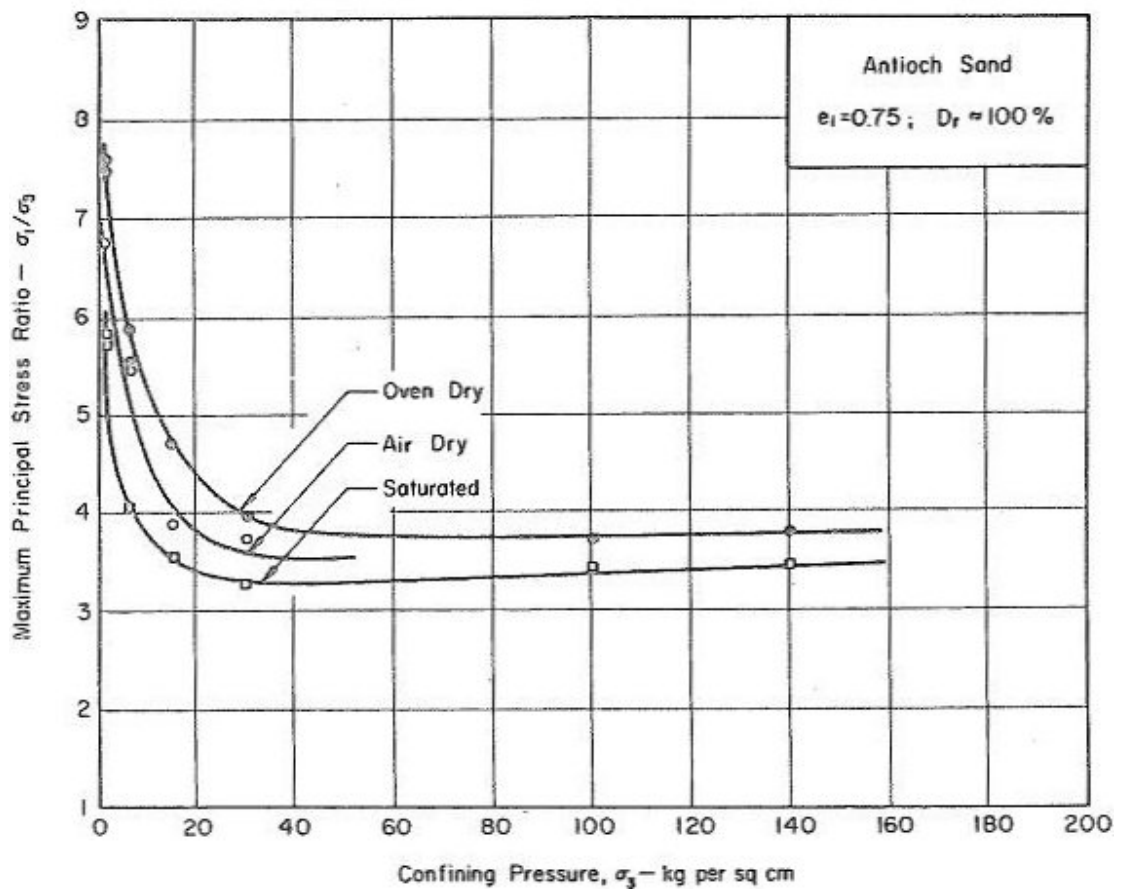


Figure 2.50. Variation of drained maximum principal stress ratio with confining pressure at different moisture conditions (after Lee et al. 1967).

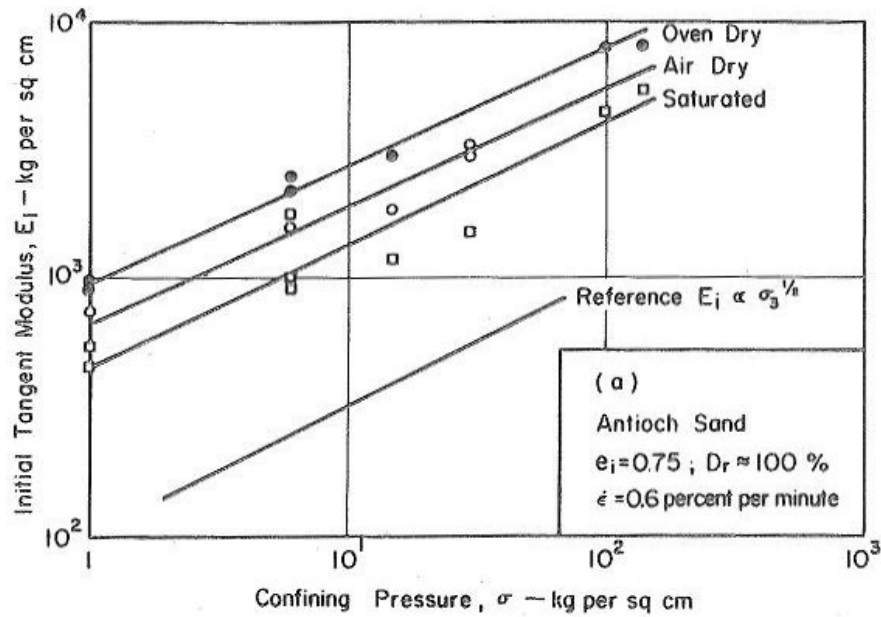


Figure 2.51. Variation of initial tangent modulus with logarithm of confining pressure at different moisture conditions (after Lee et al. 1967).

Table 2.2. Comparison of deviator stress of various types of sand under dry and saturated conditions (after Lee et al. 1967).

Sand	Confining Pressure, in kilograms per square centimeter	Drained Strength $(\sigma_1 - \sigma_3)_{\max}$, in kilograms per square centimeter		Ratio of Strengths Oven Dry Saturated
		Oven Dry	Saturated	
Antioch	1.00	6.60	4.70	1.41
Antioch (No. 50 to No. 100 sieve)	6.0	28.0	18.5	1.51
Sacramento River (No. 50- No. 100 Sieve)	1.00	5.70	4.90	1.16
Monterey (No. 20-30 sieve)	6.0	25.0	23.9	1.05
Ottawa (No. 20-30 sieve)	1.00	3.10	3.10	1.00

were applied to the specimen, followed by rapidly applying desired deviator stress and subsequently creep tests were initiated. As an illustration, Fig. 2.52 shows the effect of introducing water after 20 min and 1170 min of sustained load. In almost all cases of introducing water into the soil, the specimens failed. However, repeating these tests on Ottawa sand showed no effect of water, also indicated in Table 2.2. The main difference between Ottawa sand and other tested materials was that Ottawa sand particles had rounded shapes and the grains were free of minute cracks. Therefore, it was concluded that the presence of microscopic cracks is required for water to affect the sand behavior. This was analogous to the mechanism proposed by Sowers et al. (1965). It was also suggested that effects of water on the behavior of granular material would be more visible at elevated confining pressures as the fractures in particles at the contact points may help the occurrence of this phenomenon.

In an extensive research study, Miura and Yamanouchi (1975) investigated the influence of water on the mechanical properties of quartz sands by performing high confining pressure triaxial tests on both dry and saturated specimens. From the ratio of the volumetric strain of saturated specimens to dry specimens, they postulated that saturated specimens compressed more than dry specimens. In other words, saturated specimens underwent more particle crushing (crushing was quantified with percent finer than of 74 micron), as illustrated in Fig. 2.53.

Fig. 2.54 shows that the ratio of deviator stress of saturated specimens to dry specimens is less than unity for a wide range of confining pressures. This means that saturated specimens had a lower deviator stress at failure.

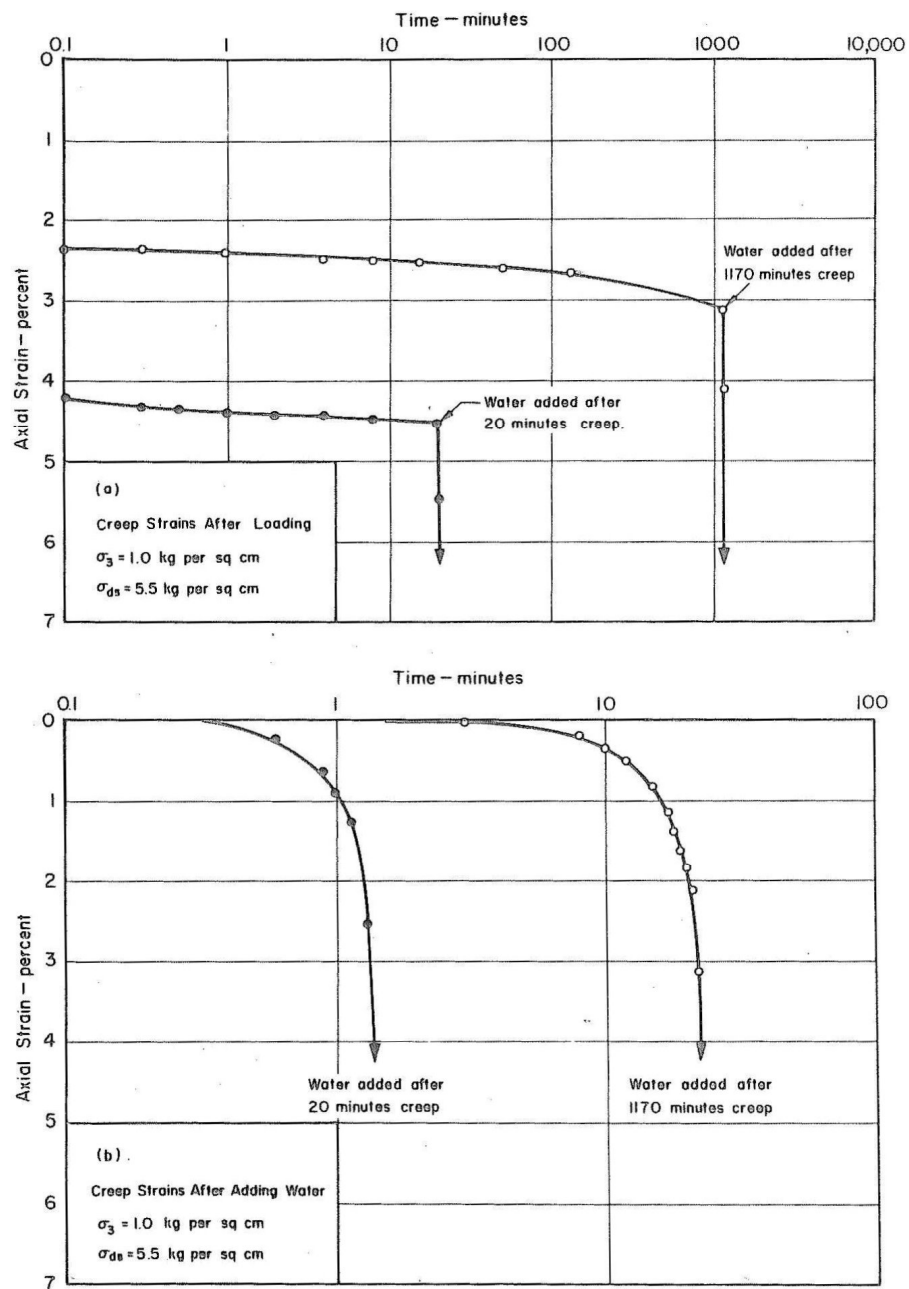


Figure 2.52. Effect of introducing water on the creep behavior of oven-dried Antioch sand specimens (after Lee et al. 1967).

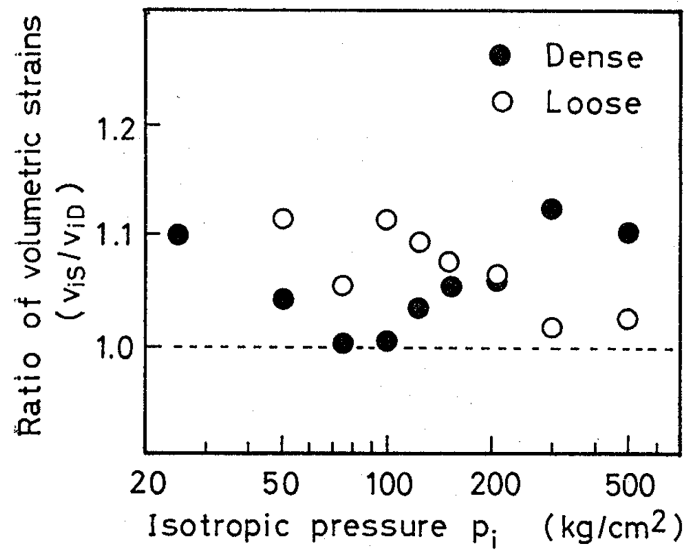


Figure 2.53. Variation of volumetric strain of saturated to dry specimens with logarithm of confining pressure (Miura and Yamanouchi 1975).

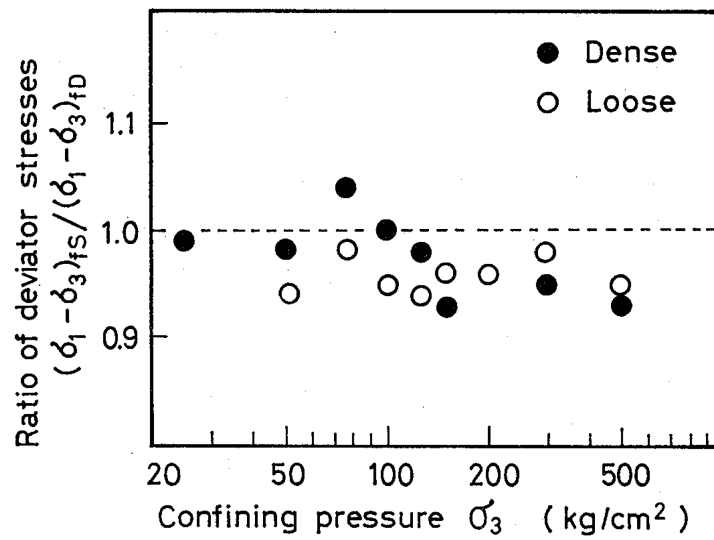


Figure 2.54. Variation of ratio of deviator stress of saturated to dry specimens with the logarithm of confining pressure (Miura and Yamanouchi 1975).

Fig. 2.55 shows that according to the sieve analyses after each test, the presence of water serves as an accelerating agent in particle crushing of sand. The hypothesis proposed by Miura and Yamanouchi (1975) regarding the effect of water on particle crushing was based on the suggestion by Orowan (1955). They mentioned that high stresses at contact points of particles cause induced cracks (there can be some intrinsic surface cracks as well). When the surrounding water enters a fresh crack, adsorption of water molecules causes release of the strain at the crack tip and reduction of the surface energy of the crack, which may lead to further growth of the crack. To prove this hypothesis, water and some other types of liquid as well as vacuum were used in the experiments performed by Miura and Yamanouchi (1975). The results showed that among all fluids tested, water had the greatest effect on the amount of particle crushing, and this was considered to be due to its high polarity, low viscosity and small molar volume of the water molecules. The effect of water was also investigated by changing the way the specimens were prepared. The following five methods were chosen: saturation by boiling, submerging for 10 min, boiling and air-equilibrating, oven-drying and air equilibrating, and oven-drying. Fig. 2.56 illustrates the variation in the amount of crushing at various confining pressures for different preparation methods. Specimens that had been saturated by boiling underwent the greatest amount of crushing, while the oven-dried specimen experienced the least crushing. This implies that higher degrees of water penetration into microscopic cracks of the specimen particles results in higher amount of crushing.

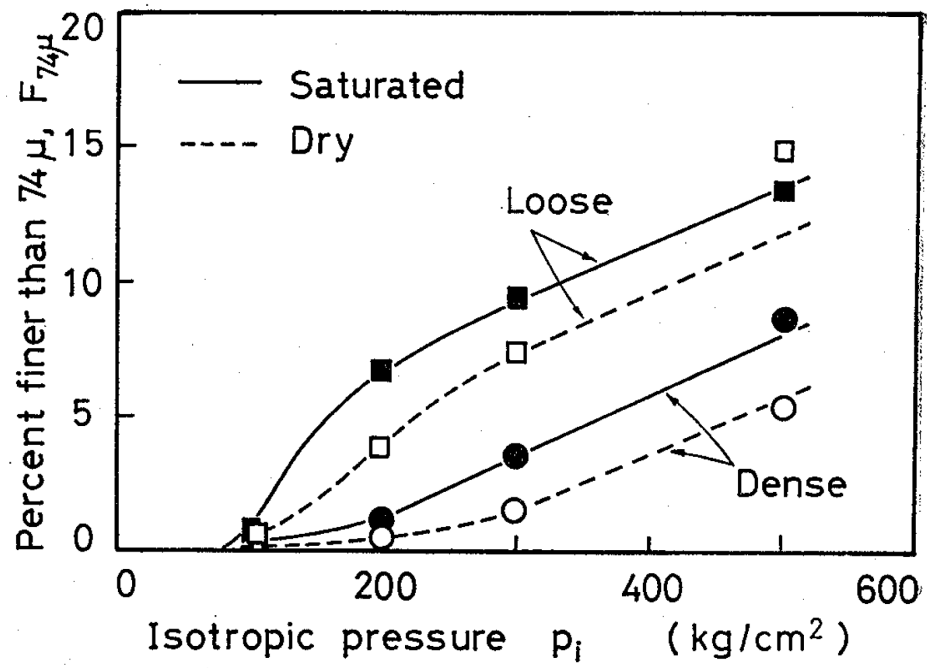


Figure 2.55. Change in degree of particle crushing with confining pressure for dry and saturated specimens (Miura and Yamanouchi 1975).

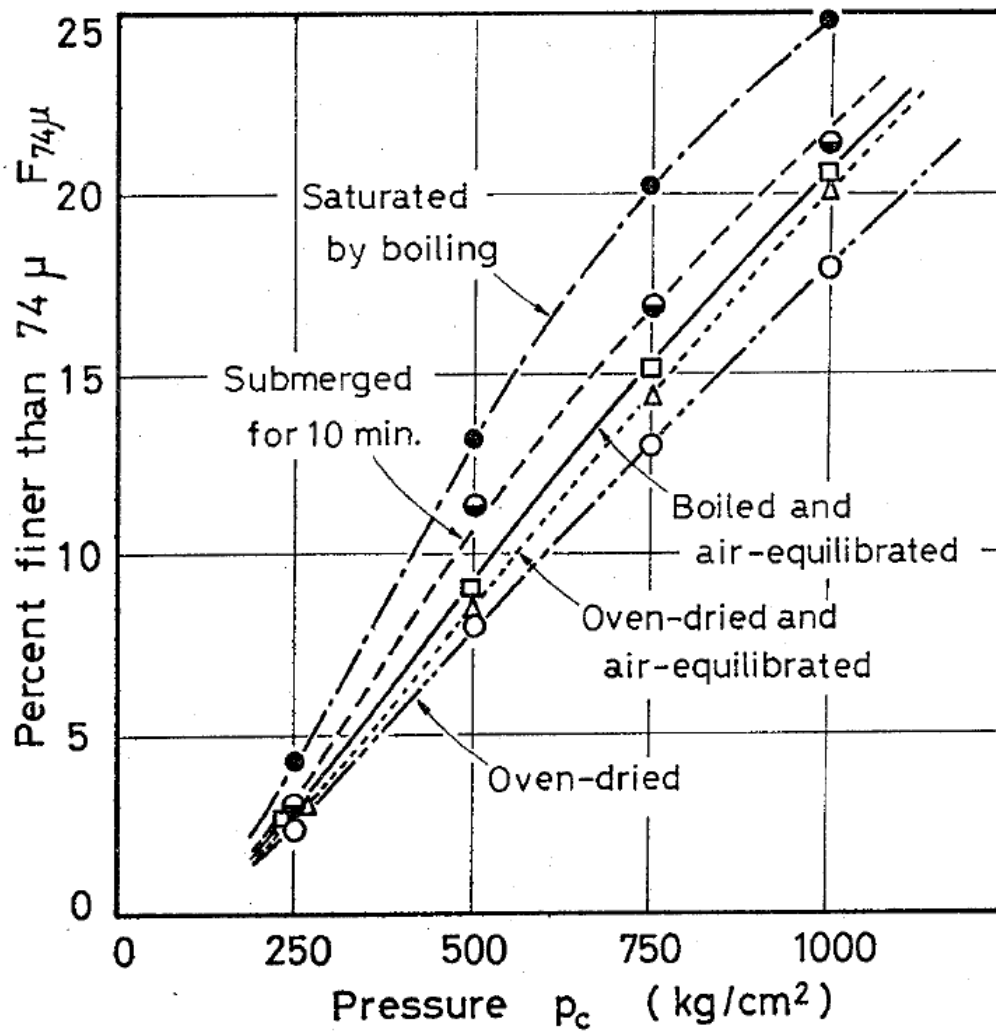


Figure 2.56. Variation of amount of particle crushing with one-dimensional pressure for different levels of presence of water (Miura and Yamanouchi 1975).

Ham et al. (2010) investigated the effect of presence of water on different minerals by performing single-particle and one-dimensional compression tests. Fig. 2.57 illustrates the schematic plot of force-displacement for a single-particle crushing test. According to this figure, they defined the first peak load, F_c , representing a force at the first breakage (fracturing of corners and surficial portions of the particle) and the maximum peak load, F_f , corresponding to the total fracture of the single particle. Dividing these two loads by the square of the initial height of the particle results in the first crushing strength, σ_c , and the maximum crushing stress, σ_f , respectively.

Results of single-particle tests confirmed that for quartz, feldspar and mica the average maximum crushing strengths were almost similar for wet and dry conditions. However, for quartz and feldspar, the average first crushing strengths were considerably lower for wet than for dry cases. This can be seen in Fig. 2.58 where the probability of survival has been plotted against the first and maximum crushing strength.

The probability of survival has been calculated according to Equation (2-4), where σ can be either the first crushing strength or the maximum crushing stress. Parameter m , denoted in Fig. 2.58, is the Weibull modulus as used in Equation (2-4). Furthermore, several one-dimensional compression tests were performed on three types of decomposed granite soil together with silica sand. It was seen that the behavior of all of the aforementioned granular materials were influenced by the presence of water. Fig. 2.59 shows the $e\text{-log}(\sigma_v)$ for these tests. Observations showed that for wet specimens of decomposed granite soils no clear break-point was recognized. The same trend can

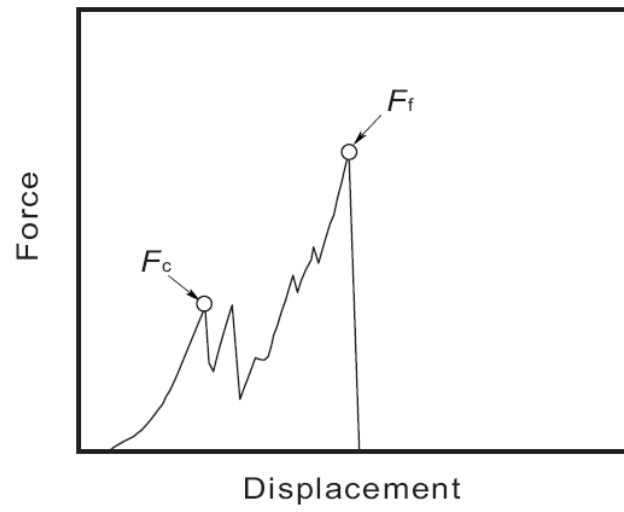


Figure 2.57. Schematic plot of force-displacement for single particle crushing test and definition of first peak load and the maximum peak load (after Ham et al. 2010).

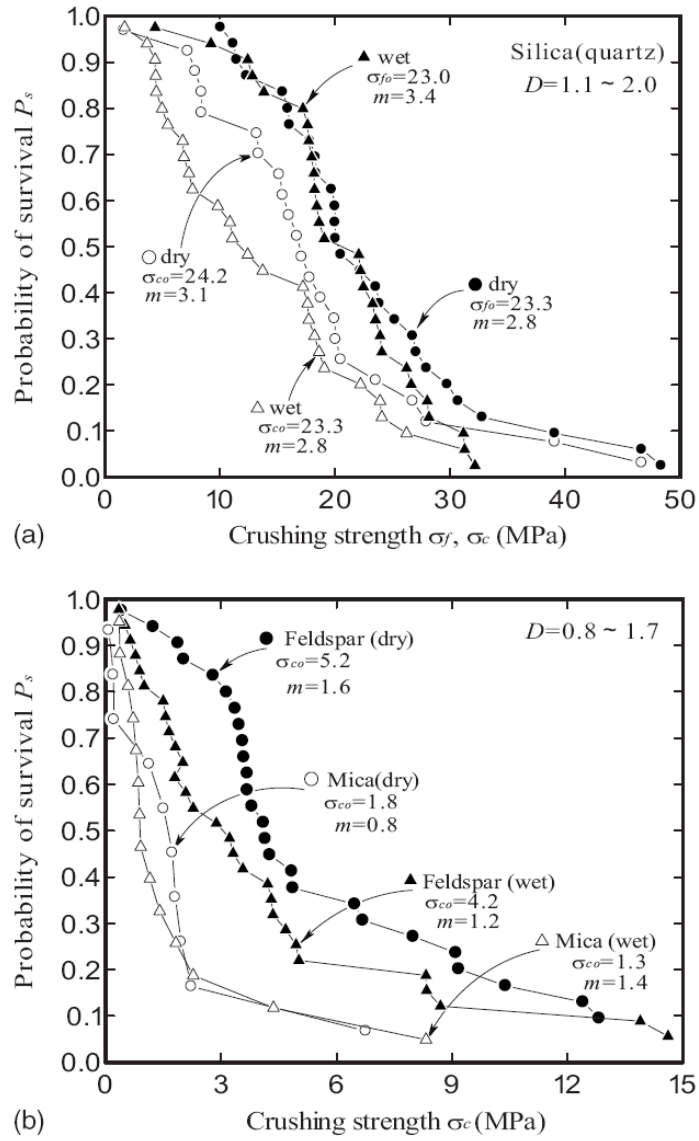
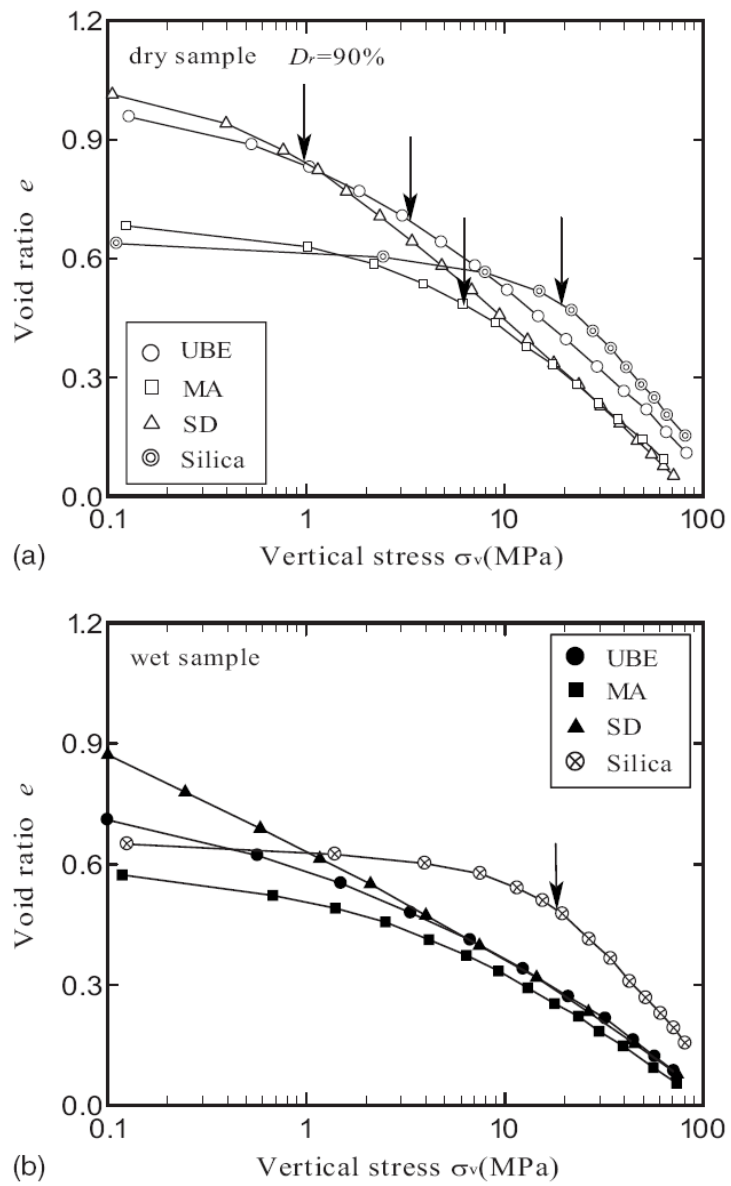


Figure 2.58. Comparison of probability of survival for particle crushing under dry and wet conditions for (a) Silica, and (b) Feldspar and Mica (after Ham et al. 2010).



**Figure 2.59. One-dimensional consolidation test for (a) dry , and (b) wet specimens
(after Ham et al. 2010).**

be seen in Fig. 2.60 which shows stress-strain behavior in one-dimensional compression tests. They stated that the presence of water has two effects. First, water lubricates the contact points of grains and avoids interlocking between grains; second, it lowers the crushing strength of individual grains.

2.5. Constitutive Models Incorporating Time Effects or Particle Crushing Effects

A large number of constitutive models have been proposed in the literature and many of these models may incorporate time-dependent phenomena or effect of evolution of the grading as time elapses. Each model may have some limitation or advantage over the other ones. This depends on the conditions for which the specific model is constituted. The aim of this study is to carry out an experimental program as a basis for generation of more realistic constitutive models which account for the mechanism of time effects; therefore, only a brief description of existing models is presented. Liingaard et al. (2004) have extensively investigated and classified these models into three main categories of empirical models, rheological models and stress-strain-time models. They concluded that these models and concepts could be utilized only for isotach materials whose behavior has been explained previously. The reader is referred to the study by Liingaard et al. (2004) for more detailed information.

2.5.1. Empirical Models

In general, empirical models are based on closed-form solutions of relations which have been achieved from fitting experimental data; therefore, they are greatly

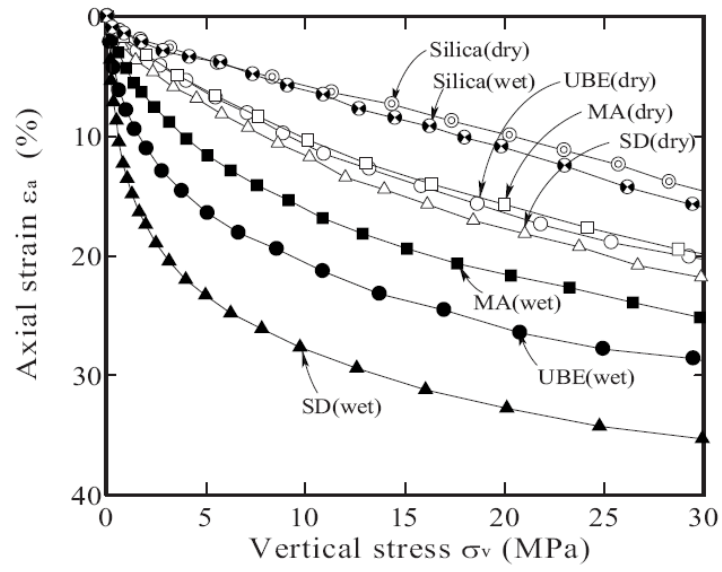


Figure 2.60. Stress-strain behavior in one-dimensional consolidation test under dry and wet conditions (after Ham et al. 2010).

affected by boundary and loading conditions. However, these models are widely used because of their simplicity in application for many practical problems in which similar boundary conditions are present. They could also be used as the basis of more complicated and advanced models. Empirical models are categorized into two basic groups of primary and secondary models, of which the latter usually consists of a combination of the former models.

Examples of Primary Empirical Relations

These relations are achieved based on a straight fitting of experimental data with mathematical equations. The following models are considered as primary empirical relations:

Semi-Logarithmic Creep Law:

This model is based on curve fitting of secondary consolidation curves extracted from one-dimensional consolidation tests (oedometer test). Depending on the assumptions, it correlates the logarithm of time by means of one or two coefficients, which may be considered functions of time, to void ratio change or vertical strain and/or vertical effective stress (Mesri, 1973; Mesri and Godlewski, 1977; Yin, 1999). However, application of this type of model is in practice limited to one-dimensional conditions from which they have been derived.

Singh and Mitchell's Creep Model:

This model was developed by Singh and Mitchell (1968) based on the analyses of drained and undrained triaxial creep tests on different types of clays, and it connects the axial creep strain rate to time and stress level by three parameters which are considered as soil properties. One parameter is defined to model whether the relation between axial strain and time whether it is linear or nonlinear. The second parameter controls the impact of stress level on axial creep strain, while the third parameter works as a scale fitting parameter. Although this model is better than the semi-logarithmic model as it can capture fading and non-fading creep behavior, it involves a constant level of stress in a one-dimensional condition and it is valid for the first time loading only.

Lacerda and Houston's Relaxation Model:

Lacerda and Houston (1973) proposed a model to predict the relaxation behavior of clays. They utilized a similar equation as that used by Singh and Mitchell (1968) for creep; however, instead of linear reduction of deviator stress with time, it is linearly reduced with the logarithm of time. Therefore, a relationship between stress relaxation and creep parameters can be achieved. Also, a term “delay time” was defined as the time between the initiation of the relaxation test (when further deformation is stopped) and the moment that stress begins to drop. This “delay time” was found to be directly related to the shearing strain rate. Lade et al. (2009, 2010) observed “delay time” in crushed coral sand and reported its dependency on shearing strain rate applied prior to initiation of creep and relaxation tests. Similar to Singh and Mitchell's Creep Model, the model

proposed by Lacerda and Houston (1973) can be used in one-dimensional analyses. Although the measured pore pressure generation during the relaxation tests was practically zero, they performed their tests in the undrained condition. Since the relationship between reduction of stress level and the logarithm of time is linear, this model is incapable of predicting fading stress relaxation. In other words, the stress will be reduced as long as the time is increased.

Prevost's Relaxation Model:

This model was proposed by Prevost (1976) based on a series of undrained triaxial tests on saturated clay performed at constant strain rate, and it incorporates six input parameters. Analogous to all aforementioned models, its application is limited to one-dimensional conditions. In addition, in this model, the final level of stress reduction is an input parameter which makes the model difficult to apply. However, the fading nature of stress relaxation can be captured. Silvestri et al. (1998) utilized Prevost's Relaxation formula to predict undrained relaxation of a soft sensitive clay.

Strain Rate Approach:

In this approach, which was originally proposed by Suklje (1957), and later extended by Leroueil et al. (1985), independent of stress-strain-time path prior to the current stress level, the vertical effective stress and strain are uniquely correlated for a given constant strain rate. Since this concept has been developed based on results of tests on normally consolidated clays, and plastic deformations are of importance in this range, there may be a significant deficiency when it comes to heavily overconsolidated clays in

which the elastic deformations may be dominant. Also, it should be mentioned that no rebounding conditions have been considered in this approach; therefore, it cannot be applied to unloading conditions of clays or even to relaxation cases under constant strain. The principal advantage of this approach is the direct connection of viscous properties to the primary deformation properties.

Examples of Secondary Empirical relations

A brief description of Kavazanjian and Mitchell's (1977), Tavenas et al.'s (1978), Bjerrum's (1967), and Yin and Graham's (1994) models are presented as follows:

Kavazanjian and Mitchell's Model:

This model was presented by Kavazanjian and Mitchell (1977) and is the advanced version of Singh and Mitchell's Creep Model that correlates volumetric strain rate as well as axial strain rate to time in two different equations. Therefore, multiaxial behavior of stress-strain-time is expected to be predictable.

Tavenas et al.'s Model:

In a similar manner, Tavenas et al. (1978) decomposed creep strains into deviator and volumetric strains and utilized a function analogous to the Singh and Mitchell's creep model for both creep strains with replacement of the effective stress function (the original equation consisted of only an exponential relation for the vertical effective stress). Therefore, any function of current effective stress, which works as a yield surface, can be employed.

Bjerrum's Model:

The concept of this model was proposed by Bjerrum (1967) based on previous studies by Buisman (1936) and Taylor (1942) to estimate the settlement of normally and lightly overconsolidated clays, and it may be called a delayed compression theory. In fact, a family of lines parallel to the virgin compression line in the $e-\log \sigma'_z$ are defined as equilibrium lines which can be reached after different periods of sustained loading. This resulted in the definition of young and aged normally consolidated clays. The concept is shown in Fig. 2.61. Later, Garlanger (1972) formulated Bjerrum's concept by expressing void ratio change by elastic, elastoplastic and creep components. These components can be defined based on recompression, compression and secondary compression indices, respectively.

Yin and Graham's Model:

This model is an advanced combination of the strain rate approach and Bjerrum's model by Yin and Graham (1989a,b, 1994, 1996), and it is based on the following four definitions shown schematically in Fig. 2.62: equivalent time, reference time line, instant time line and limit time line. Equivalent time, t_e , is described as creep time needed from a reference time line to current axial strain and constant effective stress. This value is simply the time for each increment in load in a traditional multistage loading test for normally consolidated clays. However, this is not the case for overconsolidated soils. The reference time line provides the condition from which equivalent time is calculated. In

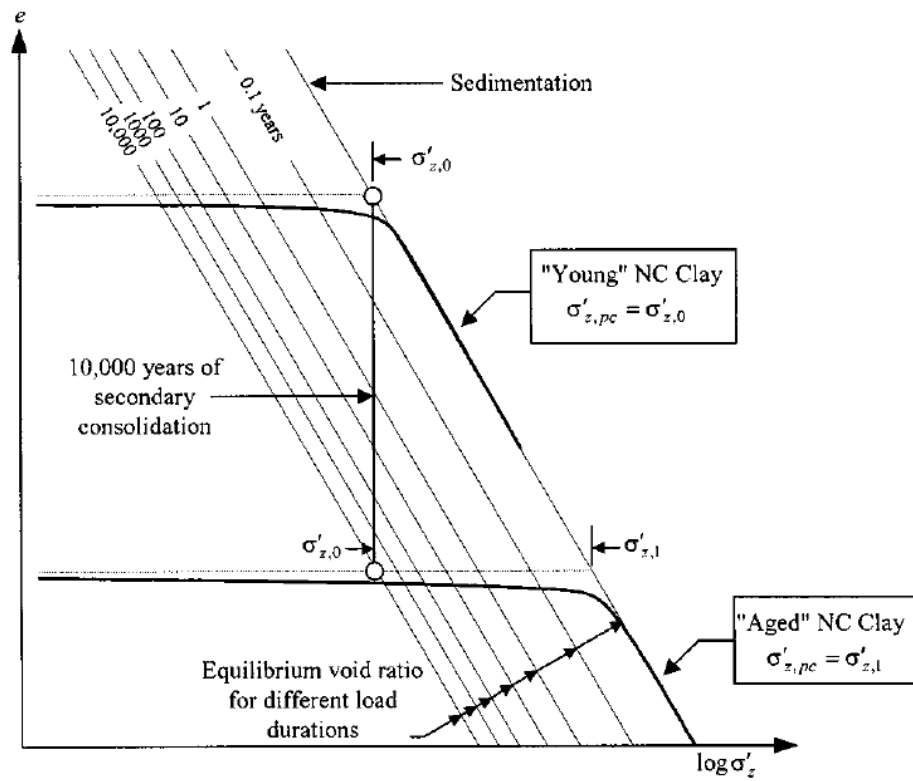


Figure 2.61. Compressibility and geological history of young and aged normally consolidated clay (after Bjerrum 1973)

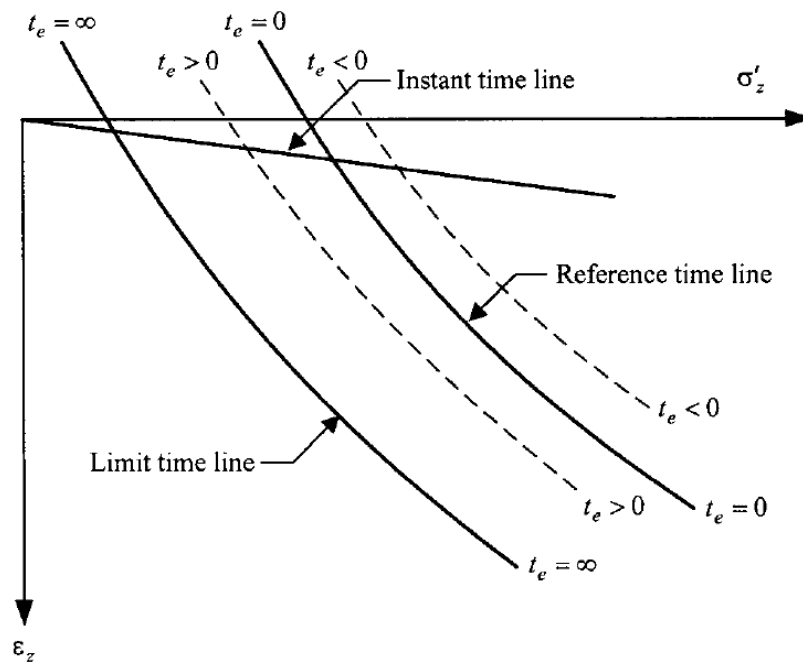


Figure 2.62. Graphical definition of instant time line, reference time line, limit time line and positive and negative time lines in stress-strain space (after Yin and Graham 1994).

other words, it is a time line at which equivalent time is zero in stress-strain space. The instant time line, which is assumed to be related to the elastic response of the medium, is employed to clarify the instant strains. According to Yin and Graham (1994), there is a state in the stress-strain space after which there is no time dependency; this is referred to as the limit time line and equivalent time is equal to infinity at this state. It should be noted that two types of logarithmic function with five parameters and a power function with eleven parameters have been suggested to cover this concept and have been fully described in the references given above.

2.5.2. Rheological Models

In comparison to Empirical Models, rheological models are described in form of mathematical closed-form equations in one dimension and are aimed to provide a better understanding of the concept of time effects. Rheological methods are commonly categorized in three main groups of: differential approach, engineering theories and hereditary approach.

Differential Approach

In this approach a combination of basic mechanical elements of elastic springs, plastic sliders and viscous dashpots are employed to constitute relations of time-dependent behavior of materials. These elements represent Hookean, Saint-Venant's and Newtonian materials in solid mechanics, respectively. Fig. 2.63 illustrates the behavior of each individual basic element.

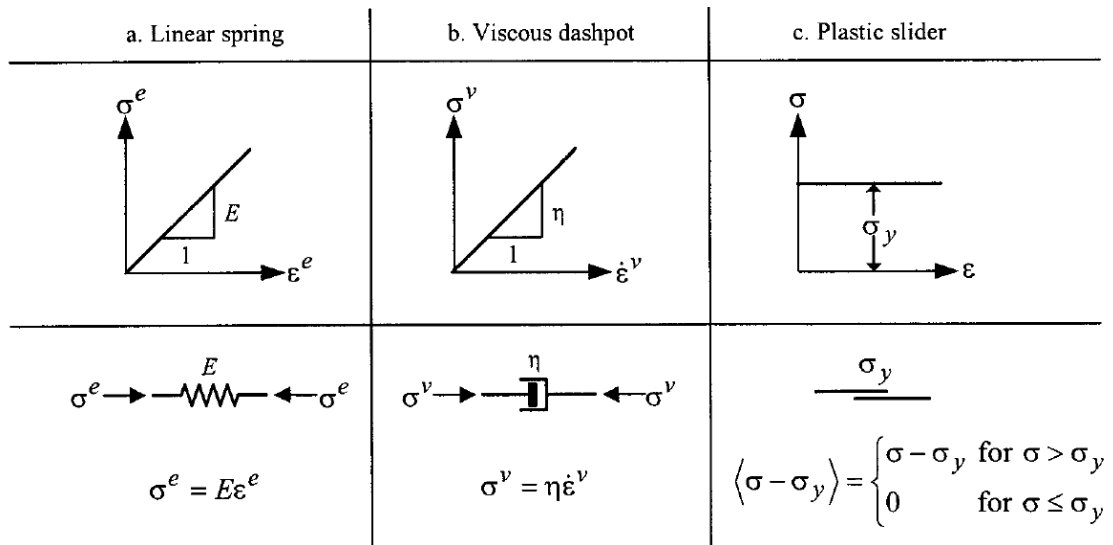


Figure 2.63. Schematic explanation of three basic material models: (a) Hookean spring; (b) Newtonian dashpot; and (c) Saint Venant's slider (after Liingaard et al. 2004).

There are certain reasons that application of these models is limited for soils. The first reason is the linearity of the response of constituent components because it is widely known that behavior of soils is nonlinear, both in elastic and plastic types of behavior. Secondly, soils may undergo both primary and secondary creep, but these models are only capable of capturing one stage of creep. Moreover, these models are commonly derived for one-dimensional conditions.

According to Singh and Mitchell (1968), expanding these equations in three dimensions makes the parameter calibration and their application extremely difficult. Last but not the least, all these models assume the isotach behavior (Tatsuoka et al., 2008) for materials which may not be the case for all soils. Here, three principal models of Maxwell, Kelvin-Voigt and Bingham are briefly described. More complicated rheological models of soils have been proposed by Murayama (1983) and Tatsuoka et al. (2008).

Maxwell Model:

This model is the most basic model for time-dependent behavior of materials and is constructed by putting a spring and a dashpot in series. By writing the constitutive equations described in Fig. 2.63, in case of creep, this model is able to capture an instantaneous elastic strain together with a linear change in strain with time, whereas for relaxation, solving the equations results in an exponential damping of stress level which approaches zero as time goes to infinity. Creep and relaxation responses of the Maxwell model are shown in Fig. 2.64.

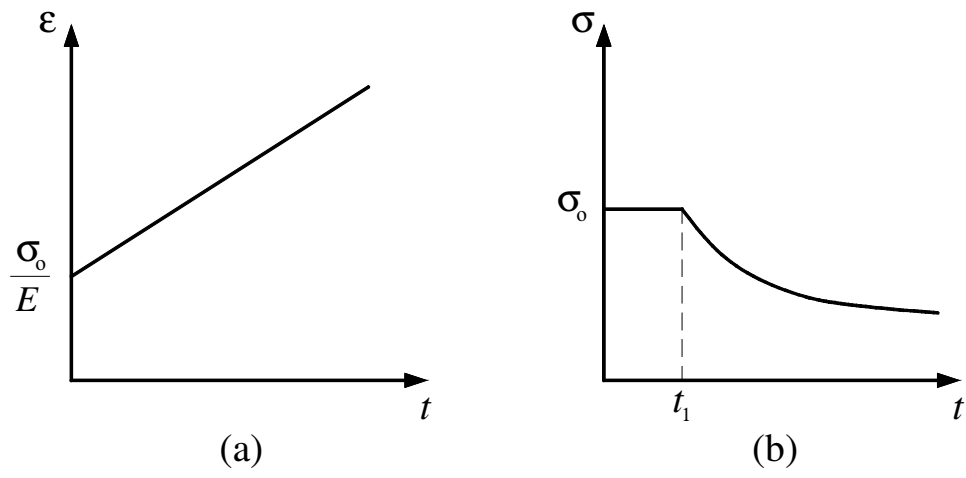


Figure 2.64. Response of the Maxwell Model: (a) creep; (b) relaxation.

Kelvin-Voigt Model:

In comparison with the Maxwell model, in the Kelvin-Voigt model, two basic elements of a spring and a dashpot are set parallel. In this case, solving the constitutive equations for creep conditions results in an exponential increase of strain with time. However, no instantaneous strain can be predicted. This problem can be overcome by putting a spring in series with the current model and making a new model which is called the corrected Kelvin model. On the other hand, by solving the relations for relaxation conditions, there is only a step reduction in stress level right at the beginning of stress relaxation and the stress level is kept constant afterwards. The output of the Kelvin-Voigt model for creep and relaxation conditions is displayed in Fig. 2.65.

Bingham Model:

This model is composed of a slider element with a parallel dashpot element together with an elastic spring in series. Under the yield stress of σ_y , the response is purely elastic whereas viscoplastic behavior is observed beyond this stress. However, assuming $\sigma_y = 0$ and a material without hardening results in the Maxwell's model. The response of the Bingham model for creep, relaxation and constant rate of strain is schematically illustrated in Fig. 2.66.

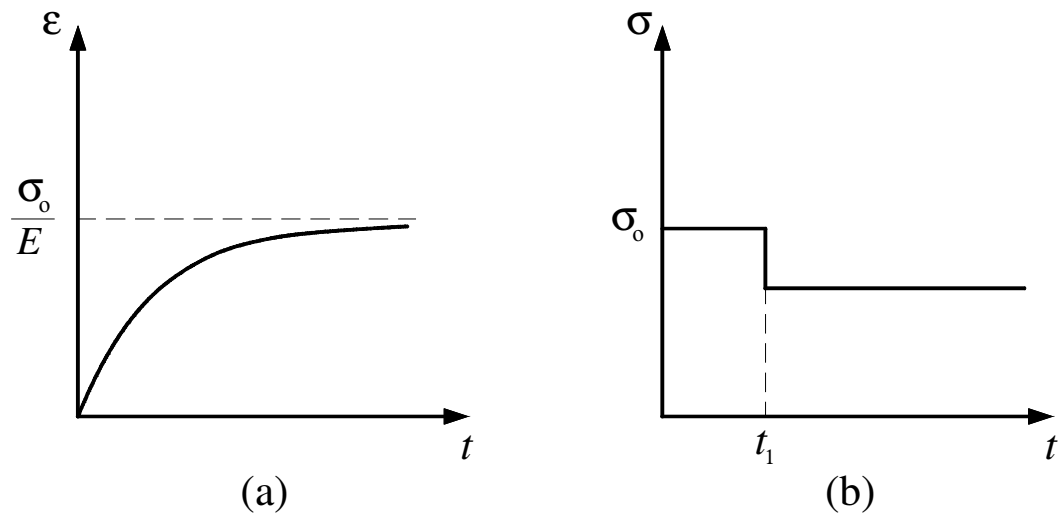


Figure 2.65. Response of the Kelvin-Voigt Model: (a) creep; (b) relaxation.

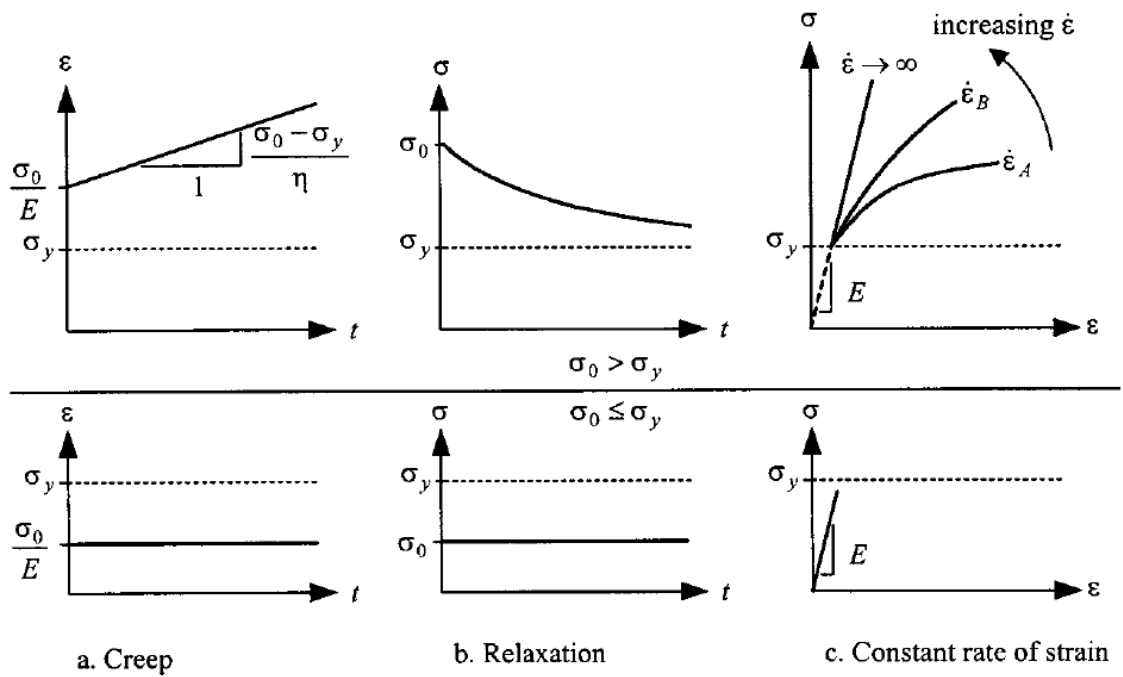


Figure 2.66. Reaction of Bingham model: (a) creep; (b) relaxation; (C) constant rate of strain (after Liingaard et al. 2004).

Engineering Theories

These theories do not follow a certain method to describe creep; instead, they are based on phenomenological laws which have been extracted from experimental observations. It should be emphasized that they are often used for materials which are loaded below their initial yield stress, i.e. metals, concrete, etc. However, Skrzypek (1993) proposed three models of Total Strain, Time-Hardening and Strain-Hardening models in the form of Engineering Creep Theories for plastic, normally consolidated clays. These models are briefly discussed below.

Total Strain Model:

This model assumes that strain is composed of instantaneous elastic and creep strain components. The elastic component is calculated from the elastic properties of the soil, while the creep component of the strain is considered as a function of applied stress and time. Any function can be adopted for the relation between applied stress and creep strain or between time and creep strain. However, power functions have been widely used for the former relations, whereas exponential, hyperbolic and power functions have been utilized in the literature for the latter. The simplicity and ease in choosing these relations are their advantages in comparison to rheological models which only employ linear relations. Conversely, instead of creep strain rate, creep strain has a direct relationship with time and stress, which is a deficiency of this model. This model works the same way as the semi-logarithmic law when the stress and time functions are assumed constant and logarithmic, respectively.

Time-Hardening Model:

To overcome the deficiency of the total strain model which considers random changes of stress, in time-hardening models, creep strain rate is assumed to be any arbitrary function of applied stress and time. Detailed observation of the time-hardening model reveals that considering exponential stress function and power function for time turns this model into Singh and Mitchell's model. The main deficiency of both total strain and time hardening models is that the governing equations are dependent on the origin of time.

Strain-Hardening Model:

In this model, as it appears from its name, hardening is calculated based on creep strains in such a way that the rate of creep is defined as a function of applied stress and creep strain. A hardening mechanism is observed with accumulation of plastic strains or work. This avoids the problem which occurs in the previous two models. This feature resembles the strain rate approach (an empirical model), defined as a unique relation between stress, strain and strain rate.

Although the aforementioned models are intended to be used for creep, their relaxation versions have also been discussed by many researchers (Rabotnov, 1969; Borm and Haupt, 1988; Huneault, 1992; Ladanyi and Melouki, 1993; Ladanyi and Benyamina, 1995).

Hereditary Approach

This approach is a very complex way of facing time-dependent behaviors in geomaterials. It is based on calculating the strain by integrating over all extremely small stress increments in stress history up to the current time. In the condition of considering nonlinear behavior for the material, which is the case for soils, more than 28 tests are required in order to model a uniaxial stress test (Feda, 1992). Many researchers (e.g. Rabotnov, 1969; Feda, 1992; Skrzypek, 1993; Meschyan, 1995) have tried to lessen the number of required tests by assuming simple boundary conditions.

2.5.3. General Constitutive Models Incorporating Time-Effects

Generally, time-dependent constitutive models present a relation between stress, strain and time in a framework to be used with different numerical tools such as finite element methods, finite difference methods, etc. on an incremental basis; thus, there are no restrictions in terms of boundary or loading conditions. However, there are certain limitations since some basic assumptions are involved in the evolution of these models. It seems to be difficult and time-consuming to explain all time-dependent constitutive models in the literature since a large number of them have been proposed. Therefore, it suffices to categorize these models in terms of the theory on which they are based. In this regard, over stress and nonstationary flow surface theories are explained briefly as they are the basis of the majority of proposed stress-strain-time models.

Overstress Theory

According to Liingaard et al. (2004), this theory was proposed for the first time by Ludwick (1922) and it has been expanded by many other researchers. The version introduced here follows the presentation by Perzyna (1963a,b,c, 1966), Olszak and Perzyna (1966, 1970) and Sekiguchi (1985). In the definition of this theory, the total strain rate tensor is composed of an elastic component, which is assumed to be independent of time, and a viscoplastic component, which consists of combined viscous and plastic strain rate tensors. While the elastic component follows the generalized Hooke's law, the theory adopts a nonassociated flow rule to define viscoplastic strain rate. In this flow rule, a viscous nucleus exists that is commonly assumed as either a power or an exponential function of the overstress function (Adachi and Okano, 1974; Akai et al., 1977). In this theory, two surfaces of static and dynamic yield surfaces are considered as shown in Fig. 2.67. The overstress function represents the distance between the current stress point, located on the dynamic yield surface, and the static yield surface. Therefore, only when the current stress point is beyond the static yield surface is a viscoplastic strain obtained. Similar to the direction of plastic strain rate in classic constitutive models, the viscoplastic strain rate direction is perpendicular to the potential surface while the magnitude is calculated from the product of the fluidity parameter (analogous to the multiplier of the plastic flow rule, λ) and the viscous nucleus function. This theory is a generalized three-dimensional version of the Bingham's model discussed earlier.

For a creep condition, while the current stress point is located outside of the static yield surface, two types of responses are expected depending on the assumption of hardening or non-hardening behavior for the material. These two cases are schematically shown in Fig. 2.68.

In the case of non-hardening material, the size of the static yield surface is constant; therefore, the overstress remains constant, and consequently, the viscoplastic strain rate is constant. On the other hand, considering hardening for the behavior of the material, the size of the static yield surface continues to increase, and in the mean time the overstress is decreasing; therefore, the viscoplastic strain rate continues to decrease until it reaches zero and the yield surfaces coincide. It should be noted that this theory is unable to capture any viscous strain in cases where the current stress point is inside the static yield surface.

For relaxation behavior, where the total strain rate is zero, if the current stress point is located beyond the static yield surface, then the dynamic yield surface starts to contract, and consequently, the stress level decreases, and so does the overstress. In fact, this is due to the main definition of the total strain rate. In other words, when the total strain rate is zero, then the elastic strain rate has to be equal to the viscoplastic strain rate in the opposite direction, and this forces the dynamic surface to diminish in size. However, when the stress point is located inside the static yield surface, the over-stress is zero and there is no viscoplastic deformation. Now, according to the definition of total strain, the elastic strain rate needs to be zero as well, and this is completely incorrect in

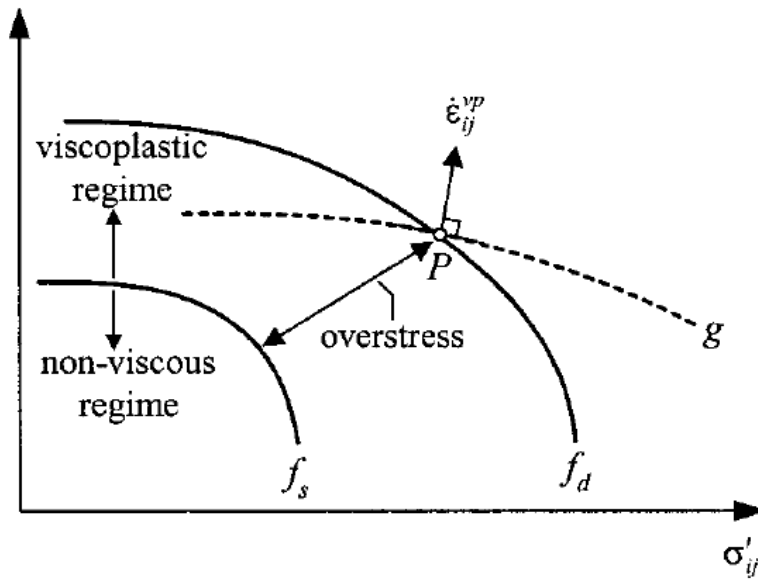


Figure 2.67. Definition of static and dynamic yield surfaces together with potential surface for current stress point, P , in overstress theory (after Liingaard et al. 2004).

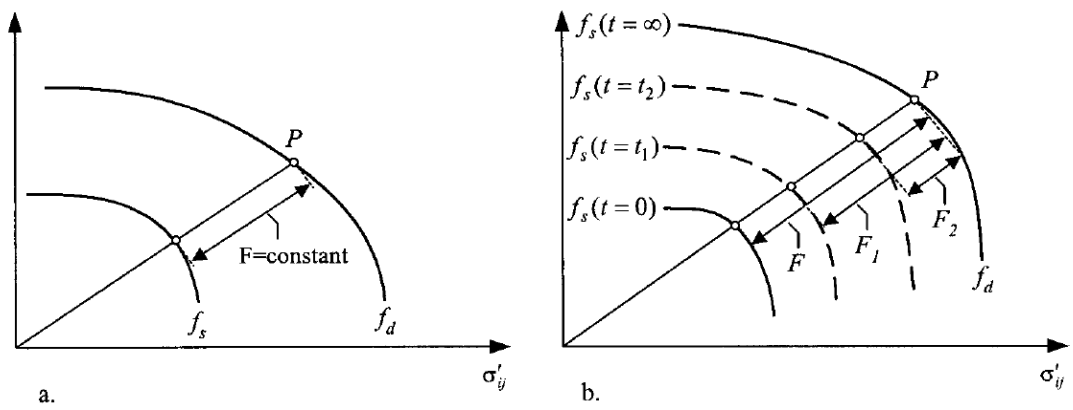


Figure 2.68. Overstress theory for creep in a (a) non-hardening material (b) hardening material (after Liingaard et al. 2004).

the relaxation process. Many different researchers have used this theory to develop constitutive models incorporating time effects for various types of geomaterials and different purposes such as Adachi and Okano (1974), Zienkiewicz and Corneau (1974), Zienkiewicz et al. (1975), Akai et al. (1977), Adachi and Oka (1982a,b), Katona (1984), Katona and Mulert (1984), Adachi et al. (1987), Desai and Zhang (1987), Oka et al. (1988), Adachi et al. (1996), di Prisco and Imposimato (1996) and di Prisco et al. (2000).

Nonstationary Flow Surface Theory

The basis of this theory is very analogous to classical elastoplasticity. The difference is in the constituent components of the yield surface. In classical elastoplasticity, the yield surface equation is a function of effective stress and plastic strain tensors. However, in this theory the yielding relation is a function of the effective stress tensor, the viscoplastic strain tensor and a time-dependent function, β . For a constant plastic strain, the yield surface does not change in classical elastoplasticity while in this theory, the yield surface undergoes changes with time and is nonstationary, even if the viscoplastic strain is kept constant. This is due to variation of β with time. The strain rate tensor is composed of elastic and viscoplastic strain rates. The elastic response usually follows Hooke's generalized law, whereas the viscoplastic strain can be calculated from the flow rule when the stress point is located on the yield surface, and otherwise is zero when the stress point is within the yield surface. In comparison with the overstress theory, in this theory, the consistency condition is applied and the multiplier of the flow rule, λ , can be calculated based on this condition. However, in nonstationary

flow surface theory, this multiplier is a function of β since the derivatives of the yield surface contain this function.

If the relaxation or creep begins when the stress point is inside the yield surface, this theory is unable to capture viscoplastic behavior of the material, because only an elastic response is expected. For creep conditions initiating at a stress point on the yield surface, a new yield surface is constructed as time passes. The stress point is now located inside the new yield surface and theoretically, no further viscoplastic strain should be allowed. However, as an exception for cases in which creep initiates at a stress point on the yield surface, the viscoplastic strain is allowed to continue. For relaxation starting from a stress point located on the yield surface, no clear procedure has been mentioned in the literature, but it seems that nonstationary flow surface theory can capture the behavior. This theory has been utilized in many different constitutive models in the literature. The most cited models have been proposed by Sekiguchi and Ohta (1977), Dragon and Mroz (1979), Nova (1982), Sekiguchi (1984), and Matsui and Abe (1985a,b).

2.5.4. Constitutive Models Incorporating Particle Crushing

Kikumoto et al. (2010) stated that particle crushing broadens the grain size distribution curve and the main consequence is lowering the critical state line. Also, according to Lade et al. (2009, 2010), particle crushing may have a direct impact on time-dependent phenomena in granular material; therefore, constitutive models which are capable of considering particle crushing and gradual evolution of the material may

intrinsically capture related phenomena. In this regard, three recent constitutive models incorporating particle crushing are briefly explained.

Model of Yao et al. (2008)

It is stated that due to the increase in confining pressure, the dilatancy tendency decreases in granular material due to particle crushing. Yao et al. (2008) have therefore used a crushing stress parameter, p_s , in the hardening part of the Cam-Clay model to be able to capture dilatant and contractive behavior at low and high confining pressures, respectively. In fact, three different lines of M , M_f and M_c are defined as critical state, failure and characteristic lines in the p - q space. M_f and M_c are functions of M , p_c and n (a material parameter) as follows:

$$M_f = M \left(\frac{p}{p_c} \right)^{-n} \quad (2-12)$$

$$M_c = M \left(\frac{p}{p_c} \right)^{-n} \quad (2-13)$$

The hardening equation is then defined as:

$$d\varepsilon_v^p = \frac{M_f^4}{M_c^4} \cdot \frac{M_c^4 - \eta^4}{M_f^4 - \eta^4} \quad (2-14)$$

where $\eta=q/p$ is the current stress ratio. Depending on the initial mean effective stress, three different triaxial stress path of AB, CD and EF are possible. These stress paths as

well as the aforementioned lines are schematically shown in Fig. 2.69. Furthermore, these stress paths and their expected stress-strain behaviors are shown in Fig. 2.70.

Stress path AB is explained as follows. For any point on the p axis, say point A , the stress ratio is equal to zero. Inserting this value in Equation (2-14) gives that $d\varepsilon_v^p > 0$; that is, isotropic compression. From A to K since $\eta < M_c$, again $d\varepsilon_v^p > 0$ is obtained. At point K the stress state is on the characteristic line, $\eta = M_c$, and it implies the maximum contraction, so $d\varepsilon_v^p = 0$. Any points beyond K describe $\eta > M_c$ which results in $d\varepsilon_v^p < 0$. In this model, Yao et al. (2008) employed an associated flow rule and used the following stress-dilatancy equation:

$$\frac{d\varepsilon_v^p}{d\varepsilon_d^p} = \frac{M_c^2 - \eta^2}{2\eta} \quad (2-15)$$

together with the Cam-Clay equations. The yield (potential) surface is defined as:

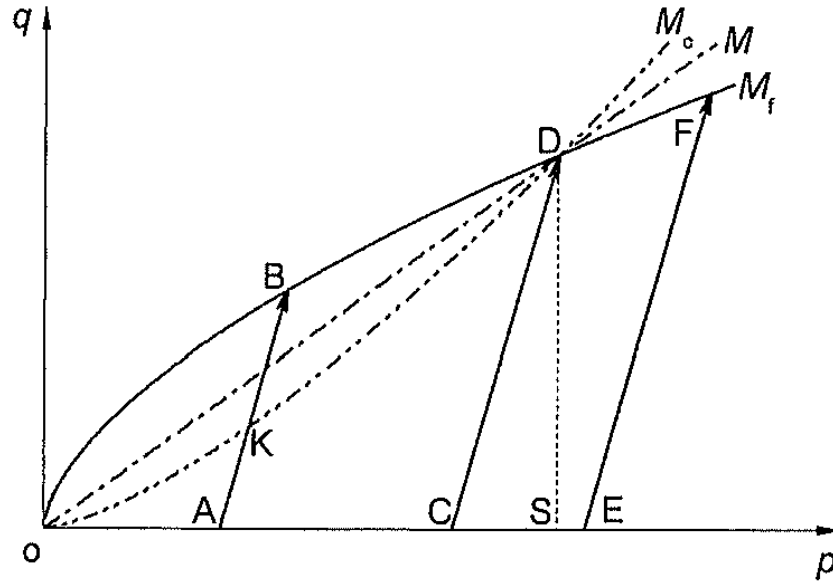


Figure 2.69. Illustration of M_c , M_f and M lines and different stress paths in p' - q space (after Yao et al. 2008).

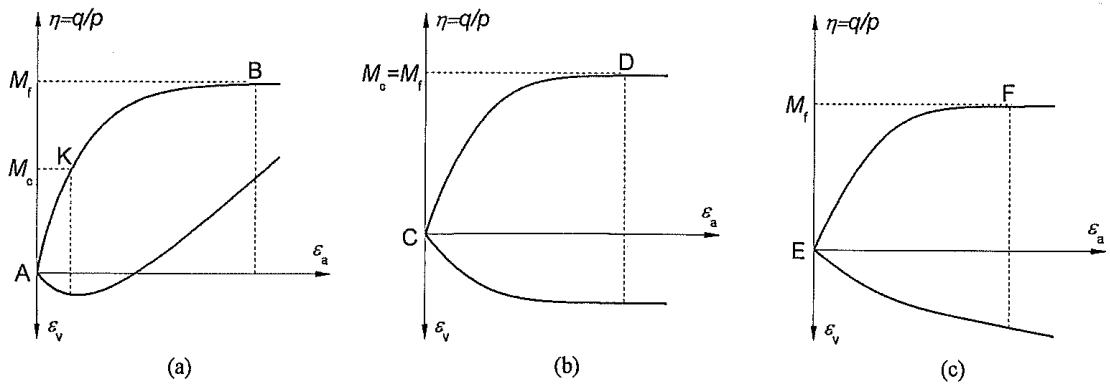


Figure 2.70. Stress-strain and volume change behavior related to triaxial compression stress paths of (a) AB , (b) CD , and (c) EF (after Yao et al. 2008).

$$f = g = (2n+1) \cdot \frac{p_c^{2n}}{M^2} \cdot \frac{q^2}{p} + p^{2n+1} - p_x^{2n+1} = 0 \quad (2-16)$$

where p_x is the mean effective stress at isotropic stress. Applying $n=0$ produces the original Cam-Clay model. A series of schematic yield (potential) surfaces are illustrated in Fig. 2.71. This model has 7 parameters. Based on the predictions of triaxial tests on Toyoura sand, it was claimed to be able to capture both drained and undrained behavior of granular material as shown in Fig. 2.72 and Fig. 2.73.

Daouadji and Hicher's (2010) Model

It is known that particle breakage increases the tendency for contraction and vanishing dilatancy. The concept of this model is to use a critical state base model, originally proposed by Salim and Indraratna (2004) and Wood (2007), and to introduce a new parameter which is able to describe the effects of changes in the critical state line due to grain crushing and the evolution of the grain size distribution curve. The original model involves the following four mechanisms in predicting the soil behavior: three plane strain deviator and one isotropic mechanisms. Thus, in the places where they are needed, different model parameters may be used.

It has been mentioned that the coefficient of uniformity, $C_u = d_{60}/d_{10}$, may be used to model the evolution of the grain size distribution. This is based on a study of change in the critical state line due to particle breakage in a series of isotropic (or one dimensional) compression tests. Fig. 2.74 illustrates the change in position of the critical state line when C_u is changing as a result of the particle crushing.

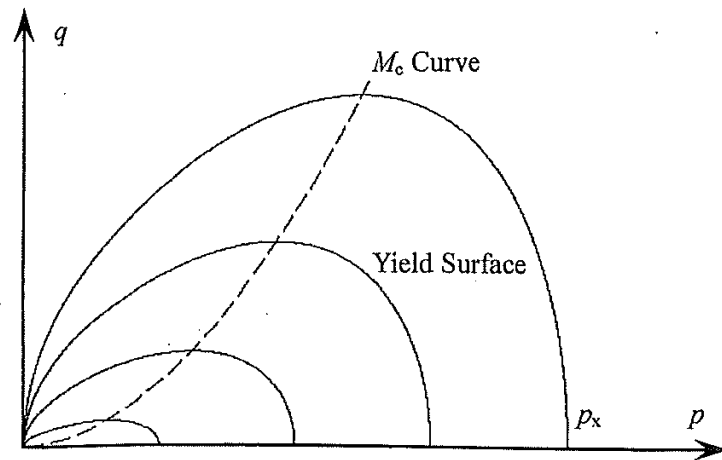


Figure 2.71. A family of yield (potential) surfaces in the p' - q space (after Yao et al. 2008).

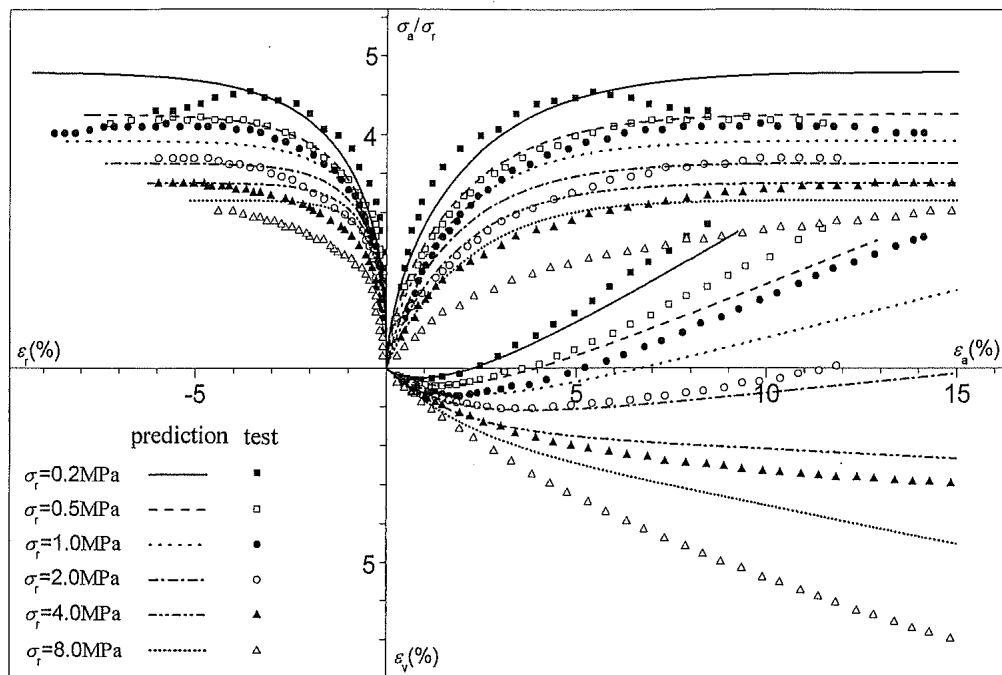


Figure 2.72. Predictions of drained stress-strain behavior of Toyoura sand by the proposed model by Yao et al. (2008).

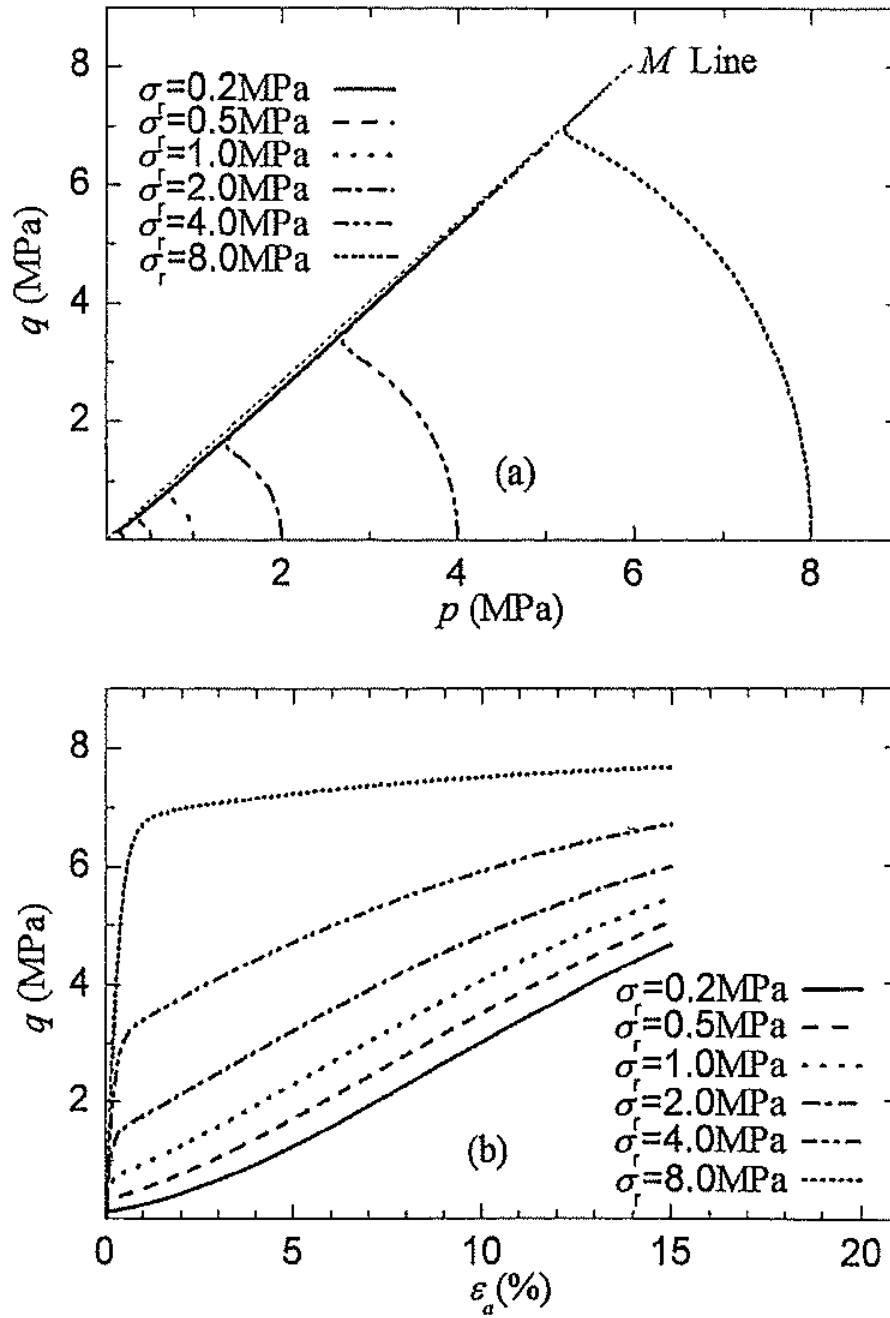


Figure 2.73. Predictions of undrained stress-strain behavior of Toyoura sand by the proposed model by Yao et al. (2008).

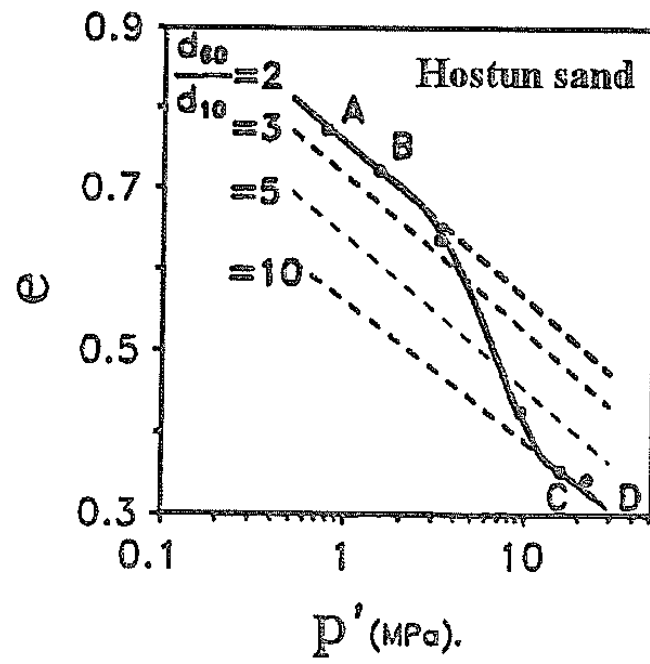


Figure 2.74. Impact of particle crushing on the location of critical state line (after Daouadji and Hicher 2010).

The dependency of the critical state line in the constitutive model is described by an internal variable, ω , which is a function of “natural” parameters such as individual particle strength and initial grading curve, defined as:

$$\omega = \int \sigma \, d\varepsilon^p \quad (2-17)$$

On the other hand, in the original model, the critical state pressure, p_c , is calculated as:

$$p_c = p_{co} \cdot \exp(\beta \varepsilon_v^p) \quad (2-18)$$

where p_{co} is a model parameter and $1/\beta$ and ε_v^p are the slope of the critical state line in $\varepsilon_v^p - \log p'$ plane and the volumetric plastic strain, respectively. However, in the revised model, p_{co} was experimentally found to be a function of ω as:

$$p_{co} = p_{coi} \cdot \left(1 - \frac{\omega}{B + \omega}\right) \quad (2-19)$$

where p_{coi} is the critical state reference pressure before particle breakage initiates and B is a material constant which includes initial properties of the particles such as shape, size, mineralogy, etc. It is noted that parameter B can be different for each mechanism involved in the revised constitutive model. The new critical state pressure is then expressed as:

$$p_c = p_{coi} \cdot \left(1 - \frac{\omega}{B + \omega}\right) \cdot \exp(\beta \varepsilon_v^p) \quad (2-20)$$

The revised constitutive model was utilized for the prediction of Hostun sand, calcareous sand and rockfill material which were tested in a triaxial testing device over a wide range of confining pressures. The parameters dealing with particle breakage needed to be estimated by a curve fitting procedure; however, it was emphasized that the model parameters were uniquely found at low confining pressures and the model was able to accurately capture the true impact of particle breakage at high confining pressures.

Russell and Khalili's (2004) Model

Russell and Khalili have developed a bounding surface model to incorporate the effect of particle crushing. In fact, this effect is considered by defining a three segment critical state line which has a constant shift from the three segment isotropic compression line that correlates with particle rearrangement, particle crushing and pseudoelastic deformation. The schematic critical state line in the $v - \log p'$ space is shown in Fig. 2.75.

It is seen that, in the low confining pressure range (A to B), the main deformation mechanism is due to the rearrangement and rotation of the grains. By increase in confining pressure and passing point B , the principal mechanism of deformation is particle crushing; therefore, particles can fit better together and the slope of the critical state line and the isotropic compression line are increased considerably. This continues until the mean effective stress reaches point C , where the mechanism of deformation changes to a pseudoelastic type because of great increase in the coordination number of particles. This critical state line needs six parameters for definition.

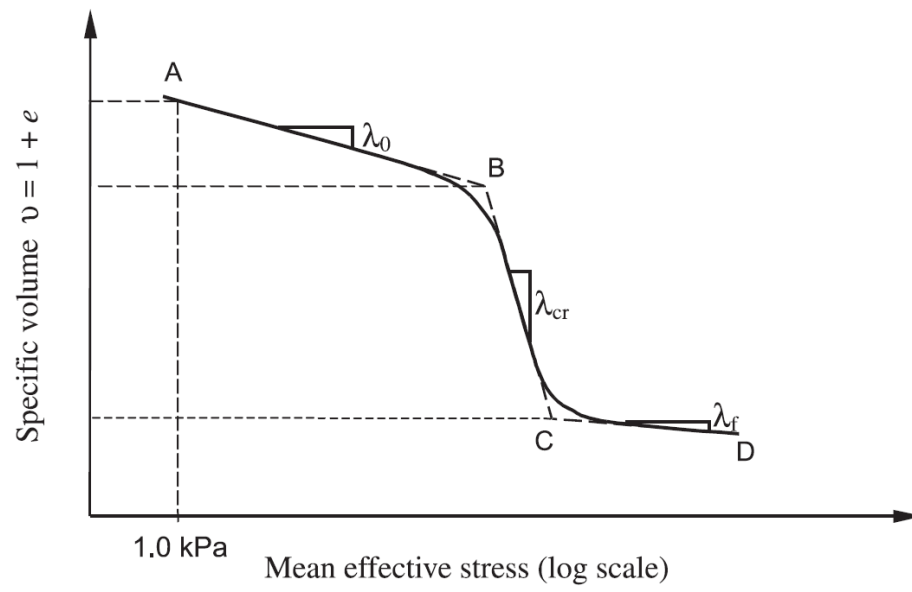


Figure 2.75. Definition of the new critical state line (after Russell and Khalili 2004).

The bounding surface formulation employed by Russell and Khalili (2004) is analogous to that proposed by Dafalias (1986) and only the radial mapping rule has been considered to define loading and bounding surfaces which have simple functions. Because of the small range of pure elastic deformations in soils, this type of behavior has been neglected in the constitutive equations. The potential function of this model does not intersect the mean effective stress axis perpendicularly, as shown in Fig. 2.76. Therefore, a considerable problem occurs in case of isotropic compression and stress paths close to the mean effective stress axis. This has been taken care of by assuming a horizontal vector of plastic strain when the shear stress is zero. However, the problem is that isotropic compression along a stress path that includes a small amount of deviator stress results in very different predictions than a stress path along the p' -axis. Thus, for a case from which only volumetric plastic strains are calculated, suddenly, a huge amount of plastic deviator strains is captured, which is incorrect.

A series of drained and undrained triaxial tests were performed over a wide range of confining pressures on Kurnell silica sand to validate the ability of this model to capture the effect of particle crushing on the behavior of the granular materials. It was shown that prepeak behavior of the tested material has been simulated well and there is good agreement between the experimental results and predictions of this model.

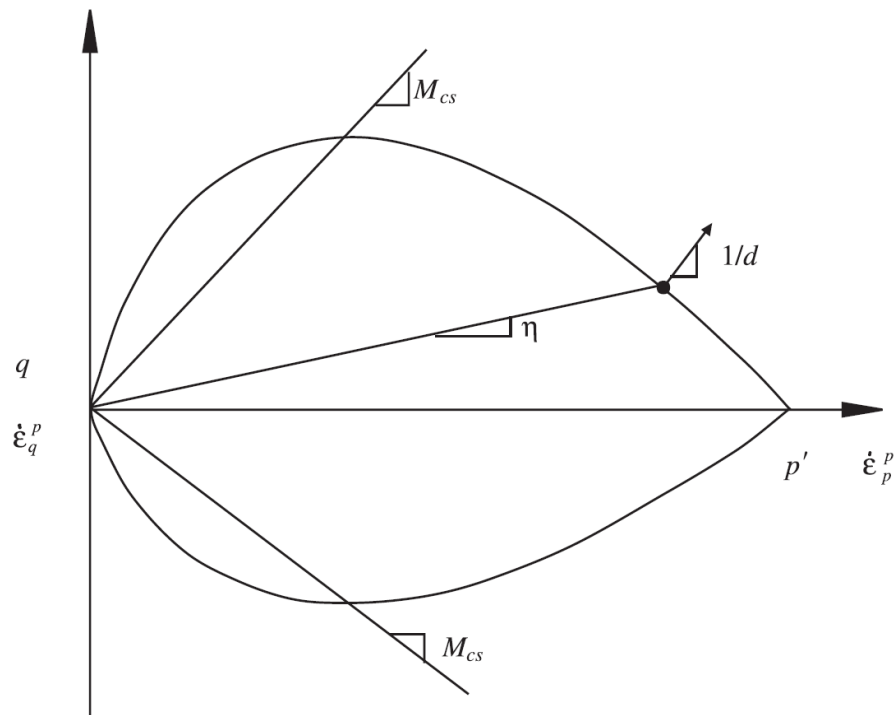


Figure 2.76. Plastic potential surface in p' - q space (after Russell and Khalili 2004).

3. Experimental Program

3.1. Materials

The following two types of materials were used in the experimental program which was composed of single particle crushing and triaxial compression tests:

3.1.1. Glass Beads Tested

Three sizes of industrially produced spherical beads of sodium lime glass were used in single particle strength and crushing experiments. The glass beads with diameters of 2, 3, and 6 mm were used to simulate the behavior of brittle, granular materials such as sands. Spherical glass beads were used to obtain the highest amount of consistency in the experimental results. The specific gravity, Young's modulus and Poisson's ratio of these beads are 2.530, 72 GPa, and 0.22, respectively.

3.1.2. Sand Tested

Six different grain size distribution curves of Virginia Beach sand composed of subangular to subrounded grains were used in the entire triaxial testing program. X-ray fluorescence analysis was employed to determine the mineralogy of the sand, and the results showed that the sand consisted of 96.09% of SiO_2 , 2.19% of Al_2O_3 , 0.43% of Fe_2O_3 and 1.29% of other chemical compounds. The specific gravity of Virginia Beach sand is 2.65. The six grain size distribution curves are shown in Fig. 3.1 and their characteristics are tabulated in Table 3.1. The grain size distribution of the grains finer

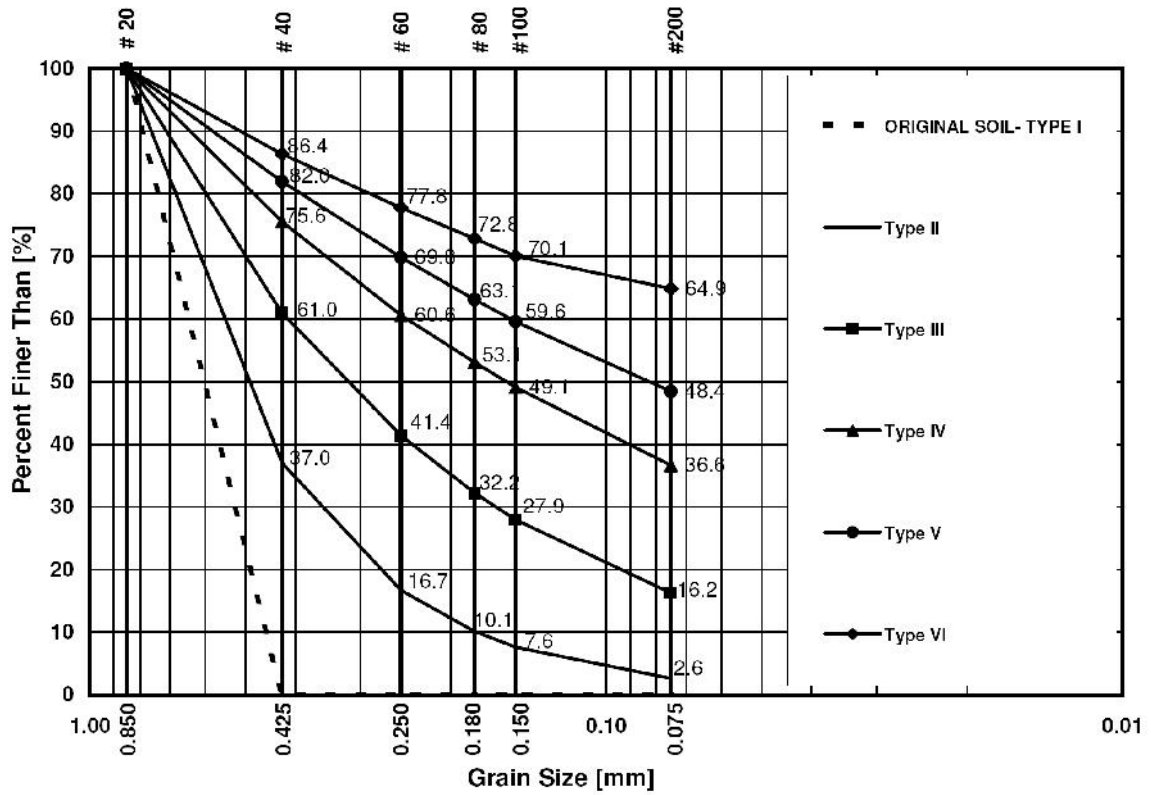


Figure 3.1. Various grading curves used in the experimental program.

Table 3.1. Properties of Virginia Beach sand.

Grading Type	Void Ratio	Uniformity Coefficient $C_u = \frac{D_{60}}{D_{10}}$	Curvature Coefficient $C_c = \frac{(D_{30})^2}{D_{10} \cdot D_{60}}$	Percent Finer than Sieve #200
Type I	0.530	1.41	0.92	0.0
Type II	0.461	3.30	1.31	2.6
Type III	0.462	10.90	1.72	16.2
Type IV	0.468	79.06	2.69	37.0
Type V	0.555	392.50	3.86	48.3
Type VI	0.822	7776.00	7.59	61.54

than U.S. sieve No. 200 (75 μm), which was determined by a hydrometer test performed according to ASTM D3360-96, is illustrated in Fig. 3.2.

Most triaxial experiments were performed on the uniform gradation, Type I, while a small portion of experiments was performed on sand with other gradations to study the effect of the grading curve. The minimum and maximum void ratios of Type I soil were 0.530 and 0.759, respectively. The minimum void ratio was believed to be obtained by pouring 1000 gr of oven-dried Type I soil from a height of 50 cm into a measured cylindrical beaker. In fact, different heights were tried and it was concluded that the achieved void ratio became independent of dropping height after the height of about 40 cm. For calculation of the minimum void ratio, a same amount of oven-dried Type I soil (i.e. 1000 gr) was poured into another measured cylindrical beaker with a cap and the beaker was turned 3 times slowly. In both cases, the dry density was calculated by dividing the weight to the measured volume and the corresponded void ratios were calculated accordingly. Void ratios presented in Table 3.1 were all attained from the same method as the method used for obtaining the minimum void ratio for Type I soil and they do not necessarily represent the minimum void ratio for Type II to Type VI soils.

Using the uniform soil in the experimental program was not only due to boosting the amount of particle crushing, which is of great importance in this study, during testing, but also it made it simpler to identify any probable changes in the gradation curve after each test. It should be noted that grading curves of Type II to Type VI were chosen based on the following equation which was suggested by Talbot and Richart (1923):

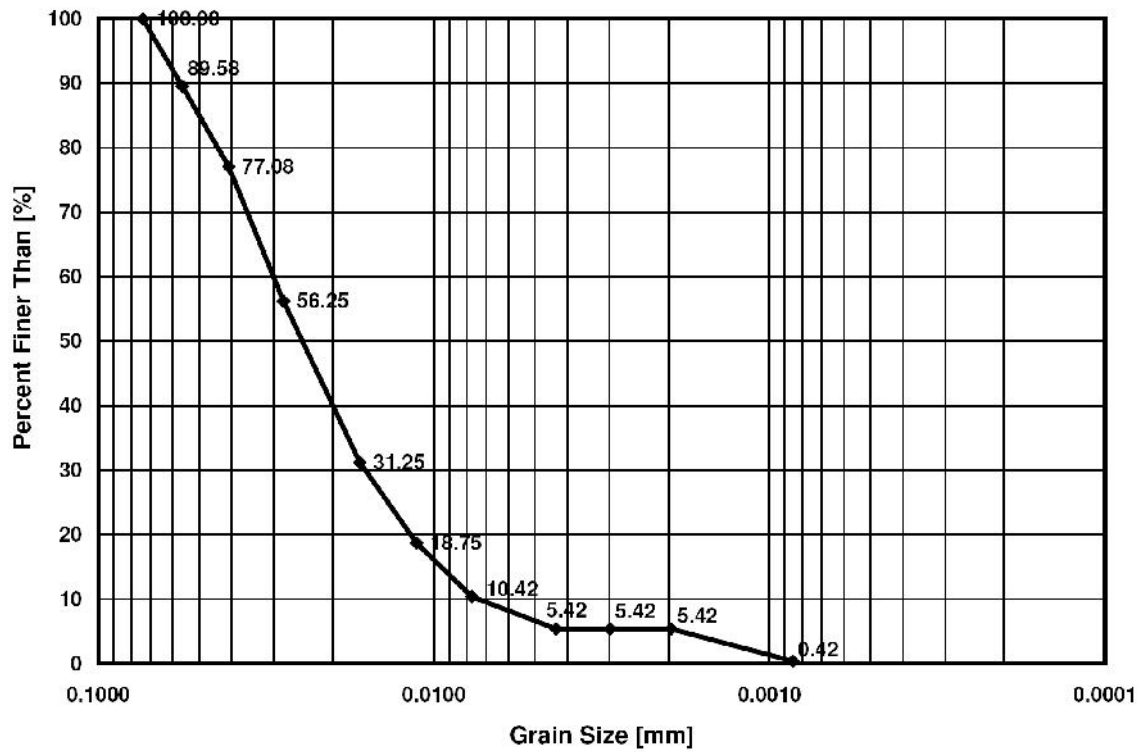


Figure 3.2. Grain distribution curve for particles finer than 75 μm .

$$P(D_i) = 100 \cdot \left(\frac{D_i}{D_{\max}} \right)^q \quad (3-1)$$

where D_{\max} equals to 0.850 mm and the corresponding values of q for soils Type II to Type VI are 0.2, 0.3, 0.41, 0.75 and 1.50, respectively. Therefore, uniformity and curvature coefficients, stated in Table 3.1, were calculated based on Talbot and Richart's equation. It is also noted that since the original Virginia Beach sand was a uniform soil between sieves #60 (0.250 mm) and #20 (0.850 mm), smaller particles were obtained from previously sheared specimens of Type I to make grading curves of Type II to Type VI.

3.2. Apparatuses, Specimen Preparation and Measurements

3.2.1. Apparatuses

Glass Bead Crushing Device

A loading frame which is usually employed for consolidation experiments was prepared to perform single glass bead crushing tests. Each glass bead is placed between two parallel, hardened high-carbon steel plates and a small seating load is applied to hold the glass bead in place. Loading was controlled using two pressure regulators for high and low ranges of applied pressures. The compression of the beads in the direction of the load was monitored by a dial gage installed on the cross bar of the apparatus.

Triaxial Compression Apparatus

All the compression tests on the Virginia Beach sand were performed in two similar triaxial cells with a confining pressure capacity of 14,000 kPa. The nominal height and diameter of specimens are 108.0 and 38.1 mm, respectively. This corresponded to a height-to-diameter ratio of 2.83. The principal cross section of the cells is shown in Fig. 3.3.

The deviator load for shearing the specimen was applied under deformation control or under load control with the possibility of switching between the two. The deformation control was supplied by a Tri-Scan 100 Advanced Digital Triaxial System whose frame had a capacity of 50 kN. The load control device consisted of a Bellofram (rolling diaphragm) cylinder operated by regulated air pressure from the same house pressure line as employed for the back pressure.

The loading piston, with the diameter of 0.75 in, is attached to the specimen cap from the beginning of the experiments in the triaxial setting. This prevents the cell pressure from being applied completely on the top of the specimen; therefore, a correction is necessary on all stress paths for isotropic compression. The pressures acting on a specimen during cell pressure increase is illustrated in Fig. 3.4.

According to the following calculations, during increasing cell pressure the stress applied on the top of the specimen is $0.250 \cdot \sigma_3$ lower than that on the sides of the specimen.

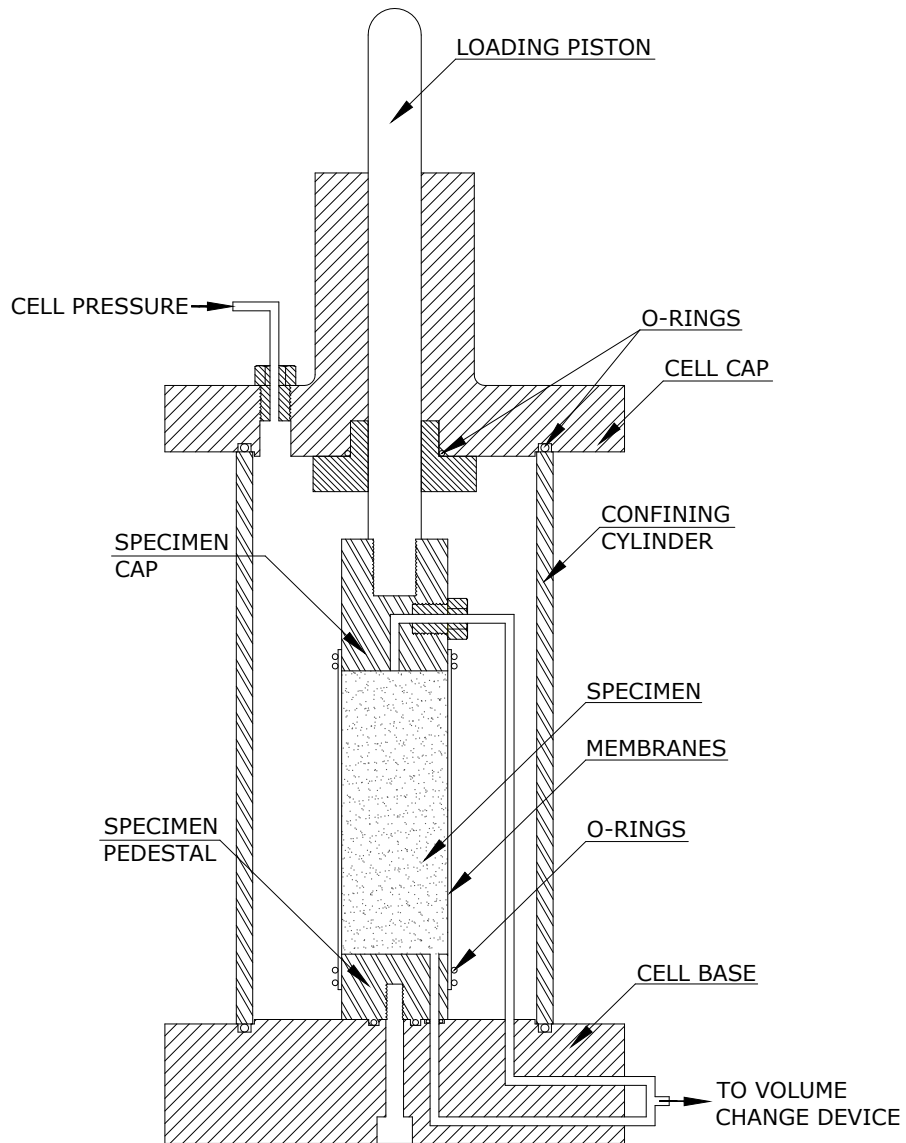


Figure 3.3. Principal cross section of the triaxial cell used in the experimental program.

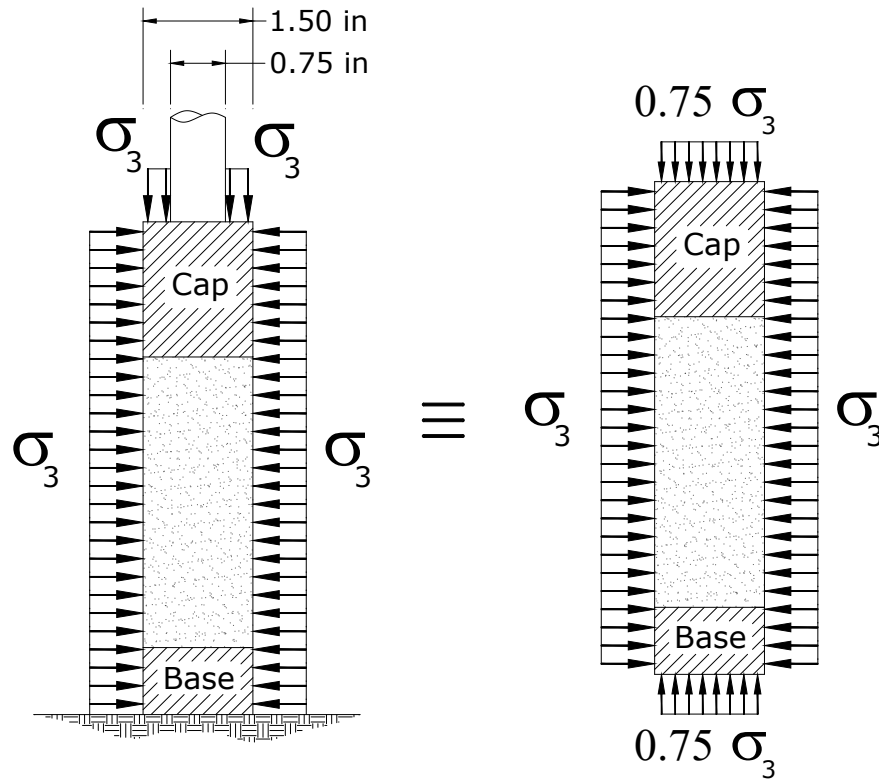


Figure 3.4. Pressures acting on a specimen during cell pressure increase.

$$\begin{aligned}
 & \left. \begin{aligned} D_{piston} &= 0.75 \quad in \\ D_{cap} &= 1.50 \quad in \end{aligned} \right\} \Rightarrow A_{piston} = 0.25 \cdot A_{cap} \\
 & \Rightarrow \sigma_{ave}|_{top} = \frac{\sigma_3 \cdot (A_{cap} - A_{piston})}{A_{cap}} = 0.75 \cdot \sigma_3
 \end{aligned} \tag{3-2}$$

where A_{piston} and A_{cap} are the areas of piston and specimen cap, while σ_3 and $\sigma_{ave}|_{top}$ are cell pressure and the average stress acting on the top of the specimen, respectively. To throw further light on the condition in the stress space, Fig. 3.5 displays the stress path during increasing confining pressure together with the isotropic compression stress path in the triaxial stress plane.

As observed, when the desired confining pressure of σ_3 is reached, the stress point is located at point A which is $0.250 \cdot \sigma_3$ below the isotropic compression stress path. Then, the axial load is applied. Applying axial load increases σ_1 ; thus, the stress point moves vertically until reaching point B at which the isotropic condition is achieved. The load that has been measured from point A to point B should not be assumed as deviator load. In fact, the deviator load is the load applied when the stress point exceeds point B and continues along the triaxial stress path. Since the load cell always measures the vertical load, the amount of $0.250 \cdot \sigma_3 \cdot A_{cap} = \sigma_3 \cdot A_{piston}$ must be deducted from all calculated vertical loads to obtain the correct deviator load and consequently the deviator stress. Therefore, this correction has been made for the entire experimental program and results shown correspond to the corrected values. The following relation is then used to calculate the deviator stress:

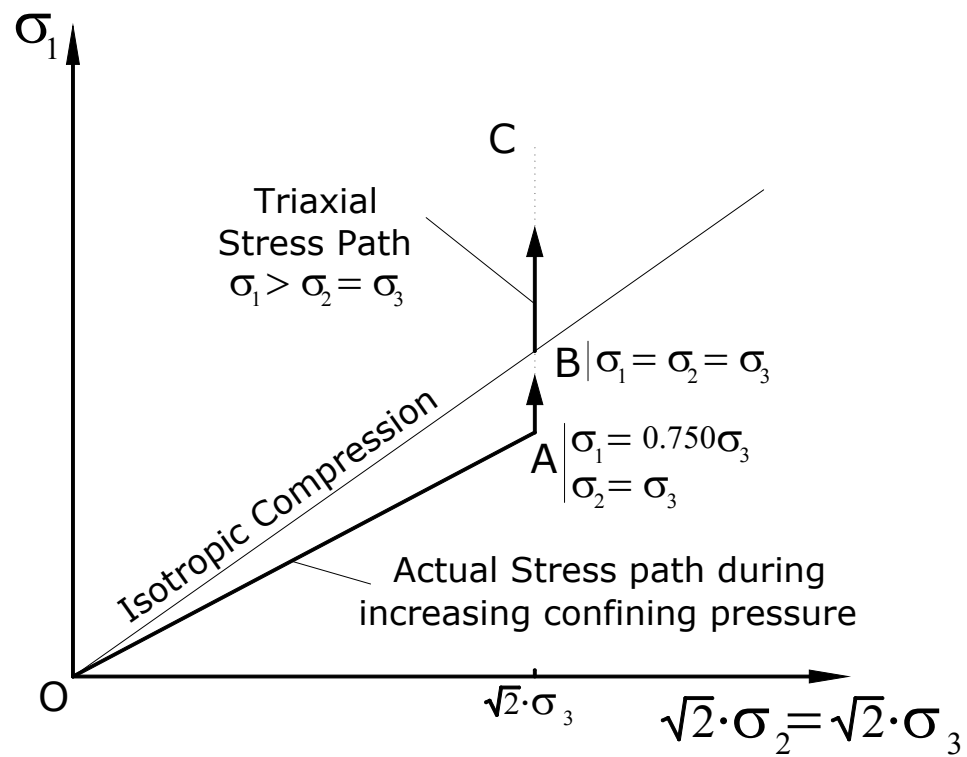


Figure 3.5. Actual stress path during increasing confining pressure and correction of the deviator stress.

$$\sigma_{deviator} = \frac{(F_{vertical} - 0.250 \cdot \sigma_3 \cdot A_{cap})}{A_{specimen}} = \frac{(F_{vertical} - \sigma_3 \cdot A_{piston})}{A_{specimen}} \quad (3-3)$$

where $F_{vertical}$ is the vertical load measured by the load cell, and $A_{specimen}$ is the corresponding specimen area.

3.2.2. Triaxial Specimen Preparation and Measurements

All specimens were built by the dry pluviation method with approximately 50 cm drop-height. To make sure that a homogenous mixture of different particle sizes is produced through the specimen for Type II to Type VI specimens, a specific method was used. In this method, particles of each size were evenly poured in layers from the largest to smallest size in a halved paper-tube with a diameter of 2 inches. Then, using a piece of circular cardboard with the same inside diameter as the tube, the layered soil was dropped into the pluviation funnel from the same height i.e. 50 cm.

The average initial void ratio for Type I specimens was 0.533 with the maximum deviation of 0.012. This corresponded to a relative density of 97.8%. The average actual height and diameter of these specimens were 107.8 and 36.7 mm, respectively. However, the initial void ratios used for Type II to Type VI specimens were presented in Table 3.1.

All specimens were initially enclosed in a 0.65 mm thick latex rubber membrane and filter stones were used at both ends. Even though the filter stones provided full friction at the ends, the specimens were observed to deform essentially as right cylinders due to the high confining pressures employed in this study. The initially dry specimen was saturated using the CO₂-method (Lade and Duncan, 1973) and Skempton's B-value

($= \Delta u / \Delta \sigma_3$) (Skempton, 1954) was determined to ensure that the specimen was fully saturated. Based on the dense state of the specimens, B-values of 0.94 indicated acceptable degrees of saturation for the drained tests in this study.

During an experiment the axial deviator load, the axial deformation, the volume change, and the time were recorded. The cross-sectional area of the specimen was determined from the measured volume change (water expelled out or sucked in) and axial deformation. The axial deviator load was measured by a 45 kN load cell, and the axial deformation was measured by a digital dial gage attached to the loading piston. According to Lade and Liu (1998), this classical system of measurement is as accurate as those measured by a much more sophisticated and elaborate measurement systems that measure movement of points directly on the specimen for determination of strains.

Aforementioned data were taken both by an operator while conducting an experiment and also by a photographic setup which included a camera and a computer. Using WebcamXP 5.0 software, pictures were taken by the camera from the deviator load display, the axial deformation dial gage and the volume change device at various time intervals which were specified according to experiments types and was recorded on the computer. This photographic setup also helped to avoid difficulties for the operator for data recording during long term experiments.

3.2.3. Membrane Leakage

To avoid membrane puncture during testing at high confining pressure which was supplied from a nitrogen bottle and controlled by a high pressure regulator, the latex

rubber membrane containing the specimen was smeared with a layer of silicone grease (Dow Corning High Vacuum), and three layers of 0.28 mm continuous rubber sheets with layers of silicone grease were wrapped around the specimen. A vertical strip of glue (Barge) was smeared at the edge of each complete wrap to glue the layers together. In addition, on the last, vertical wrap edge, a strip of liquid latex rubber was applied and allowed to dry. Even with this four-layer thick assembly of membranes, which was sealed by two O-rings at each end, leakage was observed for long term experiments at high confining pressures. This can be seen in Fig. 3.6 where the volume change results of three tests at the effective confining pressure of 8000 kPa are compared. In Test *A*, it only took 33 minutes to shear the specimen up to 22% of axial strain, while for Test *B* it took 528 minutes for the same amount of axial strain. No obvious leakage was detected for these two tests. However, for Test *C*, after reaching about 1.20% of axial strain (about 460 minutes), the volume change began to deviate due to leakage. The volume change rate increased until reaching a steady rate at which continuation of the test was not possible.

Close observation of the nature of the leakage and other clues implied that it was a kind of diffusion problem. It was discovered that nitrogen from the nitrogen bottle which supplied the high confining pressure dissolved in the de-aired water inside the cell, traveled toward the specimen and penetrated through the four-layer membrane. Once the nitrogen reached inside the specimen, since the pressure was much lower and equal to the back pressure, the nitrogen came out of solution and formed bubbles which increased in size with time. This resulted in a false volume change response and the observation of

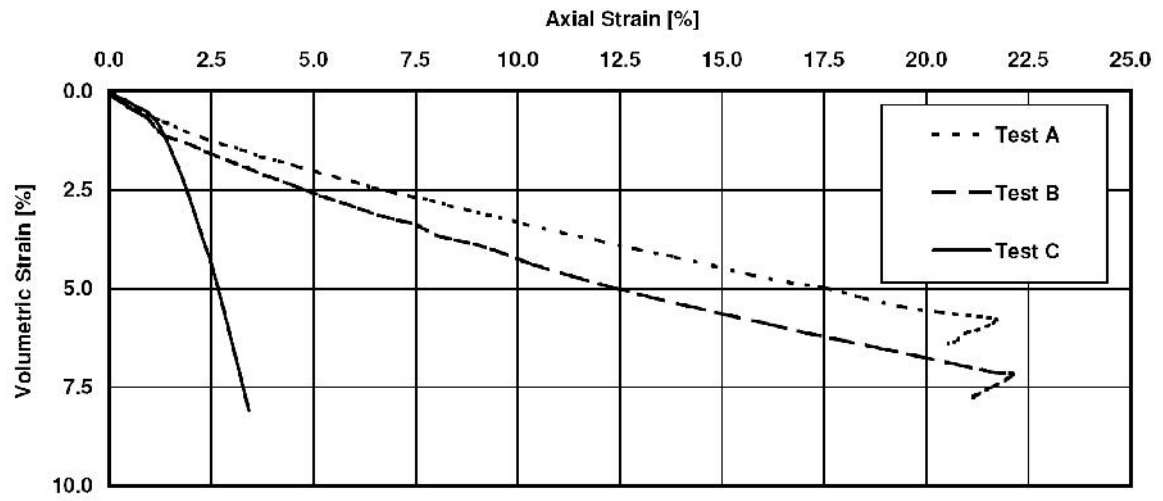


Figure 3.6. Volume change response of three triaxial tests with different time-to-failures before installation of spiral tubing.

leakage. To avoid this problem, rather than applying the nitrogen pressure directly at the top of the triaxial cell, it was decided to apply the nitrogen pressure at the end of a long spiral of stainless steel tubing full of de-aired water (see Fig. 3.3). Since gas travels by diffusion, a sufficiently long tube would prevent the nitrogen from reaching the specimen within the time of the test. The total length of the spiral tubing used was 3.6 m. It turned out that this length was enough to avoid the diffusion of nitrogen into a specimens for a test under $\sigma'_3=8000$ kPa lasting for two months.

Fig. 3.7 compares the volume change results of experiments similar to Test *A*, Test *B* and Test *C* after installation of the spiral tubing. It is observed that Test *A'* which took only 33 min exhibited 0.30% less volume change than Test *A*. In comparison, when the spiral tubing was installed, Test *B'* that lasted for 528 minutes showed 1.30% lower volume change than Test *B*. Higher difference in the error in Test *B'* in comparison to Test *A'* was due to the longer testing time. The third test, Test *C'*, demonstrated volume change of 6.20% after 8460 minutes, while Test *C* had been terminated after about 460 minutes due to leakage as explained above.

Piston friction may decrease the accuracy of the application and measurement of the vertical load. Specifically, locking of the loading piston may happen during a long period of time in creep or relaxation tests where the deformation rate is significantly reduced. Two ball-bushings were placed in the cap of the triaxial cell to minimize the amount of friction and to provide guidance for the vertical movement of the piston.

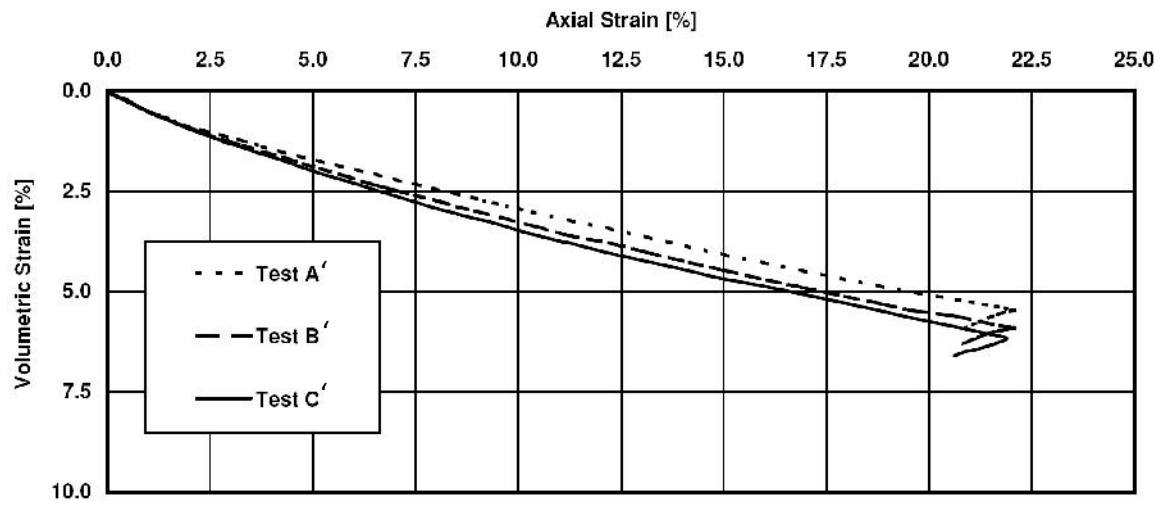


Figure 3.7. Volume change response of three triaxial tests with different time-to-failures after installation of spiral tubing.

Similarly, at high confining pressure, O-ring jamming may result in additional piston friction. However, inspection and application of silicon grease on O-rings at the end of each experiment confirmed that jamming does not occur. No correction of friction forces was made to the measured data as it was judged that the discussed friction forces can be ignored in comparison with the measured deviator loads.

3.2.4. Volume Change Error Correction

In a few experiments, small leaks were observed. Since all triaxial experiments were performed under drained conditions, these leaks could not affect the progress of the experiments. However, measuring a wrong volume change due to a leak will change the stress-strain curve. Either these experiments were repeated or in case of similar tests, their volume change behaviors were corrected based on the modified Rowe's stress-dilatancy method. This method was used by Tatsuoka et al. (2008) to calculate the volume change response of dry specimens in drained triaxial experiments. It is performed as explained in the following steps:

- Plot the R - D diagram (R is the principal stress ratio and $D = 1 - (d\varepsilon_V / d\varepsilon_1)$, where $d\varepsilon_V$ and $d\varepsilon_1$ are increments of volumetric and axial strains, respectively) for the results of the similar test and fit the nonlinear modified Rowe's stress-dilatancy relation (the original Rowe's (1962) stress-dilatancy is $R = \tan^2(45 + \phi_f / 2) \cdot (1 - d\varepsilon_V / d\varepsilon_1)$ in which ϕ_f is the friction angle of granular materials at failure after deducting dilatancy effects):

$$R = C_0 + C_1 \cdot D + C_2 \cdot D^2 + C_3 \cdot D^3 \quad (3-4)$$

- Calculate $d\varepsilon_V$ by substituting each R and $d\varepsilon_1$ from the test with the leak into the fitted relation. By summing of all $d\varepsilon_V$ from the beginning of the test, the corrected volumetric response of the test with the leak is obtained.
- Recalculate stresses according to the corrected volume change response.

3.3. Single Particle Strength Tests

Two types of tests were performed on single glass beads. In both types, glass beads were placed between two parallel, hardened high-carbon steel plates and a small seating load was applied to keep the glass sphere in place. They were then loaded under load control by increasing the load with one minute intervals. This created tensile stresses across a vertical mid-section of the spherical glass bead.

In the first type of tests, the short term fracture strength of glass beads of each of the three sizes were determined by increasing the load until fracture occurred. 16 glass beads of each size were broken. Time-to-fracture, axial compression of the glass bead and load at which the glass beads broke were recorded for each experiment. In the other type of tests, static fatigue was investigated by loading glass beads of each size up to various constant stress levels, and measuring the time-to-fracture. A total number of 22 beads of size 2 mm, 19 beads of size 3 mm and 14 beads of size 6 mm were broken in this series. As discussed in Chapter 2, it was expected that static fatigue would result in the fracture of the glass beads after some time if they were loaded up to the vicinity of their short term fracture strengths.

3.4. Isotropic Compression–Drained Triaxial Compression Tests

Effects of confining pressure and initial axial strain rate on the behavior of Virginia Beach sand were investigated in triaxial compression tests as follows:

3.4.1. Effect of Confining Pressure

A wide range of constant effective confining pressures (25, 50, 250, 500, 1000, 2000, 4000, 8000 and 14000 kPa) was considered to determine where significant particle crushing would occur significantly. This was also done to study the influence of confining pressure on the behavior of Virginia Beach sand. It should be noted that tests performed at confining pressures of 14000 kPa showed a considerable amount of crushing. However, due to many experimental difficulties such as membrane puncture and nitrogen diffusion, it was consequently decided to study time effects under a constant effective confining pressure of 8000 kPa where the significance of particle crushing and experimental feasibility criteria were both met. The states of stress during shearing of the triaxial specimens at 8000 kPa correspond to those experienced near tips of relatively long piles (15-30 m or 50-100 ft), near the bottom of deep wells, and near deep tunnels.

Following the saturation of each specimen, the confining pressure was increased in a number of steps to achieve the final desired confining pressure. In this regard for confining pressures of 25 and 50 kPa no steps were required as the specimens were built at the same effective pressure. For confining pressures of 250, 500 and 1000 kPa, steps of 100 kPa were employed, while the confining pressure was increased in steps of 500 kPa for confining pressures higher than 1000 kPa until the desired confining pressure was reached. For each increment in confining pressure, the specimen was allowed to creep for

2 minutes before the volume change and the axial deformation were recorded. The confining pressure was then increased to the next value. After the desired confining pressure had been achieved, the specimen was allowed to creep for 45 minutes before shearing was initiated at a deformation rate of 0.0448 mm/min which corresponds to 0.0416 %/min. The specimens were then sheared up to the axial strain of about 22.0% where failure.

Unlike consolidation, no specific time period can be recognized to identify the termination of the creep process because creep proceeds with logarithmic time, and no particular time is ideal for the next pressure increment. It is emphasized that the 2-minute periods of time allowed at each new confining pressure were not sufficient to reach any particular amount or proportion of creep; however, it was judged to be a practical method of reaching the desired confining pressure under a controllable situation while readings were being recorded along the way. It was also found that waiting for longer time periods would produce a stress-strain relation that would be similar to that produced after 2 minutes of creep.

The 45 minutes of creep at the desired confining pressure before shearing was initiated provided enough time for the creep rate to reduce to a small value. From a practical point of view, it granted a sufficient amount of time to the operator to check all test settings and data-logging systems before applying the deviator stress. Miura and Yamanouchi (1973) observed that under confining pressures of 300 to 500 kg/cm², specimens of Toyoura sand required 350 to 570 hours to reach 100% compression i.e. end of creep. Since waiting for these periods of time was not practical, they decided to

start the shearing of the triaxial specimens when the rate of volume change was reduced to the value of $0.1 \text{ cm}^3/\text{hr}$ or less. Similarly, Vesic and Clough (1968) in an experimental program on Chattahoochee River sand observed that waiting for 30, 60 and 150 min before applying deviator stress under confining pressures of 70, 211 and 422 kg/cm^2 corresponded to 100% compression of the specimens. They argued that although the nature of this volume change at high confining pressures was similar to consolidation, “no reasonable interpretation was possible by means of the theory of primary consolidation”.

3.4.2. Effect of Initial Axial Strain Rates

The effect of initial axial strain rate on the stress-strain behavior, strength, stiffness and volume change of different types of sand was addressed in Chapter 2. Yamamuro and Lade (1993), Matsushita et al. (1999), Santucci de Magistris and Tatsuoka (1999), Tatsuoka et al. (2000, 2002, 2006), Di Benedetto et al. (2002), Kuwano and Jardine (2002), AnhDan et al. (2006), Kiyota and Tatsuoka (2006), Lade (2007) and Lade et al. (2009, 2010) studied the effects of initial axial strain rate on the behavior of geomaterials. As a general conclusion, it was observed that the effects of strain rate are small enough to be neglected for granular materials.

Effects of initial strain rates were investigated for Virginia Beach sand. Three deformation rates of 0.0028, 0.0448 and 0.7168 mm/min which corresponded to strain rates of 0.00260, 0.0416 and 0.666 \%/min , (the maximum strain rate is 256 times higher than the minimum strain rate) were employed to perform a total of six triaxial

compression tests under two constant confining pressures of 250 and 8000 kPa. Therefore, reaching 22% of axial strain, where failure was achieved, required approximately 8460, 528 and 33 minutes, respectively.

3.4.3. Effect of Isotropic Aging

Four experiments were performed to explore the effect of aging under an isotropic stress of 8000 kPa on the properties of Virginia Beach sand. The desired confining pressure was reached incrementally as explained above. No time was allowed for consolidation of the first specimen and it was subjected to shearing instantaneously after a confining pressure of 8000 kPa. The three other specimens were isotropically consolidated for 45 min, 1 day and 1 week before application of deviator stress. The middle strain rate of 0.0416 %/min was used for application of deviator load in all four experiments. Daramola (1980) performed a similar study to determine the effect of aging under isotropic stresses applied for periods up to 152 days on the stiffness of Ham River sand at low confining pressures.

3.5. K_0 Stress State Compression-Drained Triaxial Compression Tests

Similar to the study of isotropic aging effects on the behavior of Virginia Beach sand, the effect of aging under K_0 stress state was investigated by performing four experiments in the triaxial apparatus with lateral pressure (cell pressure) of 8000 kPa. Analogous to the procedure of increasing the confining pressure described in Section 3.4.1, increments of 500 kPa was used for increasing the lateral pressure in these tests. To maintain the K_0 condition after each increment of lateral pressure, the axial load was applied (under load control) such that combinations of changes in volume change and

axial deformation resulted in a constant cross sectional area of the specimen. This procedure was used until the final lateral pressure was reached. In other words, the decrease in the cross-sectional area due to increase in the lateral pressure was compensated by applying a vertical load on the specimen which would increase the cross-sectional area. After reaching the desired lateral pressure, further loading was performed by switching to deformation control. One specimen was sheared right after switching to deformation control, while the three other specimens were aged under the K_0 condition for 45 min, 1 day and 1 week before there were sheared. All four specimens were sheared at a strain rate of 0.0416 %/min.

3.6. Creep Tests

All creep tests performed in this research were carried out under fully drained conditions as creep deformations in undrained conditions result in the production of pore pressure which in turn cause a change in effective stress. Consequently, part of the deformation is correlated to a change in effective stress level, and separation of creep deformation and plastic deformation makes the study of creep more complicated. These experiments including are explained in the following categories:

3.6.1. Effect of Initial Shearing Rate on Subsequent Creep

Experimental studies of creep in granular materials have been mostly performed with the same initial strain rate. Therefore, the influence of the initial shearing strain rate on the subsequent amounts of creep is investigated for Virginia Beach sand. In this regard, the three aforementioned strain rates of 0.00260, 0.0416 and 0.666 %/min were

used to shear a total number of six specimens under low and high effective confining pressures of 250 and 8000 kPa.

Lade et al. (1996) stated that the amount of particle crushing is related to the energy input. It was also pointed out by Lade et al. (2009, 2010) that the time effects in granular materials may be connected to particle crushing. Thus, input energy should have an important impact on time effects such as creep. The total energy input per unit volume of specimen during each experiment was calculated for each test according to the following equation:

$$E = \sum \sigma'_c \cdot \Delta \varepsilon_v + \sum (\sigma_1 - \sigma_3) \cdot \Delta \varepsilon_a \quad (3-5)$$

in which σ'_c , $(\sigma_1 - \sigma_3)$, $\Delta \varepsilon_v$ and $\Delta \varepsilon_a$ are the effective confining pressure, deviator stress, volumetric strain increment, and axial strain increment, respectively.

To compare the creep of the specimens sheared at different rates, different criteria may be considered to choose a point where creep is initiated. For example, a creep test may start at the same deviator stress or at the same axial strain. However, since particle crushing may relate to energy input, creep testing was initiated when the same total input energy had been reached. Therefore, under each confining pressure, all three specimens were sheared up to a stress point which corresponded to the same amount of total energy input calculated from Equation (3-5). These points on the stress-strain curves were chosen to be at approximately 70-75% of their deviator strengths. Creep then initiated while the stress was held constant by switching from deformation control to load control and it continued for one day (1440 minutes). During a creep test the cross-sectional area

of the specimen was determined from the measured volume change and axial deformation, and the deviator stress was maintained constant by frequently calculating the cross-sectional area and increasing the air pressure in the Bellofram cylinder to increase the deviator load to achieve the desired constant deviator stress.

3.6.2. Effect of Soil Gradation Curve on Subsequent Creep

Six different grain size distribution curves were used to explore the creep behavior of Virginia Beach sand under the confining pressure of 8000 kPa and an initial loading strain rate of 0.0416 %/min. The same deviator stress was used as the criterion of initiating creep tests.

3.6.3. 1-Day Creep Curve

Lade (2007) presented results of a series of 1-day creep experiments at different deviator stresses on Antelope Valley sand. Connecting the ending points of each creep test provided a curved called a “1-day creep curve.” This curve helped to identify the viscous type behavior of the sand as well as finding where other creep tests would end in case they initiated at different deviator stresses. A similar curve was extracted by Lade et al. (2010) from a series of creep tests on crushed coral sand. The same idea was considered for Virginia Beach sand and seven specimens were sheared under a confining pressure of 8000 kPa at a strain rate of 0.0416 %/min. Therefore, the creep process started at seven different deviator stresses by switching from strain control to stress control and creep was measured for one day in each test. The 1-day creep curve for this sand would thus be plotted by connecting seven final creep points in the stress-strain

diagram. Lagioia (1998) noticed that when a specimen was held under constant stress and crept, further loading was accompanied by structuration effects. Lade et al. (2009, 2010) also observed structuration effects upon further loading after creep and relaxation experiments on crushed coral sand. However, Lade and Liu (1998) did not report this phenomenon from the similar experiments on Antelope Valley sand. In this regard, an experiment was performed to investigate whether Virginia Beach sand would exhibit such an effect. In this test, creep was measured at three levels of deviator stresses followed by further loading to the next desired stress level for initiation of the next 1-day creep event.

3.6.4. Long Term Creep

Most studies presented on creep behavior of granular materials in the literature have been conducted for short periods of time due to various practical difficulties (Murayama et al., 1984; Leung et al., 1996; Lagioia, 1998; Bowman and Soga, 2003; Lade, 2007; Lade et al., 2009). To shed further light on creep behavior for longer periods of time, a 2-month creep experiment was performed on a specimen that had been sheared initially at strain rate of 0.0416 %/min under a confining pressure of 8000 kPa.

3.7. Stress Relaxation Tests

3.7.1. Effect of Initial Shearing Rate on Subsequent Stress Relaxation

The effect of shearing strain rate on the subsequent stress relaxation in granular materials has not been widely studied. Therefore, strain rates of 0.00260, 0.0416 and 0.666 %/min were used to perform six experiments for investigation of the subsequent

stress relaxation under confining pressures of 250 and 8000 kPa. To be able to produce a comparison between creep and relaxation results, the same criterion as used for the initiation of creep tests was used for initiation of stress relaxation tests. Thus, each specimen was loaded at different strain rates up to a deviator stress level (in the range of 70-75% of their deviator strength) that corresponds to the same total energy input as in the corresponding creep tests. At these stress points, further shearing was stopped and specimens were allowed to relax for 1 day.

It was observed that even after loading stopped, the specimens experienced some axial deformation. Theoretically, deformations should be zero during stress relaxation tests. This creates a fundamental experimental difficulty in performing these tests. The reduction in deviator stress after deformation has been stopped needs to be recorded by a load cell, which must be located in series with the triaxial specimen inside the loading frame. However, the load cell expands during the decrease in load because of stress relaxation of the specimen. This expansion compresses the specimen in the axial direction and results in measurement of stresses higher than those corresponding to stress relaxation with zero axial strain.

Therefore, three experiments were carried out at the same three initial deformation rates used in the experiments explained above to investigate the sensitivity of the measured stress relaxation to the small amounts of axial deformation imposed by expansion of the load cell during decreasing load. The axial deformation of each specimen was continuously monitored by a digital dial gage. The dial gage reading was very accurately maintained constant by small adjustment in the deformation control

loading machine thereby changing the deviator load slightly corresponding to the truly constant height of the specimen.

On the other hand, specimens exposed to stress relaxation under zero axial strain may undergo volume changes since they are not controlled in drained stress relaxation tests. Therefore, in addition to the drained stress relaxation experiments, three stress relaxation experiments were conducted under undrained conditions initiated at an effective confining pressure of 8000 kPa. The only difference between these tests and the tests with adjustment of axial deformation was closing the drainage valve right after loading stopped and before stress relaxation began. This provided a condition in which the specimen experienced completely zero deformation in any direction during stress relaxation. The pore pressure generation was monitored, recorded and analyzed instead.

3.7.2. 1-Day Stress Relaxation Curve

Similar to the 1-day creep curve, Lade (2007) and Lade et al. (2010) presented a series of 1-day relaxation experiments on Antelope Valley and crushed coral sands, respectively. Comparison of 1-day creep and 1-day stress relaxation curves showed that these two curves were located at different positions. Lade et al. (2010) found that the mechanism behind time effects in granular materials is related to crushing of particles. However, due to the friability of the two types of sand previously tested, the grain size distributions were not determined after the experiments for the purpose of proving the direct connection between time effects and crushing.

Therefore, similar testing was carried out on Virginia Beach sand followed by determination of grain size distribution curves. Six specimens were built and sheared under a confining pressure of 8000 kPa at the strain rate of 0.0416%/min up to six different deviator stresses where 1-day relaxation was initiated. It has been stated in the literature that if granular materials age under stress they would exhibit structuration during further loading. Since the previous six 1-day relaxation experiments were terminated at the end of 1-day relaxation to investigate the particle crushing during relaxation in each individual test, another specimen was built, consolidated and sheared under the same conditions. 1-day relaxation tests were performed at four different deviator stresses followed by further loading to identify structuration effects after the end of stress relaxation. As mentioned earlier, structuration effects were reported by Lade et al. (2009, 2010) on crushed coral sand while Lade (2007) did not observe this effect for Antelope Valley sand.

3.7.3. Long Term Stress Relaxation

Not many studies have been conducted to explore the stress relaxation behavior of granular materials. Because of some practical problems that may occur in the longterm, such studies have been limited to short periods of time such as 1 day (Lacerda and Houston, 1973; Ladanyi and Benyamina, 1995; Lade, 2007; Lade et al. 2010). Therefore, for further clarification of relaxation behavior of granular materials a long-term relaxation test was carried out on Virginia Beach sand. In this test, the specimen after isotropic consolidation up to 8000 kPa was loaded at a strain rate of 0.0416 %/min up to a

desired deviator stress level and allowed to stress relax for more than two months with correction of the axial deformation to achieve zero axial strain.

3.8. Mixed Creep-Stress Relaxation Tests

Experiments were also performed in which either drained creep or stress relaxation were followed by stress relaxation or creep, respectively, to throw further light on consecutive or concurrent effects of these two phenomena on each other.

3.8.1. Tests with Creep, then Stress Relaxation

Four experiments were performed to study the stress-strain behavior of Virginia Beach sand subjected to creep for different amounts of time followed by stress relaxation for 1 week. All four tests were performed with a confining pressure of 8000 kPa and sheared at 0.0416 %/min prior to initiation of creep and relaxation. Fig. 3.8 schematically shows the procedure of these tests.

As seen, all four specimens were sheared up to a desired deviator stress. The first specimen underwent instantaneous stress relaxation for 1 week. In the second test after switching from deformation control to load control, the specimen was allowed to creep for 3 hours followed by stress relaxation for 1 week by switching back to deformation control with no further deformation. Two other specimens were allowed to creep for 1 day and 1 week, respectively, before they underwent stress relaxation for a period of 1 week. It is emphasized that corrections of axial load were made due to change in the specimen cross sectional area during creep together with maintaining zero axial deformation during relaxation for all three experiments.

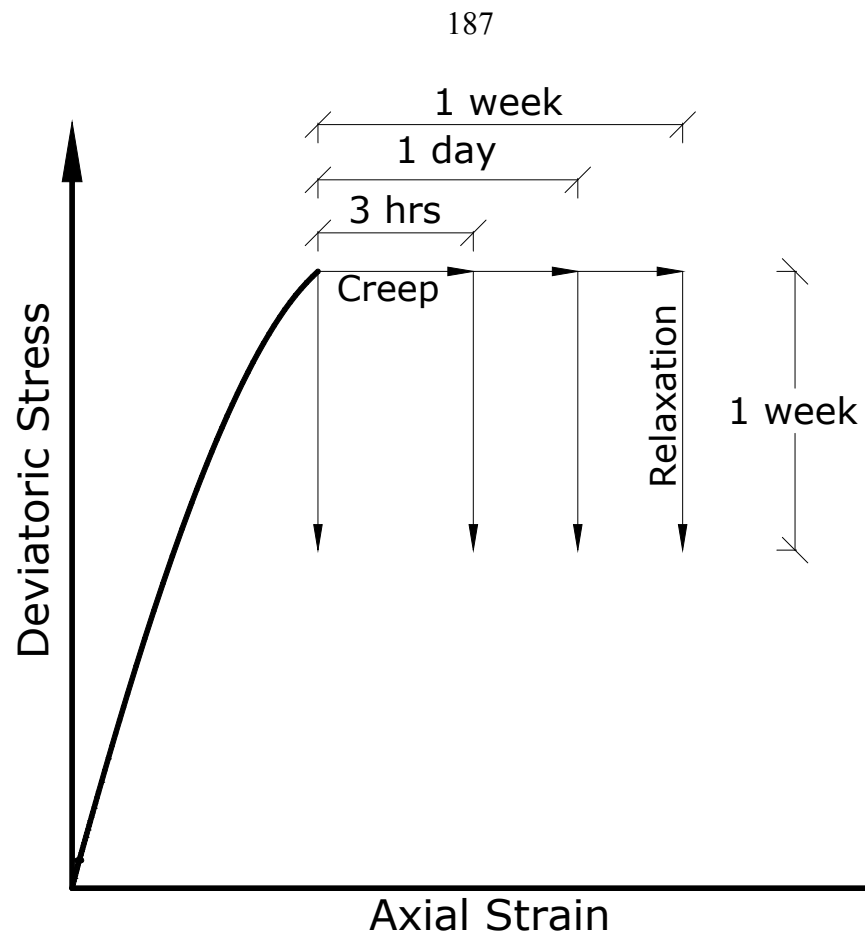


Figure 3.8. Schematic stress-strain path for creep-relaxation experiments.

3.8.2. Tests with Stress Relaxation, then Creep

Reverse loading conditions were used to explore the consecutive effects of stress relaxation and creep on Virginia Beach sand. Four tests were performed with a confining pressure of 8000 kPa. Specimens were loaded at the rate of 0.0416 %/min up to the same stress level as in the previous series of tests. Deformation control was changed to load control quickly and the first specimen was allowed to creep for 1 week. However, three other specimens initially relaxed for 3 hours, 1 day and 1 week, respectively. The loading was then switched to load control, and specimens were allowed to creep for 1 week. As mentioned earlier, the same types of correction were made to keep the stress constant during creep and maintain the deformation constant during stress relaxation. A schematic stress-strain diagram of these four tests is shown in Fig. 3.9.

3.8.3. Combined Creep-Stress Relaxation

Simultaneous effects of creep and relaxation in granular materials were studied by performing five experiments under confining pressures of 8000 kPa. Fig. 3.10 illustrates the desired stress-strain relations for these tests.

As seen, once the desired energy input was reached, the first specimen crept for 1 week by switching to load control. The second, third and fourth specimen experienced a combination of creep and relaxation for 1 week. These were performed by installing springs with different stiffness in series with the load cell and the specimen. In fact during loading of the specimens, springs were compressing according to Hooke's law

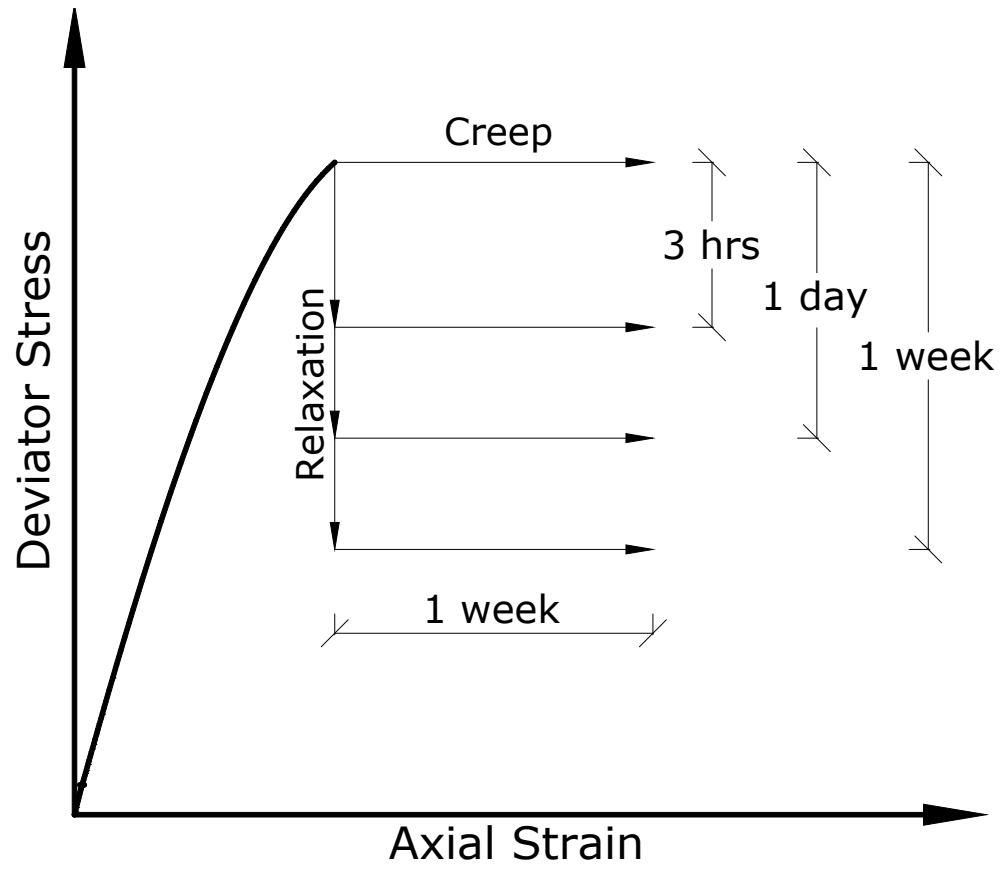


Figure 3.9. Schematic stress-strain path for relaxation-creep experiments.

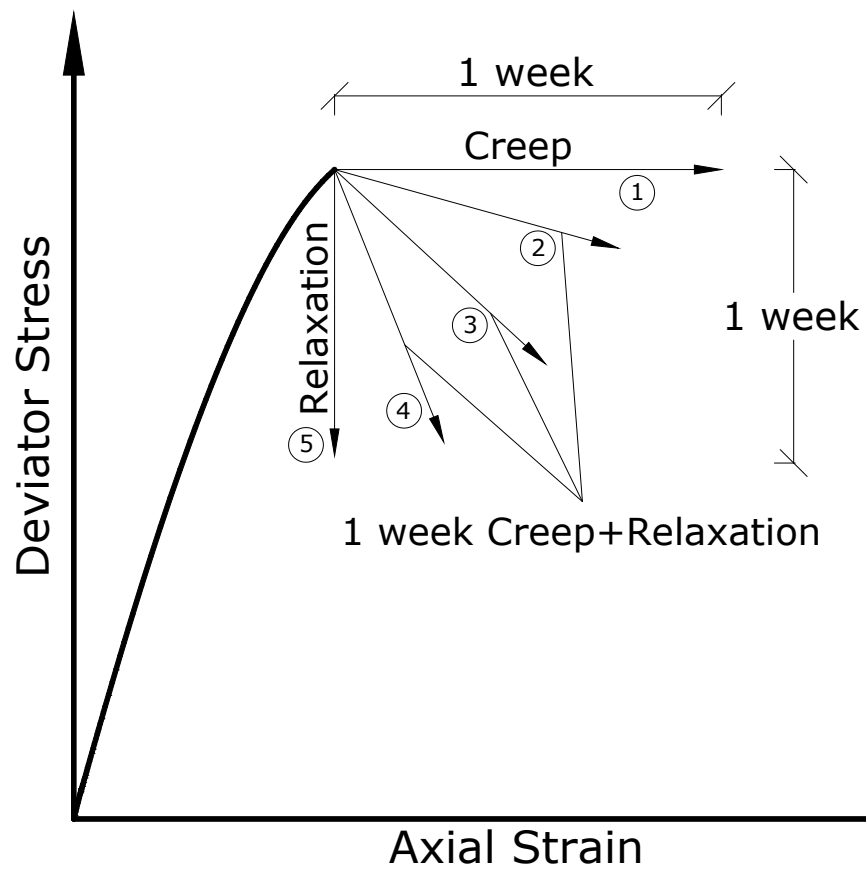


Figure 3.10. Schematic stress-strain path for combined creep-relaxation experiments.

until loading stopped. At this moment, these springs had a stored energy and worked as a loading force on the specimen with a decreasing rate because as the springs were expanded, their stored energy reduced. Various stiffnesses produced different inclination of the stress-strain relations. This idea came from the problem of the expansion of the load cell which imposed an axial deformation during stress relaxation. In test number five, when the desired deviator stress was reached deformation was stopped and the specimen relaxed for 1 week.

3.8.4. Multiple 1-Day Creep-Shear-Stress Relaxation

An experiment was performed to study creep and relaxation followed by further loading. In this test, after consolidation under 8000 kPa, the specimen was loaded at the strain rate of 0.0416 %/min up to the first desired deviator stress where the first creep process initiated for 1 day by switching to load control. It was then further sheared under deformation control to reach the second stress level where the specimen underwent 1-day stress relaxation. The experiment was continued by loading to the third deviator stress level. Loading was switched back to load control and the specimen crept for 1-day. Further loading was pursued under deformation control again to the last deviator stress level and the second 1-day stress relaxation was carried out.

3.9. Stress Drop- Creep Tests

3.9.1. Stress Drop-Creep

To expose the nature and details of creep in sand, special stress drop tests were performed. Stress drop-creep experiments began in a similar manner as the

aforementioned creep tests. However, after reaching a desired deviator stress, in three different experiments three different stress drops were imposed and creep was initiated afterward by holding the deviator stress constant for 1 week. Lade et al. (2009) described that the rate of drop in stress is not important as long as it happens relatively fast.

3.9.2. Multiple Stress Drop-Creep-Shear

Three multi stress drop-creep tests were also performed. In the first test after reaching the first desired deviator stress a specified stress drop was enforced and the specimen crept for 1 day by switching to load control. Following creep, the loading system was switched back to deformation control and the specimen was sheared to the next stress level where the deviator stress was dropped the same amount prior to initiation of another 1-day creep. The same procedure was used at the third stress level as well. The two other tests were carried out and sheared to the same deviator stresses; however, different stress drops were imposed. In this series of tests, the structuration effect due to 1 week of aging during creep was also investigated.

3.10. Stress Drop- Relaxation Tests

3.10.1. Stress Drop-Stress Relaxation

Similar to stress drop-creep experiments, the same procedure was employed for three stress drop-relaxation tests. However, instead of creep, stress relaxation was performed for 1 week. Therefore, no change was required in loading system and all experiments were performed in deformation control.

3.10.2. Multiple Stress Drop-Stress Relaxation-Shear

Structuration effects developed during relaxation of Stress Drop-Relaxation-Shear tests was studied by performing two experiments. In the first test after reaching the first desired deviator stress, a specified stress drop was enforced and stress relaxation initiated for 1 day. Following relaxation, the specimen was loaded to the next stress level where the same stress drop was implemented prior to initiation of another 1-day relaxation. The same procedure was used for the third stress level and relaxation as well. In the other test the specimen loaded to the same deviator stresses; however, a different amount of stress drop was imposed.

3.11. Sieve Analyses and Characterization of Crushing

Particles undergo crushing if the acting stresses exceed their short term strengths or they are held for enough time at a sufficiently high stress level. According to static fatigue, crushing is a time-dependent phenomenon. Thus, particle crushing may be the principal phenomenon to explain time effects in granular materials. This is in accordance with observation of smaller time effects under low confining pressures where crushing is not pronounced in comparison to high confining pressures where significant amount of crushing occurs. It should be noted that depending on the confining stress level different types of breakage may happen. For example, abrasion may be the only type of breakage under low confining pressures while the elevating confining pressure may change the breakage type to attrition or even total fracture. This indicates exhibit the importance of investigation of particle breakage.

Based on observations by Fukumoto (1992) and Lade et al. (1996), the amount of crushing is related to the amount of energy input to the soil. Therefore, time effects can be associated with energy input and crushing. To quantify breakage of particles, various methods have been proposed in different studies presented in the literature. These methods can be categorized in the following two groups.

3.11.1. Methods That Assume a Specific Grain Size

Lee and Farhoomand (1967) described “relative crushing” as the ratio of the size corresponding to 15 percent finer before testing, D_{15i} , to the same value after testing, D_{15a} while they were investigating compressibility and crushing of granular media. It can be observed that the minimum limit of “relative crushing” is unity while there is no upper limit.

Change in median diameter size, D_{50} , and D_{70}/D_{40} were used by Hagerty et al. (1993) to quantify particle crushing during the investigation on one-dimensional high pressure testing of granular materials. Lade et al. (1996) defined a particle breakage factor called B_{10} which can be estimated by deduction of the ratio of the final grain size related to 10% finer, D_{10f} , to the initial grain size related to 10% finer, D_{10i} , from unity. Therefore, similar to “relative crushing” defined by Lee and Farhoomand (1967) zero amount of crushing produces a value of unity, whereas the upper limit is infinity. In fact, D_{10} , called the effective grain size, was used to make a connection to Hazen’s formula used to estimate permeability based on D_{10} for granular materials. On the other

hand, Leung et al. (1996) also utilized a sieve with opening of 212 μm to evaluate the amount of particle crushing in a series of one-dimensional compression tests on sands.

Nakata et al. (1999) presented a new particle breakage factor, B_f , which was simply defined as the percentage of particles smaller than the initial minimum grain size after the test. They used this breakage factor to quantify evolution of the grading curve during triaxial testing on granular materials.

3.11.2. Methods That Consider Changes in the Whole Grain Size Distribution Curve

Marsal (1967) proposed “Particle breakage, B” which is calculated as the difference between the sum of positive portions of differences in percentage retained, (can be positive or negative) in each size after crushing. He used this measure in connection with the design and construction of earth and rockfill dams. Theoretically, “B” has an upper limit of 100% and a lower limit of zero.

Fukumoto (1992) in a comprehensive study of particle breakage characteristic of granular materials introduced a quantitative index called “S.I.” which is the logarithm of the ratio of specific surface area (in cm^2/gr) from grain size distribution after testing to the same value before testing. In a similar manner, Miura and O-Hara (1979) indicated that an increase in the surface area of the specimen (in cm^2/cm^3) can numerically relate particle breakage. The surface area itself is calculated from the product of current value of dry density and the specific surface area. The Blaine method (Blaine, 1943) could be employed to evaluate the specific surface area of soils finer than US standard sieve

No.200 although this method considers grains to be shaped as spheres. For larger particles specific surface can be calculated based on each grain size and dry density.

Hardin (1985) suggested a particle breakage factor which seems to be the most widely used particle breakage index in the literature. This index, B is the ratio of total breakage, B_t , to breakage potential, B_p . The definition of these parameters is illustrated in Fig. 3.11.

B_p is defined as the area between the original grading curve and the US standard sieve No. 200. In other words, this shows the maximum theoretically possible change in grain size distribution curve and means that all particles have been broken to grains finer than 75 μm . The value of B_t is calculated by measuring the area between the original and the final grading curves. Hardin's breakage factor has a lower limit of zero and a theoretical upper limit of unity.

A total number of 118 triaxial compression experiments was performed on Virginia Beach sand. Virginia Beach sand was sieved before each test to produce the desired grain size distribution curve. To determine the amount of crushing that occurred after each test, the specimen was retrieved, put in an oven for 24 hours at 105°C and sieved. The sieving procedure for each specimen, which originally weighed an average of 197 g, was performed by small sieves with diameter of 3 in. To produce accurate results, each specimen was sieved in three equal parts using a Humboldt motorized sieve shaker (model H-4326). The sieving time is also of importance as the amount of soil

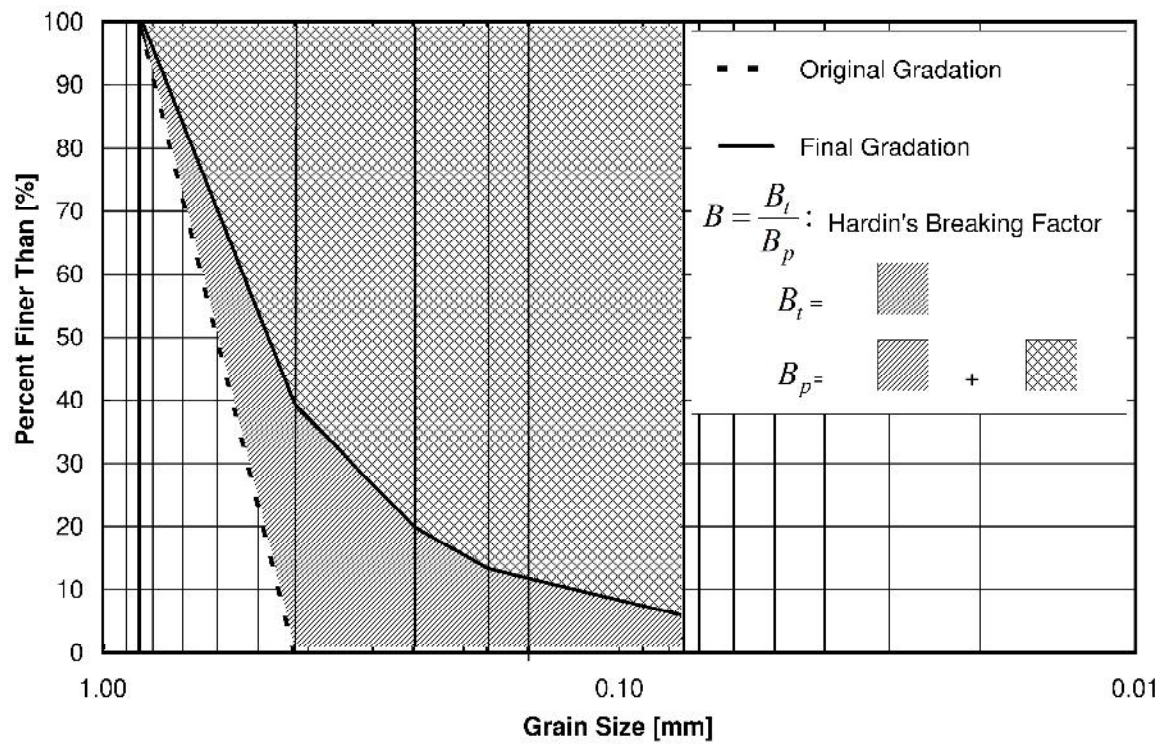


Figure 3.11. Definition of parameters of Hardin's particle breakage index.

passing through a sieve may increase with the time of sieving. This increase is dependent on the friability of the sand particles. Therefore, a time of 13 min was given to all specimens for sieving. Hardin's breakage factor has been used in the entire study to quantify the amount of crushing, and to correlate time effects with particle breakage through energy input.

4. Isotropic and K_0 Stress States Compression-Drained Triaxial Experiments, and Single Particle Strength Tests

4.1. Effect of Confining Pressure

A wide range of confining pressures of 25, 50, 250, 500, 1000, 2000, 4000, 8000, 12000 and 14000 kPa were used to study their effect on the behavior of Virginia Beach sand. The procedure and details of performed experiments were described in Chapter 3. Fig. 4.1 shows the effect of the confining pressure on the stress-strain and volumetric behavior of Virginia Beach sand for confining pressures equal to and lower than 250 kPa, while Fig. 4.2 illustrate the same curves for higher confining pressures.

Based on the experimental results it can be concluded that the behavior of dense Virginia Beach sand is considerably different under low and high confining pressures. Fig. 4.3 illustrates the variation of the principal stress ratio with respect to axial strain for the aforementioned experiments. As it is seen, at high confining pressures no significant post-failure strength drop is observed, whereas at low confining pressures failure is followed by a considerable reduction in strength. For confining pressure of 14000 kPa, no clear failure is observed up to 22 % axial deformation. Failure occurs at just about the same axial strain under confining pressure of 8000 kPa, while for lower confining pressures strain-to-failure is reduced with decrease in confining pressure.

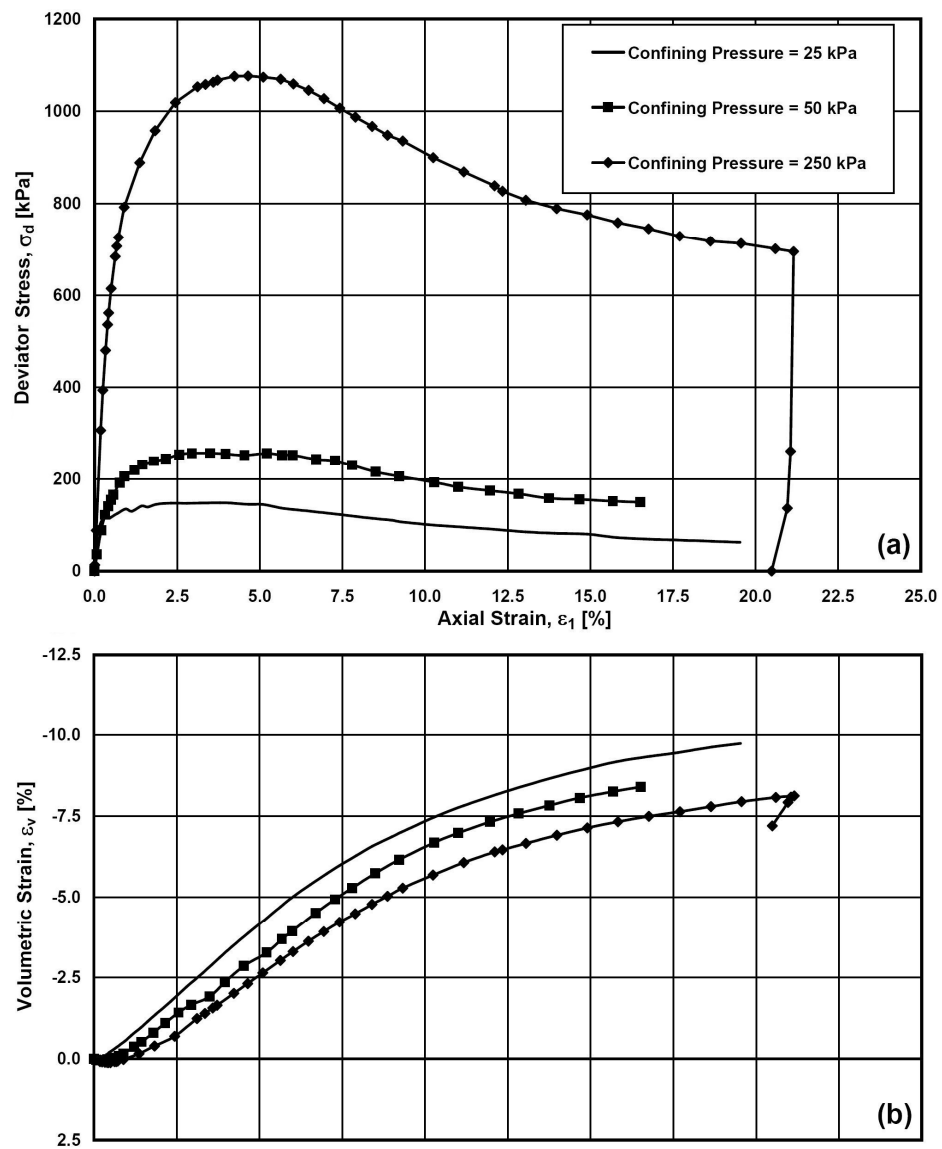


Figure 4.1. Effect of confining pressures equal to and lower than 250 kPa on (a) stress-strain, and (b) volumetric behavior of Virginia Beach sand.

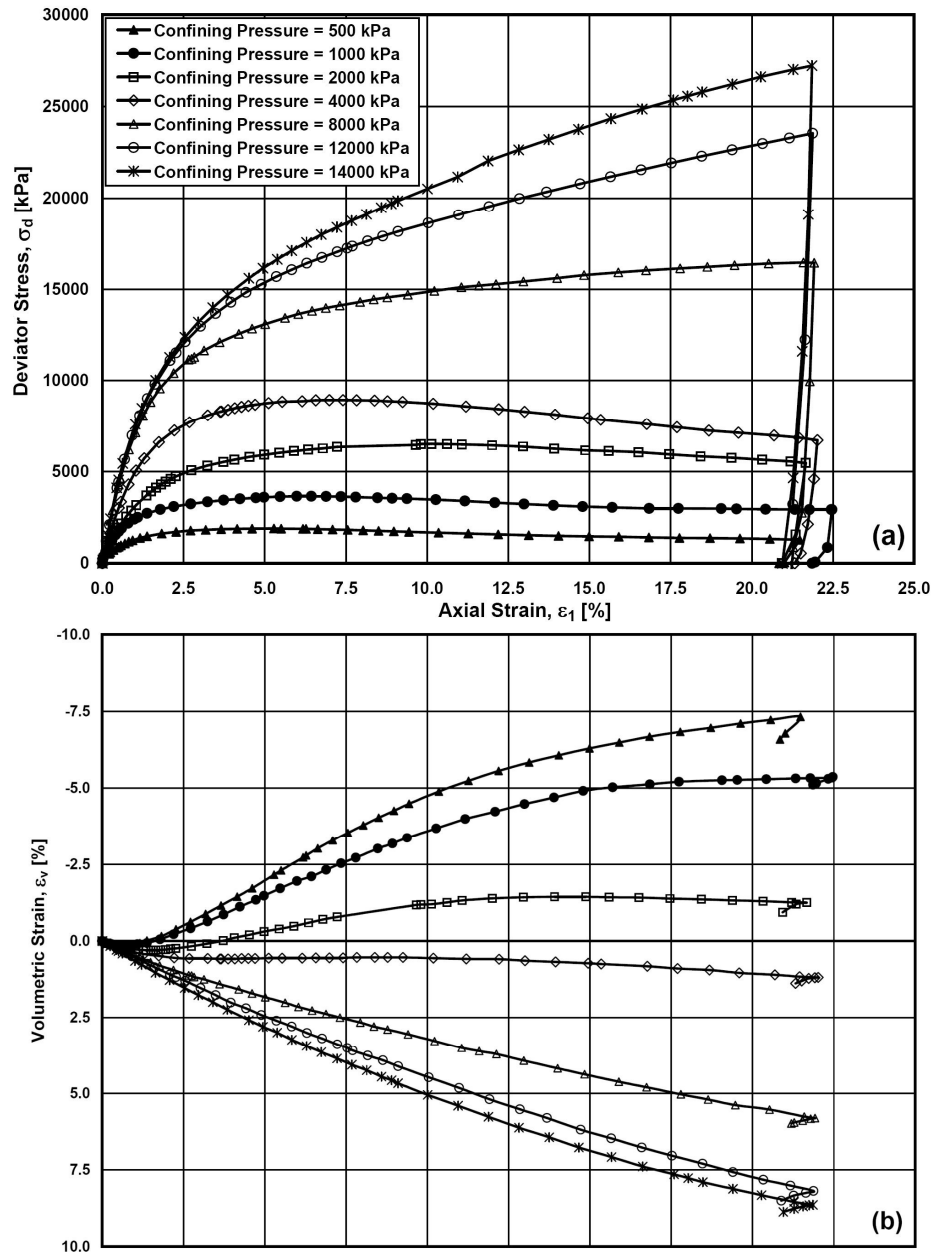


Figure 4.2. Effect of confining pressures higher than 250 kPa on (a) stress-strain, and (b) volumetric behavior of Virginia Beach sand.

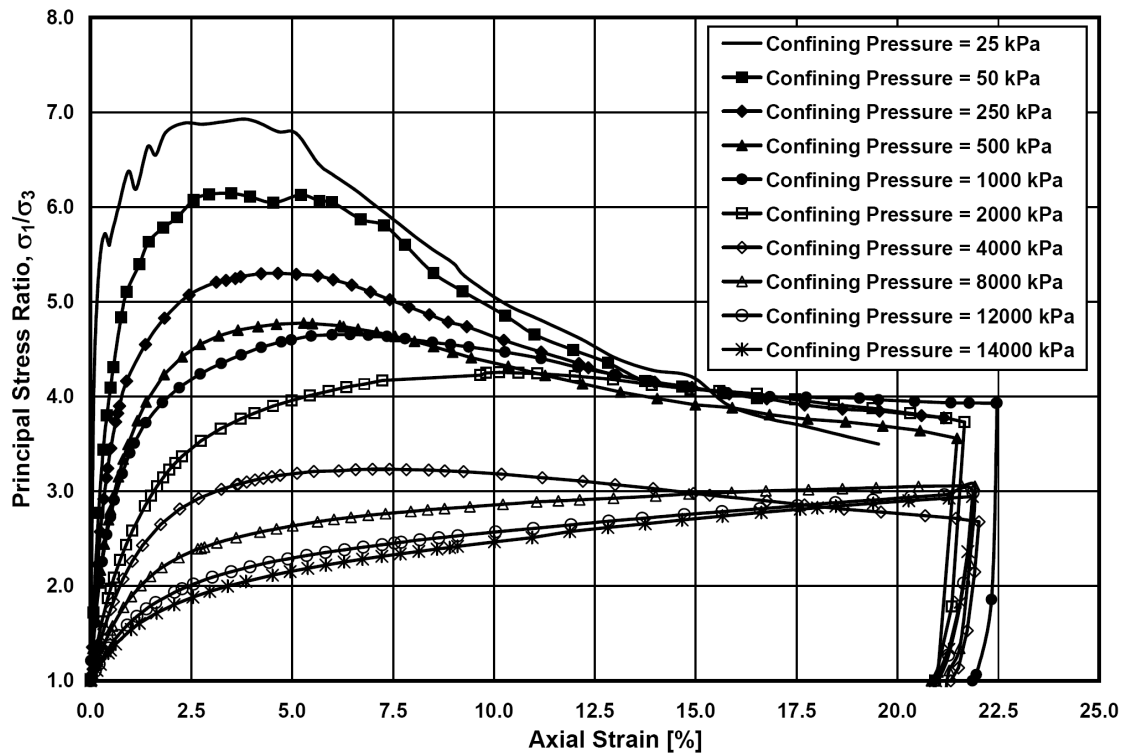


Figure 4.3. Principal stress ratio versus axial strain under confining pressures ranging from 25 kPa to 14000 kPa for Virginia Beach sand.

Fig. 4.3 shows that the critical strength of specimens sheared under confining pressures of 4000 kPa and beyond merges to the same value (approximately, principal stress ratio of 3.0). However, the average critical principal stress ratio is about one unit higher for specimens sheared at the lower pressures. This can be explained based on the post failure behavior of the specimens sheared at lower pressures. Comparison of volume change curves illustrated in Fig. 4.1(b) and 4.2(b) reveals that in experiments performed under confining pressures of 4000 kPa and beyond, specimens undergo no dilation. In contrast, specimens sheared under lower confining pressures experience a significant amount of dilation specifically after reaching failure. In fact, shear banding which occurs during dilation violates the assumption of specimens remaining in cylindrical shape during tests. Thus, the assumed area for specimens experiencing shear banding is smaller than the real area and higher stresses are calculated. The visual inspection of the specimens also confirmed that the shape of specimens sheared under low and high confining pressures are quite different. For instance, Fig. 4.4 shows the shape of two specimens sheared up to 22 % axial strain under confining pressures of 250 and 14000 kPa.

Shear banding together with significant amount of dilation at the middle part of specimen are clearly observed in Fig. 4.4(a) associated with the specimen sheared under confining stress of 250 kPa, while the upper and the lower parts of the specimen remained cylindrical. In the other specimen shown in Fig. 4.4(b), no pronounced failure

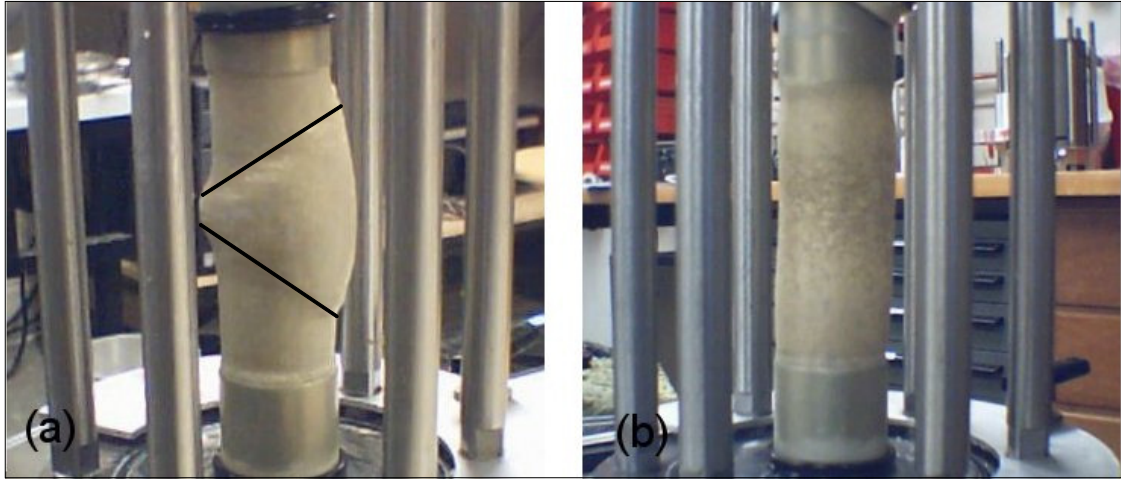


Figure 4.4. Appearance of specimens after 22 % axial strain under confining pressures of (a) 250 kPa, and (b) 14000 kPa.

planes can be detected and the specimen remains approximately cylindrical. No attempt was made to correct the area of specimens due to occurrence of shear banding during dilation. It is observed that higher confining pressures result in higher deviator stresses and lower dilation tendency in such a way that specimens undergo no dilation for confining pressures higher than 2000 kPa and subsequently specimens remain their cylindrical shape. As mentioned in Chapter 2, this is mainly due to particle crushing.

Lee et al. (1967) carried out a series of triaxial tests on Antioch sand and reported that the variation of the initial tangent modulus may be described by a power function of the confining pressure. That is, the logarithm of initial tangent modulus varies linearly with the logarithm of confining pressure. A similar analysis was performed for Virginia Beach sand and the results, as illustrated in Fig. 4.5 (a), indicate the same type of behavior. It is noted that the initial tangent modulus and the confining pressure were normalized by dividing to atmosphere pressure, $p_a=100$ kPa. In other words, the logarithm of the normalized initial tangent modulus increases linearly with increase in the logarithm of the normalized confining pressure. In Fig. 4.5 (b), the maximum principal stress ratio (failure condition) and the axial strain-to-failure is plotted against the normalized confining pressure to throw further light on the variation in the behavior of Virginia Beach sand under low and high pressures.

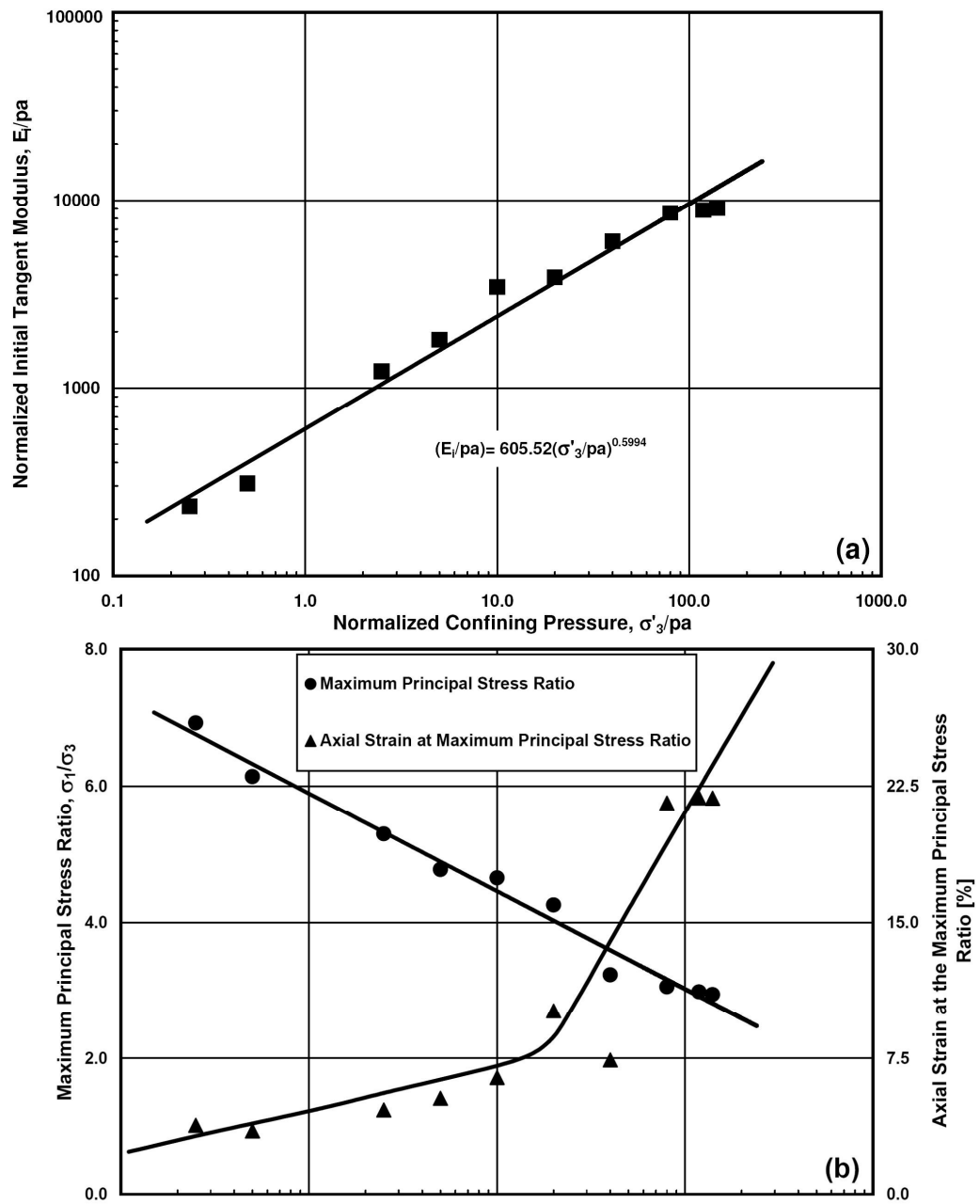


Figure 4.5. Variation of (a) normalized initial tangent modulus, and (b) maximum principal stress ratio and its corresponding axial strain with normalized confining pressure.

As seen, there is a linear relationship between the strain-to-failure and the logarithm of confining stress for the confining pressures below 2000 kPa. Although the same trend exists after confining pressures of 2000 kPa, where no dilation is observed, the slope of the trendline is significantly increased. It is noted that the test performed at 4000 kPa does not follow the trend. Based on the inspection of the specimen, this could be due to buckling that probably had taken place around the axial strain of 6%, where the maximum stress ratio starts dropping (see Fig. 4.3). The magnitude of the maximum stress ratio is not affected due to buckling since the stress-strain curve was approximately horizontal around the axial strain of 6%. Therefore, this experiment was not repeated.

Furthermore, Fig. 4.5(b) demonstrates that the maximum principal stress ratio decreases linearly with increase in logarithm of the confining pressure. Marsal (1967) reported the same type of behavior while performing large triaxial experiments up to confining pressures of 25 kg/cm² on rockfill materials. He also noticed that presence of water has a weakening effect and it shifts this line downward while the slope remains the same. According to Mohr failure criterion, the maximum principal stress ratio is connected to the friction angle, ϕ , for granular non-cohesive materials through the following equation:

$$\phi = \sin^{-1} \left(\frac{\sigma_1/\sigma_3 - 1}{\sigma_1/\sigma_3 + 1} \right)_f \quad (4-1)$$

or

$$(\sigma_1/\sigma_3)_s = \tan^2(45 + \phi/2) \quad (4-2)$$

However, Bishop (1954) stated that the dilation has an impact on the principal stress ratio. He suggested the following equation to calculate the friction angle after deducting the dilatancy component, ϕ_{dr} , at failure:

$$\tan^2(45 + \phi_{dr}/2) = (\sigma_1/\sigma_3)_f + d\varepsilon_v/d\varepsilon_1 \quad (4-3)$$

in which $d\varepsilon_1$ and $d\varepsilon_v$ are the increments of axial and volumetric strains at the maximum principal stress ratio ($d\varepsilon_v < 0$ during dilation and $d\varepsilon_v > 0$ during compression); consequently, $d\varepsilon_v/d\varepsilon_1$ is the slope of the volumetric strain-axial strain diagram (rate of dilatancy) at failure. Rowe (1962) also mentioned that the measured friction angle is affected by dilatancy and particle reorientation, and ϕ_{dr} , calculated in Equation (4-3), still overestimates the angle of friction, ϕ_μ , in granular materials. He derived the following equation to calculate the friction angle of granular materials at failure after deducting dilatancy effects, ϕ_f :

$$\tan^2(45 + \phi_f/2) = (\sigma_1/\sigma_3)_f / (1 - d\varepsilon_v/d\varepsilon_1) \quad (4-4)$$

While the confining stress is increased, the dilation tendency is decreased due to particle crushing. Consequently, the measured friction angle decreases as the dilation component decreases. It is noted that the rate of dilatancy at failure merges to zero for experiments performed at high confining pressures, or performed at low confining pressures on loose specimens. Variation of the measured friction angle with the logarithm of the normalized confining pressure for Virginia Beach sand is shown in Fig. 4.6.

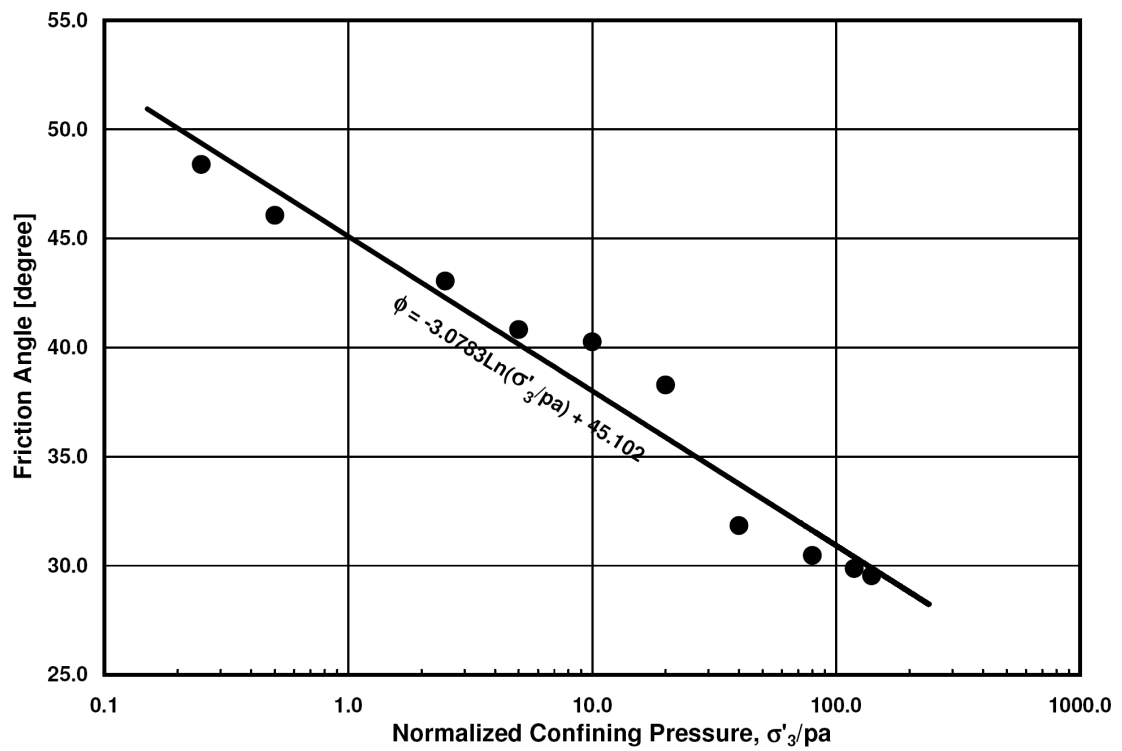


Figure 4.6. Variation of measured friction angle with logarithm of normalized confining pressure.

Similar to the maximum principal stress ratio, a linear relationship is detected between the measured friction angle and the logarithm of the confining pressure. Vesic and Clough (1968) observed the same behavior for Chattahoochee River sand. They stated that after a certain high confining pressure, this trendline merges with a horizontal line and the friction angle will not vary with the confining pressure. They called this confining pressure the “breakdown stress” since it describes a stress after which dilatancy effects vanishes. However, this was not observed for Virginia Beach sand up to the confining pressure of 14000 kPa. Similar to Vesic and Clough (1968), Hall and Gordon (1963) and Leslie (1963) reported a linear reduction of the measured friction angle versus the logarithm of the mean normal stress.

All specimens were retrieved for sieve analyses at the end of the experiments. Sieving was then performed as explained in Chapter 3. The energy input in each experiment was calculated according to Equation (3-1) during consolidation and shearing. Fig. 4.7 illustrates the grain size distribution curve at the end of the experiments together with the original grading curve. As expected, a higher confining pressure has resulted in larger amount of particle crushing.

Hardin’s breakage factor corresponding to each individual curve has been calculated and plotted against the amount of energy input for each experiment in Fig. 4.8. It can be concluded that, the amount of particle crushing increases with the amount of energy input; however, this trend is not linear. For confining pressures below 500 kPa where rotation and rearrangement of grains are the main mechanisms of the shearing, the

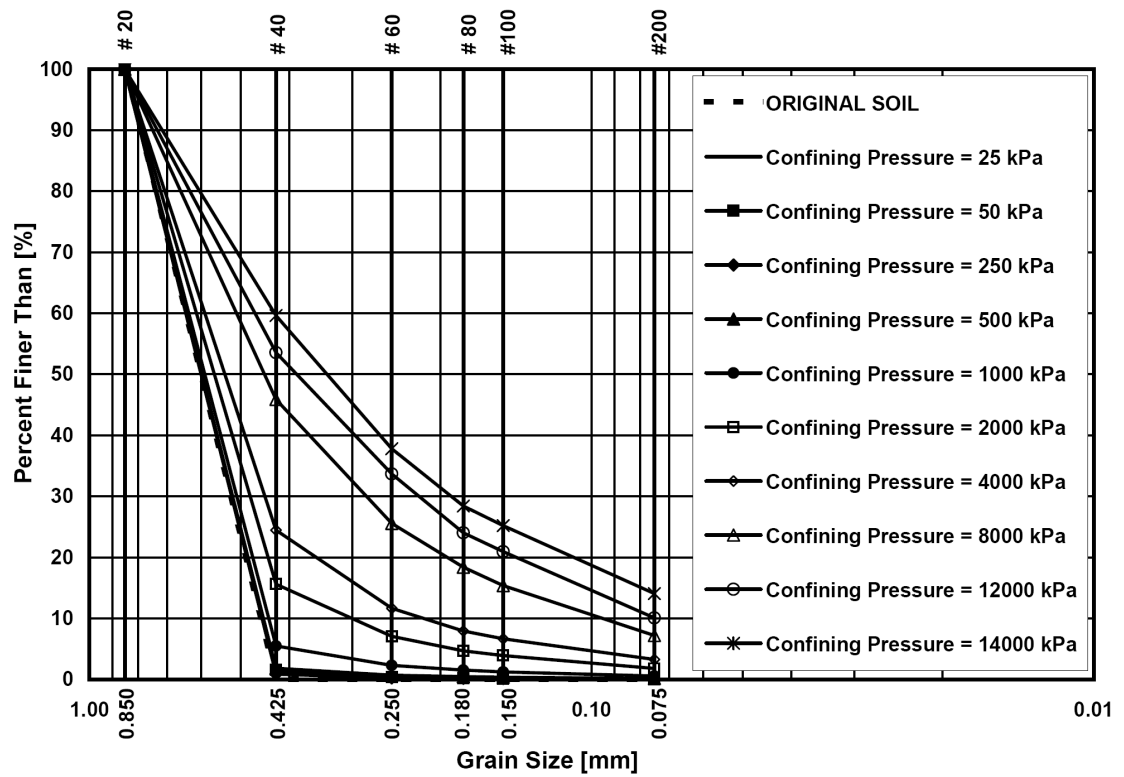


Figure 4.7. Effect of confining pressure on evolution of grain size distribution curve.

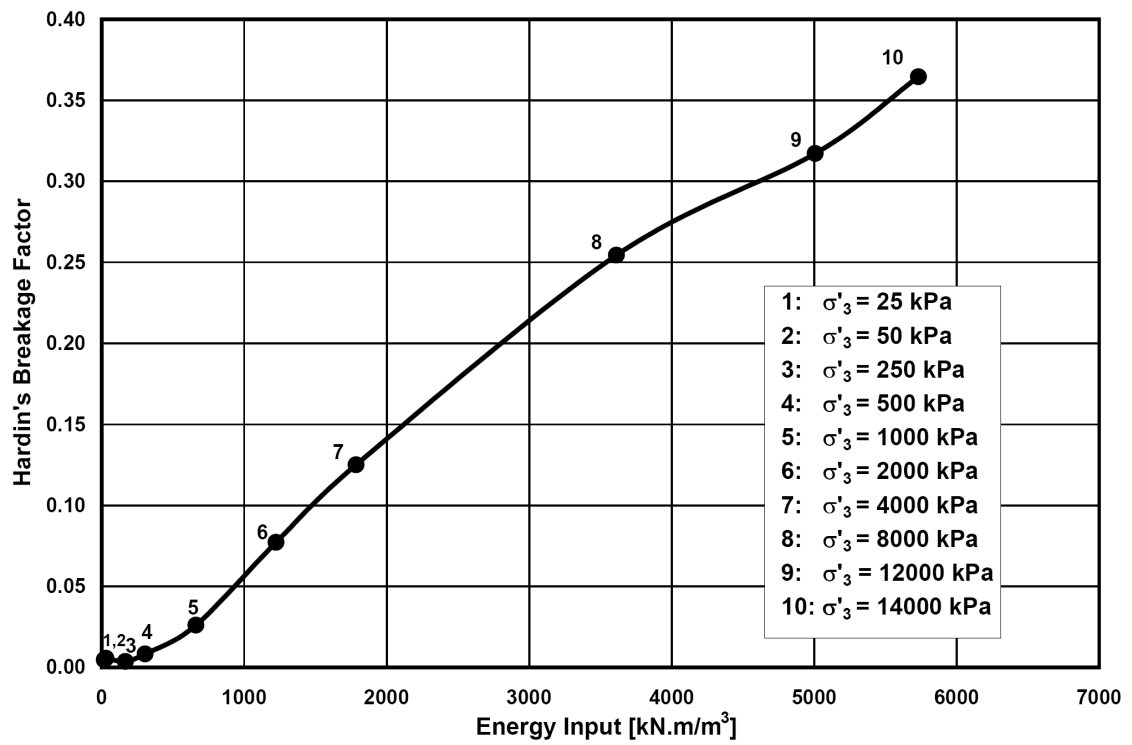


Figure 4.8. Hardin's breakage factor versus energy input.

energy input is spent on friction among grains without breaking them. In fact, possible crushing is in the form of abrasion. Consequently, more or less the same breakage factor has been achieved for experiments below this pressure. As the confining pressure is increased, the particle breakage mechanism is added to the rotation and rearrangement of particles, so the slope of the curve increases. However, for pressures beyond 8000 kPa, the amount of particle breakage increases in a declining manner. This may be due to the prior significant amount of crushing and considerable increase in the coordination number for the particles in the specimen.

4.2. Effect of Initial Shearing Strain Rate

Six triaxial compression tests were carried out on dense specimens of Virginia Beach sand at deformation rates of 0.0028, 0.0448, and 0.7168 mm/min under confining pressures of 250 kPa and 8000 kPa. These deformation rates correspond to strain rates of 0.00260, 0.0416, and 0.666%/min. Each specimen was sheared up to the axial strain of about 22%. Therefore, experiments lasted for approximately 6 days, 9 hours, and 33 minutes, respectively.

Fig. 4.9 and Fig. 4.10 show the effect of the initial loading rate on the stress-strain and volumetric behavior of Virginia Beach sand under confining stresses of 250 and 8000 kPa, respectively. In Fig. 4.9(a), approximately the same stiffness is achieved for experiments performed under constant confining pressure of 250 kPa for different shearing strain rates. Moreover, a similar behavior is observed for the strength of Virginia Beach sand. In other words, under low confining pressure, pre-failure stress-strain

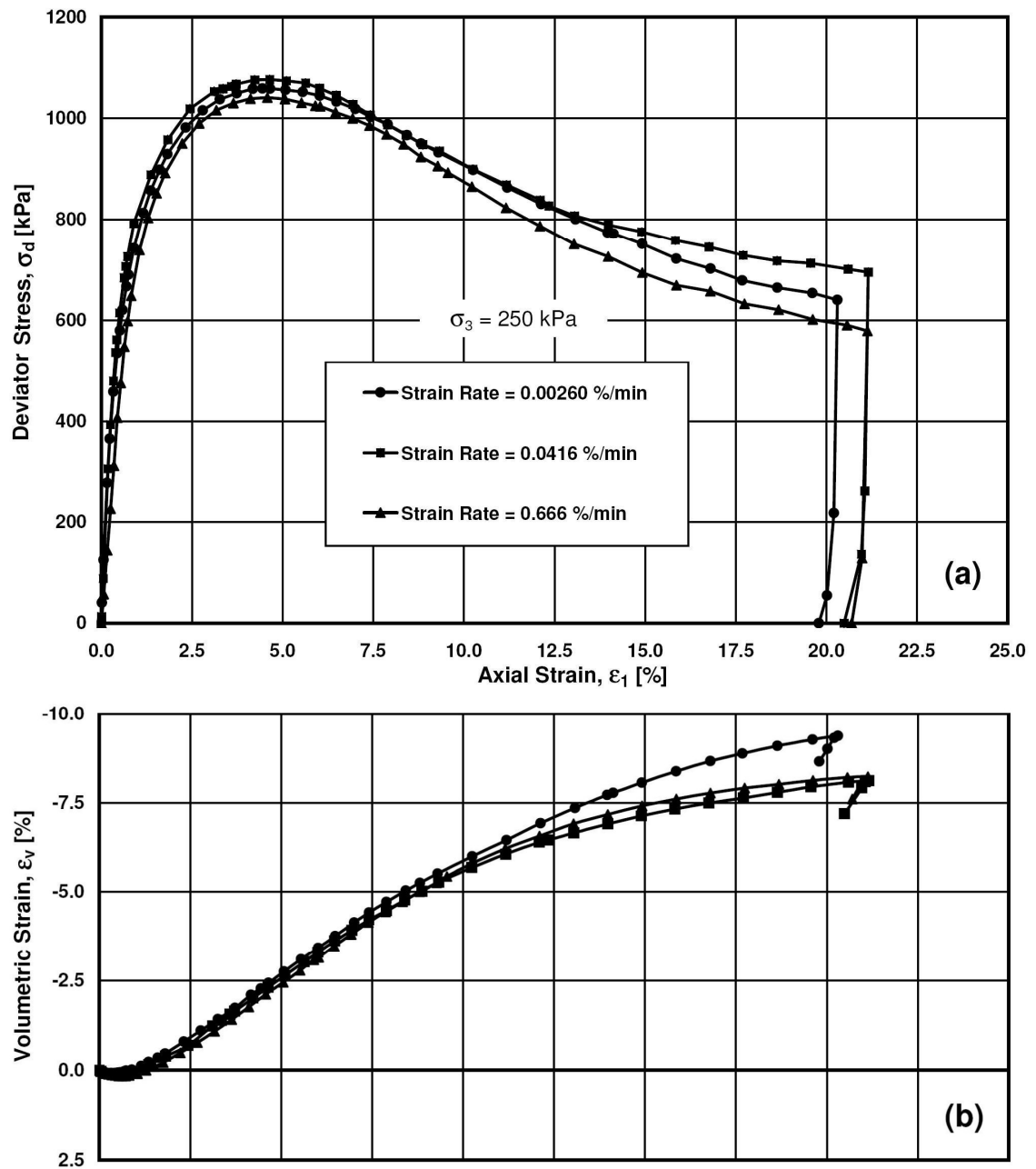


Figure 4.9. Effect of shearing strain rate on stress-strain and volumetric behavior under confining pressure of 250 kPa.

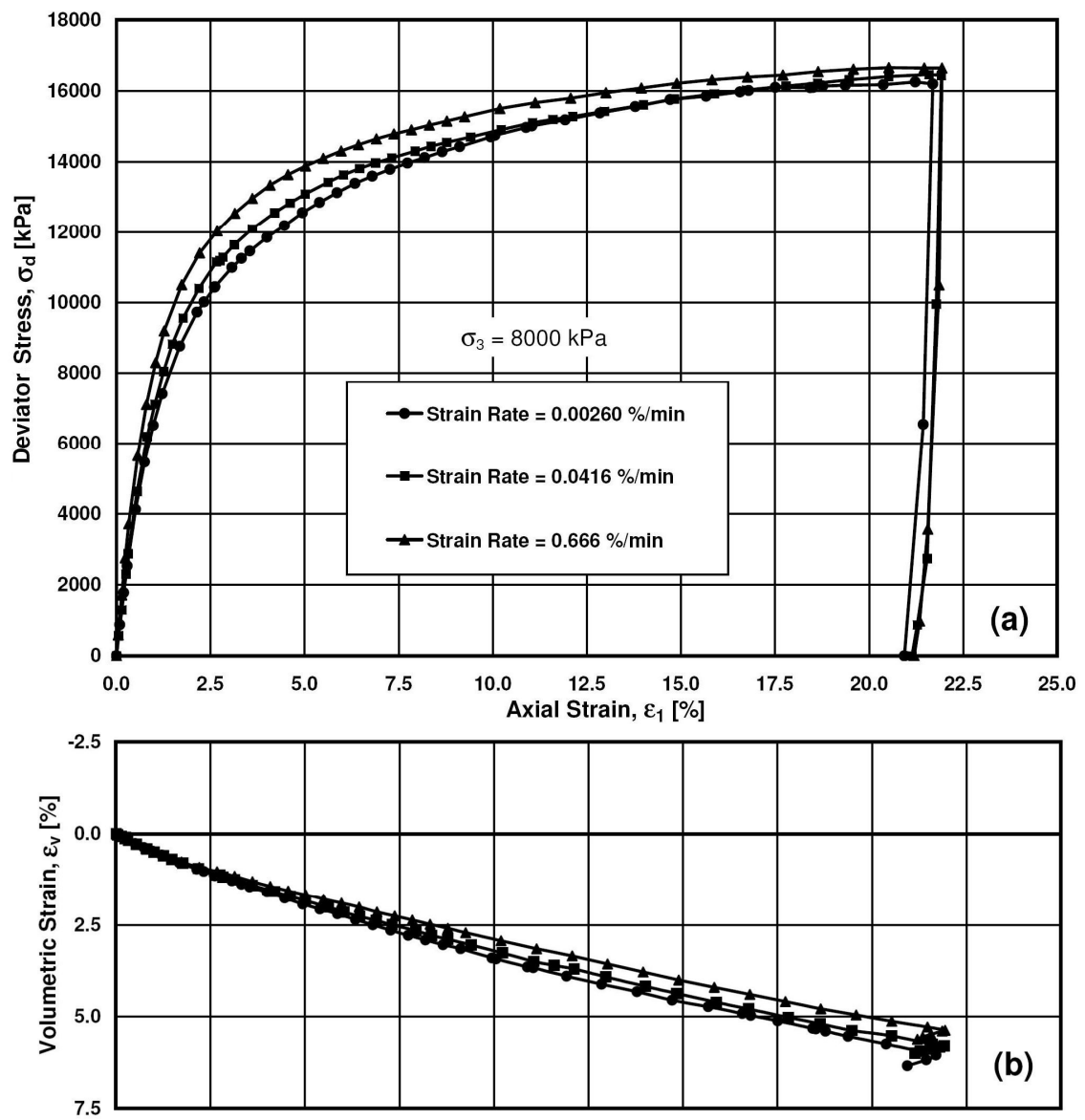


Figure 4.10. Effect of shearing strain rate on stress-strain and volumetric behavior under confining pressure of 8000 kPa.

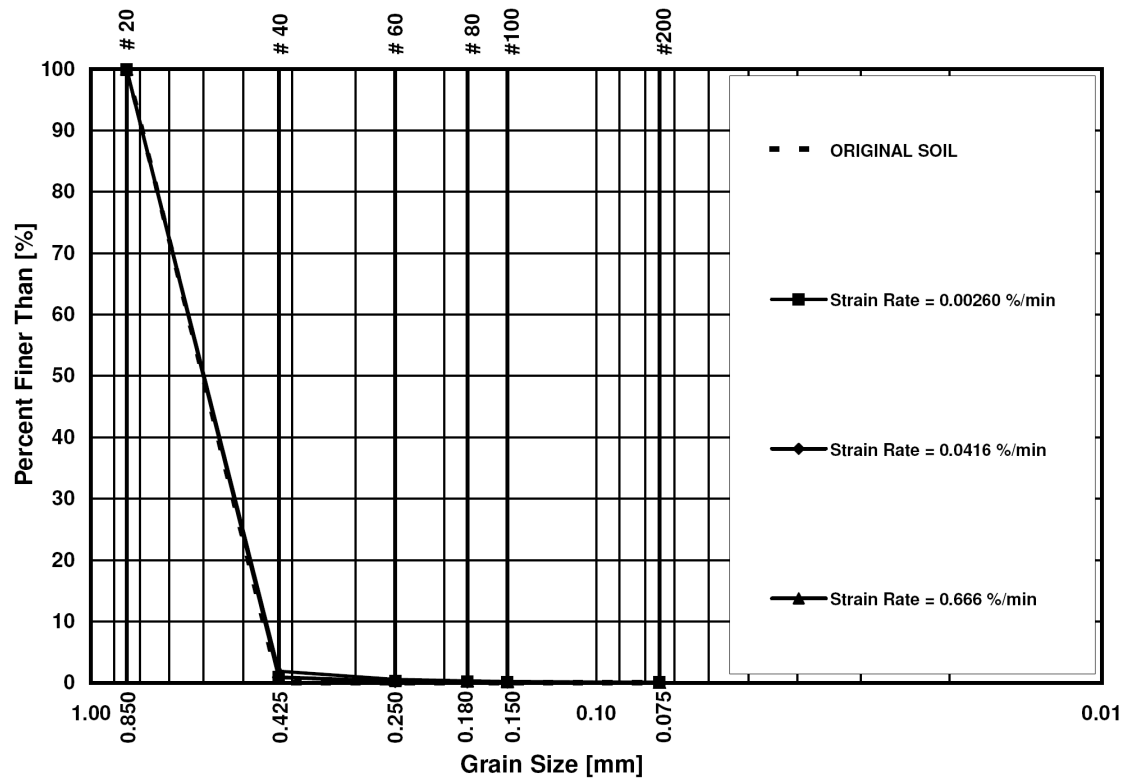
behavior is independent of strain rate at which the specimens sheared. The difference between the minimum and maximum deviator stresses is about 3% which is in the range of the experimental scatter. However, the post-failure behavior (beyond 7.5% of axial strain) of these experiments can not be correctly compared due to occurring shear banding as explained in section 4.1 and as seen in Fig. 4.4.

The friction angles calculated at the maximum deviator stresses for the slowest to the fastest experiments are 42.8° , 43.0° , and 42.5° corresponding to axial strain of 4.18, 4.65, and 4.58%. Fig. 4.9(b) shows that the volumetric strains at failure for experiments sheared at the lowest to the highest strain rate are -2.10, -2.31, and -2.12%. In summary, the stress-strain and volumetric behavior of Virginia Beach sand under low confining pressures exhibits negligible dependency on shearing strain rate.

Fig. 4.10(a) demonstrates that the higher strain rate results in a slightly stiffer response for the experiments performed at the confining stress of 8000 kPa. Also, in the middle range of the axial strain, higher magnitudes of the deviator stresses are produced when specimens are sheared at the higher loading rates. However, in the vicinity of failure all curves merge and no significant difference is observed. This means that the initial loading rate has only little influence on the strength. The friction angles corresponding to the maximum deviator stresses increase slightly with the strain rate and magnitudes of 30.3° , 30.5° , and 30.7° are achieved. The related axial strains are 21.2, 21.6, and 21.9%. On the other hand, Fig. 4.10(b) illustrates that higher strain rates produce lower volumetric compression. The volumetric strains at failure for the slowest to the fastest test are 5.9, 5.7 and 5.4%. Although it has been stated that effects of the

strain rate on the strength, stress-strain and volumetric behavior can be neglected in granular materials, the experimental results show that there is a consistent relationship between the strain rate and stress-strain behavior of Virginia Beach sand. To maintain consistency in presenting future results where the effect of the initial shearing rate on other phenomena is considered, these stress-strain and volume change relations will be used as reference curves.

All six specimens were sieved and Hardin's breakage factors were calculated after testing. Fig. 4.11 and Fig 4.12 exhibit the grain size distribution curves of the test series performed under confining pressures of 250 kPa and 8000 kPa. In Fig. 4.11, no significant particle crushing is observed for low confining pressure and approximately the same grain size distribution curve has been achieved for experiments sheared at different strain rates. This is similar to the corresponding stress-strain curves. It is seen that at low pressures, abrasion, which can not be adequately detected by sieving, may be the only type of particle crushing that occurs in the experiments. In contrast, experiments show that considerable crushing occurs at higher confining pressures where small amounts of time effects are observed. Although similar in magnitude, Fig. 4.12 shows that the lowest amounts of particle crushing is related to the experiment performed at the highest strain rate, while the lowest strain rate has produced the highest amount of particle crushing. This in turn reveals that particle crushing is a phenomenon that progresses with time. de Souza (1958), Lee and Farhoomand (1967) and Leung et al. (1996) also observed that particle breakage increased with the time that stress is applied. Moreover, R  sch (1960)



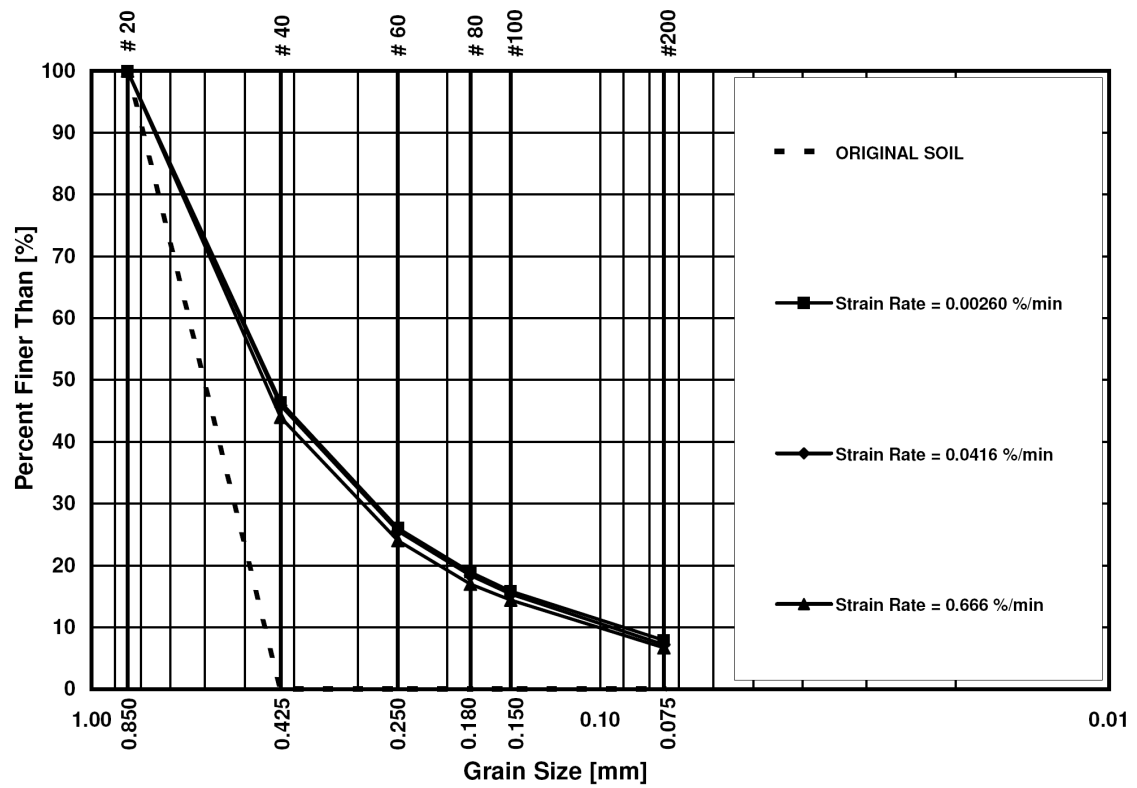


Figure 4.12. Effect of shearing strain rate on evolution of grain size distribution curve under confining pressure of 8000 kPa.

showed that the strengths of brittle materials are dependent on time as discussed in Section 2.3 and indicated in Fig. 2.27.

It is believed that particle breakage is the fundamental behavior that accounts for time effects in granular materials. As discussed in Section 3.11, this is due to the time-dependent fracture, i.e. the static fatigue of the sand particles. In other words, if there is more time available for the applied stress, there is more time for the particles to crush and more contractive volume changes are therefore observed provided that applied stress has been high enough to fracture the particles. If the amount of crushing relates to the amount of energy input to the soil, time effects are related to the energy input and particle crushing. Fig. 4.13 shows the variation of Hardin's breakage factor with respect to the energy input for experiments performed at the three different strain rates and at the two confining pressures of 250 and 8000 kPa.

Particles do not undergo crushing under confining pressure of 250 kPa as the input energy is not high enough. Thus, more or less the same Hardin's factor is achieved for different strain rates. This proves that if the stress level is not sufficiently high, the time during which the stress is applied may not have a crucial influence on the behavior. However, due to considerable amounts of input energy at the confining pressure of 8000 kPa, the strain rate and consequently the time period of applied stress have an essential impact on the particle crushing. Fig. 4.13 shows that although the experiment with the highest strain rate has the largest amount of energy input (3710 kN.m/m^3), it has undergone the lowest amount of particle crushing. In contrast, the experiment sheared at

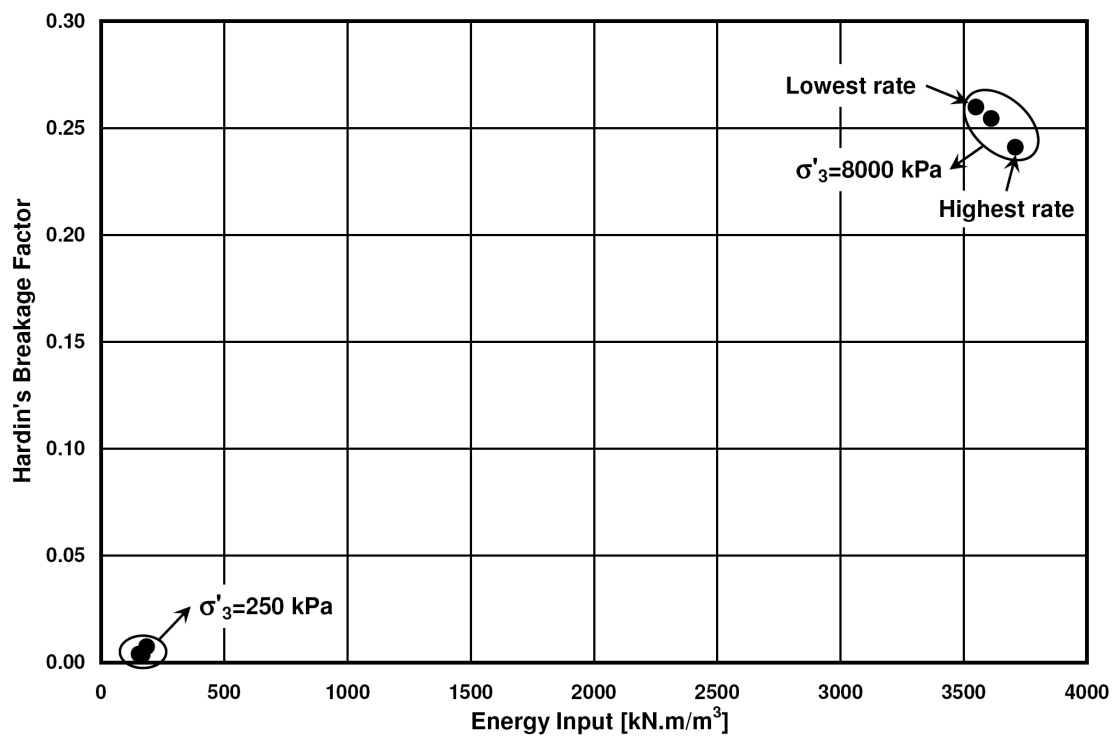


Figure 4.13. Variation of Hardin's breakage factor with respect to energy input.

the lowest rate has the lowest energy input (3550 kN.m/m^3), but it has experienced the highest amount of particle breakage. These observations confirm that static fatigue of particles is at the root of time effects in granular materials.

4.3. Effect of Aging under Isotropic Stresses

The effect of aging under isotropic stresses was studied by performing four experiments at a cell pressure of 8000 kPa and each tested at the strain rate of 0.416 %/min. The first specimen was sheared right after reaching the desired cell pressure. The two other specimens were aged under this confining pressure for 45 min, 1 day and 1 week prior to initiation of deviator loading. Seed (1976) stated that specimens aged for 100 days had shown up to 25% increase in strength. Daramola (1980) performed a similar study under confining pressure of 400 kPa and aged specimens of Ham River sand up to 152 days before they were sheared. In contrast to Seed (1976), he found that the strength remains approximately the same, but the stiffness changes considerably.

Fig. 4.14 shows the stress-strain and volumetric behavior of four experiments on Virginia Beach sand. Although the specimen with lower aging time produced a slightly higher strength, it can be concluded that the aging occurring under isotropic pressures does not considerably affect the stiffness and strength of Virginia Beach sand.

Daramola (1980) has suggested that to circumvent the unavoidable bedding errors connected with the overall strain measurement on the calculation of the stiffness, the initial tangent modulus should not be used for comparison. Herein, points of 10% and 25% of the maximum deviator stress have been used to calculate the stiffness as follows:

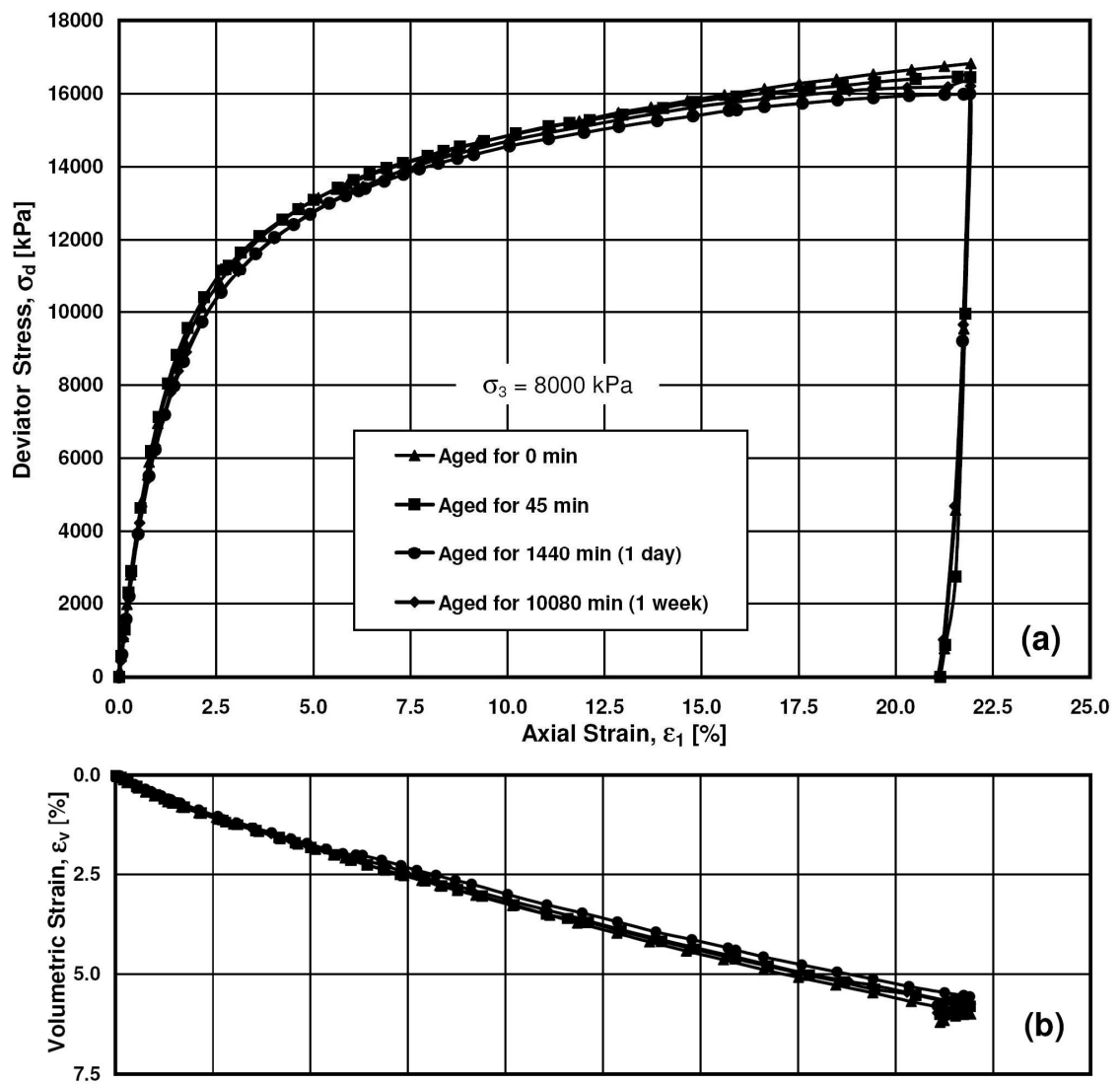


Figure 4.14. Effect of isotropic aging on (a) stress-strain, and (b) volumetric behavior of Virginia Beach sand.

$$stiffness = \frac{0.25 \cdot \sigma_{d_{max}} - 0.10 \cdot \sigma_{d_{max}}}{\varepsilon_1|_{0.25 \cdot \sigma_{d_{max}}} - \varepsilon_1|_{0.10 \cdot \sigma_{d_{max}}}} \quad (4-1)$$

The calculated stiffnesses, the maximum friction angles, and the axial and volumetric strains at failure have been compared in Table 4.1. To have a better understanding of the variation of the stiffness and the strength with the isotropic aging time, Fig. 4.15 illustrates the variation of the friction angle and the ratio of the stiffness of the isotropically aged specimens to the stiffness of the non-aged specimen with respect to the logarithm of the isotropic aging time.

The stiffness ratio is seen to be approximately constant with increase in the consolidation time. In fact, the average stiffness is about 7784 kPa with the standard deviation is 4.6%. Although the change in the friction angle with the logarithm of the isotropic consolidation time has a declining trend, the average value of the friction angle is 30.4° with the standard deviation of 1.2%. Overall, it is concluded that the small differences in the stiffnesses and strengths may be due to the experimental scatter and the time during which specimens are isotropically consolidated has no significant impact on the stiffness and strength of Virginia Beach sand.

Fig. 4.14 (b) illustrates a similar volumetric behavior for specimens isotropically aged for time periods up to 1 week. In terms of grain crushing and evolution of grain size distribution curve, Fig. 4.16 shows that the specimen exhibiting higher volume change has undergone slightly more particle crushing. However, the difference in the amount of particle breakage is not significant.

Table 4.1. Initial stiffnesses, maximum friction angles, and axial and volumetric strains at failure for specimens aged under isotropic stress state.

Isotropic aging time [min]	Stiffness [kPa]	Friction angle [degrees]	(ϵ_1, ϵ_v) at failure [%]
0	7767.11	30.8	(21.93, 6.00)
45	8289.20	30.5	(21.59, 5.75)
1440	7592.60	30.0	(21.91, 5.56)
10080	7485.85	30.2	(21.92, 5.74)

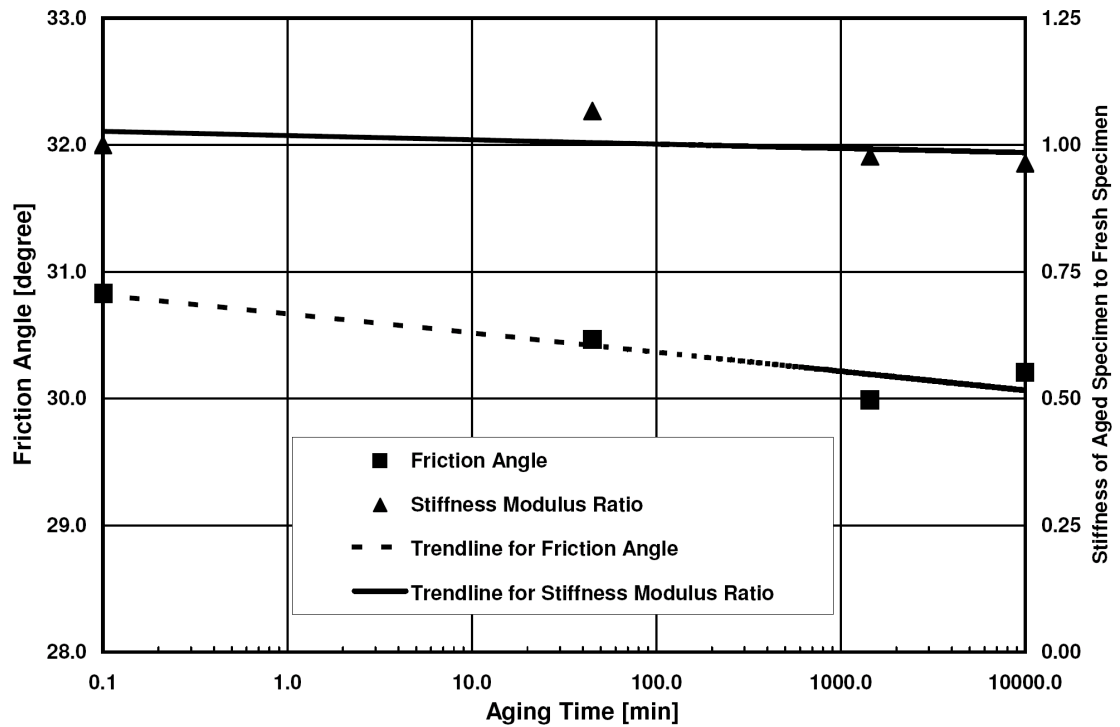


Figure 4.15. Variation of stiffness ratio and maximum friction angle with isotropic consolidation time.

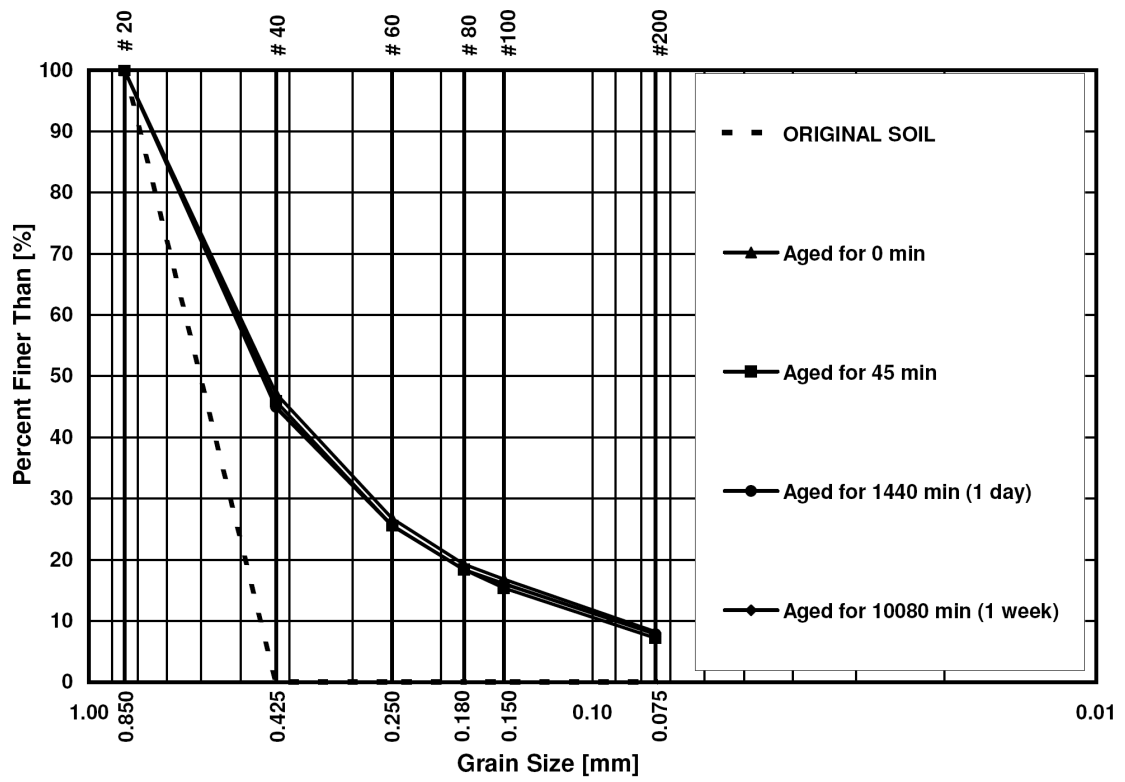


Figure 4.16. Grain size distribution curve for specimens sheared after various isotropic aging times.

Table 4.2 shows the energy input in each individual experiment and the corresponding Hardin's breakage factor calculated from Fig. 4.16. The results imply that the isotropic aging time does not have considerable impact on the final amount of particle breakage.

As explained in Section 3.11, the effect of time is noticeable when a sufficient amount of energy is applied. In the present tests, specimens were aged under a constant cell pressure before they were sheared up to the axial strain of 22%. According to Table 4.2, application of the confining stress up to 8000 kPa produced from 1.8 to 6.2% of the total energy input for the specimen without isotropic aging to the specimen aged for 1 week. These values are not adequately high to produce fractures in particles. Since all specimens have been loaded under the same strain rate during shearing, an equal time has been given to all specimens under a significant stress level at which static fatigue may occur. As a result, the isotropic aging time does not have a significant effect on the final crushing. In other words, the severe crushing during shearing overwhelms the effects of the small amounts of crushing during the isotropic aging.

4.4. Effect of the Aging under K_0 Stress States

As mentioned in the previous section, the aging under isotropic stresses did not have a significant influence on the stiffness and strength of Virginia Beach sand. Herein, the effect of aging during K_0 stress conditions is studied by performing triaxial experiments with lateral pressure (cell pressure) of 8000 kPa. In these tests, the cell pressures and deviator stresses were applied to maintain the K_0 stress state under

Table 4.2. Energy input and Hardin's breakage factor for specimens aged under isotropic stress state.

Isotropic aging time [min]	Energy input at the end of aging [kN.m/m ³]	Total energy input [kN.m/m ³]	Hardin's breakage factor
0	68	3640	0.266
45	66	3610	0.254
1440	78	3520	0.254
10080	231	3720	0.254

increasing stresses. Similar aging time periods were employed as in the tests with aging under isotropic stresses. That is, the first specimen was sheared instantaneously when the lateral pressure reached 8000 kPa while the three other specimens were aged under K_0 stress conditions for 45 min, 1 day and 1 week before they were sheared at the rate of 0.0416 %/min. It is noted that the application of K_0 stress conditions was performed by load control whereas the subsequent shearing was performed by switching to deformation control at the end of the aging time period.

The stress-strain and volume change relations for application of both K_0 stress conditions and shearing are shown in Fig. 4.17. Since the details might not be clearly seen, these results are split into application of K_0 stress conditions and shearing. Fig. 4.18 illustrates the stress-strain and volumetric behavior while vertical and lateral stresses were increased during K_0 conditions until reaching the lateral stress of 8000 kPa. Good agreement is observed among the results of the K_0 condition experiments. The final experimental points, which are specified with larger markers in Fig. 4.18, indicate the response corresponding to the end of aging period. These points show how much axial and volumetric strains have been produced during aging at the K_0 condition. As explained in Section 3.5, instead of using deformation boundary conditions, loading boundary conditions were used to reach the final desired lateral stress under K_0 conditions. This in turn resulted in an axial and volumetric strain of about 3% at the lateral pressure of 8000 kPa. Fig. 4.18 (b) reveals that the K_0 condition has been precisely maintained for all experiments.

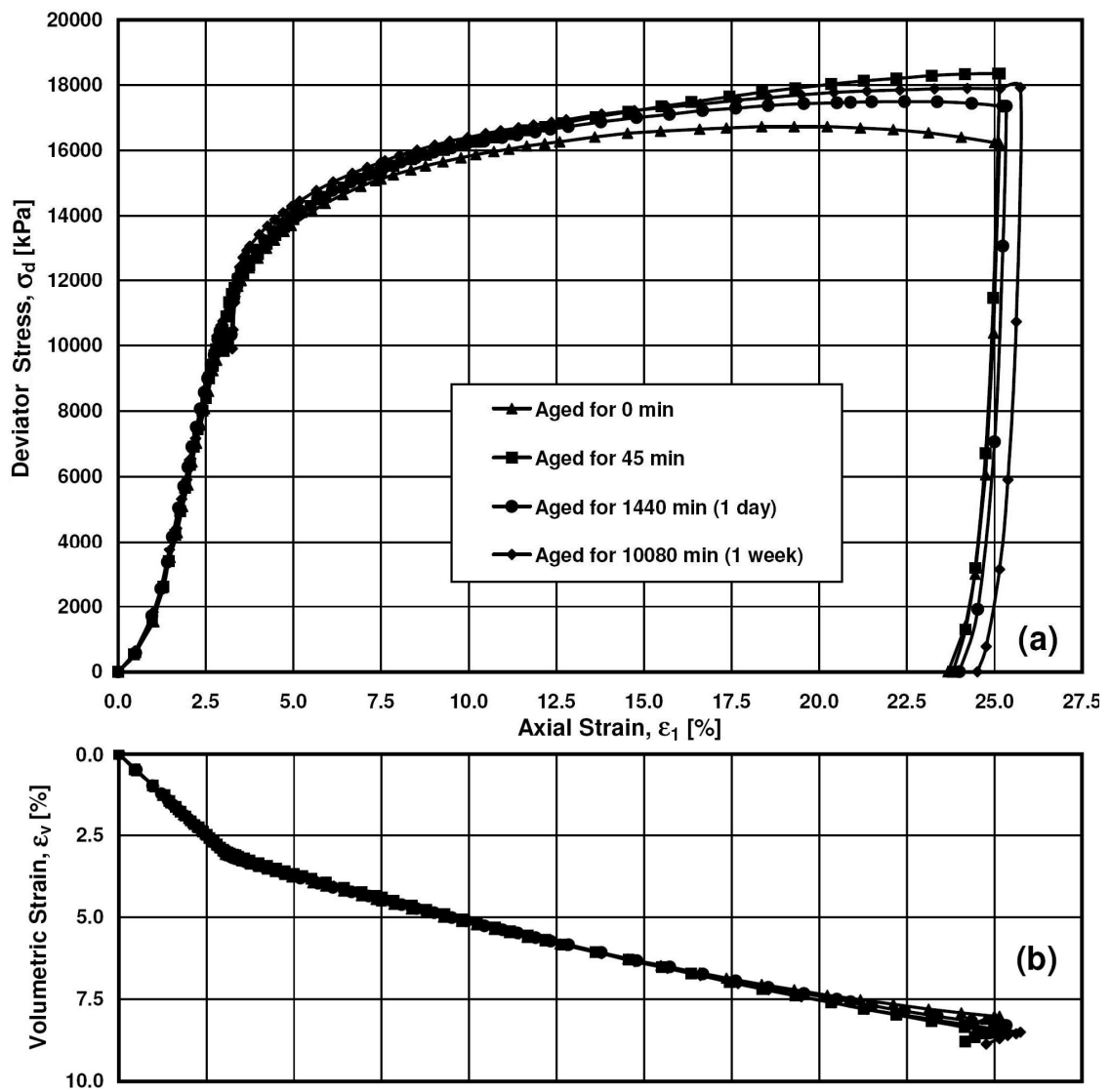


Figure 4.17. (a) Stress-strain, and (b) volume change behavior during K0 stress states compression, aging and shearing.

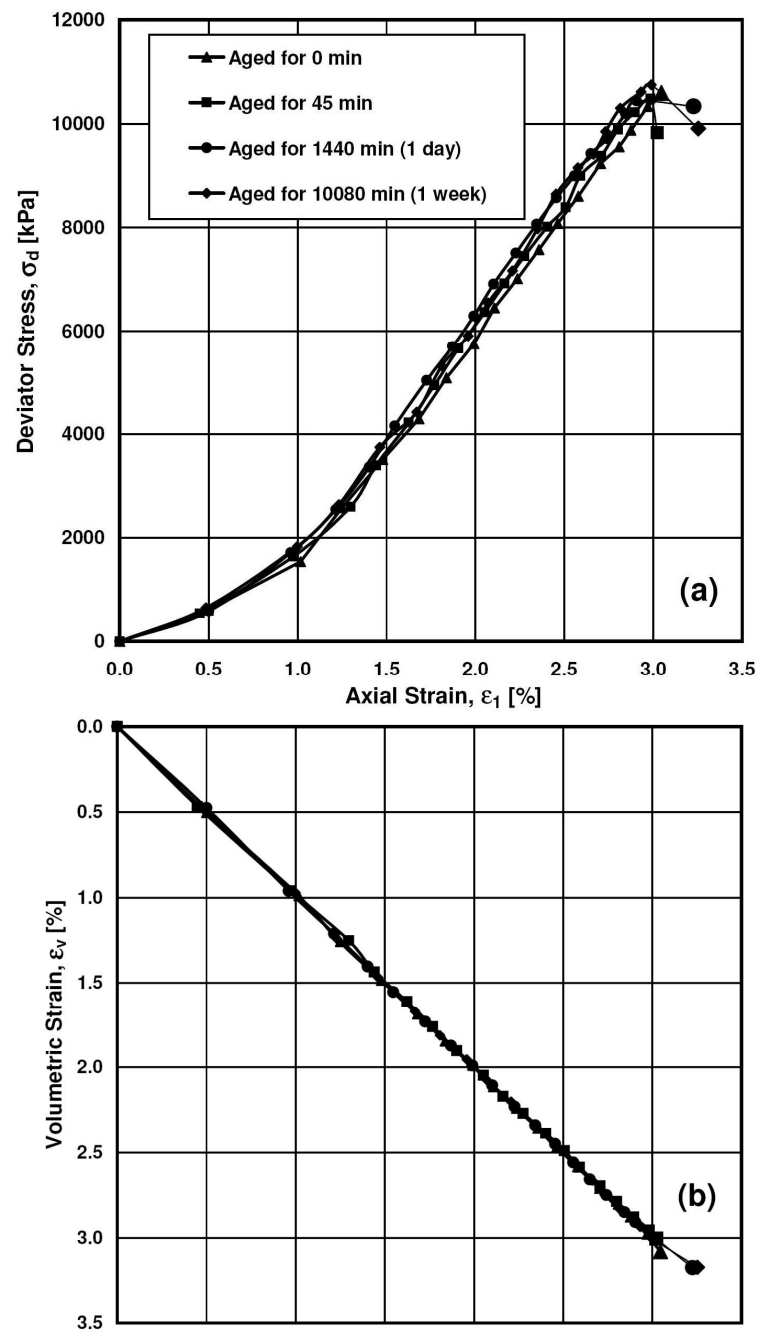


Figure 4.18. (a) Stress-strain, and (b) volumetric behavior during K0 stress states compression, aging and shearing.

Fig. 4.19 shows the stress-strain and volumetric strain-axial strain curves during shearing. As clearly observed, the K_0 condition aging time has a considerable impact on the stiffness and strength of Virginia Beach sand. For the tests aged under isotropic conditions, points of 10% and 25% of the maximum deviator stress were used to calculate the stiffness. In contrast, the high curvature of the stress-strain curve at the initiation of shearing following K_0 -compression, the tangent initial stiffnesses are compared. It was found that the stiffness increases linearly with the logarithm of the K_0 condition aging time, as shown in Fig. 4.20.

Assuming the stiffness of the freshly K_0 -consolidated specimen as E , the stiffness of the specimen consolidated for 45 min under K_0 condition was found to be $2.15E$. The corresponding stiffnesses for the specimen consolidated for 1440 min and 10080 min under K_0 condition are $2.42E$ and $2.92E$, respectively. That is, for every log cycle of time in minutes, the stiffness of the specimen increases approximately 40%. In other words, after a time period of 20 years the stiffness becomes 4 times of that observed for freshly deposited sand at the same density. Inspection of the specimens at the end of experiments disclosed that the specimens aged for 0, 1440 and 10080 minutes had buckled during testing, as shown in Fig. 4.21. Therefore, lower maximum deviator stresses were achieved. In this regard, change in the strength of the specimen because of the K_0 condition aging was studied by calculation of the friction angle at 7.5% of axial strain, where the specimens were most likely still in cylindrical shape.

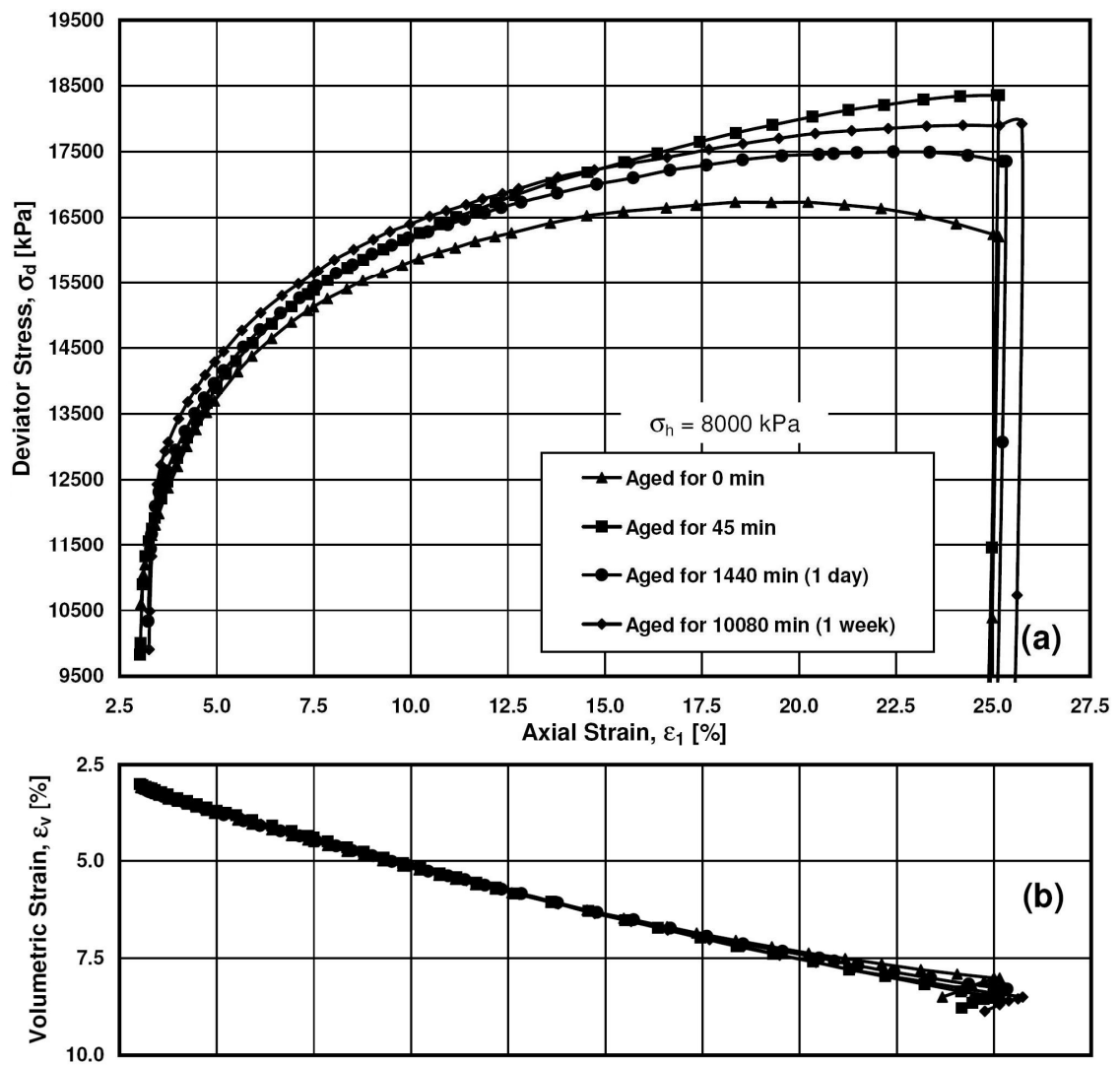


Figure 4.19. (a) Stress-strain, and (b) volumetric behavior during shearing.

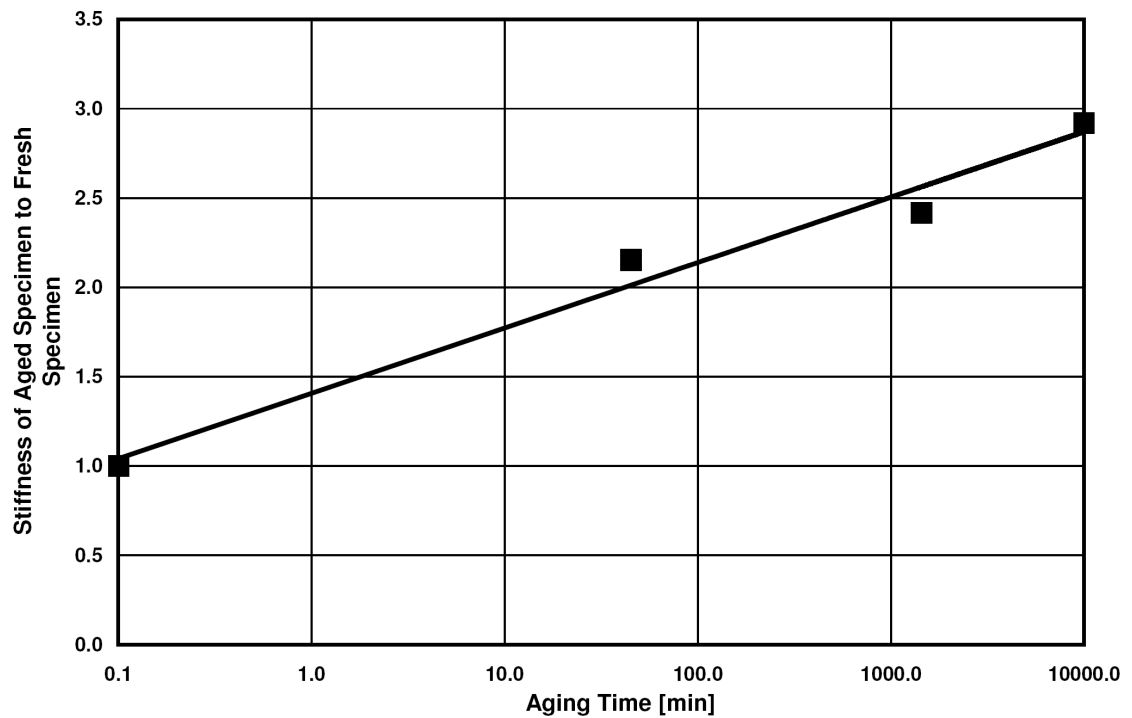


Figure 4.20. Variation of stiffness ratio with consolidation time under K_0 stress states.

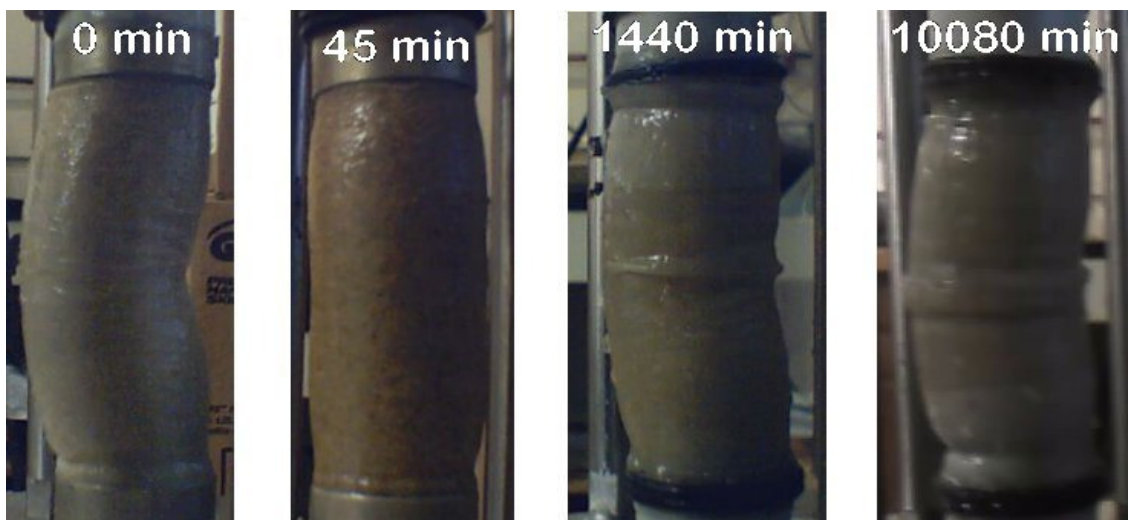


Figure 4.21. Appearance of specimens aged under K_0 stress states at end of shearing.

Variation of the friction angle corresponding to 7.5% axial strain with respect to the aging time has been plotted in Fig. 4.22 together with the axial and volumetric creep during the K_0 consolidation aging. There is a linear relationship between the friction angle and the logarithm of K_0 consolidation time. Moreover, it is observed that higher amounts of axial and volumetric strains have been obtained when specimens are consolidated for a longer period of time.

Sieve analyses were performed on the retrieved specimens at the end of shearing and Hardin's breakage factor was calculated. The grain size distribution curves have been plotted in Fig. 4.23 while the energy input at the end of aging at the K_0 stress condition have been tabulated in Table 4.3 together with the corresponding total energy input and Hardin's breakage factor.

Similar to the specimens aged isotropically, herein, the amount of energy input at the end of the K_0 aging varies from 4.5 to 5.2% of the total energy input. Therefore, the aging time can not significantly affect the amount of final crushing as much as does the shearing time. However, shearing time is essentially the same for all specimens as they were loaded at the same strain rate up to a similar axial strain. Although the specimen with zero aging time has undergone the lowest amount of particle crushing, and the specimen with the highest aging time has exhibited the highest particle crushing, as shown in Fig. 4.23, this was found to be related to the corresponding energy input values and not to the aging time. This is illustrated in Fig. 4.24 where the variation of Hardin's breakage factor has been plotted against the final energy input.

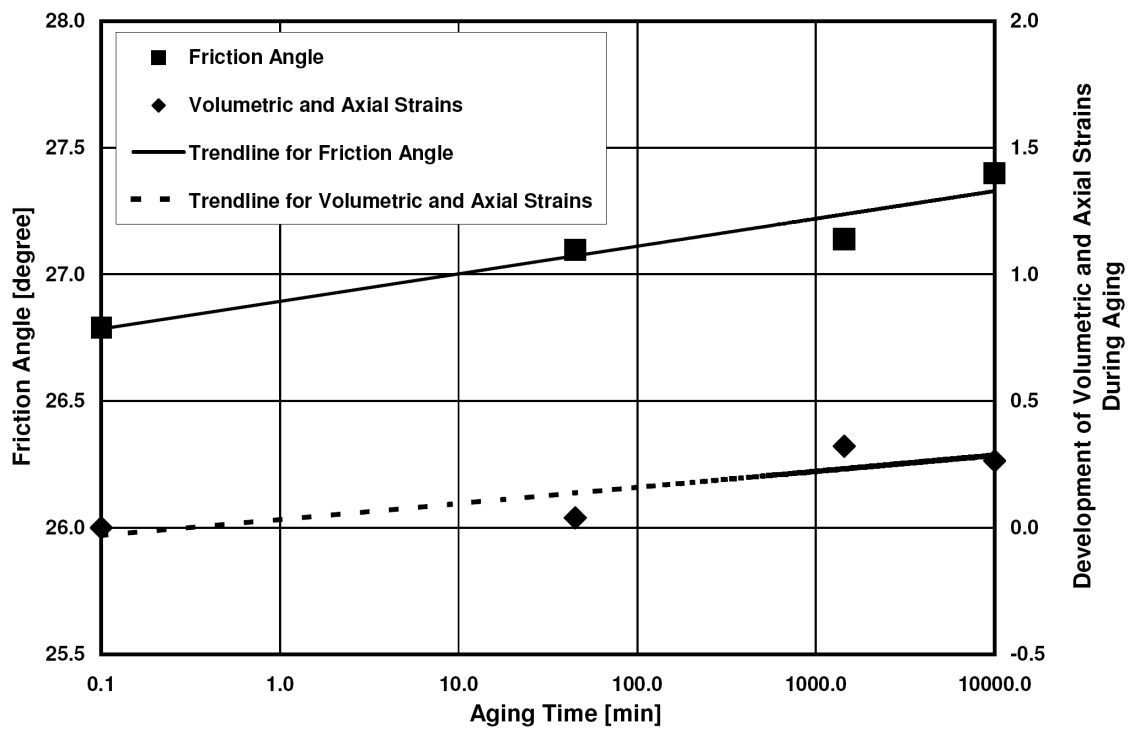


Figure 4.22. Variation of friction angle at axial strain of 7.5%, and axial and volumetric creep during aging under K_0 stress states with respect to aging time.

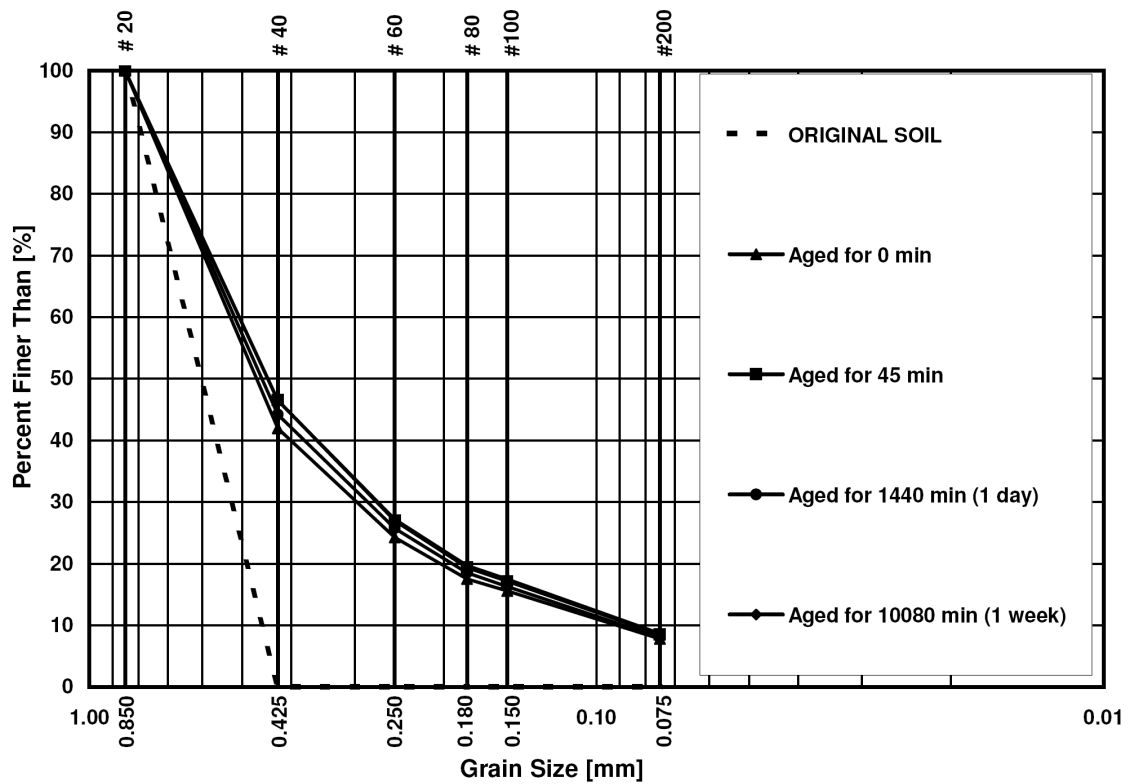


Figure 4.23. Grain size distribution curve for specimens sheared after various aging times under K_0 stress states.

Table 4.3. Energy input and Hardin's breakage factor for specimens aged under K_0 stress states.

Isotropic aging time [min]	Energy input at the end of aging [kN.m/m ³]	Total energy input [kN.m/m ³]	Hardin's breakage factor
0	183	4080	0.241
45	184	4320	0.266
1440	222	4260	0.253
10080	221	4410	0.268

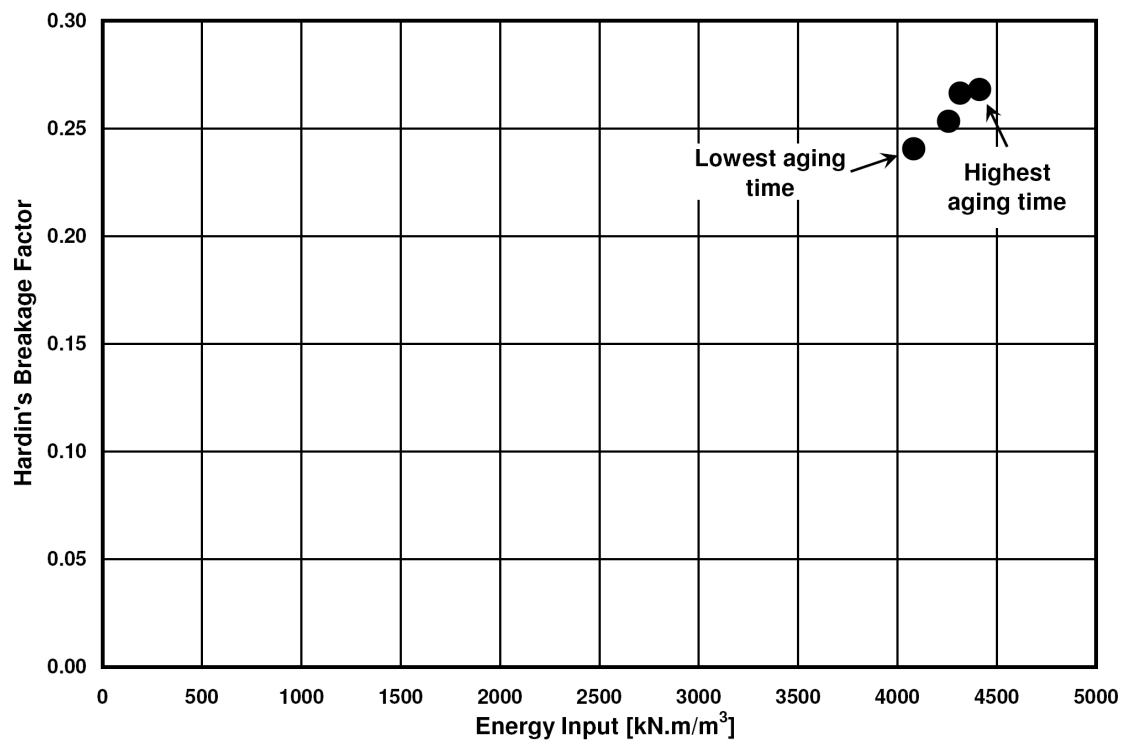


Figure 4.24. Variation of Hardin's breakage factor with respect to energy input for specimens sheared after various aging times under K_0 stress states.

4.5. Single Particle Strength Tests

In the recent years, a number of experimental studies have been carried out on single particle crushing (McDowell and Bolton, 1998; Nakata et al., 1999, 2001a, b; Tang et al., 2001; Kou et al., 2001; Bolton et al., 2008). However, influence of time has not been considered yet. To throw further light on the phenomenon of static fatigue, two types of experiments were performed on industrially produced spherical sodium lime glass beads, as discussed in Chapter 3. Spherical glass beads with diameters of 2, 3, and 6 mm, rather than irregularly shaped sand particles, were used to achieve the highest consistency in the experimental results. Considerable amounts of scatter have been reported in the results of brittle fracture tests since the existence of uncontrolled defects play an important role in the strength of such materials (Scholz, 1972). The main difference between testing single glass bead and testing many glass beads in triaxial tests is the coordination number, i.e. the number of contacts one glass bead has with the surrounding beads. In single glass bead tests, the coordination number is always 2; however, in a soil assembly, this number depends on the grain size distribution, but it is larger than 2.

In the first series of experiments the short term fracture strength was studied by breaking 16 glass beads of each size. These tests were performed by increasing the load until fracture occurred. The time-to-fracture was found to be independent of glass bead size and no discernable pattern was detected for the time-to-fracture, which varied from 5 to 27 minutes. Wijk (1978) has proposed some analytical relations to express the normal stresses of σ_r (radial stress) and σ_θ (circumferential or hoop stress) for spherical brittle

materials subjected to point loads. θ and r are spherical coordinates as defined according to Fig. 4.25. These relations are expressed by a series of Legendre's polynomials and are based on the elastic behavior of the material.

Wijk (1978) stated that the hoop stress at the center of the spherical specimen right before breakage describes the tensile strength of the sphere and it can be estimated as follows:

$$"stress" = \sigma_{\theta}(r = 0, \theta) \Big|_{\theta_o=0} = \beta \cdot \frac{P}{d^2} \quad (4-5)$$

in which d is the diameter, P is the applied load, θ_o is the central angle defining the width over which P is applied (Fig.4.25), and β is a function of Poisson's ratio, ν . He derived that if the reverse value of Poisson's ratio, $1/\nu$, varies in the range of

$$3 \leq \frac{1}{\nu} \leq 10 \quad (4-6)$$

then the parameter β varies as follows:

$$0.77 \leq \beta \leq 0.89 \quad (4-7)$$

Since the Poisson's ratio of the glass beads tested is 0.22, the linear interpolation results in β of 0.80. Furthermore, "strain" is calculated as

$$"strain" = \frac{\Delta d}{d} \quad (4-8)$$

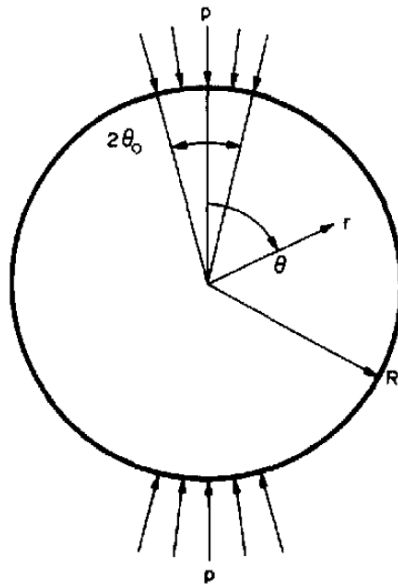


Figure 4.25. Definition of point load test and spherical coordinates of r and θ (after Wijk, 1978).

where Δd is the axial dial gage reading. The resulting “stress-strain” relations are presented in Fig. 4.26. Considerable scatter in the “stress-strain” behavior is observed in this figure. To maintain a consistent condition in terms of surface defects of the glass beads, 5 beads of each size were treated for 2 minutes in Hydrofluoric Acid before testing. However, similar fluctuations were observed in the results on the treated beads. Statistical analysis of the results produces the average breakage stress and the standard deviation for each bead size as follows: 2 mm: 231.0 ± 59.2 MPa; 3 mm: 138.5 ± 69.5 MPa; and 6 mm: 81.3 ± 6.5 MPa.

According to Weibull (1939) (Equation 2-2), there is a linear relationship between the logarithm of the crushing stress and the volume of the particles. Fig. 4.27 illustrates the average crushing stress versus the volume of the glass beads of each size in a Log-Log diagram. Equation (2-2) is applied to the data points in Fig. 4.27 and it results in the exponent of n equal to 3.16 with the R-squared value of 0.981. It is clearly observed that a power function can adequately describe the relationship.

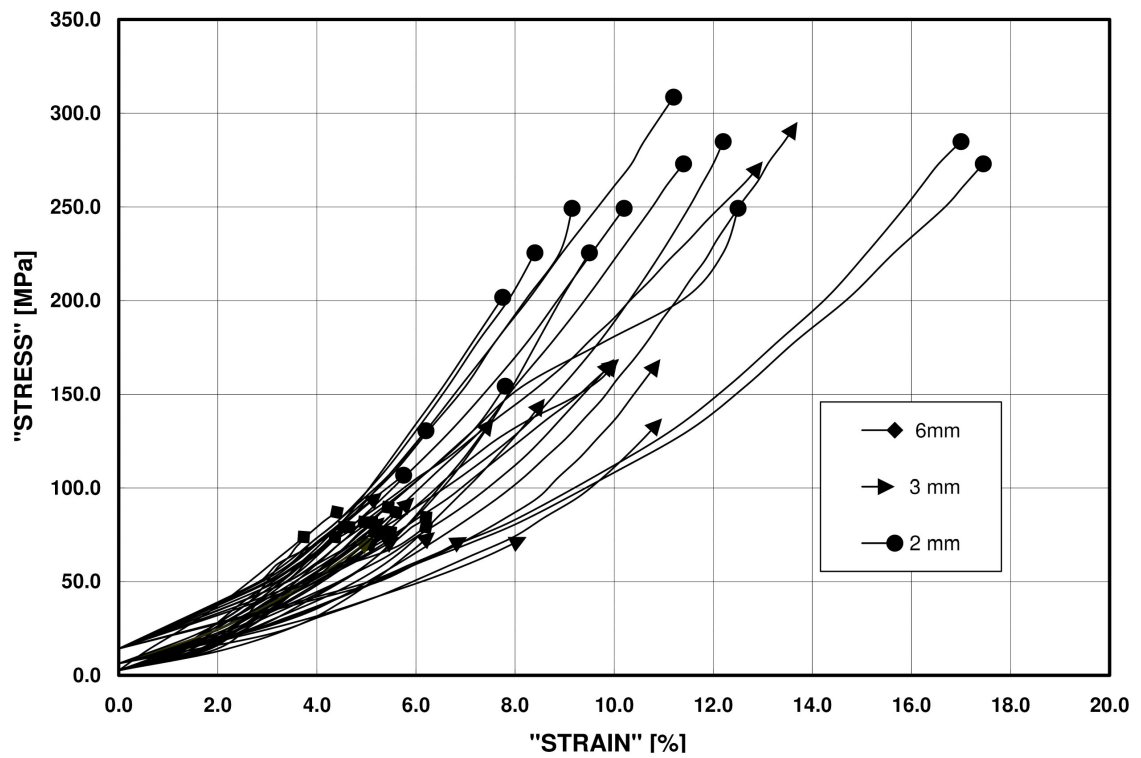


Figure 4.26. “Stress-strain” relations for different size soda lime glass beads tested in compression.

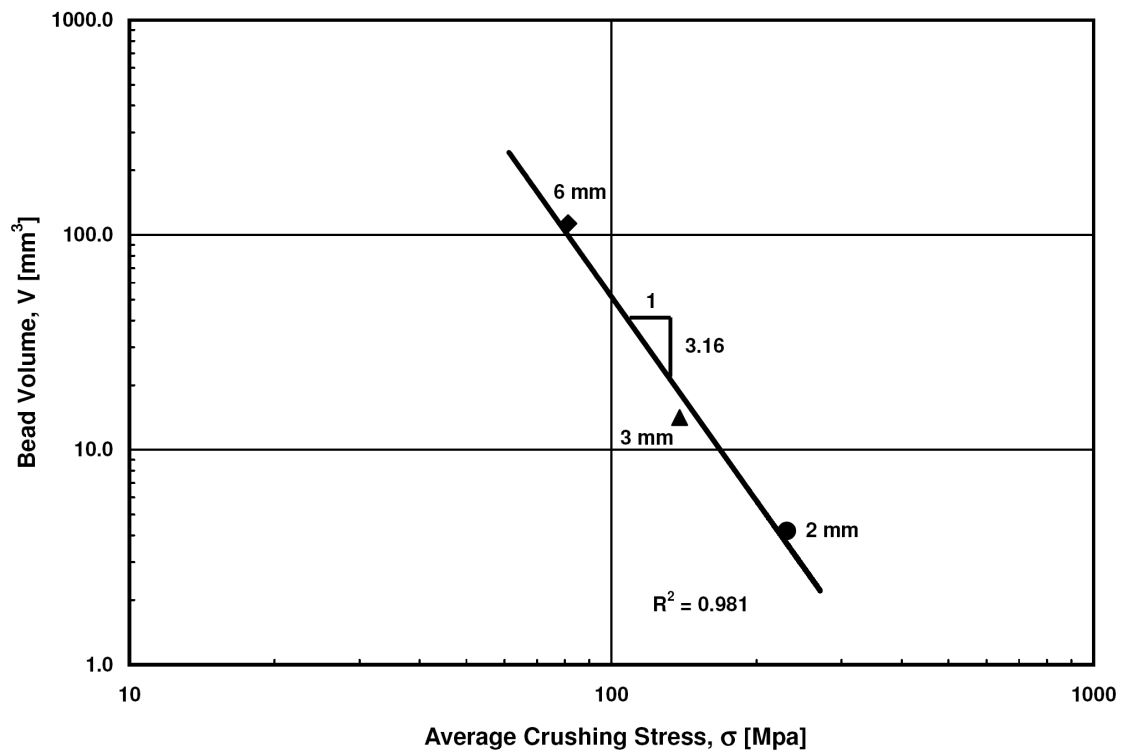


Figure 4.27. Curve fitting to evaluate the exponent of n in Equation (2-2).

McDowell and Bolton (1998), Nakata et al. (1999, 2001a,b) and Ham et al. (2010) utilized survival probability to analyze the results of their experiments on single particles. In this regard, survival probability has been calculated according to Equation (2-4) and the results are plotted in Fig. 4.28(a). The graph implies that beads with smaller size exhibit higher amount of scatter. This indicates that although smaller beads fracture at higher stresses than larger ones because they enclose fewer critically oriented microcracks, their strengths are highly influenced by these microcracks, flaws and defects. This result has been normalized with a stress value at which 36.8% of the beads of each size have survived. The normalized curves are shown in Fig. 4.28(b). It is observed that the curves merge after normalization and more or less, a same curve is obtained beyond the normalized stress of 0.9.

Equation (2-3) can be written as follows:

$$\ln \left[\ln \left(\frac{1}{P_s(V_0)} \right) \right] = m \cdot \ln \left(\frac{\sigma}{\sigma_0} \right) \quad (4-9)$$

Fig. 4.29 shows the data points in a $\ln[\ln(1/P_s(V_0))]-\ln(\sigma/\sigma_0)$ diagram. Therefore, the slope of the trendline passing through these data reveals that the Weibull modulus, m , in Equation (2-3) equals to 3.10. Inasmuch as Equation (2-2) is a special case of Equation (2-3) where $P_s = 1/e = 0.368 = 36.8\%$, the value of the exponent n is very close to the Weibull modulus, m .

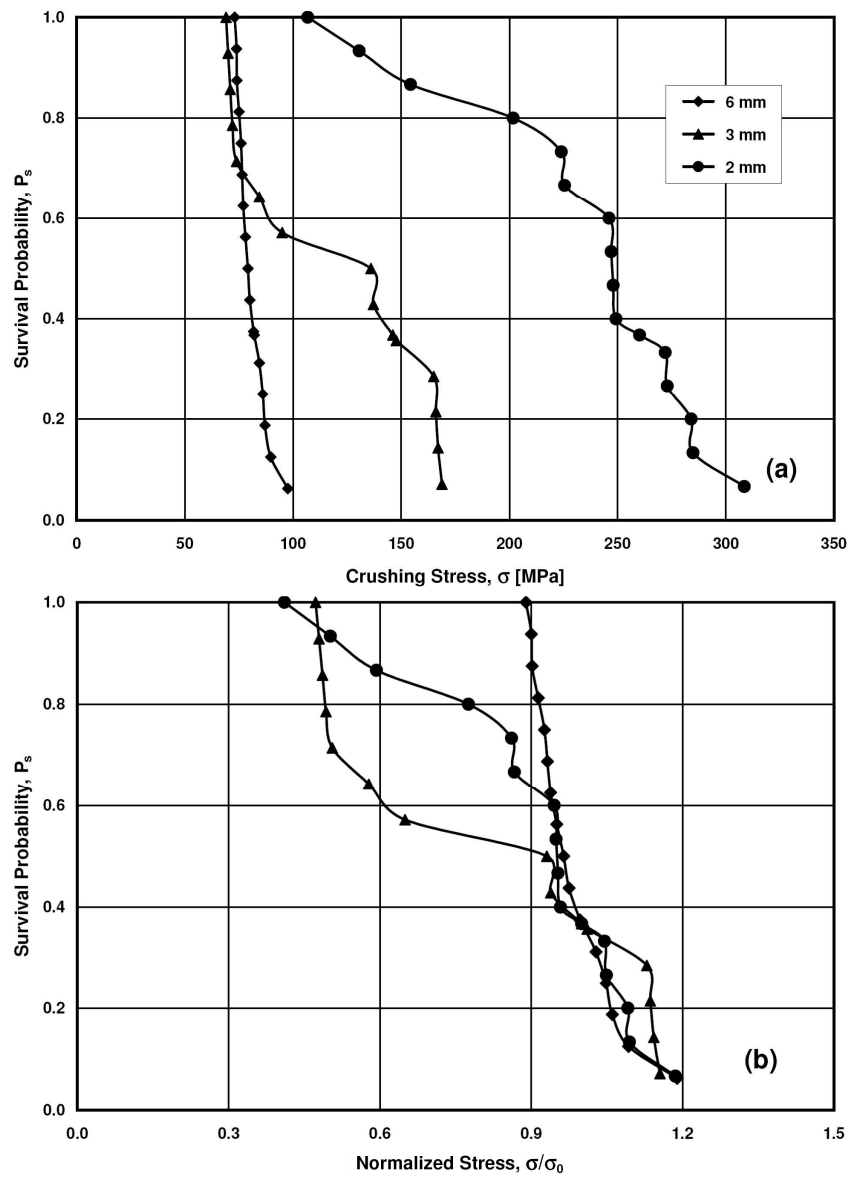


Figure 4.28. Survival probability versus (a) crushing stress, and (b) normalized stress.

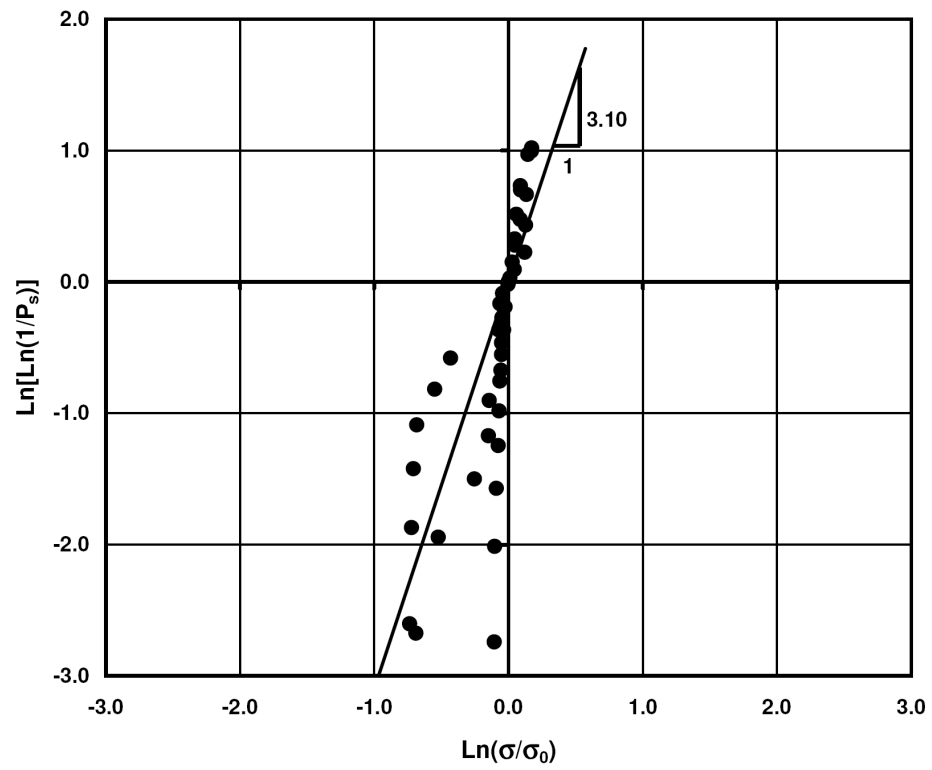


Figure 4.29. Curve fitting to obtain Weibull modulus, m .

In the second series of the single glass bead experiments, static fatigue was studied by holding glass beads of each size under various stress levels while time-to-fracture was measured. The following numbers of beads were tested: 2 mm: 22, 3 mm: 19, and 6 mm: 14. Many beads fractured during loading toward the desired stress, whereas others fractured under constant stresses with time-to-fracture varying from seconds to several days. The time-dependent behavior of glass beads is shown in Fig. 4.30 for ones the beads fractured within the first 10 minutes.

Although the pattern obtained is basically erratic and does not follow the behavior indicated in Fig. 2.27 for concrete specimens or the expressions in Section 2.3.2 for prediction of the time-to-fracture under static fatigue, this phenomenon is clearly observed in the sense that fracture will occur after some time when the beads are loaded up to the vicinity of their short term fracture strengths. This suggests that the prediction of the time-dependent strength of non-spherical single grains with a variety of shapes is likely to be even more complicated. However, as discussed earlier, while fracture time prediction might be difficult and may require sophisticated methods to control the observed scatter, the average behavior in an assembly of millions of particles may be quite consistent. For instance, Lade et al. (2009, 2010) presented a consistent time-dependent behavior for crushed coral sand in a series of triaxial creep and relaxation experiments.

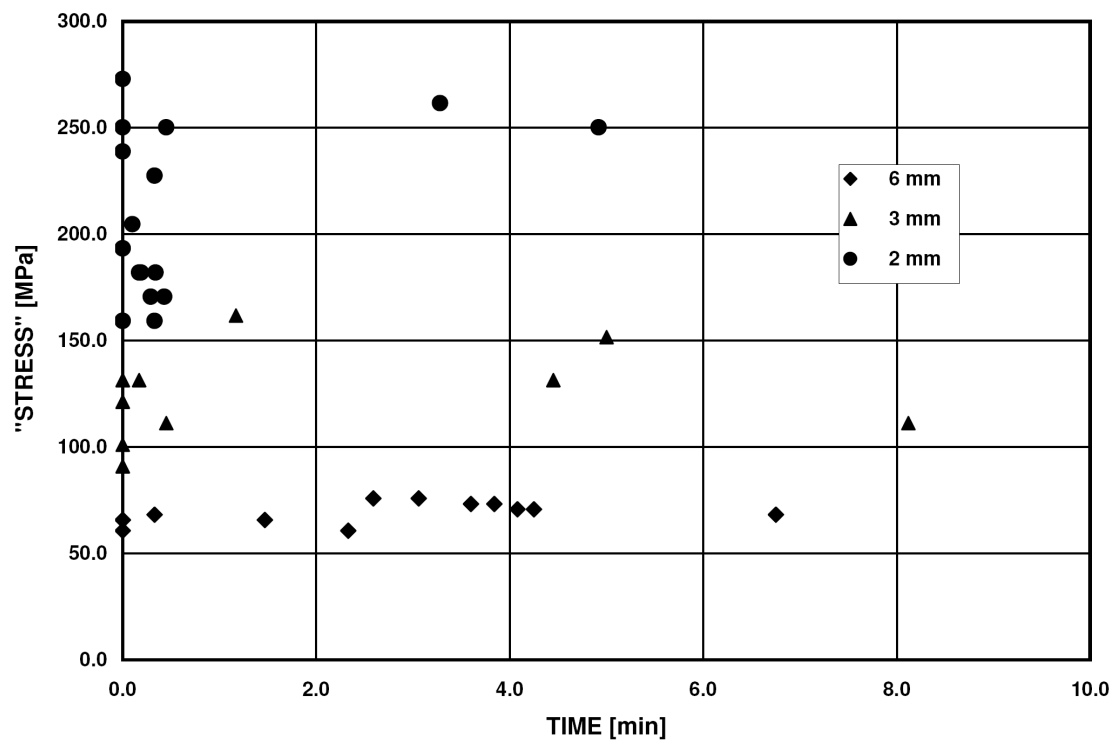


Figure 4.30. Relation between sustained stress and time-to-fracture for different size soda lime glass beads tested in compression.

5. Creep Experiments

The drained creep behavior of Virginia Beach sand was investigated as follows:

5.1. Effect of Initial Shearing Rate on Subsequent Creep

Since the previous experiments to study creep were all performed with the same loading strain rate, the effects of the initial loading strain rate on the subsequent amounts of creep and stress relaxation had not been investigated before. Thus, three strain rates of 0.00260, 0.0416 and 0.666 %/min were used to shear a total number of six specimens under low and high effective confining pressures of 250 and 8000 kPa.

Inasmuch as there was a small difference in the stress-strain behavior of dense Virginia Beach sand when specimens were sheared under different strain rates, the criterion of equal input energy was used for the stress point at which creep experiments were initiated. The input energy was calculated according to Equation (3-5).

For experiments performed under a confining pressure of 250 kPa, specimens were sheared up to points on stress-strain curves where $[(\sigma_1 - \sigma_3), \epsilon_1] = [723 \text{ kPa}, 1.09\%]$, $[825 \text{ kPa}, 0.94\%]$, and $[795 \text{ kPa}, 1.17\%]$ for the lowest to the highest shearing rate, respectively. These points were located in the vicinity of 70-75% of their deviator strengths found in Section 4.2 and they corresponded to points where the energy input per unit volume, calculated from Equation (3-5), reached the same level of $6 \text{ kN.m/m}^3 = 6 \text{ kN/m}^2 = 6 \text{ kPa}$. Then, specimens were allowed to creep for a day. Due to axial and

volumetric creep deformations, the cross sectional area of the specimens would vary during creep. In spite of the fact that the deviator load was adjusted periodically to maintain a constant deviator stress, some reduction in the deviator stress level was observed for specimens sheared at strain rates of 0.0416 and 0.666%/min. The stress-strain behavior and volume change of these experiments are shown in Fig. 5.1. The X-axis (axial strain) has been magnified 10 times in comparison to the experimental results shown in Chapter 4 to show the details; otherwise, the observed discrepancies are within the experimental scatter as described in Chapter 4.

Fig. 5.1(b) shows that different strain rates have resulted in more or less the same axial and volumetric creep after 1440 minutes. The axial and volumetric creep behaviors of these experiments are illustrated in Fig. 5.2. For specimens sheared from the lowest to the highest strain rates, the axial creep strains of 0.14%, 0.06% and 0.07% were achieved after 1 day creep, whereas the corresponding values for volumetric creep strains were -0.08%, -0.14% and -0.08%, respectively. These values are so small that they can easily be affected by experimental errors.

As shown in Fig. 5.1(b) and Fig. 5.2(b), the specimens underwent dilation during creep at low confining pressures. In fact, just before creep is initiated the specimens are in the dilation mode. Previously, Bowman and Soga (2003), and Ladanyi and Benyamina (1995) had reported dilation during creep under low confining stresses. It is known that the surfaces of particles of granular materials are very uneven and full of rough features. As a result, inter-connections of particles take place at extremely small asperities where

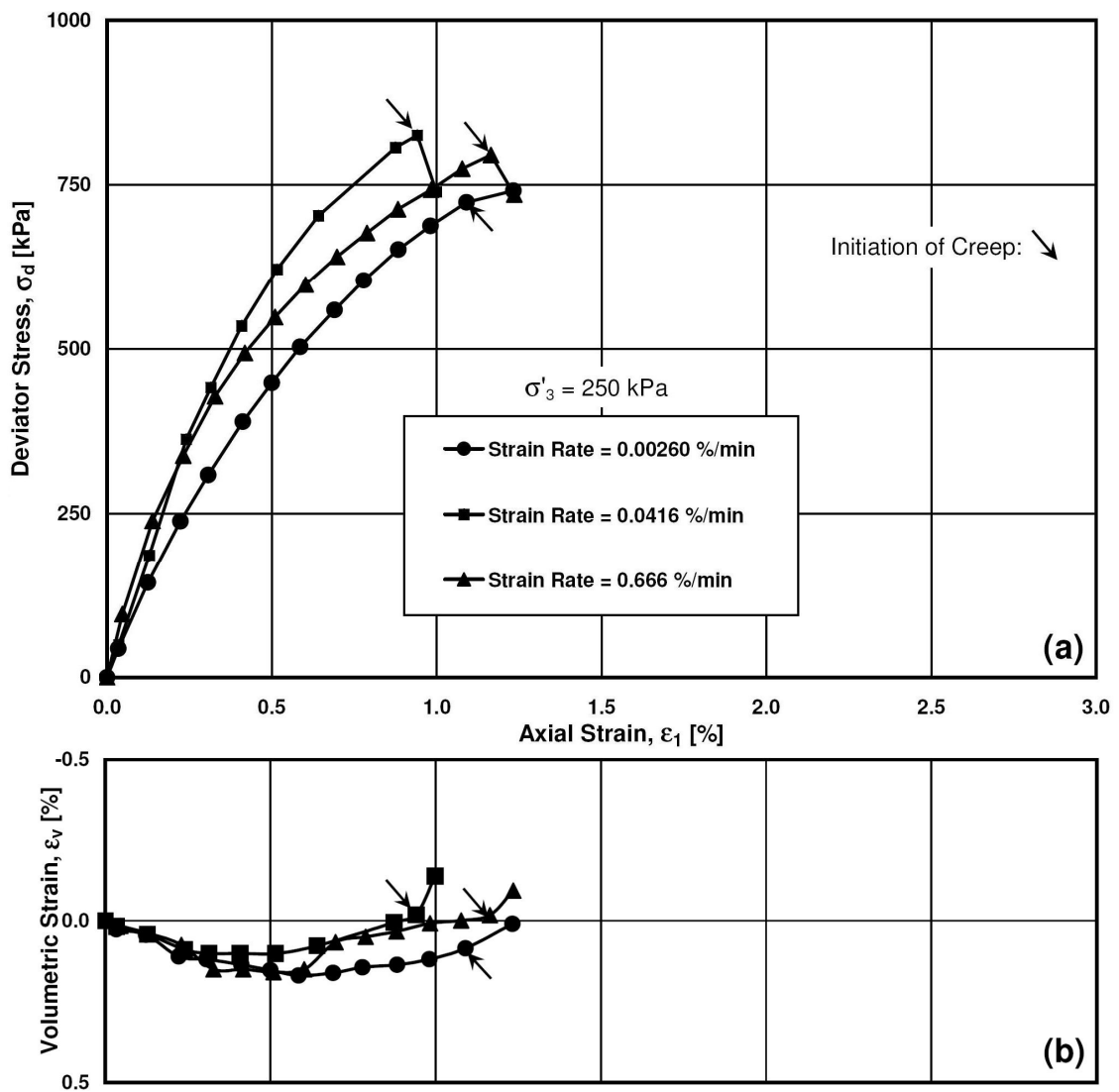


Figure 5.1. Effect of the shearing strain rate on the subsequent creep behavior under $\sigma'_3=250$ kPa: (a) Stress-strain curve; (b) volume change curve.

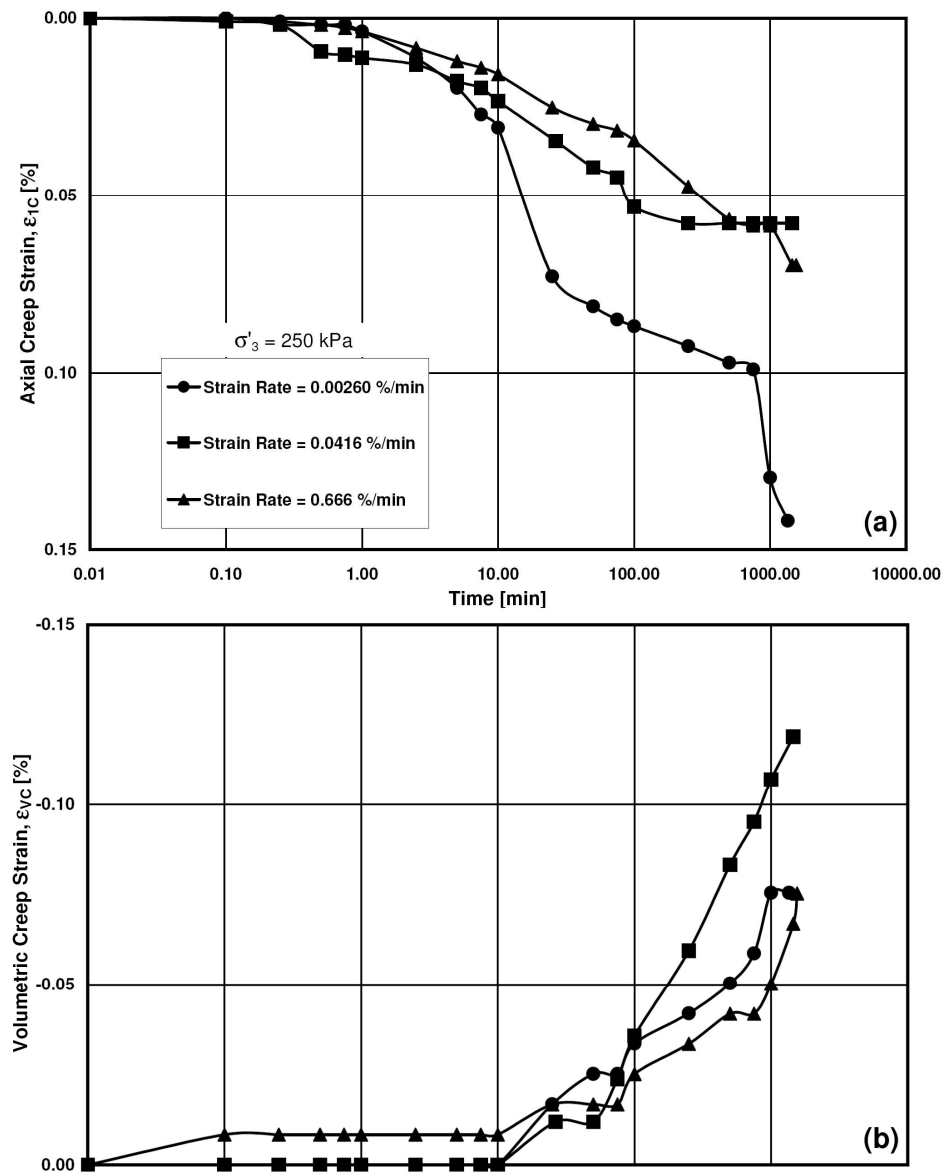


Figure 5.2. Effect of the initial shearing strain rate on the variation of (a) axial and (b) volumetric creep strains with time.

stress concentrations may result in the breakage of these asperities. This type of breakage is called as abrasion which can not be detected by sieving. It is believed that particle crushing is the root of time effects. However, as mentioned, there is no measurable particle crushing at low confining stress. It may be concluded that the rotation and rearrangement of particles, which result in observation of dilation, are the governing mechanisms of creep behavior in low confining stresses. However, breakage of asperities may trigger the rotation and rearrangement of grains. While no clear rate dependency pattern is recognized in the subsequent creep under low confining pressures, it is observed that the rate of dilation is equal to or higher than the rate observed during loading (see Fig. 4.9). Results of sieve analyses are shown in Fig. 5.3. As seen, almost no particle crushing has been experienced under low confining stresses.

In the second series of these tests, specimens were loaded at three different shearing rates to approximately 70-75% of their deviator strengths at a confining pressure of 8000 kPa as obtained in Section 4.2. Similar amounts of initial energy/volume (410 kPa) were applied before creep experiments were performed. For specimens loaded with the strain rate of 0.00260, 0.0416 and 0.666 %/min, the corresponding stress-strain points were $[(\sigma_1 - \sigma_3), \epsilon_1] = [10594 \text{ kPa}, 2.85\%]$, $[11246 \text{ kPa}, 2.81\%]$, and $[11881 \text{ kPa}, 2.76\%]$, respectively. The loading was stopped at these points and the specimens were allowed to creep for 1 day. For specimens sheared at different strain rates, dissimilar conditions in terms of the amount of particle crushing and the grain structure were expected. This was due to static fatigue and the different times under which the specimens were sheared.

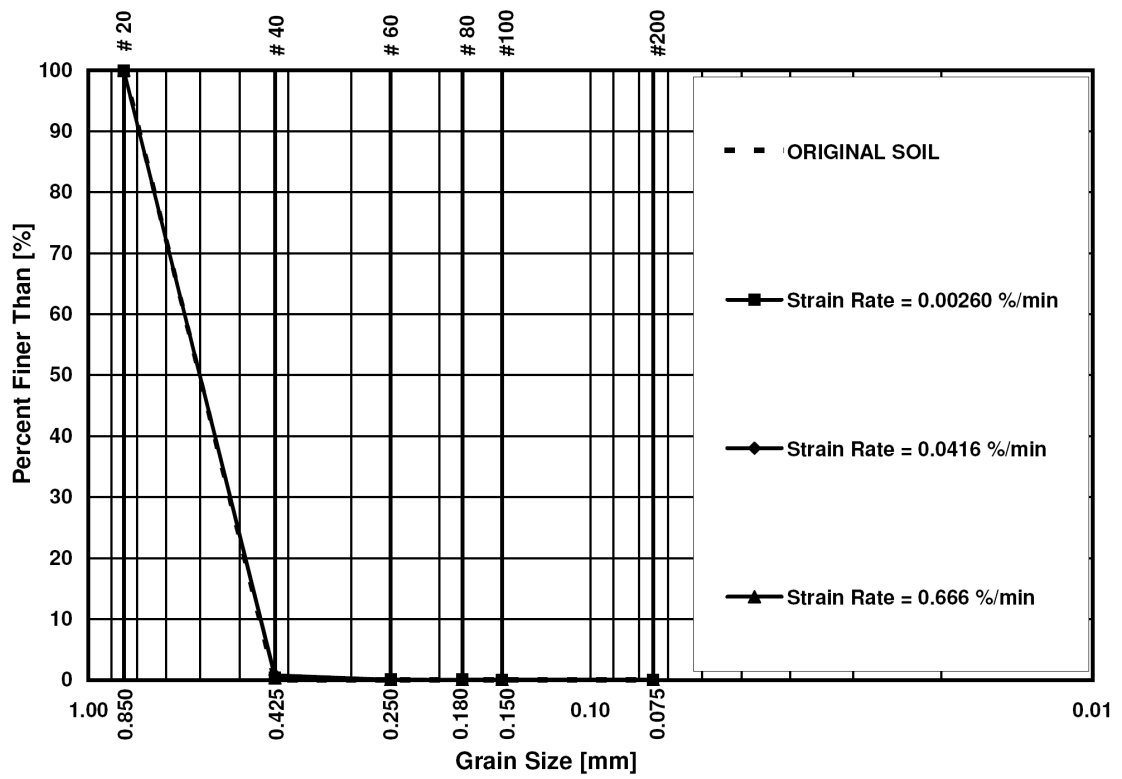


Figure 5.3. Effect of the initial shearing strain rate on the crushing of the particles.

Fig. 5.4 illustrates the stress-strain and volumetric curves for creep experiments performed under a confining pressure of 8000 kPa. To show the repeatability of experiments, the stress-strain curves shown in Fig. 4.10, corresponding to the same strain rates, have been superimposed as reference curves. As it can be seen, the discrepancies between creep experiment curves and reference curves are within experimental scatter and the coincidence of curves indicates the repeatability of the experiments.

It is clearly observed that loading under initial higher strain rates produce subsequent more creep deformation within 1 day. Furthermore, Fig. 5.4(a) shows that there is a jump in the axial strain at the moment of switching from deformation control to load control to initiate creep at a constant deviator stress. This is most clearly seen in Fig. 5.5. The higher the initial shearing rate, the more pronounced the jump will be. Interestingly, as better observed in the magnified portion of Fig. 5.4(b), once the switch occurs, volumetric strains leap along their related reference curves. In other words, the volume change has no tendency to deviate from its corresponding reference curve as was also reported by Lade (2007) for creep tests performed on Antelope Valley sand,. This may suggest that an identical potential function may be used for modeling inelastic creep deformations. In contrast, Lade et al. (2010), after performing creep experiments on crushed coral sand, argued that there was a tendency of more contraction during the creep process than indicated by the reference curve. To throw further light on the creep behavior, the axial and volumetric strains during creep have been plotted against elapsed creep time in Fig. 5.5.

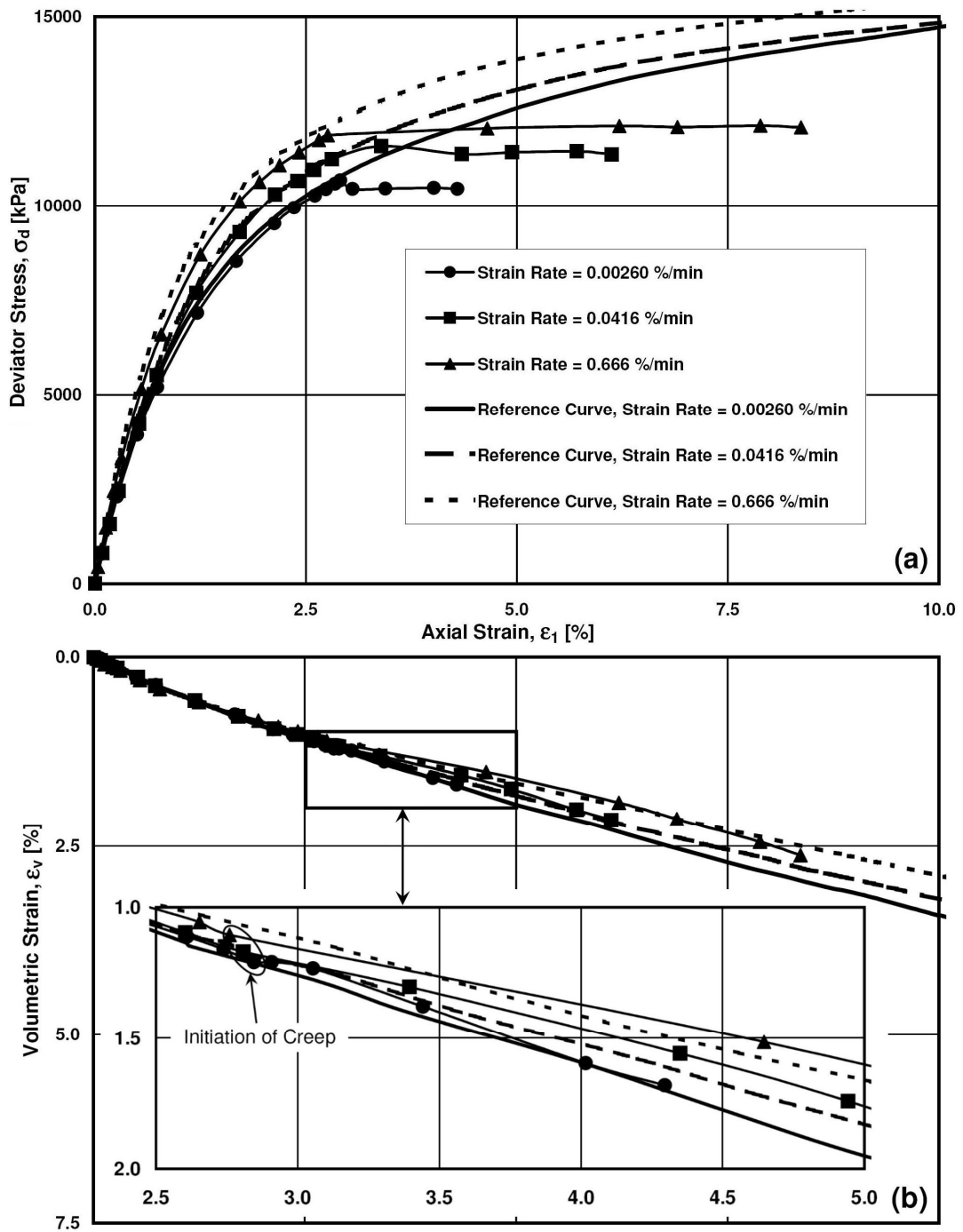


Figure 5.4. Effect of the shearing strain rate on the subsequent creep behavior under $\sigma'_3 = 8000$ kPa: (a) Stress-strain curve; (b) volume change curve.

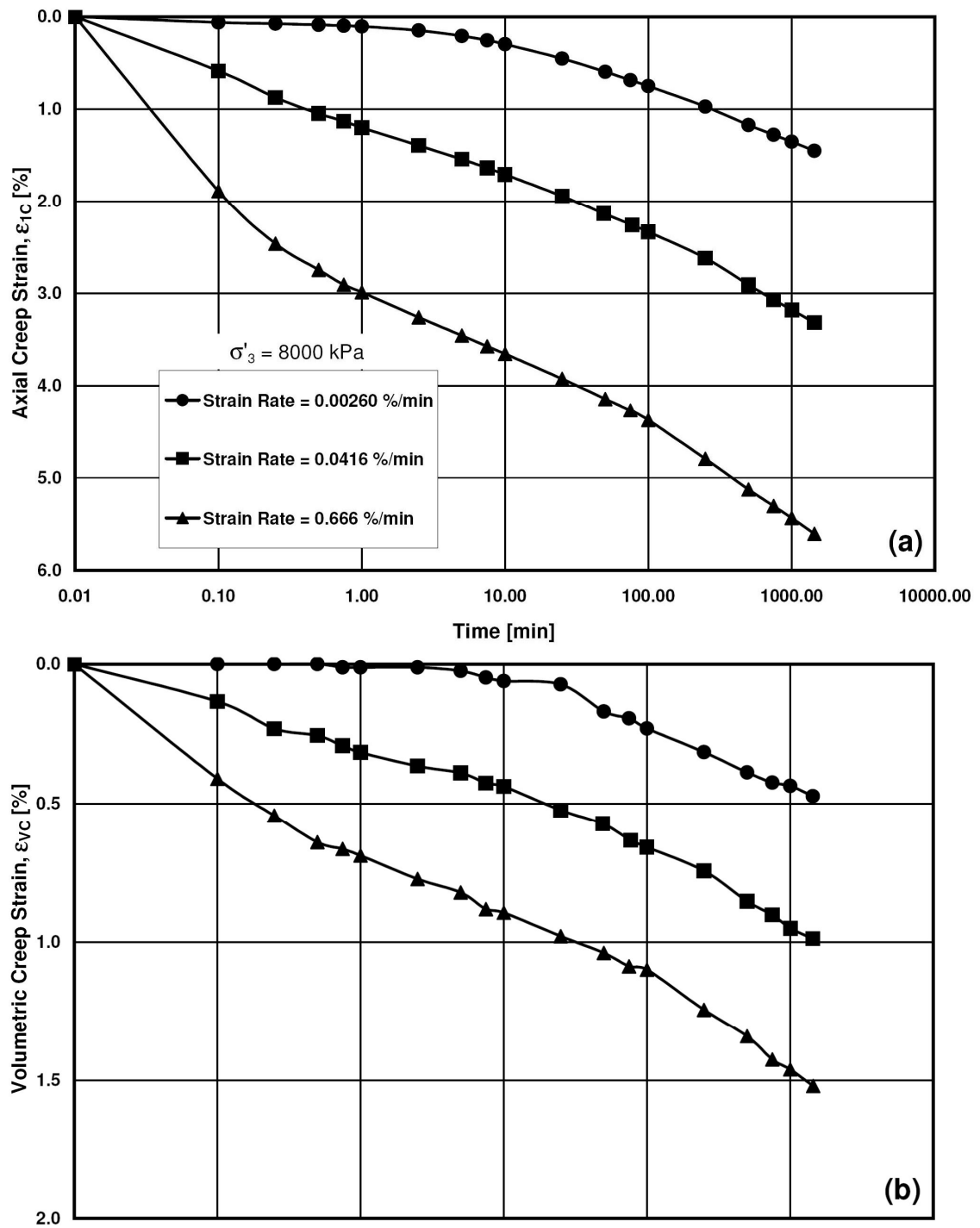


Figure 5.5. Effect of initial shearing strain rate on variation of (a) axial, and (b) volumetric creep strains with time.

Similar patterns are observed for the axial and volumetric creep strains. In the first one minute of creep, the specimen sheared under a strain rate of 0.00260 %/min experienced almost no axial and volumetric creep strains, while the specimen loaded under the strain rate of 0.666 %/min has shown 2.99% axial and 0.69% volumetric creep strains. However, the axial and volumetric creep strains progress at similar rates with time following the initial 10 to 25 minutes. That is, the curves on Fig. 5.5 tend to become parallel for different initial shearing strain rates. The total axial creep deformation of 5.61%, 3.31% and 1.45% were achieved after creeping for 1 day for the highest to the lowest initial shearing strain rates, while the corresponding volumetric strains were 1.52%, 0.99%, and 0.47%, respectively. For the middle strain rate of 0.0416 %/min, an almost linear creep relation is observed with the logarithm of time. However, for the specimen sheared at the highest strain rate, the highest creep rate is observed in the first 15 seconds.

Different creep deformation means different energy input and subsequently dissimilar amounts of particle crushing. Fig. 5.6 exhibits the grain size distribution curves for creep experiments under confining pressure of 8000 kPa. This graph again confirms that creep behavior and particle crushing are intimately connected. The experiment which showed the highest creep deformations has experienced the highest particle breakage, whereas the specimen with the lowest axial and volumetric creep deformation exhibits the lowest particle breakage. The corresponding total energy input at the end of 1 day creep were 560, 830, and 1160 kPa from the slowest to the fastest, respectively. Variation

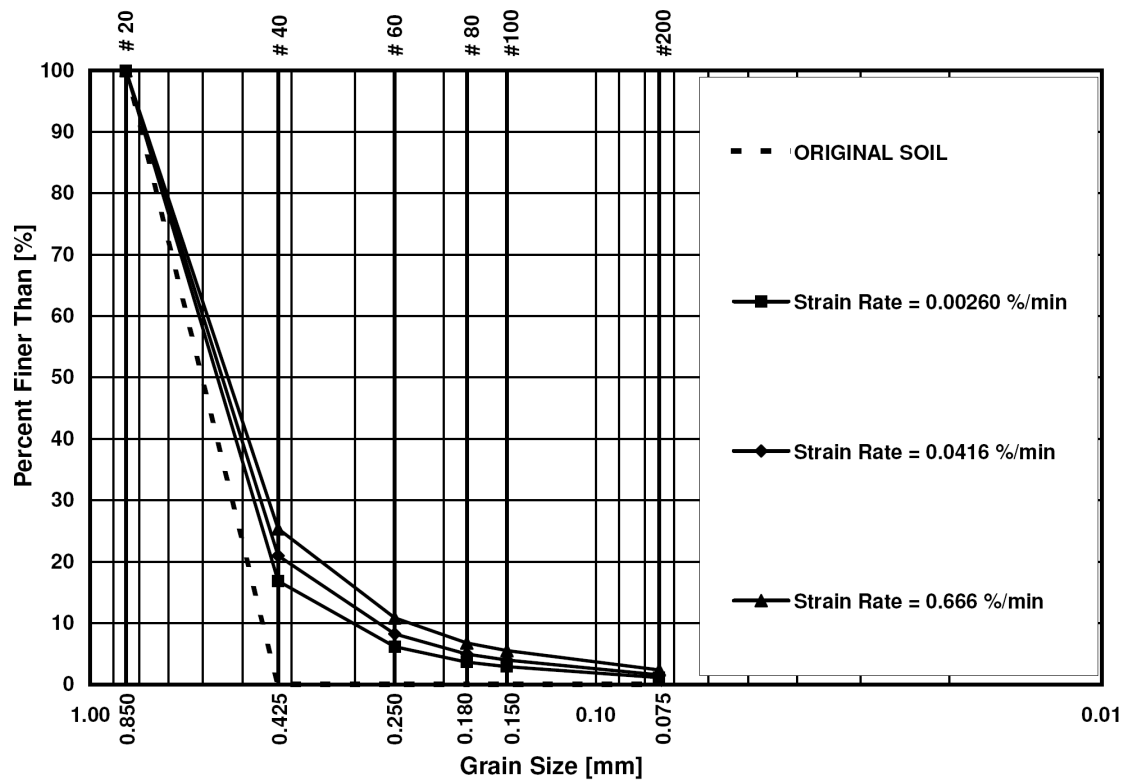


Figure 5.6. Effect of initial shearing strain rate on crushing of particles.

of Hardin's breakage factor versus energy input is plotted in Fig. 5.7 indicating a linear relationship between Hardin's breakage factors with the energy input (the R-squared value equals to unity).

5.2. Effect of Soil Gradation Curve on Subsequent Creep

Previous experimental results showed that the rate of creep decreases as particle crushing progresses and a more distributed grain size curve is achieved. Therefore, to study whether specimens with more distributed grain size curves would exhibit smaller creep deformations and to explore dependency of the creep behavior of Virginia Beach sand on the initial grain size distribution curve, triaxial creep experiments on six different grading curves were performed under a confining stress of 8000 kPa by performing. All specimens were built using a similar method which was pouring the oven-dried soils from a height of 50 cm into the specimen mold. These grading curves were shown in Fig. 3.1, and they involved a wide range of uniformity ranging from very uniform to well-graded soils with different amounts of fine particles. These soils were expected to exhibit different stress strain behaviors; thus, the same deviator stress was found to be more logical from which to initiate creep experiments. All six specimens were sheared at the middle strain rate of 0.0416 %/min to the deviator stress level of about 6500 kPa. The loading system was then switched to load control to sustain the deviator load and the specimens were allowed to creep for 1 day. The stress-strain and volumetric relation of these experiments during shearing and creep are shown in Fig. 5.8.

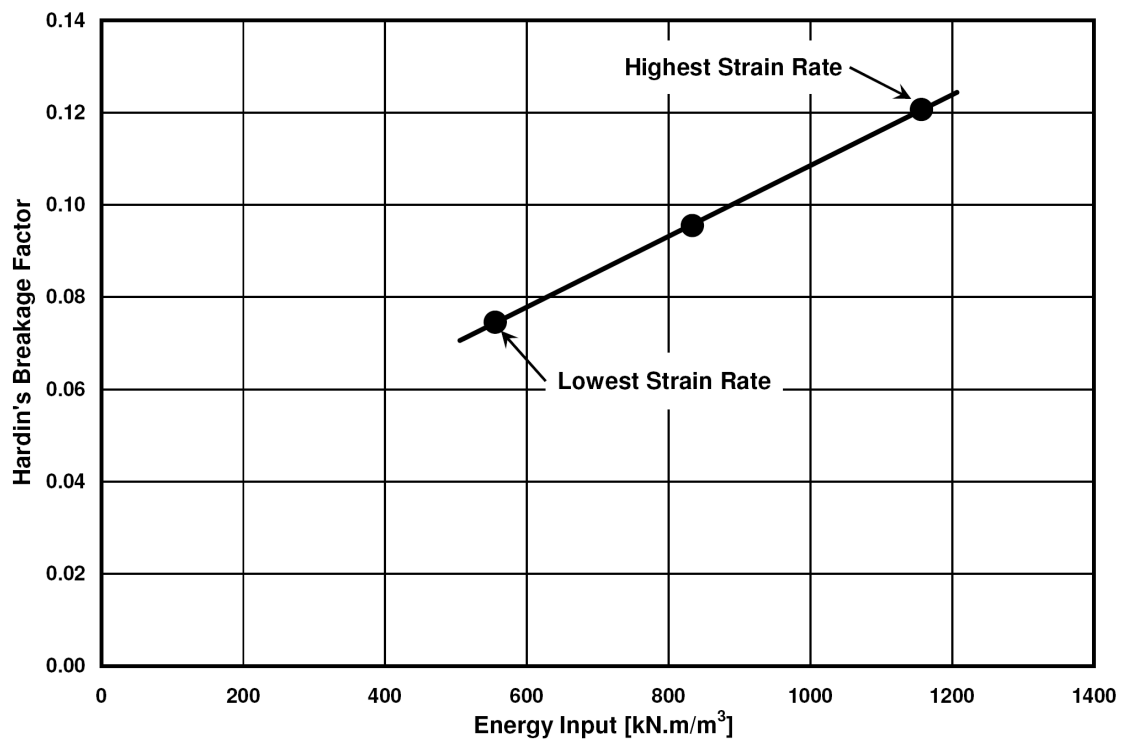


Figure 5.7. Relationship between Hardin's breakage factor and the amount of energy input for creep tests initially sheared at different strain rates.

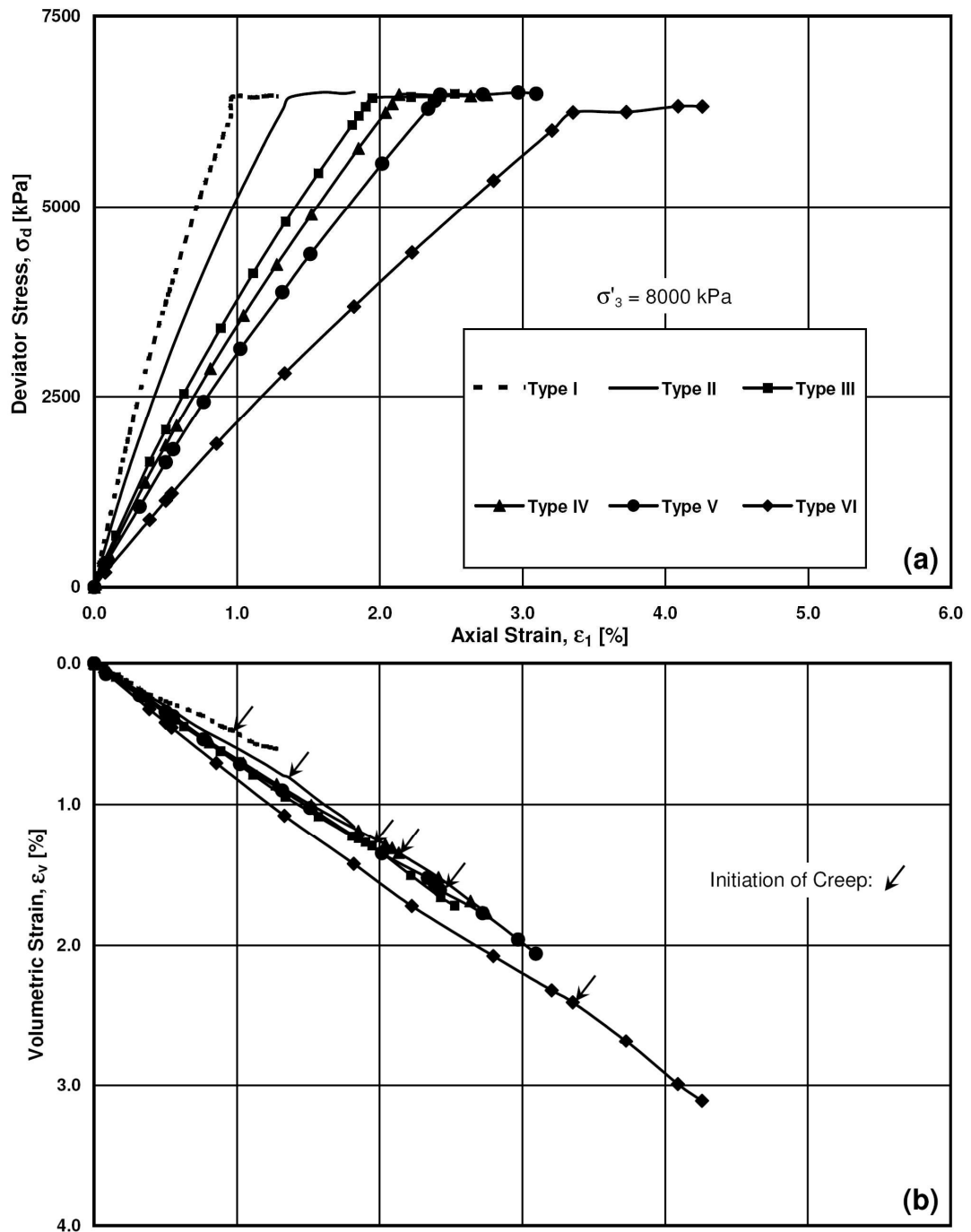


Figure 5.8. Effect of the grain size distribution curve on the subsequent creep behavior under $\sigma'_3=8000$ kPa: (a) Stress-strain curve; (b) volume change curve.

Fig. 5.8(a) shows that the more uniform the soil is, the stiffer the response will be. Therefore, a smaller axial strain is necessary to reach the target creep deviator stress level. In this regard, the soil Type I was sheared up to an axial strain of 0.97%, while soil Type VI was loaded to the axial strain of 3.35% to reach the same deviator stress level for initiation of the 1-day creep. In addition, Fig. 5.8(b) shows that less volumetric strains were experienced for specimens which were more uniform. In other words, at the same axial strain, a higher deviator stress and a lower volume change were observed for specimens with higher uniformity coefficients. Similar to the creep behavior presented in the previous section, Fig. 5.8(b) reveals that the volume change curves follow the same trend during creep as they had during shearing. This suggests employing a similar potential function to evaluate the direction of inelastic creep and plastic strain increments. For each experiment, the initial tangent modulus has been calculated and plotted versus the uniformity and curvature coefficients of the corresponding grain size distribution curve in Fig. 5.9. It may be concluded that the logarithm of the initial tangent modulus is reduced with the logarithm of the uniformity and curvature coefficients.

Fig. 5.8 also reveals that specimens with more uniform grading have undergone lower amounts of axial and volumetric creep deformation for 1 day. This can be better observed in Fig. 5.10, where the axial and volumetric creep strains are plotted against elapsed creep time. The total 1-day axial and volumetric creep strains are 0.31% and 0.13% for the specimen of Type I, whereas these values are 0.90% and 0.71% for the specimen of Type VI. Fig. 5.10 shows that up to somewhere between 7.5 and 10 minutes

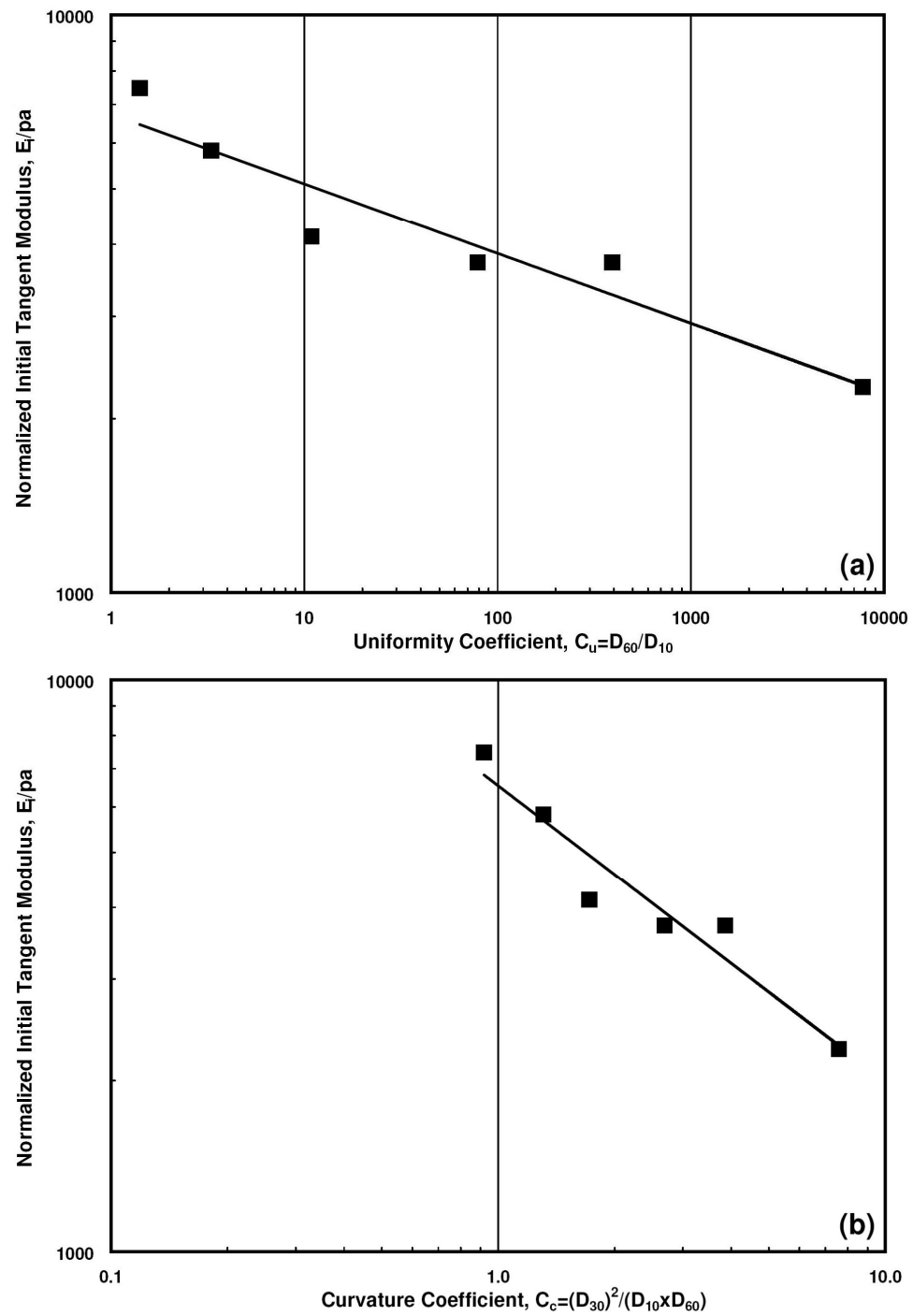


Figure 5.9. Variation of the initial tangent modulus with (a) uniformity and (b) curvature coefficients.

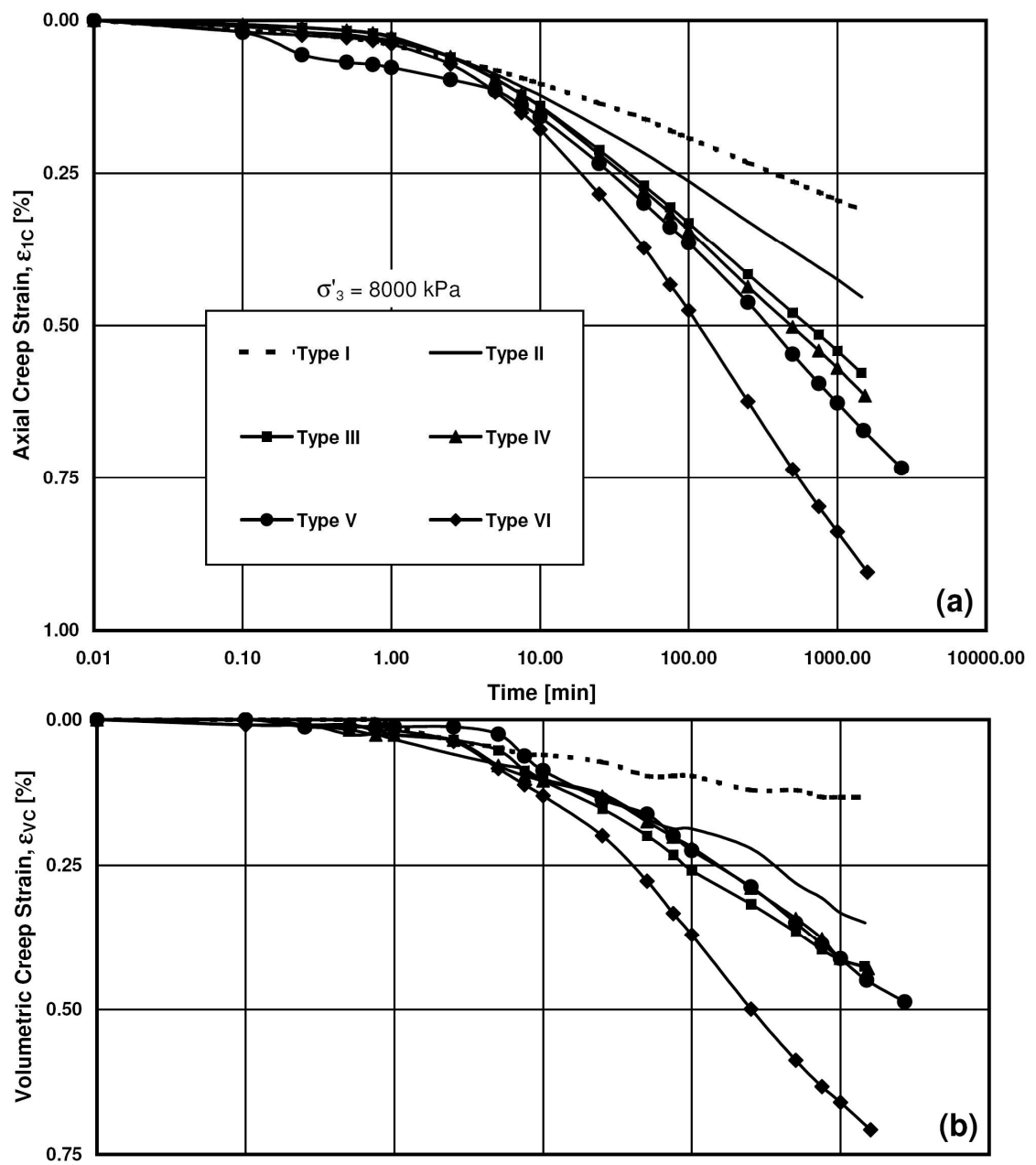


Figure 5.10. Effect of the grain distribution curve on the variation of (a) axial and (b) volumetric creep strains with time.

after initiation of creep, very similar amounts of axial and volumetric creep strains have been achieved for all specimens. This is believed to be because of the shearing strain rate prior to creep. That is, all specimens have had the same amount of time to form a stable structure. Therefore, by switching to load control and initiation of creep, more or less, the same response was obtained during the first 10 minutes. It was previously noticed in Section 5.1 that the time for reaching a structure that can resist and sustain loads is dependent on the strain rate at which the specimen had been sheared.

However, different tendencies are observed after this time period. Specimens with a higher uniformity and curvature coefficients have responded with a higher axial and volumetric creep strains. This may be explained by the initial soil structure, the amount of fine particles (smaller than 75 μm) in each specimen and coordination number as discussed below. In this regard, the initial amount of fine particles, the initial void ratio, and the reduction in void ratio, axial and volumetric strains at the end of isotropic compression of 8000 kPa have been tabulated in Table 5.1.

Lade et al. (1998) have investigated the effect of non-plastic fines on the minimum and maximum void ratio of sand. In their study, they considered a uniform soil with large particles (at least 10 times larger than the fine particles) to be mixed with different amounts of fine particles. All particles were assumed to be spherical. They proposed a theoretical packing diagram, as illustrated in Fig. 5.11, to obtain the amount of fine particles that must be mixed with large particles to achieve the minimum void

Table 5.1. Change in void ratio, axial and volumetric strains at the end of isotropic compression.

Grading Type	Before Isotropic Compression		At the End of Isotropic Compression		
	Minimum Void Ratio	Particles Finer than 75 μ m [%]	Reduction in Void Ratio	Axial Strain [%]	Volumetric Strain [%]
Type I	0.531	0.0	0.034	0.52	2.27
Type II	0.461	2.6	0.037	0.75	2.52
Type III	0.462	16.2	0.050	0.83	3.44
Type IV	0.468	37.0	0.060	1.00	4.06
Type V	0.555	48.3	0.075	0.74	4.80
Type VI	0.822	61.54	0.130	1.35	7.14

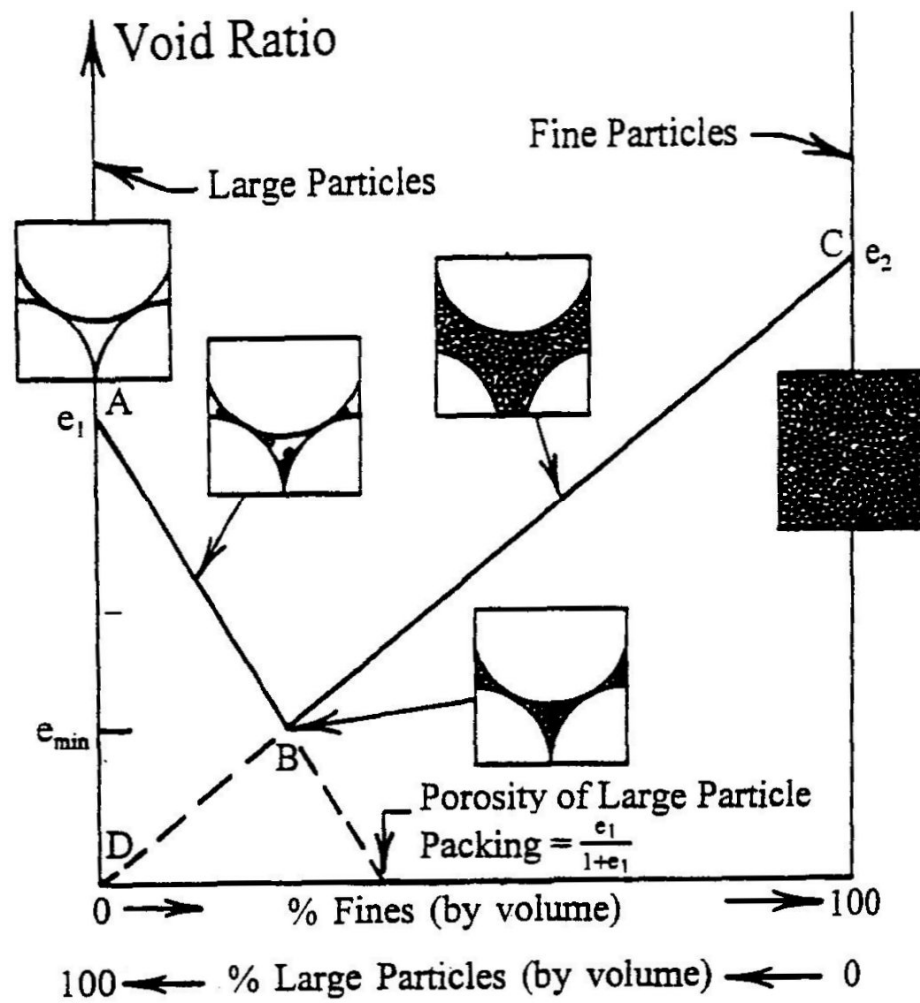


Figure 5.11. Schematic variation of minimum void ratio for the mixture of large and fine spherical particles (after Lade et al., 1998).

ratio. In fact, the minimum void ratio is obtained when all existing voids in the original fabric is filled with small particles. In this graph, the percentage of fine grains corresponding to point *B* will produce the overall minimum void ratio. Point *B* is the intersection of two lines. The first line starts from a point corresponding to the minimum void ratio of large particles on the Y-axis and ends in the point corresponding to the porosity of large grains on the X-axis. The other line is drawn from the origin of the diagram and ends in a point equal to the minimum void ratio of fine particles on the Y-axis. This gives an insight on how the minimum void ratio changes by adding fine particles.

As it discussed in Chapter 3, the dry pluviation method has been used to make dense specimens for the entire experimental program. Visual observation during specimen preparation revealed that particles finer than sieve #200 did not drop as quickly as larger particles because the air resistance affected their dropping velocity. This results in particles having less energy when they reach the surface of the specimen. It can be seen that adding smaller particles to the original uniform soil (Type I) results in a decrease in the minimum void ratio from 0.531 to 0.461 for Type II. However, after this point, adding smaller particles results in increases in the minimum void ratio up to 0.822 for soil Type VI. Obviously, the percentage of fine particles increases by adding smaller particles, as shown in Table 5.1 for soil Type I to Type VI. Fine particles residing in the voids decrease the void ratio of the soil without having influence on the mechanical properties mainly because they are not part of the soil skeleton which resists sustained loads. Those fine particles, which are parts of the load-bearing skeleton by sitting at

contact points of larger grains and holding them apart, may even reduce the overall mechanical properties of the soil. This is because they have to carry the same amount of load as the adjacent large grains. In fact, due to their small cross-sectional area, higher stresses are produced which results in the breakage of these particles and triggering more deformations.

In Table 5.1, it is observed that although adding smaller particles has reduced the initial void ratio, the reduction of void ratio and amount of axial and volumetric strains are more pronounced in these specimens after isotropic compression. This means that the presence of fine particles has increased the compressibility of the soils of Type II to Type VI. Therefore, the higher the amount of fine particle, the higher the creep deformations will be. Sieving was performed on the retrieved specimens and the results are shown in Fig. 5.12. The particle crushing can be detected in Type I and Type II, while it is more pronounced in the former as the soil was more uniform. For the other four soil types, particle crushing may have occurred in the fine particles, but this can not be distinguished by sieve analyses. This in turn elucidates why soil Type I with a rather uniform particle size distribution has been used in the entire experimental program rather than any other grain size distribution curve.

It is concluded that the creep behavior was strongly connected to the soil structure as it was formed during loading and not only did not performing creep tests on specimens with a wider distribution curve reduce the amount of creep deformation, it resulted in a larger amount of creep deformations. The results exhibited that creep deformations were more pronounced when the amount of fine particles (<0.075 mm) increased.

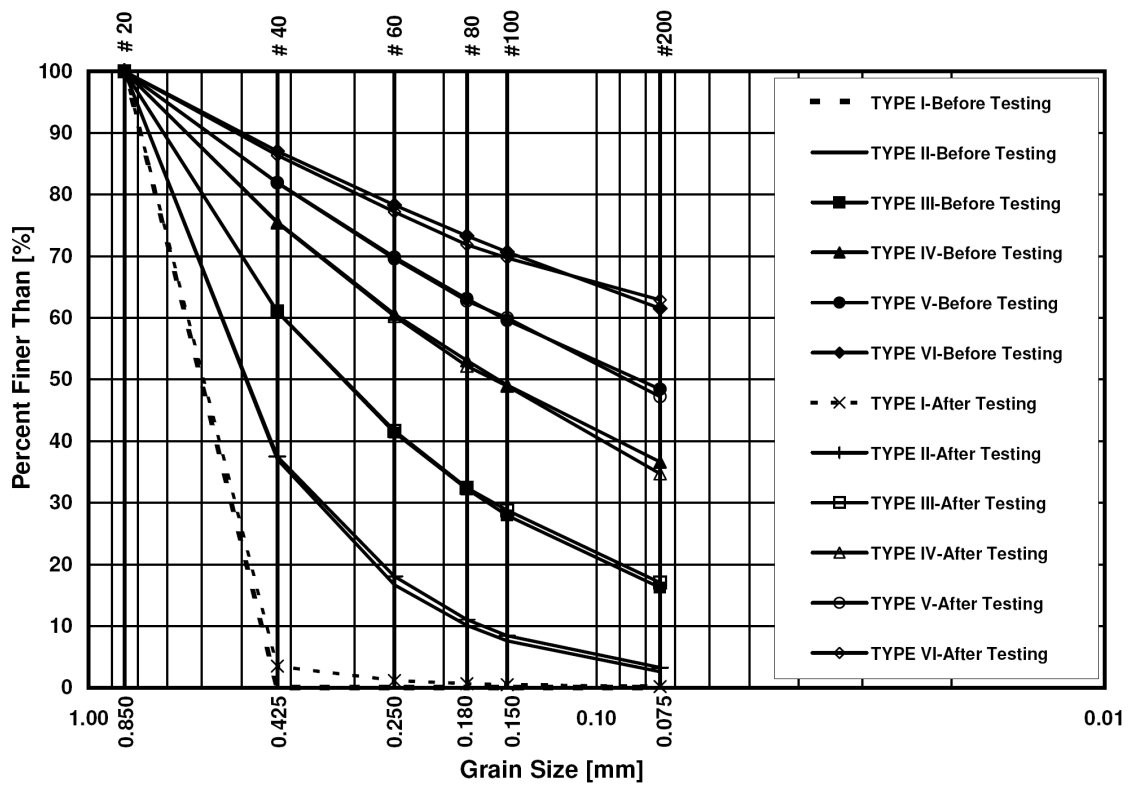


Figure 5.12. Comparison of grain size distribution curves before and after creep tests.

5.3. 1-Day Creep Curve

To identify the creep behavior of Virginia Beach sand, 7 experiments of 1-day creep were performed under a confining stress of 8000 kPa. In all these tests, the specimens were loaded at a strain rate of 0.0416 %/min up to the desired deviator stress levels where 1-day creep was initiated by switching to load control. For an easier presentation, these creep tests were named C1 to C7. They were initiated at the following deviator stress levels: 3830, 6440, 9000, 10210, 11050, 13770, and 14050 kPa, respectively. The creep parts of the experiments have been extracted from the individual experiments and superimposed on the corresponding reference stress-strain curve as shown in Fig. 5.13. Connecting the ending points of creep tests produces the overall “1-day creep curve” for dense Virginia Beach sand under confining pressure of 8000 kPa. This helps to discover where other creep experiments end if they begin at different deviator stresses. Lade (2007) and Lade et al. (2010) plotted the same graphs for Antelope Valley and crushed coral sand. In their tests, specimens were additionally sheared after creeping for 1 day to reach the next desired creep stress level, while the specimens were unloaded at the end of each 1-day creep in this series of tests. In fact, this enabled the possibility of investigation of the particle crushing for individual tests.

The overall “1-day creep curve” is similar to the stress-strain reference curve. The horizontal distance between these two curves represents the axial creep for 1 day. In general, the distance between the reference curve and 1-day creep curve increases as the deviator stress level is increased. This exhibits the effect of stress level on the subsequent

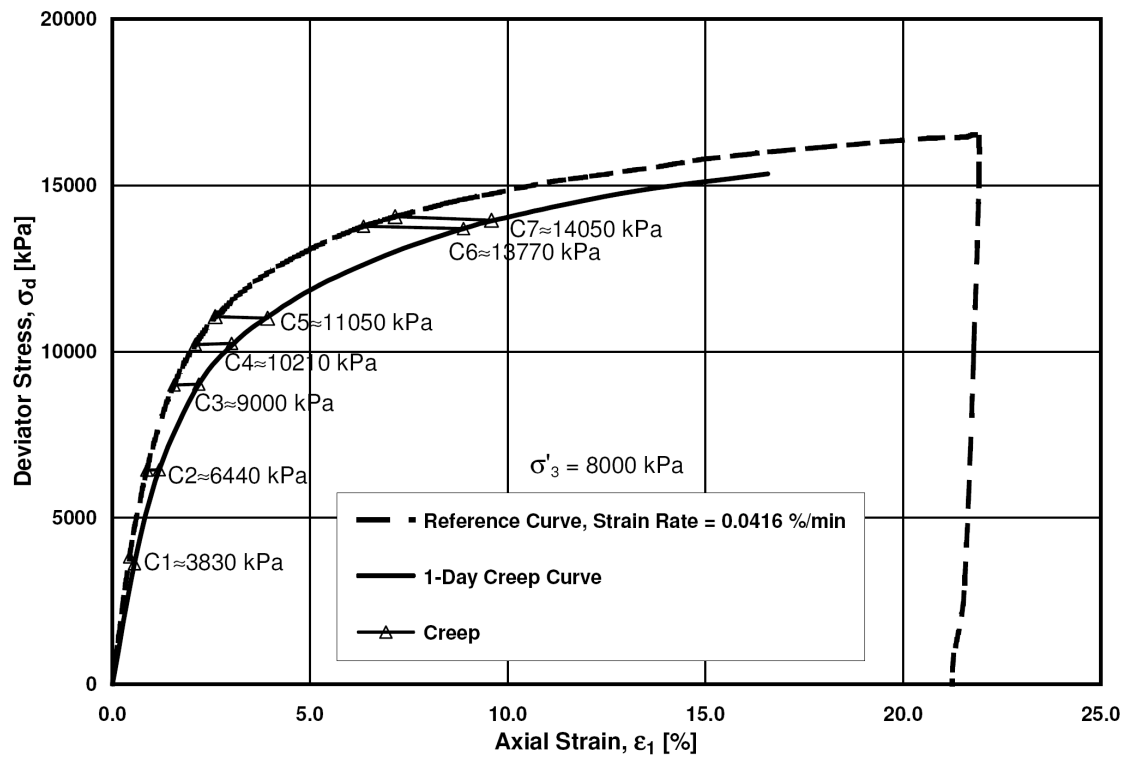


Figure 5.13. 1-day creep curve for Virginia Beach sand under $\sigma'_3=8000$ kPa.

creep and it is in agreement with the effect of load on the static fatigue. Fig. 5.14 illustrates the variation of the axial and volumetric creep strains versus the logarithm of elapsed creep time.

The general trend of all curves is similar. Approximately no axial and volumetric creep strains are observed for the first 1 min. This is a time that is required for the soil structure to reach a stable condition and for force chains to stabilize. From this moment microscopic cracks propagate in grains and particle breakage occurs. Once particles start to crush, smaller parts fill into the voids and axial and volumetric creep deformations are observed. As seen, there is a systematic response in both creep strains. The higher the deviator stress level is, the larger the axial and volumetric strains will be. In test C1 performed at a stress level of 3830 kPa, 1 day creep results in 0.12% axial creep strain and 0.12% contraction, whereas these values are 2.49% and 0.76% for test C7 at a deviator stress of 14050 kPa, respectively.

Inasmuch as all 1-day creep tests were terminated at the end of creep, the structuration effect was not studied in these tests. Thus, a multiple 1-day creep test was carried out with the same strain rate and confining pressure. In this test, the specimen was sheared at a strain rate of 0.0416 %/min. Once the desired deviator stresses of 6210, 11140, and 13550 kPa had been reached, the specimen was allowed to creep for 1 day. These deviator stresses were chosen to be approximately equal to C2, C5 and C6 in the experiments presented above.

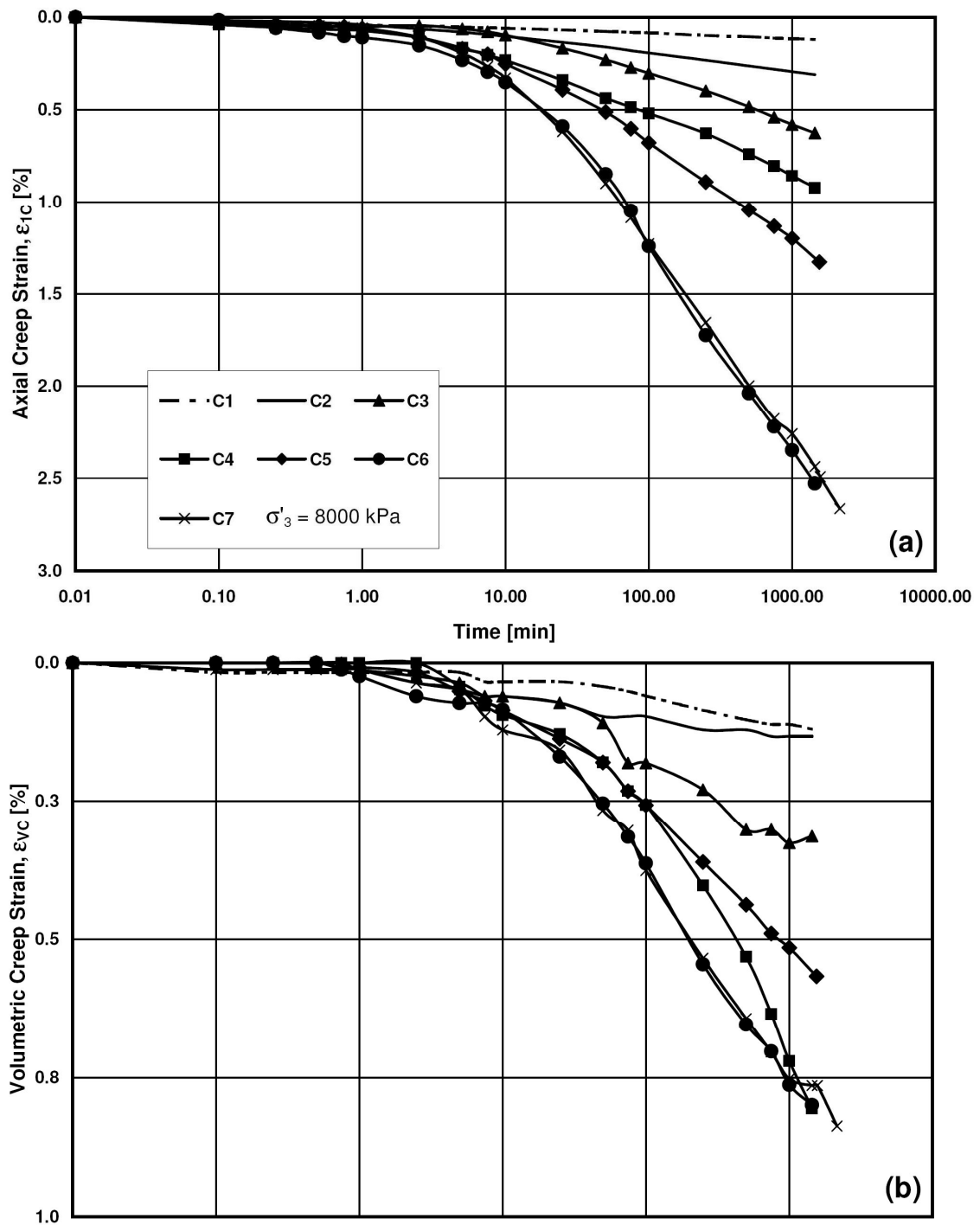


Figure 5.14. Effect of the deviator stress level on the (a) axial, and (b) volumetric creep strains with time.

At the end of each creep stage, the deviator stress was increased to the next desired deviator stress level. However, after the last 1-day creep branch, the specimen was further sheared to the deviator stress of 15340 kPa where it was stress-relaxed for 1 day. The stress-strain and volume change behavior of this test have been superimposed on the reference curve as demonstrated in Fig. 5.15.

The three horizontal parts on the stress-strain curve are the three creep stages of the test, while the last vertical line shows the stress relaxation at the end of the experiment. At the end of each creep stage, the stress-strain curve increases at a steeper slope to reach the original curve. According to Bjerrum (1973) and Lade (1994), the yield surface increases in size during creep. Therefore, the current stress point is located inside the yield surface. Therefore, continuation of loading generates elastic strains until the new yield surface is reached, which corresponds to a point located either on or above the original stress-strain curve depending on the occurrence of structuration effects. Lade (2007) presented the results of multiple creep tests on Antelope Valley sand. The results showed no structuration effects and further loading after creep merged with the original stress-strain curve. However, Lade et al. (2009) reported structuration effects after performing similar experiments on crushed coral sand. Herein, rather than a small scatter with respect to the reference curve at the middle part of axial strain, it is observed that creep for 1-day has produced no structuration effect when the specimen was sheared following the creep. In this case, the new yield surface is related to a point on the original stress-strain curve.

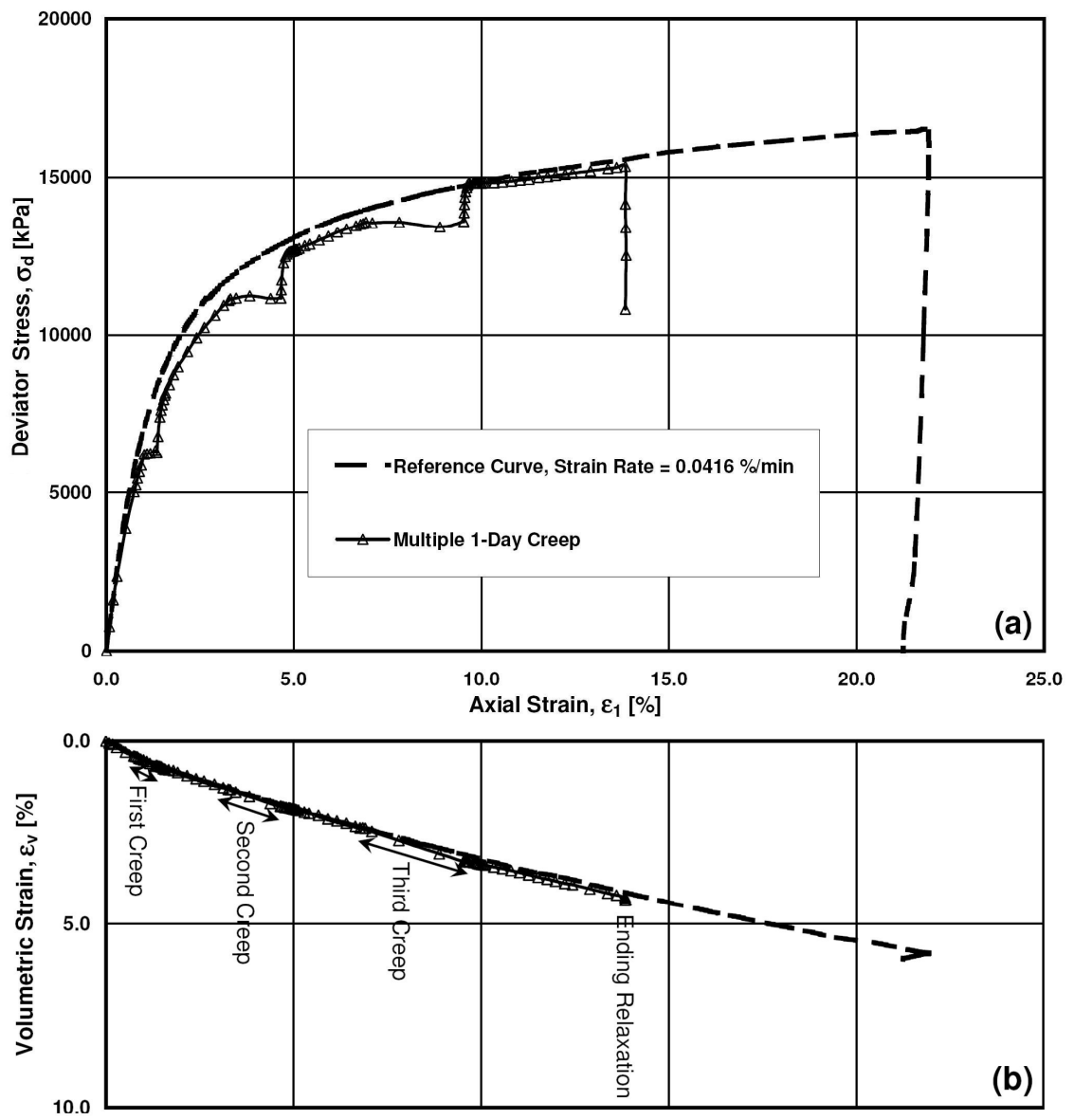


Figure 5.15. (a) Stress-strain, and (b) volume change curves for the multiple 1-day creep test on Virginia Beach sand.

Moreover, dissimilar to the previous experiments on crushed coral sand performed by Lade et al (2009), and analogous to what Lade (2007) presented for Antelope Valley sand, the volume change curves corresponding to creep stages do not deviate from the reference curve. This means that the directions of plastic strain increments are the same as inelastic creep strain increments. That is, an identical function may be utilized for evaluating the direction of inelastic creep and plastic strains for Virginia Beach sand. The axial and volumetric strains during creep have been superimposed on the results of the equivalent 1-day creep tests of C2, C5 and C6 in Fig. 5.16. These results confirm the repeatability of the experimental data.

The results of sieve analyses on specimens tested to study creep after 1 day are illustrated in Fig. 5.17. Clearly, creep tests performed at a higher stress level produced greater amounts of higher particle crushing, as expected according to the static fatigue hypothesis. This is in accordance with the observed axial and volumetric creep strains in Fig. 5.14 and Fig. 5.16.

To show the relationship between the particle crushing and creep behavior of Virginia Beach sand, Fig. 5.18 compares the Hardin's breakage factors, calculated from Fig. 5.17, against the corresponding axial and volumetric creep strains. Furthermore, Fig. 5.19 shows the relation between the energy input and Hardin's breakage factor. The results of the sieve analysis of the multiple creep test specimen is also included in Fig. 5.19. Obviously, larger Hardin's breakage factors are related to higher energy input and larger amounts of axial and volumetric creep strains, validating the particle crushing phenomenon as the root of time-dependent behavior in brittle granular materials.

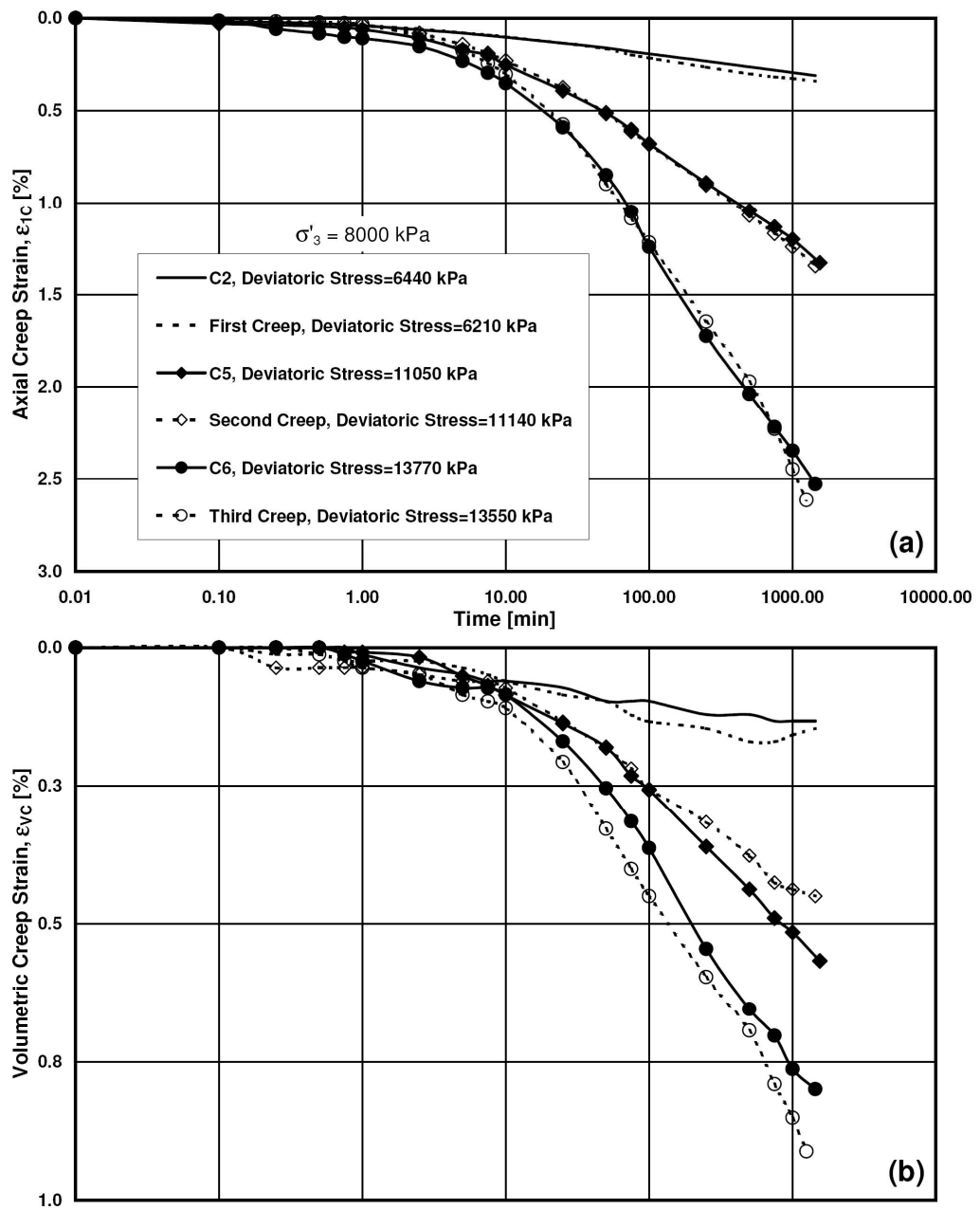


Figure 5.16. Variation of (a) axial, and (b) volumetric creep strains of the multiple 1-day creep test with time.

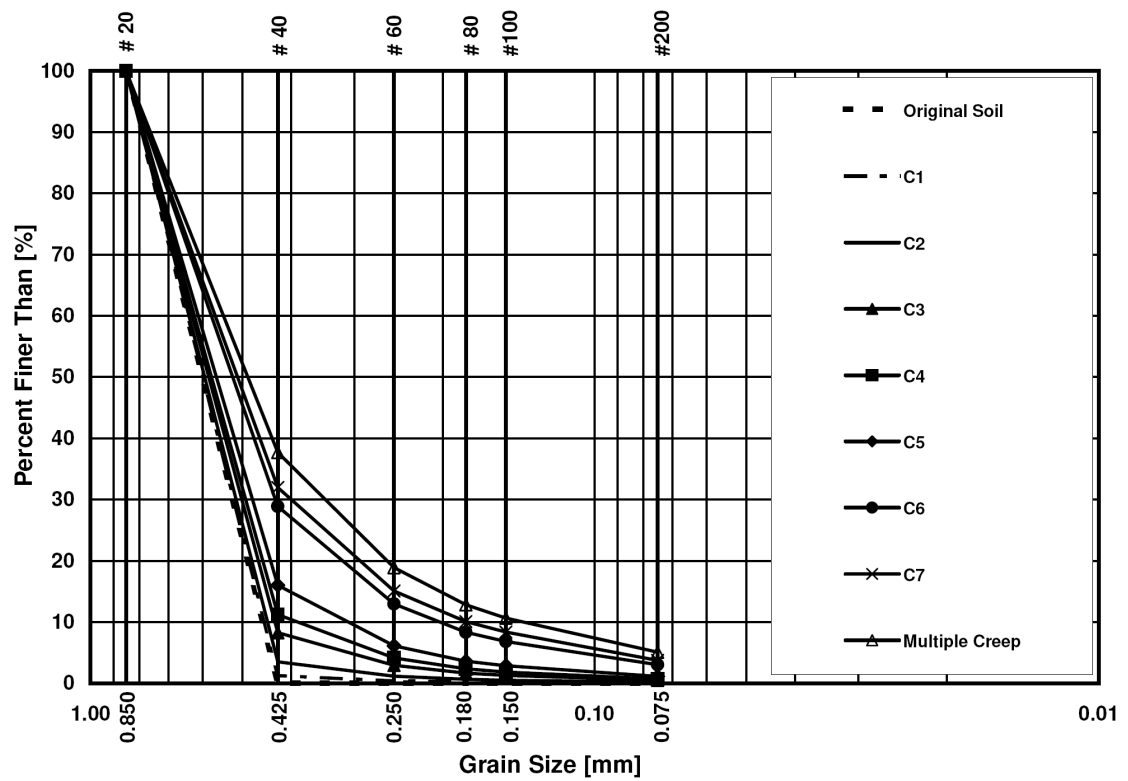


Figure 5.17. Evolution of grain size distribution curve for the 1-day creep tests.

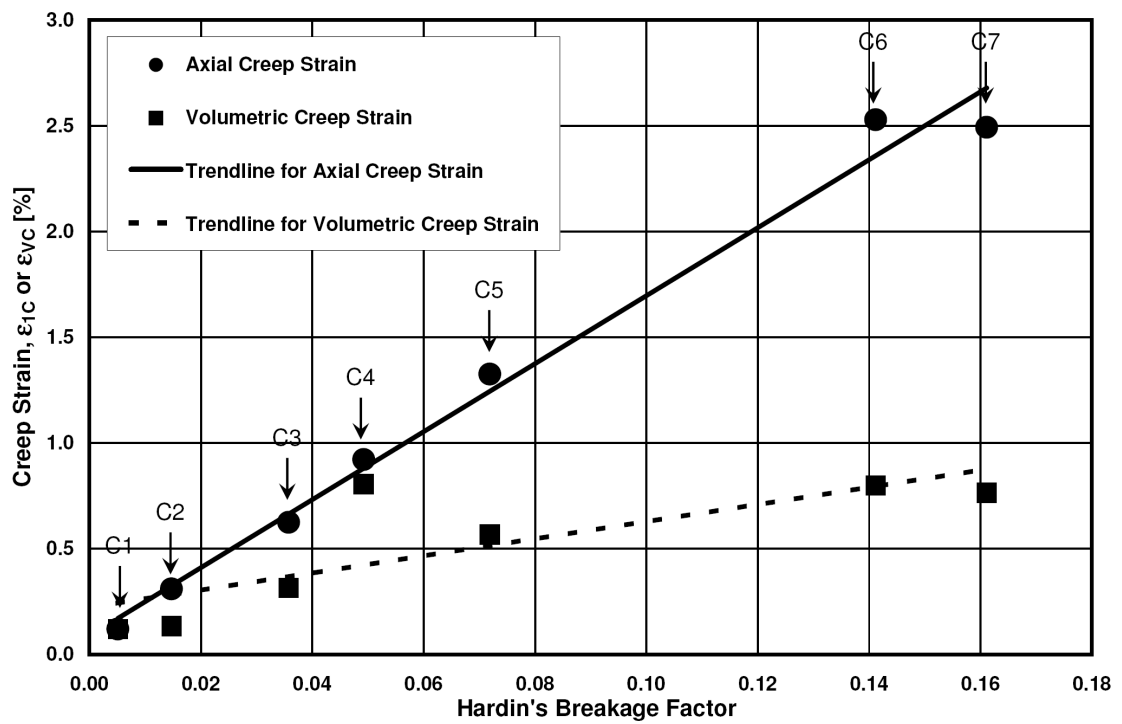


Figure 5.18. The relationship between the axial and volumetric creep strains, and Hardin's breakage factor for the 1-day creep tests.

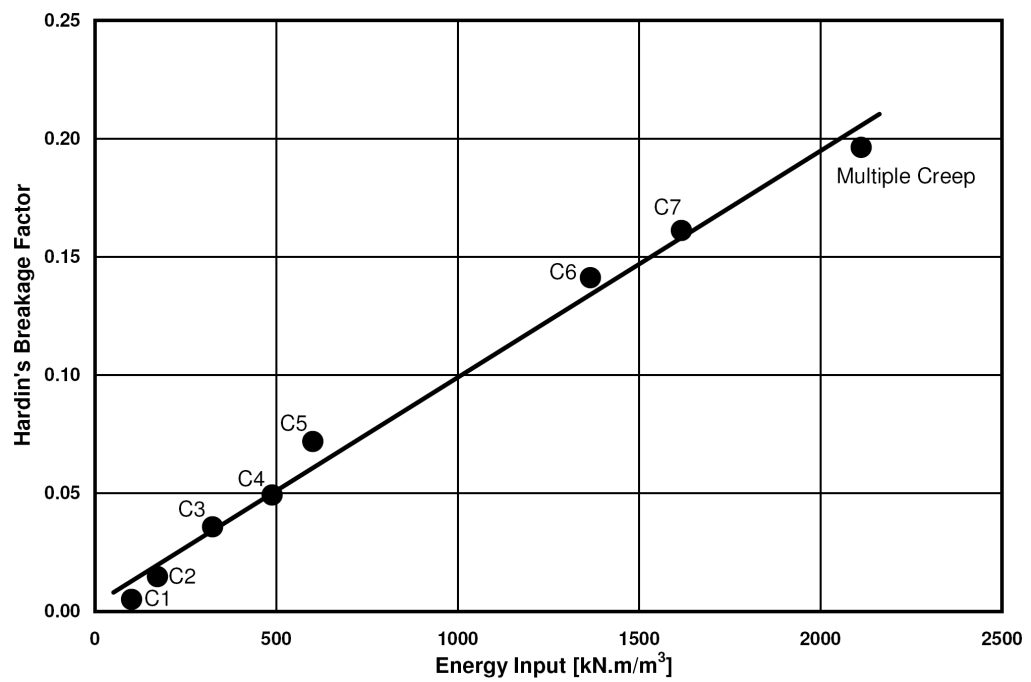


Figure 5.19. The relationship between the energy input and Hardin's breakage factor for the 1-day creep tests.

5.4. Long Term Creep

Previous studies of creep behavior of granular materials have been limited to short creep times. Therefore, a specimen was sheared at the strain rate of 0.0416 %/min under confining stress of 8000 kPa up to the deviator stress of 11290 kPa where it was allowed to creep for two months. As creep proceeds, the cross-sectional area of the specimen changes and the deviator load was therefore continuously adjusted to maintain the desired deviator stress constant. The stress-strain and volume change behavior are illustrated in Fig. 5.20.

In addition, the axial and volumetric creep strains are shown in Fig. 5.21 together with the results of the 1-day creep test C5 which was performed at approximately the same deviator stress level. Coincidence of data from the 2-month creep experiment and test C5 indicates the repeatability and consistency in the experiments. Moreover, this graph indicates that even after two months, the axial and volumetric creep strains increase at approximately the same rate as the rate that they had at the vicinity of 1 day with the logarithm of time. This may suggest that there is no end to creep deformations of Virginia Beach sand. In the view of the settlement observation of fills over many years, as observed by Crawford and Morrison (1996), it appears that creep of granular materials will continue along a straight line on strain-log(time) diagram similar to that in Fig. 5.21. As concluded for Virginia Beach sand and according to the static fatigue phenomenon as the origin of time effects, granular materials may not show any end to creep deformations.

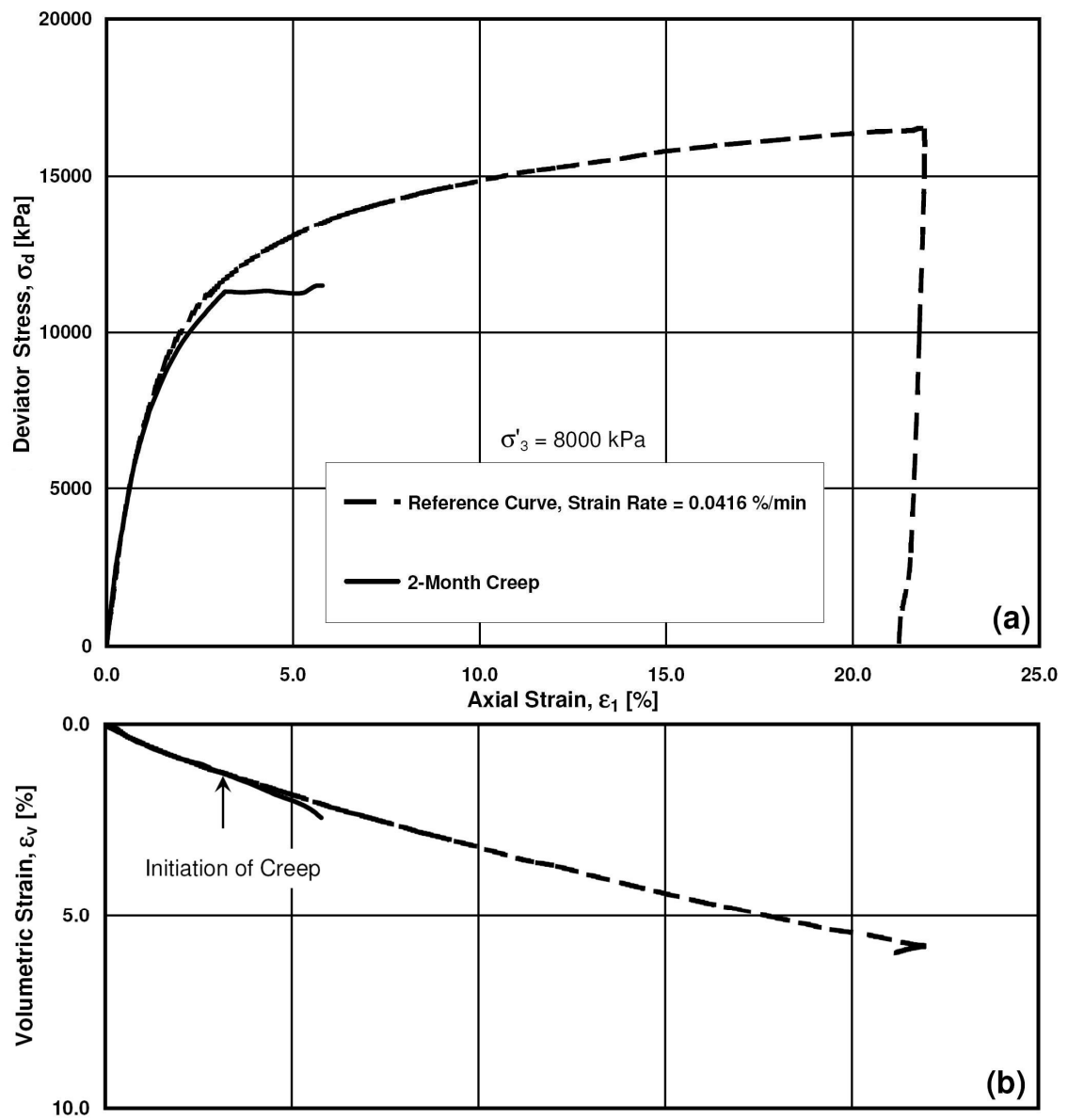


Figure 5.20. (a) Stress-strain, and (b) volume change curves for the 2-month creep test on Virginia Beach sand.

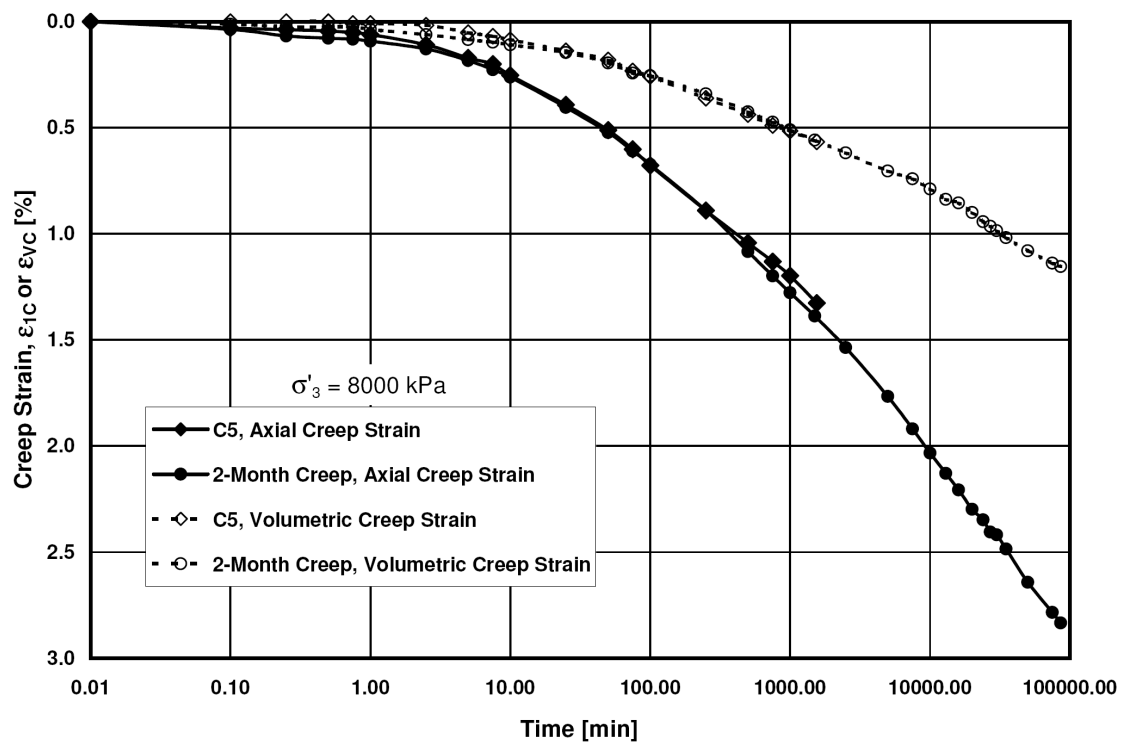


Figure 5.21. Variation of axial and volumetric creep strains of the 2-month creep test with time.

5.5. Mechanism of Creep Behavior

It is believed that the mechanism behind the observations presented above can be explained by static fatigue and the proposed mechanistic picture of time effects for granular materials proposed by Lade et al. (2009). At low confining pressures, friction and rearrangement of particles govern the behavior. Particle crushing occurs in the form of abrasion which does not affect the quantity of particle breakage indices. In view of the fact that particles do not crush into smaller parts at low pressures, either compression or dilation may occur with as observed and presented above. This means that specimens undergoing dilation before initiation of time-dependent phenomena would exhibit dilation, whereas specimens experiencing contraction prior to time effects would show contraction. Generally, since very little particle breakage takes place at low confining pressures in sands with strong particles, time effects achieved are insignificant.

At high pressures, grains are tightly put together and the energy input is spent on their breakage instead of sliding and rearrangement. Therefore, force chains form due to rearrangement, reorientation and specific breakage of particles, and are based on the change in the boundary condition of specimens. This results in contractive behavior at high pressures. Obviously, when a grain is crushed, smaller parts will be rearranged and reoriented and may fit into available voids. At each increment of time during deformation control loading, some displacement is applied to a specimen. Therefore, force chains are continuously changing to form a stable structure that resist the applied load.

Since particle crushing is a time-dependent phenomenon, loading rate has an important role on the establishment of a stable structure. The higher the strain rate, the less time will be available for reestablishment of the structure. Once creep is initiated (at the time of switching from strain control to load control), specimens sheared at a high strain rate prior to initiation of creep exhibit a high creep deformation rate, whereas specimens loaded under a low strain rate show a delay in initiation of the creep deformation meaning the rate of deformation is close to zero.

During creep, particles may keep their position until breakage of a number of particles located in the force chain due to static fatigue. The position of the broken parts will be changed. On the grounds that the stress level on the boundaries is constant, rearrangement and reorientation of the broken parts will culminate in formation of a new force chain and creep deformation is observed. As particles fracture and fit into available voids, the coordination number increases and the critical forces passing through the particles decreases with time. Therefore, the rates of particle breakage and creep deformations decrease with time. Once the impact of initial shearing strain rate disappears after a short period of time, specimens loaded at high and low strain rates prior to creep behave similarly and the same creep deformation rate is obtained.

6. Stress Relaxation Experiments

Lacerda and Houston (1973) and Matsushita et al. (1999) have performed some stress relaxation experiments on Monterey sand, and Hostun and Toyoura sands, respectively. Moreover, Ladanyi and Benyamina (1995) have carried out several relaxation tests on frozen sand. However, there is not a large amount of research in the literature on the relaxation behavior of granular materials. Therefore, the relaxation behavior of Virginia Beach sand was studied by performing drained and undrained triaxial relaxation tests as follows:

6.1. Effect of Initial Shearing Rate on Subsequent Stress Relaxation

The influence of shearing strain rate has not been considered in the study of the subsequent relaxation behavior. Herein, three loading strain rates of 0.00260, 0.0416 and 0.666 %/min have been utilized to perform six drained relaxation experiments on specimens of dense Virginia Beach sand under two confining pressures of 250 and 8000 kPa. Similar to creep experiments, explained in Chapter 5, the criterion of equal energy input calculated from Equation (3-1) was used for stress points at which relaxation experiments began. This helped to produce an accurate comparison between the creep and relaxation experimental results. The deviator stress at these points is in the range of 70-75% of the maximum deviator strength presented in Chapter 4. In fact, specimens were loaded under deformation control at these three shearing rates and loading was then stopped at the points with the same energy input and specimens were allowed to relax for 1 day.

The results of stress relaxation experiments at a confining pressure of 250 kPa are plotted in Fig. 6.1. Approximately the same stress-strain behavior is achieved for all three shearing rates. Stress relaxation started at the stress-strain points of $[(\sigma_1 - \sigma_3), \epsilon_1] = [790 \text{ kPa}, 0.91\%]$, $[780 \text{ kPa}, 0.96\%]$, and $[780 \text{ kPa}, 0.98\%]$ for the lowest to the highest loading rate. These points correspond to an energy input of 5 kN.m/m^3 . The almost vertical lines indicate the stress reduction during relaxation. Slightly higher stress relaxations have been obtained for specimens sheared faster. The specimen sheared at strain rate of 0.0026 \%/min exhibits a stress relaxation of 84 kPa, while the fastest experiment shows a stress relaxation of 127 kPa.

Fig. 6.1(b) illustrates that the specimens undergo dilation during stress relaxation. The rationale behind this behavior is analogous to that described for creep experiments at low confining pressures in Chapter 5. The mechanism that can explain this behavior is discussed later in detail. Fig. 6.2 displays the variation of the amount of stress relaxation with the logarithm of time for different loading strain rates.

The results of sieve analyses are described in Fig. 6.3. As expected, particle crushing is not significant under low confining pressure. Therefore, identical grain size distribution curves have been obtained. Despite the fact that various stress relaxation values have been achieved, the shearing strain rate does not have an effect on the quantity of particle breakage at low pressures.

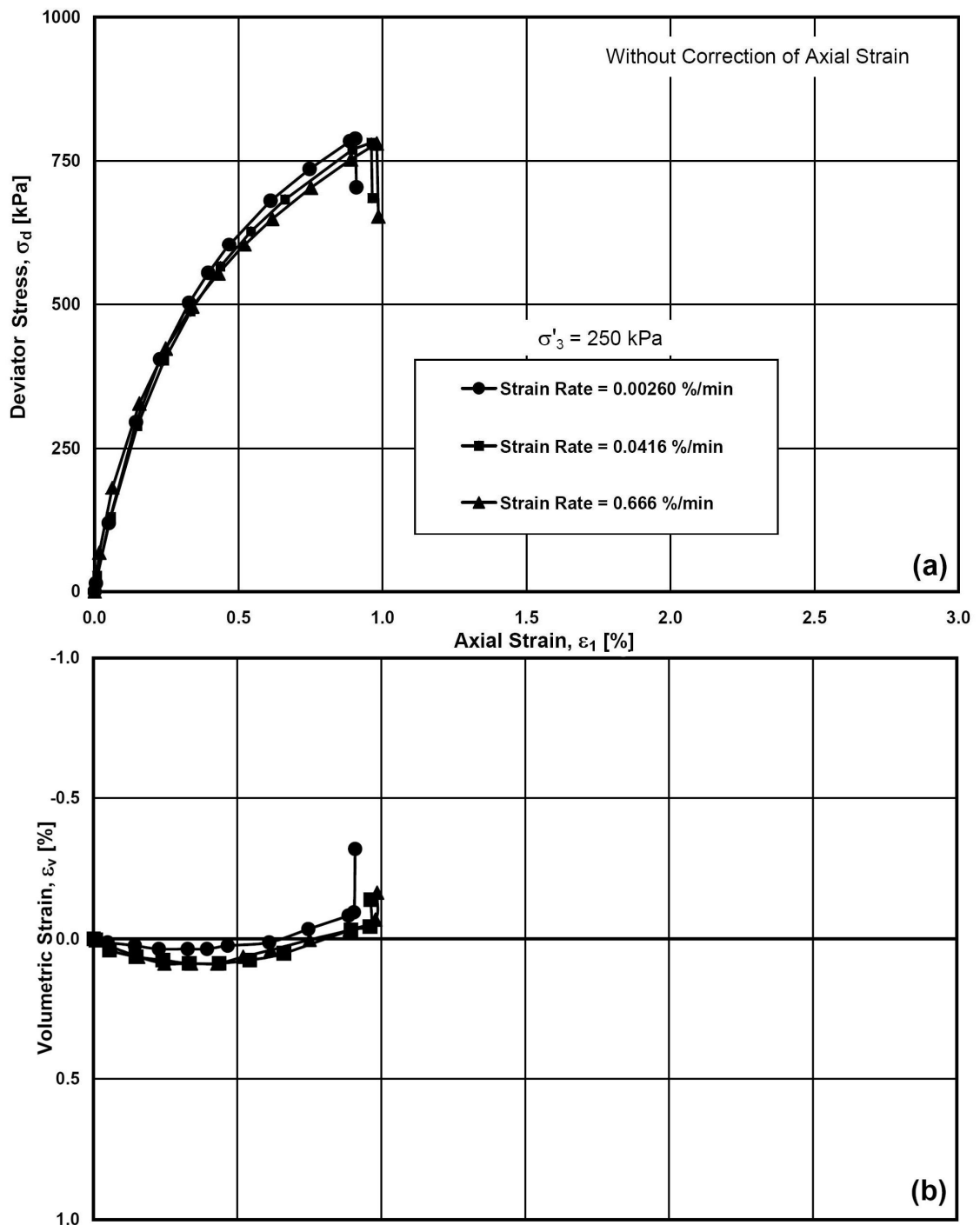


Figure 6.1. Effect of shearing strain rate on subsequent stress relaxation under

$\sigma'_3=250$ kPa: (a) stress-strain curves; (b) volume change curves.

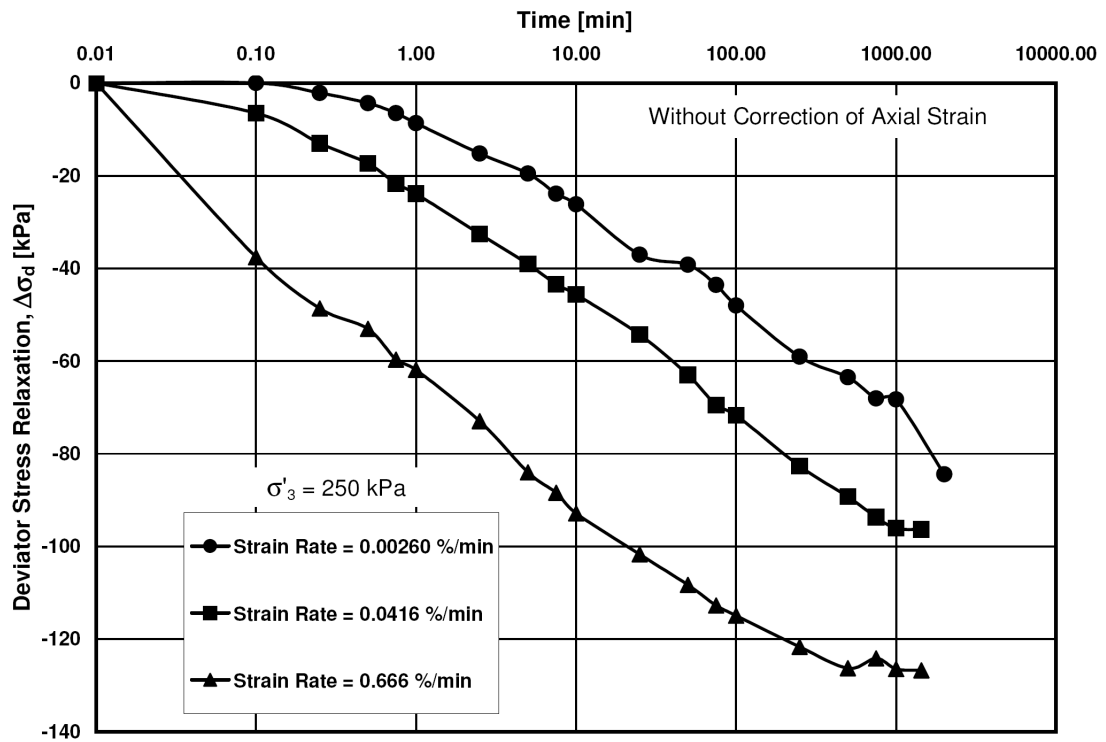


Figure 6.2. Effect of initial shearing strain rate on variation of stress relaxation.

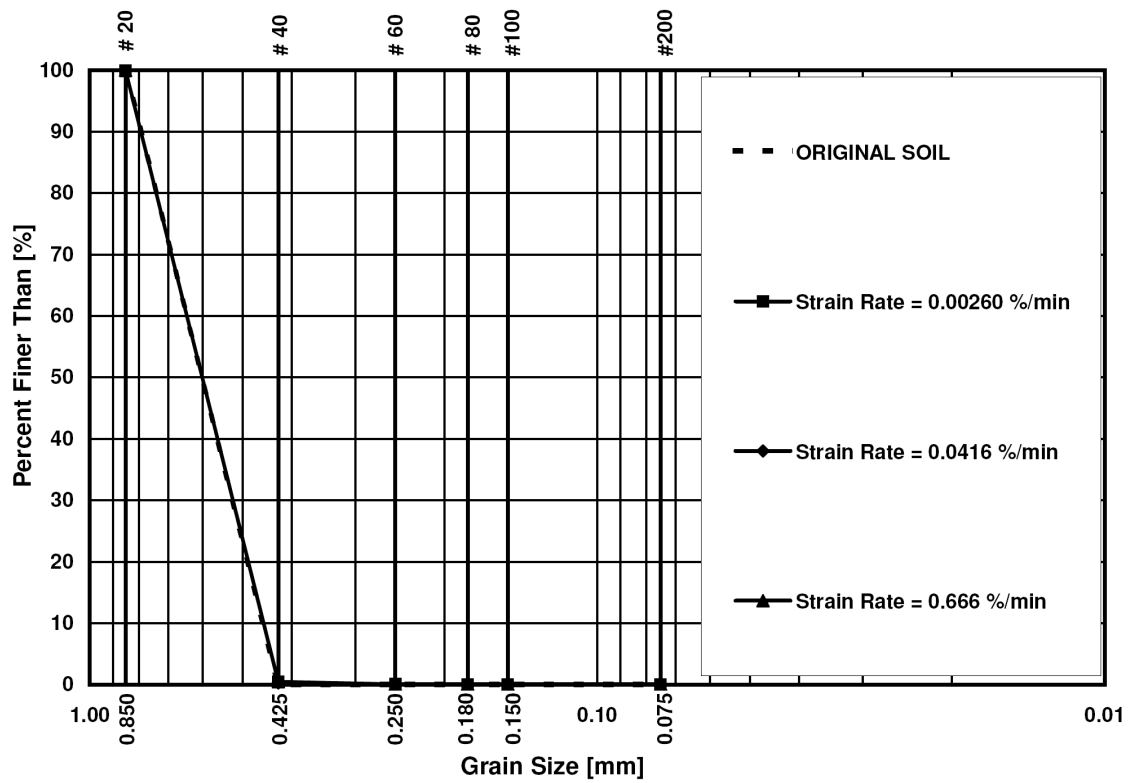


Figure 6.3. Effect of initial shearing strain rate on crushing of particles.

The stress-strain and volumetric behavior of the three 1-day relaxation experiments under confining pressure of 8000 kPa are shown in Fig. 6.4. Since these specimens were sheared at different rates, dissimilar time periods were given to particles to fracture due to static fatigue. Subsequently, different soil structures were expected prior to stress relaxation. Corresponding stress-strain and volume change reference curves from Fig. 4.10 have been superimposed in this graph to illustrate the repeatability of the experiments. An excellent agreement is observed between the experimental results and the reference curves. For the lowest to the highest shearing rate, the corresponding stress-strain points where relaxation initiated were $[(\sigma_1 - \sigma_3), \epsilon_1] = [10600 \text{ kPa}, 2.86\%]$, $[11240 \text{ kPa}, 2.81\%]$, and $[11880 \text{ kPa}, 2.75\%]$, respectively. The total energy input up to these points were equal to 390 kN.m/m^3 .

Fig. 6.4(b) indicates that very small volumetric strains developed during stress relaxation and the responses have not deviated from the reference curves. According to Lade (2007), Antelope Valley sand exhibited a similar type of response during stress relaxation experiments, whereas Lade et al. (2010) observed a considerable amount of contraction for similar experiments on crushed coral sand.

The variation of stress relaxation with respect to the logarithm of time is illustrated in Fig. 6.5, both in terms of the deviator stress relaxation and actual deviator stress. Stress relaxations of 1529, 2339 and 2962 kPa were achieved in connection with strain rates of 0.00260, 0.0416 and 0.666 %/min. Based on Fig. 6.5(b), although stress relaxation is initiated at different deviator stress levels, the ending points more or less

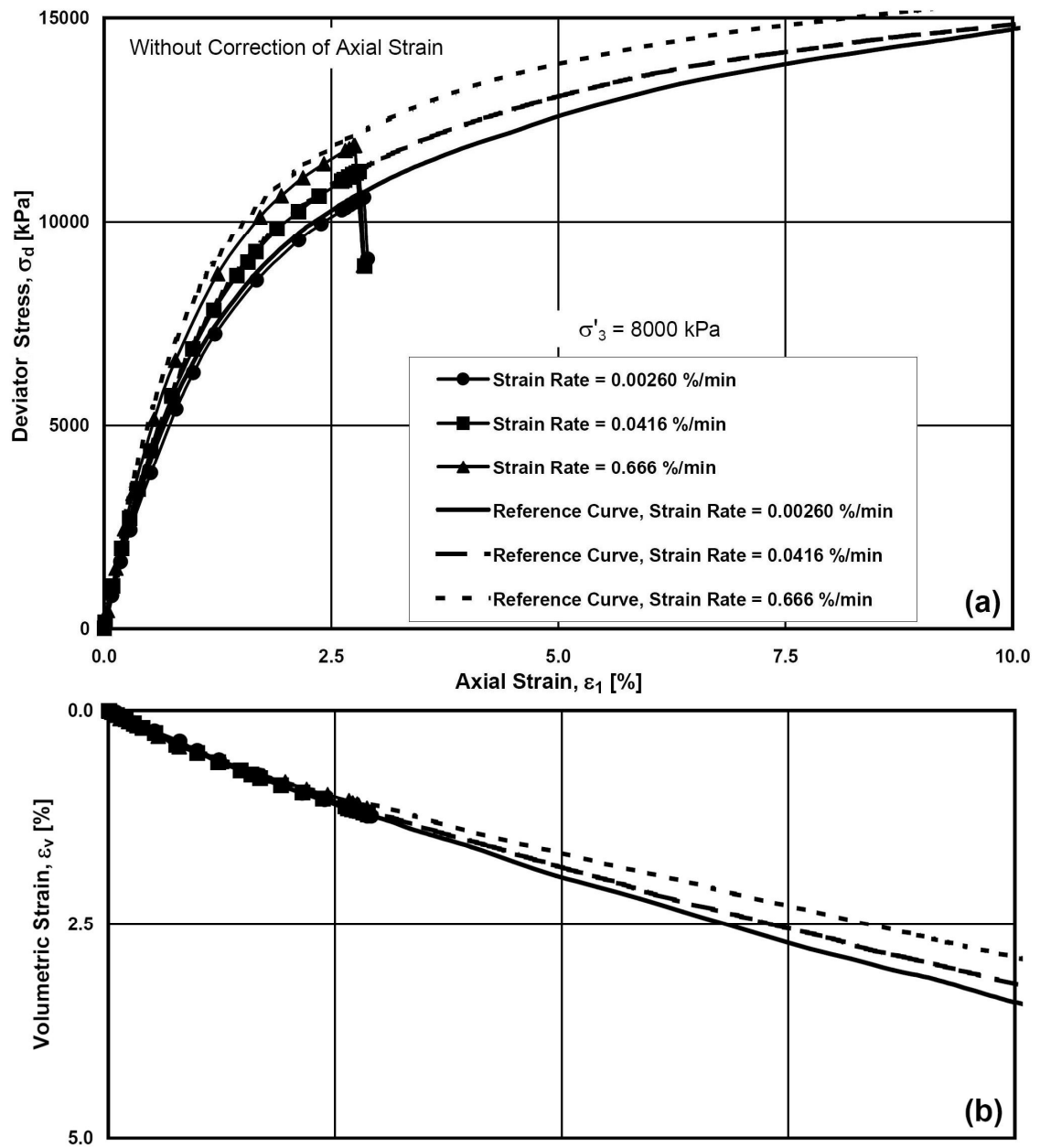


Figure 6.4. Effect of shearing strain rate on subsequent stress relaxation under

$\sigma'_3=8000$ kPa: (a) Stress-strain curves; (b) volume change curves.

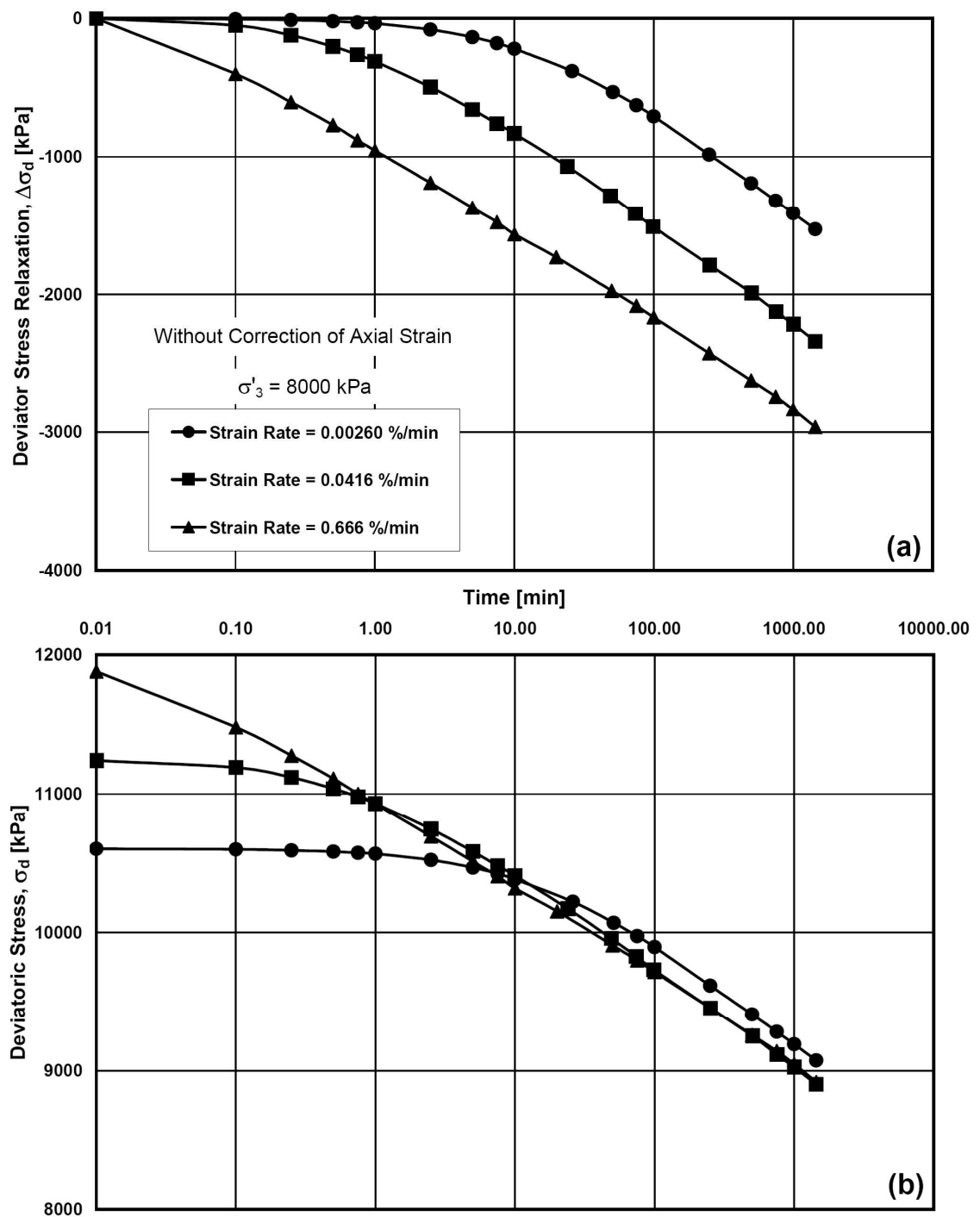


Figure 6.5. Effect of initial shearing strain rate on variation stress relaxation: (a) deviator stress relaxation, and (b) actual deviator stresses.

have the same magnitudes. This is because specimens sheared at higher strain rates start their stress relaxation at higher deviator stress levels and have experienced larger amounts of stress relaxation. As discussed below in detail, this may suggest that specimens have reached analogous structures to transfer the load since a similar value of energy input has been applied to all three tests before stress relaxation initiates.

Fig. 6.5 shows that the specimen sheared at the lowest strain rate, has shown almost no stress relaxation for the first 2 minutes after stopping deformation, while an immediate reduction in the deviator stress was observed for the specimen sheared at the highest strain rate. Interestingly, after about 10-25 minutes from the initiation of stress relaxation, further stress reduction with time continued at a same rate for all three specimens. The exact same pattern was observed for creep deformations after initiation of creep, as illustrated in Fig. 5.5. Murayama and Shibata (1961) and Vialov and Skibitsky (1961) reported similar trends for stress relaxation experiments on clay. They mentioned that there is a delay in stress reduction related to the strain rate prior to stress relaxation; the lower the strain rate is, the greater the delay will be. Lacerda and Houston (1973) tested several clays and sands. They mentioned that stress relaxation for all soils varies linearly with the logarithm of time while the strain rate prior to initiation the stress relaxation and confining stress have no effect on the slope. Furthermore, Mitchell (1993) explained that clays and sands behave in the same way during stress relaxation.

It is anticipated that the three stress relaxation experiments experience the same amount of crushing as the same amount of energy input has been applied, and the same relaxation time has been given. Fig. 6.6 confirms this expectation and it shows that approximately the same grain size distribution curves have been achieved after 1 day relaxation for the three initial strain rates.

As explained in Chapter 3, expansion of the load cell imposes some axial deformations on the specimen during stress relaxation. This can be roughly seen in Fig. 6.4(a) where the relaxation lines are not completely vertical. The variation of the axial strains is shown in Fig. 6.7. The trend is analogous to the stress relaxation of the specimens shown in Fig. 6.5(a). Based on the definition, no deformation should occur during stress relaxation because it may affect the amount of stress relaxation. Since no correction was made in the aforementioned experiments, it was decided to perform three relaxation experiments at the similar strain rates under confining pressure of 8000 kPa with correction of the axial deformation. The dial gage reading, which showed the axial deformation of the specimen, was maintained constant very accurately by small adjustment in the displacement of deformation control loading machine. This helped to explore the sensitivity of the measured stress relaxation to the small amounts of axial deformation imposed by the expansion of the load cell during stress relaxation.

The results of these three experiments are compared in Fig. 6.8 with the results of the stress relaxation experiments without correction of the axial strain. To better exhibit the comparison, the diagram has been magnified to show the stress relaxation stage of the

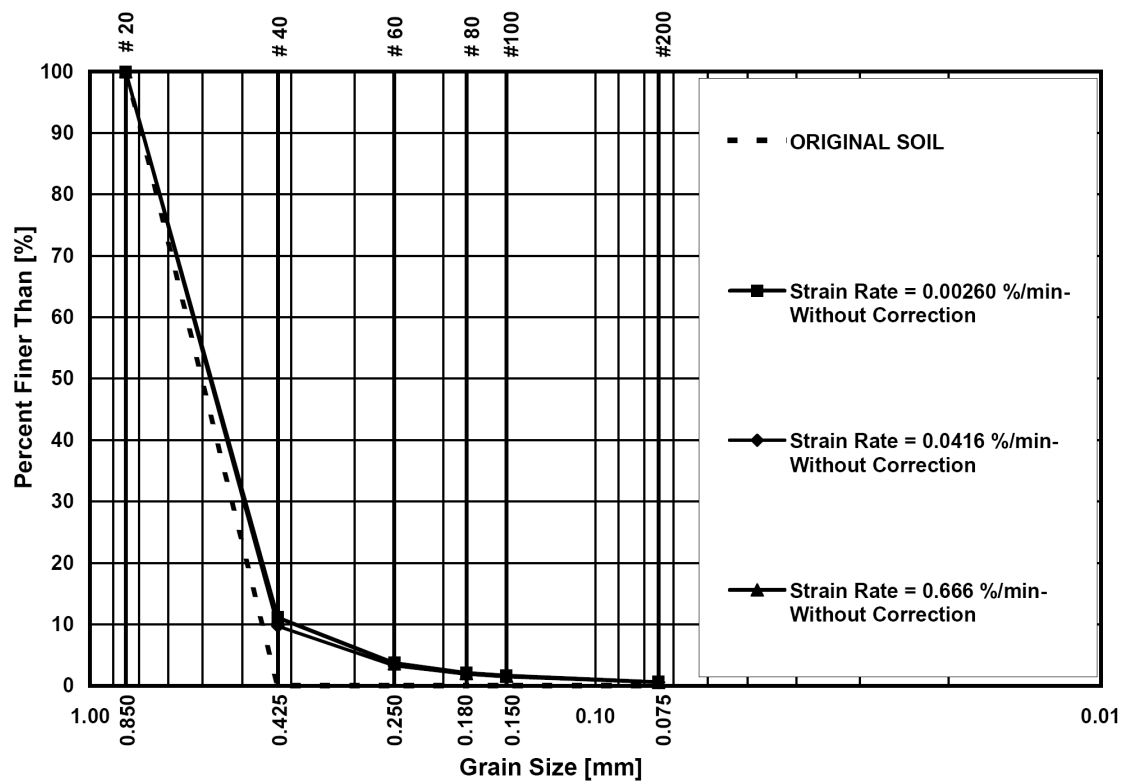


Figure 6.6. Effect of initial shearing strain rate on crushing of particles.

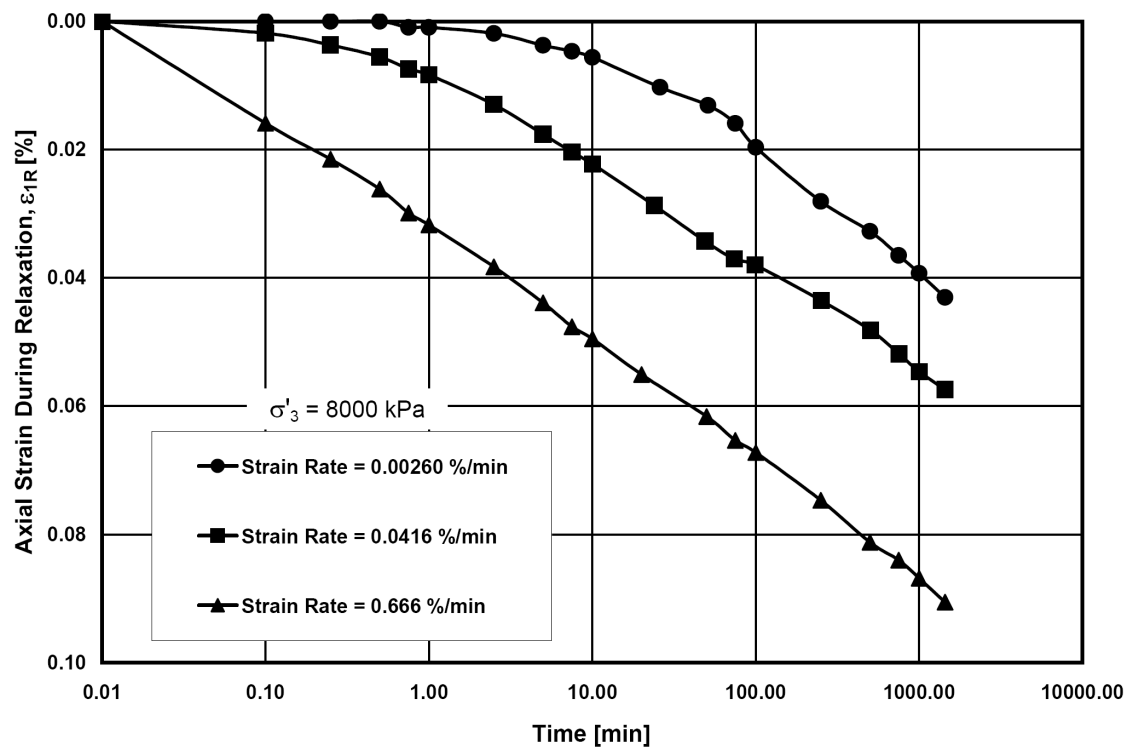


Figure 6.7. Development of axial strain during stress relaxation due to expansion of load cell.

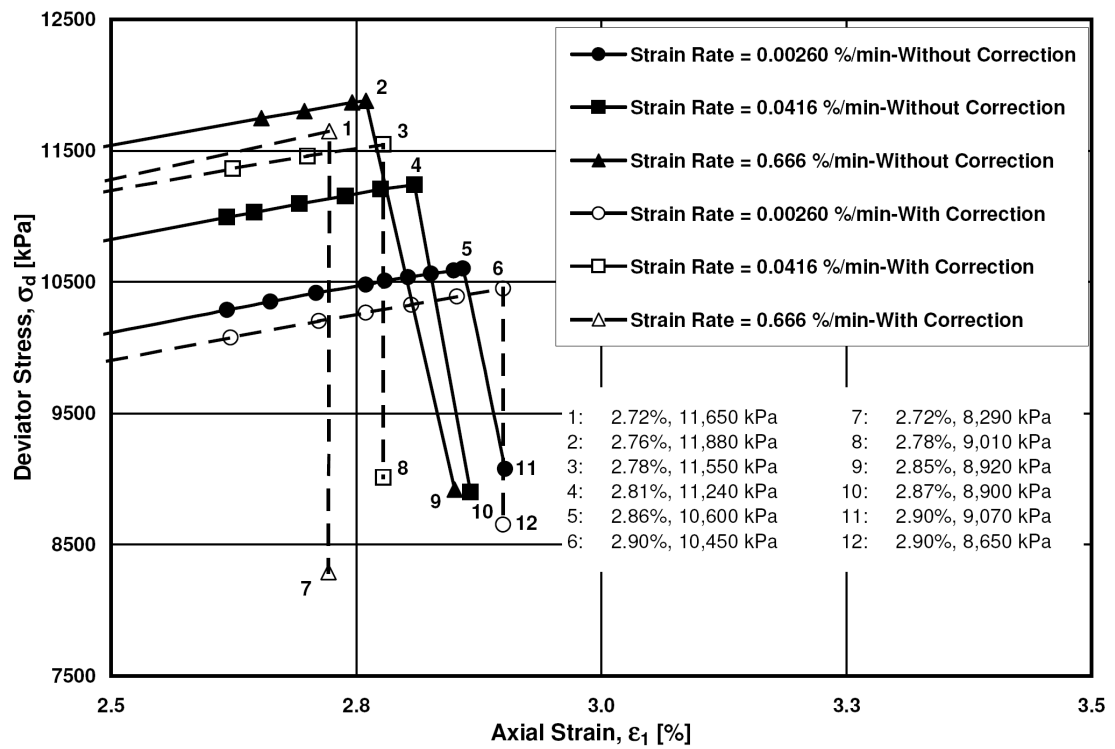


Figure 6.8. Comparison of drained stress relaxation experiments with and without correction of axial strains.

experiments and the coordinates of the initiation and ending points have been tabulated. The slightly inclined lines indicate stress relaxation without correction, while the vertical lines include experimental correction. Thus, the vertical lines correspond to stress relaxation at zero axial strain.

The trend of exhibiting greater amounts of stress relaxation for higher strain rates is observed for tests with correction of axial strain. To throw further light on the details of the difference between the two types of tests, Fig. 6.9 shows a comparison of the stress relaxation behavior with the logarithm of time. This graph reveals that experiments with correction of axial strains demonstrate more stress relaxation. The differences in amount of 1-day stress relaxation for the lowest to the highest strain rates are $(1800-1530)=270$ kPa, $(2530-2340)=190$ kPa, and $(3360-2960)=400$ kPa. These errors indicate that ignoring axial deformation correction results in underestimating stress relaxation by 7.5% to 15%. It is noted that sudden jumps on the results of stress relaxation tests with correction are due to lack of adjustment for experiments that required performance overnight.

The slopes of the inclined relaxation lines indicate the stiffness of the load cell used in this experimental program. This stiffness was found to be 3.6×10^6 kPa. It is expected that a stiffer load cell would reduce error in determination of stress relaxation. As a result, this may avoid the continuous manual adjustment of the displacement of the deformation control loading machine.

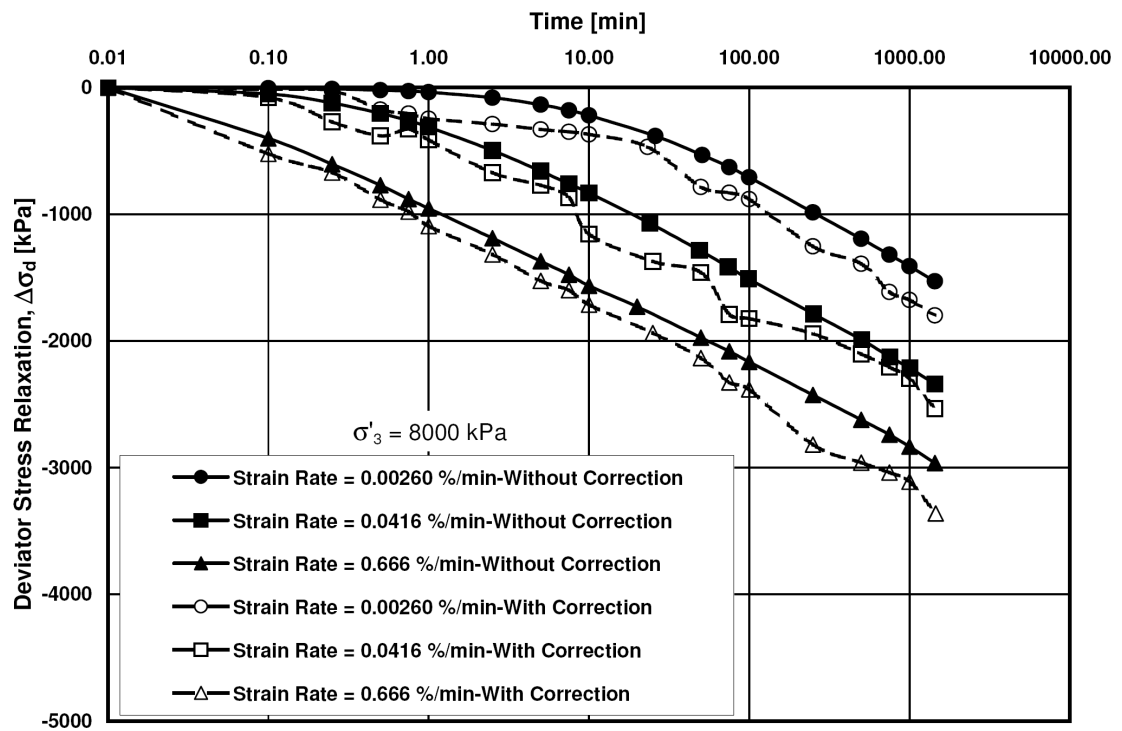


Figure 6.9. Comparison of stress relaxation magnitudes in experiments with and without correction of axial strains.

Theoretically, during stress relaxation all deformations must remain zero. It was observed that specimens may undergo volume change together with the imposed axial deformation. In the relaxation experiments performed so far no attempt was made to preserve the volumetric strain constant. The volume change behaviors versus the logarithm of time for the experiments under confining pressure of 8000 kPa with and without axial strain correction are compared in Fig. 6.10. While the developed volumetric strains for 1 day are very small, this graph indicates that the correction of the axial strain does not significantly impact the volume change behavior.

To study the importance of influence of the small volume change on the observed stress relaxation, three other specimens were built to perform undrained stress relaxation with correction of axial strain such that no deformation is imposed on the specimens. The only difference between these tests and the experiments with correction of axial strain was closing the drainage valve right at the initiation of the 1-day relaxation. This presented a condition in which the specimens experienced totally zero deformation during stress relaxation. Instead, the pore pressure that may be generated under the undrained condition was monitored and recorded for analysis. The stress-strain and volumetric behavior of the undrained stress relaxation tests are shown in Fig. 6.11 together with the reference curves from Fig. 4.10. In spite of the fact that the stress-strain curves follow the same sequence as the reference curves, approximately the same stress-strain curves were obtained with no discernable effect of initial strain rate before initiation of the stress relaxation stages. It is noted that the undrained relaxation

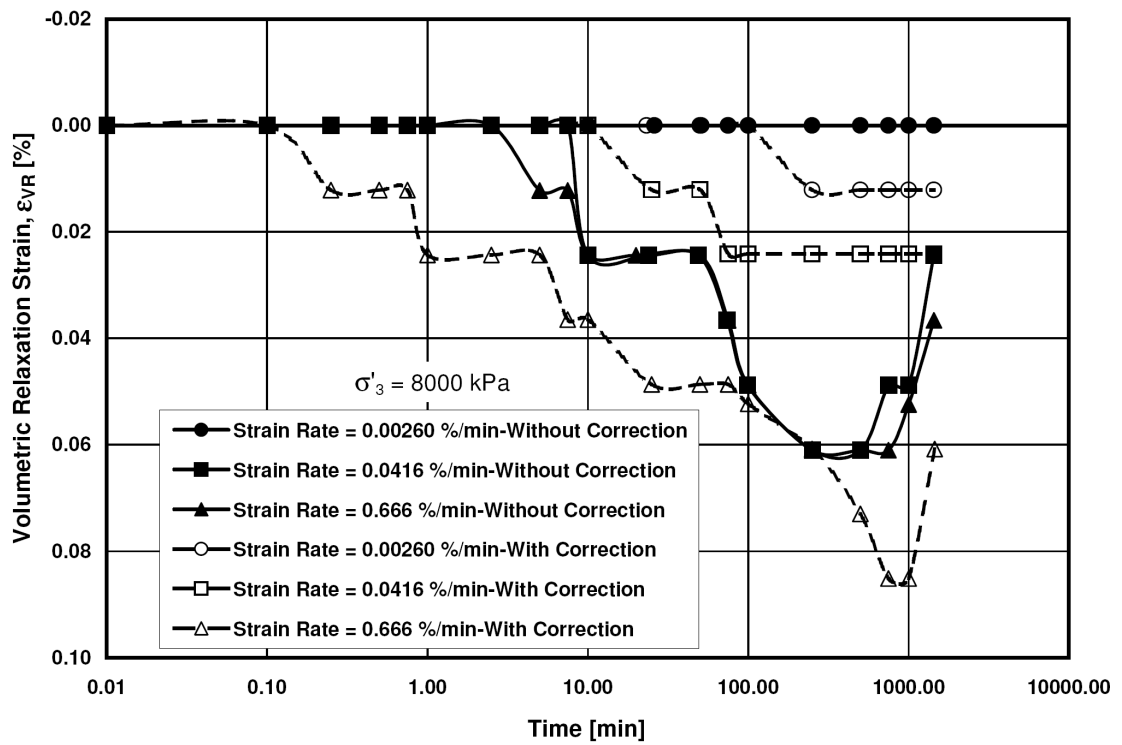


Figure 6.10. Comparison of volumetric strains during stress relaxation for experiments with and without correction of axial strains.

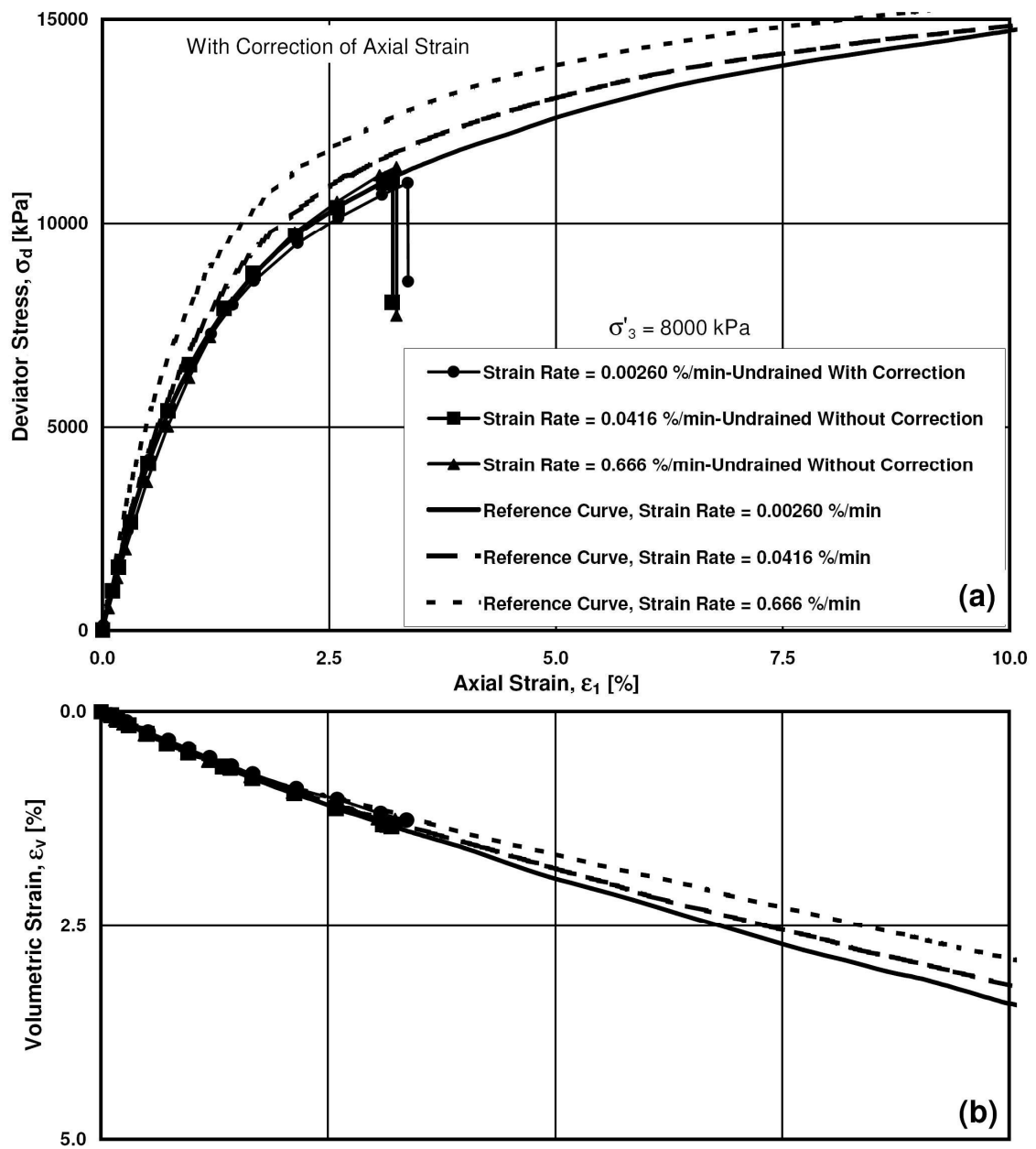


Figure 6.11. Effect of shearing strain rate on subsequent undrained stress relaxation under $\sigma'_3 = 8000$ kPa: (a) stress-strain curves; (b) volume change curves.

experiments were performed using equipment including the triaxial cell, loading cell, loading frame and volume change device, and they were performed approximately one year after the reference relaxation experiments were performed. In addition, a new sample was taken from the stock of Virginia Beach sand and sieved to make the specimens. However, Fig. 6.11(b) shows that there is good agreement between the volume change of reference curves and the results of experiments before initiation of undrained stress relaxation. It seems difficult to put a finger on a specific issue that may have caused these discrepancies while supposedly testing procedure other experimental details were the same.

For the lowest to the highest strain rate, stress relaxation began at stress-strain points of $[(\sigma_1 - \sigma_3), \epsilon_1] = [10990 \text{ kPa}, 3.37\%]$, $[11100 \text{ kPa}, 3.20\%]$, and $[11380 \text{ kPa}, 3.24\%]$, respectively. The corresponding energy input at these points is 430 kN.m/m^3 , about 9% higher than the energy input prior to initiation of the equivalent drained relaxation tests. Variation of the stress reduction with respect to the stress relaxation elapsed time is compared with the drained stress relaxation results in Fig. 6.12.

A similar trend is obtained for the drained and the undrained stress relaxation experiments. However, the final stress relaxation is slightly lower than the corresponding drained tests. Systematically, the lower the strain rate, the higher the final difference will be after 1 day stress relaxation. Thus, 19%, 15% and 9% more stress reduction is observed in the experiments with the slowest to the fastest initial shearing strain rate. The undrained stress relaxation tests were performed at a higher energy input as mentioned

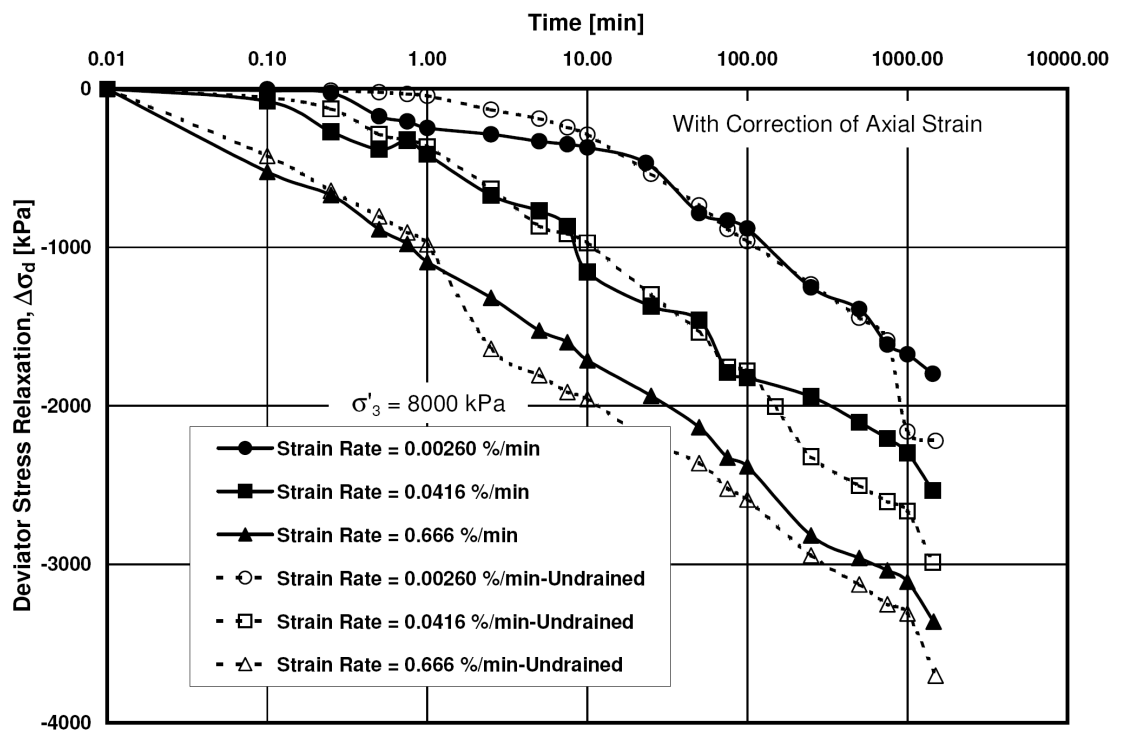


Figure 6.12. Comparison of stress relaxation magnitudes in drained and undrained experiments both with correction of axial strain.

above. It is reasonable to normalize the results in Fig. 6.12 with respect to the corresponding energy input at the beginning of stress relaxation for each individual experiment because higher energy input may result in greater stress relaxation. Fig. 6.13 exhibits the normalized curves for all three types of stress relaxation experiments performed at the confining pressure of 8000 kPa. This graph indicates that similar stress relaxation for drained and undrained conditions is obtained as long as the axial strain remains constant during stress relaxation.

The variation of pore pressure was recorded during the undrained stress relaxation tests instead of monitoring the volume change during the drained experiments. The pore pressures and the volume changes have been compared in Fig. 6.14. It was explained before that the experiments performed at the higher strain rate exhibited larger volume changes during stress relaxation. The pore pressure generation also follows a systematic pattern. Positive pore pressures which are initially generated for some time are followed by significant reductions.

For the slowest test, no pore pressure was generated in the first minute. However, positive pore pressures up to 20 kPa were produced within 10 minutes. Afterwards, a reverse tendency was observed and the pore pressures started to decrease until it reached a value of -180 kPa at 1440 minutes. For the middle shearing strain rate, it only took a few seconds for the pore pressure to be produced. The pore pressure continued to increase and it reached 370 kPa at 100 minutes after the initiation of stress relaxation. A reversal was then seen and the pore pressure decreased to -40 kPa at the end of 1 day

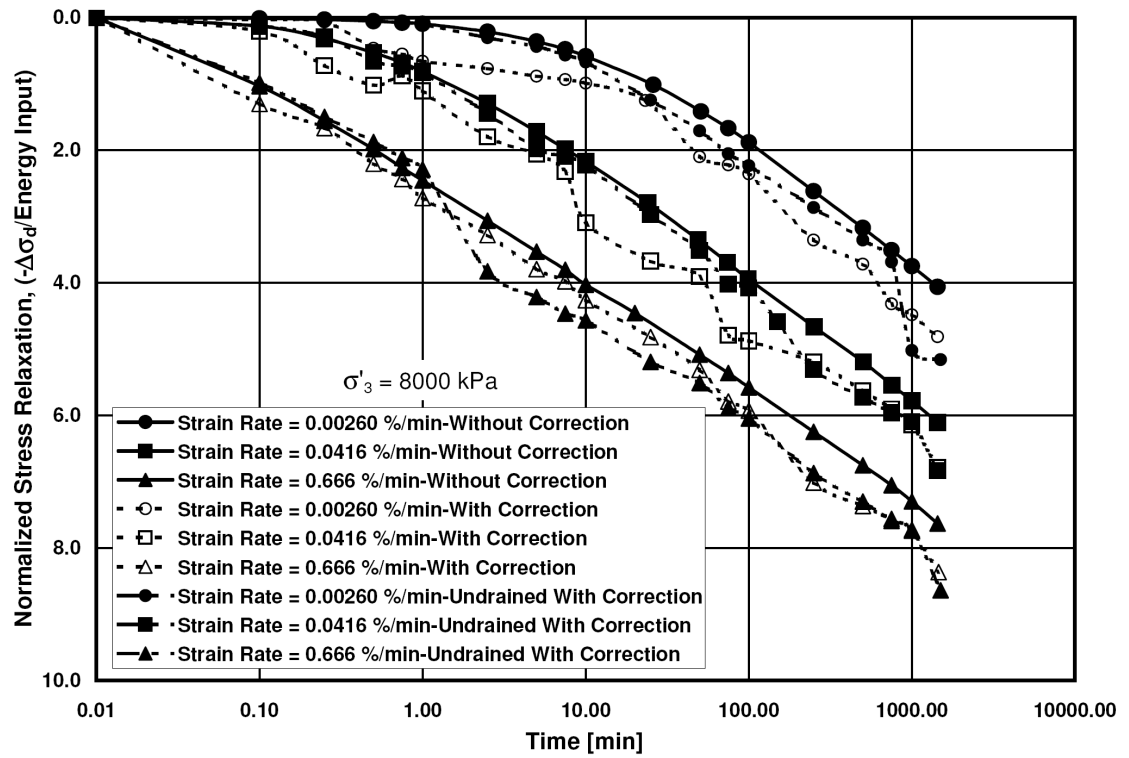


Figure 6.13. Comparison of normalized stress relaxation magnitudes in drained and undrained experiments, with and without correction of axial strains.

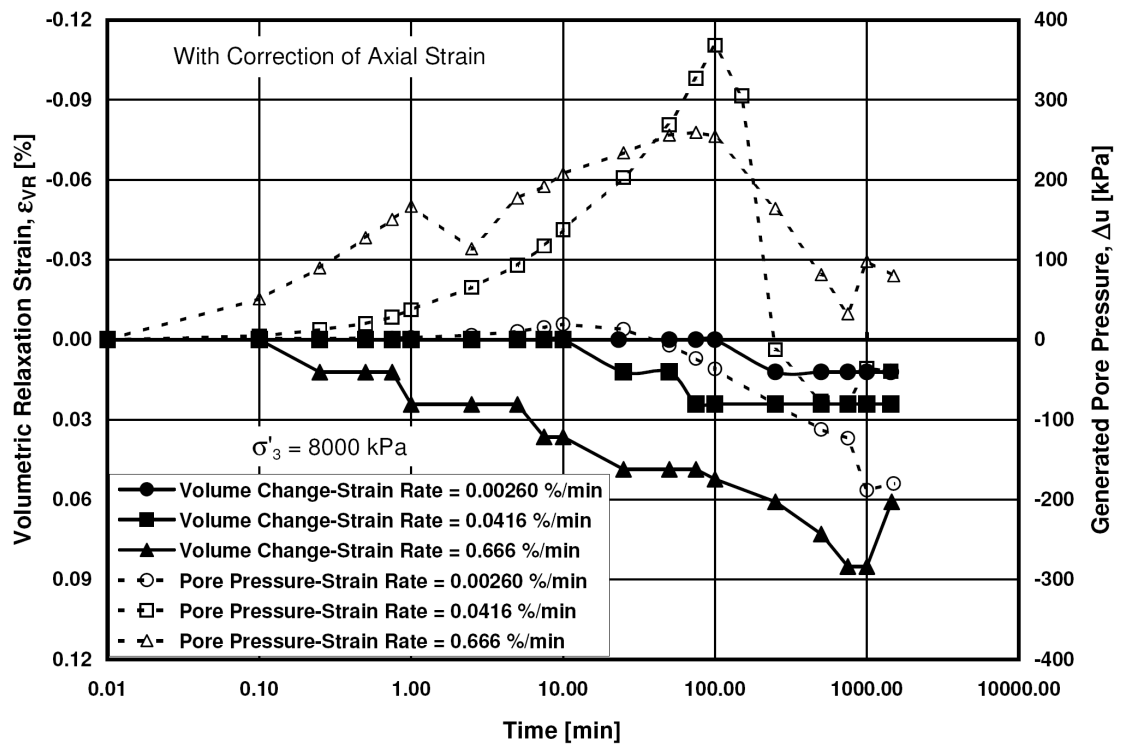


Figure 6.14. Comparison of volumetric strain response during drained stress relaxation with pore pressure generation during equivalent undrained tests.

stress relaxation. In the fastest experiment, the pore pressure was generated as soon as stress relaxation initiated. It increased for 75 minutes, up to the value of 260 kPa where it started to decrease and it finally reached to 80 kPa at the end of stress relaxation. Although a systematic pattern has been obtained for pore pressure generation, this phenomenon is not well understood because the corresponding drained experiments showed contraction during stress relaxation. This tendency for contraction was expected to produce positive pore pressures in the equivalent undrained tests. However, these pore pressures are small compared with the effective confining pressure of 8000 kPa. Similarly, after performing a series of drained and undrained relaxation experiments on clays and sands, Lacerda and Houston (1973) concluded that the variation of pore pressure during stress relaxation is negligible. They used the hypothesis of the magnitude of pore pressure being exclusively dependent on the amount of strain, proposed by Lo (1969), to support their observations. Murayama and Shibata (1961) also reported similar observations for clays.

Moreover, grain size distribution curves at the end of drained and undrained stress relaxation tests are compared in Fig. 6.15. As observed, all curves coincide. Since approximately the same amount of energy input has been applied to the specimens, the same grain size distribution curve is expected. This is better seen in Fig. 6.16 where the related Hardin's breakage factors are plotted against the corresponding energy inputs. The energy input during stress relaxation is practically zero, and so is the crushing. This

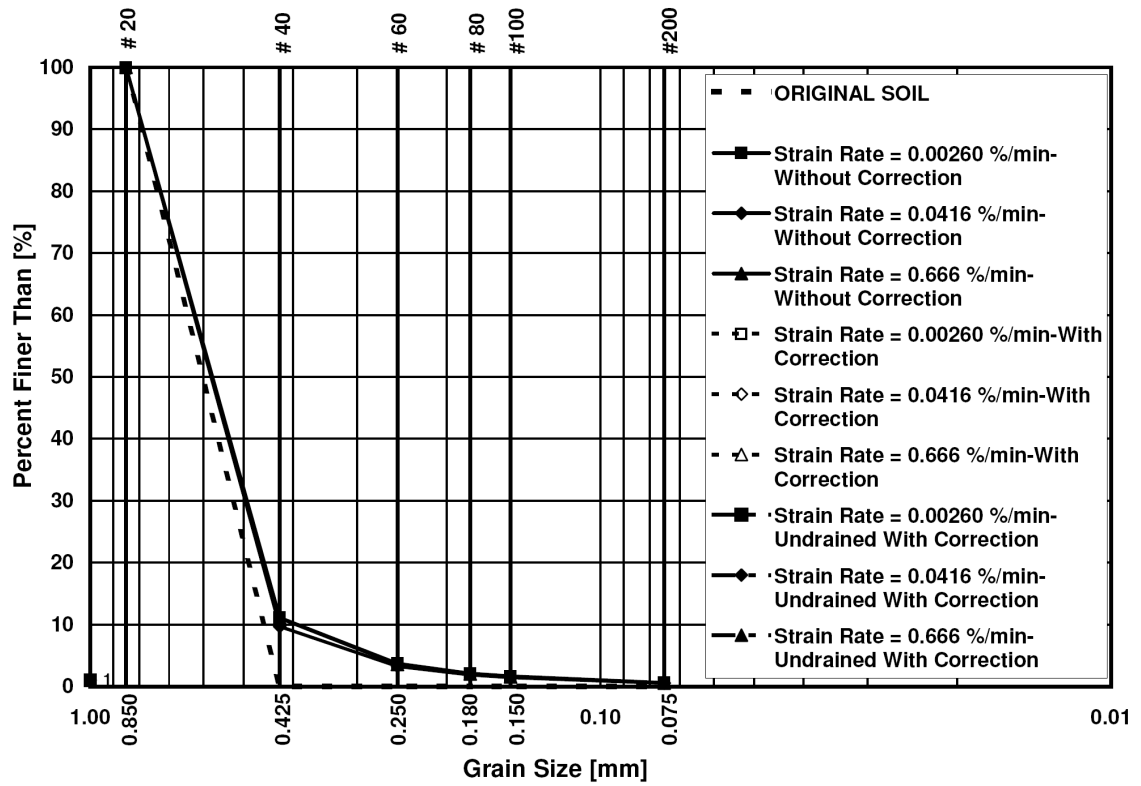


Figure 6.15. Grain size distribution curves at the end of drained and undrained stress relaxation tests, with and without correction of axial strain.

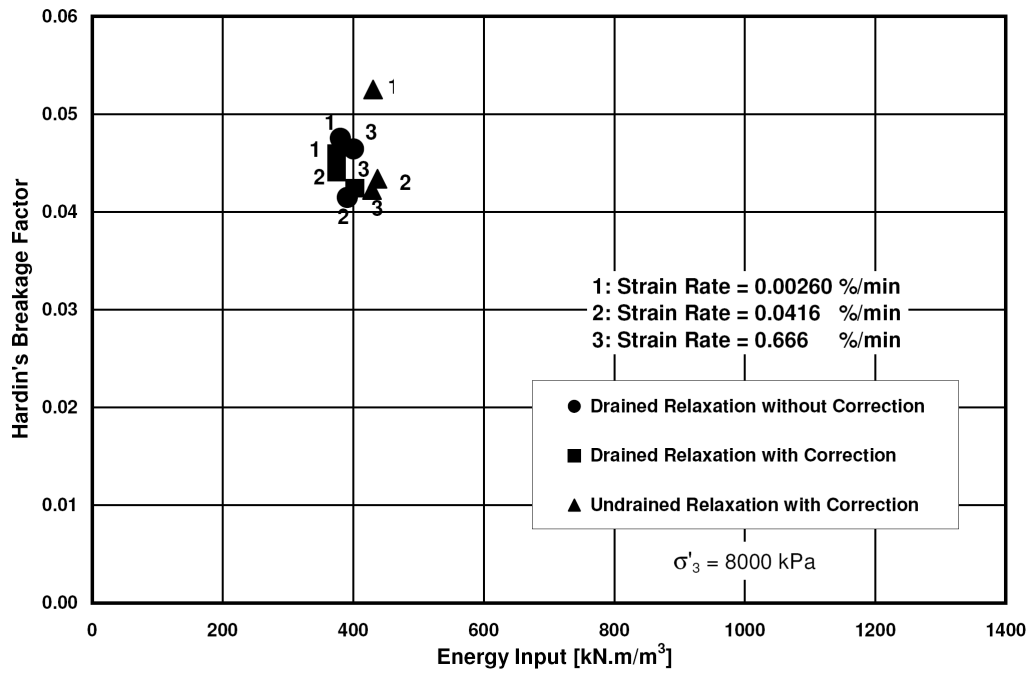


Figure 6.16. Relationship between Hardin's breakage factor and the amount of energy input for stress relaxation tests shown in Fig. 6.15.

is because the axial or volumetric strains are both zero. Therefore, the crushing due to creep can be obtained by subtracting the grain size curves presented in Fig. 6.15 from the equivalent curves for creep experiments as exhibited in Fig. 5.6.

6.2. 1-Day Stress Relaxation Curve

To explore the “1-day relaxation curve” for Virginia Beach sand, 6 tests of 1-day stress relaxation with correction of axial strain were carried out under a confining pressure of 8000 kPa. The specimens were sheared at the middle strain rate (0.0416 %/min) until the desired stress levels were reached where the stress relaxation tests began. These experiments have been labeled as to R1 to R6 for ease in presentation. The desired deviator stress levels at which stress relaxation tests were initiated are 2890, 5920, 11550, 13690, 15100 and 15570 kPa. Fig 6.17 illustrates the stress relaxation part of the experiments superimposed on the relevant reference stress-strain curve from Fig. 4.10. The resulting “1-day relaxation curve” for dense Virginia Beach sand is achieved by connecting the ending points of these stress relaxation tests. These stress levels have been chosen in such a way that the “1-day relaxation curve” would help produce a smooth curve.

The general shape of the 1-day relaxation curve is analogous to, but lower than the stress-strain reference curve. Obviously, the vertical distances between these two curves exhibit the amount of stress relaxation for 1 day at any chosen initial deviator stress. It seems that as the deviator stress level is increased, the amount of stress

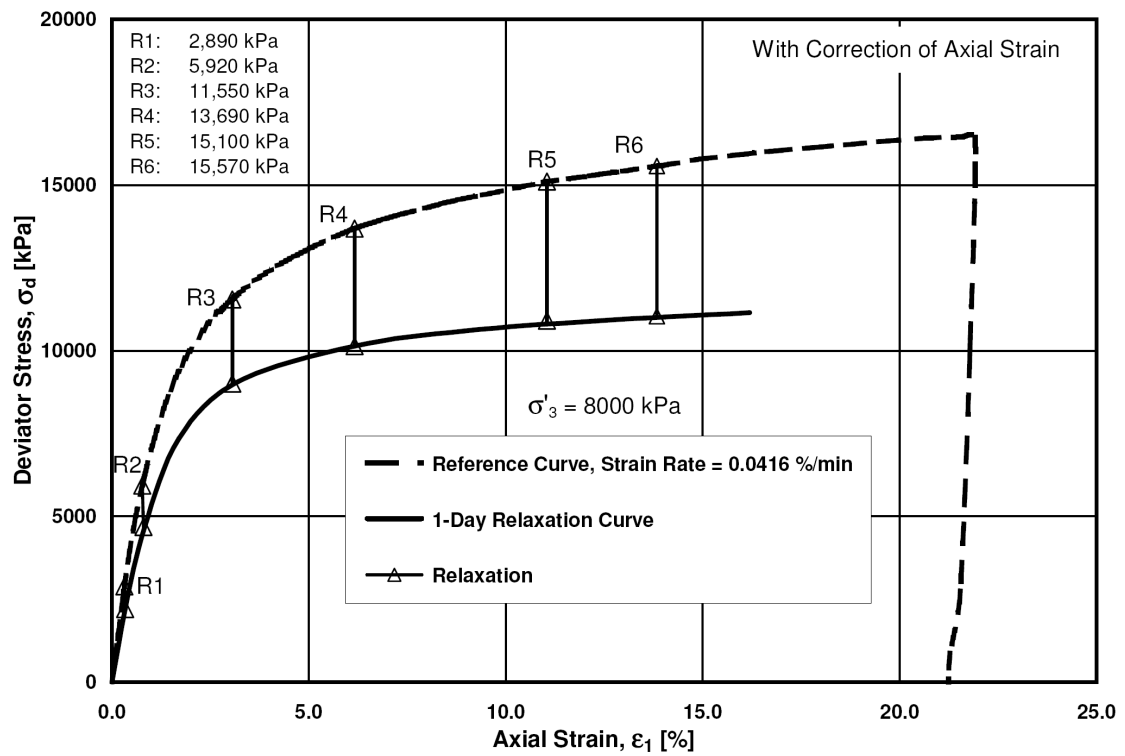


Figure 6.17. 1-day stress relaxation curve for Virginia Beach sand under $\sigma'_3=8000$ kPa.

relaxation increases. This is in accordance with influence of load on the progress of static fatigue. The variation of the stress relaxation with respect to the logarithm of elapsed relaxation time is illustrated in Fig. 6.18 for experiments R1 to R6. As mentioned earlier, lack of adjustment for experiments that required performance overnight caused irregular jumps on the results of stress relaxation tests with correction. These are seen for experiments R4, R5 and R6 in the vicinity of 750 minutes in Fig. 6.18.

A systematic response is observed for the stress relaxation. If stress relaxation begins at higher deviator stresses, larger stress reduction values are observed. In test R1 performed at the initial deviator stress level of 2890 kPa, stress reduction of 680 kPa is obtained, while in test R6 initiated at the deviator stress level of 15570 kPa, a stress relaxation of 4450 kPa is observed after 1 day.

As explained before, all experiments were terminated at the end of 1-day stress relaxation. Although, it was explained in the previous chapter that there is no structuration effect by loading after 1-day creep experiments, one multiple 1-day stress relaxation experiment was performed under the same confining pressure to study this effect after stress relaxation. Four 1-day stress relaxation stages with correction of axial strain were produced at deviator stress levels of 6620, 11180, 13620 and 15300 kPa. The specimen was sheared at the middle rate of 0.0416 %/min to the deviator stress level of 6620 kPa, where the first stress relaxation test started and lasted for 1 day by stopping further deformation. The specimen was then loaded to the next desired deviator level to perform the second 1-day stress relaxation. This procedure continued until the last

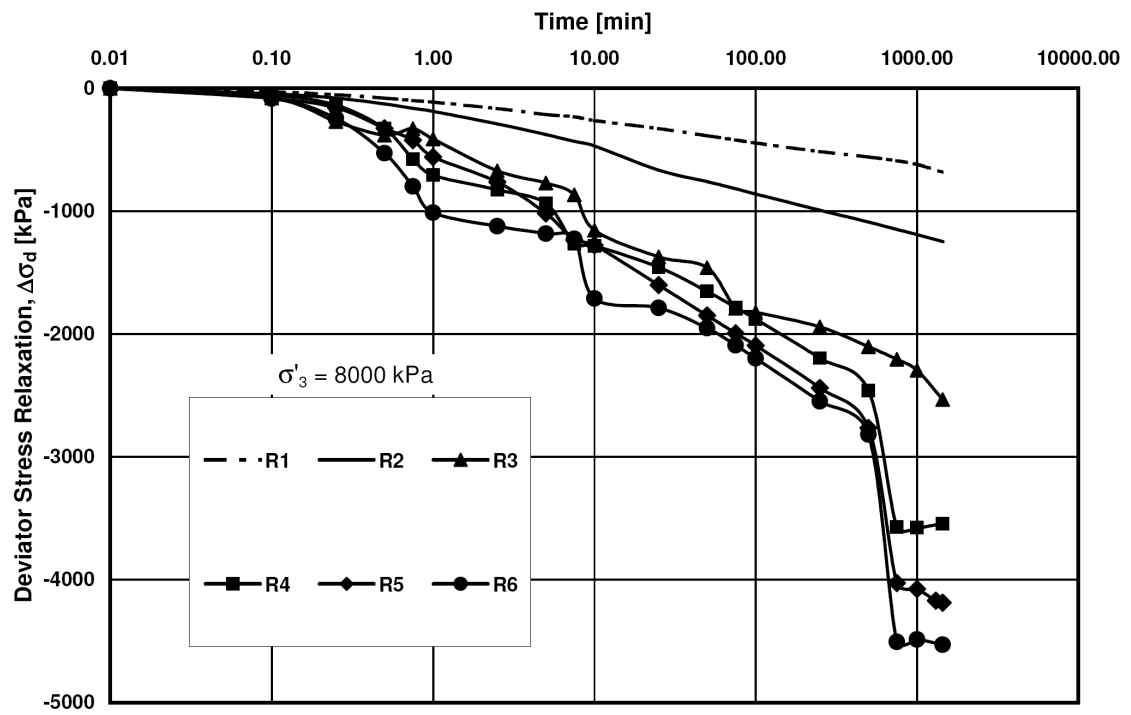


Figure 6.18. Effect of deviator stress level on magnitudes of stress relaxation.

desired stress level of 15280 was reached and the last stress relaxation was conducted. The deviator stresses employed were close to the stress levels at which experiments R2, R3, R4 and R5 had been initiated. Fig. 6.19 shows the stress-strain and volume change behavior in this test compared with the corresponding reference curve.

Fig. 6.19(a) indicates that the stress-strain curve increases at a steeper slope to rejoin the reference curve when the specimen is further loaded at the end of each stress relaxation stage. During stress relaxation, the stress point moves toward the inside of the yield surface due to reduction of the stress level. Therefore, further loading initially produces elastic strains until the stress point is reached at the current yield surface where plastic strains are generated. If a structuration effect exists, the stress point overshoots the reference stress-strain curve. Otherwise, it smoothly rejoins the reference curve. Lade (2007) showed that Antelope Valley sand underwent no structuration effects, whereas Lade et al. (2010) reported structuration effects after performing multiple stress relaxation tests on crushed coral sand. Fig. 6.19(a) shows that there is no structuration effects in dense Virginia Beach sand because the stress-strain curve merges with the reference curve after further loading at the end of each stress relaxation cycle without demonstrating any extra strength. Fig. 6.19(b) shows that there are insignificant volume changes during stress relaxation and the axial-volumetric strain curve perfectly follows the reference curve. Points corresponding to stress relaxation stages have been noted on this graph. Variation of stress relaxation in the various stages with time elapsed is presented in Fig. 6.20 together with the result of individual stress relaxation tests of R2, R3, R4 and R5.

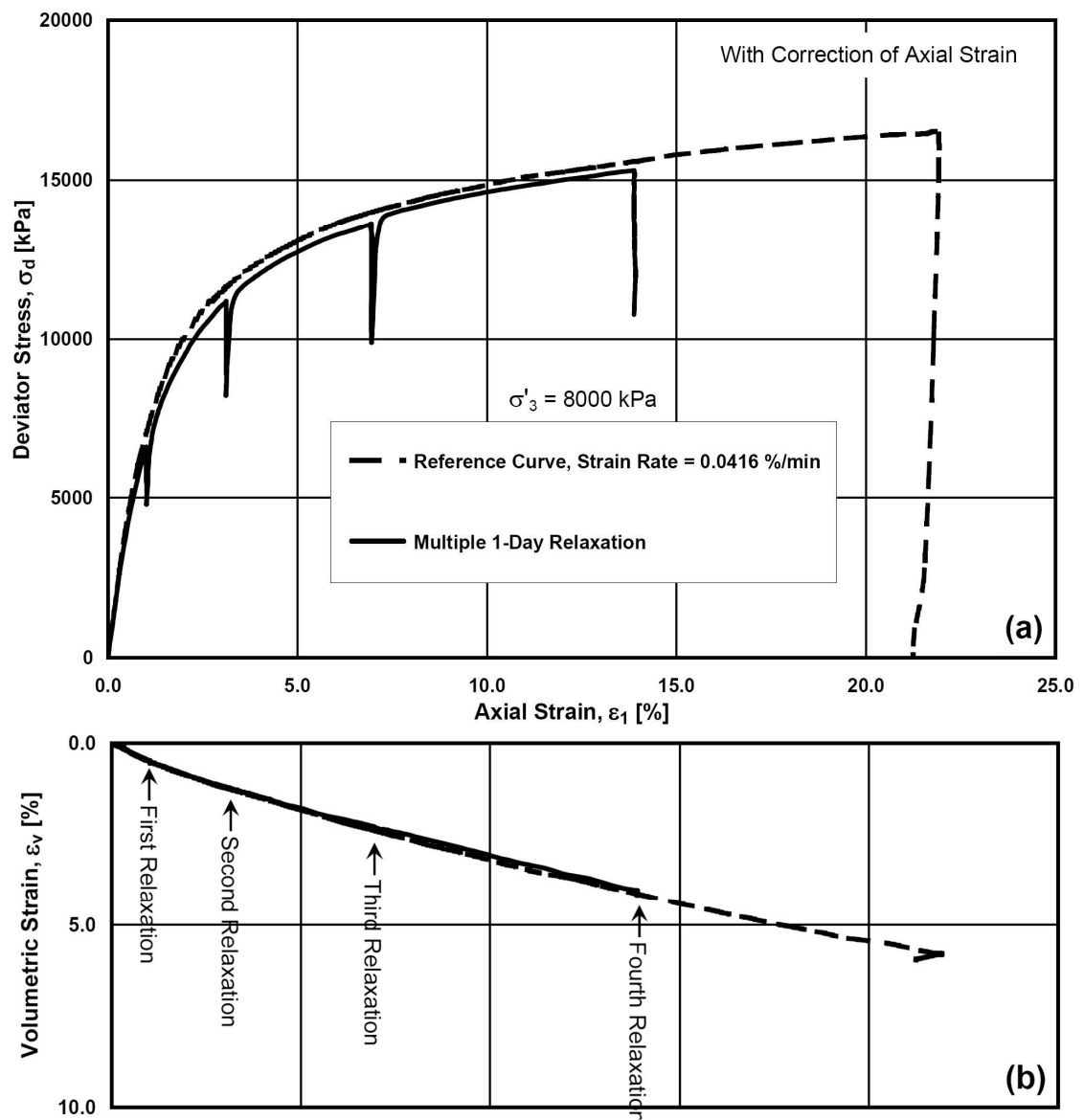


Figure 6.19. (a) Stress-strain, and (b) volume change curves for multiple 1-day stress relaxation test on Virginia Beach sand.

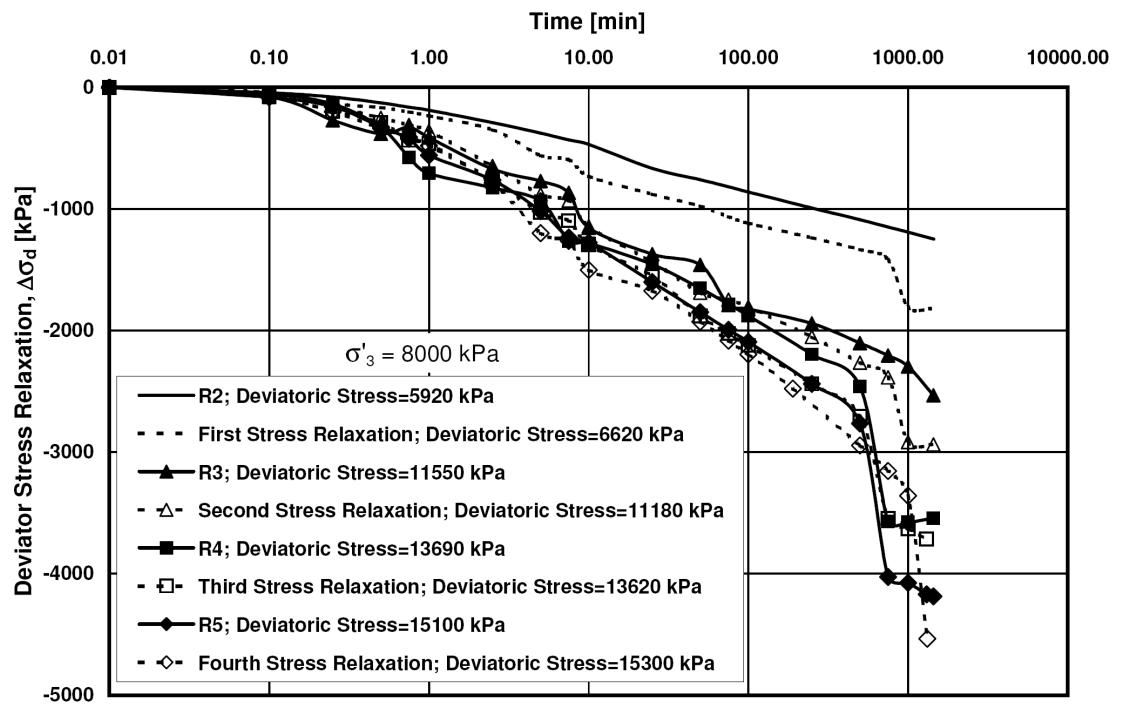


Figure 6.20. Variation of magnitudes of stress relaxation at different deviator stress levels for multiple 1-day stress relaxation tests with time.

As observed, very similar responses have been achieved. The highest difference of 31% is observed between the results of the first stress relaxation and test R2. However, the deviator stress level at which the former was initiated was 11% higher than that in test R2. Fig. 6.17 indicated that a small difference in the deviator stress level at low axial strains (under 5%) results in a considerable difference in the amount of stress relaxation. On the other hand, the smallest difference is 4.6% between the third stage of relaxation and test R4; the difference of the deviator stress levels was 1%. For the higher axial strains (over 10%), the “1-day relaxation curve” and the stress-strain curve tend to become parallel. Therefore, the deviator stress level is not as important as it is at low axial strains.

Sieve analyses have been performed on all specimens and the results are presented in Fig. 6.21. The relaxation experiments performed at higher deviator stresses have produced larger amounts of particle crushing as reaching higher stresses and strains requires more energy input. This is in agreement with the static fatigue phenomenon which is at the root of time-dependent grain crushing. The amount of energy input during stress relaxation is basically zero as the amount of axial and volumetric strains occurring during this stage can be neglected. Accordingly, the amounts of energy input and particle crushing are related to those at the points of initiation of stress relaxation. Here, the experiments of R5 and R6 and the multiple stress relaxation test have been sheared to similar energy inputs of 2100, 2110 and 2150 kPa, respectively. Therefore, more or less the same grain size curves are expected as confirmed in Fig. 6.21.

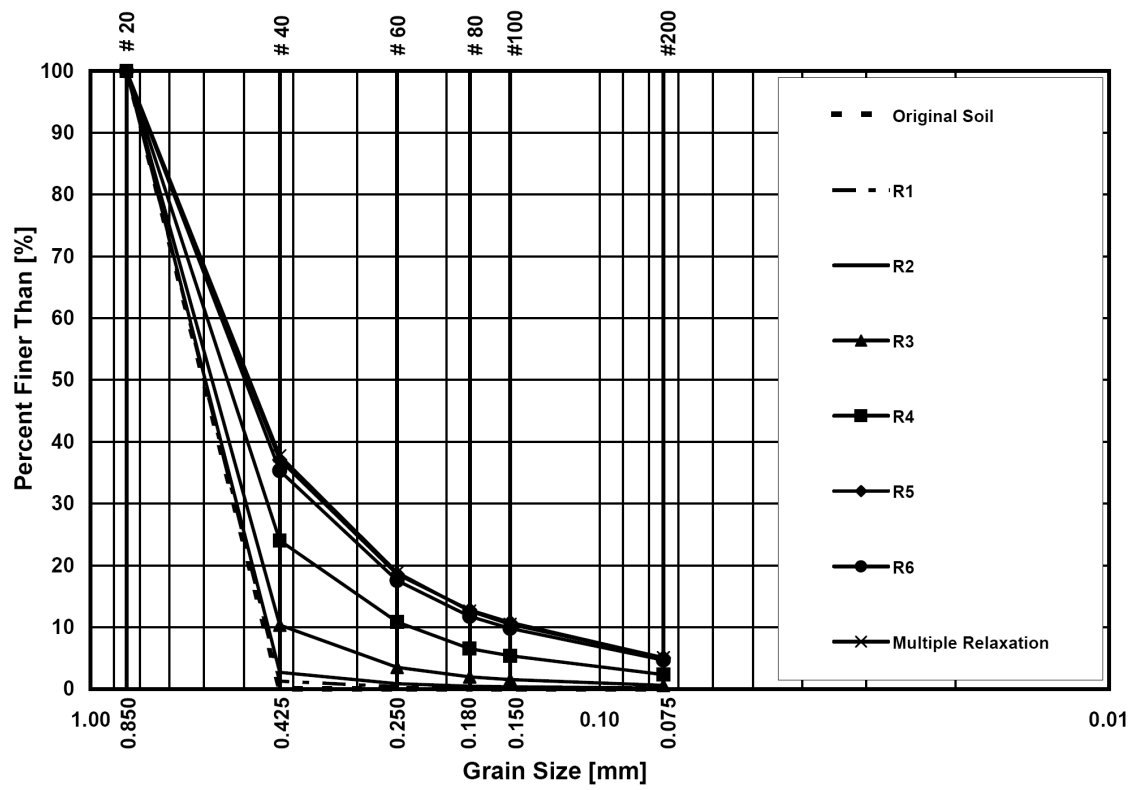


Figure 6.21. Evolution of grain size distribution curve for 1-day stress relaxation tests.

Fig. 6.22 throws further light on the relationship between energy input and Hardin's breakage factor for the grain size distribution curves shown in Fig. 6.21. Approximately the same breakage factor has been obtained for tests R5 and R6 and the multiple stress relaxation test. As a general trend, the higher the energy inputs are, the larger the Hardin's breakage factors will be.

6.3. Long Term Stress Relaxation

Not many studies have been presented in the literature on stress relaxation in granular materials and those presented have been limited to short periods of time. For instance, Lacerda and Houston (1973) studied stress relaxation behavior of Monterey sand up to 100 minutes, and Ladanyi and Benyamina (1995) performed stress relaxation experiments on frozen Ottawa sand for 1 day. In addition, Lade (2007) and Lade et al. (2010) presented results of stress relaxation experiments up to 1 week. These studies were all conducted at low confining pressures where experimental difficulties are considerably less in comparison to high confining pressures where membrane puncture and gas diffusion problems are much more pronounced. Here is presented the results of a 2-month drained stress relaxation experiment with correction of axial strain performed on dense Virginia Beach sand to study this phenomenon for a longer period of time. Before the specimen was allowed to stress relax for two months, it was sheared under a confining stress of 8000 kPa at a strain rate of 0.0416 %/min up to the deviator stress level of 11240 kPa. Fig. 6.23 exhibits the stress-strain and volumetric behavior of the experiment.

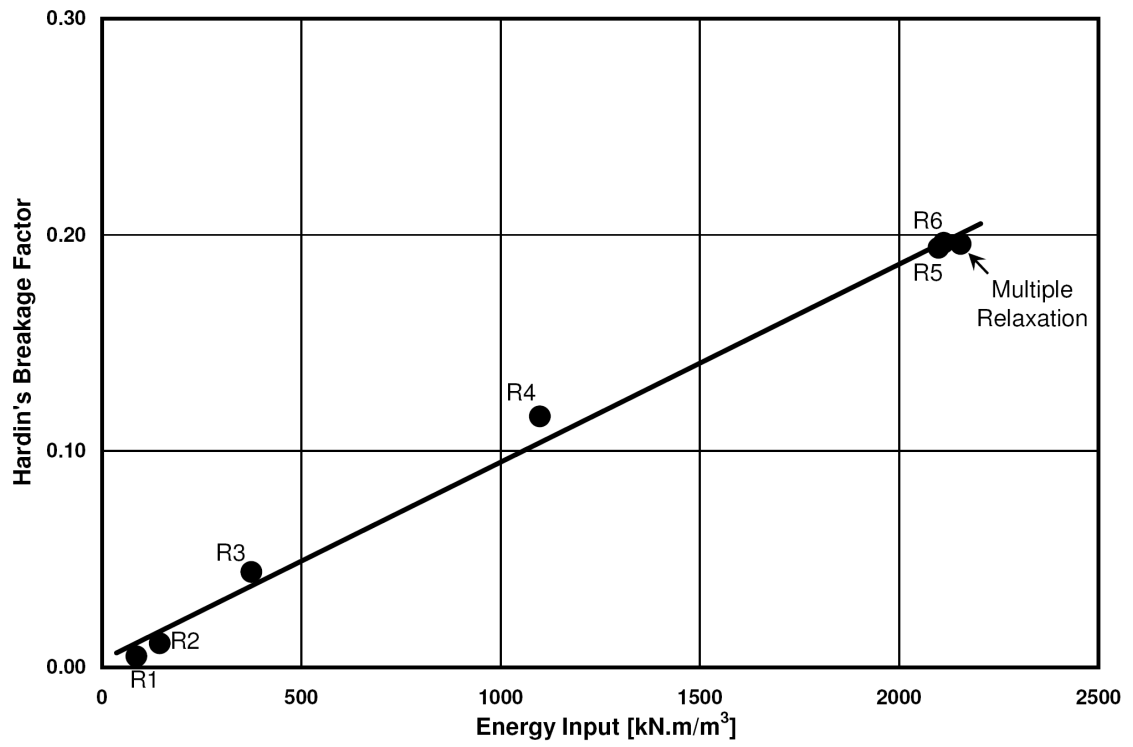


Figure 6.22. Relationship between energy input and Hardin's breakage factor for 1-day stress relaxation tests.

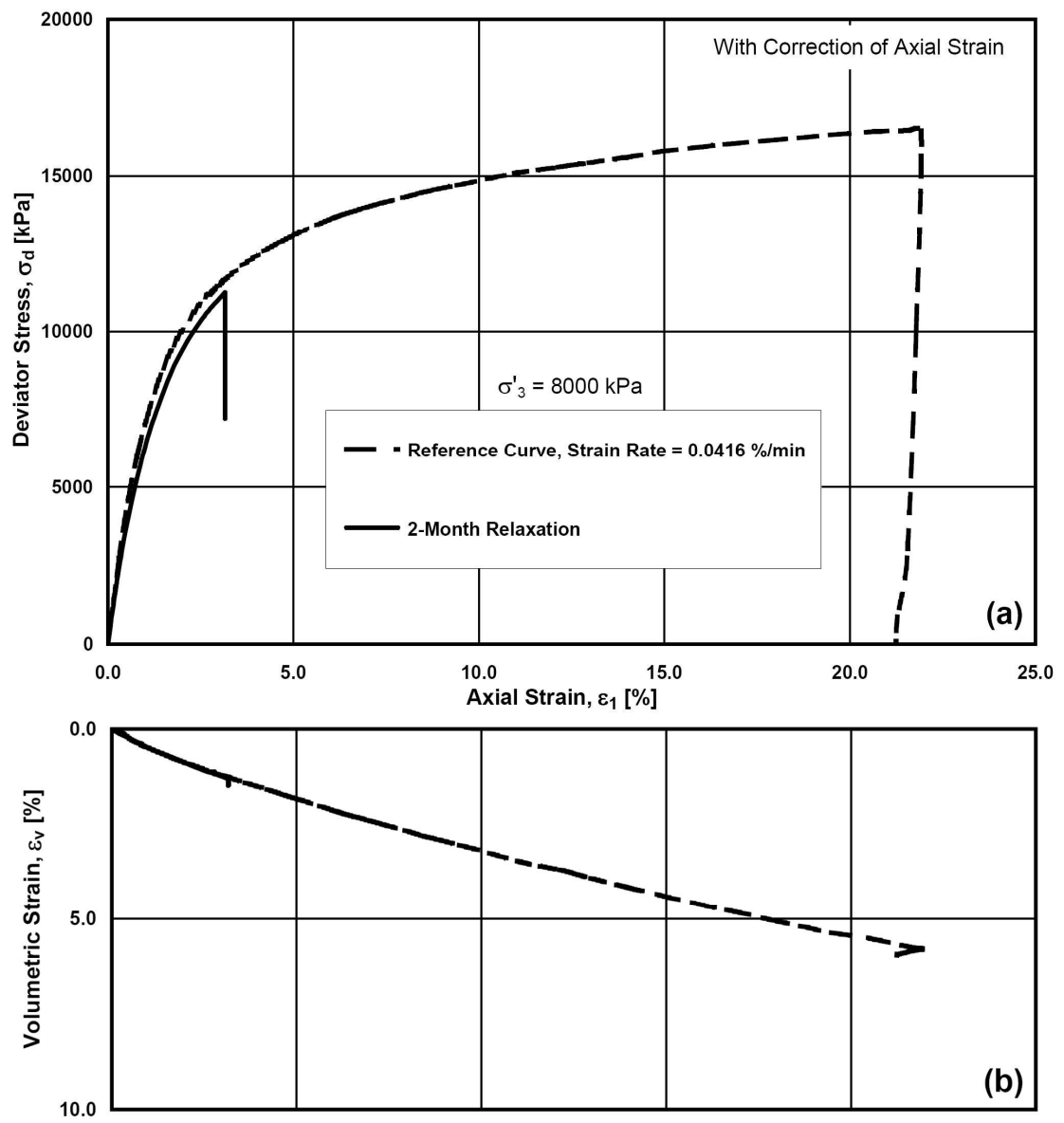


Figure 6.23. (a) Stress-strain, and (b) volume change curves for 2-month stress relaxation test on Virginia Beach sand.

Fig. 6.23(a) indicates that the stress reduction of 4020 kPa over the period of two months. This is approximately 37% of the deviator stress at the beginning of stress relaxation. Additionally, the variation of the stress relaxation with time elapsed is presented in Fig. 6.24 where the results of the 1-day stress relaxation test of R3 are also plotted. As seen on the graph, stress relaxation has initiated at approximately the same deviator stress level for both experiments. There is very good agreement between the results of the experiments indicating the repeatability and steadiness in the experimental program. As observed, even after two months, the deviator stress level continues to decrease with the logarithm of time and with the same rate as it had at around 10 minutes, suggesting that there is no limit for the stress relaxation. This is in contrast to the hypothesis of Murayama and Shibata (1961) stated that there is a certain final relaxed level of stress.

6.4. Comparison between 1-Day Creep and Stress Relaxation

The results of six 1-day stress relaxation and seven 1-day creep experiments have been superimposed on the corresponding stress-strain curve from Fig 4.10 to provide a comparison between creep and stress relaxation behaviors as shown in Fig. 6.25. The vertical lines illustrate stress relaxation experiments, whereas the horizontal lines exhibit the creep tests. Both stress relaxation and creep deformation increase with the stress level from which they initiated. The data from both types of experiments are very consistent, but they are located at quite different positions with respect to the reference curve. In other words, the measured stress relaxation behavior does not correspond with the

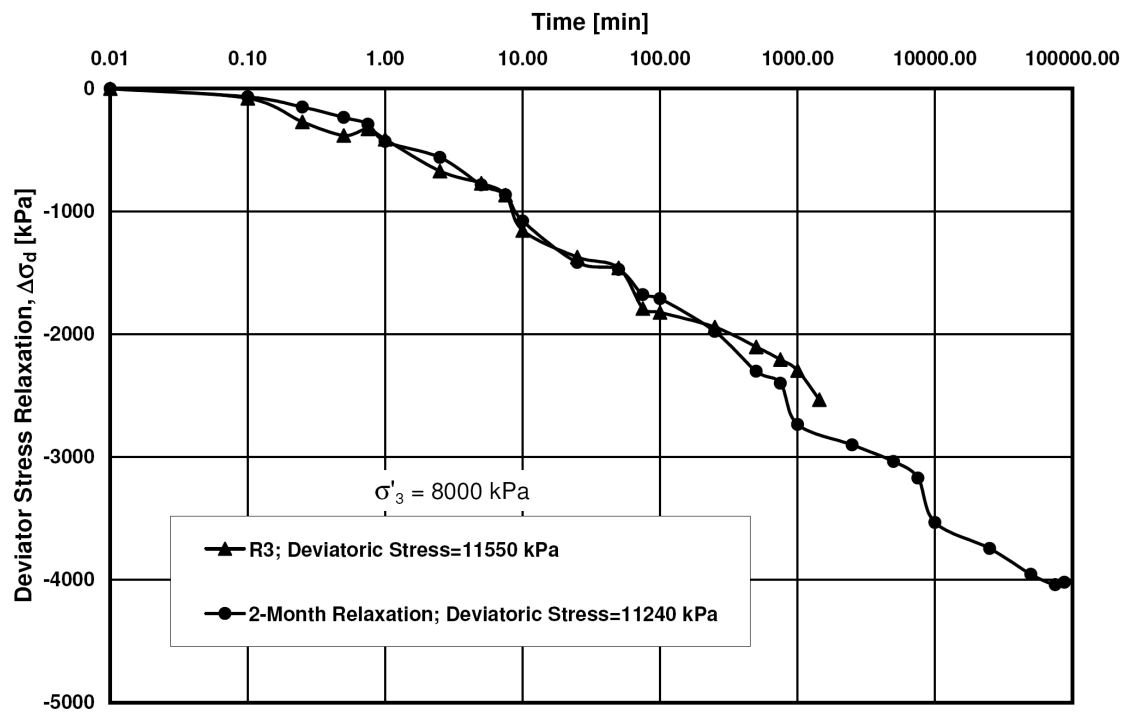


Figure 6.24. Variation of deviator stress in the 2-month stress relaxation test with time.

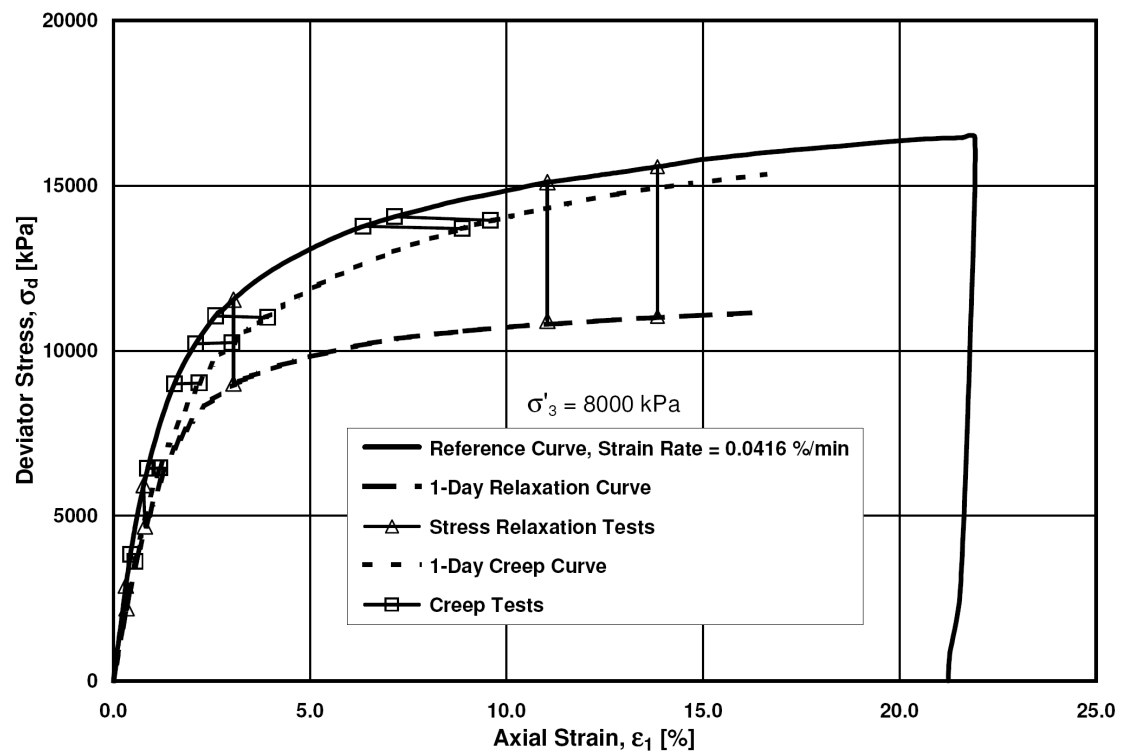


Figure 6.25. Comparison between 1-day creep and 1-day stress relaxation curves.

observed creep behavior and the two curves cannot be obtained from each other. These observations confirm that in contrast with clays, Virginia Beach sand does not follow isotach behavior.

6.5. Mechanism of Stress Relaxation Behavior Observed

It is believed that the mechanism behind these observations can be explained by particle crushing due to static fatigue, and this is proposed as the root of observed time effects in granular materials. The same mechanism of creep behavior was explained for low and high confining pressures in Section 5.5. Stress relaxation behavior of granular materials under low confining stresses is explained in a similar manner to creep at these pressures. However, stress relaxation under high confining stresses is described as follows.

When loading is stopped, the boundaries are kept stationary thus allowing stress relaxation. However, the soil structure needs to transmit the applied stress level. Once a number of particles fracture due to static fatigue and are excluded from the existing force chains, new force chains are mobilized. Because the boundaries are not allowed to move, the stress level is reduced. This reduction of stress level is referred to as stress relaxation. For the same reasons as explained for creep, the rate of stress reduction is also influenced by the strain rate before initiation of stress relaxation. Accordingly, at the commencement of stress relaxation, a larger rate of stress decrease is attained for an initial high shearing strain rate, while stress relaxation is delayed for an initial low shearing strain rate. During stress relaxation, some new particles may fracture due to static fatigue. Particle crushing

results in increase in coordination numbers and consequently, reduction in forces on particles. Since no deformation is allowed, stress reduction occurs and particle breakage is reduced with time. Once an adequate amount of time has passed, the effect of shearing strain rate vanishes. Therefore, specimens sheared at very high and very low strain rates prior to stress relaxation exhibit the same rate of stress reduction following a short period of time for adjustment.

7. Creep-Stress Relaxation Experiments

The following four series of tests were designed to study consecutive and concurrent effects of stress relaxation and creep. The confining pressure of 8000 kPa and an initial shearing strain rate of 0.0416 %/min were used in these experiments.

7.1. Tests with Creep, then Stress Relaxation

The consecutive effect of creep and stress relaxation were studied by performing four experiments in which the specimens were sheared to a desired energy input and subjected to creep for different time periods before they were allowed to relax for 1 week. The four specimens experienced 0 minutes, 3 hours, 1 day and 1 week of creep before initiation of stress relaxation. In these experiments, the initial shearing was performed under strain control; loading was then changed to load control to carry out the creep phase. To maintain the deformation constant during the following 1-week stress relaxation phase, the loading was changed back to deformation control. This allowed time for an axial deformation correction during stress relaxation. The energy inputs at the beginning of the creep phase of the tests were 422, 416, 406 and 420 kN.m/m³ for the experiments with creep times of 0 minute, 3 hours, 1 day and 1 week, corresponding to stress-strain points of $[(\sigma_1 - \sigma_3), \epsilon_1] = [11260 \text{ kPa}, 3.18\%]$, $[11520 \text{ kPa}, 3.11\%]$, $[11050 \text{ kPa}, 3.15\%]$, and $[11200 \text{ kPa}, 3.17\%]$, respectively. The stress-strain and volumetric behavior of these tests are presented in Fig. 7.1.

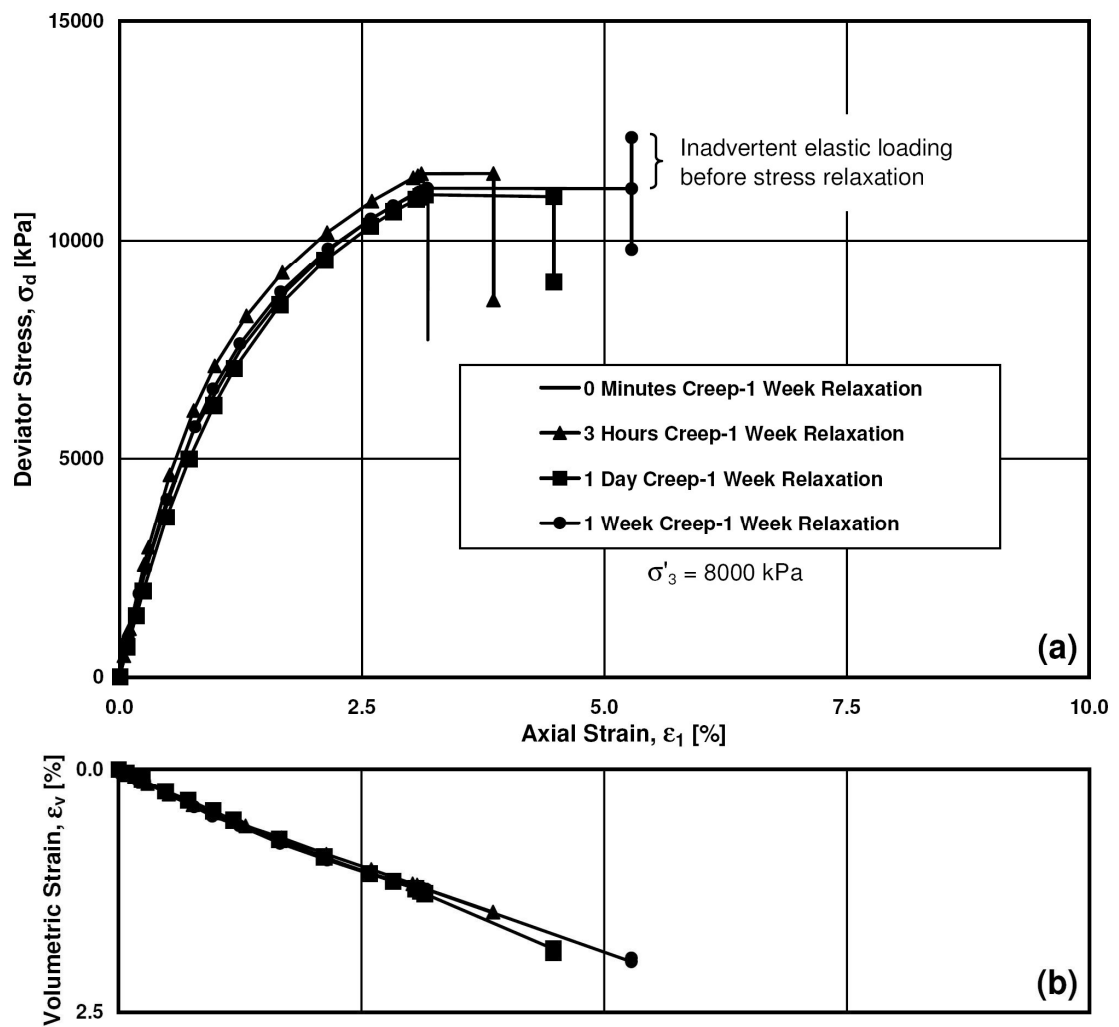


Figure 7.1. (a) Stress-strain behavior, and (b) volumetric response for experiments starting with creep and ending with stress relaxation.

The test in which the specimen underwent no creep produced the largest deviator stress reduction (3540 kPa) for 1 week of stress relaxation. The second specimen crept axially for 0.74% and volumetrically for 0.25% during 3 hours of creep, while it showed a stress reduction of 2900 kPa after 1 week stress relaxation. In the third experiment, axial and volumetric creep strains of 1.33% and 0.57% were achieved after 1 day. This was followed by stress relaxation of 1960 kPa in 1 week. The fourth specimen produced axial and volumetric creep strains of 2.11% and 0.74% after 1 week of creep. At the initiation of the stress relaxation phase and during switching from load control to deformation control an error occurred in this experiment and due to inadvertent elastic loading during switching to deformation control, the 1-week stress relaxation started at a higher deviator stress level, which is indicated in Fig. 7.1(a). However, a net stress drop of 1150 kPa was experienced after 1 week stress relaxation with respect to the deviator stress level at which the specimen was allowed to creep for 1 week. Fig. 7.2(a) shows the variation of axial and volumetric creep strains during the creep phase and Fig. 7.2(b) illustrates the subsequent stress reduction during the stress relaxation phase with respect to the logarithm of elapsed time for the aforementioned experiments.

Fig. 7.2(a) confirms the repeatability of creep tests as the variation of axial and volumetric creep strains are matched for their common time periods. However, as seen in Fig. 7.2(b), a different trend is observed for the stress relaxation phase of the experiments. In other words, even though the stress relaxations initiated at the same deviator stress level, dissimilar variations of stress is observed. This behavior pattern can

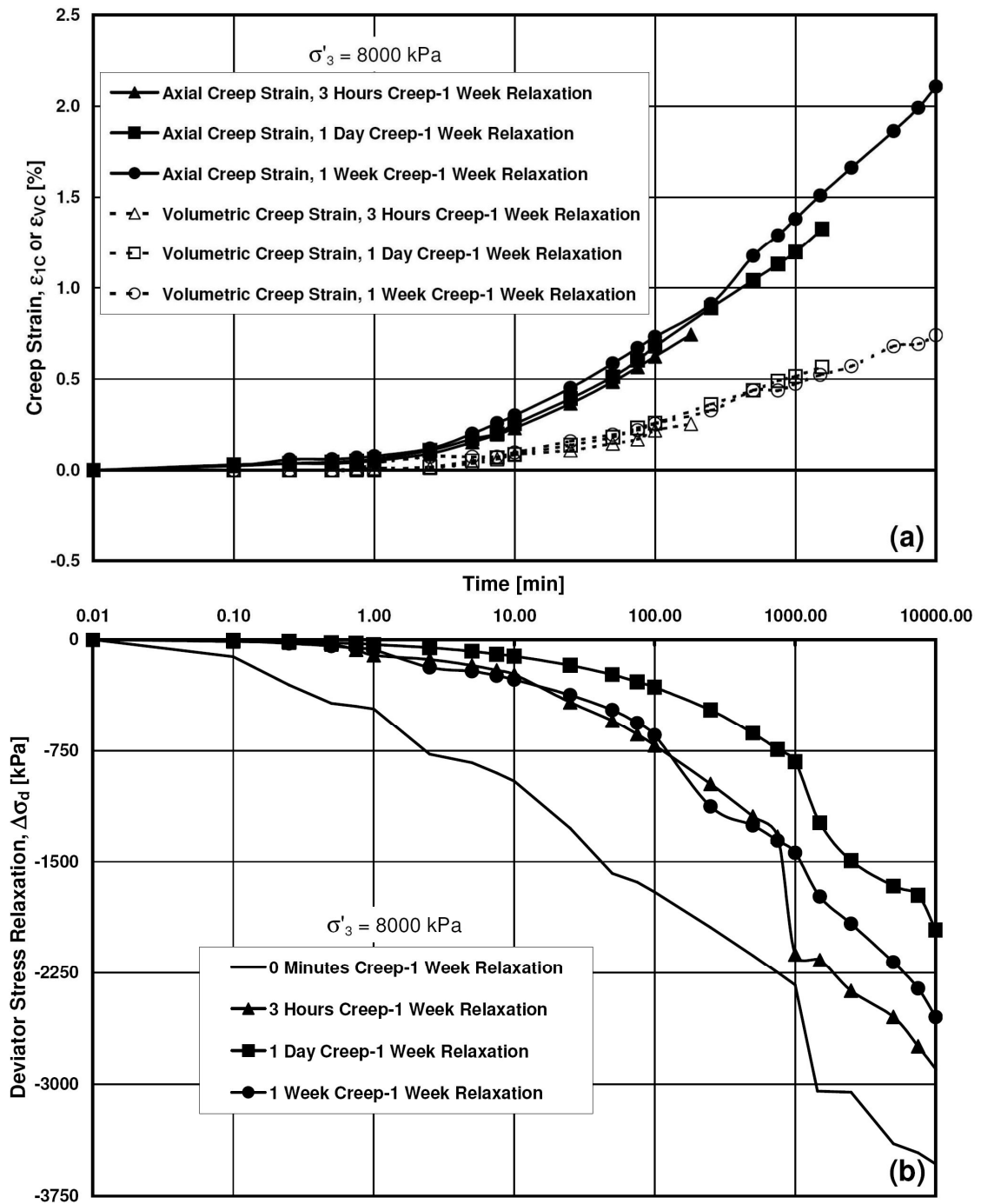


Figure 7.2. (a) Variation of axial and volumetric creep strains during creep phase;
(b) variation of deviator stress during stress relaxation phase.

be explained according to particle crushing and the soil structure at the initiation of each phase in the experiments. Once the shearing phase is finished, all specimens have more or less the same structure, because the same time has been given to all specimens under a similar stress path. Therefore, the same response is expected at similar elapsed times during the creep procedures. However, since the specimens have crept for various time periods, different soil structures are expected at the initiation of the stress relaxation phases and different responses are achieved for the same relaxation time periods. Thus, specimens exposed to longer periods of creep show less stress relaxation, because the particles that would have crushed during relaxation already had crushed during creep.

Fig. 7.3 shows the sieve analyses results for these experiments. It can be observed that the higher the creep time is, the greater the amounts of breakage of particles will be. The energy inputs at the end of the experiments were 426, 522, 600 and 720 kN.m/m³ for the experiments with creep times of 0 minute, 3 hours, 1 day and 1 week, respectively. Hardin's breakage factor has been calculated and the result has been plotted against the energy input at the end of each experiment in Fig.7.4 which shows that a larger amounts of particle breakage is attained for longer creep times, implying static fatigue as at the root of time-dependent phenomena in granular materials.

7.2. Tests with Stress Relaxation, then Creep

To study the consecutive effects of relaxation and creep on Virginia Beach sand, a series of experiments was carried out in the reverse sequence of the experiments

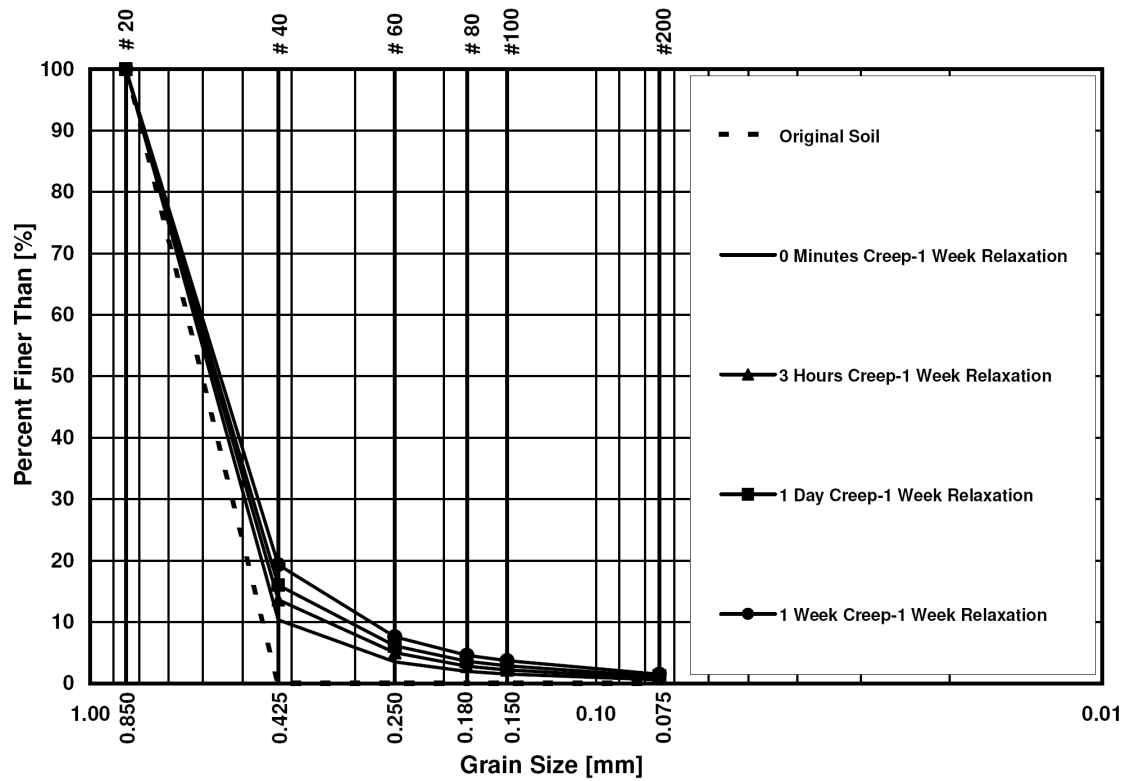


Figure 7.3. Grain size distribution curve for experiments starting with creep and ending with stress relaxation.

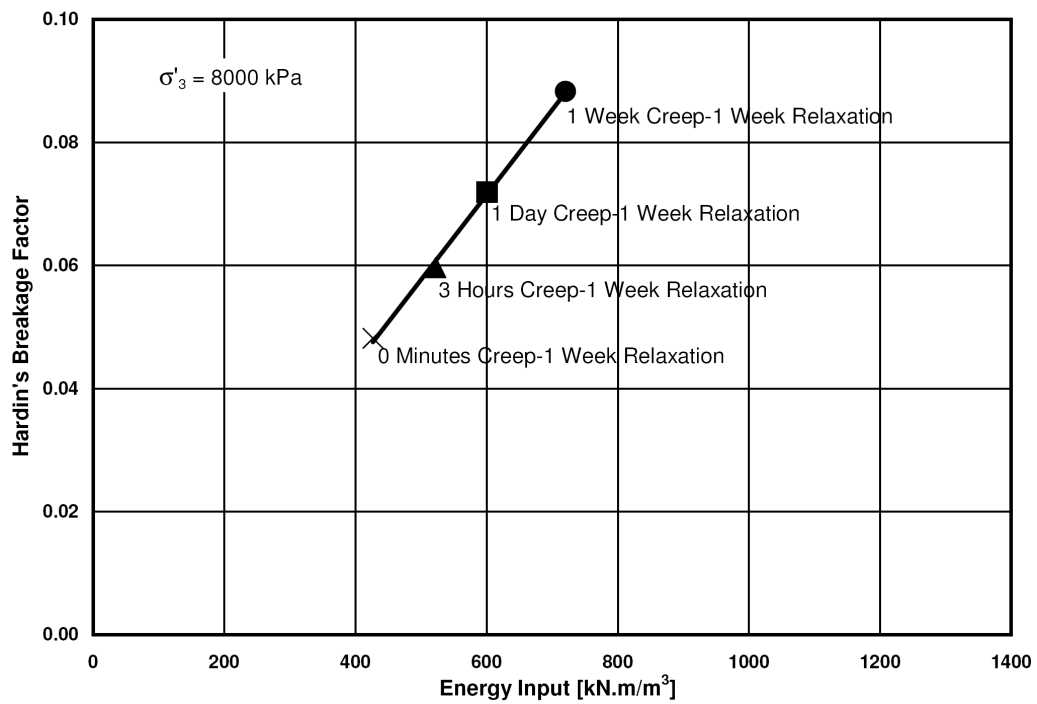


Figure 7.4. Energy input versus Hardin's breakage factor for experiments starting with creep and ending with stress relaxation.

explained in the previous section. That is, once shearing stopped, a stress relaxation phase was allowed prior to the creep phase. Four experiments were dedicated to this series of experiments in which the first specimen was allowed to creep for 1 week without prior stress relaxation phase (This experiment was referred to as 0 minutes stress relaxation-1 week creep). The three other specimens underwent 3 hours, 1 day and 1 week of stress relaxation before they were subjected to 1 week creep. The stress-strain points at which the shearing was stopped and time dependent phases initiated were $[(\sigma_1 - \sigma_3), \epsilon_1] = [11260 \text{ kPa}, 3.18\%]$, $[11520 \text{ kPa}, 3.11\%]$, $[11050 \text{ kPa}, 3.15\%]$, and $[11200 \text{ kPa}, 3.17\%]$, and these were associated with the energy inputs of 420, 413, 450 and 422 kN.m/m^3 for the experiments with the initial stress relaxation times of 0 minute, 3 hours, 1 day and 1 week, respectively. The stress-strain curves and volumetric responses of this series of tests are plotted in Fig. 7.5.

It is observed that the experiment with 0 minutes stress relaxation shows a considerably higher creep deformation in comparison to the other experiments in which the specimens experienced initial stress relaxation. In this experiment, the axial and volumetric creep strains of 2.11% and 0.74% have been obtained after 1 week of creep, while the second specimen crept axially for 0.16% and volumetrically for 0.03% when it was subjected to a 3-hour stress relaxation phase prior to 1 week creep. A stress reduction of 2010 kPa was observed during the relaxation phase for the second specimen. The third specimen was stress relaxed for 1 day and the deviator stress level dropped 3080 kPa,

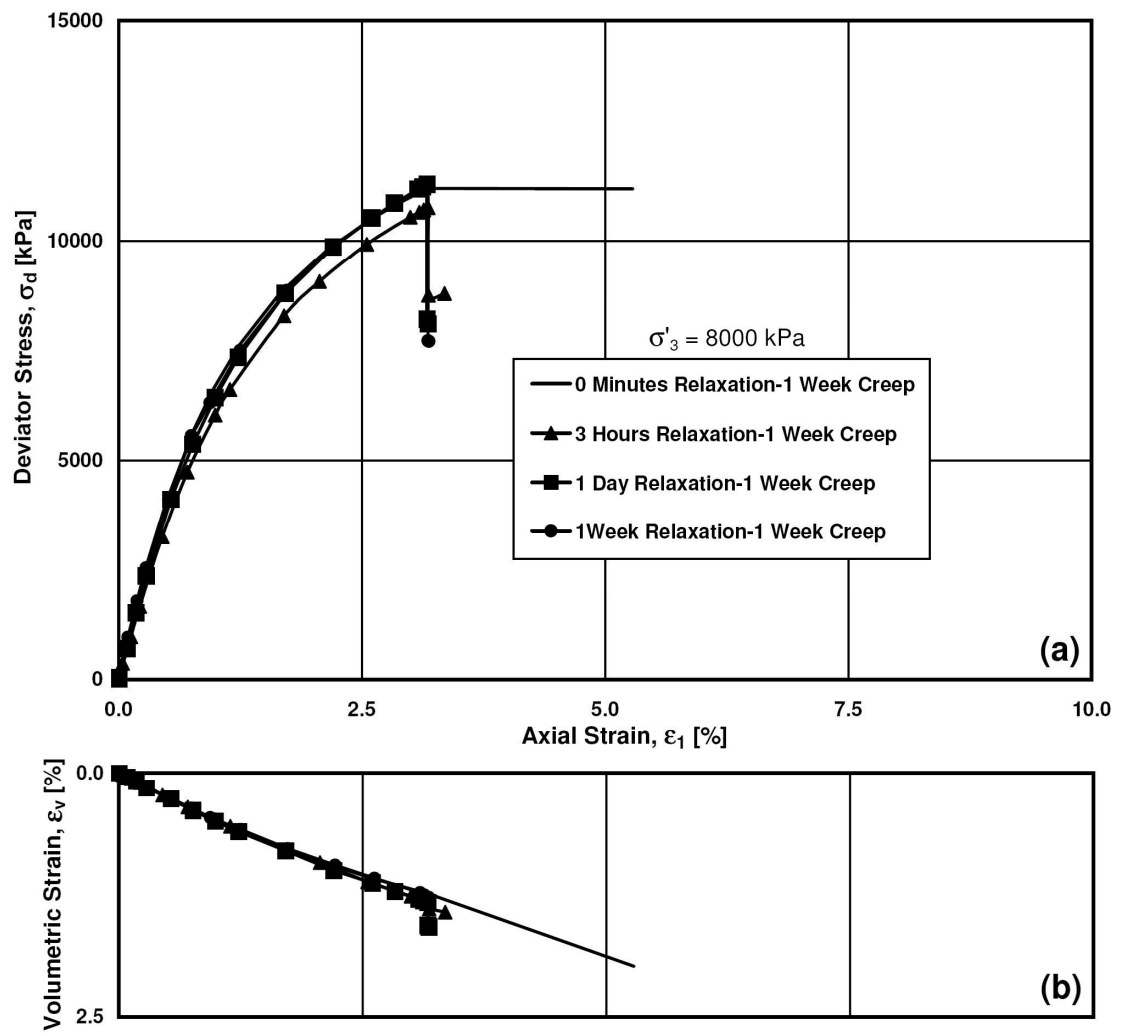


Figure 7.5. (a) Stress-strain behavior, and (b) volumetric response for experiments starting with stress relaxation and ending with creep.

whereas negligible creep deformation was observed during the creep phase. The fourth specimen experienced a stress decrease of 3540 kPa during 1 week stress relaxation, while it did not exhibit any creep deformation in the subsequent creep phase.

The repeatability of the experimental program is confirmed again in Fig. 7.6(a) where a similar variation in deviator stress was observed for the stress relaxation phases of the experiments. Moreover, the variation of the axial and volumetric creep deformation during the creep phases with respect to the elapsed time is shown in Fig. 7.6(b) and Fig. 7.6(c). These figures show that the experiment without stress relaxation starts to exhibit axial and volumetric creep strains as soon as the creep phase is initiated while the test experiencing 3 hours of stress relaxation shows no axial deformation and volume change within the first 1000 minutes of the creep phase. For the tests with 1 day and 1 week stress relaxation prior to the creep phase, absolutely no creep deformations are captured even after 1 week of creep.

The explanation behind this observation can be based on static fatigue of particles. As reported in the previous chapters and noted in many studies, the stress level and time under which the stress is kept on the particles severely influence the static fatigue phenomenon and subsequently the time effects. When a specimen has stress relaxed for a longer period of time, higher stress reduction is observed. Therefore, when the specimen is subjected to a creep phase at a lower stress level, a lower number of particles would crush under a longer period of time thus explaining why the first

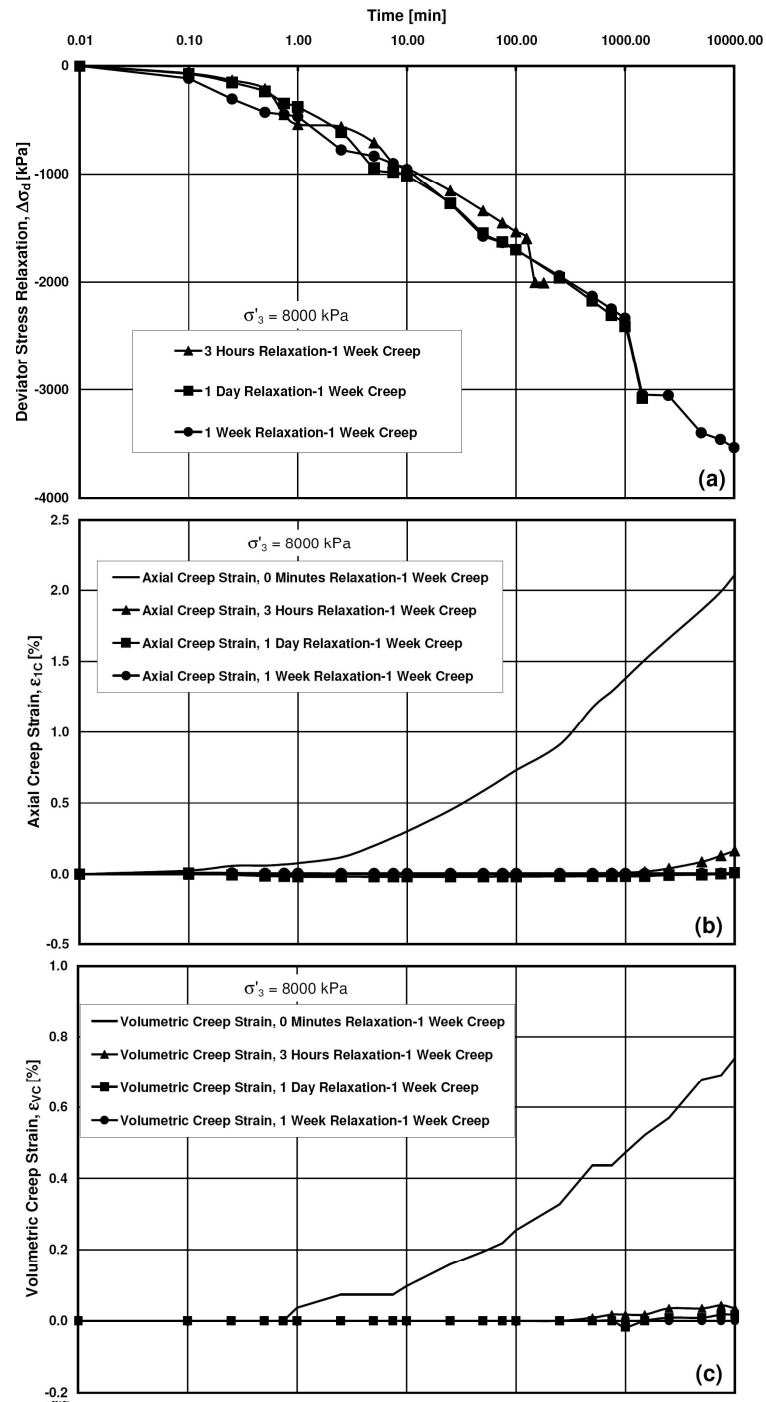


Figure 7.6. (a) Variation of deviator stress during stress relaxation phase, (b) variation of axial, and (c) volumetric creep strains during creep phase.

specimen instantly undergoes creep deformations, while the second specimen exhibits little deformation but only after 1000 minutes, and the two remaining tests did not exhibit any creep strains within 10000 minutes of creep.

The results of sieve analyses performed on the retrieved specimens at the end of the experiments are presented in Fig. 7.7, while the variation of Hardin's breakage factor, calculated from Fig. 7.7, versus the final energy input is illustrated in Fig. 7.8. It is observed that approximately the same grain distribution curves and subsequently similar breakage factors are obtained for experiments with stress relaxation times of 3 hours, 1 day and 1 week. However, since the first specimen did not undergo stress relaxation and crept considerably, a higher energy input has been reached and therefore a larger particle breakage factor is expected.

7.3. Combined Creep-Stress Relaxation

Five drained triaxial compression experiments, as explained in Chapter 3, were performed to evaluate the concurrent effects of creep and stress relaxation in granular materials. All of these tests were performed with a confining pressure of 8000 kPa and a strain rate of 0.0416 %/min and their time-dependent phase lasted for 1 week. The time-dependent phase of the first and the fifth experiments were dedicated to "100% creep" and "100% relaxation", respectively, whereas the three other experiments experienced stress paths composed of creep and stress relaxation. These specific tests help understand the phenomena that consist of combinations of creep and stress relaxation.

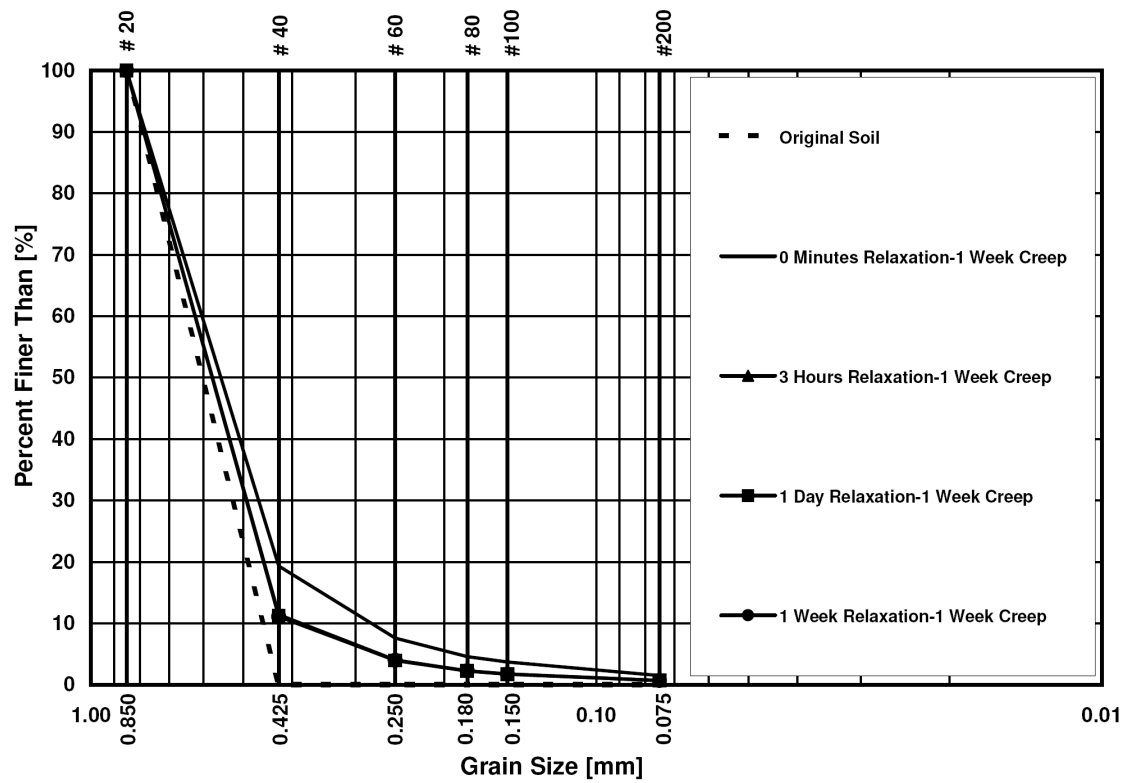


Figure 7.7. Grain size distribution curve for experiments starting with stress relaxation and ending with creep.

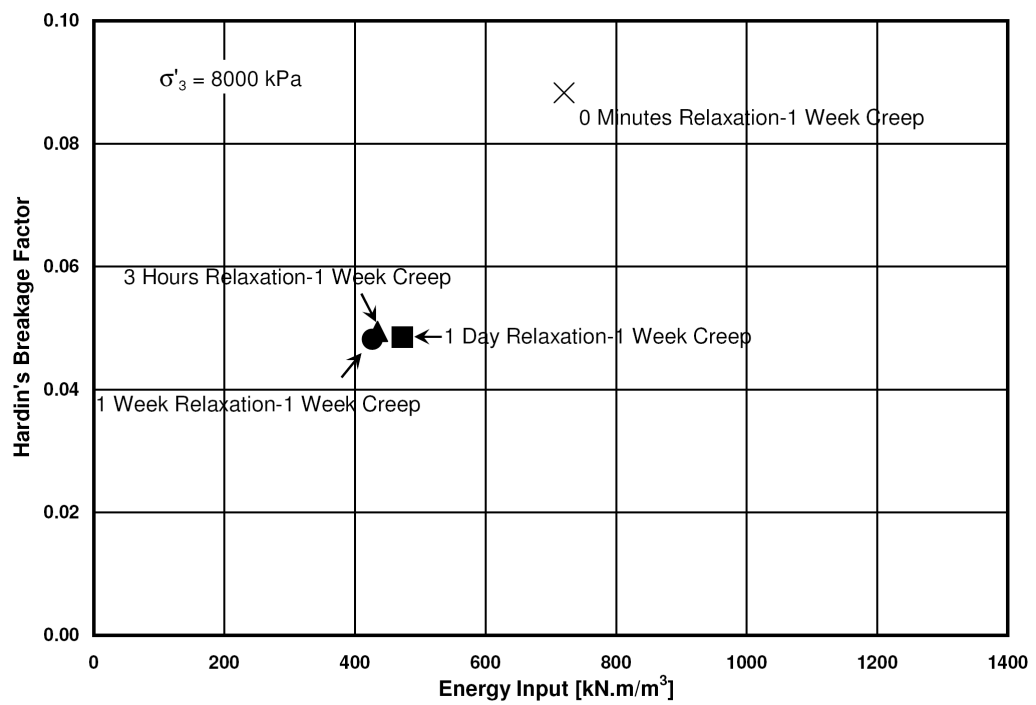


Figure 7.8. Energy input versus Hardin's breakage factor for experiments starting with stress relaxation and ending with creep.

Such cases are found frequently in practice. An example was presented by Leung et al. (1996) in their experimental studies of creep of piles installed in sand layers. In this study, the measured stress at the tip of a pile decreased with time whereas the side resistance increased. They called this phenomenon stress relaxation, whereas the pile was still creeping, i.e. stress reduction was accompanied by deformation at the tip of the pile. Clearly, this phenomenon is neither creep, nor stress relaxation, but a combination of creep and stress relaxation. The structure of the sand at the pile tip was readjusted due to breakage and rearrangement of particles. As a result, the frictional shear forces on the sides were affected and the side resistance was observed to increase. However, the side resistance could not keep the pile stationary and some creep deformation was observed at the pile tip. Thus, the observed behavior at the pile tip was a combined creep-stress relaxation condition.

The stress-strain and volume change behavior observed in these five tests are shown in Fig. 7.9. Moreover, stress-strain points and corresponding energy inputs at the beginning and end of the time-dependent phases of these tests are tabulated in Table 7.1.

Fig. 7.9(b) shows that the volumetric response of the “100% creep” test follows the same trend as observed during shearing. As the involvement of creep becomes smaller and relaxation dominates, smaller amounts of axial and volumetric strains are observed. Therefore, the curves deviate from their original trends until the test of “100% relaxation” is reached in which no axial and volumetric response is achieved. Due to negligible scatter in the experimental data and to show the consistency in the comparison

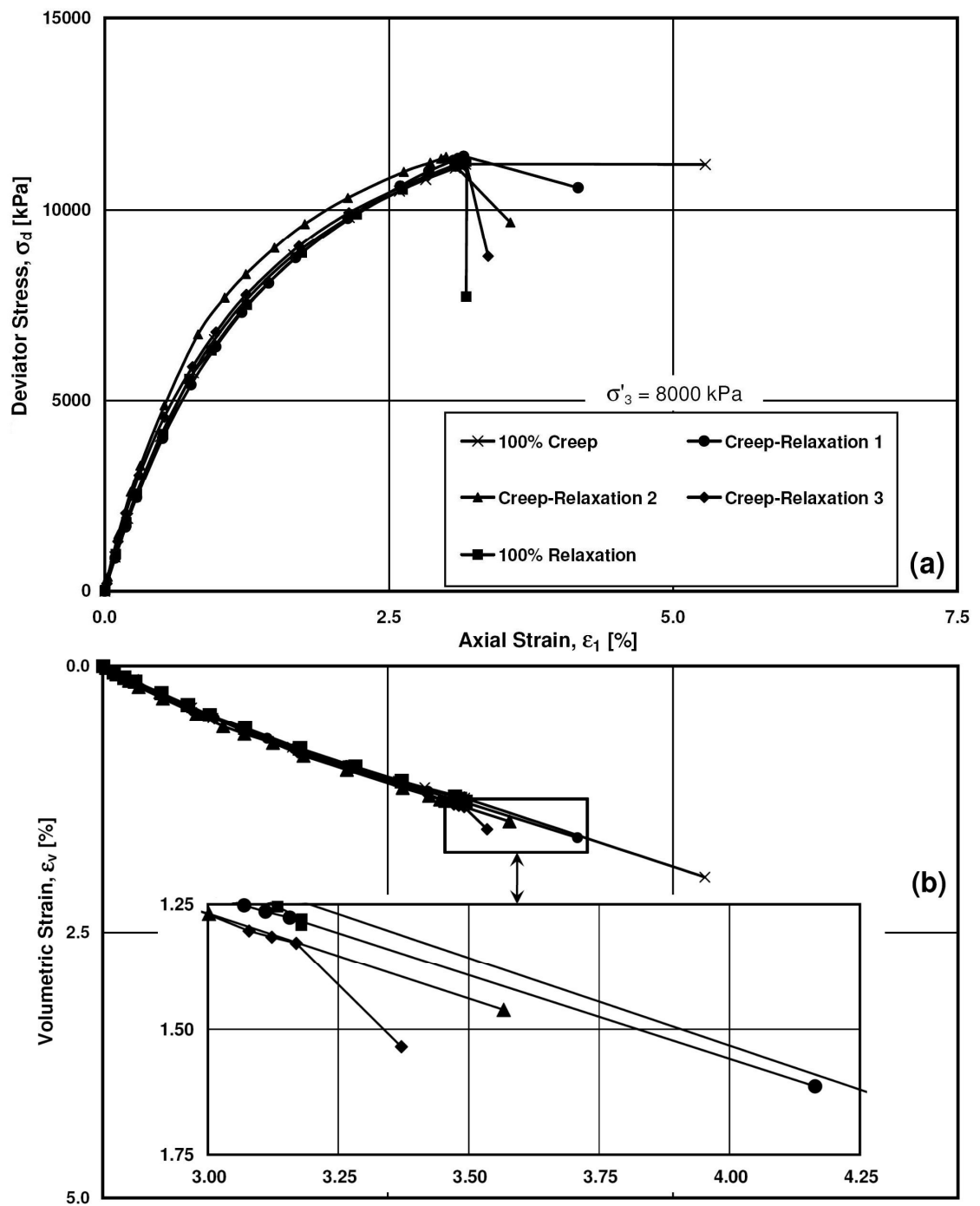


Figure 7.9. (a) Stress-strain behavior, and (b) volumetric response for combined creep-stress relaxation experiments.

Table 7.1. Stress-strain points and energy input at the beginning and end of time-dependent phases of combined creep-stress relaxation experiments.

Test	Stress-Strain Point [(σ_1 - σ_3) kPa, ϵ_1 %]		Energy Input kN.m/m ³	
	Beginning	End	Beginning	End
100% Creep	(11200, 3.17)	(11190, 5.28)	421	720
Creep-Relaxation 1	(11400, 3.16)	(10580, 4.16)	424	558
Creep-Relaxation 2	(11380, 3.00)	(9680, 3.57)	422	493
Creep-Relaxation 3	(11280, 3.17)	(8770, 3.37)	443	479
100% Relaxation	(11260, 3.18)	(7720, 3.18)	423	427

of the experimental data, the time-dependent phase of these experiments were superimposed on the corresponding reference curve from Fig. 4.10 and presented in Fig. 7.10. Points related to 10 min, 250 min, 1440 min and 10000 min have been connected with dashed lines to show the contours of progress in the time-dependent phase.

Fig. 7.11 presents the variation of deviator stress level, and the axial and volumetric strains with the logarithm of the elapsed time. In the first experiment, “100% creep”, once the desired energy input was reached, the loading was switched to load control and the specimen was allowed to creep for 1 week while the deviator stress level was consistency adjusted to remain constant. In this test, the axial and volumetric strains of 2.11% and 0.74% were achieved after 10000 min. The second test was performed by switching to load control once the input energy of 424 kN.m/m^3 was achieved. In contrast to the previous experiment, the deviator stress level was reduced smoothly in a systematic way to obtain the planned stress path while the axial and volumetric creep strains were being recorded. At the end of the time-dependent part, the stress reduction of 820 kPa, and the axial and volumetric strains of 1.01% and 0.34% were attained in the “creep-relaxation 1” test. The “creep-relaxation 2” test was performed in an innovative way, so that the deviator stress was reduced automatically. As mentioned in Chapter 3, the idea of this method came from the expansion of the load cell in relaxation tests. In the present test, a proving ring was placed in series with the load cell and the triaxial cell. As soon as an energy input of 422 kN.m/m^3 was reached, the loading stopped and the proving ring was allowed to expand thus deforming the specimen under a decreasing load. Of course,

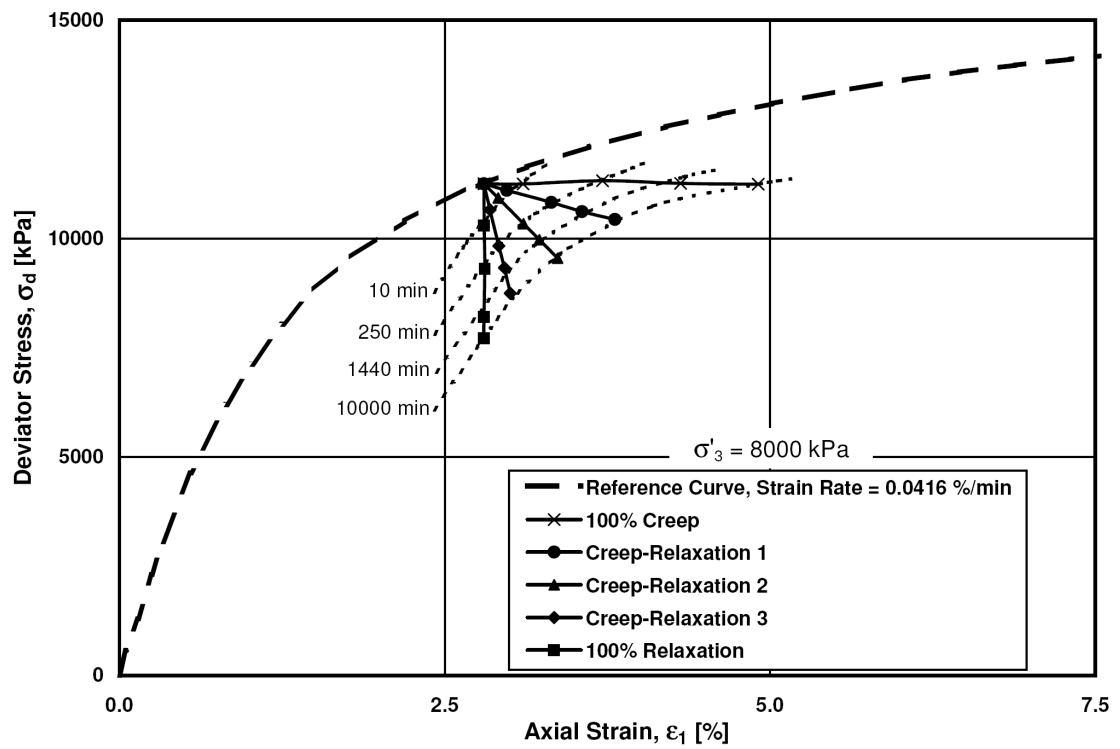


Figure 7.10. Time-dependent phase of combined creep-stress relaxation shown initially from the same points on reference stress-strain curve.

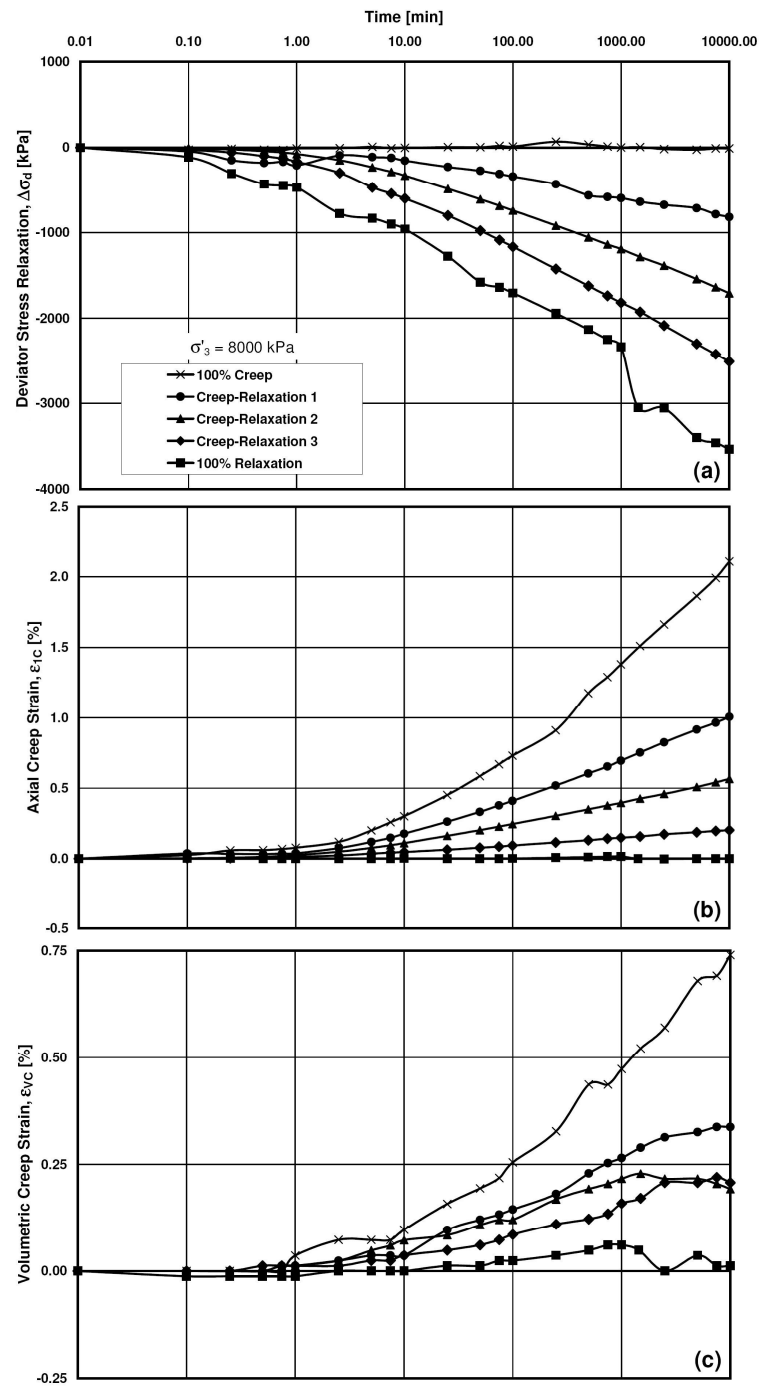


Figure 7.11. (a) Variation of deviator stress, (b) axial and (c) volumetric creep strains during time dependent phase of combined creep-stress relaxation tests.

the stiffness of the proving ring was chosen in such a way that it provided a sufficient deflection and stress reduction. The reduction of the deviator stress occurred in a very smooth pattern as seen in Fig. 7.9 and Fig. 7.10. The readings showed the stress decrease of 1710 kPa along with axial and volumetric strains of 0.57% and 0.19% at the end of 1 week.

The fourth experiment, “creep-relaxation 2”, was carried out in a manners similar to the third experiment, but with a stiffer proving ring which provided a larger stress drop with a smaller deflection during 1 week, as illustrated in Fig. 7.9 and Fig. 7.10. The stress reduction, and the axial and volumetric strains associated with this test were 2510 kPa, 0.20% and 0.21%. The “100% relaxation” test was performed in a similar manner as the other stress relaxation tests including correction of axial deformation. As expected, the largest amount of stress relaxation was observed in this experiment during which no axial and volumetric strains were captured. Similar to the explanations in the previous two sections on the subsequent creep and stress relaxation tests, the static fatigue phenomenon and soil structure are the basis of the observed behavior.

7.4. Multiple 1-Day Creep-Shear-Stress Relaxation

A multiple creep-stress relaxation test was carried out on Virginia Beach sand. In this experiment four different deviator stress levels were chosen at which 1-day creep and 1-day stress relaxation tests were performed. The stress-strain and volumetric behavior of the specimen are illustrated in Fig. 7.12. As seen, the first 1-day creep phase was initiated

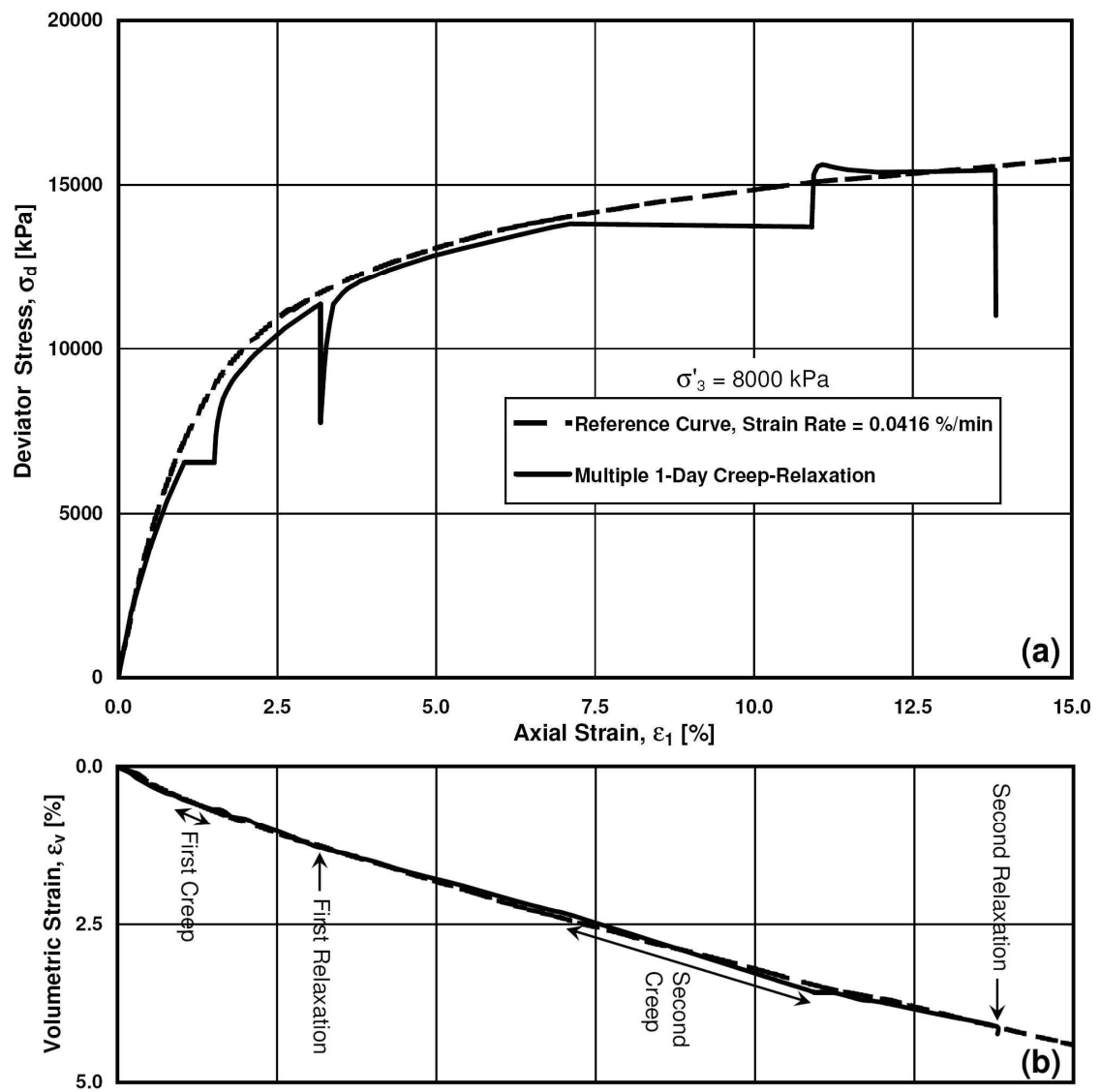


Figure 7.12. (a) Stress-strain behavior, and (b) volumetric response for multiple 1-day creep-stress relaxation experiment.

once the stress-strain point of $[(\sigma_1 - \sigma_3), \epsilon_1] = [6550 \text{ kPa}, 1.04\%]$, corresponding to energy input of 157 kN.m/m^3 , had been reached. During this period, the axial and volumetric creep strains of 0.47% and 0.16% were obtained. The loading system was switched back to deformation control to pursue further loading to the deviator stress level of 11350 kPa where the first 1-day stress relaxation started. During this phase, a stress decrease of 3582 kPa was recorded. The loading continued to the stress-strain point of $[(\sigma_1 - \sigma_3), \epsilon_1] = [13810 \text{ kPa}, 7.11\%]$ where the loading was changed to load control to maintain the stress level constant during the second 1-day creep phase. The axial and volumetric creep strains of 3.80% and 1.21% were attained at the end of the second creep phase. The specimen was further loaded to the deviator stress of 15440 kPa at which the second 1-day stress relaxation phase was performed and the stress reduction of 4450 kPa was observed.

As mentioned in Chapter 5 and Chapter 6 where multiple 1-day creep and stress relaxation experiments were presented, no structuration effect was observed when specimens were further sheared at the end of stress relaxation and creep phases. However, Fig. 7.12(a) demonstrates a very small amount of strength gain was observed after the second creep part. In terms of the volumetric behavior, Fig. 7.12(b) shows no deviation from the reference volume change curve during the time-dependent phases of the experiment. Fig. 7.13(a) illustrates the variation of axial and volumetric creep strains of the first and second 1-day creep parts of the experiment, while the decrease in deviator stress during the first and second 1-day stress relaxation phases is exhibited in Fig. 7.13(b).

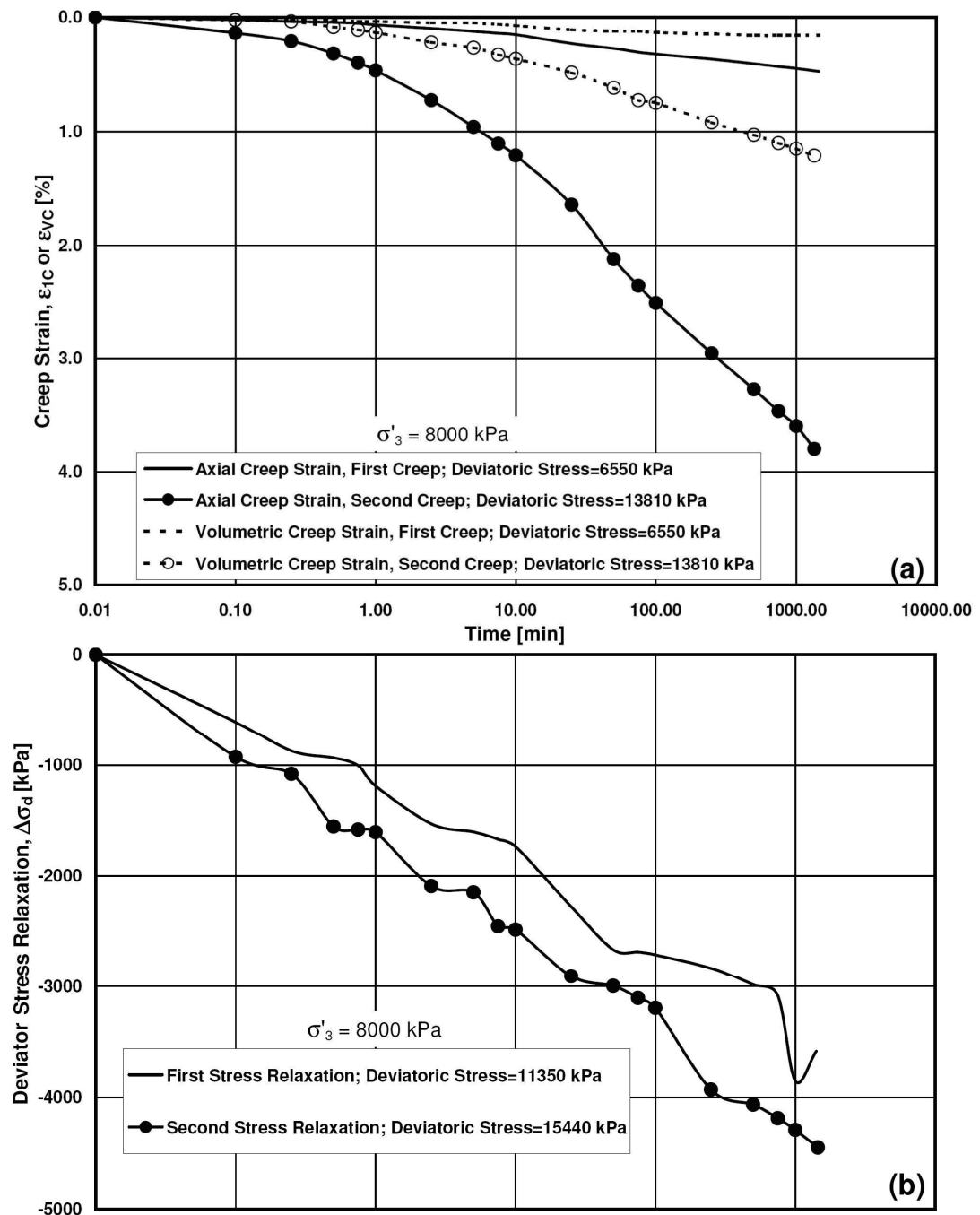


Figure 7.13. (a) Variation of axial and volumetric strains during first and second creep phases, and (b) variation of deviator stress during first and second stress relaxation phases for multiple 1-day creep-stress relaxation experiment.

The grain size distribution curves of combined creep-stress relaxation and multiple creep-stress relaxation tests are exhibited in Fig. 7.14. The largest amount of particle crushing is observed for the multiple creep-stress relaxation experiment. The “100% creep” test shows the highest amount of particle crushing among combined creep-stress relaxation tests, while the lowest belongs to “100% relaxation” test and the three other curves are located in between in a sequence according to the input energy. The Hardin’s breakage factor was then calculated and plotted in Fig. 7.15 against their energy input at the end of the experiments in Fig. 7.15. As seen, the higher the energy input, the larger the amount of crushing observed in the experiments.

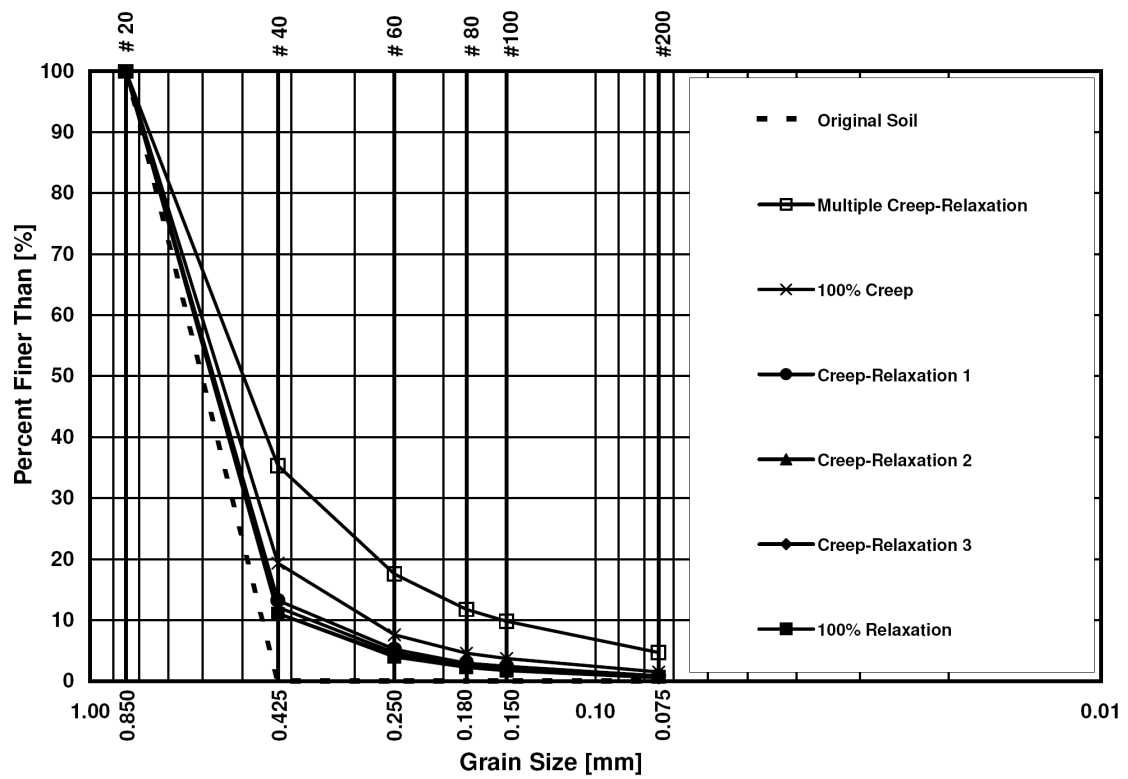


Figure 7.14. Grain size distribution curve for combined creep-stress relaxation experiments and multiple 1-day creep-stress relaxation test.

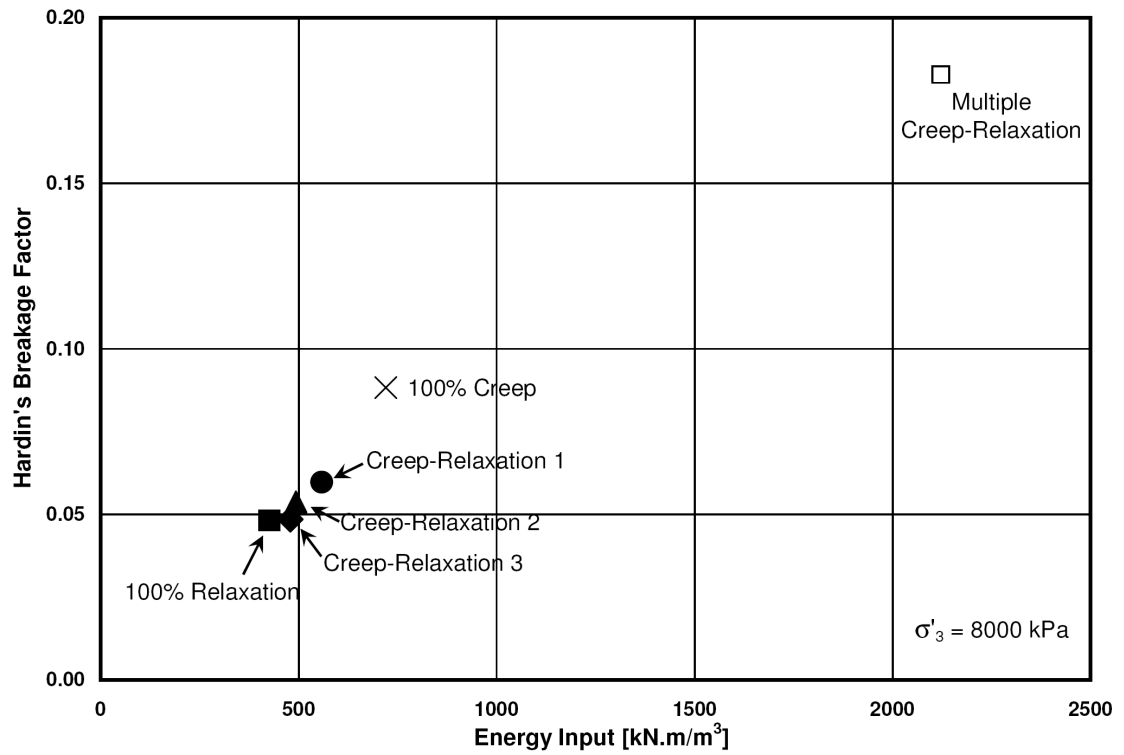


Figure 7.15. Energy input versus Hardin's breakage factor for combined creep-stress relaxation experiments and multiple 1-day creep-stress relaxation test.

8. Stress Drop-Creep and Stress Drop-Stress Relaxation

Increases in confining pressure and creep stress level to the failure strength result in an increase in the magnitude of delayed plastic deformations. Also, the closer the creep stress point is to the plastic yield surface, the higher the rate of creep strains will be. Lade (1994) and Bjerrum (1973) mentioned that the yield surface moves outward as creep proceeds, thus implying reduction in the creep strain rate as the distance between the current stress point and yield surface increases. This means that the highest creep deformation rate occurs at the moment at which creep is initiated while the current stress point is on the yield surface. To identify the creep and stress relaxation behavior of crushed coral sand at different stress points with respect to the yield surface, Lade et al. (2009, 2010) performed stress drop tests followed by creep or stress relaxation. In this chapter, a similar approach is considered for Virginia Beach sand under a confining pressure of 8000 kPa and with an initial shearing strain rate of 0.0416 %/min. In these tests, three stress drops of 0 kPa, 2500 kPa and 5000 kPa have been employed to explore the subsequent stress relaxation and creep behavior. No stress drop tests are equal to the regular creep and stress relaxation experiments as presented in Chapters 5 and 6. Tests with 2500 kPa and 5000 kPa stress drop will show the dependency of time effects on the proximity of the stress point to the yield surface.

8.1. Stress Drop-Creep Tests

8.1.1. Stress Drop-Creep

Three tests were performed to discover the influence of distance of stress point from the yield surface on the creep behavior of Virginia Beach sand. In the first experiment, the specimen was sheared to the stress point of $[(\sigma_1 - \sigma_3), \epsilon_1] = [11200 \text{ kPa}, 3.17\%]$ where it was subjected to creep for 1 week by switching to load control. The total axial and volumetric creep strains of 2.11% and 0.74% were achieved during the creep phase. The second specimen was loaded to the stress-strain point of $[11220 \text{ kPa}, 3.19\%]$ where the stress level was reduced to 8710 kPa. The creep phase initiated at this stress level and the specimen axially and volumetrically crept for 0.13% and 0.15% under load control, respectively. The third specimen was sheared to the stress-strain point of $[11354 \text{ kPa}, 3.01\%]$ and a stress drop of 5000 kPa was imposed and kept constant for 1 week. No axial deformation was observed during the creep phase, while a volume change of 0.12% was observed. It is noted that the stress drop phase of these experiments was executed under deformation control and using the same shearing strain rate as the one by which the specimens had originally been loaded, i.e. at 0.0416%/min. Fig. 8.1 shows the stress-strain and volume change curves of this series of the experiments.

The variation of the axial and volumetric creep strains have been plotted against the logarithm of the elapsed creep time in Fig. 8.2. It is seen that creep deformations are significantly reduced with an increase in amount of stress drop. However, this

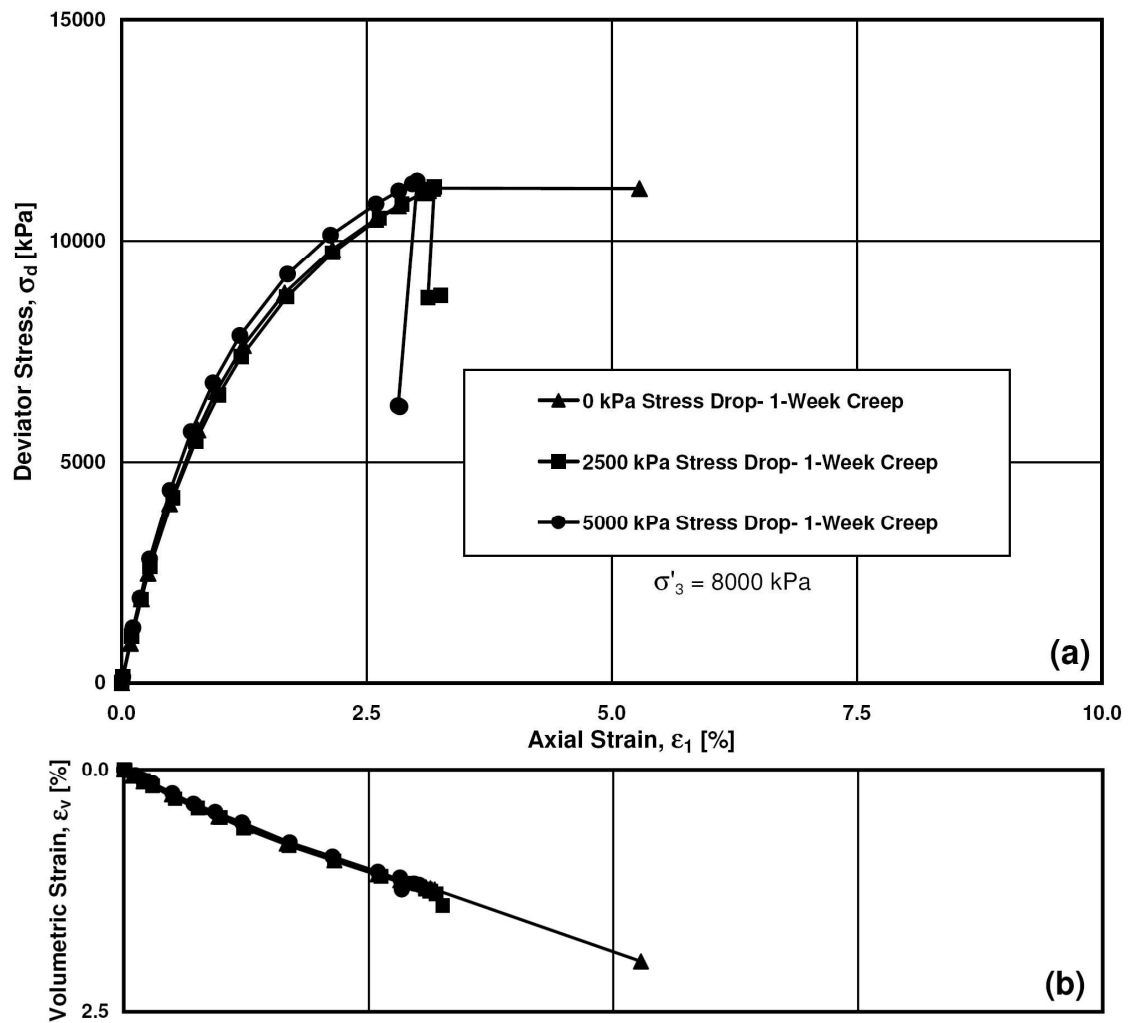


Figure 8.1. (a) Stress-strain behavior, and (b) volumetric response for stress drop- 1-week creep experiments.

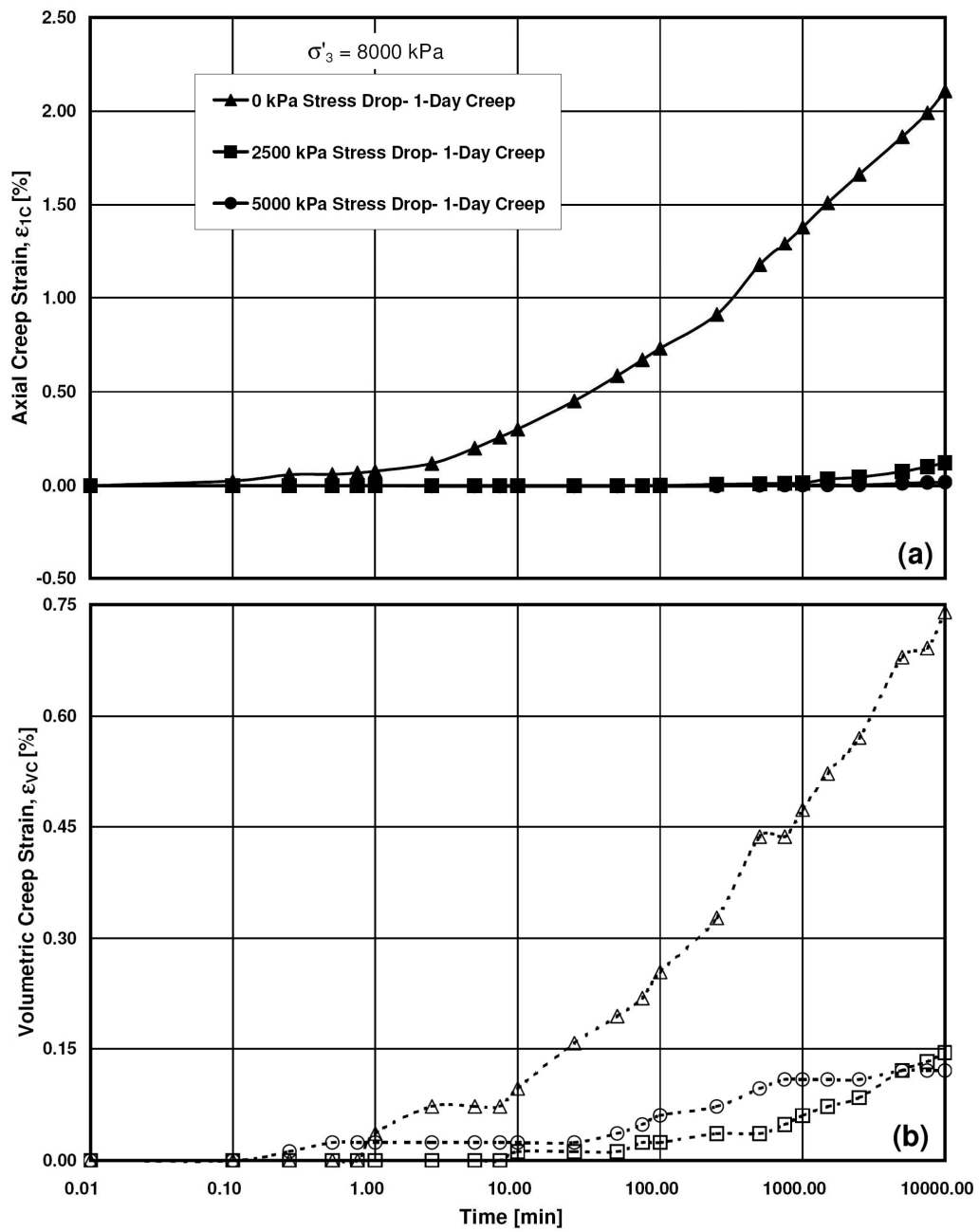


Figure 8.2. Variation of (a) axial, and (b) volumetric strains during creep.

relationship is less pronounced for volumetric creep strain. A similar observation was made in Chapter 7 where the specimens underwent stress relaxation prior to the creep phase. Lade et al. (2009) also observed the same behavior for crushed coral sand.

For the tests with zero stress drop, the creep strains are initiated as soon as the creep phase started. However, it took about 1000 minutes before axial deformations started to occur in the test with a stress drop of 2500 kPa, while the volumetric deformation were initiated after 10 minutes. In the test with a stress drop of 5000 kPa, no axial deformation was captured after 1 week creep, but the volume change began to change from the first minutes of the creep phase. In this series of tests the influence of the deviator stress level and further loading after the creep phase were not studied; therefore, in the next section a series of multiple stress drop-creep tests is explored.

8.1.2. Multiple Stress Drop-Creep

This series of experiments were performed similarly to the tests explained in the previous section. However, after the first 1-day creep phase, the specimens were further sheared to the next stress level where a stress drop was followed by another 1-day creep phase. This procedure was followed at three desired stress level for three stress drops of 0 kPa, 2500 kPa and 5000 kPa, and all three experiments ended with a 1-day stress relaxation phase. Further loading at the end of time-dependent phases also help to identify possible structuration effects in Virginia Beach sand. The stress-strain and volume change results of these tests are exhibited in Fig. 8.3. As seen, there is an

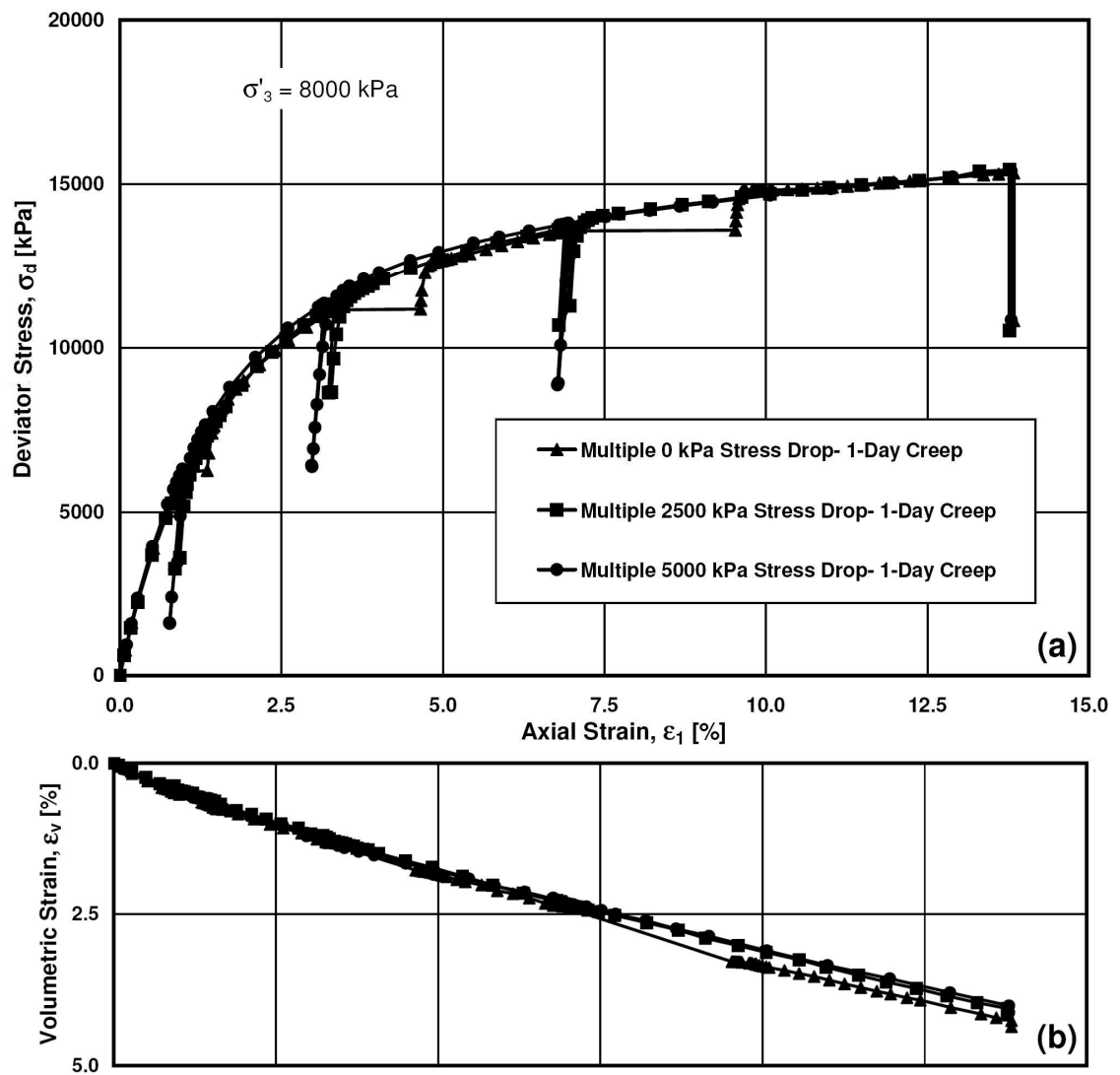


Figure 8.3. Stress-strain behavior, and (b) volumetric response for multiple stress drop-creep experiments.

excellent agreement between these results, which confirms the repeatability of the experimental program. In the first test with zero stress drop, the 1-day creep phases were initiated at the following stress-strain points: $[(\sigma_1 - \sigma_3), \epsilon_1] = [6210 \text{ kPa}, 1.01\%]$, $[11140 \text{ kPa}, 3.31\%]$, and $[13570 \text{ kPa}, 6.91\%]$. In the second test, a stress drop of 2500 kPa was imposed at the stress-strain points of $[6050 \text{ kPa}, 0.98\%]$, $[11310 \text{ kPa}, 3.32\%]$, and $[13640 \text{ kPa}, 6.88\%]$ before each 1-day creep phase. In the last experiment of this series, a stress drop of 5000 kPa was employed. The stress-strain points at which the stress drops were imposed were $[6310 \text{ kPa}, 0.97\%]$, $[11340 \text{ kPa}, 3.16\%]$, and $[13812 \text{ kPa}, 6.94\%]$. In contrast to crushed coral sand, it was observed in Fig. 8.3 that Virginia Beach sand does not show structuration effects when subjected to shearing after experiencing creep conditions for some amount of time. This confirms the findings in Chapter 5 regarding the lack of structuration effects in Virginia Beach sand.

The variation of axial and volumetric strains with the logarithm of time for each creep phase of the experiments in the present test series is shown in Fig. 8.4. As observed, the specimen with no stress drop has experienced the largest axial and volumetric creep strains for all three creep phases and the difference between these results becomes larger at higher stress levels. Moreover, the experiment with stress drop of 2500 kPa exhibits larger creep deformations in comparison to the tests with stress drop of 5000 kPa. This confirms that the higher the stress drop is, the lower the following creep strains will be. The axial and volumetric creep deformations at the end of 1 day creep together with the deviator stress level at which creep had been initiated have been tabulated in Table 8.1 for the sake of better comparison.

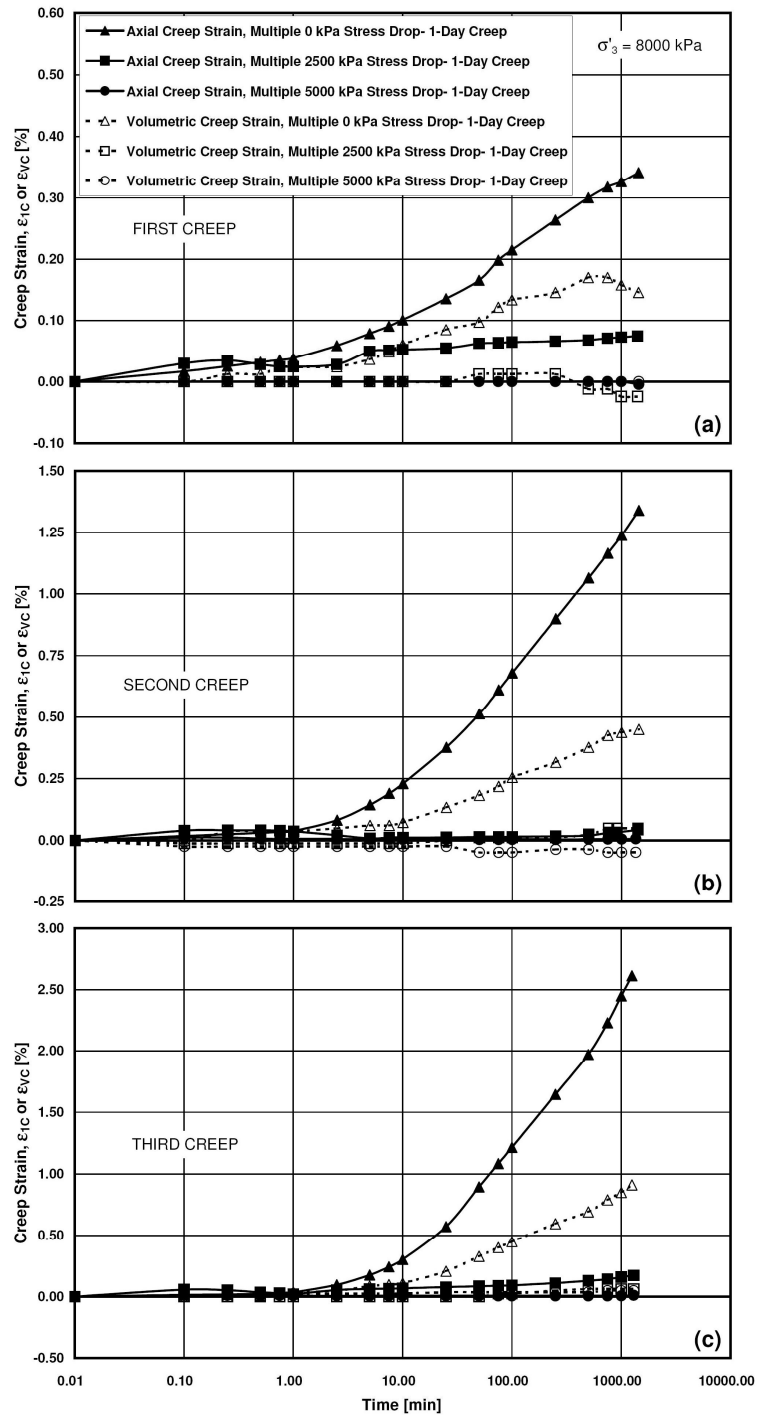


Figure 8.4. Variation of axial and volumetric creep strains during (a) first, (b) second, and (c) third creep phase of multiple stress drop-creep experiments.

Table 8.1. Details of multiple stress drop-creep experiments.

Experiments	Stress Drop								
	0 kPa			2500 kPa			5000 kPa		
	σ_d [kPa]	ϵ_{1C} [%]	ϵ_{VC} [%]	σ_d [kPa]	ϵ_{1C} [%]	ϵ_{VC} [%]	σ_d [kPa]	ϵ_{1C} [%]	ϵ_{VC} [%]
First Creep	6210	0.34	0.15	3250	0.07	-0.02	1580	0.01	0.00
Second Creep	11140	1.34	0.45	8620	0.04	0.05	6420	0.01	-0.05
Third Creep	13570	2.61	0.91	10680	0.17	0.06	8860	0.01	0.05
Total Energy Input at the end of test [kN.m/m ³]	2110			2110			2130		

As a general trend, creep at higher deviator stresses results in larger creep deformations, as also confirmed in Chapter 5. This trend is observed clearly for the test with no stress drops involved. However, it is not as pronounced for the tests with stress drop of 2500 kPa. On the other hand, for the tests with stress drop of 5000 kPa, almost no creep deformations are captured, independent of the creep deviator stress level. Similar to the previous multiple creep and stress relaxation experiments, no signs of structuration were detected during the reloading process at the end of each time dependent phase.

According to studies by Lade et al. (2009, 2010), an identical potential surface may be used to estimate the plastic and creep deformations, depending on the soil type. This was also observed in Chapter 5, where the creep deformations did not deviate from the reference curves. Since in the classic constitutive models no plastic deformation and subsequently no plastic potential surface is defined for stress points inside the yield surface, observing inelastic deformations with time after a stress drop requires defining a separate surface for predicting creep deformations. However, more experiments are required to make a more rigid conclusion.

To identify the particle crushing and its connection to the observed time effects in these tests, sieve analyses were performed on all specimens. Fig. 8.5 shows the grain size distribution curves for stress drop-creep experiments. Approximately the same grading curves have been achieved for 1-week creep tests after stress drops of 2500 kPa and 5000 kPa. In comparison, the 1-week creep test with no stress drop showed a larger amount of particle crushing. Moreover, a similar grain size distribution curve was obtained for

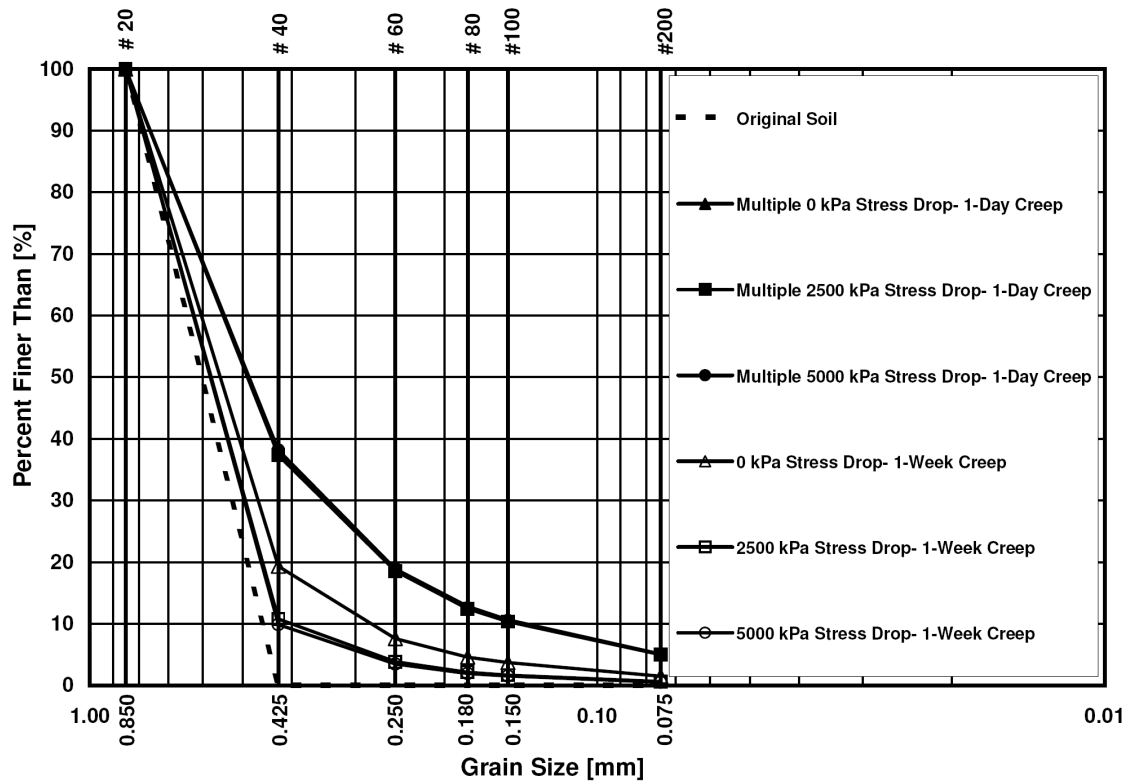


Figure 8.5. Grain size distribution curves for stress drop-creep experiments.

multiple stress drop-creep experiments. The mechanism behind these observations may be explained in terms of the energy input and Hardin's breakage factor which was calculated from Fig. 8.5 for each individual test. Fig. 8.6 illustrates the variation of the final energy input with respect to the Hardin's breakage factors for stress drop-creep experiments. As it can be seen and was shown in Table 8.1, more or less the same amount of energy (during the same time periods) has been applied to the specimens of multiple stress drop-creep tests, thus indicating a similar amount of particle crushing due to the static fatigue phenomenon. This also is observed for the 1-week creep tests with stress drops of 2500 kPa and 5000 kPa. Therefore, analogous grain size distribution curves have been attained.

8.2. Stress Drop-Stress Relaxation Tests

A similar approach as used in the stress drop-creep tests was considered for stress drop relaxation experiments. These tests have been categorized into the following two groups: stress drop- stress relaxation and multiple stress drop-stress relaxation.

8.2.1. Stress Drop-Stress Relaxation

As mentioned in Chapter 3, three stress drop- 1-week stress relaxation experiments were performed. These tests were initiated similarly to the original stress relaxation experiments explained in Chapter 6. However, stress drops of 0 kPa, 2500 kPa, and 5000 kPa were imposed once the deviator stress of approximately 11250 kPa had been achieved. This was done under deformation control and with the same shearing strain rate as the one specimens had been sheared with prior to the stress drop. The exact

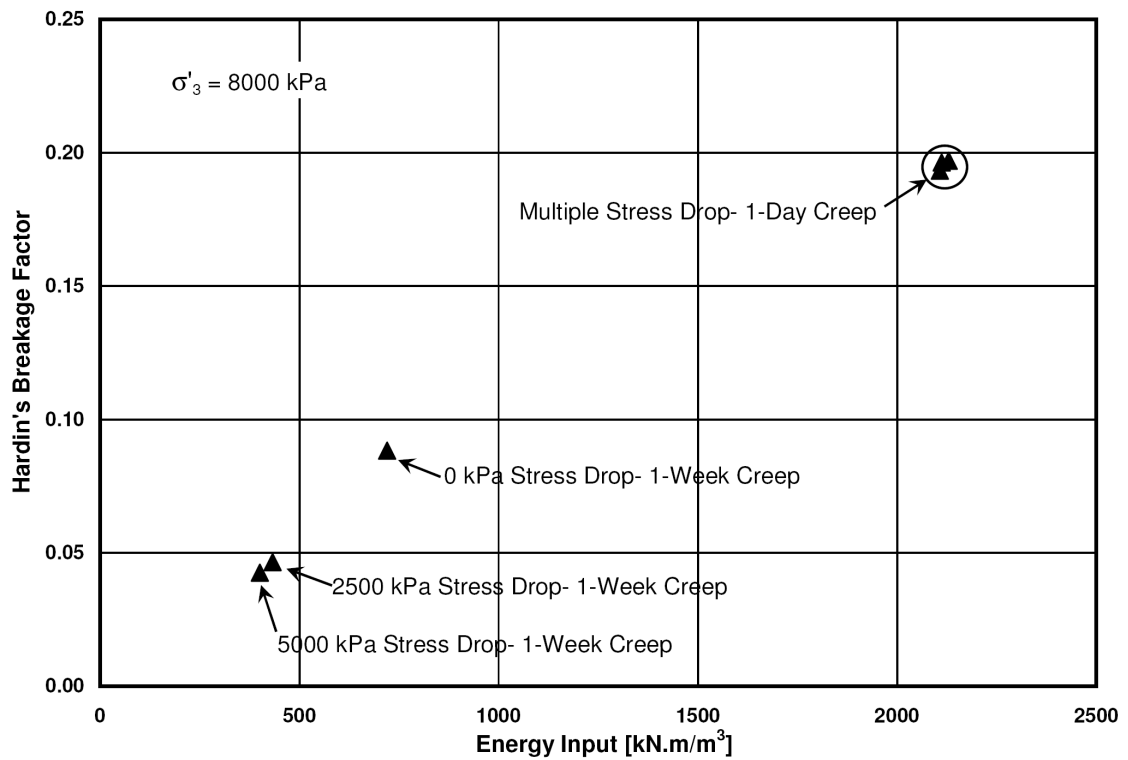


Figure 8.6. Variation of Hardin's breakage actor with the energy input for stress drop-creep experiments.

stress-strain points, where the stress drop phase initiated were $[(\sigma_1 - \sigma_3), \epsilon_1] = [11260 \text{ kPa}, 3.18\%]$, $[11260 \text{ kPa}, 3.21\%]$ and $[11280 \text{ kPa}, 3.31\%]$ for the lowest to the highest stress drop. Once the desired stress drop was obtained, 1-week stress relaxation phases were initiated. The test with no stress drop underwent stress reduction of 3540 kPa over the course of 1 week. However, the specimen which experienced a stress drop of 2500 kPa showed a stress relaxation of 1370 kPa during the same period of time. In the third specimen with a stress drop of 5000 kPa, a stress decrease of 280 kPa was observed after 1 week stress relaxation. The results of stress-strain and volumetric response of these three tests are shown in Fig. 8.7, while the detailed variation of deviator stress level with respect to the logarithm of the elapsed stress relaxation time is plotted in Fig. 8.8.

While no considerable volume change had been detected previously during stress relaxation experiments, the observed large volume change during the stress relaxation phase of the test with a stress drop of 5000 kPa, shown in Fig. 8.7(b), is associated with a small leak in the specimen membrane. This is clearly seen in Fig. 8.8 where the variation of volume change of 0, 2500 and 5000 kPa stress drop- 1 week stress relaxation experiments with the logarithm of time are compared. The tests with stress drop of 0 and 2500 kPa exhibited approximately no change in volumetric response within 1-week of stress relaxation, whereas in the tests with stress drop of 5000 kPa, the volumetric strain curve started to deviate from two other curves after 100 minutes when the leak probably occurred. Since these experiments were performed under drained condition, a leak in the membrane does not affect the recorded stress relaxation.

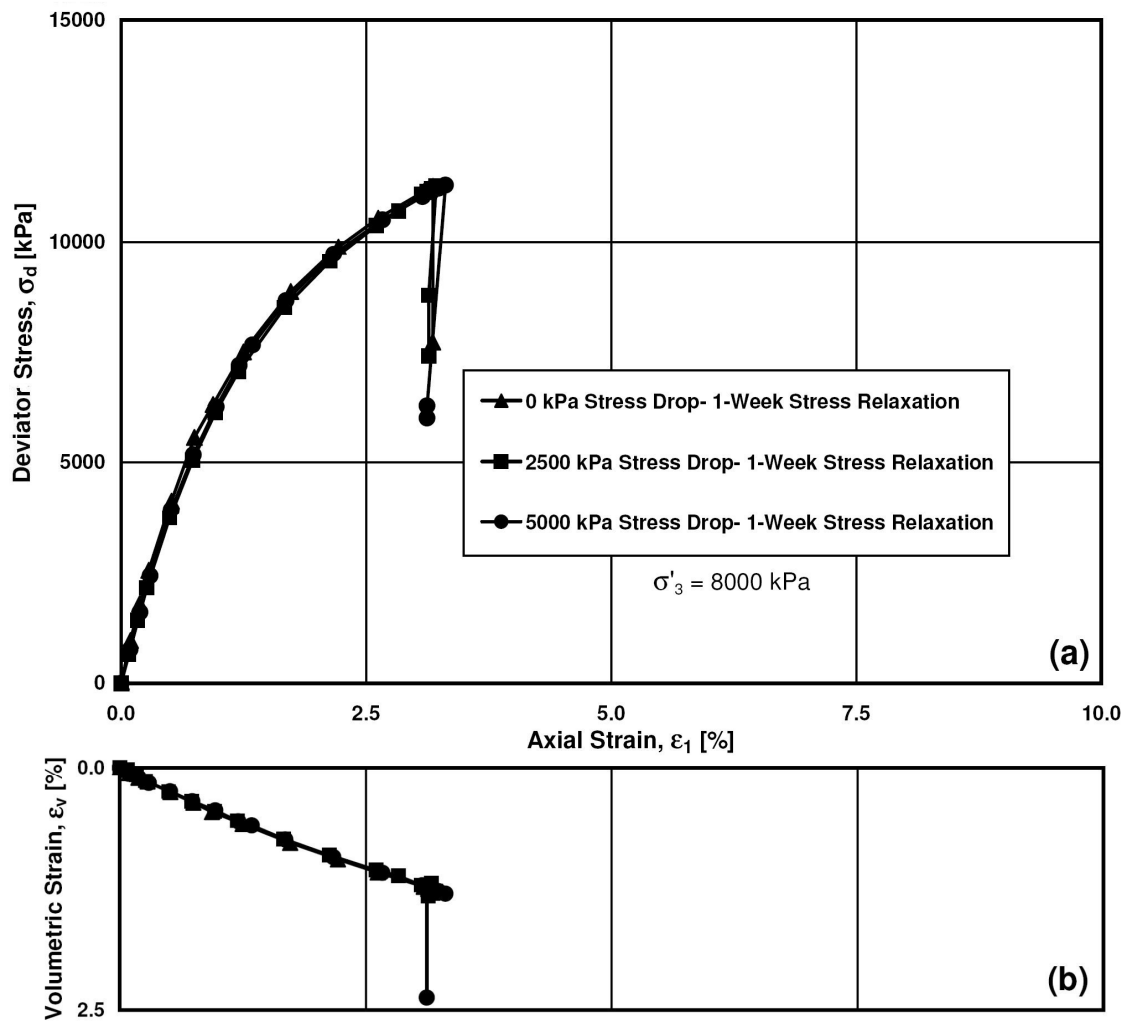


Figure 8.7. (a) Stress-strain behavior, and (b) volumetric response for stress drop- 1-week stress relaxation experiments.

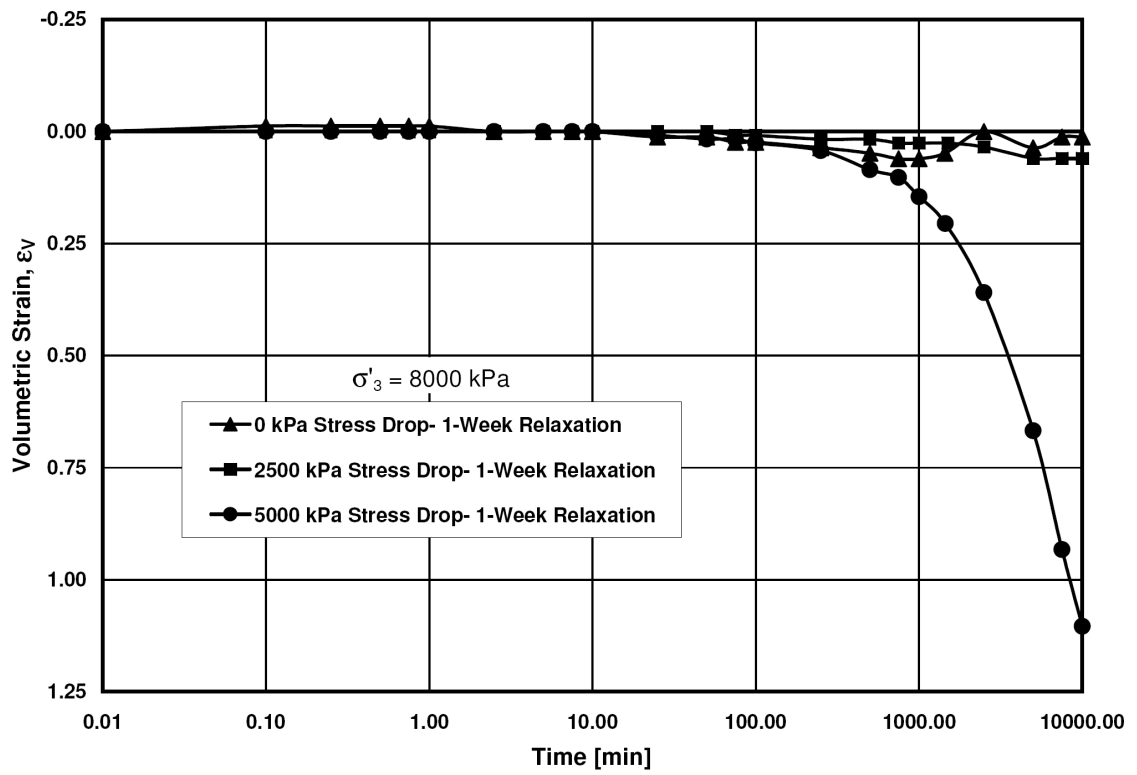


Figure 8.8. Variation of volume change with time for stress drop- 1- week stress relaxation experiments.

As seen in Fig. 8.9, once the stress relaxation is initiated, there is a delay time for the deviator stress level to start relaxing whose magnitude depends on the prior stress drop. Lade et al. (2010) also reported this type of response for crushed coral sand. The first experiment that involved no stress drop immediately showed stress reduction when deformation was stopped. The largest stress relaxation was attained in this test. Interestingly, once the stress relaxation phase was initiated, the other two specimens showed small stress increases within the first 10 min. After this period, the deviator stress level began to reduce, while the rate of stress relaxation in the test with a stress drop of 2500 kPa was more pronounced than the specimen undergoing a stress drop of 5000 kPa. As a pattern, larger stress drops result in longer time delays before the deviator stress begins to reduce and in smaller amounts of stress relaxation.

8.2.2. Multiple Stress Drop-Stress Relaxation

In a similar manner to the stress drop-creep tests, three experiments were performed to explore the effect of the location of the current stress point on the subsequent stress relaxation. Also, by further shearing of the specimens at the end of each time-dependent phase, structuration phenomenon could be studied. Three tests involving stress drops of 0 kPa, 2500 kPa and 5000 kPa at three different deviator stress levels were performed. All three specimens were subjected to a final 1-day stress relaxation phase at an axial strain of about 13.80%. It is noted that the axial deformation was consistently adjusted to correct for the effect of the application of axial loads due to expansion of the load cell. Fig. 8.10 shows the stress-strain and volumetric response of these experiments. The graph clearly indicates repeatability of the experimental results.

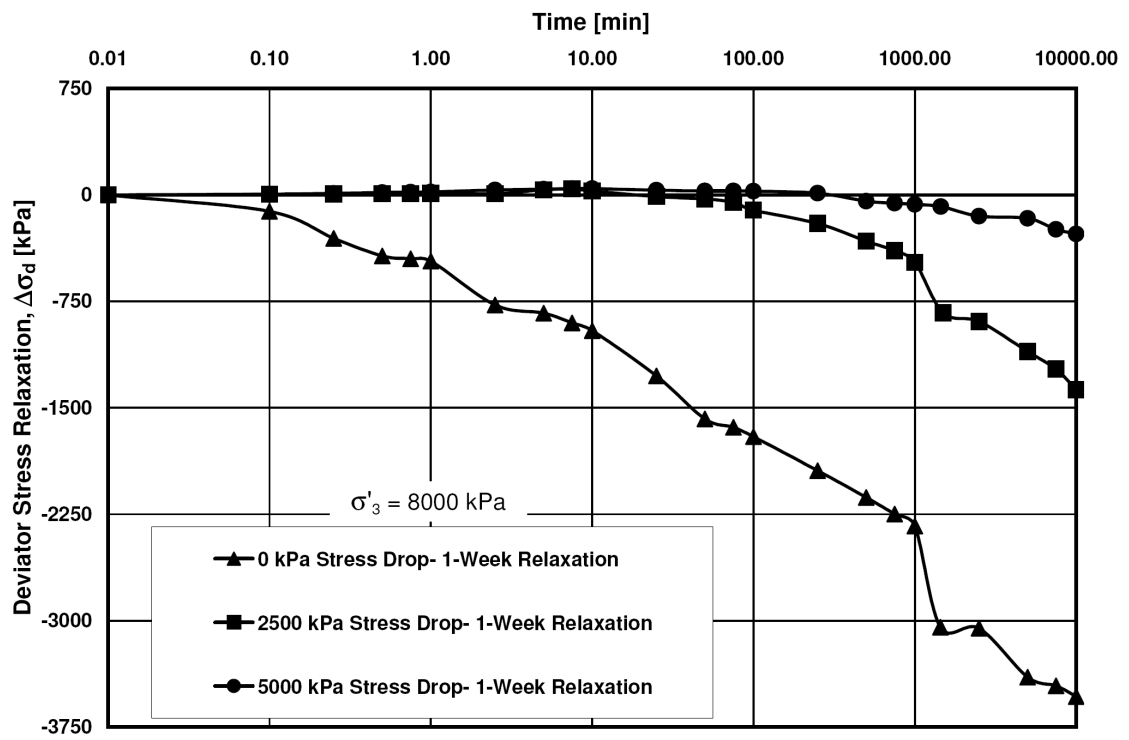


Figure 8.9. Variation of deviator stress level with creep time for multiple stress drop- 1-week stress relaxation experiments.

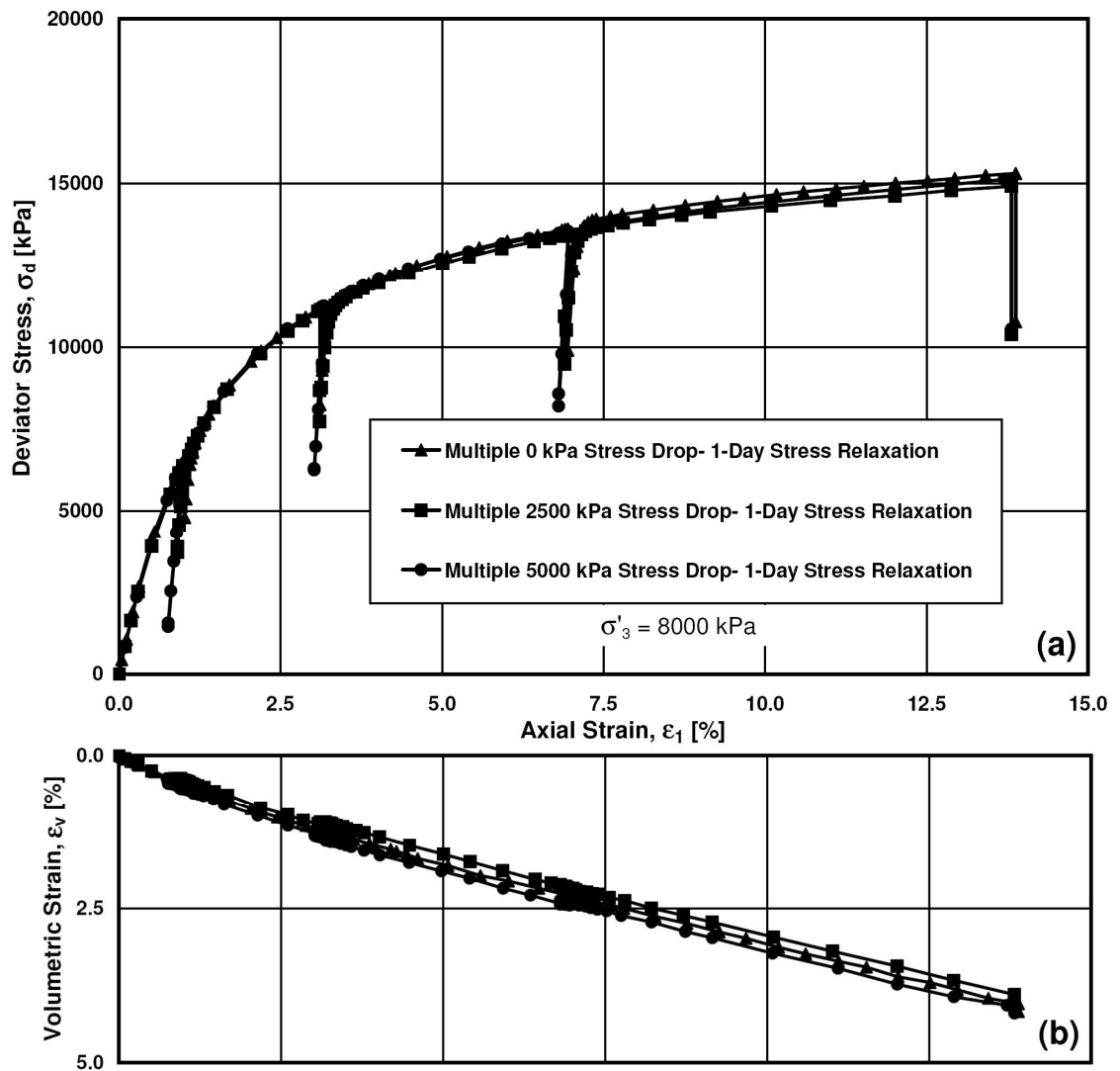


Figure 8.10. Stress-strain behavior, and (b) volumetric response for multiple stress drop-stress relaxation experiments.

In the test with no stress drop, the three 1-day stress relaxation phases were performed at stress-strain points of $[(\sigma_1 - \sigma_3), \epsilon_1] = [6620 \text{ kPa}, 1.01\%]$, $[11180 \text{ kPa}, 3.11\%]$ and $[13620 \text{ kPa}, 6.95\%]$, and stress relaxations of 1820 kPa, 2940 kPa and 3720 kPa were recorded, respectively. For the test with stress drops of 2500 kPa, the specimen was sheared to the following stress points to perform the stress drop prior to 1-day stress relaxation phases: $[6380 \text{ kPa}, 0.98\%]$, $[11190 \text{ kPa}, 3.17\%]$ and $[13440 \text{ kPa}, 6.96\%]$. After imposing the stress drop, stress reductions of 170 kPa, 940 kPa and 1450 kPa were achieved. In the third test, stress drops of 5000 kPa was enforced at stress levels of $[6410 \text{ kPa}, 0.98\%]$, $[11260 \text{ kPa}, 3.17\%]$ and $[13540 \text{ kPa}, 6.95\%]$ subsequently, the specimen was subjected to 1-day stress relaxation phases and deviator stress decreases of -120 kPa, 40 kPa and 380 kPa were attained. As seen, during the first stress relaxation phase of the latter experiment, the deviator stress level was increased. This is further shown in Fig. 8.11 where the detailed variation of the deviator stress level with respect to the logarithm of elapsed stress relaxation time is plotted.

Fig. 8.11(a) illustrates the first stress relaxation phase of the three experiments. The specimen with no stress drop experienced stress drop as soon as the deformation stopped. However, in the second experiment, once the stress drop of 2500 kPa was imposed, the deviator stress level increased slightly for the first 2.5 min and started to decrease slowly with time. After 50 min, the stress level reached back to the value from which the stress relaxation phase had been started. In the test with a stress drop of

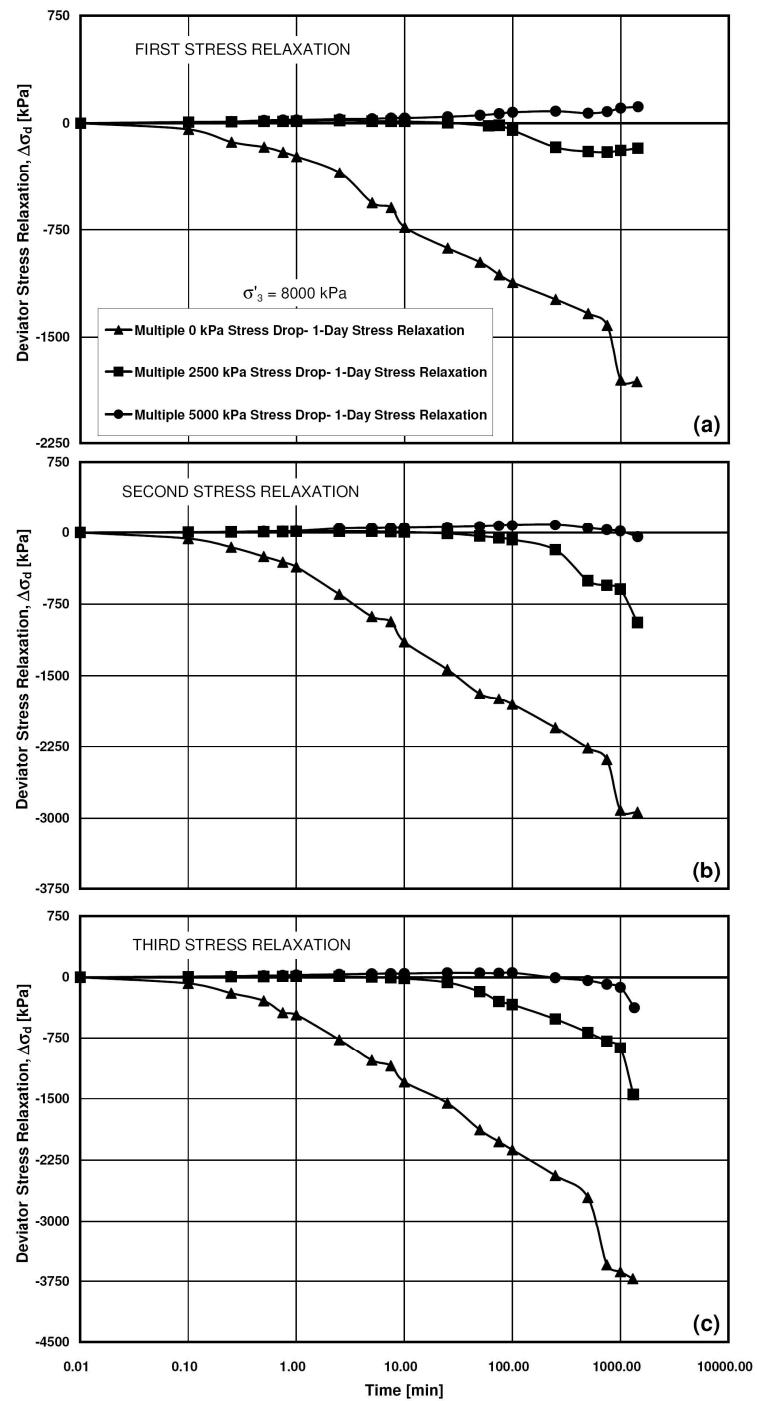


Figure 8.11. Variation of the deviator stress level during (a) first, (b) second, and (c) third stress relaxation phase for multiple stress drop-creep experiments.

5000 kPa, the stress level started to increase immediately when the stress drop was completed and unloading was stopped. Interestingly, while the recording lasted (1440 min) the stress level continued to increase.

The second stress relaxation phase is shown in Fig. 8.11(b). The experiment with zero stress drop behaved as it did in the first stress relaxation phase. In other words, once the loading stopped, the stress level began to decrease. However, the final stress reduction after 1 day increased 61% in comparison with the first stress relaxation phase. Also, in the test with a stress drop of 2500 kPa, a similar behavior to the first stress relaxation phase was observed in which the stress level increased for 2.5 min and started to reduce subsequently at a higher rate relative to that observed in the first phase. Therefore, as explained above, a much higher stress reduction was achieved after 1 day. In the third test, when the stress drop of 5000 kPa was applied, the deviator stress increased by 80 kPa in the first 250 min before it started to decrease.

An analogous trend to the second stress relaxation was obtained in the third phase as illustrated in Fig. 8.11(c). For the test with no stress drop, the specimen experienced stress reduction as soon as shearing stopped, while the deviator stress began to increase for 1 min in the second experiment. Afterwards, a regular stress reduction was observed at a higher rate in comparison to its previous two stress relaxation phases. In the test with a stress drop of 5000 kPa, the deviator stress level increased by 60 kPa in the first 100 min after which it began to decrease.

As a general trend, it was observed that the rate of stress reduction increases with the stress level at which stress relaxation begins. Furthermore, when a specimen experiences a stress drop before initiating stress relaxation, there would be a delay in the beginning of stress reduction; the larger the stress drop is, the longer the delay will be. Also, it is seen that if the stress drop is high enough, there might be a reverse effect. In other words, at the beginning of stress relaxation, the deviator stress level increases for a period of time (depending on the amount of stress drop and deviator stress level) before the stress reduction initiates.

Lade et al. (2009) performed stress drop-creep tests on crushed coral sand and noted that for significant amounts of stress drop, a negative axial creep strain was achieved for a period of time. They related this behavior to the Bauchinger effect i.e. the stress point reaching the kinematic yield surface inside the plastic yield surface during unloading which activates the creep deformations as soon as unloading stops. They speculated that after a period of time, the specimen realizes that the effective deviator stress is still positive; as a result, creep deformations change direction and compressive creep deformation is recorded. Lade et al. (2010) also performed stress drop-stress relaxation experiments on crushed coral sand and captured the same type of behavior as observed for Virginia Beach sand, i.e. a slight increase in deviator stress level is observed for a period of time after specimens were subjected to a sufficiently large stress drop. They speculated that this was the mirror effect of that observed in the case of stress drop-creep experiments. That is, the increase in the deviator stress cannot carry on and the

increments of stress increase reduce with time. Subsequently, their direction changes and the deviator stress decreases over longer periods of time.

Particle crushing during stress drop-stress relaxation experiments has been studied by performing sieve analyses before and after each experiment. Fig. 8.12 illustrates the grain size distribution curves for these experiments. As seen for each group of stress drop-stress relaxation experiments, a similar grain size curve has been obtained. This is due to applying a same amount of energy input during the same period of time (Table 8.2). Also, the variation of Hardin's breakage factor with respect to the energy input has been plotted in Fig. 8.13. This figure once more confirms that a higher energy input results in larger amounts of particle crushing, provided that it is applied in a same period of time.

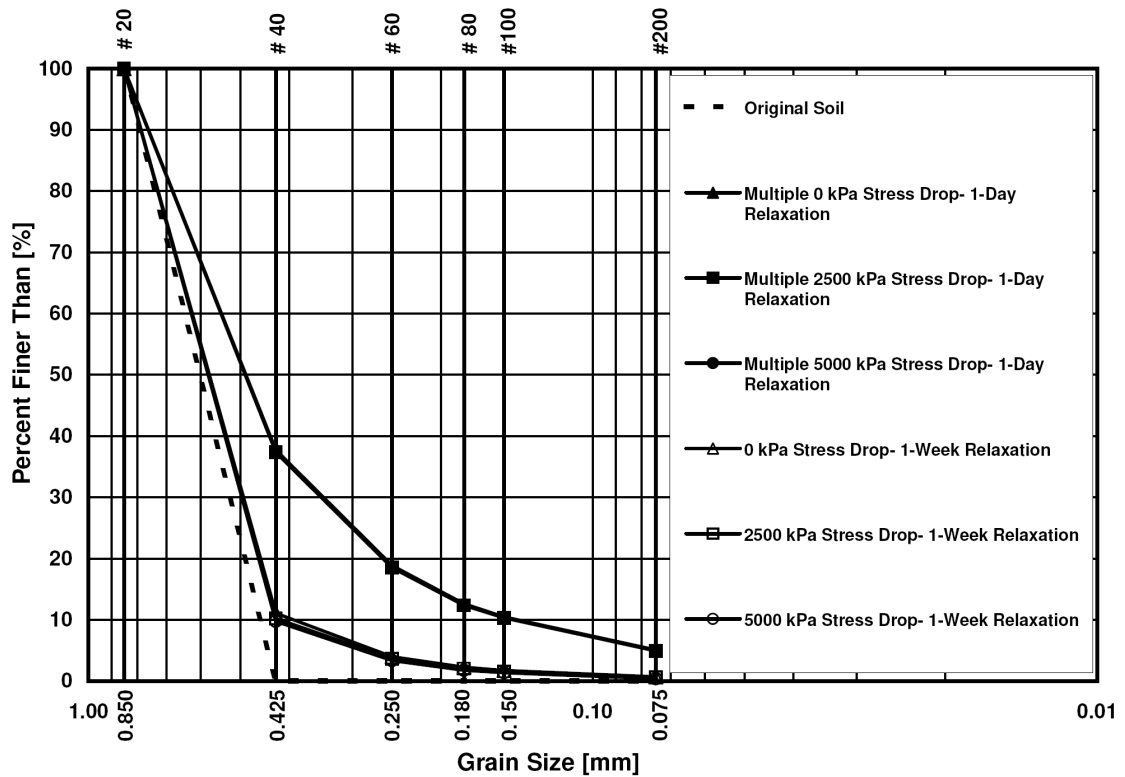


Figure 8.12. Grain size distribution curve for stress drop-stress relaxation experiments.

Table 8.2. Hardin's breakage factor and energy input for stress drop-stress relaxation experiments.

Experiments	Hardin's Breakage Factor	Energy Input [kN.m/m ³]
0 kPa Stress Drop- 1-week Relaxation	0.196	2150
2500 kPa Stress Drop- 1-week Relaxation	0.193	2080
5000 kPa Stress Drop- 1-week Relaxation	0.194	2110
Multiple 0 kPa Stress Drop- 1-day Relaxation	0.048	430
Multiple 2500 kPa Stress Drop- 1-day Relaxation	0.044	420
Multiple 5000 kPa Stress Drop- 1-day Relaxation	0.041	430

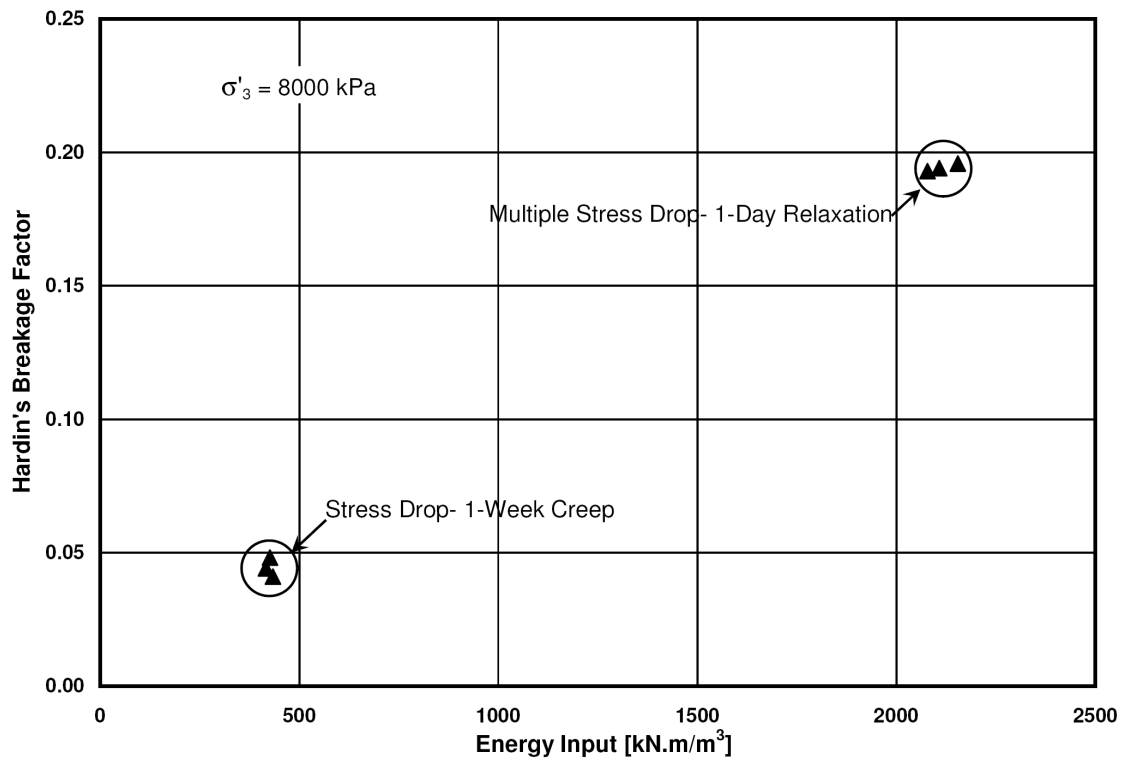


Figure 8.13. Variation of Hardin's breakage factor with the energy input for stress drop-stress relaxation experiments.

9. Sieve Analyses

After presenting the results of sieve analyses for individual series of experiments in the previous chapters, the relation between Hardin's breakage factor and energy input is studied in the following groups of tests:

9.1. Particle Crushing During Isotropic Compression

Three isotropic experiments were conducted up to confining pressures of 6000, 8000 and 12000 kPa to obtain a better understanding of breakage factor-energy input relations during isotropic compression. The sieve analyses results shown in Fig. 9.1 indicate that very small amounts of particle crushing occurred during isotropic compression tests.

Fig. 9.2 illustrates the variation of Hardin's breakage factor versus energy input for these tests. As seen, particle crushing increases with the amount of energy input similar to the data exhibited in previous chapters. The best linear trendline for the variation of particle crushing versus energy input under isotropic condition has been plotted to compare these data with data from triaxial compression tests. Energy input is only a function of volumetric strain under isotropic compression conditions and the variation of Hardin's breakage factor is also plotted against the applied confining pressure in Fig. 9.3. It is noted that assuming a linear trend between breakage factor and confining pressure may overestimate the prediction of breakage factor at higher stresses.

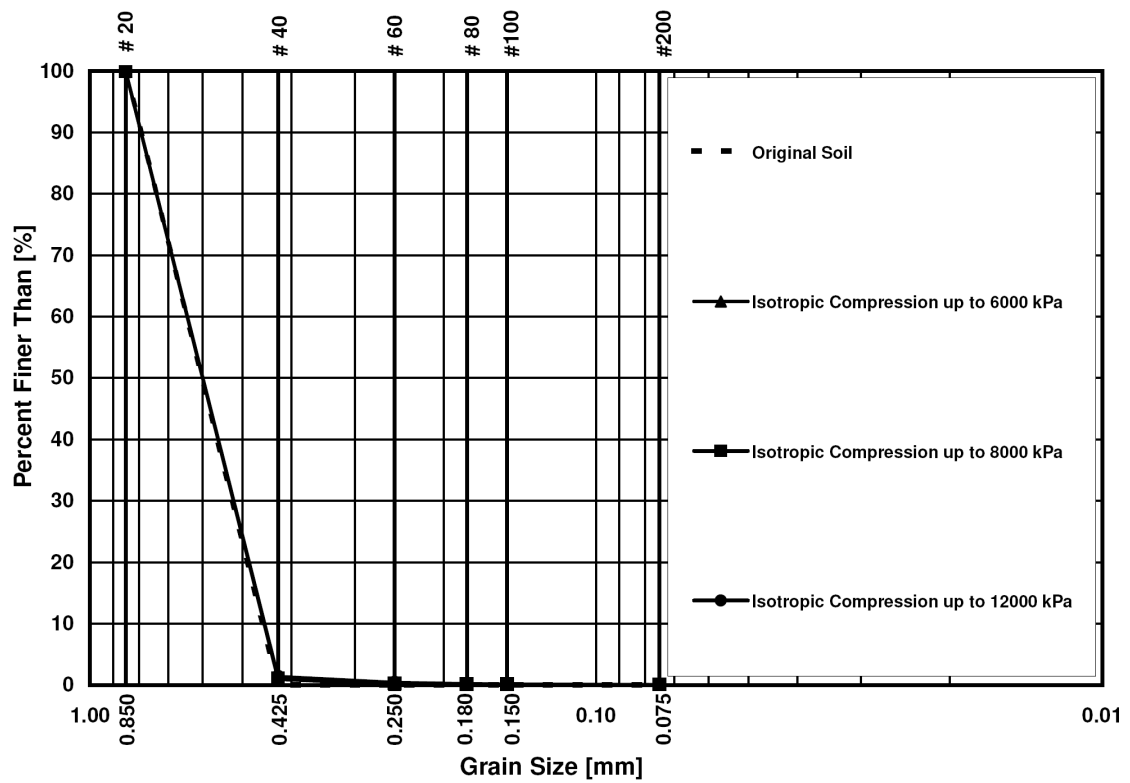


Figure 9.1. Grain size distribution curves for isotropic compression tests.

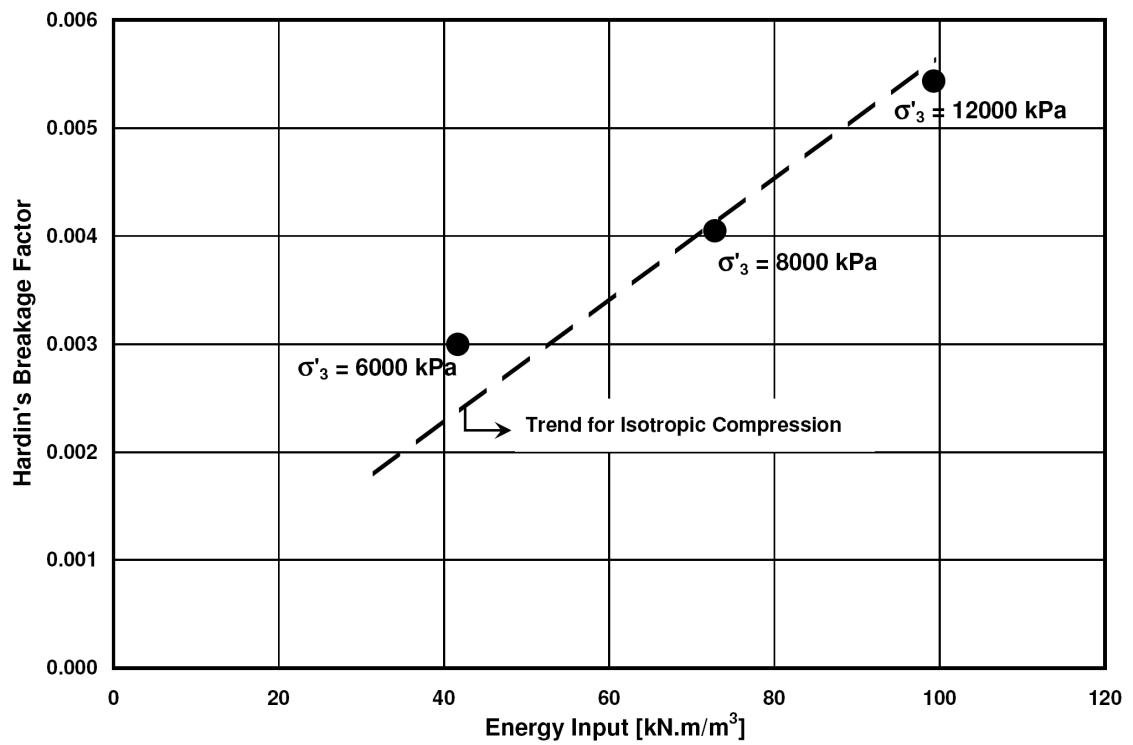


Figure 9.2. Hardin's breakage factor versus energy input for isotropic compression tests.

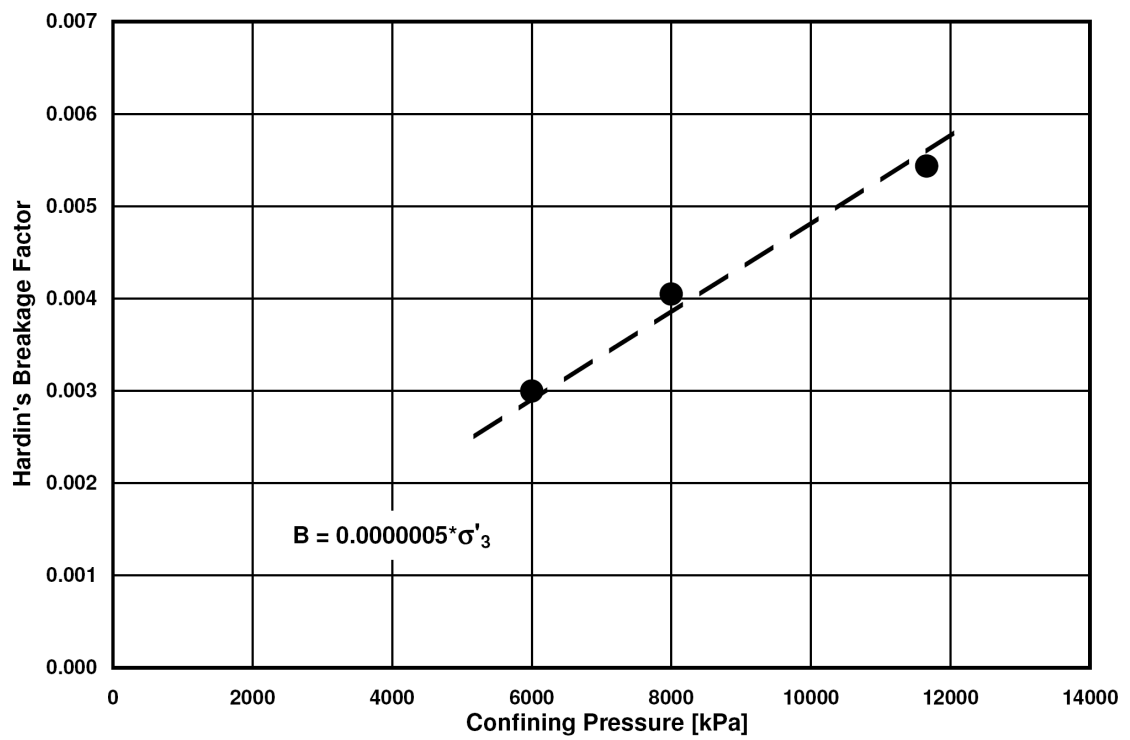


Figure 9.3. Hardin's breakage factor versus confining pressure for isotropic compression tests.

The reason may be associated with increase in coordination number and reduction in forces acting at grains contacts as particle crushing progresses. However, the linear trend is indicated in Fig. 9.2 and Fig. 9.3 for ease in comparisons.

9.2. Particle Crushing During Triaxial Compression

9.2.1. Effect of Confining Pressure

Grain size distribution curves for a series of triaxial compression tests performed at a strain rate of 0.0416 %/min up to axial strains of 22% over a wide range of confining pressures varying from 25 kPa to 14000 kPa are shown in Fig. 9.4. Subsequently, the variation of calculated breakage factors against energy input is plotted in Fig. 9.5 along with the trendline for isotropic compression tests from Fig. 9.2.

By comparison between the results of particle crushing during isotropic compression and triaxial compression, it is found that a much larger amount of particle crushing is produced during shearing. As a case in point, it is observed that a triaxial test performed under a confining pressure of 25 kPa has experienced the same amount of grain breakage as does the isotropic compression test up to 8000 kPa. Nakata et al. (1999) observed a similar behavior and stated that shearing produces more severe crushing than isotropic compression, because shearing forms strong force chains that transmit the major principal stress. In spite of the fact that the linear relationship between breakage factor and confining pressure shown in Fig. 9.3 may underestimate the confining pressures at higher stresses, as explained earlier, it can be calculated that the required confining pressure to create a Hardin's breakage factor of 0.254 corresponding to point 8 on

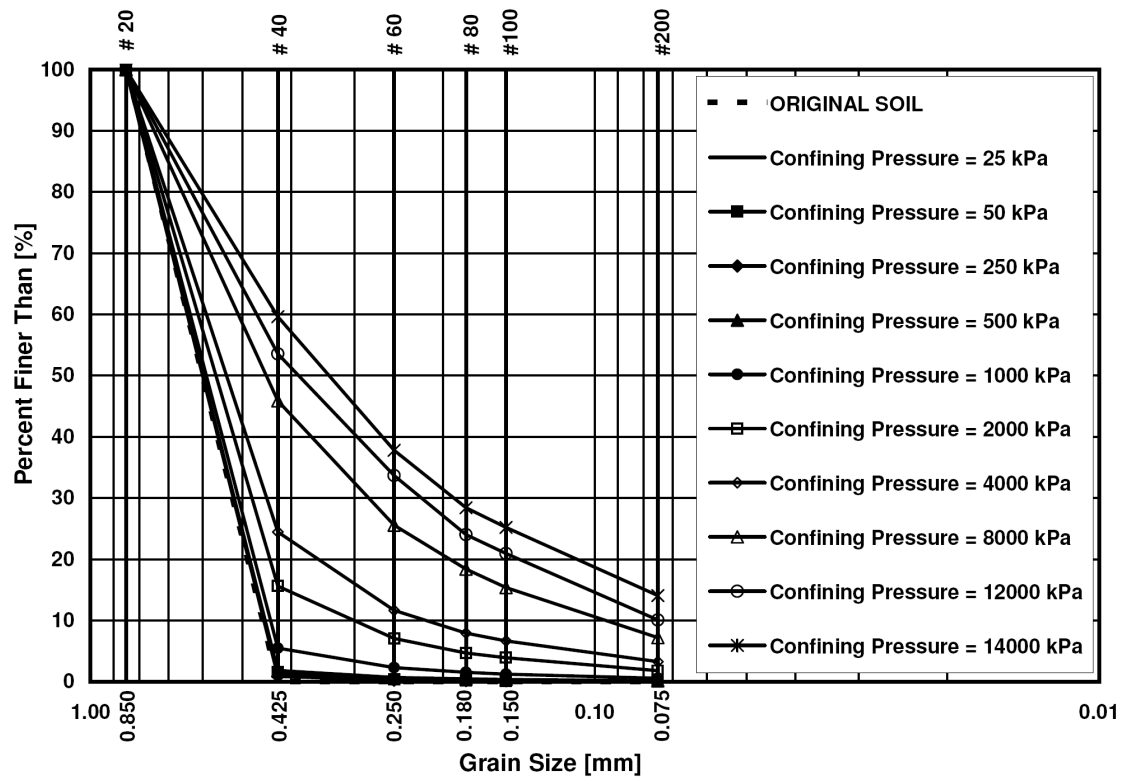


Figure 9.4. Grain size distribution curves for triaxial compression tests under different confining pressures.

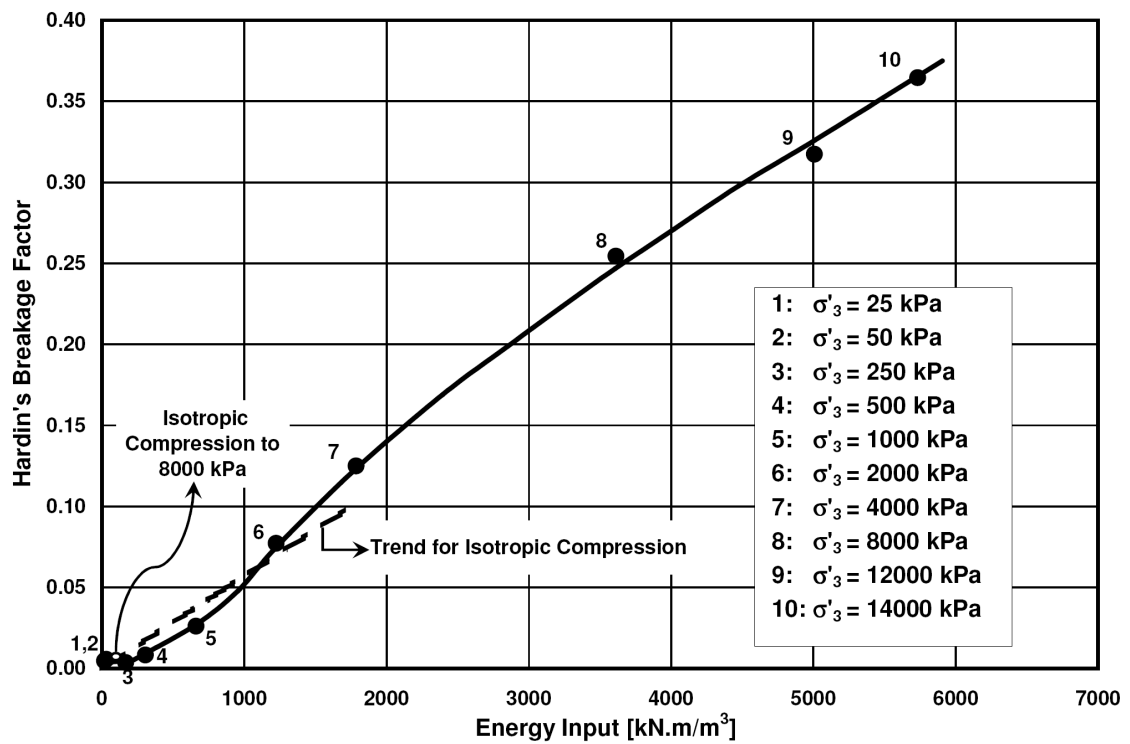


Figure 9.5. Hardin's breakage factor versus energy input for triaxial compression tests under different confining pressures.

Fig. 9.5 (22% of axial strain in a triaxial compression test under confining stress of 8000 kPa) is equal to 508000 kPa. Sieving results also implies that in tests performed at larger confining pressures, Hardin's breakage factor varies at higher rates than at lower confining pressures.

9.2.2. Effect of Shearing Strain Rate

The results of sieve analyses of all experiments performed at a confining pressure of 8000 kPa are shown in Fig. 9.6 together with the observed linear trend for isotropic compression tests from Fig. 9.2. Since it was observed in Chapter 6 that negligible particle crushing occurs and negligible energy is applied during stress relaxation tests, the results shown in Fig. 9.6 include the data of stress relaxation experiments as well. These tests were performed at three strain rates of 0.00260, 0.0416 and 0.666 %/min. A point corresponding to breakage and energy input under isotropic compression of 8000 kPa is also illustrated in Fig. 9.6. The variation of particle breakage factor versus energy input is proposed by a trendline for each strain rate according to the presented results. Obviously, specimens sheared at lower strain rates have experienced larger amount of crushing, while higher strain rates have produced smaller particle breakage factors. According to the static fatigue hypothesis, this is mainly because shorter time periods were available for particle crushing in specimens sheared at higher strain rates.

9.3. Particle Crushing During Creep

Two series of creep experiments are employed to show the effect of shearing strain rate prior to creep and confining pressure on the amount of particle crushing during

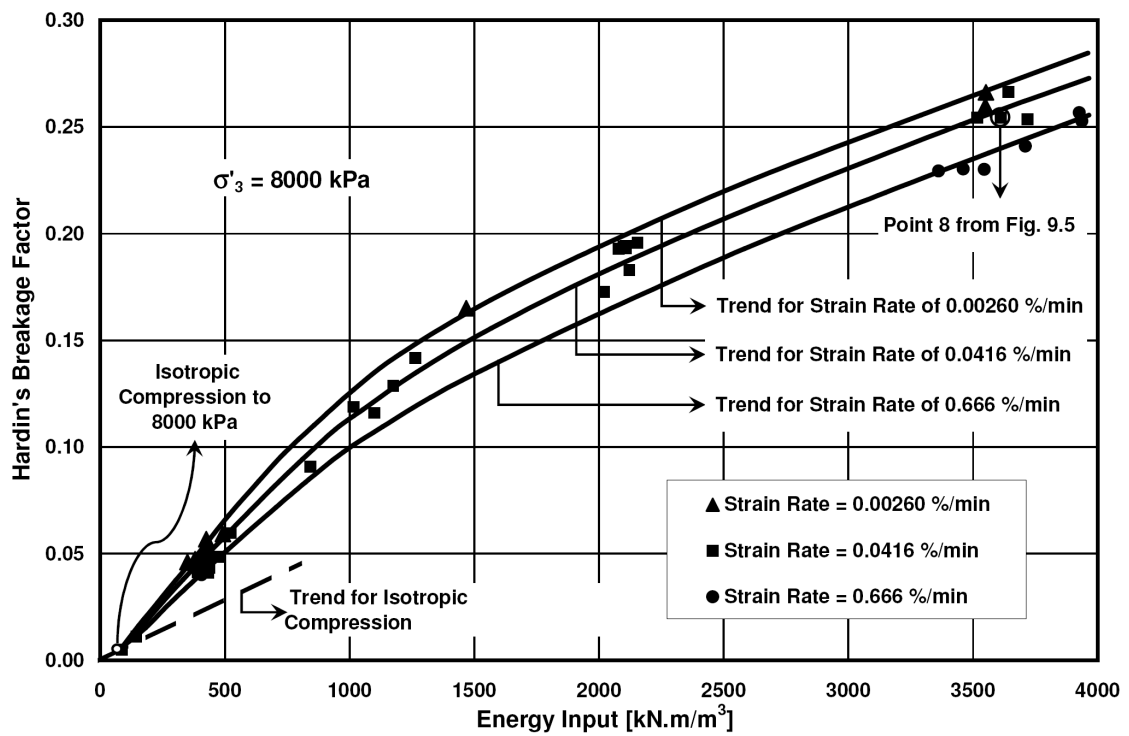


Figure 9.6. Hardin's breakage factor versus energy input for triaxial compression tests under confining pressure of 8000 kPa.

creep and to illustrate effects of creep time on the subsequent particle crushing. Fig. 9.7 and Fig. 9.8 show the grain size distribution curves for experiments presented in the first test series discussed in Chapter 4, while the particle crushing-energy input relations for these experiments are plotted in Fig. 9.9. In these figures, points “1 and 7”, “2 and 8” and “3 and 9” are associated with tests that have been performed at the three strain rates of 0.00260, 0.0416 and 0.666 %/min up to initiation of creep testing, whereas points of “4 and 10”, “5 and 11” and “6 and 12” correspond to 1-day creep tests at the same rates, respectively. Therefore, the distances illustrated with arrows between these points indicate the amount of particle crushing that occurred during creep. As seen, more or less the same points have been achieved for experiments performed with a confining stress of 250 kPa as shown in the inserted diagram with magnified axes in Fig 9.9. Small discrepancies observed in the magnified zone can be considered to be experimental scatter. However, considerable differences are observed for tests carried out with the confining pressure of 8000 kPa. In general, as seen in Fig. 9.6, a larger amount of breakage is achieved at lower strain rates for the same amount of energy input. This fits perfectly in the concept of static fatigue explained in previous chapters.

Fig. 9.10 and Fig. 9.11 show the grain size distribution curves and their particle crushing-energy input relations for creep experiments lasting for over different time periods. Point “1” corresponds to the beginning of creep tests, while points “2”, “3” and “4” are associated with creep time periods of 3 hours, 1 day and 1 week. The trends of particle breakage versus energy input for isotropic compression conditions and triaxial

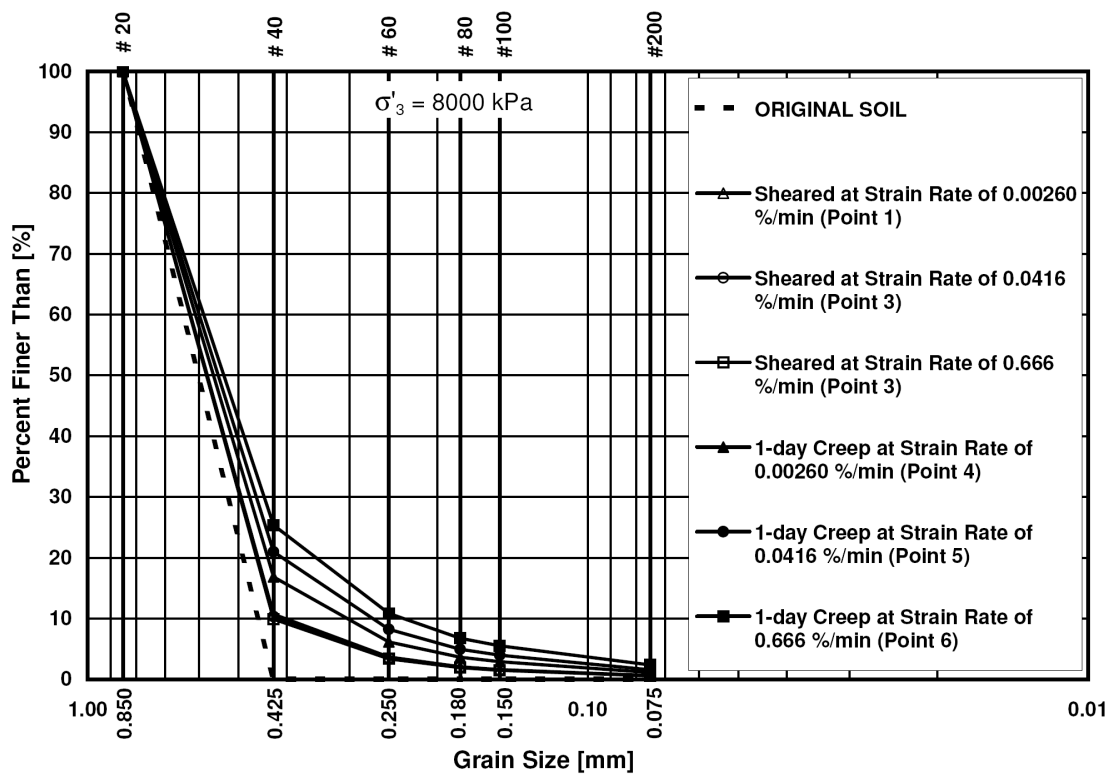


Figure 9.7. Grain size distribution curves for creep experiments under confining pressure of 8000 kPa.

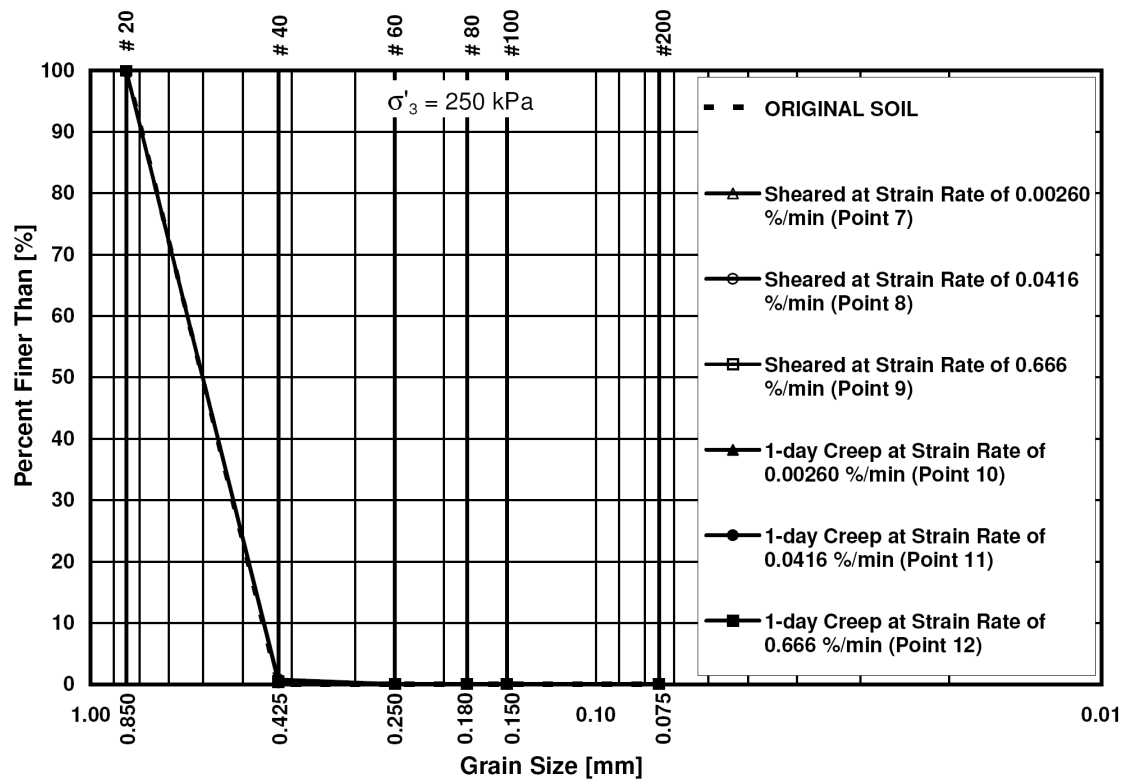


Figure 9.8. Grain size distribution curves for creep experiments under confining pressure of 250 kPa.

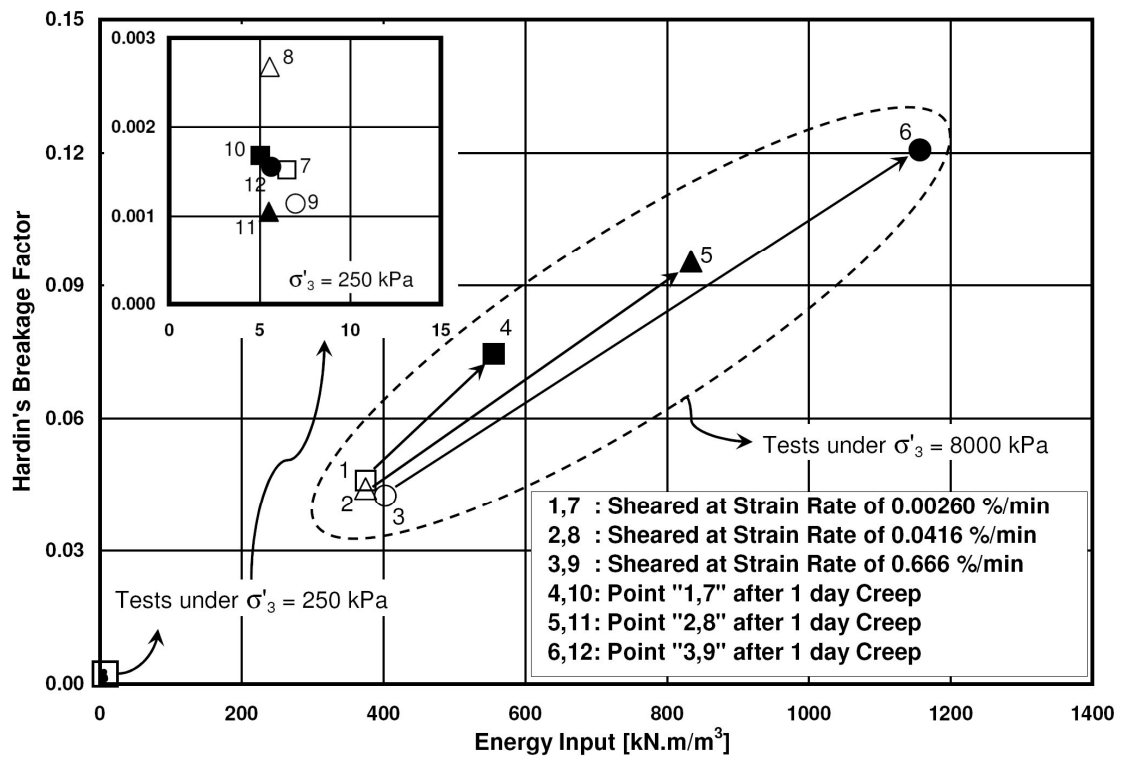


Figure 9.9. Hardin's breakage factor versus energy input for creep experiments under confining pressure of 250 and 8000 kPa.

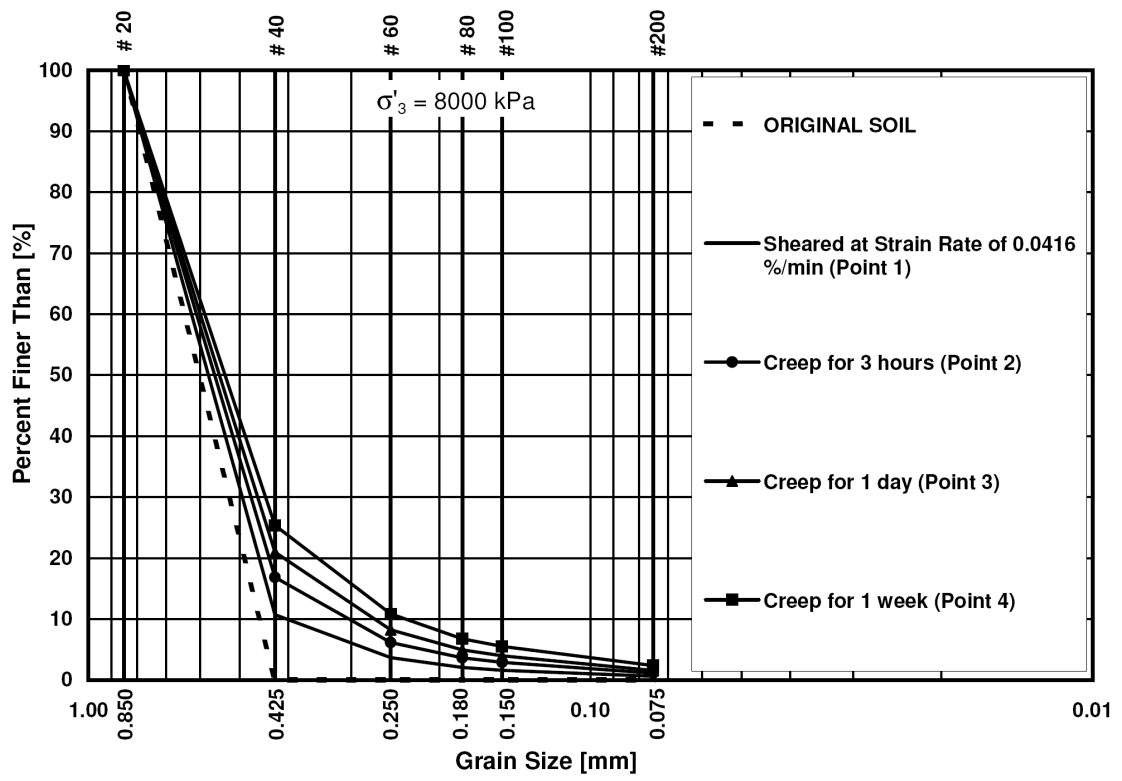


Figure 9.10. Grain size distribution curves for creep experiments under confining pressure of 8000 kPa.

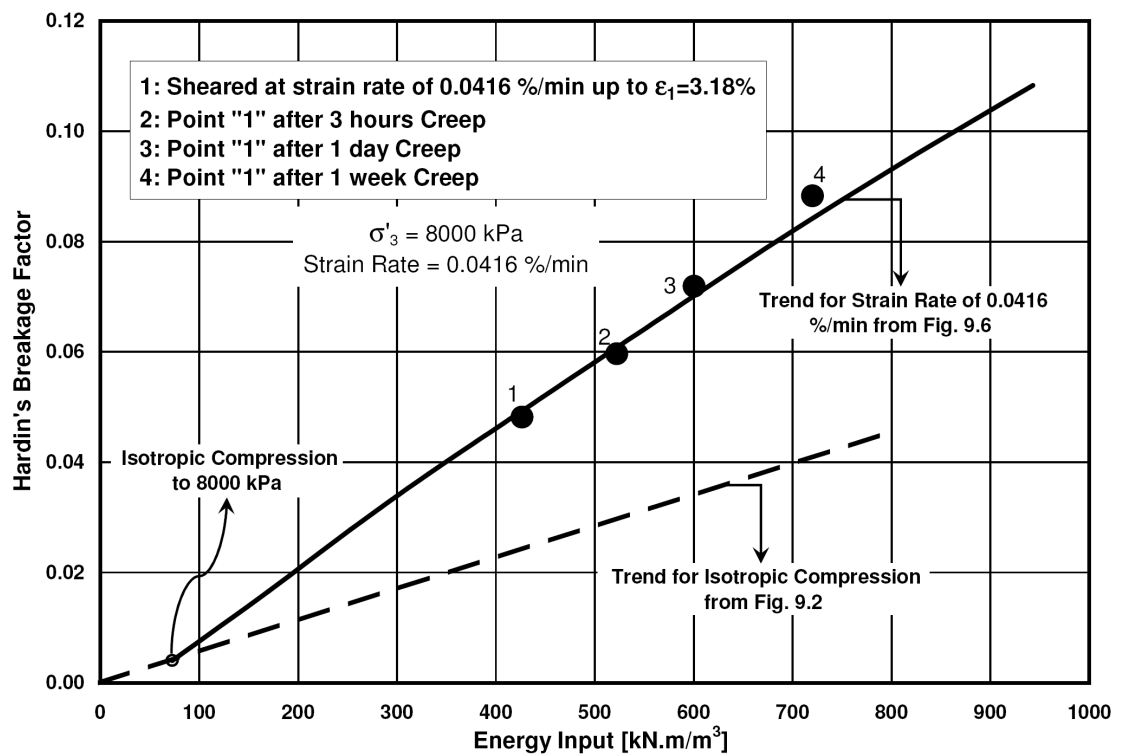


Figure 9.11. Hardin's breakage factor versus energy input for creep experiments under confining pressure of 8000 kPa.

conditions at strain rate of 0.0416 %/min are also superimposed along with a point related to the isotropic compression of 8000 kPa. It is seen that the longer the creep time is, the larger the particle crushing will be. This also can be perfectly explained in terms of static the fatigue phenomenon discussed in previous chapters.

In the next following analysis, a comparison is made between particle crushing during stress relaxation and creep experiments. As presented in Fig. 7.9, five experiments were performed to compare creep and stress relaxation behavior of Virginia Beach sand. The grain size distribution curves for these tests are shown in Fig. 7.14 and the relation between Hardin's breakage factor and energy input for these tests is illustrated in Fig. 9.12. It is observed that as the creep component of the experiment increases, larger amounts of particle crushing and energy input are obtained. This increase follows the proposed trend from Fig. 9.6.

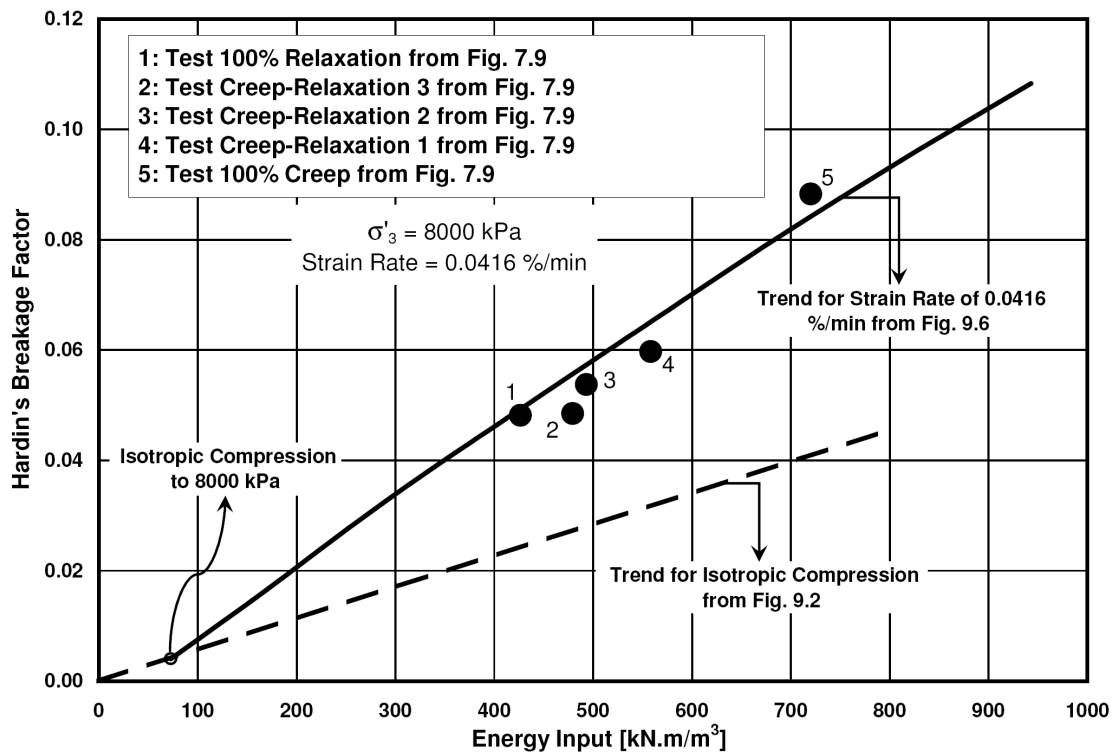


Figure 9.12. Hardin's breakage factor versus energy input for creep-relaxation experiments under confining pressure of 8000 kPa.

10. Summary and Conclusions

This study has focused on time effects in connection with crushing in granular materials. Since particle crushing was not investigated in previous related studies due to friability of the material used, a much stronger type of sand, Virginia Beach sand, was used in this study. A comprehensive experimental program was designed to cover all possible trends that might help to explore time effects in granular materials. This program included (1) performing different triaxial compression experiments over a wide range of confining stresses on dense Virginia Beach sand and (2) single particle strength tests on glass beads.

10.1. Single Particle Strength Tests

Although it is known that strength tests on brittle materials involve considerable amounts of scatter due to the important role of uncontrolled defects in the microscopic structure, two groups of experiments were performed on glass beads in three sizes of 2, 3 and 6 mm to show static fatigue as the root of time dependent phenomena in single particles.

The first group included obtaining the short term strengths of the beads by breaking 16 beads of each size. As predicted, a significant amount of scatter in “stress-strain” behavior and time-to-fracture was observed. The average strength of smaller particles was considerably larger, which was due to a distribution of fewer critically oriented flaws. The second group of experiments consisted of static fatigue experiments in which glass beads of each size were held under various constant stress levels until

breakage occurred. These stresses were fractions of the short term strengths obtained from the first group of tests. Although the pattern attained was erratic and different times-to-fractures varying from seconds to several days were obtained, the phenomenon of static fatigue was clearly visible in the manner that beads fractured after some time under stresses which were smaller than their short term strength. This resulted in the consideration that more consistent behavior might be achieved in a triaxial specimen consists of an assembly of millions of particles. The difference between testing single glass beads and testing triaxial tests with millions of particles is that in single particle tests, the number of contacts with other particles referred to as the coordination number is always 2, while the coordination number for particles in an assembly depends on the soil distribution in triaxial tests. However, this number is greater than 2 and the particles are stabilized and less susceptible to erratic fracture.

10.2. Triaxial Compression Tests

Effects of confining pressure and shearing strain rate on the behavior of dense Virginia Beach sand were studied by performing triaxial compression experiments. Confining pressures varying from 25 to 14000 kPa were used and it was observed that post-failure strength did not drop at high confining pressures, whereas failure was followed by a considerable decrease in strength at low confining pressures. The higher the confining pressure was, the larger the strains-to-failure were. Moreover, the logarithm of initial tangent modulus increased linearly with the logarithm of confining pressure, while the maximum principal stress ratio and the friction angle decreased linearly with increase in the logarithm of the confining pressure. No “breakdown stress” beyond which

the maximum principal stress ratio becomes constant was detected for dense Virginia Beach sand for confining pressures up to 14000 kPa. In terms of crushing, a larger amount of particle crushing was achieved for higher confining pressures. The variation of energy input versus Hardin's breakage factor revealed that experiments performed below confining pressure of 500 kPa did not show noticeable amounts of crushing. However, beyond this pressure, the slope of the energy-crushing curve increased significantly thus suggesting a transition of the principal shearing mechanism from rotation and rearrangement of grains at low confining pressures to crushing of particles at high confining pressures.

Three strain rates of 0.00260, 0.0416 and 0.666 %/min were utilized to study their effects on the stiffness and strength at low (250 kPa) and high (8000 kPa) confining pressures. The same modulus were attained under low confining pressures independent of strain rate, while a slightly stiffer response was achieved at higher strain rates for specimens confined under higher stresses. The critical strength of dense Virginia Beach sand was found to be independent of shearing strain rate at both low and high confining pressures. Sieving results indicated that while insignificant amount of crushing were experienced at low pressures, experiments performed at high confining stresses showed the lowest amount of particle crushing occurred in the specimen sheared at highest strain rate and the largest amount occurred in specimens tested at low strain rates. This proposed that crushing of particles is a function of time.

10.3. Isotropic Compression and K_0 Aging Tests

The effects of aging under isotropic compression and K_0 conditions were studied by holding triaxial specimens under these conditions for various time periods up to a week followed by shearing. Aging under isotropic compression did not show a noticeable impact on the stiffness and strength of dense Virginia Beach sand. This was explained by the fact that insignificant crushing occurred during isotropic condition. On the other hand, it was observed that the stiffness modulus and friction angle increased linearly with the logarithm of the K_0 condition aging time.

10.4. Creep Tests

Creep behavior of dense Virginia Beach sand was investigated under low and high confining pressures for specimens which had been sheared at the three strain rates prior to creep. Since insignificant particle crushing occurred under low stresses, creep behavior was negligible. A small amount of dilation was observed during creep under these pressures. It was suggested that the observed volume change was associated with frictional sliding, rotation and rearrangements of particles which were triggered by breakage of asperities.

Shearing strain rate prior to creep was found to have a crucial influence on the creep behavior under high confining pressures. Once loading was switched from strain control to load control to perform the creep phase, there was a delay in initiation of the axial creep strain for low strain rates, while a considerable jump in axial strain was noticed for high strain rates. The static fatigue phenomenon and the proposed mechanistic picture by Lade et al. (2009) sufficiently explain this observation. During creep, volume

change-axial strain relation followed the reference curves suggesting that the same potential function may be used to model creep as well as plastic deformations.

Results of 1-day creep experiments indicated that the creep response was more pronounced at higher deviator stresses as is the case for static fatigue. After a period of time, the rate of axial and volumetric deformations became approximately the same and independent of the initial shearing strain rate. The immediate change in the creep deformation at the beginning of creep is a function of the strain rate prior to creep. The results of a 2-month creep experiment showed that even after two months both axial and volumetric creep strains increase with the logarithm of time at approximately the same rates as they had in the vicinity of 1 day. This may suggest that there is no ending to creep deformations of dense Virginia Beach sand. Also, further loading at the end of creep phases performed at different stress levels indicated that there were no structuration effects for dense Virginia Beach sand.

Five different grain size distributions were tested to study effects of soil gradation on creep behavior of dense Virginia Beach sand. The test results showed that the more uniform the soil was, the stiffer the responses were and smaller axial strains were necessary to reach the desired creep deviator stress. Although quite different stress-strain responses were achieved for different grain size distributions, similar delays were observed in the initiation of creep, suggesting that these delays were functions of the strain rate prior to creep. Moreover, greater axial and volumetric creep responses were obtained for specimens with larger uniformity and curvature coefficients.

Sieve analyses data indicated that crushing was not detectable for tests performed under low confining pressures, whereas at high confining stresses, specimens that were allowed to creep for a longer period of time showed greater amounts of crushing.

10.5. Stress Relaxation Tests

The three strain rates were also considered to explore stress relaxation behavior of dense Virginia Beach sand under low and high confining pressures. Under low pressures, slightly larger amounts of stress relaxation were obtained for specimens initially sheared faster.

Due to expansion of the load cell during stress relaxation under high pressures resulting in small amounts of axial compression, experiments were performed under three different conditions: drained-without correction of axial strains, drained-with correction of axial strains (to achieve axial strains of zero) and undrained-with correction of axial strains. Similar trends in soil behavior were observed for all three types of experiments. In each type, the specimen sheared at the lowest strain rate showed a delay in stress relaxation after stopping deformation, while an immediate reduction in the deviator stress was observed for the specimen sheared at the highest strain rate. After a period of time, the deviator stress reduced with time at approximately the same rate for all three specimens. This behavior was understandable in view of the static fatigue phenomenon and the proposed mechanistic picture. Overall, undrained stress relaxation tests with correction of the axial strains exhibited the maximum stress reduction, while drained experiments without correction resulted in the minimum stress decrease. Sieve analyses

showed that specimens of all stress relaxation experiments had undergone the same amount of particle crushing, i.e. negligible crushing occurred during stress relaxation.

Several 1-day stress relaxation experiments started at various deviator stress levels revealed that tests performed at higher deviator stress levels resulted in larger amounts of stress relaxation. Similar to creep tests, stress relaxation did not cease, even after two months, suggesting that there is no limit for the stress relaxation. Besides, no structuration effect was detected when specimens were further loaded at the end of the stress relaxation phases. Results of analyses of the particle crushing showed that the stress relaxation phase did not noticeably affect the amount of particle breakage at either low or high confining pressures.

10.6. Creep-Stress Relaxation Tests

Consecutive effects of stress relaxation and creep were studied by performing two series of experiments. In the first series, the time-dependent phase of the experiments started with creep and stress relaxation initiated after different creep times. Results indicated that longer creep time periods resulted in smaller amounts of stress relaxation. In the second series, a reverse procedure was employed in which the time-dependent phases started with stress relaxation. After similar time periods, the experiments were switched to creep. In a similar manner, the longer the relaxation was, the smaller the following creep deformations were.

Static fatigue of particles and subsequently, the soil structure can adequately explain these observations. It is known that the stress level and the time under which the stress is kept constant severely influence the static fatigue phenomenon. Since the same

time was given to all specimens during the initial shearing, all specimens had approximately the same structure at the end of the shearing phase. As a result, the same response was expected at similar elapsed times during the following creep or stress relaxation procedures. Obviously, when specimens crept for various time periods, they would achieve different soil structures at the initiation of the stress relaxation phase implying different responses during the stress relaxation phase. In the second series, stress relaxation for different time periods resulted in dissimilar soil structures and stress distributions. Therefore, dissimilar behaviors were achieved during the following creep phases.

Concurrent effects of stress relaxation and creep were investigated by performing five time dependent experiments. Two experiments were dedicated to pure creep and pure stress relaxation, whereas stress-strain paths of the three other tests included both stress relaxation (reduction in stress level) and creep (increase in deformations). The largest stress reduction was observed in the pure stress relaxation experiment, so called “100% stress relaxation”. The other experiments showed a smooth transition in which the amount of stress relaxation decreased while increasing amounts of creep deformations were obtained until the pure creep experiment where no stress reduction was recorded and the specimen showed the largest creep deformation. Sieve analyses results confirmed that the amount of particle breakage during stress relaxation could be ignored, whereas it was quite considerable during creep and increased with the time of creep.

10.7. Stress Drop-Creep and Stress Drop-Stress Relaxation Tests

Dependency of creep and stress relaxation behavior on the proximity of the stress point to the yield surface was studied by performing stress drop-creep and stress drop-stress relaxation experiments. Results of the stress drop-creep tests showed that creep deformations were considerably reduced with increasing amounts of stress drop. However, this relationship was less pronounced for volumetric creep strains. Depending on the amount of stress drop, a delay was detected before creep deformations were initiated. This behavior was similar to the observations made for consecutive creep-stress relaxation experiments where the stress relaxation phase was followed by creep. Experimental data indicated that no creep deformations were obtained for high stress drops over the period that tests were conducted. Multiple stress drop-creep experiments were also performed. While no structuration effect was observed when specimens were further sheared, larger creep deformations were attained when the stress drops occurred at higher stress levels.

Stress drop-stress relaxation experiments were also performed. The mirror effect of stress drop-creep experiments was obtained. In other words, for larger stress drops, longer delays were observed before stress relaxation began. As a result, for the same period of time, a larger stress drop ended in a smaller stress relaxation. These results implied that if the stress drop was high enough, there might be a reverse effect. That is, the deviator stress level increased for a period of time at the beginning of stress relaxation before the stress reduction initiated. This temporary increase depended on the amount of stress drop and deviator stress level. Multiple stress drop-stress relaxation tests revealed

that the rate of stress relaxation increased with the stress level at which it was commenced. In addition, no structuration effect was observed when specimens were further loaded at the end of stress relaxation.

During creep experiments, it was observed that the axial and volumetric deformations did not deviate from the reference curves established for conventional shearing, and the same potential surface may therefore be used to predict the plastic and the creep deformations. In classic elasto-plastic constitutive models, no plastic deformation and subsequently no plastic potential surface is defined for stress points inside the yield surface. Observation of creep deformations after stress drops suggested that definition of a separate surface for predicting inelastic deformations with time is required. A similar explanation may be utilized when stress relaxation was followed by creep because reduction of stress during stress relaxation brought the stress point inside the yield surface.

10.8. Sieve Analyses

A comprehensive sieve analyses was performed after each experiment and particle crushing was quantified according to a method proposed by Hardin (1985) and utilized in many other studies presented in the literature. Sieve analyses results showed that, as a general rule, particle breakage increases with the energy input. Shearing produces more severe crushing than isotropic compression due to formation of strong force chains that transmit the major principal stress during shearing. This means that for the same amount of energy input, larger amounts of particle breakage are experienced. Therefore, a larger amount of energy input is required during isotropic compression in

comparison with shearing to produce the same amount of particle crushing. For instance, a specimen sheared up to 22% axial strain in a triaxial compression test under a confining pressure of 25 kPa experienced the same amount of particle breakage as did an isotropic compression test up to 8000 kPa. Variation of Hardin's breakage factor with the energy input and confining pressure was estimated with a linear function in this study. According to this trendline, which tends to underestimate the crushing, an isotropic compression test to more than 500000 kPa was required to produce the same amount of crushing attained in a triaxial compression test under confining stress of 8000 kPa (sheared up to the axial strain of 22%). It was also observed that specimens sheared at lower strain rates experienced larger amount of crushing, while higher strain rates produced smaller particle breakage factors. That is, the longer the application of load lasted, the higher the amount of particle crushing.

Particle crushing was also analyzed for stress relaxation and creep experiments. The results indicated that no crushing was obtained during stress relaxation as there was no energy input during stress relaxation. However, significant amounts of particle breakage were achieved during creep depending on the creep time. The specimens that crept for longer periods of time exhibited larger values of Hardin's breakage factor.

10.9. Overall Observations

Among the time effects discussed, it was found that dense Virginia Beach sand did not exhibit structuration effects with time. This was examined for many different conditions where specimens were subject to further loading at the end of different time-dependent phases. Also, it was observed that although the shearing strain rate did not

significantly influence the behavior of granular materials in regular triaxial compression experiments, it had a considerable impact on the subsequent time effects i.e. creep and stress relaxation.

The difference between creep and stress relaxation curves indicated that transition from one phenomenon to the other is not possible. This behavior fits into the category of nonisotach behavior which is quite different from the viscous behavior exhibited by isotach materials like clays. The long term experimental results imply that there is no end to either stress relaxation or creep. If there are lower limits for these two phenomena, then according to the static fatigue phenomenon and the mechanistic picture, they are required to be associated with the strength of grains rather than their frictional characteristics.

10.10. The Hypothesis of Creep and Stress Relaxation Behavior

At low confining pressures frictional sliding and rearrangement of particles dominate the behavior of granular materials and particle crushing is in the form of abrasion which does not affect the results of sieve analyses. On the grounds that particles do not crush into smaller parts, either a contractive or a dilative behavior may be observed during time effects, depending on the previous volumetric regime. That is, specimens undergoing dilation before initiation of creep or relaxation would exhibit dilation, whereas specimens experiencing contraction would show contraction. Since very little particle breakage occurs at low confining pressures in granular materials with strong particles, time effects are negligible. This was clearly indicated by the modest slope of the curve of Hardin's breakage versus energy input.

As the confining pressure and the shear stresses increase, particle crushing starts to dominate the behavior. This is because the particles are held tightly together at these higher stresses and the energy is expended on particle crushing. As a result, strains produced have their origin in crushing rather than rearrangement and frictional sliding. This is the reason for observations of contraction at high pressures. All data and analyses confirm the connection between particle breakage and time effects in granular materials. This relationship is perfectly explained by the static fatigue phenomenon as follows.

It is assumed that an assembly of soil particles is loaded up to a certain deviator stress. A grain in the middle of this assembly breaks at the beginning of either creep or stress relaxation. Two different responses may be obtained according to each boundary condition. In case of creep, the vertical stress on the assembly is kept constant while the associated boundary is free to move. Subsequently, the structure of the assembly is adjusted in order to resist the stress applied and to maintain physical stability. Therefore, new force chains are formed and the engagement of grains in carrying the applied load changes and some vertical displacements, namely creep deformations, are caused. The rate of deformation at the beginning of the creep is controlled by the strain rate at which the assembly was sheared prior to creep because the number of particles that did not have time to fracture is much higher at high strain rates in comparison with low strain rates. Therefore, at the commencement of creep, larger deformation rates are observed at the macro level from accumulation of deformations for high strain rates, whereas a delay is observed in initiation of creep deformation for low strain rates. The experimental results strongly support this hypothesis. During the creep procedure, new particles fracture due

to propagation of microscopic cracks and static fatigue and further deformations are captured. However, as the particles break and fit into the voids, the coordination number increases and the critical forces which pass through the grains are reduced with time. As a result, the rate of particle breakage and the rate of creep deformation are decreased with time and after a sufficient time period assemblies sheared at very high and very low strain rates prior to creep exhibit the same behavior, i.e. the same creep deformation rate is obtained.

As an alternative, the particle assembly experiences stress relaxation when the deformation is kept constant. Consider that a middle particle breaks and the crushed parts leave the existing force chain. Since the vertical boundary is constrained, the measured stress level is reduced and new force chains are formed. Similar to the explanation of the effect of the initial shearing strain rate on the subsequent creep deformation, the speed of stress relaxation is also affected by the initial shearing strain rate. Therefore, at the beginning of stress relaxation, larger stress reduction rates are attained for initially high strain rates, while stress relaxation is delayed at low strain rates. This hypothesis is also strongly supported by experimental data. New particles may fracture because of propagation of microscopic cracks and static fatigue during stress relaxation. Particle crushing directly results in increase in coordination number and decrease in forces on particles. Considering the boundary condition, this resulted in continuation of stress relaxation. Once an adequate amount of time has passed, assemblies sheared at high and low strain rates prior to stress relaxation show the same behavior.

Appendices

A: Stress-Strain Data for Tests presented

Tests Presented in Chapter 4

Test:

Confining Pressure=25 kPa

Initial Height [mm]	107.70	Void ratio	0.528
Initial Area [mm ²]	1073.6	Saturation Index, B	-
Mass [gr]	200.5	Shearing Rate [%/min]	0.0416
Back Pressure [kPa]	200.0	Confining Pressure [kPa]	25

	Time	ϵ_1	ϵ_v [%]	σ'_3	σ'_d		Time	ϵ_1 [%]	ϵ_v [%]	σ'_3	σ'_d
	[min]	[%]		[kPa]	[kPa]		[min]			[kPa]	[kPa]
Triaxial Compression	-	0.00	0.00	25	0	Triaxial Compression	-	6.03	-5.02	25	133
	-	0.09	0.02	25	78		-	6.53	-5.38	25	130
	-	0.18	0.01	25	103		-	7.04	-5.72	25	126
	-	0.27	-0.04	25	115		-	7.41	-5.97	25	123
	-	0.36	-0.10	25	118		-	7.92	-6.28	25	118
	-	0.46	-0.19	25	115		-	8.42	-6.57	25	114
	-	0.69	-0.36	25	125		-	9.00	-6.86	25	110
	-	0.94	-0.54	25	134		-	9.28	-7.00	25	107
	-	1.13	-0.72	25	130		-	10.28	-7.46	25	100
	-	1.42	-0.96	25	141		-	11.16	-7.81	25	95
	-	1.61	-1.14	25	139		-	12.17	-8.17	25	90
	-	1.87	-1.37	25	145		-	13.04	-8.44	25	85
	-	2.31	-1.76	25	147		-	13.91	-8.70	25	82
	-	2.79	-2.21	25	147		-	14.91	-8.96	25	80
	-	3.29	-2.64	25	148		-	15.79	-9.17	25	73
	-	3.80	-3.11	25	148		-	16.79	-9.34	25	69
	-	4.16	-3.45	25	147		-	17.63	-9.45	25	67
	-	4.66	-3.87	25	145		-	18.66	-9.63	25	65
	-	5.10	-4.24	25	144		-	19.53	-9.73	25	62
	-	5.65	-4.70	25	136						

Test:

Confining Pressure=50 kPa

Initial Height [mm]	107.95	Void ratio	0.530
Initial Area [mm ²]	1068.1	Saturation Index, B	0.857
Mass [gr]	199.7	Shearing Rate [%/min]	0.0416
Back Pressure [kPa]	200.0	Confining Pressure [kPa]	50

	Time	ε_1	ε_v	σ'_3	σ'_d					
	[min]	[%]	[%]	[kPa]	[kPa]	Time	ε_1	ε_v	σ'_3	σ'_d
Triaxial Compression	-	0.00	0.00	50	0					
	-	0.07	0.03	50	36					
	-	0.20	0.04	50	89					
	-	0.32	0.04	50	122					
	-	0.41	0.02	50	140					
	-	0.57	-0.02	50	165					
	-	0.76	-0.08	50	192					
	-	0.90	-0.16	50	205					
	-	1.21	-0.37	50	220					
	-	1.44	-0.52	50	232					
	-	1.80	-0.80	50	239					
	-	2.15	-1.10	50	245					
	-	2.56	-1.42	50	254					
	-	2.95	-1.66	50	257					
	-	3.49	-1.91	50	257					
	-	3.96	-2.36	50	255					
	-	4.53	-2.86	50	252					
	-	5.22	-3.27	50	256					
	-	5.68	-3.69	50	253					
	-	5.99	-3.93	50	253					
	-	6.70	-4.50	50	244					
	-	7.28	-4.92	50	240					
	-	7.80	-5.28	50	230					
	-	8.50	-5.73	50	215					
	-	9.22	-6.15	50	206					
	-	10.28	-6.68	50	193					
	-	11.00	-6.97	50	183					
	-	11.96	-7.32	50	175					
	-	12.83	-7.57	50	168					
	-	13.75	-7.82	50	158					
	-	14.67	-8.06	50	155					
	-	15.68	-8.25	50	152					
	-	16.51	-8.39	50	149					

Test:

Confining Pressure=250 kPa

Initial Height [mm]	106.68	Void ratio	0.531
Initial Area [mm ²]	1063.5	Saturation Index, B	0.932
Mass [gr]	196.4	Shearing Rate [%/min]	0.0416
Back Pressure [kPa]	200.0	Confining Pressure [kPa]	250

	Time [min]	ε_1 [%]	ε_v [%]	σ'_3 [kPa]	σ'_d [kPa]		Time [min]	ε_1 [%]	ε_v [%]	σ'_3 [kPa]	σ'_d [kPa]
Isotropic Comp.	-	0.00	0.00	114	-		-	9.33	-5.27	250	936
	-	0.01	0.19	199	-		-	10.24	-5.68	250	900
	-	0.02	0.32	250	-		-	11.17	-6.06	250	869
	-	0.03	0.45	250	-		-	12.10	-6.39	250	838
Triaxial Compression	-	0.00	0.00	250	0	Triaxial Compression	-	12.34	-6.45	250	827
	-	0.00	0.00	250	13		-	13.05	-6.66	250	807
	-	0.05	0.04	250	88		-	13.98	-6.91	250	789
	-	0.18	0.08	250	307		-	14.90	-7.13	250	775
	-	0.25	0.10	250	394		-	15.83	-7.32	250	758
	-	0.33	0.11	250	480		-	16.76	-7.49	250	745
	-	0.40	0.11	250	536		-	17.70	-7.63	250	728
	-	0.43	0.12	250	561		-	18.63	-7.79	250	717
	-	0.50	0.12	250	614		-	19.56	-7.94	250	712
	-	0.63	0.08	250	684		-	20.60	-8.07	250	701
	-	0.67	0.08	250	706		-	21.15	-8.12	250	695
	-	0.72	0.07	250	726		-	21.05	-8.08	250	261
	-	0.90	0.02	250	792		-	20.96	-7.92	250	136
	-	1.36	-0.15	250	888		-	20.49	-7.19	250	0
	-	1.83	-0.39	250	958		-	20.40	-7.06	250	-25
	-	2.44	-0.69	250	1019		-	19.79	-6.42	250	-96
	-	3.12	-1.24	250	1053						
	-	3.36	-1.39	250	1058						
	-	3.59	-1.56	250	1063						
	-	3.72	-1.64	250	1067						
	-	4.23	-2.01	250	1076						
	-	4.65	-2.31	250	1076						
	-	5.10	-2.64	250	1074						
	-	5.63	-3.02	250	1070						
	-	6.01	-3.30	250	1059						
	-	6.48	-3.62	250	1045						
	-	6.94	-3.92	250	1027						
	-	7.42	-4.21	250	1007						
	-	7.89	-4.48	250	987						
	-	8.40	-4.77	250	967						
	-	8.87	-5.02	250	948						

Test:

Confining Pressure=500 kPa

Initial Height [mm]	106.93	Void ratio	0.532
Initial Area [mm ²]	1061.4	Saturation Index, B	0.950
Mass [gr]	196.3	Shearing Rate [%/min]	0.0416
Back Pressure [kPa]	200.0	Confining Pressure [kPa]	500

	Time [min]	ε_1 [%]	ε_v [%]	σ'_3 [kPa]	σ'_d [kPa]		Time [min]	ε_1 [%]	ε_v [%]	σ'_3 [kPa]	σ'_d [kPa]
Isotropic Compression	-	0.00	0.00	100	-		-	8.97	-4.26	500	1736
	-	0.01	0.19	199	-		-	9.44	-4.49	500	1707
	-	0.02	0.32	300	-		-	10.35	-4.89	500	1661
	-	0.03	0.45	399	-		-	11.27	-5.24	500	1613
	-	0.03	0.53	500	-		-	12.19	-5.56	500	1569
	-	0.03	0.53	500	-		-	13.13	-5.84	500	1525
Triaxial Compression	-	0.00	0.00	500	0	Triaxial Compression	-	14.04	-6.07	500	1491
	-	0.00	0.00	500	11		-	14.99	-6.30	500	1457
	-	0.06	0.03	500	171		-	15.90	-6.49	500	1442
	-	0.21	0.09	500	517		-	16.83	-6.68	500	1406
	-	0.25	0.10	500	586		-	17.77	-6.84	500	1382
	-	0.34	0.12	500	723		-	18.71	-6.97	500	1368
	-	0.45	0.13	500	851		-	19.63	-7.11	500	1346
	-	0.57	0.13	500	976		-	20.56	-7.23	500	1321
	-	0.69	0.13	500	1078		-	21.47	-7.33	500	1281
	-	0.81	0.12	500	1171		-	21.00	-6.79	500	47
	-	0.93	0.11	500	1249		-	20.84	-6.59	500	0
	-	1.16	0.07	500	1374						
	-	1.38	-0.01	500	1473						
	-	1.82	-0.15	500	1617						
	-	2.27	-0.38	500	1711						
	-	2.72	-0.62	500	1777						
	-	3.18	-0.88	500	1822						
	-	3.66	-1.15	500	1852						
	-	4.15	-1.44	500	1871						
	-	4.61	-1.71	500	1883						
	-	5.28	-2.15	500	1889						
	-	5.50	-2.30	500	1886						
	-	6.18	-2.73	500	1876						
	-	6.27	-2.79	500	1871						
	-	6.63	-3.02	500	1858						
	-	7.09	-3.29	500	1841						
	-	7.55	-3.54	500	1819						
	-	8.03	-3.79	500	1793						
	-	8.50	-4.04	500	1765						

Test:

Confining Pressure=1000 kPa

Initial Height [mm]	107.19	Void ratio	0.530
Initial Area [mm ²]	1057.8	Saturation Index, B	0.945
Mass [gr]	196.4	Shearing Rate [%/min]	0.0416
Back Pressure [kPa]	200.0	Confining Pressure [kPa]	1000

	Time [min]	ε_1 [%]	ε_v [%]	σ'_3 [kPa]	σ'_d [kPa]		Time [min]	ε_1 [%]	ε_v [%]	σ'_3 [kPa]	σ'_d [kPa]
Isotropic Compression	-	0.00	0.00	100	-	Triaxial Compression	-	11.17	-3.99	997	3390
	-	0.02	0.26	291	-		-	12.08	-4.23	997	3299
	-	0.05	0.52	585	-		-	12.99	-4.48	997	3221
	-	0.07	0.62	781	-		-	13.89	-4.70	997	3152
	-	0.08	0.72	997	-		-	14.79	-4.91	997	3087
	-	0.08	0.74	997	-		-	15.70	-5.03	997	3035
Triaxial Compression	-	0.00	0.00	997	0		-	16.84	-5.13	997	2989
	-	0.01	0.01	997	211		-	17.74	-5.21	997	2982
	-	0.11	0.07	997	611		-	19.06	-5.26	997	2973
	-	0.23	0.09	997	1052		-	19.53	-5.27	997	2957
	-	0.29	0.11	997	1253		-	20.42	-5.30	997	2940
	-	0.40	0.14	997	1539		-	21.33	-5.32	997	2925
	-	0.59	0.17	997	1901		-	21.78	-5.33	997	2922
	-	0.79	0.15	997	2178		-	22.45	-5.34	997	2922
	-	0.98	0.14	997	2398		-	22.47	-5.37	997	2922
	-	1.09	0.11	997	2500		-	22.33	-5.31	997	855
	-	1.37	0.07	997	2715		-	21.95	-5.16	997	65
	-	1.78	-0.05	997	2928		-	21.86	-5.11	997	0
	-	2.20	-0.22	997	3083						
	-	2.72	-0.41	997	3229						
	-	3.24	-0.63	997	3340						
	-	3.74	-0.86	997	3430						
	-	4.24	-1.11	997	3508						
	-	4.73	-1.34	997	3567						
	-	4.98	-1.47	997	3587						
	-	5.47	-1.71	997	3629						
	-	5.99	-1.95	997	3642						
	-	6.44	-2.10	997	3643						
	-	6.89	-2.32	997	3637						
	-	7.35	-2.53	997	3624						
	-	7.80	-2.71	997	3600						
	-	8.48	-3.01	997	3562						
	-	8.93	-3.18	997	3539						
	-	9.38	-3.37	997	3512						
	-	10.27	-3.68	997	3459						

Test:

Confining Pressure=2000 kPa

Initial Height [mm]	108.20	Void ratio	0.538
Initial Area [mm ²]	1055.1	Saturation Index, B	0.945
Mass [gr]	196.7	Shearing Rate [%/min]	0.0416
Back Pressure [kPa]	200.0	Confining Pressure [kPa]	2000

	Time [min]	ε_1 [%]	ε_v [%]	σ'_3 [kPa]	σ'_d [kPa]		Time [min]	ε_1 [%]	ε_v [%]	σ'_3 [kPa]	σ'_d [kPa]
Isotropic Compression	-	0.00	0.00	100	-	Triaxial Compression	-	9.66	-1.17	1997	6444
	-	0.02	0.26	291	-		-	9.80	-1.19	1997	6492
	-	0.05	0.51	585	-		-	10.13	-1.20	1997	6504
	-	0.09	0.67	879	-		-	10.61	-1.26	1997	6491
	-	0.11	0.80	1173	-		-	11.07	-1.32	1997	6477
	-	0.14	0.91	1468	-		-	12.00	-1.39	1997	6428
	-	0.17	1.01	1762	-		-	12.95	-1.42	1997	6351
	-	0.19	1.10	1997	-		-	13.91	-1.44	1997	6243
	-	0.19	1.11	1997	-		-	14.88	-1.44	1997	6148
	-	0.00	0.00	1997	0		-	15.59	-1.42	1997	6112
Triaxial Compression	-	0.15	0.06	1997	711	Triaxial Compression	-	16.51	-1.41	1997	6051
	-	0.28	0.14	1997	1251		-	17.46	-1.38	1997	5928
	-	0.43	0.17	1997	1745		-	18.42	-1.35	1997	5822
	-	0.58	0.22	1997	2170		-	19.38	-1.32	1997	5745
	-	0.73	0.26	1997	2542		-	20.32	-1.29	1997	5638
	-	0.89	0.27	1997	2869		-	21.20	-1.26	1997	5542
	-	1.04	0.28	1997	3167		-	21.66	-1.25	1997	5455
	-	1.35	0.30	1997	3688		-	21.34	-1.20	1997	1568
	-	1.50	0.30	1997	3905		-	20.93	-0.93	1997	0
	-	1.65	0.30	1997	4102						
	-	1.80	0.29	1997	4287						
	-	1.95	0.28	1997	4449						
	-	2.11	0.26	1997	4594						
	-	2.27	0.24	1997	4730						
	-	2.74	0.17	1997	5062						
	-	3.23	0.09	1997	5319						
	-	3.73	-0.01	1997	5521						
	-	4.06	-0.10	1997	5641						
	-	4.52	-0.20	1997	5791						
	-	4.98	-0.30	1997	5907						
	-	5.44	-0.39	1997	6014						
	-	5.90	-0.48	1997	6104						
	-	6.34	-0.59	1997	6193						
	-	6.79	-0.70	1997	6256						
	-	7.23	-0.78	1997	6333						

Test:

Confining Pressure=4000 kPa

Initial Height [mm]	106.93	Void ratio	0.534
Initial Area [mm ²]	1061.4	Saturation Index, B	0.933
Mass [gr]	196.1	Shearing Rate [%/min]	0.0416
Back Pressure [kPa]	200.0	Confining Pressure [kPa]	4000

	Time [min]	ε_1 [%]	ε_v [%]	σ'_3 [kPa]	σ'_d [kPa]		Time [min]	ε_1 [%]	ε_v [%]	σ'_3 [kPa]	σ'_d [kPa]
Isotropic Compression	-	0.00	0.00	100	-	Triaxial Compression	-	6.99	0.55	3999	8928
	-	0.02	0.24	291	-		-	7.41	0.55	3999	8930
	-	0.09	0.62	781	-		-	7.83	0.54	3999	8915
	-	0.14	0.85	1272	-		-	8.38	0.54	3999	8895
	-	0.18	1.03	1762	-		-	8.78	0.54	3999	8864
	-	0.22	1.17	2253	-		-	9.25	0.54	3999	8823
	-	0.25	1.30	2743	-		-	10.19	0.56	3999	8725
	-	0.29	1.41	3234	-		-	11.20	0.58	3999	8570
	-	0.32	1.51	3724	-		-	12.20	0.60	3999	8424
	-	0.33	1.56	3999	-		-	13.00	0.65	3999	8283
Triaxial Compression	-	0.33	1.56	3999	-		-	13.94	0.68	3999	8114
		0.00	0.00	3999	0		-	14.95	0.73	3999	7914
		0.07	0.04	3999	492		-	15.35	0.75	3999	7837
		0.15	0.08	3999	1037		-	16.76	0.83	3999	7595
	-	0.24	0.10	3999	1631		-	17.69	0.90	3999	7420
	-	0.33	0.15	3999	2178		-	18.68	0.95	3999	7239
	-	0.57	0.24	3999	3345		-	19.59	1.04	3999	7119
	-	0.80	0.32	3999	4291		-	20.68	1.10	3999	6968
	-	1.04	0.38	3999	5049		-	21.45	1.16	3999	6855
	-	1.29	0.43	3999	5715		-	22.02	1.19	3999	6707
	-	1.74	0.49	3999	6602		-	21.91	1.20	3999	4590
	-	2.21	0.55	3999	7249		-	21.73	1.22	3999	2120
	-	2.68	0.57	3999	7698		-	21.51	1.31	3999	546
	-	3.24	0.57	3999	8081		-	21.32	1.39	3999	0
	-	3.63	0.58	3999	8278						
	-	3.66	0.58	3999	8293						
	-	3.87	0.58	3999	8387						
	-	4.08	0.58	3999	8480						
	-	4.28	0.57	3999	8545						
	-	4.50	0.57	3999	8614						
	-	4.70	0.57	3999	8671						
	-	5.12	0.56	3999	8761						
	-	5.53	0.56	3999	8834						
	-	6.15	0.56	3999	8860						
	-	6.57	0.55	3999	8912						

Test:

Confining Pressure=8000 kPa

Initial Height [mm]	106.93	Void ratio	0.536
Initial Area [mm ²]	1062.3	Saturation Index, B	0.938
Mass [gr]	195.8	Shearing Rate [%/min]	0.0416
Back Pressure [kPa]	200.0	Confining Pressure [kPa]	8000

	Time [min]	ε_1 [%]	ε_v [%]	σ'_3 [kPa]	σ'_d [kPa]		Time [min]	ε_1 [%]	ε_v [%]	σ'_3 [kPa]	σ'_d [kPa]
Isotropic Compression	-	0.00	0.00	100	-	Triaxial Compression	-	3.61	1.41	8000	12097
	-	0.02	0.28	291	-		-	4.20	1.58	8000	12557
	-	0.07	0.70	781	-		-	4.61	1.71	8000	12833
	-	0.12	0.95	1272	-		-	5.01	1.83	8000	13087
	-	0.14	1.14	1762	-		-	5.62	2.02	8000	13423
	-	0.16	1.28	2253	-		-	6.03	2.15	8000	13632
	-	0.19	1.41	2743	-		-	6.46	2.27	8000	13810
	-	0.21	1.54	3234	-		-	6.88	2.38	8000	13966
	-	0.24	1.65	3724	-		-	7.31	2.50	8000	14105
	-	0.26	1.75	4215	-		-	7.94	2.66	8000	14299
	-	0.28	1.85	4705	-		-	8.36	2.79	8000	14436
	-	0.30	1.94	5196	-		-	8.78	2.89	8000	14546
	-	0.32	2.01	5686	-		-	9.40	3.05	8000	14696
	-	0.35	2.10	6177	-		-	10.22	3.27	8000	14904
	-	0.37	2.18	6667	-		-	11.06	3.50	8000	15103
	-	0.39	2.25	7158	-		-	11.59	3.61	8000	15188
	-	0.42	2.32	7648	-		-	12.12	3.70	8000	15272
Triaxial Compression	-	0.43	2.38	8000	-		-	12.96	3.92	8000	15420
	-	0.44	2.40	8000	-		-	14.01	4.18	8000	15604
	-	0.00	0.00	8000	0		-	14.83	4.37	8000	15766
	-	0.05	0.03	8000	574		-	15.89	4.61	8000	15911
	-	0.14	0.06	8000	1295		-	16.74	4.79	8000	16025
	-	0.25	0.10	8000	2310		-	17.79	5.03	8000	16132
	-	0.31	0.12	8000	2884		-	18.63	5.20	8000	16217
	-	0.55	0.28	8000	4638		-	19.47	5.38	8000	16309
	-	0.82	0.42	8000	6200		-	20.52	5.52	8000	16405
	-	1.02	0.50	8000	7122		-	21.59	5.75	8000	16457
	-	1.25	0.60	8000	8042		-	21.92	5.80	8000	16434
	-	1.49	0.69	8000	8819		-	21.79	5.83	8000	9954
	-	1.77	0.80	8000	9560		-	21.54	5.89	8000	2744
	-	2.19	0.95	8000	10401		-	21.28	5.95	8000	868
	-	2.66	1.12	8000	11152		-	21.14	6.00	8000	0
	-	2.75	1.13	8000	11188						
	-	2.83	1.18	8000	11289						
	-	3.13	1.25	8000	11639						

Test:

Confining Pressure=12000 kPa

Initial Height [mm]	107.70	Void ratio	0.533
Initial Area [mm ²]	1054.0	Saturation Index, B	0.949
Mass [gr]	196.2	Shearing Rate [%/min]	0.0416
Back Pressure [kPa]	200.0	Confining Pressure [kPa]	11865

	Time [min]	ε_1 [%]	ε_v [%]	σ'_3 [kPa]	σ'_d [kPa]		Time [min]	ε_1 [%]	ε_v [%]	σ'_3 [kPa]	σ'_d [kPa]
Isotropic Compression	-	0.00	0.00	100	-	Triaxial Compression	-	2.09	1.09	11865	11096
	-	0.05	0.67	300	-		-	2.27	1.18	11865	11520
	-	0.12	1.15	800	-		-	2.55	1.30	11865	12117
	-	0.17	1.41	1300	-		-	3.02	1.53	11865	12966
	-	0.21	1.54	1800	-		-	3.49	1.77	11865	13668
	-	0.24	1.69	2300	-		-	3.96	2.01	11865	14278
	-	0.28	1.84	2800	-		-	4.42	2.20	11865	14821
	-	0.31	1.97	3300	-		-	4.89	2.42	11865	15266
	-	0.35	2.05	3800	-		-	5.36	2.60	11865	15682
	-	0.38	2.16	4300	-		-	5.83	2.79	11865	16063
	-	0.41	2.24	4800	-		-	6.30	3.00	11865	16414
	-	0.43	2.32	5300	-		-	6.76	3.18	11865	16730
	-	0.46	2.39	5800	-		-	7.23	3.38	11865	17046
	-	0.49	2.45	6300	-		-	7.54	3.50	11865	17245
	-	0.52	2.54	6800	-		-	7.70	3.59	11865	17353
	-	0.54	2.61	7300	-		-	8.17	3.75	11865	17644
	-	0.57	2.70	7800	-		-	8.63	3.91	11865	17904
	-	0.58	2.72	8000	-		-	9.10	4.11	11865	18165
	-	0.58	2.73	8000	-		-	10.04	4.47	11865	18630
	-	0.58	2.73	8000	-		-	10.98	4.82	11865	19082
Triaxial Compression	-	0.62	2.83	8800	-		-	11.91	5.19	11865	19539
	-	0.67	2.98	9866	-		-	12.85	5.51	11865	19978
	-	0.71	3.08	10800	-		-	13.68	5.80	11865	20343
	-	0.77	3.19	11865	-		-	14.72	6.18	11865	20790
	-	0.77	3.19	11865	-		-	15.65	6.46	11865	21172
	-	0.00	0.00	11865	0		-	16.59	6.77	11865	21551
	-	0.03	0.01	11865	288		-	17.52	7.03	11865	21933
	-	0.12	0.07	11865	1199		-	18.46	7.29	11865	22293
	-	0.21	0.11	11865	2092		-	19.40	7.57	11865	22642
	-	0.45	0.25	11865	4082		-	20.33	7.82	11865	22987
	-	0.68	0.38	11865	5663		-	21.16	8.01	11865	23283
	-	0.92	0.50	11865	6967		-	21.87	8.19	11865	23544
	-	1.15	0.62	11865	8061		-	21.64	8.25	11865	12232
	-	1.39	0.74	11865	9004		-	21.27	8.34	11865	3201
	-	1.62	0.86	11865	9792		-	21.24	8.59	11865	0

Test:

Confining Pressure=14000 kPa

Initial Height [mm]	107.44	Void ratio	0.530
Initial Area [mm ²]	1058.8	Saturation Index, B	0.953
Mass [gr]	197.0	Shearing Rate [%/min]	0.0416
Back Pressure [kPa]	200.0	Confining Pressure [kPa]	14000

	Time [min]	ε_1 [%]	ε_v [%]	σ'_3 [kPa]	σ'_d [kPa]		Time [min]	ε_1 [%]	ε_v [%]	σ'_3 [kPa]	σ'_d [kPa]
Isotropic Compression	-	0.00	0.00	100	-	Triaxial Compression	-	3.85	2.24	14000	14680
	-	0.01	0.30	291	-		-	4.51	2.58	14000	15596
	-	0.05	0.66	781	-		-	4.95	2.80	14000	16141
	-	0.08	0.91	1272	-		-	5.38	3.00	14000	16634
	-	0.11	1.08	1762	-		-	5.83	3.23	14000	17104
	-	0.13	1.21	2253	-		-	6.28	3.43	14000	17556
	-	0.16	1.34	2743	-		-	6.74	3.64	14000	17985
	-	0.18	1.43	3234	-		-	7.22	3.85	14000	18391
	-	0.20	1.53	3724	-		-	7.68	4.06	14000	18765
	-	0.22	1.62	4215	-		-	8.14	4.24	14000	19113
	-	0.25	1.70	4705	-		-	8.59	4.45	14000	19478
	-	0.29	1.88	5686	-		-	8.90	4.57	14000	19696
	-	0.34	2.02	6667	-		-	9.10	4.67	14000	19851
	-	0.38	2.16	7648	-		-	10.01	5.04	14000	20510
	-	0.42	2.29	8629	-		-	10.94	5.40	14000	21166
	-	0.47	2.41	9610	-		-	11.88	5.76	14000	22041
	-	0.51	2.53	10591	-		-	12.82	6.12	14000	22643
	-	0.55	2.65	11572	-		-	13.75	6.43	14000	23203
	-	0.59	2.77	12553	-		-	14.66	6.76	14000	23758
	-	0.63	2.87	13534	-		-	15.66	7.08	14000	24341
Triaxial Compression	-	0.65	2.94	14000	-		-	16.62	7.38	14000	24870
	-	0.65	2.99	14000	-		-	17.59	7.64	14000	25349
	-	0.00	0.00	14000	0		-	18.02	7.76	14000	25567
	-	0.02	0.01	14000	177		-	18.47	7.90	14000	25794
	-	0.16	0.09	14000	1544		-	19.40	8.11	14000	26216
	-	0.25	0.17	14000	2422		-	20.28	8.32	14000	26618
	-	0.44	0.29	14000	4106		-	21.28	8.54	14000	27016
	-	0.62	0.41	14000	5436		-	21.86	8.64	14000	27225
	-	1.01	0.66	14000	7586		-	21.74	8.65	14000	19097
	-	1.21	0.78	14000	8480		-	21.56	8.69	14000	11598
	-	1.64	1.03	14000	10013		-	21.27	8.76	14000	4645
	-	2.07	1.28	14000	11264		-	20.94	8.87	14000	0
	-	2.54	1.53	14000	12368						
	-	2.96	1.76	14000	13199						
	-	3.40	2.00	14000	13981						

Test:

Strain Rate=0.00260 %/min, $\sigma'_3=250$ kPa

Initial Height [mm]	107.19	Void ratio	0.530
Initial Area [mm ²]	1060.9	Saturation Index, B	0.950
Mass [gr]	197.0	Shearing Rate [%/min]	0.00260
Back Pressure [kPa]	200.0	Confining Pressure [kPa]	250

	Time [min]	ϵ_1 [%]	ϵ_v [%]	σ'_3 [kPa]	σ'_d [kPa]		Time [min]	ϵ_1 [%]	ϵ_v [%]	σ'_3 [kPa]	σ'_d [kPa]
Isotropic Comp.	-	0.00	0.00	110	-		-	8.82	-5.25	250	950
	-	0.01	0.14	199	-		-	9.30	-5.52	250	933
	-	0.02	0.21	250	-		-	10.25	-6.00	250	898
	-	0.02	0.22	250	-		-	11.19	-6.45	250	863
Triaxial Compression		0.00	0.00	250	0	Triaxial Compression	-	12.13	-6.93	250	831
		0.02	0.01	250	40		-	13.08	-7.35	250	801
		0.06	0.02	250	125		-	13.96	-7.72	250	774
		0.16	0.06	250	277		-	14.13	-7.78	250	772
		0.23	0.08	250	366		-	14.91	-8.06	250	751
	-	0.33	0.08	250	459		-	15.85	-8.38	250	722
	-	0.44	0.08	250	534		-	16.80	-8.67	250	702
	-	0.51	0.07	250	579		-	17.68	-8.88	250	678
	-	0.59	0.06	250	620		-	18.64	-9.10	250	664
	-	0.69	0.03	250	667		-	19.61	-9.27	250	654
	-	0.74	0.01	250	690		-	20.30	-9.38	250	640
	-	0.90	-0.01	250	743		-	20.20	-9.32	250	217
	-	1.15	-0.12	250	813		-	20.02	-9.01	250	55
	-	1.36	-0.23	250	857		-	19.79	-8.66	250	0
	-	1.61	-0.35	250	899						
	-	1.82	-0.47	250	929						
	-	2.33	-0.80	250	982						
	-	2.80	-1.11	250	1015						
	-	3.27	-1.43	250	1038						
	-	3.73	-1.73	250	1049						
	-	4.18	-2.10	250	1058						
	-	4.44	-2.28	250	1059						
	-	4.65	-2.43	250	1059						
	-	5.08	-2.75	250	1056						
	-	5.55	-3.10	250	1052						
	-	6.02	-3.43	250	1044						
	-	6.49	-3.76	250	1033						
	-	7.01	-4.14	250	1019						
	-	7.42	-4.42	250	1003						
	-	7.90	-4.72	250	988						
	-	8.43	-5.04	250	967						

Test:

Strain Rate=0.0416 %/min, $\sigma'_3=250$ kPa

Initial Height [mm]	106.68	Void ratio	0.531
Initial Area [mm ²]	1063.5	Saturation Index, B	0.932
Mass [gr]	196.4	Shearing Rate [%/min]	0.0416
Back Pressure [kPa]	200.0	Confining Pressure [kPa]	250

	Time [min]	ε_1 [%]	ε_v [%]	σ'_3 [kPa]	σ'_d [kPa]		Time [min]	ε_1 [%]	ε_v [%]	σ'_3 [kPa]	σ'_d [kPa]
Isotropic Comp.	-	0.00	0.00	114	-		-	9.33	-5.27	250	936
	-	0.01	0.19	199	-		-	10.24	-5.68	250	900
	-	0.02	0.32	250	-		-	11.17	-6.06	250	869
	-	0.03	0.45	250	-		-	12.10	-6.39	250	838
Triaxial Compression	-	0.00	0.00	250	0	Triaxial Compression	-	12.34	-6.45	250	827
	-	0.00	0.00	250	13		-	13.05	-6.66	250	807
	-	0.05	0.04	250	88		-	13.98	-6.91	250	789
	-	0.18	0.08	250	307		-	14.90	-7.13	250	775
	-	0.25	0.10	250	394		-	15.83	-7.32	250	758
	-	0.33	0.11	250	480		-	16.76	-7.49	250	745
	-	0.40	0.11	250	536		-	17.70	-7.63	250	728
	-	0.43	0.12	250	561		-	18.63	-7.79	250	717
	-	0.50	0.12	250	614		-	19.56	-7.94	250	712
	-	0.63	0.08	250	684		-	20.60	-8.07	250	701
	-	0.67	0.08	250	706		-	21.15	-8.12	250	695
	-	0.72	0.07	250	726		-	21.05	-8.08	250	261
	-	0.90	0.02	250	792		-	20.96	-7.92	250	136
	-	1.36	-0.15	250	888		-	20.49	-7.19	250	0
	-	1.83	-0.39	250	958						
	-	2.44	-0.69	250	1019						
	-	3.12	-1.24	250	1053						
	-	3.36	-1.39	250	1058						
	-	3.59	-1.56	250	1063						
	-	3.72	-1.64	250	1067						
	-	4.23	-2.01	250	1076						
	-	4.65	-2.31	250	1076						
	-	5.10	-2.64	250	1074						
	-	5.63	-3.02	250	1070						
	-	6.01	-3.30	250	1059						
	-	6.48	-3.62	250	1045						
	-	6.94	-3.92	250	1027						
	-	7.42	-4.21	250	1007						
	-	7.89	-4.48	250	987						
	-	8.40	-4.77	250	967						
	-	8.87	-5.02	250	948						

Test:

Strain Rate=0.666 %/min, $\sigma'_3=250$ kPa

Initial Height [mm]	106.43	Void ratio	0.530
Initial Area [mm ²]	1065.2	Saturation Index, B	0.953
Mass [gr]	196.4	Shearing Rate [%/min]	0.666
Back Pressure [kPa]	200.0	Confining Pressure [kPa]	250

	Time [min]	ϵ_1 [%]	ϵ_v [%]	σ'_3 [kPa]	σ'_d [kPa]		Time [min]	ϵ_1 [%]	ϵ_v [%]	σ'_3 [kPa]	σ'_d [kPa]
Isotropic Comp.	-	0.00	0.00	100	-		-	9.56	-5.44	250	893
	-	0.03	0.21	200	-		-	10.22	-5.78	250	865
	-	0.05	0.31	250	-		-	11.16	-6.21	250	823
	-	0.05	0.31	250	-		-	12.10	-6.57	250	787
Triaxial Compression	-	0.00	0.00	250	0	Triaxial Compression	-	13.04	-6.91	250	751
	-	0.07	0.03	250	57		-	13.98	-7.17	250	726
	-	0.16	0.07	250	144		-	14.92	-7.41	250	694
	-	0.25	0.11	250	226		-	15.86	-7.60	250	669
	-	0.35	0.13	250	312		-	16.80	-7.77	250	657
	-	0.44	0.14	250	407		-	17.74	-7.91	250	632
	-	0.54	0.16	250	476		-	18.68	-8.02	250	620
	-	0.63	0.16	250	547		-	19.62	-8.13	250	601
	-	0.73	0.16	250	598		-	20.56	-8.21	250	590
	-	0.82	0.14	250	648		-	21.13	-8.23	250	578
	-	1.05	0.10	250	739		-	20.98	-8.11	250	129
	-	1.29	0.00	250	803		-	20.70	-7.61	250	0
	-	1.52	-0.11	250	852						
	-	1.76	-0.21	250	892						
	-	2.23	-0.49	250	950						
	-	2.70	-0.77	250	990						
	-	3.17	-1.08	250	1016						
	-	3.64	-1.41	250	1030						
	-	4.11	-1.76	250	1039						
	-	4.58	-2.12	250	1041						
	-	5.06	-2.45	250	1038						
	-	5.52	-2.78	250	1031						
	-	5.90	-3.08	250	1025						
	-	6.03	-3.15	250	1024						
	-	6.46	-3.47	250	1012						
	-	6.93	-3.81	250	1000						
	-	7.40	-4.14	250	986						
	-	7.87	-4.44	250	968						
	-	8.34	-4.72	250	949						
	-	8.81	-5.01	250	924						
	-	9.28	-5.26	250	906						

Test:

Strain Rate=0.00260 %/min, $\sigma'_3=8000$ kPa

Initial Height [mm]	107.95	Void ratio	0.544
Initial Area [mm ²]	1058.3	Saturation Index, B	0.913
Mass [gr]	196.0	Shearing Rate [%/min]	0.00260
Back Pressure [kPa]	200.0	Confining Pressure [kPa]	8000

	Time [min]	ε_1 [%]	ε_v [%]	σ'_3 [kPa]	σ'_d [kPa]		Time [min]	ε_1 [%]	ε_v [%]	σ'_3 [kPa]	σ'_d [kPa]
Isotropic Compression	-	0.00	0.00	100	-	Triaxial Compression	-	4.00	1.59	8000	11850
	-	0.01	0.31	291	-		-	4.47	1.76	8000	12189
	-	0.05	0.73	781	-		-	4.94	1.93	8000	12556
	-	0.12	1.00	1272	-		-	5.40	2.07	8000	12850
	-	0.14	1.20	1762	-		-	5.86	2.20	8000	13126
	-	0.17	1.35	2253	-		-	6.34	2.36	8000	13388
	-	0.20	1.50	2743	-		-	6.80	2.50	8000	13590
	-	0.24	1.61	3234	-		-	7.27	2.64	8000	13784
	-	0.26	1.73	3724	-		-	7.74	2.79	8000	13960
	-	0.30	1.85	4215	-		-	8.19	2.91	8000	14117
	-	0.33	1.93	4705	-		-	8.66	3.04	8000	14281
	-	0.36	2.02	5196	-		-	9.12	3.15	8000	14422
	-	0.38	2.11	5686	-		-	9.95	3.41	8000	14699
	-	0.41	2.19	6177	-		-	10.06	3.43	8000	14744
	-	0.44	2.27	6667	-		-	10.89	3.65	8000	14964
	-	0.47	2.34	7158	-		-	11.04	3.67	8000	15011
	-	0.49	2.43	7648	-		-	11.92	3.90	8000	15181
Triaxial Compression	-	0.51	2.47	8000	-		-	12.85	4.12	8000	15374
	-	0.51	2.52	8000	-		-	13.79	4.32	8000	15554
	-	0.00	0.00	8000	0		-	14.72	4.55	8000	15752
	-	0.09	0.04	8000	877		-	15.67	4.73	8000	15844
	-	0.19	0.07	8000	1780		-	16.57	4.92	8000	15964
	-	0.28	0.13	8000	2534		-	16.80	4.97	8000	16007
	-	0.51	0.27	8000	4128		-	17.51	5.12	8000	16093
	-	0.74	0.37	8000	5463		-	18.44	5.32	8000	16091
	-	0.98	0.47	8000	6520		-	18.52	5.34	8000	16095
	-	1.21	0.58	8000	7414		-	18.77	5.40	8000	16131
	-	1.68	0.78	8000	8760		-	19.37	5.54	8000	16157
	-	2.14	0.97	8000	9724		-	20.38	5.75	8000	16170
	-	2.33	1.03	8000	10018		-	21.23	5.94	8000	16249
	-	2.61	1.14	8000	10428		-	21.69	6.05	8000	16192
	-	2.62	1.15	8000	10448		-	21.44	6.18	8000	6544
	-	3.07	1.28	8000	10990		-	20.94	6.34	8000	0
	-	3.32	1.38	8000	11252						
	-	3.54	1.45	8000	11461						

Test:

Strain Rate=0.0416 %/min, $\sigma'_3=8000$ kPa

Initial Height [mm]	106.93	Void ratio	0.536
Initial Area [mm ²]	1062.3	Saturation Index, B	0.938
Mass [gr]	195.8	Shearing Rate [%/min]	0.0416
Back Pressure [kPa]	200.0	Confining Pressure [kPa]	8000

	Time [min]	ε_1 [%]	ε_v [%]	σ'_3 [kPa]	σ'_d [kPa]		Time [min]	ε_1 [%]	ε_v [%]	σ'_3 [kPa]	σ'_d [kPa]
Isotropic Compression	-	0.00	0.00	100	-	Triaxial Compression	-	3.61	1.41	8000	12097
	-	0.02	0.28	291	-		-	4.20	1.58	8000	12557
	-	0.07	0.70	781	-		-	4.61	1.71	8000	12833
	-	0.12	0.95	1272	-		-	5.01	1.83	8000	13087
	-	0.14	1.14	1762	-		-	5.62	2.02	8000	13423
	-	0.16	1.28	2253	-		-	6.03	2.15	8000	13632
	-	0.19	1.41	2743	-		-	6.46	2.27	8000	13810
	-	0.21	1.54	3234	-		-	6.88	2.38	8000	13966
	-	0.24	1.65	3724	-		-	7.31	2.50	8000	14105
	-	0.26	1.75	4215	-		-	7.94	2.66	8000	14299
	-	0.28	1.85	4705	-		-	8.36	2.79	8000	14436
	-	0.30	1.94	5196	-		-	8.78	2.89	8000	14546
	-	0.32	2.01	5686	-		-	9.40	3.05	8000	14696
	-	0.35	2.10	6177	-		-	10.22	3.27	8000	14904
	-	0.37	2.18	6667	-		-	11.06	3.50	8000	15103
	-	0.39	2.25	7158	-		-	11.59	3.61	8000	15188
	-	0.42	2.32	7648	-		-	12.12	3.70	8000	15272
Triaxial Compression	-	0.43	2.38	8000	-		-	12.96	3.92	8000	15420
	-	0.44	2.40	8000	-		-	14.01	4.18	8000	15604
	-	0.00	0.00	8000	0		-	14.83	4.37	8000	15766
	-	0.05	0.03	8000	574		-	15.89	4.61	8000	15911
	-	0.14	0.06	8000	1295		-	16.74	4.79	8000	16025
	-	0.25	0.10	8000	2310		-	17.79	5.03	8000	16132
	-	0.31	0.12	8000	2884		-	18.63	5.20	8000	16217
	-	0.55	0.28	8000	4638		-	19.47	5.38	8000	16309
	-	0.82	0.42	8000	6200		-	20.52	5.52	8000	16405
	-	1.02	0.50	8000	7122		-	21.59	5.75	8000	16457
	-	1.25	0.60	8000	8042		-	21.92	5.80	8000	16434
	-	1.49	0.69	8000	8819		-	21.79	5.83	8000	9954
	-	1.77	0.80	8000	9560		-	21.54	5.89	8000	2744
	-	2.19	0.95	8000	10401		-	21.28	5.95	8000	868
	-	2.66	1.12	8000	11152		-	21.14	6.00	8000	0
	-	2.75	1.13	8000	11188						
	-	2.83	1.18	8000	11289						
	-	3.13	1.25	8000	11639						

Test:

Strain Rate=0.666 %/min, $\sigma'_3=8000$ kPa

Initial Height [mm]	106.93	Void ratio	0.534
Initial Area [mm ²]	1058.0	Saturation Index, B	0.922
Mass [gr]	195.4	Shearing Rate [%/min]	0.666
Back Pressure [kPa]	200.0	Confining Pressure [kPa]	8000

	Time [min]	ε_1 [%]	ε_v [%]	σ'_3 [kPa]	σ'_d [kPa]		Time [min]	ε_1 [%]	ε_v [%]	σ'_3 [kPa]	σ'_d [kPa]
Isotropic Compression	-	0.00	0.00	100	-	Triaxial Compression	-	5.02	1.67	8000	13877
	-	0.02	0.29	291	-		-	5.50	1.79	8000	14096
	-	0.06	0.70	781	-		-	5.97	1.90	8000	14304
	-	0.11	0.94	1272	-		-	6.43	2.01	8000	14481
	-	0.13	1.13	1762	-		-	6.91	2.14	8000	14644
	-	0.16	1.30	2253	-		-	7.37	2.25	8000	14781
	-	0.19	1.43	2743	-		-	7.84	2.36	8000	14901
	-	0.21	1.56	3234	-		-	8.31	2.48	8000	15029
	-	0.24	1.66	3724	-		-	8.78	2.59	8000	15147
	-	0.26	1.77	4215	-		-	9.25	2.72	8000	15266
	-	0.29	1.85	4705	-		-	10.19	2.93	8000	15500
	-	0.32	1.95	5196	-		-	11.13	3.15	8000	15666
	-	0.34	2.02	5686	-		-	12.07	3.35	8000	15790
	-	0.36	2.09	6177	-		-	13.01	3.57	8000	15942
	-	0.39	2.19	6667	-		-	13.95	3.79	8000	16076
	-	0.41	2.26	7158	-		-	14.89	4.01	8000	16208
	-	0.43	2.32	7648	-		-	15.83	4.20	8000	16310
	-	0.45	2.38	8000	-		-	16.77	4.40	8000	16384
Triaxial Compression	-	0.45	2.43	8000	-		-	17.71	4.59	8000	16438
	-	0.00	0.00	8000	0		-	18.64	4.79	8000	16540
	-	0.05	0.03	8000	588		-	19.58	4.96	8000	16608
	-	0.14	0.07	8000	1714		-	20.52	5.13	8000	16650
	-	0.23	0.13	8000	2761		-	21.47	5.29	8000	16641
	-	0.33	0.18	8000	3723		-	21.94	5.37	8000	16638
	-	0.56	0.29	8000	5655		-	21.86	5.40	8000	10498
	-	0.80	0.40	8000	7111		-	21.56	5.48	8000	3569
	-	1.04	0.50	8000	8299		-	21.34	5.55	8000	983
	-	1.27	0.58	8000	9193		-	21.20	5.62	8000	0
	-	1.73	0.77	8000	10503						
	-	2.21	0.91	8000	11407						
	-	2.67	1.03	8000	12035						
	-	3.14	1.16	8000	12537						
	-	3.61	1.30	8000	12966						
	-	4.08	1.44	8000	13338						
	-	4.56	1.56	8000	13637						

Test:

Isotropically Aged for 0 Minutes

Initial Height [mm]	107.95	Void ratio	0.531
Initial Area [mm ²]	1053.3	Saturation Index, B	0.952
Mass [gr]	196.8	Shearing Rate [%/min]	0.0416
Back Pressure [kPa]	200.0	Confining Pressure [kPa]	8000

	Time [min]	ε_1 [%]	ε_v [%]	σ'_3 [kPa]	σ'_d [kPa]		Time [min]	ε_1 [%]	ε_v [%]	σ'_3 [kPa]	σ'_d [kPa]
Isotropic Compression	-	0.00	0.00	100	-	Triaxial Compression	-	4.68	1.74	8000	12872
	-	0.01	0.32	300	-		-	5.13	1.87	8000	13147
	-	0.06	0.70	800	-		-	5.59	2.01	8000	13387
	-	0.10	0.95	1300	-		-	5.89	2.09	8000	13517
	-	0.13	1.11	1800	-		-	6.44	2.26	8000	13768
	-	0.16	1.28	2300	-		-	6.92	2.40	8000	13934
	-	0.19	1.40	2800	-		-	7.39	2.53	8000	14099
	-	0.22	1.51	3300	-		-	7.85	2.65	8000	14241
	-	0.25	1.62	3800	-		-	8.31	2.78	8000	14380
	-	0.28	1.72	4300	-		-	8.76	2.90	8000	14520
	-	0.30	1.81	4800	-		-	9.24	3.03	8000	14649
	-	0.33	1.89	5300	-		-	10.18	3.28	8000	14880
	-	0.36	2.00	5800	-		-	11.14	3.52	8000	15090
	-	0.38	2.09	6300	-		-	11.85	3.72	8000	15245
	-	0.40	2.19	6800	-		-	12.86	3.97	8000	15477
	-	0.43	2.28	7300	-		-	13.70	4.19	8000	15624
Triaxial Compression	-	0.45	2.35	7800	-		-	14.64	4.42	8000	15804
	-	0.46	2.40	8000	-		-	15.59	4.64	8000	15962
	-	0.46	2.40	8000	-		-	16.62	4.88	8000	16134
	-	0.00	0.00	8000	0		-	17.51	5.07	8000	16278
	-	0.02	0.01	8000	174		-	18.47	5.27	8000	16391
	-	0.11	0.07	8000	1109		-	19.42	5.46	8000	16527
	-	0.20	0.12	8000	1986		-	20.41	5.68	8000	16652
	-	0.29	0.19	8000	2787		-	21.25	5.85	8000	16745
	-	0.58	0.32	8000	4811		-	21.93	6.00	8000	16820
	-	0.77	0.42	8000	5896		-	21.75	6.01	8000	9536
	-	0.99	0.52	8000	6951		-	21.54	6.04	8000	4583
	-	1.34	0.66	8000	8204		-	21.25	6.15	8000	778
	-	1.46	0.70	8000	8553		-	21.14	6.21	8000	0
	-	1.69	0.80	8000	9185						
	-	2.14	0.94	8000	10119						
	-	2.58	1.07	8000	10821						
	-	3.02	1.24	8000	11401						
	-	3.68	1.43	8000	12092						
	-	4.23	1.61	8000	12548						

Test:

Isotropically Aged for 45 Minutes

Initial Height [mm]	106.93	Void ratio	0.536
Initial Area [mm ²]	1062.3	Saturation Index, B	0.938
Mass [gr]	195.8	Shearing Rate [%/min]	0.0416
Back Pressure [kPa]	200.0	Confining Pressure [kPa]	8000

	Time [min]	ε_1 [%]	ε_v [%]	σ'_3 [kPa]	σ'_d [kPa]		Time [min]	ε_1 [%]	ε_v [%]	σ'_3 [kPa]	σ'_d [kPa]
Isotropic Compression	-	0.00	0.00	100	-	Triaxial Compression	-	3.61	1.41	8000	12097
	-	0.02	0.28	291	-		-	4.20	1.58	8000	12557
	-	0.07	0.70	781	-		-	4.61	1.71	8000	12833
	-	0.12	0.95	1272	-		-	5.01	1.83	8000	13087
	-	0.14	1.14	1762	-		-	5.62	2.02	8000	13423
	-	0.16	1.28	2253	-		-	6.03	2.15	8000	13632
	-	0.19	1.41	2743	-		-	6.46	2.27	8000	13810
	-	0.21	1.54	3234	-		-	6.88	2.38	8000	13966
	-	0.24	1.65	3724	-		-	7.31	2.50	8000	14105
	-	0.26	1.75	4215	-		-	7.94	2.66	8000	14299
	-	0.28	1.85	4705	-		-	8.36	2.79	8000	14436
	-	0.30	1.94	5196	-		-	8.78	2.89	8000	14546
	-	0.32	2.01	5686	-		-	9.40	3.05	8000	14696
	-	0.35	2.10	6177	-		-	10.22	3.27	8000	14904
	-	0.37	2.18	6667	-		-	11.06	3.50	8000	15103
	-	0.39	2.25	7158	-		-	11.59	3.61	8000	15188
Triaxial Compression	-	0.42	2.32	7648	-		-	12.12	3.70	8000	15272
	-	0.43	2.38	8000	-		-	12.96	3.92	8000	15420
	-	0.44	2.40	8000	-		-	14.01	4.18	8000	15604
	-	0.00	0.00	8000	0		-	14.83	4.37	8000	15766
	-	0.05	0.03	8000	574		-	15.89	4.61	8000	15911
	-	0.14	0.06	8000	1295		-	16.74	4.79	8000	16025
	-	0.25	0.10	8000	2310		-	17.79	5.03	8000	16132
	-	0.31	0.12	8000	2884		-	18.63	5.20	8000	16217
	-	0.55	0.28	8000	4638		-	19.47	5.38	8000	16309
	-	0.82	0.42	8000	6200		-	20.52	5.52	8000	16405
	-	1.02	0.50	8000	7122		-	21.59	5.75	8000	16457
	-	1.25	0.60	8000	8042		-	21.92	5.80	8000	16434
	-	1.49	0.69	8000	8819		-	21.79	5.83	8000	9954
	-	1.77	0.80	8000	9560		-	21.54	5.89	8000	2744
	-	2.19	0.95	8000	10401		-	21.28	5.95	8000	868
	-	2.66	1.12	8000	11152		-	21.14	6.00	8000	0
	-	2.75	1.13	8000	11188						
	-	2.83	1.18	8000	11289						
	-	3.13	1.25	8000	11639						

Test:

Isotropically Aged for 1440 Minutes

Initial Height [mm]	107.70	Void ratio	0.535
Initial Area [mm ²]	1058.2	Saturation Index, B	0.950
Mass [gr]	196.8	Shearing Rate [%/min]	0.0416
Back Pressure [kPa]	200.0	Confining Pressure [kPa]	8000

	Time [min]	ε_1 [%]	ε_v [%]	σ'_3 [kPa]	σ'_d [kPa]		Time [min]	ε_1 [%]	ε_v [%]	σ'_3 [kPa]	σ'_d [kPa]
Isotropic Compression	-	0.00	0.00	100	-	Triaxial Compression	-	4.92	1.72	8000	12695
	-	0.03	0.43	300	-		-	5.42	1.87	8000	12995
	-	0.08	0.84	800	-		-	5.83	1.98	8000	13202
	-	0.12	1.09	1300	-		-	6.17	2.01	8000	13333
	-	0.15	1.26	1800	-		-	6.33	2.02	8000	13399
	-	0.18	1.41	2300	-		-	6.83	2.14	8000	13599
	-	0.21	1.52	2800	-		-	7.33	2.28	8000	13783
	-	0.24	1.65	3300	-		-	7.73	2.40	8000	13935
	-	0.27	1.75	3800	-		-	8.22	2.52	8000	14086
	-	0.30	1.85	4300	-		-	8.72	2.65	8000	14222
	-	0.32	1.95	4800	-		-	9.13	2.74	8000	14326
	-	0.35	2.03	5300	-		-	10.06	3.00	8000	14559
	-	0.38	2.11	5800	-		-	11.06	3.26	8000	14763
	-	0.40	2.20	6300	-		-	11.97	3.47	8000	14930
	-	0.43	2.27	6800	-		-	12.87	3.69	8000	15092
	-	0.45	2.35	7300	-		-	13.86	3.94	8000	15253
Triaxial Compression	-	0.48	2.41	7800	-		-	14.78	4.13	8000	15383
	-	0.49	2.45	8000	-		-	15.71	4.34	8000	15530
	-	0.49	2.65	8000	-		-	15.91	4.39	8000	15546
	-	0.00	0.00	8000	0		-	16.62	4.56	8000	15638
	-	0.07	0.03	8000	610		-	17.60	4.76	8000	15732
	-	0.18	0.08	8000	1575		-	18.50	4.94	8000	15817
	-	0.26	0.11	8000	2201		-	19.43	5.12	8000	15881
	-	0.49	0.23	8000	3924		-	20.35	5.30	8000	15939
	-	0.77	0.35	8000	5508		-	21.26	5.46	8000	15975
	-	0.93	0.42	8000	6233		-	21.75	5.52	8000	15977
	-	1.17	0.51	8000	7184		-	21.91	5.56	8000	15989
	-	1.42	0.61	8000	7974		-	21.72	5.57	8000	9201
	-	1.66	0.69	8000	8641		-	21.50	5.63	8000	4604
	-	2.14	0.87	8000	9723		-	21.22	5.72	8000	1007
	-	2.63	1.03	8000	10532		-	21.06	5.79	8000	0
	-	3.11	1.19	8000	11167						
	-	3.52	1.32	8000	11614						
	-	4.01	1.46	8000	12063						
	-	4.50	1.61	8000	12415						

Test:

Isotropically Aged for 10080 Minutes

Initial Height [mm]	107.95	Void ratio	0.529
Initial Area [mm ²]	1052.0	Saturation Index, B	0.950
Mass [gr]	196.8	Shearing Rate [%/min]	0.0416
Back Pressure [kPa]	200.0	Confining Pressure [kPa]	8000

	Time [min]	ε_1 [%]	ε_v [%]	σ'_3 [kPa]	σ'_d [kPa]		Time [min]	ε_1 [%]	ε_v [%]	σ'_3 [kPa]	σ'_d [kPa]
Isotropic Compression	-	0.00	0.00	100	-	Triaxial Compression	-	4.46	1.60	8000	12397
	-	0.04	0.42	300	-		-	4.90	1.74	8000	12705
	-	0.12	0.88	800	-		-	5.35	1.87	8000	12979
	-	0.16	1.11	1300	-		-	5.82	2.00	8000	13238
	-	0.20	1.28	1800	-		-	6.28	2.11	8000	13454
	-	0.23	1.43	2300	-		-	6.96	2.30	8000	13759
	-	0.26	1.55	2800	-		-	7.42	2.44	8000	13941
	-	0.29	1.66	3300	-		-	7.72	2.52	8000	14039
	-	0.31	1.77	3800	-		-	8.19	2.66	8000	14197
	-	0.35	1.87	4300	-		-	8.65	2.77	8000	14338
	-	0.37	1.95	4800	-		-	9.12	2.88	8000	14465
	-	0.40	2.04	5300	-		-	10.06	3.14	8000	14706
	-	0.43	2.13	5800	-		-	11.01	3.38	8000	14914
	-	0.45	2.21	6300	-		-	11.95	3.61	8000	15098
	-	0.48	2.30	6800	-		-	12.88	3.86	8000	15277
Triaxial Compression	-	0.51	2.38	7300	-		-	13.81	4.09	8000	15450
	-	0.53	2.47	7800	-		-	14.75	4.31	8000	15616
	-	0.54	2.52	8000	-		-	15.70	4.52	8000	15745
	-	0.54	4.58	8000	-		-	16.64	4.74	8000	15851
	-	0.00	0.00	8000	0		-	17.57	4.95	8000	15948
	-	0.04	0.02	8000	433		-	18.80	5.18	8000	16073
	-	0.11	0.06	8000	1034		-	19.38	5.26	8000	16113
	-	0.18	0.09	8000	1632		-	20.29	5.45	8000	16160
	-	0.31	0.17	8000	2756		-	21.34	5.66	8000	16184
	-	0.53	0.26	8000	4232		-	21.92	5.74	8000	16201
	-	0.74	0.35	8000	5415		-	21.74	5.75	8000	9653
	-	0.93	0.43	8000	6341		-	21.51	5.77	8000	4688
	-	1.32	0.59	8000	7793		-	21.23	5.92	8000	1020
	-	1.52	0.66	8000	8388		-	21.07	5.96	8000	0
	-	1.72	0.72	8000	8906						
	-	2.13	0.87	8000	9746						
	-	2.61	1.05	8000	10527						
	-	3.07	1.18	8000	11106						
	-	3.55	1.33	8000	11625						
	-	3.99	1.48	8000	12028						

Test:

K₀ Condition-Aged for 0 Minutes

Initial Height [mm]	108.20	Void ratio	0.530
Initial Area [mm ²]	1047.9	Saturation Index, B	0.951
Mass [gr]	196.4	Shearing Rate [%/min]	0.0416
Back Pressure [kPa]	200.0	Confining Pressure [kPa]	8000

	Time [min]	ε_1 [%]	ε_v [%]	σ'_3 [kPa]	σ'_d [kPa]		Time [min]	ε_1 [%]	ε_v [%]	σ'_3 [kPa]	σ'_d [kPa]
K ₀ Compression	-	0.00	0.00	100	0	Triaxial Compression	-	6.92	4.35	8000	14898
	-	0.50	0.50	300	601		-	7.34	4.46	8000	15075
	-	1.02	0.99	800	1538		-	7.50	4.50	8000	15129
	-	1.25	1.26	1300	2580		-	7.85	4.61	8000	15256
	-	1.48	1.49	1800	3511		-	8.35	4.75	8000	15405
	-	1.68	1.69	2300	4296		-	8.77	4.87	8000	15532
	-	1.84	1.85	2800	5092		-	9.27	5.00	8000	15651
	-	1.99	1.99	3300	5751		-	9.78	5.13	8000	15774
	-	2.11	2.12	3800	6455		-	10.21	5.23	8000	15872
	-	2.24	2.24	4300	7019		-	10.72	5.37	8000	15969
	-	2.36	2.36	4800	7576		-	11.15	5.47	8000	16039
	-	2.46	2.47	5300	8082		-	11.66	5.61	8000	16136
	-	2.58	2.59	5800	8605		-	12.17	5.72	8000	16209
	-	2.70	2.71	6300	9235		-	12.59	5.82	8000	16264
	-	2.81	2.80	6800	9556		-	13.60	6.07	8000	16413
	-	2.87	2.88	7300	9878		-	14.53	6.27	8000	16526
Triaxial Compression	-	2.97	2.98	7800	10332		-	15.47	6.48	8000	16592
	-	3.05	3.08	8000	10597		-	16.59	6.69	8000	16649
	-	3.05	3.08	8000	10597		-	17.35	6.86	8000	16687
	-	3.05	3.09	8000	10597		-	18.36	7.05	8000	16733
	-	3.11	3.11	8000	11050		-	19.29	7.21	8000	16728
	-	3.15	3.12	8000	11196		-	20.23	7.38	8000	16733
	-	3.22	3.15	8000	11384		-	21.18	7.52	8000	16689
	-	3.33	3.20	8000	11643		-	22.11	7.66	8000	16637
	-	3.42	3.24	8000	11815		-	23.12	7.80	8000	16539
	-	3.51	3.28	8000	11984		-	24.05	7.92	8000	16405
	-	3.75	3.38	8000	12376		-	25.00	8.02	8000	16244
	-	3.99	3.45	8000	12702		-	25.15	8.02	8000	16208
	-	4.23	3.53	8000	13007		-	24.98	8.05	8000	10388
	-	4.46	3.61	8000	13261		-	24.75	8.11	8000	6062
	-	4.73	3.70	8000	13524		-	24.45	8.22	8000	2993
	-	4.94	3.77	8000	13701		-	24.17	8.33	8000	1426
	-	5.54	3.95	8000	14143		-	23.67	8.50	8000	4
	-	5.91	4.05	8000	14378						
	-	6.41	4.20	8000	14649						

Test:

K₀ Condition-Aged for 45 Minutes

Initial Height [mm]	107.70	Void ratio	0.534
Initial Area [mm ²]	1059.1	Saturation Index, B	0.946
Mass [gr]	197.0	Shearing Rate [%/min]	0.0416
Back Pressure [kPa]	200.0	Confining Pressure [kPa]	8000

	Time [min]	ε_1 [%]	ε_v [%]	σ'_3 [kPa]	σ'_d [kPa]		Time [min]	ε_1 [%]	ε_v [%]	σ'_3 [kPa]	σ'_d [kPa]
K ₀ Compression	-	0.00	0.00	100	0	Triaxial Compression	-	5.92	3.95	8000	14575
	-	0.45	0.47	300	542		-	6.42	4.10	8000	14869
	-	0.97	0.96	800	1637		-	6.93	4.24	8000	15132
	-	1.30	1.25	1300	2600		-	7.35	4.36	8000	15318
	-	1.44	1.44	1800	3395		-	7.50	4.40	8000	15384
	-	1.62	1.61	2300	4221		-	7.85	4.49	8000	15536
	-	1.77	1.76	2800	4947		-	8.36	4.65	8000	15726
	-	1.90	1.90	3300	5662		-	8.78	4.77	8000	15854
	-	2.05	2.04	3800	6364		-	9.29	4.91	8000	16015
	-	2.16	2.17	4300	6921		-	9.81	5.06	8000	16158
	-	2.27	2.27	4800	7449		-	10.23	5.16	8000	16264
	-	2.40	2.39	5300	8017		-	10.75	5.32	8000	16399
	-	2.51	2.49	5800	8397		-	11.17	5.42	8000	16505
	-	2.59	2.59	6300	9002		-	11.68	5.56	8000	16612
	-	2.71	2.70	6800	9386		-	12.18	5.69	8000	16726
	-	2.80	2.79	7300	9883		-	12.69	5.84	8000	16837
Triaxial Compression	-	2.90	2.88	7800	10222		-	13.62	6.06	8000	17025
	-	2.98	2.95	8000	10482		-	14.56	6.29	8000	17186
	-	3.02	3.00	8000	9830		-	15.50	6.52	8000	17342
	-	3.02	3.00	8000	9830		-	16.35	6.72	8000	17475
	-	3.03	3.00	8000	10001		-	17.45	6.98	8000	17652
	-	3.10	3.03	8000	10893		-	18.37	7.20	8000	17784
	-	3.17	3.06	8000	11324		-	19.31	7.39	8000	17906
	-	3.25	3.09	8000	11567		-	20.34	7.60	8000	18031
	-	3.33	3.12	8000	11752		-	21.28	7.80	8000	18132
	-	3.41	3.16	8000	11918		-	22.20	7.98	8000	18207
	-	3.57	3.20	8000	12214		-	23.21	8.18	8000	18291
	-	3.74	3.27	8000	12474		-	24.15	8.36	8000	18343
	-	3.99	3.36	8000	12832		-	25.10	8.51	8000	18357
	-	4.24	3.43	8000	13141		-	25.15	8.52	8000	18359
	-	4.49	3.52	8000	13412		-	24.97	8.53	8000	11452
	-	4.74	3.60	8000	13663		-	24.75	8.55	8000	6720
	-	4.99	3.68	8000	13893		-	24.45	8.66	8000	3184
	-	5.24	3.74	8000	14107		-	24.17	8.79	8000	1299
	-	5.50	3.82	8000	14300		-	23.82	8.95	8000	8

Test:

K₀ Condition-Aged for 1440 Minutes

Initial Height [mm]	107.95	Void ratio	0.532
Initial Area [mm ²]	1055.2	Saturation Index, B	0.951
Mass [gr]	197.0	Shearing Rate [%/min]	0.0416
Back Pressure [kPa]	200.0	Confining Pressure [kPa]	8000

	Time [min]	ε_1 [%]	ε_v [%]	σ'_3 [kPa]	σ'_d [kPa]		Time [min]	ε_1 [%]	ε_v [%]	σ'_3 [kPa]	σ'_d [kPa]
K ₀ Compression	-	0.00	0.00	100	0	Triaxial Compression	-	7.14	4.36	8000	15262
	-	0.50	0.48	300	582		-	7.50	4.47	8000	15420
	-	0.96	0.96	800	1712		-	7.56	4.49	8000	15449
	-	1.22	1.21	1300	2544		-	8.07	4.62	8000	15645
	-	1.40	1.40	1800	3361		-	8.50	4.74	8000	15779
	-	1.55	1.55	2300	4160		-	9.00	4.87	8000	15945
	-	1.73	1.73	2800	5043		-	9.51	5.01	8000	16078
	-	1.87	1.87	3300	5703		-	9.93	5.12	8000	16187
	-	1.99	1.99	3800	6294		-	10.44	5.26	8000	16283
	-	2.10	2.11	4300	6913		-	10.96	5.39	8000	16391
	-	2.23	2.23	4800	7510		-	11.39	5.48	8000	16473
	-	2.34	2.34	5300	8067		-	11.90	5.63	8000	16568
	-	2.45	2.45	5800	8573		-	12.33	5.73	8000	16649
	-	2.56	2.56	6300	8998		-	12.84	5.84	8000	16731
	-	2.65	2.66	6800	9427		-	13.77	6.08	8000	16870
	-	2.74	2.75	7300	9714		-	14.79	6.33	8000	17006
Triaxial Compression	-	2.84	2.85	7800	10193		-	15.73	6.52	8000	17103
	-	2.91	2.91	8000	10442		-	16.68	6.73	8000	17220
	-	3.23	3.18	8000	10335		-	17.62	6.94	8000	17296
	-	3.23	3.18	8000	10335		-	18.55	7.14	8000	17376
	-	3.29	3.20	8000	11435		-	19.56	7.33	8000	17437
	-	3.32	3.21	8000	11673		-	20.51	7.50	8000	17460
	-	3.42	3.24	8000	12097		-	20.89	7.58	8000	17469
	-	3.51	3.27	8000	12313		-	21.50	7.70	8000	17487
	-	3.62	3.31	8000	12496		-	22.44	7.86	8000	17497
	-	3.71	3.34	8000	12631		-	23.37	8.02	8000	17492
	-	3.94	3.43	8000	12949		-	24.35	8.17	8000	17443
	-	4.18	3.50	8000	13234		-	25.24	8.29	8000	17355
	-	4.43	3.58	8000	13508		-	25.34	8.30	8000	17353
	-	4.68	3.66	8000	13741		-	25.24	8.30	8000	13071
	-	4.93	3.75	8000	13964		-	25.00	8.33	8000	7066
	-	5.18	3.81	8000	14160		-	24.53	8.54	8000	1917
	-	5.69	3.97	8000	14517		-	24.00	8.73	8000	4
	-	6.12	4.09	8000	14780						
	-	6.64	4.23	8000	15033						

Test:

K₀ Condition-Aged for 10080 Minutes

Initial Height [mm]	108.71	Void ratio	0.533
Initial Area [mm ²]	1044.9	Saturation Index, B	0.958
Mass [gr]	196.4	Shearing Rate [%/min]	0.0416
Back Pressure [kPa]	200.0	Confining Pressure [kPa]	8000

	Time [min]	ε_1 [%]	ε_v [%]	σ'_3 [kPa]	σ'_d [kPa]		Time [min]	ε_1 [%]	ε_v [%]	σ'_3 [kPa]	σ'_d [kPa]
K₀ Compression	-	0.00	0.00	100	0	Triaxial Compression	-	6.68	4.22	8000	15299
	-	0.48	0.49	300	647		-	7.10	4.35	8000	15480
	-	1.00	0.97	800	1832		-	7.50	4.46	8000	15639
	-	1.23	1.24	1300	2638		-	7.61	4.49	8000	15683
	-	1.46	1.47	1800	3748		-	8.03	4.62	8000	15853
	-	1.67	1.67	2300	4428		-	8.53	4.75	8000	16009
	-	1.81	1.81	2800	5321		-	9.03	4.89	8000	16164
	-	1.96	1.95	3300	5911		-	9.46	5.00	8000	16286
	-	2.07	2.07	3800	6550		-	9.97	5.13	8000	16396
	-	2.21	2.20	4300	7168		-	10.49	5.26	8000	16517
	-	2.35	2.34	4800	7978		-	10.91	5.37	8000	16601
	-	2.45	2.46	5300	8645		-	11.42	5.51	8000	16694
	-	2.58	2.57	5800	9153		-	11.85	5.62	8000	16781
	-	2.66	2.66	6300	9413		-	12.36	5.74	8000	16862
	-	2.73	2.75	6800	9849		-	12.78	5.86	8000	16939
	-	2.81	2.83	7300	10297		-	13.79	6.11	8000	17113
Triaxial Compression	-	2.93	2.94	7800	10613		-	14.73	6.35	8000	17222
	-	2.99	3.00	8000	10749		-	15.67	6.56	8000	17324
	-	3.25	3.17	8000	9909		-	16.61	6.78	8000	17414
	-	3.25	3.17	8000	9909		-	17.68	7.03	8000	17536
	-	3.28	3.17	8000	10490		-	18.55	7.21	8000	17621
	-	3.32	3.19	8000	11322		-	19.49	7.43	8000	17702
	-	3.40	3.21	8000	12076		-	20.42	7.61	8000	17776
	-	3.47	3.23	8000	12430		-	21.36	7.81	8000	17820
	-	3.56	3.27	8000	12722		-	22.30	7.97	8000	17854
	-	3.67	3.31	8000	12934		-	23.29	8.13	8000	17886
	-	3.75	3.33	8000	13073		-	24.22	8.28	8000	17903
	-	4.02	3.42	8000	13426		-	25.16	8.43	8000	17896
	-	4.26	3.52	8000	13685		-	25.74	8.51	8000	17924
	-	4.46	3.56	8000	13879		-	25.62	8.55	8000	10730
	-	4.70	3.65	8000	14092		-	25.38	8.60	8000	5905
	-	4.95	3.72	8000	14291		-	25.14	8.70	8000	3138
	-	5.18	3.78	8000	14450		-	24.76	8.87	8000	779
	-	5.65	3.91	8000	14770		-	24.51	8.97	8000	6
	-	6.13	4.05	8000	15036						

Tests Presented in Chapter 4

Test:

Strain Rate=0.00260 %/min- σ'_3 =250 kPa

Initial Height [mm]	107.19	Void ratio	0.536
Initial Area [mm ²]	1060.9	Saturation Index, B	0.950
Mass [gr]	196.2	Shearing Rate [%/min]	0.00260
Back Pressure [kPa]	200.0	Confining Pressure [kPa]	250

	Time [min]	ϵ_1 [%]	ϵ_v [%]	σ'_3 [kPa]	σ'_d [kPa]		Time [min]	ϵ_1 [%]	ϵ_v [%]	σ'_3 [kPa]	σ'_d [kPa]
Isotropic Comp.	-	0.00	0.00	110	-		0.01	1.09	0.09	250	723
	-	0.02	0.21	199	-		0.10	1.09	0.09	250	721
	-	0.03	0.28	250	-		0.25	1.09	0.09	250	726
	-	0.03	0.29	250	-		0.50	1.09	0.09	250	723
Triaxial Compression	-	0.00	0.00	250	0		0.75	1.09	0.09	250	723
	-	0.03	0.03	250	44		1.00	1.09	0.09	250	728
	-	0.12	0.04	250	144		2.50	1.10	0.09	250	726
	-	0.22	0.11	250	239		5.00	1.11	0.09	250	728
	-	0.31	0.12	250	308		7.50	1.12	0.09	250	725
	-	0.41	0.14	250	389		10.00	1.12	0.09	250	725
	-	0.50	0.15	250	448		25.00	1.16	0.07	250	736
	-	0.59	0.17	250	502		50.00	1.17	0.06	250	725
	-	0.69	0.16	250	559		75.00	1.18	0.06	250	722
	-	0.78	0.14	250	604		100.00	1.18	0.05	250	720
	-	0.88	0.14	250	651		250.00	1.18	0.04	250	714
	-	0.98	0.12	250	687		500.00	1.19	0.04	250	707
	-	1.09	0.09	250	723		750.00	1.19	0.03	250	707
							1000.0	1.22	0.01	250	735
							1350.0	1.23	0.01	250	741

Test:

Strain Rate=0.0416 %/min- σ'_3 =250 kPa

Initial Height [mm]	107.19	Void ratio	0.530
Initial Area [mm ²]	1057.2	Saturation Index, B	0.951
Mass [gr]	196.3	Shearing Rate [%/min]	0.0416
Back Pressure [kPa]	200.0	Confining Pressure [kPa]	250

	Time [min]	ε_1 [%]	ε_v [%]	σ'_3 [kPa]	σ'_d [kPa]		Time [min]	ε_1 [%]	ε_v [%]	σ'_3 [kPa]	σ'_d [kPa]
Isotropic Comp.	-	0.00	0.00	100	-		0.01	0.94	-0.02	250	825
	-	0.01	0.18	199	-		0.10	0.94	-0.02	250	819
	-	0.02	0.25	250	-		0.25	0.94	-0.02	250	814
	-	0.02	0.26	250	-		0.50	0.95	-0.02	250	830
Triaxial Compression	-	0.00	0.00	250	0		0.75	0.95	-0.02	250	812
	-	0.04	0.02	250	49		1.00	0.95	-0.02	250	808
	-	0.13	0.04	250	186		2.50	0.95	-0.02	250	799
	-	0.24	0.09	250	363		5.00	0.96	-0.02	250	806
	-	0.32	0.10	250	441		7.50	0.96	-0.02	250	803
	-	0.41	0.10	250	534		10.00	0.96	-0.02	250	803
	-	0.52	0.10	250	621		26.50	0.98	-0.03	250	799
	-	0.64	0.08	250	703		50.00	0.98	-0.03	250	805
	-	0.87	0.01	250	807		75.00	0.99	-0.04	250	792
	-	0.94	-0.02	250	825		100.00	0.99	-0.05	250	809
							250.00	1.00	-0.08	250	763
							500.00	1.00	-0.10	250	757
Creep							750.00	1.00	-0.11	250	757
							1000.0	1.00	-0.12	250	759
							1450.0	1.00	-0.14	250	739

Test:

Strain Rate=0.666 %/min- σ'_3 =250 kPa

Initial Height [mm]	107.70	Void ratio	0.536
Initial Area [mm ²]	1058.2	Saturation Index, B	0.952
Mass [gr]	196.6	Shearing Rate [%/min]	0.666
Back Pressure [kPa]	200.0	Confining Pressure [kPa]	250

	Time [min]	ϵ_1 [%]	ϵ_v [%]	σ'_3 [kPa]	σ'_d [kPa]		Time [min]	ϵ_1 [%]	ϵ_v [%]	σ'_3 [kPa]	σ'_d [kPa]
Isotropic Comp.	-	0.00	0.00	110	-		0.01	1.17	-0.02	250	795
	-	0.02	0.18	199	-		0.10	1.17	-0.03	250	752
	-	0.03	0.25	250	-		0.25	1.17	-0.03	250	749
	-	0.03	0.25	250	-		0.50	1.17	-0.03	250	747
Triaxial Compression	-	0.00	0.00	250	0		0.75	1.17	-0.03	250	747
	-	0.05	0.02	250	96		1.00	1.17	-0.03	250	745
	-	0.14	0.04	250	239		2.50	1.17	-0.03	250	749
	-	0.23	0.07	250	338		5.00	1.18	-0.03	250	745
	-	0.33	0.15	250	428		7.50	1.18	-0.03	250	743
	-	0.42	0.15	250	493		10.00	1.18	-0.03	250	741
	-	0.51	0.16	250	548		25.00	1.19	-0.03	250	745
	-	0.60	0.15	250	598		50.00	1.20	-0.03	250	743
	-	0.70	0.07	250	640		75.00	1.20	-0.03	250	745
	-	0.79	0.05	250	677		100.00	1.20	-0.04	250	762
	-	0.88	0.03	250	713		250.00	1.21	-0.05	250	744
	-	0.98	0.01	250	743		500.00	1.22	-0.06	250	740
	-	1.08	0.00	250	774		750.00	1.22	-0.06	250	733
	-	1.16	-0.02	250	795		1000.0	1.22	-0.07	250	720
							1450.0	1.24	-0.08	250	733
							1550.0	1.24	-0.09	250	735

Creep

Test:

Strain Rate=0.00260 %/min- σ'_3 =8000 kPa

Initial Height [mm]	107.70	Void ratio	0.540
Initial Area [mm ²]	1053.6	Saturation Index, B	0.930
Mass [gr]	195.6	Shearing Rate [%/min]	0.00260
Back Pressure [kPa]	200.0	Confining Pressure [kPa]	8000

	Time [min]	ε_1 [%]	ε_v [%]	σ'_3 [kPa]	σ'_d [kPa]		Time [min]	ε_1 [%]	ε_v [%]	σ'_3 [kPa]	σ'_d [kPa]
Isotropic Compression	-	0.00	0.00	100	-	Creep	0.01	2.85	1.21	8000	10594
	-	0.03	0.25	291	-		0.10	2.91	1.21	8000	10687
	-	0.11	0.64	781	-		0.25	2.92	1.21	8000	10573
	-	0.17	0.90	1272	-		0.50	2.93	1.21	8000	10502
	-	0.21	1.08	1762	-		0.75	2.94	1.22	8000	10454
	-	0.24	1.21	2253	-		1.00	2.95	1.22	8000	10416
	-	0.26	1.34	2743	-		2.50	3.00	1.22	8000	10456
	-	0.29	1.45	3234	-		5.00	3.05	1.23	8000	10464
	-	0.32	1.55	3724	-		7.50	3.10	1.26	8000	10470
	-	0.34	1.65	4215	-		10.00	3.14	1.27	8000	10462
	-	0.37	1.73	4705	-		25.00	3.30	1.28	8000	10459
	-	0.40	1.81	5196	-		50.00	3.44	1.38	8000	10468
	-	0.42	1.88	5686	-		75.00	3.53	1.40	8000	10469
	-	0.45	1.96	6177	-		100.00	3.60	1.44	8000	10456
	-	0.47	2.03	6667	-		250.00	3.82	1.52	8000	10470
	-	0.50	2.10	7158	-		500.00	4.02	1.60	8000	10489
	-	0.52	2.17	7697	-		750.00	4.12	1.63	8000	10461
	-	0.54	2.20	8000	-		1000.0	4.20	1.64	8000	10444
	-	0.54	2.22	8000	-		1440.0	4.30	1.68	8000	10465
Triaxial Compression	-	0.00	0.00	8000	0						
	-	0.08	0.02	8000	782						
	-	0.18	0.09	8000	1607						
	-	0.26	0.13	8000	2293						
	-	0.50	0.26	8000	3919						
	-	0.74	0.37	8000	5194						
	-	1.21	0.59	8000	7159						
	-	1.68	0.76	8000	8534						
	-	2.13	0.95	8000	9530						
	-	2.36	1.03	8000	9960						
	-	2.61	1.11	8000	10281						
	-	2.69	1.15	8000	10386						
	-	2.74	1.16	8000	10455						
	-	2.79	1.17	8000	10522						
	-	2.83	1.20	8000	10578						
	-	2.85	1.21	8000	10594						

Test

Strain Rate=0.0416 %/min- σ'_3 =8000 kPa

Initial Height [mm]	107.70	Void ratio	0.535
Initial Area [mm ²]	1051.4	Saturation Index, B	0.939
Mass [gr]	195.4	Shearing Rate [%/min]	0.04
Back Pressure [kPa]	200.0	Confining Pressure [kPa]	8000

	Time [min]	ϵ_1 [%]	ϵ_v [%]	σ'_3 [kPa]	σ'_d [kPa]		Time [min]	ϵ_1 [%]	ϵ_v [%]	σ'_3 [kPa]	σ'_d [kPa]
Isotropic Compression	-	0.00	0.00	100	-	Tri. Comp.	-	2.70	1.12	8000	11093
	-	0.01	0.30	291	-		-	2.74	1.13	8000	11160
	-	0.07	0.74	781	-		-	2.81	1.17	8000	11246
	-	0.11	1.00	1272	-	Creep	0.01	2.81	1.17	8000	11246
	-	0.15	1.19	1762	-		0.10	3.39	1.30	8000	11588
	-	0.19	1.34	2253	-		0.25	3.68	1.40	8000	11491
	-	0.22	1.48	2743	-		0.50	3.86	1.42	8000	11465
	-	0.24	1.60	3234	-		0.75	3.94	1.46	8000	11456
	-	0.27	1.72	3724	-		1.00	4.01	1.49	8000	11447
	-	0.30	1.83	4215	-		2.50	4.20	1.53	8000	11381
	-	0.32	1.91	4705	-		5.00	4.35	1.56	8000	11381
	-	0.35	2.00	5196	-		7.50	4.44	1.60	8000	11368
	-	0.38	2.08	5686	-		10.00	4.52	1.61	8000	11396
	-	0.41	2.15	6177	-		25.00	4.75	1.69	8000	11386
	-	0.43	2.24	6667	-		49.00	4.94	1.74	8000	11424
	-	0.46	2.32	7158	-		77.00	5.07	1.80	8000	11344
	-	0.48	2.39	7648	-		100.00	5.14	1.83	8000	11405
	-	0.50	2.45	8000	-		250.00	5.42	1.91	8000	11444
	-	0.50	2.49	8000	-		500.00	5.71	2.02	8000	11451
	-	0.00	0.00	8000	0		750.00	5.88	2.07	8000	11405
	-	0.09	0.05	8000	803		1006.00	5.99	2.12	8000	11396
	-	0.18	0.08	8000	1573		1440.00	6.12	2.16	8000	11374
	-	0.28	0.15	8000	2434						
	-	0.53	0.27	8000	4216						
	-	0.74	0.38	8000	5520						
	-	1.20	0.57	8000	7691						
	-	1.72	0.78	8000	9301						
	-	2.14	0.95	8000	10308						
	-	2.40	1.02	8000	10673						
	-	2.43	1.04	8000	10711						
	-	2.46	1.05	8000	10765						
	-	2.51	1.06	8000	10832						
	-	2.56	1.08	8000	10903						
	-	2.60	1.10	8000	10966						
	-	2.65	1.11	8000	11028						
Triaxial Compression											

Test:

Strain Rate=0.666 %/min- σ'_3 =8000 kPa

Initial Height [mm]	108.21	Void ratio	0.540
Initial Area [mm ²]	1054.3	Saturation Index, B	0.922
Mass [gr]	195.7	Shearing Rate [%/min]	0.666
Back Pressure [kPa]	200.0	Confining Pressure [kPa]	8000

	Time [min]	ε_1 [%]	ε_v [%]	σ'_3 [kPa]	σ'_d [kPa]		Time [min]	ε_1 [%]	ε_v [%]	σ'_3 [kPa]	σ'_d [kPa]
Isotropic Compression	-	0.00	0.00	100	-	Creep	0.01	2.87	1.09	8000	11277
	-	0.04	0.37	291	-		0.10	4.76	1.50	8000	12060
	-	0.12	0.77	781	-		0.25	5.33	1.63	8000	12150
	-	0.18	1.04	1272	-		0.50	5.61	1.73	8000	12155
	-	0.23	1.23	1762	-		0.75	5.77	1.75	8000	12143
	-	0.27	1.36	2253	-		1.00	5.86	1.78	8000	12136
	-	0.30	1.47	2743	-		2.50	6.13	1.86	8000	12122
	-	0.33	1.59	3234	-		5.00	6.32	1.91	8000	12126
	-	0.36	1.70	3724	-		7.50	6.44	1.97	8000	12115
	-	0.39	1.79	4215	-		10.00	6.52	1.98	8000	12113
	-	0.42	1.87	4705	-		25.00	6.79	2.07	8000	12084
	-	0.45	1.95	5196	-		50.00	7.01	2.13	8000	12099
	-	0.48	2.02	5686	-		75.00	7.14	2.17	8000	12060
	-	0.50	2.10	6177	-		100.00	7.24	2.19	8000	12156
	-	0.53	2.16	6667	-		250.00	7.66	2.33	8000	12196
	-	0.56	2.23	7158	-		500.00	7.99	2.43	8000	12130
	-	0.58	2.29	7697	-		750.00	8.17	2.51	8000	12101
	-	0.60	2.33	8000	-		1000.0	8.30	2.55	8000	12101
	-	0.60	2.33	8000	-		1440.0	8.47	2.61	8000	12085
Triaxial Compression	-	0.00	0.00	8000	0						
	-	0.00	0.00	8000	20						
	-	0.09	0.04	8000	875						
	-	0.19	0.10	8000	1681						
	-	0.28	0.15	8000	2431						
	-	0.52	0.27	8000	4096						
	-	0.75	0.38	8000	5422						
	-	1.21	0.53	8000	7569						
	-	1.67	0.71	8000	9026						
	-	1.91	0.79	8000	9607						
	-	2.14	0.88	8000	10126						
	-	2.37	0.92	8000	10555						
	-	2.61	1.02	8000	10926						
	-	2.87	1.09	8000	11277						

Test:

Type I

Initial Height [mm] 107.70
Initial Area [mm²] 1056.6
Mass [gr] 197.0
Back Pressure [kPa] 200.0

Void ratio 0.531
Saturation Index, B 0.942
Shearing Rate [%/min] 0.0416
Confining Pressure [kPa] 8000

	Time [min]	ε_1 [%]	ε_v [%]	σ'_3 [kPa]	σ'_d [kPa]		Time [min]	ε_1 [%]	ε_v [%]	σ'_3 [kPa]	σ'_d [kPa]
Isotropic Compression	-	0.00	0.00	100	-	Creep	0.01	0.97	0.47	8000	6440
	-	0.04	0.27	300	-		0.10	0.98	0.47	8000	6528
	-	0.12	0.63	800	-		0.25	0.99	0.47	8000	6453
	-	0.18	0.86	1300	-		0.50	1.00	0.47	8000	6424
	-	0.21	1.03	1800	-		0.75	1.00	0.47	8000	6412
	-	0.25	1.18	2300	-		1.00	1.01	0.48	8000	6406
	-	0.28	1.29	2800	-		2.50	1.03	0.51	8000	6402
	-	0.31	1.41	3300	-		5.00	1.05	0.52	8000	6403
	-	0.34	1.50	3800	-		7.50	1.06	0.53	8000	6428
	-	0.36	1.60	4300	-		10.00	1.07	0.53	8000	6427
	-	0.40	1.69	4800	-		25.00	1.10	0.54	8000	6423
	-	0.43	1.77	5300	-		50.00	1.13	0.57	8000	6434
	-	0.45	1.86	5800	-		75.00	1.15	0.57	8000	6477
	-	0.48	1.93	6300	-		100.00	1.16	0.57	8000	6474
	-	0.50	2.00	6800	-		250.00	1.20	0.59	8000	6468
	-	0.53	2.07	7300	-		500.00	1.23	0.59	8000	6461
	-	0.56	2.15	7800	-		750.00	1.25	0.61	8000	6456
	-	0.57	2.19	8000	-		1000.0	1.26	0.61	8000	6452
	-	0.57	2.21	8000	-		1440.0	1.28	0.61	8000	6449
Triaxial Compression	-	0.00	0.00	8000	0						
	-	0.05	0.04	8000	429						
	-	0.18	0.10	8000	1500						
	-	0.25	0.13	8000	2019						
	-	0.38	0.22	8000	3003						
	-	0.52	0.28	8000	3889						
	-	0.74	0.36	8000	5136						
	-	0.90	0.45	8000	5912						
	-	0.96	0.47	8000	6184						
	-	0.97	0.47	8000	6440						

Test:

Type II

Initial Height [mm] 107.70
Initial Area [mm²] 1065.5
Mass [gr] 208.1
Back Pressure [kPa] 200.0

Void ratio 0.461
Saturation Index, B 0.951
Shearing Rate [%/min] 0.0416
Confining Pressure [kPa] 8000

	Time [min]	ε_1 [%]	ε_v [%]	σ'_3 [kPa]	σ'_d [kPa]		Time [min]	ε_1 [%]	ε_v [%]	σ'_3 [kPa]	σ'_d [kPa]
Isotropic Compression	-	0.00	0.00	100	-	Creep	0.01	1.37	0.81	8000	6435
	-	0.07	0.29	300	-		0.10	1.38	0.82	8000	6822
	-	0.16	0.61	800	-		0.25	1.39	0.82	8000	6662
	-	0.22	0.83	1300	-		0.50	1.39	0.84	8000	6499
	-	0.27	1.01	1800	-		0.75	1.40	0.84	8000	6501
	-	0.31	1.14	2300	-		1.00	1.40	0.84	8000	6494
	-	0.35	1.29	2800	-		2.50	1.43	0.87	8000	6503
	-	0.40	1.42	3300	-		5.00	1.45	0.89	8000	6500
	-	0.44	1.53	3800	-		7.50	1.48	0.89	8000	6514
	-	0.48	1.64	4300	-		10.00	1.49	0.91	8000	6508
	-	0.52	1.78	4800	-		25.00	1.54	0.94	8000	6488
	-	0.56	1.87	5300	-		50.00	1.58	0.98	8000	6501
	-	0.59	1.97	5800	-		75.00	1.61	1.00	8000	6511
	-	0.63	2.07	6300	-		100.00	1.63	1.00	8000	6503
	-	0.66	2.17	6800	-		250.00	1.70	1.03	8000	6509
	-	0.69	2.29	7300	-		500.00	1.74	1.09	8000	6488
	-	0.73	2.38	7800	-		750.00	1.77	1.12	8000	6497
	-	0.74	2.44	8000	-		1000.0	1.79	1.14	8000	6477
	-	0.75	2.52	8000	-		1460.0	1.82	1.16	8000	6507
Triaxial Compression	-	0.00	0.00	8000	0						
	-	0.07	0.04	8000	456						
	-	0.15	0.09	8000	1000						
	-	0.27	0.17	8000	1711						
	-	0.50	0.30	8000	2888						
	-	0.71	0.44	8000	3911						
	-	0.95	0.57	8000	4901						
	-	1.19	0.71	8000	5814						
	-	1.32	0.79	8000	6280						
	-	1.37	0.81	8000	6435						

Test:

Type III

Initial Height [mm]	106.68	Void ratio	0.462
Initial Area [mm ²]	1057.7	Saturation Index, B	0.871
Mass [gr]	204.5	Shearing Rate [%/min]	0.0416
Back Pressure [kPa]	200.0	Confining Pressure [kPa]	8000

	Time [min]	ε_1 [%]	ε_v [%]	σ'_3 [kPa]	σ'_d [kPa]		Time [min]	ε_1 [%]	ε_v [%]	σ'_3 [kPa]	σ'_d [kPa]
Isotropic Compression	-	0.00	0.00	100	-	Creep	0.01	1.95	1.29	8000	6429
	-	0.05	0.29	300	-		0.10	1.96	1.29	8000	6687
	-	0.13	0.69	800	-		0.25	1.96	1.30	8000	6523
	-	0.20	0.97	1300	-		0.50	1.96	1.30	8000	6451
	-	0.26	1.21	1800	-		0.75	1.97	1.31	8000	6433
	-	0.32	1.43	2300	-		1.00	1.98	1.32	8000	6438
	-	0.37	1.64	2800	-		2.50	2.01	1.33	8000	6442
	-	0.43	1.84	3300	-		5.00	2.04	1.35	8000	6439
	-	0.47	1.99	3800	-		7.50	2.07	1.38	8000	6435
	-	0.52	2.16	4300	-		10.00	2.09	1.40	8000	6437
	-	0.57	2.34	4800	-		25.00	2.16	1.46	8000	6438
	-	0.61	2.48	5300	-		50.00	2.22	1.50	8000	6441
	-	0.65	2.62	5800	-		75.00	2.25	1.56	8000	6436
	-	0.69	2.77	6300	-		100.00	2.28	1.59	8000	6453
	-	0.73	2.90	6800	-		250.00	2.36	1.74	8000	6461
	-	0.77	3.05	7300	-		500.00	2.43	1.94	8000	6448
	-	0.81	3.19	7800	-		750.00	2.46	2.10	8000	6450
	-	0.82	3.27	8000	-		1000.0	2.49	2.25	8000	6468
	-	0.83	3.44	8000	-		1450.0	2.52	2.43	8000	6485
Triaxial Compression	-	0.00	0.00	8000	0						
	-	0.07	0.05	8000	312						
	-	0.15	0.10	8000	676						
	-	0.39	0.27	8000	1642						
	-	0.63	0.45	8000	2539						
	-	0.88	0.62	8000	3403						
	-	1.11	0.79	8000	4123						
	-	1.34	0.95	8000	4803						
	-	1.57	1.09	8000	5446						
	-	1.81	1.22	8000	6078						
	-	1.85	1.24	8000	6197						
	-	1.90	1.27	8000	6314						
	-	1.95	1.29	8000	6429						

Test:

Type IV

Initial Height [mm]	106.93	Void ratio	0.468
Initial Area [mm ²]	1060.0	Saturation Index, B	0.857
Mass [gr]	204.6	Shearing Rate [%/min]	0.0416
Back Pressure [kPa]	200.0	Confining Pressure [kPa]	8000

	Time [min]	ε_1 [%]	ε_v [%]	σ'_3 [kPa]	σ'_d [kPa]		Time [min]	ε_1 [%]	ε_v [%]	σ'_3 [kPa]	σ'_d [kPa]
Isotropic Compression	-	0.00	0.00	100	-	Creep	0.01	2.13	1.35	8000	6473
	-	0.07	0.36	300	-		0.10	2.14	1.35	8000	6727
	-	0.20	0.87	800	-		0.25	2.15	1.35	8000	6594
	-	0.28	1.22	1300	-		0.50	2.15	1.36	8000	6487
	-	0.36	1.54	1800	-		0.75	2.15	1.37	8000	6465
	-	0.42	1.81	2300	-		1.00	2.16	1.37	8000	6469
	-	0.49	2.06	2800	-		2.50	2.19	1.38	8000	6480
	-	0.53	2.27	3300	-		5.00	2.23	1.42	8000	6476
	-	0.59	2.49	3800	-		7.50	2.26	1.44	8000	6473
	-	0.64	2.69	4300	-		10.00	2.28	1.45	8000	6465
	-	0.70	2.89	4800	-		25.00	2.35	1.48	8000	6467
	-	0.75	3.05	5300	-		50.00	2.41	1.52	8000	6459
	-	0.79	3.14	5800	-		75.00	2.45	1.55	8000	6463
	-	0.84	3.39	6300	-		100.00	2.48	1.56	8000	6471
	-	0.88	3.55	6800	-		250.00	2.57	1.63	8000	6480
	-	0.93	3.69	7300	-		500.00	2.64	1.69	8000	6456
	-	0.97	3.83	7800	-		750.00	2.68	1.72	8000	6467
	-	0.98	3.91	8000	-		1000.0	2.70	1.76	8000	6452
	-	1.00	4.06	8000	-		1533.0	2.75	1.77	8000	6470
Triaxial Compression	-	0.00	0.00	8000	0						
	-	0.01	0.01	8000	38						
	-	0.10	0.07	8000	424						
	-	0.36	0.23	8000	1371						
	-	0.58	0.39	8000	2117						
	-	0.81	0.56	8000	2871						
	-	1.04	0.71	8000	3569						
	-	1.28	0.85	8000	4238						
	-	1.52	1.00	8000	4899						
	-	1.85	1.19	8000	5770						
	-	2.04	1.28	8000	6238						
	-	2.09	1.31	8000	6353						
	-	2.13	1.35	8000	6473						

Test:

Type V

Initial Height [mm] 107.19
Initial Area [mm²] 1056.3
Mass [gr] 192.9
Back Pressure [kPa] 200.0

Void ratio 0.555
Saturation Index, B 0.913
Shearing Rate [%/min] 0.0416
Confining Pressure [kPa] 8000

	Time [min]	ε_1 [%]	ε_v [%]	σ'_3 [kPa]	σ'_d [kPa]		Time [min]	ε_1 [%]	ε_v [%]	σ'_3 [kPa]	σ'_d [kPa]
Isotropic Compression	-	0.00	0.00	100	-	Creep	0.01	2.42	1.61	8000	6472
	-	0.01	0.24	300	-		0.10	2.44	1.61	8000	6952
	-	0.04	0.86	800	-		0.25	2.48	1.62	8000	6829
	-	0.11	1.31	1300	-		0.50	2.49	1.62	8000	6695
	-	0.17	1.70	1800	-		0.75	2.50	1.62	8000	6590
	-	0.23	2.02	2300	-		1.00	2.50	1.62	8000	6539
	-	0.27	2.33	2800	-		2.50	2.52	1.62	8000	6451
	-	0.32	2.60	3300	-		5.00	2.54	1.64	8000	6464
	-	0.37	2.90	3800	-		7.50	2.56	1.67	8000	6461
	-	0.41	3.12	4300	-		10.00	2.58	1.70	8000	6464
	-	0.46	3.36	4800	-		25.00	2.66	1.75	8000	6475
	-	0.51	3.59	5300	-		50.00	2.72	1.77	8000	6473
	-	0.55	3.79	5800	-		75.00	2.76	1.81	8000	6471
	-	0.59	3.97	6300	-		100.00	2.79	1.84	8000	6464
	-	0.63	4.18	6800	-		250.00	2.89	1.90	8000	6472
	-	0.67	4.37	7300	-		500.00	2.97	1.96	8000	6500
	-	0.71	4.53	7800	-		750.00	3.02	2.00	8000	6492
	-	0.73	4.63	8000	-		1000.0	3.05	2.02	8000	6489
	-	0.74	4.80	8000	-		1500.0	3.09	2.06	8000	6484
Triaxial Compression	-	0.00	0.00	8000	0		2700.0	3.16	2.10	8000	6477
	-	0.08	0.08	8000	314						
	-	0.32	0.23	8000	1051						
	-	0.55	0.38	8000	1803						
	-	0.77	0.54	8000	2429						
	-	1.02	0.71	8000	3130						
	-	1.32	0.90	8000	3872						
	-	1.51	1.02	8000	4375						
	-	2.02	1.35	8000	5570						
	-	2.34	1.52	8000	6287						
	-	2.39	1.56	8000	6391						
	-	2.42	1.61	8000	6472						

Test:

Type VI

Initial Height [mm] 107.44
Initial Area [mm²] 1023.9
Mass [gr] 160.0
Back Pressure [kPa] 200.0

Void ratio 0.822
Saturation Index, B 0.951
Shearing Rate [%/min] 0.0416
Confining Pressure [kPa] 8000

	Time [min]	ε_1 [%]	ε_v [%]	σ'_3 [kPa]	σ'_d [kPa]		Time [min]	ε_1 [%]	ε_v [%]	σ'_3 [kPa]	σ'_d [kPa]
Isotropic Compression	-	0.00	0.00	100	-	Creep	0.01	3.35	2.40	8000	6240
	-	0.05	0.51	300	-		0.10	3.37	2.41	8000	6706
	-	0.17	1.39	800	-		0.25	3.38	2.41	8000	6423
	-	0.30	2.04	1300	-		0.50	3.38	2.41	8000	6193
	-	0.42	2.60	1800	-		0.75	3.39	2.42	8000	6234
	-	0.51	3.07	2300	-		1.00	3.39	2.42	8000	6229
	-	0.60	3.51	2800	-		2.50	3.42	2.44	8000	6216
	-	0.69	3.95	3300	-		5.00	3.47	2.49	8000	6252
	-	0.76	4.32	3800	-		7.50	3.50	2.51	8000	6242
	-	0.84	4.66	4300	-		10.00	3.53	2.53	8000	6246
	-	0.91	4.94	4800	-		25.00	3.64	2.60	8000	6252
	-	0.98	5.27	5300	-		50.00	3.73	2.68	8000	6244
	-	1.05	5.52	5800	-		75.00	3.79	2.74	8000	6277
	-	1.11	5.75	6300	-		100.00	3.83	2.77	8000	6271
	-	1.18	6.03	6800	-		250.00	3.98	2.90	8000	6341
	-	1.24	6.30	7300	-		500.00	4.09	2.99	8000	6320
	-	1.30	6.55	7800	-		750.00	4.15	3.04	8000	6306
Triaxial Compression	-	1.32	6.66	8000	-	Creep	1000.0	4.19	3.06	8000	6302
	-	1.35	7.14	8000	-		1593.0	4.26	3.11	8000	6317
	-	0.00	0.00	8000	0						
	-	0.08	0.06	8000	192						
	-	0.39	0.32	8000	882						
	-	0.54	0.45	8000	1227						
	-	0.86	0.71	8000	1878						
	-	1.33	1.08	8000	2806						
	-	1.82	1.42	8000	3684						
	-	2.22	1.72	8000	4395						
	-	2.80	2.08	8000	5346						
	-	3.20	2.32	8000	6004						
	-	3.35	2.40	8000	6240						

Test:

C1

Initial Height [mm] 107.44
Initial Area [mm²] 1059.6
Mass [gr] 197.0
Back Pressure [kPa] 200.0

Void ratio 0.531
Saturation Index, B 0.920
Shearing Rate [%/min] 0.0416
Confining Pressure [kPa] 8000

	Time [min]	ε_1 [%]	ε_v [%]	σ'_3 [kPa]	σ'_d [kPa]		Time [min]	ε_1 [%]	ε_v [%]	σ'_3 [kPa]	σ'_d [kPa]
Isotropic Compression	-	0.00	0.00	100	-	Creep	0.01	0.30	0.17	8000	3141
	-	0.00	0.39	300	-		0.10	0.33	0.18	8000	3828
	-	0.01	0.77	800	-		0.25	0.34	0.18	8000	3787
	-	0.01	1.00	1300	-		0.50	0.34	0.18	8000	3753
	-	0.02	1.17	1800	-		0.75	0.34	0.18	8000	3735
	-	0.03	1.32	2300	-		1.00	0.34	0.18	8000	3724
	-	0.04	1.45	2800	-		2.50	0.35	0.18	8000	3712
	-	0.06	1.56	3300	-		5.00	0.35	0.18	8000	3716
	-	0.09	1.67	3800	-		7.50	0.36	0.20	8000	3710
	-	0.11	1.76	4300	-		10.00	0.36	0.20	8000	3706
	-	0.14	1.86	4800	-		25.00	0.37	0.20	8000	3694
	-	0.16	1.96	5300	-		50.00	0.38	0.21	8000	3714
	-	0.18	2.02	5800	-		75.00	0.38	0.22	8000	3701
	-	0.21	2.10	6300	-		100.00	0.38	0.23	8000	3704
	-	0.23	2.17	6800	-		250.00	0.40	0.25	8000	3686
	-	0.25	2.23	7300	-		500.00	0.41	0.27	8000	3637
	-	0.27	2.32	7800	-		750.00	0.41	0.28	8000	3673
	-	0.28	2.35	8000	-		1000.0	0.42	0.28	8000	3624
	-	0.28	2.37	8000	-		1440.0	0.42	0.29	8000	3615
Triaxial Comp.	-	0.00	0.00	8000	0						
	-	0.02	0.01	8000	200						
	-	0.11	0.06	8000	1189						
	-	0.20	0.12	8000	2204						
	-	0.30	0.17	8000	3141						

Test:

C2

Initial Height [mm] 107.70
Initial Area [mm²] 1056.6
Mass [gr] 197.0
Back Pressure [kPa] 200.0

Void ratio 0.531
Saturation Index, B 0.942
Shearing Rate [%/min] 0.0416
Confining Pressure [kPa] 8000

	Time [min]	ε_1 [%]	ε_v [%]	σ'_3 [kPa]	σ'_d [kPa]		Time [min]	ε_1 [%]	ε_v [%]	σ'_3 [kPa]	σ'_d [kPa]
Isotropic Compression	-	0.00	0.00	100	-	Creep	0.01	0.97	0.47	8000	6440
	-	0.04	0.27	300	-		0.10	0.98	0.47	8000	6528
	-	0.12	0.63	800	-		0.25	0.99	0.47	8000	6453
	-	0.18	0.86	1300	-		0.50	1.00	0.47	8000	6424
	-	0.21	1.03	1800	-		0.75	1.00	0.47	8000	6412
	-	0.25	1.18	2300	-		1.00	1.01	0.48	8000	6406
	-	0.28	1.29	2800	-		2.50	1.03	0.51	8000	6402
	-	0.31	1.41	3300	-		5.00	1.05	0.52	8000	6403
	-	0.34	1.50	3800	-		7.50	1.06	0.53	8000	6428
	-	0.36	1.60	4300	-		10.00	1.07	0.53	8000	6427
	-	0.40	1.69	4800	-		25.00	1.10	0.54	8000	6423
	-	0.43	1.77	5300	-		50.00	1.13	0.57	8000	6434
	-	0.45	1.86	5800	-		75.00	1.15	0.57	8000	6477
	-	0.48	1.93	6300	-		100.00	1.16	0.57	8000	6474
	-	0.50	2.00	6800	-		250.00	1.20	0.59	8000	6468
	-	0.53	2.07	7300	-		500.00	1.23	0.59	8000	6461
	-	0.56	2.15	7800	-		750.00	1.25	0.61	8000	6456
	-	0.57	2.19	8000	-		1000.0	1.26	0.61	8000	6452
	-	0.57	2.21	8000	-		1440.0	1.28	0.61	8000	6449
Triaxial Compression	-	0.00	0.00	8000	0						
	-	0.05	0.04	8000	429						
	-	0.18	0.10	8000	1500						
	-	0.25	0.13	8000	2019						
	-	0.38	0.22	8000	3003						
	-	0.52	0.28	8000	3889						
	-	0.74	0.36	8000	5136						
	-	0.90	0.45	8000	5912						
	-	0.96	0.47	8000	6184						
	-	0.97	0.47	8000	6440						

Test:

C3

Initial Height [mm] 107.95
Initial Area [mm²] 1055.8
Mass [gr] 197.0
Back Pressure [kPa] 200.0

Void ratio 0.533
Saturation Index, B 0.959
Shearing Rate [%/min] 0.0416
Confining Pressure [kPa] 8000

	Time [min]	ε_1 [%]	ε_v [%]	σ'_3 [kPa]	σ'_d [kPa]		Time [min]	ε_1 [%]	ε_v [%]	σ'_3 [kPa]	σ'_d [kPa]
Isotropic Compression	-	0.00	0.00	100	-	Creep	0.01	1.86	0.85	8000	8998
	-	0.02	0.28	300	-		0.10	1.89	0.85	8000	9364
	-	0.06	0.65	800	-		0.25	1.90	0.85	8000	9243
	-	0.09	0.87	1300	-		0.50	1.91	0.85	8000	9236
	-	0.12	1.05	1800	-		0.75	1.91	0.85	8000	9081
	-	0.15	1.19	2300	-		1.00	1.92	0.86	8000	9016
	-	0.17	1.31	2800	-		2.50	1.91	0.87	8000	8823
	-	0.20	1.43	3300	-		5.00	1.93	0.88	8000	8849
	-	0.23	1.52	3833	-		7.50	1.94	0.91	8000	8850
	-	0.25	1.62	4300	-		10.00	1.96	0.91	8000	8894
	-	0.28	1.72	4833	-		25.00	2.03	0.92	8000	8934
	-	0.30	1.81	5300	-		50.00	2.09	0.95	8000	8945
	-	0.32	1.88	5800	-		75.00	2.13	1.03	8000	8990
	-	0.35	1.96	6300	-		100.00	2.16	1.03	8000	8984
	-	0.37	2.04	6800	-		250.00	2.26	1.08	8000	8968
	-	0.39	2.11	7300	-		500.00	2.35	1.15	8000	9055
	-	0.42	2.18	7800	-		750.00	2.40	1.15	8000	9039
	-	0.43	2.23	8000	-		1000.0	2.44	1.17	8000	9033
	-	0.43	2.27	8000	-		1440.0	2.49	1.16	8000	9024
Triaxial Compression	-	0.00	0.00	8000	0						
	-	0.00	0.00	8000	9						
	-	0.10	0.06	8000	1001						
	-	0.19	0.12	8000	1786						
	-	0.28	0.17	8000	2493						
	-	0.51	0.30	8000	4046						
	-	0.75	0.39	8000	5311						
	-	0.98	0.51	8000	6354						
	-	1.21	0.60	8000	7213						
	-	1.44	0.68	8000	7941						
	-	1.68	0.79	8000	8572						
	-	1.75	0.81	8000	8743						
	-	1.86	0.85	8000	8998						

Test:

C4

Initial Height [mm] 107.70
Initial Area [mm²] 1055.8
Mass [gr] 197.0
Back Pressure [kPa] 200.0

Void ratio 0.531
Saturation Index, B 0.886
Shearing Rate [%/min] 0.0416
Confining Pressure [kPa] 8000

	Time [min]	ε_1 [%]	ε_v [%]	σ'_3 [kPa]	σ'_d [kPa]		Time [min]	ε_1 [%]	ε_v [%]	σ'_3 [kPa]	σ'_d [kPa]
Isotropic Compression	-	0.00	0.00	100	-	Creep	0.01	2.59	1.09	8000	10213
	-	0.04	0.29	300	-		0.10	2.63	1.09	8000	10748
	-	0.10	0.67	800	-		0.25	2.64	1.09	8000	10466
	-	0.14	0.90	1300	-		0.50	2.65	1.09	8000	10300
	-	0.18	1.07	1800	-		0.75	2.65	1.09	8000	10207
	-	0.21	1.21	2300	-		1.00	2.66	1.09	8000	10147
	-	0.25	1.35	2800	-		2.50	2.70	1.09	8000	10190
	-	0.28	1.46	3300	-		5.00	2.75	1.13	8000	10279
	-	0.31	1.56	3833	-		7.50	2.79	1.17	8000	10272
	-	0.34	1.65	4300	-		10.00	2.82	1.19	8000	10288
	-	0.37	1.75	4833	-		25.00	2.93	1.22	8000	10263
	-	0.39	1.84	5300	-		50.00	3.02	1.27	8000	10272
	-	0.42	1.91	5800	-		75.00	3.07	1.32	8000	10246
	-	0.45	1.99	6300	-		100.00	3.10	1.35	8000	10230
	-	0.47	2.07	6800	-		250.00	3.21	1.49	8000	10177
	-	0.49	2.12	7300	-		500.00	3.32	1.62	8000	10265
	-	0.52	2.20	7800	-		750.0	3.39	1.73	8000	10236
	-	0.53	2.24	8000	-		1000.0	3.44	1.81	8000	10291
	-	0.53	2.31	8000	-		1440.0	3.51	1.90	8000	10245
Triaxial Compression	-	0.00	0.00	8000	0						
	-	0.07	0.04	8000	567						
	-	0.17	0.09	8000	1434						
	-	0.25	0.13	8000	2021						
	-	0.49	0.23	8000	3574						
	-	0.72	0.35	8000	4888						
	-	0.95	0.47	8000	5978						
	-	1.19	0.56	8000	6898						
	-	1.42	0.65	8000	7679						
	-	1.65	0.73	8000	8351						
	-	2.12	0.91	8000	9409						
	-	2.45	1.01	8000	9997						
	-	2.59	1.09	8000	10213						

Test:

C5

Initial Height [mm] 107.70
Initial Area [mm²] 1054.2
Mass [gr] 196.7
Back Pressure [kPa] 200.0

Void ratio 0.530
Saturation Index, B 0.929
Shearing Rate [%/min] 0.0416
Confining Pressure [kPa] 8000

	Time [min]	ε_1 [%]	ε_v [%]	σ'_3 [kPa]	σ'_d [kPa]		Time [min]	ε_1 [%]	ε_v [%]	σ'_3 [kPa]	σ'_d [kPa]
Isotropic Compression	-	0.00	0.00	100	-	Creep	0.01	3.15	1.29	8000	11047
	-	0.04	0.30	300	-		0.10	3.18	1.29	8000	11392
	-	0.10	0.66	800	-		0.25	3.19	1.29	8000	11220
	-	0.15	0.90	1300	-		0.50	3.20	1.29	8000	11070
	-	0.18	1.07	1800	-		0.75	3.21	1.30	8000	11052
	-	0.22	1.22	2300	-		1.00	3.21	1.30	8000	11064
	-	0.26	1.35	2800	-		2.50	3.26	1.30	8000	11092
	-	0.29	1.45	3300	-		5.00	3.33	1.34	8000	11079
	-	0.32	1.58	3800	-		7.50	3.35	1.36	8000	11073
	-	0.35	1.68	4300	-		10.00	3.41	1.37	8000	11059
	-	0.38	1.77	4800	-		25.00	3.55	1.42	8000	11051
	-	0.40	1.85	5300	-		50.00	3.67	1.47	8000	11029
	-	0.43	1.95	5800	-		75.00	3.76	1.52	8000	11168
	-	0.46	2.02	6300	-		100.00	3.83	1.54	8000	11142
	-	0.48	2.10	6800	-		250.00	4.04	1.65	8000	11082
	-	0.51	2.16	7300	-		500.00	4.20	1.72	8000	11034
	-	0.53	2.25	7800	-		750.0	4.28	1.78	8000	11003
	-	0.55	2.28	8000	-		1000.0	4.35	1.80	8000	10980
	-	0.55	2.31	8000	-		1550.0	4.48	1.85	8000	11001
Triaxial Compression	-	0.00	0.00	8000	0						
	-	0.08	0.04	8000	687						
	-	0.17	0.07	8000	1403						
	-	0.24	0.11	8000	1964						
	-	0.48	0.23	8000	3656						
	-	0.72	0.33	8000	4995						
	-	0.97	0.44	8000	6212						
	-	1.18	0.53	8000	7055						
	-	1.65	0.73	8000	8516						
	-	2.12	0.91	8000	9546						
	-	2.59	1.08	8000	10327						
	-	2.83	1.16	8000	10663						
	-	3.06	1.24	8000	10943						
	-	3.11	1.26	8000	10995						
	-	3.15	1.29	8000	11047						

Test:

C6

Initial Height [mm] 107.95
Initial Area [mm²] 1053.0
Mass [gr] 196.9
Back Pressure [kPa] 200.0

Void ratio 0.530
Saturation Index, B 0.955
Shearing Rate [%/min] 0.0416
Confining Pressure [kPa] 8000

	Time [min]	ε_1 [%]	ε_v [%]	σ'_3 [kPa]	σ'_d [kPa]		Time [min]	ε_1 [%]	ε_v [%]	σ'_3 [kPa]	σ'_d [kPa]
Isotropic Compression	-	0.00	0.00	100	-	Triaxial Compression	-	4.00	1.52	8000	12112
	-	0.03	0.32	300	-		-	4.45	1.67	8000	12479
	-	0.10	0.69	800	-		-	4.90	1.79	8000	12802
	-	0.14	0.88	1300	-		-	5.42	1.91	8000	13095
	-	0.18	1.06	1800	-		-	5.82	2.00	8000	13313
	-	0.21	1.21	2300	-		-	6.28	2.13	8000	13523
	-	0.24	1.33	2800	-		-	6.81	2.29	8000	13766
	-	0.27	1.44	3300	-		0.01	6.81	2.29	8000	13766
	-	0.30	1.56	3800	-		0.10	6.83	2.29	8000	14116
	-	0.33	1.66	4300	-		0.25	6.87	2.29	8000	14273
	-	0.35	1.73	4800	-		0.50	6.90	2.29	8000	14103
	-	0.38	1.83	5300	-		0.75	6.92	2.30	8000	14035
	-	0.41	1.92	5800	-		1.00	6.92	2.31	8000	13781
	-	0.43	1.99	6300	-		2.50	6.97	2.35	8000	13707
	-	0.46	2.07	6800	-		5.00	7.05	2.36	8000	13780
Triaxial Compression	-	0.48	2.13	7300	-	Creep	7.50	7.11	2.36	8000	13771
	-	0.51	2.21	7800	-		10.00	7.17	2.37	8000	13759
	-	0.52	2.21	8000	-		25.00	7.40	2.46	8000	13734
	-	0.52	2.27	8000	-		50.00	7.66	2.54	8000	13782
	-	0.00	0.00	8000	0		75.00	7.86	2.60	8000	13909
	-	0.01	0.01	8000	156		100.00	8.05	2.65	8000	13875
	-	0.13	0.06	8000	1124		250.00	8.54	2.83	8000	13790
	-	0.31	0.14	8000	2587		500.00	8.85	2.94	8000	13736
	-	0.50	0.25	8000	3851		750.0	9.03	2.99	8000	13700
	-	0.70	0.35	8000	4978		1000.0	9.16	3.05	8000	13677
	-	0.85	0.41	8000	5729		1440.0	9.34	3.09	8000	13695
	-	1.00	0.48	8000	6366						
	-	1.11	0.51	8000	6817						
	-	1.33	0.62	8000	7563						
	-	1.54	0.70	8000	8213						
	-	1.69	0.75	8000	8616						
	-	2.13	0.91	8000	9617						
	-	2.62	1.10	8000	10484						
	-	3.13	1.23	8000	11183						
	-	3.55	1.37	8000	11665						

Test:

C7

Initial Height [mm] 108.20
Initial Area [mm²] 1051.0
Mass [gr] 197.0
Back Pressure [kPa] 200.0

Void ratio 0.530
Saturation Index, B 0.970
Shearing Rate [%/min] 0.0416
Confining Pressure [kPa] 8000

	Time [min]	ε_1 [%]	ε_v [%]	σ'_3 [kPa]	σ'_d [kPa]		Time [min]	ε_1 [%]	ε_v [%]	σ'_3 [kPa]	σ'_d [kPa]
Isotropic Compression	-	0.00	0.00	100	-	Triaxial Compression	-	6.83	2.43	8000	13344
	-	0.03	0.39	300	-		-	7.37	2.57	8000	13558
	-	0.09	0.77	800	-		-	7.59	2.60	8000	13639
	-	0.15	1.02	1300	-		-	7.76	2.67	8000	13709
	-	0.19	1.18	1800	-		-	7.99	2.72	8000	13792
	-	0.22	1.31	2300	-		-	8.22	2.79	8000	13988
	-	0.26	1.47	2800	-		-	8.36	2.83	8000	14054
	-	0.29	1.58	3300	-		0.01	8.36	2.83	8000	14054
	-	0.33	1.70	3800	-		0.10	8.38	2.84	8000	14429
	-	0.36	1.80	4300	-		0.25	8.41	2.84	8000	14489
	-	0.39	1.88	4800	-	Creep	0.50	8.41	2.84	8000	14257
	-	0.43	1.99	5300	-		0.75	8.42	2.84	8000	14127
	-	0.45	2.05	5800	-		1.00	8.42	2.84	8000	14048
	-	0.48	2.15	6300	-		2.50	8.47	2.86	8000	14113
	-	0.51	2.22	6800	-		5.00	8.56	2.88	8000	14122
	-	0.54	2.29	7300	-		7.50	8.63	2.92	8000	14120
	-	0.58	2.37	7866	-		10.00	8.69	2.95	8000	14110
	-	0.58	2.39	8000	-		25.00	8.98	2.98	8000	14121
	-	0.59	2.41	8000	-		50.00	9.26	3.09	8000	14114
	-	0.00	0.00	8000	0		75.00	9.45	3.13	8000	14051
Triaxial Compression	-	0.08	0.05	8000	700		100.00	9.59	3.20	8000	14036
	-	0.34	0.18	8000	2536		250.00	10.02	3.36	8000	14058
	-	0.54	0.30	8000	3718		500.00	10.36	3.47	8000	14014
	-	0.82	0.44	8000	5114		750.0	10.54	3.53	8000	14008
	-	1.26	0.64	8000	6834		1000.0	10.62	3.58	8000	13993
	-	2.18	1.01	8000	9234		1440.0	10.80	3.59	8000	13954
	-	2.61	1.17	8000	10036		1574.0	10.86	3.59	8000	13913
	-	3.05	1.31	8000	10668		2153.0	11.03	3.66	8000	13913
	-	3.49	1.47	8000	11204						
	-	3.94	1.61	8000	11643						
	-	4.40	1.75	8000	11996						
	-	5.09	1.93	8000	12438						
	-	5.55	2.06	8000	12711						
	-	6.01	2.18	8000	12955						
	-	6.46	2.33	8000	13186						

Test:

Multiple 1-Day Creep

Initial Height [mm]	107.44	Void ratio	0.530
Initial Area [mm ²]	1055.8	Saturation Index, B	0.949
Mass [gr]	196.5	Shearing Rate [%/min]	0.416
Back Pressure [kPa]	200.0	Confining Pressure [kPa]	8000

	Time [min]	ε_1 [%]	ε_v [%]	σ'_3 [kPa]	σ'_d [kPa]		Time [min]	ε_1 [%]	ε_v [%]	σ'_3 [kPa]	σ'_d [kPa]
Isotropic Compression	-	0.00	0.00	100	-	First Creep	0.01	1.01	0.52	8000	6213
	-	0.02	0.37	300	-		0.10	1.02	0.52	8000	6384
	-	0.08	0.79	800	-		0.25	1.03	0.53	8000	6378
	-	0.13	1.03	1300	-		0.50	1.04	0.53	8000	6312
	-	0.17	1.23	1800	-		0.75	1.04	0.54	8000	6273
	-	0.20	1.36	2300	-		1.00	1.05	0.54	8000	6239
	-	0.23	1.52	2800	-		2.50	1.07	0.54	8000	6244
	-	0.26	1.62	3300	-		5.00	1.09	0.55	8000	6243
	-	0.28	1.73	3800	-		7.50	1.10	0.56	8000	6241
	-	0.32	1.84	4300	-		10.00	1.11	0.58	8000	6243
	-	0.35	1.93	4800	-		25.00	1.14	0.60	8000	6247
	-	0.37	2.02	5300	-		50.00	1.17	0.61	8000	6254
	-	0.40	2.10	5800	-		75.00	1.21	0.64	8000	6359
	-	0.43	2.17	6300	-		100.00	1.22	0.65	8000	6356
	-	0.46	2.26	6800	-		250.00	1.27	0.66	8000	6344
	-	0.48	2.32	7300	-		500.00	1.31	0.69	8000	6336
	-	0.50	2.40	7800	-		750.00	1.33	0.69	8000	6245
Triaxial Compression	-	0.52	2.43	8000	-	Triaxial Compression	1000.0	1.33	0.67	8000	6239
	-	0.52	2.45	8000	-		1440.0	1.35	0.66	8000	6270
	-	0.00	0.00	8000	0		-	1.35	0.66	8000	6270
	-	0.08	0.05	8000	774		-	1.37	0.67	8000	6792
	-	0.18	0.09	8000	1611		-	1.43	0.69	8000	7405
	-	0.28	0.18	8000	2353		-	1.49	0.71	8000	7792
	-	0.52	0.30	8000	3873		-	1.53	0.75	8000	7964
	-	0.74	0.41	8000	5029		-	1.56	0.76	8000	8093
	-	0.79	0.42	8000	5240		-	1.58	0.77	8000	8161
	-	0.83	0.43	8000	5460		-	1.67	0.78	8000	8435
	-	0.88	0.47	8000	5665		-	1.79	0.81	8000	8738
	-	0.93	0.49	8000	5875		-	1.91	0.86	8000	8990
	-	1.01	0.52	8000	6213		-	2.16	0.94	8000	9475
							-	2.41	1.03	8000	9907
							-	2.61	1.09	8000	10231
							-	2.89	1.17	8000	10617
							-	3.13	1.27	8000	10937
							-	3.31	1.33	8000	11142

Test:

Multiple 1-Day Creep (continued)

Initial Height [mm]	107.44	Void ratio	0.530
Initial Area [mm ²]	1055.8	Saturation Index, B	0.949
Mass [gr]	196.5	Shearing Rate [%/min]	0.416
Back Pressure [kPa]	200.0	Confining Pressure [kPa]	8000

	Time [min]	ε_1 [%]	ε_v [%]	σ'_3 [kPa]	σ'_d [kPa]		Time [min]	ε_1 [%]	ε_v [%]	σ'_3 [kPa]	σ'_d [kPa]
Second Creep	0.01	3.31	1.33	8000	11142	Triaxial Compression	-	5.42	1.97	8000	12867
	0.10	3.33	1.33	8000	11481		-	5.67	2.02	8000	13004
	0.25	3.34	1.37	8000	11306		-	5.91	2.12	8000	13126
	0.50	3.34	1.37	8000	11164		-	6.15	2.17	8000	13248
	0.75	3.35	1.37	8000	11083		-	6.40	2.24	8000	13356
	1.00	3.35	1.37	8000	11045		-	6.65	2.33	8000	13462
	2.50	3.39	1.38	8000	11161		-	6.77	2.36	8000	13512
	5.00	3.46	1.39	8000	11161		-	6.84	2.36	8000	13534
	7.50	3.50	1.39	8000	11152		-	6.91	2.38	8000	13573
	10.00	3.54	1.40	8000	11166	Third Creep	0.01	6.91	2.38	8000	13573
	25.00	3.69	1.46	8000	11151		0.10	6.93	2.38	8000	13739
	50.00	3.82	1.51	8000	11233		0.25	6.93	2.38	8000	13619
	75.00	3.92	1.55	8000	11218		0.50	6.94	2.39	8000	13494
	100.00	3.99	1.59	8000	11209		0.75	6.94	2.40	8000	13417
	250.00	4.21	1.65	8000	11175		1.00	6.95	2.41	8000	13419
	500.00	4.38	1.71	8000	11151		2.50	7.01	2.42	8000	13556
	750.00	4.48	1.76	8000	11170		5.00	7.09	2.46	8000	13552
	1000.0	4.55	1.77	8000	11159		7.50	7.16	2.47	8000	13541
	1440.0	4.65	1.78	8000	11166		10.00	7.22	2.49	8000	13543
Triaxial Compression	-	4.65	1.78	8000	11166		25.00	7.49	2.58	8000	13544
	-	4.66	1.78	8000	11430		50.00	7.81	2.70	8000	13573
	-	4.67	1.78	8000	11743		75.00	8.00	2.78	8000	13552
	-	4.72	1.79	8000	12285		100.00	8.13	2.83	8000	13537
	-	4.77	1.80	8000	12481		250.00	8.56	2.97	8000	13476
	-	4.81	1.80	8000	12553		500.00	8.88	3.07	8000	13427
	-	4.87	1.82	8000	12611		750.00	9.14	3.17	8000	13604
	-	4.89	1.82	8000	12626		1000.0	9.36	3.23	8000	13571
	-	4.92	1.83	8000	12636		1252.0	9.53	3.29	8000	13598
	-	4.96	1.84	8000	12653						
	-	4.99	1.85	8000	12668						
	-	5.02	1.85	8000	12685						
	-	5.05	1.87	8000	12695						
	-	5.08	1.88	8000	12706						
	-	5.13	1.89	8000	12733						
	-	5.29	1.94	8000	12816						

Test:

Multiple 1-Day Creep (continued)

Initial Height [mm]	107.44	Void ratio	0.530
Initial Area [mm ²]	1055.8	Saturation Index, B	0.949
Mass [gr]	196.5	Shearing Rate [%/min]	0.416
Back Pressure [kPa]	200.0	Confining Pressure [kPa]	8000

	Time	ϵ_1 [%]	ϵ_v [%]	σ'_3	σ'_d		Time	ϵ_1 [%]	ϵ_v [%]	σ'_3	σ'_d
	[min]			[kPa]	[kPa]		[min]			[kPa]	[kPa]
Triaxial Compression	-	9.53	3.29	8000	13598	Ending Relaxation	0.01	13.84	4.26	8000	15343
	-	9.53	3.29	8000	13879		0.10	13.84	4.26	8000	15260
	-	9.55	3.29	8000	14144		0.25	13.84	4.26	8000	15098
	-	9.56	3.29	8000	14375		0.50	13.84	4.26	8000	14815
	-	9.58	3.29	8000	14557		0.75	13.84	4.26	8000	14544
	-	9.60	3.29	8000	14684		1.00	13.84	4.26	8000	14332
	-	9.63	3.29	8000	14761		2.50	13.84	4.26	8000	14220
	-	9.65	3.29	8000	14801		5.00	13.84	4.26	8000	14159
	-	9.68	3.30	8000	14828		7.50	13.84	4.27	8000	14117
	-	9.79	3.31	8000	14838		10.00	13.84	4.27	8000	13632
	-	9.81	3.31	8000	14831		25.00	13.84	4.27	8000	13555
	-	9.84	3.31	8000	14825		50.00	13.84	4.30	8000	13392
	-	9.88	3.32	8000	14819		75.00	13.84	4.31	8000	13251
	-	9.90	3.32	8000	14819		100.00	13.84	4.32	8000	13146
	-	9.91	3.34	8000	14822		250.00	13.85	4.33	8000	12795
	-	9.95	3.35	8000	14824		500.00	13.86	4.35	8000	12524
	-	10.00	3.36	8000	14822		750.00	13.84	4.36	8000	10837
	-	10.06	3.37	8000	14823		1000.0	13.84	4.36	8000	10857
	-	10.10	3.38	8000	14823		1440.0	13.84	4.36	8000	10814
	-	10.34	3.43	8000	14832						
	-	10.56	3.48	8000	14854						
	-	10.80	3.53	8000	14875						
	-	11.03	3.59	8000	14907						
	-	11.26	3.65	8000	14938						
	-	11.52	3.71	8000	14992						
	-	11.76	3.77	8000	15027						
	-	11.97	3.82	8000	15057						
	-	12.23	3.88	8000	15093						
	-	12.43	3.92	8000	15124						
	-	12.90	4.04	8000	15201						
	-	13.37	4.15	8000	15278						
	-	13.60	4.21	8000	15306						
	-	13.84	4.26	8000	15343						

Test:

2-Month Creep

Initial Height [mm]	108.20	Void ratio	0.533
Initial Area [mm ²]	1050.0	Saturation Index, B	0.927
Mass [gr]	196.4	Shearing Rate [%/min]	0.0416
Back Pressure [kPa]	200.0	Confining Pressure [kPa]	8000

	Time [min]	ε_1 [%]	ε_v [%]	σ'_3 [kPa]	σ'_d [kPa]		Time [min]	ε_1 [%]	ε_v [%]	σ'_3 [kPa]	σ'_d [kPa]
Isotropic Compression	-	0.00	0.00	100	-	Creep	0.01	3.18	1.28	8000	11293
	-	0.02	0.43	300	-		0.10	3.22	1.29	8000	11920
	-	0.08	0.83	800	-		0.25	3.25	1.30	8000	11618
	-	0.12	1.04	1300	-		0.50	3.26	1.30	8000	11389
	-	0.15	1.23	1800	-		0.75	3.26	1.30	8000	11311
	-	0.18	1.39	2300	-		1.00	3.27	1.32	8000	11329
	-	0.21	1.50	2800	-		2.50	3.31	1.34	8000	11298
	-	0.24	1.62	3300	-		5.00	3.36	1.36	8000	11301
	-	0.27	1.73	3800	-		7.50	3.41	1.38	8000	11307
	-	0.30	1.84	4300	-		10.00	3.44	1.39	8000	11302
	-	0.33	1.92	4800	-		25.00	3.58	1.42	8000	11289
	-	0.36	2.01	5300	-		50.00	3.70	1.47	8000	11272
	-	0.38	2.08	5800	-		75.00	3.79	1.52	8000	11315
	-	0.41	2.15	6300	-		100.00	3.85	1.53	8000	11303
	-	0.43	2.24	6800	-		250.00	4.07	1.62	8000	11304
	-	0.46	2.31	7300	-		500.00	4.26	1.70	8000	11321
	-	0.48	2.37	7800	-		750.00	4.38	1.75	8000	11303
	-	0.49	2.42	8000	-		1000.0	4.46	1.79	8000	11292
	-	0.49	2.44	8000	-		1500.0	4.57	1.84	8000	11281
Triaxial Compression	-	0.00	0.00	8000	0		2500.0	4.72	1.90	8000	11255
	-	0.01	0.01	8000	159		5000.0	4.95	1.98	8000	11226
	-	0.11	0.08	8000	1149		7500.0	5.10	2.02	8000	11263
	-	0.24	0.14	8000	2387		10000	5.21	2.07	8000	11249
	-	0.31	0.19	8000	2994		13000	5.31	2.12	8000	11249
	-	0.68	0.36	8000	5416		16000	5.39	2.13	8000	11238
	-	0.85	0.45	8000	6262		20000	5.48	2.18	8000	11292
	-	0.99	0.49	8000	6862		24000	5.53	2.22	8000	11282
	-	1.22	0.61	8000	7715		27000	5.59	2.24	8000	11449
	-	1.68	0.77	8000	8961		30000	5.60	2.26	8000	11454
	-	2.15	0.94	8000	9892		35000	5.67	2.30	8000	11497
	-	2.61	1.05	8000	10575		50000	5.82	2.36	8000	11476
	-	2.86	1.17	8000	10894		75000	5.96	2.42	8000	11461
	-	3.08	1.26	8000	11169		85950	6.01	2.43	8000	11456
	-	3.13	1.27	8000	11216						
	-	3.18	1.28	8000	11293						

Tests Presented in Chapter 6

Test: Strain Rate=0.00260 %/min-Without Correction

Initial Height [mm]	107.44	Void ratio	0.540
Initial Area [mm ²]	1060.0	Saturation Index, B	0.968
Mass [gr]	195.8	Shearing Rate [%/min]	0.0026
Back Pressure [kPa]	200.0	Confining Pressure [kPa]	8000

	Time [min]	ε_1 [%]	ε_v [%]	σ'_3 [kPa]	σ'_d [kPa]		Time [min]	ε_1 [%]	ε_v [%]	σ'_3 [kPa]	σ'_d [kPa]
Isotropic Compression	-	0.00	0.00	100	-	Triaxial Comp.	-	2.76	1.19	8000	10481
	-	0.02	0.31	291	-		-	2.78	1.20	8000	10508
	-	0.08	0.77	781	-		-	2.80	1.20	8000	10537
	-	0.13	1.03	1272	-		-	2.83	1.21	8000	10564
	-	0.17	1.20	1762	-		-	2.85	1.22	8000	10589
	-	0.20	1.37	2253	-		-	2.85	1.22	8000	10595
	-	0.23	1.50	2743	-		-	2.86	1.23	8000	10602
	-	0.26	1.62	3234	-	Relaxation	0.01	2.86	1.23	8000	10602
	-	0.29	1.74	3724	-		0.10	2.86	1.23	8000	10598
	-	0.32	1.83	4215	-		0.25	2.86	1.23	8000	10591
	-	0.34	1.94	4705	-		0.50	2.86	1.23	8000	10582
	-	0.36	2.03	5196	-		0.75	2.86	1.23	8000	10573
	-	0.38	2.11	5686	-		1.00	2.86	1.23	8000	10567
	-	0.41	2.18	6177	-		2.50	2.86	1.23	8000	10522
	-	0.43	2.27	6667	-		5.00	2.86	1.23	8000	10467
	-	0.46	2.34	7158	-		7.50	2.86	1.23	8000	10423
	-	0.48	2.41	7648	-		10.00	2.86	1.23	8000	10383
	-	0.50	2.46	8000	-		26.00	2.87	1.23	8000	10221
	-	0.50	2.49	8000	-		51.00	2.87	1.23	8000	10070
Triaxial Compression	-	0.00	0.00	8000	0		75.00	2.87	1.23	8000	9975
	-	0.09	0.02	8000	807		100.00	2.88	1.23	8000	9895
	-	0.18	0.08	8000	1628		250.00	2.89	1.23	8000	9618
	-	0.29	0.14	8000	2409		500.00	2.89	1.23	8000	9409
	-	0.51	0.24	8000	3815		750.00	2.90	1.23	8000	9283
	-	0.79	0.36	8000	5390		1000.0	2.90	1.23	8000	9192
	-	0.98	0.47	8000	6286		1440.0	2.90	1.23	8000	9075
	-	1.22	0.58	8000	7233						
	-	1.68	0.76	8000	8549						
	-	2.14	0.97	8000	9539						
	-	2.39	1.04	8000	9948						
	-	2.62	1.12	8000	10288						
	-	2.66	1.15	8000	10349						
	-	2.71	1.16	8000	10416						

Test:

Strain Rate=0.0416 %/min-Without Correction

Initial Height [mm]	108.46	Void ratio	0.530
Initial Area [mm ²]	1042.4	Saturation Index, B	0.939
Mass [gr]	195.8	Shearing Rate [%/min]	0.0416
Back Pressure [kPa]	200.0	Confining Pressure [kPa]	8000

	Time [min]	ε_1 [%]	ε_v [%]	σ'_3 [kPa]	σ'_d [kPa]		Time [min]	ε_1 [%]	ε_v [%]	σ'_3 [kPa]	σ'_d [kPa]
Isotropic Compression	-	0.00	0.00	100	-	Triaxial Compression	-	2.62	1.12	8000	10994
	-	0.01	0.29	291	-		-	2.65	1.14	8000	11030
	-	0.06	0.73	781	-		-	2.69	1.15	8000	11095
	-	0.10	0.99	1272	-		-	2.74	1.17	8000	11155
	-	0.13	1.18	1762	-		-	2.77	1.18	8000	11206
	-	0.16	1.33	2253	-		-	2.81	1.19	8000	11241
	-	0.19	1.48	2743	-	Relaxation	0.01	2.81	1.19	8000	11241
	-	0.22	1.59	3234	-		0.10	2.81	1.19	8000	11191
	-	0.24	1.71	3724	-		0.25	2.81	1.19	8000	11119
	-	0.27	1.82	4215	-		0.50	2.81	1.19	8000	11038
	-	0.30	1.92	4705	-		0.75	2.82	1.19	8000	10979
	-	0.33	2.02	5196	-		1.00	2.82	1.19	8000	10930
	-	0.35	2.11	5686	-		2.50	2.82	1.19	8000	10745
	-	0.38	2.18	6177	-		5.00	2.83	1.19	8000	10582
	-	0.40	2.26	6667	-		7.50	2.83	1.19	8000	10481
	-	0.42	2.33	7158	-		10.00	2.83	1.22	8000	10410
	-	0.45	2.40	7648	-		24.00	2.84	1.22	8000	10171
	-	0.46	2.45	8000	-		49.00	2.84	1.22	8000	9956
	-	0.46	2.50	8000	-		74.00	2.85	1.23	8000	9827
	-	0.00	0.00	8000	0		99.00	2.85	1.24	8000	9732
	-	0.01	0.01	8000	150		252.00	2.85	1.25	8000	9454
	-	0.10	0.06	8000	1038		504.00	2.86	1.25	8000	9251
	-	0.20	0.10	8000	1956		754.00	2.86	1.24	8000	9117
	-	0.28	0.15	8000	2696		1004.0	2.86	1.24	8000	9026
	-	0.38	0.20	8000	3420		1440.0	2.87	1.22	8000	8902
	-	0.52	0.26	8000	4378						
	-	0.75	0.40	8000	5721						
	-	0.98	0.50	8000	6866						
	-	1.21	0.61	8000	7817						
	-	1.46	0.70	8000	8659						
	-	1.58	0.75	8000	9002						
	-	1.67	0.79	8000	9256						
	-	1.91	0.87	8000	9820						
	-	2.14	0.96	8000	10257						
	-	2.37	1.03	8000	10636						

Test:

Strain Rate=0.666 %/min-Without Correction

Initial Height [mm]	107.70	Void ratio	0.530
Initial Area [mm ²]	1049.7	Saturation Index, B	0.956
Mass [gr]	195.8	Shearing Rate [%/min]	0.666
Back Pressure [kPa]	200.0	Confining Pressure [kPa]	8000

	Time [min]	ε_1 [%]	ε_v [%]	σ'_3 [kPa]	σ'_d [kPa]		Time [min]	ε_1 [%]	ε_v [%]	σ'_3 [kPa]	σ'_d [kPa]
Isotropic Compression	-	0.00	0.00	100	-	Relaxation	0.01	2.76	1.10	8000	11881
	-	0.02	0.26	291	-		0.10	2.78	1.10	8000	11480
	-	0.11	0.70	781	-		0.25	2.78	1.10	8000	11276
	-	0.16	0.95	1272	-		0.50	2.79	1.10	8000	11111
	-	0.21	1.18	1762	-		0.75	2.79	1.10	8000	11001
	-	0.24	1.34	2253	-		1.00	2.79	1.10	8000	10927
	-	0.27	1.48	2743	-		2.50	2.80	1.10	8000	10692
	-	0.30	1.59	3234	-		5.00	2.80	1.12	8000	10510
	-	0.34	1.73	3773	-		7.50	2.81	1.12	8000	10405
	-	0.36	1.82	4215	-		10.00	2.81	1.13	8000	10317
	-	0.39	1.92	4705	-		20.00	2.81	1.13	8000	10152
	-	0.42	2.00	5196	-		50.00	2.82	1.13	8000	9908
	-	0.44	2.08	5686	-		75.00	2.83	1.14	8000	9800
	-	0.47	2.17	6177	-		100.00	2.83	1.15	8000	9716
	-	0.49	2.24	6667	-		250.00	2.83	1.17	8000	9456
	-	0.52	2.31	7158	-		500.00	2.84	1.17	8000	9259
	-	0.54	2.38	7648	-		750.00	2.84	1.17	8000	9143
	-	0.56	2.44	8000	-		1000.00	2.85	1.16	8000	9048
	-	0.56	2.49	8000	-		1440.00	2.85	1.14	8000	8919
Triaxial Compression	-	0.00	0.00	8000	0						
	-	0.04	0.02	8000	438						
	-	0.13	0.09	8000	1482						
	-	0.22	0.13	8000	2444						
	-	0.32	0.18	8000	3309						
	-	0.55	0.30	8000	5150						
	-	0.78	0.42	8000	6592						
	-	1.25	0.59	8000	8716						
	-	1.72	0.76	8000	10120						
	-	1.95	0.84	8000	10642						
	-	2.19	0.92	8000	11081						
	-	2.42	0.98	8000	11431						
	-	2.65	1.06	8000	11749						
	-	2.70	1.08	8000	11802						
	-	2.75	1.09	8000	11868						
	-	2.76	1.10	8000	11881						

Test:

Strain Rate=0.00260 %/min-With Correction

Initial Height [mm]	106.93	Void ratio	0.540
Initial Area [mm ²]	1063.3	Saturation Index, B	0.942
Mass [gr]	195.7	Shearing Rate [%/min]	0.00260
Back Pressure [kPa]	200.0	Confining Pressure [kPa]	8000

	Time [min]	ε_1 [%]	ε_v [%]	σ'_3 [kPa]	σ'_d [kPa]		Time [min]	ε_1 [%]	ε_v [%]	σ'_3 [kPa]	σ'_d [kPa]
Isotropic Compression	-	0.00	0.00	100	-	Relaxation	0.01	2.90	1.20	8000	10451
	-	0.02	0.25	291	-		0.10	2.90	1.20	8000	10439
	-	0.08	0.60	781	-		0.25	2.90	1.20	8000	10426
	-	0.13	0.85	1272	-		0.50	2.90	1.20	8000	10277
	-	0.18	1.03	1762	-		0.75	2.90	1.20	8000	10246
	-	0.21	1.17	2253	-		1.00	2.90	1.20	8000	10205
	-	0.24	1.30	2743	-		2.50	2.90	1.20	8000	10163
	-	0.27	1.42	3234	-		5.00	2.90	1.20	8000	10120
	-	0.30	1.53	3724	-		7.50	2.90	1.20	8000	10102
	-	0.33	1.62	4215	-		10.00	2.90	1.20	8000	10081
	-	0.35	1.70	4705	-		23.25	2.90	1.20	8000	9983
	-	0.38	1.79	5196	-		50.00	2.90	1.20	8000	9666
	-	0.40	1.87	5686	-		75.00	2.90	1.20	8000	9621
	-	0.42	1.95	6177	-		100.00	2.90	1.20	8000	9571
	-	0.45	2.03	6667	-		250.00	2.90	1.21	8000	9198
	-	0.47	2.12	7158	-		500.00	2.90	1.21	8000	9061
	-	0.49	2.19	7648	-		750.00	2.90	1.21	8000	8838
	-	0.51	2.25	8000	-		1000.0	2.90	1.21	8000	8776
	-	0.51	2.28	8000	-		1440.0	2.90	1.21	8000	8653
Triaxial Compression	-	0.00	0.00	8000	0						
	-	0.08	0.03	8000	780						
	-	0.17	0.08	8000	1646						
	-	0.27	0.14	8000	2468						
	-	0.51	0.27	8000	4122						
	-	0.74	0.38	8000	5369						
	-	0.98	0.48	8000	6432						
	-	1.22	0.59	8000	7260						
	-	1.45	0.66	8000	7897						
	-	1.68	0.76	8000	8452						
	-	2.16	0.94	8000	9367						
	-	2.39	1.01	8000	9746						
	-	2.62	1.11	8000	10077						
	-	2.71	1.13	8000	10203						
	-	2.81	1.16	8000	10326						
	-	2.90	1.20	8000	10451						

Test:

Strain Rate=0.0416 %/min-With Correction

Initial Height [mm]	107.70	Void ratio	0.535
Initial Area [mm ²]	1058.4	Saturation Index, B	0.929
Mass [gr]	196.0	Shearing Rate [%/min]	0.0416
Back Pressure [kPa]	200.0	Confining Pressure [kPa]	8000

	Time [min]	ε_1 [%]	ε_v [%]	σ'_3 [kPa]	σ'_d [kPa]		Time [min]	ε_1 [%]	ε_v [%]	σ'_3 [kPa]	σ'_d [kPa]
Isotropic Compression	-	0.00	0.00	100	-	Relaxation	0.01	2.78	1.10	8000	11547
	-	0.02	0.32	291	-		0.10	2.78	1.10	8000	11470
	-	0.06	0.68	781	-		0.25	2.78	1.10	8000	11277
	-	0.09	0.92	1272	-		0.50	2.78	1.10	8000	11167
	-	0.12	1.10	1762	-		0.75	2.78	1.10	8000	11220
	-	0.15	1.24	2253	-		1.00	2.78	1.10	8000	11135
	-	0.17	1.36	2743	-		2.50	2.78	1.10	8000	10876
	-	0.20	1.47	3234	-		5.00	2.78	1.10	8000	10777
	-	0.22	1.57	3724	-		7.50	2.78	1.10	8000	10681
	-	0.25	1.66	4215	-		10.00	2.78	1.10	8000	10392
	-	0.27	1.75	4705	-		25.00	2.78	1.12	8000	10175
	-	0.29	1.83	5196	-		50.00	2.78	1.12	8000	10088
	-	0.31	1.90	5686	-		75.00	2.78	1.13	8000	9757
	-	0.34	1.97	6177	-		100.00	2.78	1.13	8000	9725
	-	0.36	2.05	6667	-		250.00	2.78	1.13	8000	9606
	-	0.38	2.11	7158	-		500.00	2.78	1.13	8000	9445
	-	0.40	2.17	7648	-		750.00	2.79	1.13	8000	9341
Triaxial Compression	-	0.42	2.22	8000	-		1000.00	2.79	1.13	8000	9251
	-	0.42	2.23	8000	-		1440.00	2.78	1.13	8000	9013
	-	0.00	0.00	8000	0	Relaxation					
	-	0.01	0.01	8000	160						
	-	0.15	0.07	8000	1698						
	-	0.20	0.10	8000	2167						
	-	0.29	0.16	8000	3054						
	-	0.54	0.27	8000	4971						
	-	0.82	0.40	8000	6751						
	-	1.28	0.61	8000	8684						
	-	1.69	0.77	8000	9820						
	-	2.18	0.91	8000	10744						
	-	2.39	0.98	8000	11050						
	-	2.62	1.04	8000	11364						
	-	2.70	1.07	8000	11459						
	-	2.78	1.10	8000	11547						

Test:

Strain Rate=0.666 %/min-With Correction

Initial Height [mm]	107.44	Void ratio	0.521
Initial Area [mm ²]	1055.4	Saturation Index, B	0.963
Mass [gr]		Shearing Rate [%/min]	0.666
Back Pressure [kPa]	200.0	Confining Pressure [kPa]	8000

	Time [min]	ε_1 [%]	ε_v [%]	σ'_3 [kPa]	σ'_d [kPa]		Time [min]	ε_1 [%]	ε_v [%]	σ'_3 [kPa]	σ'_d [kPa]
Isotropic Compression	-	0.00	0.00	100	-	Relaxation	0.01	2.72	1.04	8000	11651
	-	0.04	0.37	300	-		0.10	2.72	1.04	8000	11127
	-	0.12	0.78	800	-		0.25	2.72	1.05	8000	10981
	-	0.17	1.00	1300	-		0.50	2.72	1.05	8000	10765
	-	0.23	1.22	1840	-		0.75	2.72	1.05	8000	10673
	-	0.26	1.36	2300	-		1.00	2.72	1.06	8000	10558
	-	0.29	1.52	2800	-		2.50	2.72	1.06	8000	10333
	-	0.32	1.65	3330	-		5.00	2.72	1.06	8000	10126
	-	0.34	1.74	3800	-		7.50	2.72	1.07	8000	10052
	-	0.38	1.85	4300	-		10.00	2.72	1.07	8000	9938
	-	0.40	1.93	4800	-		25.00	2.72	1.09	8000	9714
	-	0.43	2.02	5300	-		50.00	2.72	1.09	8000	9516
	-	0.46	2.11	5800	-		75.00	2.72	1.09	8000	9324
	-	0.48	2.19	6300	-		100.00	2.72	1.09	8000	9269
	-	0.51	2.28	6860	-		250.00	2.72	1.10	8000	8833
	-	0.53	2.34	7300	-		500.00	2.72	1.11	8000	8691
	-	0.56	2.40	7800	-		750.00	2.72	1.12	8000	8612
	-	0.57	2.43	8000	-		1000.00	2.73	1.12	8000	8541
	-	0.57	2.47	8000	-		1457.00	2.72	1.10	8000	8290
Triaxial Compression	-	0.00	0.00	8000	0						
	-	0.01	0.00	8000	92						
	-	0.10	0.05	8000	901						
	-	0.19	0.09	8000	1695						
	-	0.28	0.14	8000	2436						
	-	0.51	0.25	8000	4080						
	-	0.75	0.34	8000	5499						
	-	0.98	0.45	8000	6718						
	-	1.22	0.55	8000	7751						
	-	1.47	0.64	8000	8699						
	-	1.68	0.71	8000	9403						
	-	2.15	0.87	8000	10590						
	-	2.48	0.98	8000	11243						
	-	2.72	1.04	8000	11651						

Test:

Strain Rate=0.00260 %/min-Undrained With Correction

Initial Height [mm]	107.94	Void ratio	0.538
Initial Area [mm ²]	1058.9	Saturation Index, B	0.950
Mass [gr]	196.9	Shearing Rate [%/min]	0.00260
Back Pressure [kPa]	200.0	Confining Pressure [kPa]	8000

	Time [min]	ε_1 [%]	ε_v [%]	σ'_3 [kPa]	σ'_d [kPa]		Time [min]	ε_1 [%]	Pore Pre. [kPa]	σ'_3 [kPa]	σ'_d [kPa]
Isotropic Compression	-	0.00	0.00	100	-	Undrained Relaxation	0.01	3.37	197.93	8000	10980
	-	0.03	0.35	300	-		0.10	3.37	198.62	8000	10978
	-	0.07	0.74	800	-		0.25	3.37	199.31	8000	10969
	-	0.10	0.97	1300	-		0.50	3.37	200.00	8000	10958
	-	0.13	1.16	1800	-		0.75	3.37	200.00	8000	10947
	-	0.16	1.29	2300	-		1.00	3.37	200.69	8000	10936
	-	0.18	1.42	2800	-		2.50	3.37	203.45	8000	10848
	-	0.21	1.55	3300	-		5.00	3.37	208.28	8000	10792
	-	0.24	1.66	3833	-		7.50	3.37	213.10	8000	10737
	-	0.26	1.77	4300	-		10.00	3.37	217.24	8000	10691
	-	0.29	1.86	4800	-		25.00	3.37	211.04	8000	10444
	-	0.32	1.94	5300	-		50.00	3.37	191.04	8000	10244
	-	0.34	2.02	5800	-		75.00	3.37	174.49	8000	10095
	-	0.37	2.12	6300	-		100.00	3.37	161.39	8000	10019
	-	0.39	2.19	6800	-		250.00	3.37	116.56	8000	9746
	-	0.42	2.27	7300	-		500.00	3.38	85.53	8000	9535
	-	0.44	2.33	7800	-		750.00	3.38	74.50	8000	9393
Triaxial Compression	-	0.45	2.36	8000	-		1000.0	3.36	9.68	8000	8818
	-	0.45	2.39	8000	-		1500.0	3.37	17.96	8000	8759
	-	0.01	0.00	8000	108		2800.0	3.36	17.27	8000	8570
	-	0.11	0.04	8000	986						
	-	0.18	0.07	8000	1570						
	-	0.28	0.12	8000	2418						
	-	0.52	0.24	8000	4186						
	-	0.74	0.34	8000	5416						
	-	0.97	0.44	8000	6432						
	-	1.20	0.54	8000	7270						
	-	1.43	0.64	8000	7981						
	-	1.67	0.73	8000	8568						
	-	2.15	0.90	8000	9493						
	-	2.60	1.03	8000	10126						
	-	3.08	1.19	8000	10697						
	-	3.37	1.27	8000	10980						

Test:

Strain Rate=0.0416 %/min-Undrained With Correction

Initial Height [mm]	107.70	Void ratio	0.542
Initial Area [mm ²]	1056.8	Saturation Index, B	0.950
Mass [gr]	195.6	Shearing Rate [%/min]	0.0416
Back Pressure [kPa]	200.0	Confining Pressure [kPa]	8000

	Time [min]	ε_1 [%]	ε_v [%]	σ'_3 [kPa]	σ'_d [kPa]		Time [min]	ε_1 [%]	Pore Pre. [kPa]	σ'_3 [kPa]	σ'_d [kPa]
Isotropic Compression	-	0.00	0.00	100	-		0.01	3.19	197.93	8000	11073
	-	0.04	0.44	300	-		0.10	3.19	202.07	8000	11018
	-	0.09	0.95	800	-		0.25	3.20	210.35	8000	10947
	-	0.14	1.21	1300	-		0.50	3.19	217.93	8000	10786
	-	0.17	1.44	1800	-		0.75	3.19	226.21	8000	10753
	-	0.20	1.61	2300	-		1.00	3.19	235.17	8000	10709
	-	0.23	1.76	2800	-		2.50	3.19	263.44	8000	10442
	-	0.26	1.91	3300	-		5.00	3.19	291.03	8000	10207
	-	0.29	2.02	3800	-		7.50	3.19	315.16	8000	10159
	-	0.32	2.14	4300	-		10.00	3.19	335.16	8000	10101
	-	0.34	2.24	4800	-		25.00	3.19	400.67	8000	9774
	-	0.37	2.35	5300	-		50.00	3.19	466.86	8000	9537
	-	0.39	2.46	5800	-		75.00	3.19	524.79	8000	9316
	-	0.42	2.55	6300	-		100.00	3.19	566.16	8000	9292
	-	0.45	2.64	6800	-		150.00	3.19	502.72	8000	9069
	-	0.47	2.74	7300	-		250.00	3.19	185.52	8000	8752
	-	0.50	2.83	7800	-		500.00	3.20	120.70	8000	8571
	-	0.51	2.89	8000	-		750.0	3.20	118.63	8000	8469
Triaxial Compression	-	0.51	2.94	8000	-		1000.0	3.20	162.08	8000	8409
	-	0.00	0.00	8000	0		1440.0	3.19	158.63	8000	8086
	-	0.11	0.05	8000	938						
	-	0.17	0.10	8000	1515						
	-	0.30	0.16	8000	2624						
	-	0.50	0.26	8000	4063						
	-	0.72	0.38	8000	5369						
	-	0.96	0.48	8000	6495						
	-	1.34	0.64	8000	7870						
	-	1.66	0.78	8000	8732						
	-	2.13	0.95	8000	9665						
	-	2.59	1.13	8000	10358						
	-	3.10	1.32	8000	10979						
	-	3.15	1.32	8000	11031						
	-	3.19	1.34	8000	11073						

Test:

Strain Rate=0.666 %/min-Undrained With Correction

Initial Height [mm]	107.95	Void ratio	0.545
Initial Area [mm ²]	1065.4	Saturation Index, B	0.952
Mass [gr]	197.3	Shearing Rate [%/min]	0.666
Back Pressure [kPa]	200.0	Confining Pressure [kPa]	8000

	Time [min]	ε_1 [%]	ε_v [%]	σ'_3 [kPa]	σ'_d [kPa]		Time [min]	ε_1 [%]	Pore Pre. [kPa]	σ'_3 [kPa]	σ'_d [kPa]
Isotropic Compression	-	0.00	0.00	100	-		0.01	3.24	197.93	8000	11381
	-	0.08	0.45	300	-		0.10	3.25	248.96	8000	10959
	-	0.18	0.85	800	-		0.25	3.25	287.58	8000	10739
	-	0.24	1.10	1300	-		0.50	3.26	325.50	8000	10577
	-	0.29	1.27	1800	-		0.75	3.26	348.26	8000	10474
	-	0.34	1.43	2300	-		1.00	3.26	364.81	8000	10400
	-	0.38	1.59	2800	-		2.50	3.24	311.71	8000	9740
	-	0.42	1.71	3300	-		5.00	3.24	375.15	8000	9575
	-	0.45	1.82	3800	-		7.50	3.24	389.63	8000	9468
	-	0.49	1.93	4300	-		10.00	3.24	405.49	8000	9424
	-	0.52	2.03	4800	-		25.00	3.24	431.70	8000	9156
	-	0.55	2.14	5300	-		50.00	3.24	453.76	8000	9019
	-	0.58	2.23	5800	-		75.00	3.24	457.21	8000	8857
	-	0.61	2.32	6300	-		100.00	3.24	452.38	8000	8790
	-	0.64	2.40	6800	-		250.00	3.24	362.05	8000	8436
	-	0.67	2.47	7300	-		500.00	3.24	279.30	8000	8253
	-	0.70	2.57	7800	-		750.00	3.25	230.34	8000	8128
Triaxial Compression	-	0.71	2.62	8000	-		1000.0	3.25	295.85	8000	8071
	-	0.71	2.66	8000	-		1500.0	3.24	277.92	8000	7679
	-	0.00	0.00	8000	0		2500.0	3.24	522.72	8000	7664
	-	0.07	0.03	8000	542		2800.0	3.24	475.83	8000	7611
	-	0.16	0.08	8000	1280						
	-	0.25	0.13	8000	1982						
	-	0.49	0.26	8000	3634						
	-	0.72	0.37	8000	5016						
	-	0.95	0.47	8000	6206						
	-	1.19	0.57	8000	7202						
	-	1.42	0.66	8000	8049						
	-	1.65	0.75	8000	8728						
	-	2.12	0.93	8000	9776						
	-	2.59	1.12	8000	10532						
	-	3.05	1.24	8000	11182						
	-	3.24	1.27	8000	11381						

Test:

Strain Rate=0.00260 %/min- σ'_3 =250 kPa

Initial Height [mm]	107.70	Void ratio	0.531
Initial Area [mm ²]	1056.7	Saturation Index, B	0.950
Mass [gr]	197.0	Shearing Rate [%/min]	0.00260
Back Pressure [kPa]	200.0	Confining Pressure [kPa]	250

	Time [min]	ϵ_1 [%]	ϵ_v [%]	σ'_3 [kPa]	σ'_d [kPa]		Time [min]	ϵ_1 [%]	ϵ_v [%]	σ'_3 [kPa]	σ'_d [kPa]
Isotropic Comp.	-	0.00	0.00	100	-		0.01	0.91	-0.09	250	788
	-	0.01	0.18	200	-		0.10	0.91	-0.09	250	788
	-	0.01	0.25	250	-		0.25	0.91	-0.09	250	786
	-	0.01	0.25	250	-		0.50	0.91	-0.09	250	784
	-	0.00	0.00	250	0		0.75	0.91	-0.09	250	782
Triaxial Compression	-	0.00	0.00	250	14	Relaxation	1.00	0.91	-0.09	250	780
	-	0.05	0.01	250	119		2.50	0.91	-0.09	250	773
	-	0.14	0.02	250	295		5.00	0.91	-0.09	250	769
	-	0.23	0.04	250	404		7.50	0.91	-0.09	250	764
	-	0.33	0.04	250	502		10.00	0.91	-0.11	250	762
	-	0.39	0.04	250	554		25.00	0.91	-0.11	250	751
	-	0.47	0.02	250	604		50.00	0.91	-0.11	250	749
	-	0.61	0.01	250	681		75.00	0.91	-0.11	250	745
	-	0.75	-0.03	250	736		100.00	0.91	-0.12	250	740
	-	0.89	-0.08	250	784		250.00	0.91	-0.14	250	729
	-	0.91	-0.09	250	788		500.00	0.91	-0.15	250	725
							750.00	0.91	-0.18	250	720
							1000.00	0.91	-0.20	250	720
							1450.00	0.91	-0.26	250	698
							2000.00	0.91	-0.32	250	704
							2500.00	0.91	-0.38	250	701
							3000.00	0.91	-0.44	250	701

Test:

Strain Rate=0.0416 %/min- σ'_3 =250 kPa

Initial Height [mm]	107.19	Void ratio	0.530
Initial Area [mm ²]	1057.0	Saturation Index, B	0.951
Mass [gr]	196.3	Shearing Rate [%/min]	0.0416
Back Pressure [kPa]	200.0	Confining Pressure [kPa]	250

	Time [min]	ε_1 [%]	ε_v [%]	σ'_3 [kPa]	σ'_d [kPa]		Time [min]	ε_1 [%]	ε_v [%]	σ'_3 [kPa]	σ'_d [kPa]
Isotropic Comp.	-	0.00	0.00	100	-		0.01	0.96	-0.04	250	782
	-	0.01	0.18	199	-		0.10	0.96	-0.04	250	775
	-	0.01	0.24	250	-		0.25	0.96	-0.04	250	769
	-	0.01	0.26	250	-		0.50	0.96	-0.04	250	764
	-	0.00	0.00	250	0		0.75	0.96	-0.04	250	760
Triaxial Compression	-	0.01	0.00	250	27	Relaxation	1.00	0.96	-0.04	250	758
	-	0.06	0.04	250	130		2.50	0.96	-0.04	250	749
	-	0.15	0.06	250	289		5.00	0.96	-0.04	250	743
	-	0.24	0.08	250	402		7.50	0.96	-0.04	250	738
	-	0.33	0.09	250	487		10.00	0.96	-0.04	250	736
	-	0.44	0.09	250	565		25.00	0.96	-0.04	250	727
	-	0.54	0.08	250	627		50.00	0.96	-0.04	250	719
	-	0.66	0.05	250	683		75.00	0.96	-0.04	250	712
	-	0.90	-0.03	250	769		100.00	0.96	-0.04	250	710
	-	0.96	-0.04	250	782		250.00	0.96	-0.06	250	699
							500.00	0.96	-0.07	250	693
							750.00	0.96	-0.08	250	688
							1000.00	0.96	-0.10	250	686
							1440.00	0.96	-0.14	250	685

Test:

Strain Rate=0.666 %/min- σ'_3 =250 kPa

Initial Height [mm]	108.46	Void ratio	0.531
Initial Area [mm ²]	1037.7	Saturation Index, B	0.944
Mass [gr]	194.8	Shearing Rate [%/min]	0.666
Back Pressure [kPa]	200.0	Confining Pressure [kPa]	250

	Time [min]	ϵ_1 [%]	ϵ_v [%]	σ'_3 [kPa]	σ'_d [kPa]		Time [min]	ϵ_1 [%]	ϵ_v [%]	σ'_3 [kPa]	σ'_d [kPa]
Isotropic Comp.	-	0.00	0.00	100	-		0.01	0.98	-0.07	250	780
	-	0.01	0.20	200	-		0.10	0.98	-0.07	250	743
	-	0.01	0.29	250	-		0.25	0.98	-0.07	250	732
	-	0.02	0.30	250	-		0.50	0.98	-0.07	250	727
Triaxial Compression	-	0.00	0.00	250	0		0.75	0.98	-0.07	250	721
	-	0.02	0.00	250	68		1.00	0.98	-0.07	250	718
	-	0.06	0.03	250	181		2.50	0.98	-0.07	250	707
	-	0.16	0.06	250	328		5.00	0.98	-0.07	250	696
	-	0.25	0.09	250	423		7.50	0.98	-0.07	250	692
	-	0.34	0.09	250	496		10.00	0.98	-0.07	250	688
	-	0.43	0.09	250	553		25.00	0.98	-0.07	250	679
	-	0.52	0.06	250	604		50.00	0.98	-0.07	250	672
	-	0.62	0.04	250	649		75.00	0.98	-0.07	250	668
	-	0.75	0.00	250	703		100.00	0.98	-0.07	250	665
	-	0.89	-0.03	250	753		250.00	0.98	-0.08	250	659
	-	0.98	-0.07	250	780		500.00	0.98	-0.10	250	654
							750.00	0.98	-0.12	250	656
							1000.00	0.98	-0.13	250	654
							1440.00	0.99	-0.16	250	654
							2000.00	0.99	-0.18	250	638
							2700.00	0.99	-0.20	250	640

Test:

R1

Initial Height [mm] 107.70
Initial Area [mm²] 1055.3
Mass [gr] 197.0
Back Pressure [kPa] 200.0

Void ratio 0.529
Saturation Index, B 0.941
Shearing Rate [%/min] 0.0416
Confining Pressure [kPa] 8000

	Time [min]	ϵ_1 [%]	ϵ_v [%]	σ'_3 [kPa]	σ'_d [kPa]		Time [min]	ϵ_1 [%]	ϵ_v [%]	σ'_3 [kPa]	σ'_d [kPa]
Isotropic Compression	-	0.00	0.00	100	-	Relaxation	0.01	0.30	0.16	8000	2886
	-	0.03	0.33	291	-		0.10	0.31	0.16	8000	2858
	-	0.09	0.67	781	-		0.25	0.31	0.16	8000	2833
	-	0.14	0.88	1272	-		0.50	0.31	0.16	8000	2807
	-	0.17	1.05	1762	-		0.75	0.31	0.16	8000	2787
	-	0.20	1.17	2253	-		1.00	0.31	0.16	8000	2774
	-	0.23	1.29	2743	-		2.50	0.31	0.16	8000	2721
	-	0.26	1.40	3234	-		5.00	0.31	0.17	8000	2673
	-	0.29	1.50	3724	-		7.50	0.31	0.17	8000	2655
	-	0.32	1.59	4215	-		10.00	0.31	0.17	8000	2625
	-	0.34	1.67	4705	-		25.00	0.31	0.17	8000	2558
	-	0.37	1.75	5196	-		50.00	0.31	0.17	8000	2501
	-	0.40	1.83	5686	-		75.00	0.32	0.17	8000	2465
	-	0.42	1.92	6177	-		100.00	0.32	0.18	8000	2442
	-	0.44	1.98	6667	-		250.00	0.32	0.19	8000	2371
	-	0.47	2.05	7158	-		500.00	0.32	0.19	8000	2327
	-	0.49	2.11	7648	-		750.00	0.32	0.19	8000	2296
	-	0.51	2.18	8000	-		1000.0	0.32	0.19	8000	2267
	-	0.51	2.19	8000	-		1440.0	0.32	0.19	8000	2203
Triaxial Compression	-	0.00	0.00	8000	0						
	-	0.03	0.02	8000	392						
	-	0.12	0.06	8000	1307						
	-	0.22	0.13	8000	2154						
	-	0.30	0.16	8000	2886						

Test:

R2

Initial Height [mm] 107.95
Initial Area [mm²] 1052.5
Mass [gr] 196.8
Back Pressure [kPa] 200.0

Void ratio 0.530
Saturation Index, B 0.942
Shearing Rate [%/min] 0.0416
Confining Pressure [kPa] 8000

	Time [min]	ϵ_1 [%]	ϵ_v [%]	σ'_3 [kPa]	σ'_d [kPa]		Time [min]	ϵ_1 [%]	ϵ_v [%]	σ'_3 [kPa]	σ'_d [kPa]
Isotropic Compression	-	0.00	0.00	100	-	Relaxation	0.01	0.94	0.45	8000	5924
	-	0.05	0.33	291	-		0.10	0.94	0.45	8000	5879
	-	0.14	0.70	781	-		0.25	0.95	0.45	8000	5844
	-	0.20	0.91	1272	-		0.50	0.95	0.46	8000	5796
	-	0.25	1.08	1762	-		0.75	0.95	0.46	8000	5761
	-	0.29	1.22	2253	-		1.00	0.95	0.46	8000	5737
	-	0.33	1.35	2743	-		2.50	0.95	0.46	8000	5633
	-	0.36	1.47	3234	-		5.00	0.95	0.46	8000	5547
	-	0.39	1.57	3724	-		7.50	0.95	0.46	8000	5492
	-	0.42	1.67	4215	-		10.00	0.95	0.47	8000	5455
	-	0.45	1.75	4705	-		25.00	0.96	0.50	8000	5258
	-	0.48	1.85	5196	-		50.00	0.96	0.50	8000	5165
	-	0.50	1.93	5686	-		75.00	0.96	0.50	8000	5105
	-	0.53	2.01	6177	-		100.00	0.97	0.50	8000	5063
	-	0.56	2.07	6667	-		250.00	0.97	0.51	8000	4932
	-	0.58	2.14	7158	-		500.00	0.97	0.51	8000	4835
	-	0.61	2.21	7648	-		750.00	0.97	0.51	8000	4775
	-	0.63	2.27	8000	-		1000.0	0.97	0.51	8000	4733
	-	0.63	2.33	8000	-		1450.0	0.97	0.51	8000	4675
Triaxial Compression	-	0.00	0.00	8000	0						
	-	0.06	0.03	8000	469						
	-	0.15	0.07	8000	1216						
	-	0.23	0.12	8000	1840						
	-	0.47	0.24	8000	3402						
	-	0.70	0.34	8000	4742						
	-	0.75	0.38	8000	4984						
	-	0.79	0.39	8000	5225						
	-	0.84	0.40	8000	5449						
	-	0.89	0.41	8000	5663						
	-	0.94	0.45	8000	5924						

Test:

R3

Initial Height [mm] 107.70
Initial Area [mm²] 1058.4
Mass [gr] 196.7
Back Pressure [kPa] 200.0

Void ratio 0.535
Saturation Index, B 0.929
Shearing Rate [%/min] 0.0416
Confining Pressure [kPa] 8000

	Time [min]	ϵ_1 [%]	ϵ_v [%]	σ'_3 [kPa]	σ'_d [kPa]		Time [min]	ϵ_1 [%]	ϵ_v [%]	σ'_3 [kPa]	σ'_d [kPa]
Isotropic Compression	-	0.00	0.00	100	-	Relaxation	0.01	2.78	1.10	8000	11547
	-	0.02	0.32	291	-		0.10	2.78	1.10	8000	11470
	-	0.06	0.68	781	-		0.25	2.78	1.10	8000	11277
	-	0.09	0.92	1272	-		0.50	2.78	1.10	8000	11167
	-	0.12	1.10	1762	-		0.75	2.78	1.10	8000	11220
	-	0.15	1.24	2253	-		1.00	2.78	1.10	8000	11135
	-	0.17	1.36	2743	-		2.50	2.78	1.10	8000	10876
	-	0.20	1.47	3234	-		5.00	2.78	1.10	8000	10777
	-	0.22	1.57	3724	-		7.50	2.78	1.10	8000	10681
	-	0.25	1.66	4215	-		10.00	2.78	1.10	8000	10392
	-	0.27	1.75	4705	-		25.00	2.78	1.12	8000	10175
	-	0.29	1.83	5196	-		50.00	2.78	1.12	8000	10088
	-	0.31	1.90	5686	-		75.00	2.78	1.13	8000	9757
	-	0.34	1.97	6177	-		100.00	2.78	1.13	8000	9725
	-	0.36	2.05	6667	-		250.00	2.78	1.13	8000	9606
	-	0.38	2.11	7158	-		500.00	2.78	1.13	8000	9445
	-	0.40	2.17	7648	-		750.00	2.79	1.13	8000	9341
	-	0.42	2.22	8000	-		1000.0	2.79	1.13	8000	9251
	-	0.42	2.23	8000	-		1440.0	2.78	1.13	8000	9013
Triaxial Compression	-	0.00	0.00	8000	0						
	-	0.01	0.01	8000	160						
	-	0.15	0.07	8000	1698						
	-	0.20	0.10	8000	2167						
	-	0.29	0.16	8000	3054						
	-	0.54	0.27	8000	4971						
	-	0.82	0.40	8000	6751						
	-	1.28	0.61	8000	8684						
	-	1.69	0.77	8000	9820						
	-	2.18	0.91	8000	10744						
	-	2.39	0.98	8000	11050						
	-	2.62	1.04	8000	11364						
	-	2.70	1.07	8000	11459						
	-	2.78	1.10	8000	11547						

Test:

R4

Initial Height [mm] 108.20
Initial Area [mm²] 1052.1
Mass [gr] 197.0
Back Pressure [kPa] 200.0

Void ratio 0.531
Saturation Index, B 0.928
Shearing Rate [%/min] 0.0416
Confining Pressure [kPa] 8000

	Time [min]	ϵ_1 [%]	ϵ_v [%]	σ'_3 [kPa]	σ'_d [kPa]		Time [min]	ϵ_1 [%]	ϵ_v [%]	σ'_3 [kPa]	σ'_d [kPa]
Isotropic Compression	-	0.00	0.00	100	-	Triaxial Comp.	-	5.81	2.02	8000	12876
	-	0.04	0.35	300	-		-	6.30	2.16	8000	13100
	-	0.15	0.78	800	-		-	6.70	2.26	8000	13253
	-	0.21	1.02	1300	-		-	7.16	2.39	8000	13424
	-	0.26	1.22	1835	-		-	7.83	2.59	8000	13687
	-	0.29	1.36	2300	-	Relaxation	0.01	7.83	2.59	8000	13687
	-	0.33	1.50	2800	-		0.10	7.83	2.59	8000	13632
	-	0.36	1.63	3300	-		0.25	7.83	2.59	8000	13550
	-	0.39	1.74	3800	-		0.50	7.83	2.59	8000	13357
	-	0.42	1.83	4300	-		0.75	7.83	2.59	8000	13112
	-	0.45	1.93	4800	-		1.00	7.83	2.59	8000	12980
	-	0.48	2.01	5300	-		2.50	7.83	2.59	8000	12861
	-	0.51	2.10	5800	-		5.00	7.83	2.59	8000	12750
	-	0.54	2.20	6300	-		7.50	7.83	2.59	8000	12423
	-	0.56	2.27	6800	-		10.00	7.83	2.60	8000	12404
	-	0.59	2.34	7300	-		25.00	7.83	2.60	8000	12229
	-	0.62	2.41	7800	-		50.00	7.84	2.61	8000	12033
	-	0.63	2.45	8000	-		75.00	7.84	2.61	8000	11903
	-	0.63	2.48	8000	-		100.00	7.84	2.61	8000	11808
	-	0.00	0.00	8000	0		250.00	7.85	2.62	8000	11490
	-	0.06	0.03	8000	564		500.00	7.85	2.63	8000	11226
	-	0.22	0.11	8000	1752		750.00	7.83	2.63	8000	10115
	-	0.29	0.15	8000	2392		1000.0	7.83	2.63	8000	10109
	-	0.48	0.25	8000	3493		1440.0	7.83	2.63	8000	10143
Triaxial Compression	-	0.73	0.33	8000	4791						
	-	1.18	0.56	8000	6695						
	-	1.62	0.70	8000	8069						
	-	2.05	0.87	8000	9135						
	-	2.71	1.09	8000	10306						
	-	3.15	1.24	8000	10880						
	-	3.58	1.40	8000	11369						
	-	3.99	1.52	8000	11745						
	-	4.43	1.65	8000	12087						
	-	4.88	1.77	8000	12375						
	-	5.34	1.90	8000	12649						

Test:

R5

Initial Height [mm] 107.70
Initial Area [mm²] 1056.6
Mass [gr] 197.0
Back Pressure [kPa] 200.0

Void ratio 0.529
Saturation Index, B 0.867
Shearing Rate [%/min] 0.0416
Confining Pressure [kPa] 8000

	Time [min]	ϵ_1 [%]	ϵ_v [%]	σ'_3 [kPa]	σ'_d [kPa]		Time [min]	ϵ_1 [%]	ϵ_v [%]	σ'_3 [kPa]	σ'_d [kPa]
Isotropic Compression	-	0.00	0.00	100	-	Triaxial Compression	-	6.90	2.26	8000	13403
	-	0.05	0.41	300	-		-	7.82	2.45	8000	13698
	-	0.12	0.80	800	-		-	8.23	2.60	8000	13950
	-	0.17	1.05	1300	-		-	9.14	2.82	8000	14184
	-	0.20	1.21	1800	-		-	10.06	3.06	8000	14409
	-	0.23	1.33	2300	-		-	11.46	3.40	8000	14671
	-	0.27	1.48	2800	-		-	12.41	3.64	8000	14855
	-	0.30	1.59	3300	-		-	13.35	3.89	8000	15037
	-	0.33	1.71	3800	-		-	13.81	3.98	8000	15100
	-	0.36	1.79	4300	-	Relaxation	0.01	13.81	3.98	8000	15100
	-	0.39	1.87	4800	-		0.10	13.81	3.98	8000	15018
	-	0.42	1.96	5300	-		0.25	13.81	3.98	8000	14942
	-	0.45	2.03	5800	-		0.50	13.81	3.98	8000	14774
	-	0.48	2.12	6300	-		0.75	13.81	3.98	8000	14678
	-	0.51	2.18	6800	-		1.00	13.81	3.99	8000	14541
	-	0.53	2.26	7300	-		2.50	13.81	3.99	8000	14337
	-	0.56	2.34	7866	-		5.00	13.81	4.00	8000	14082
	-	0.57	2.36	8000	-		7.50	13.81	4.01	8000	13865
	-	0.57	2.42	8000	-		10.00	13.81	4.02	8000	13823
Triaxial Compression	-	0.00	0.00	8000	0		25.00	13.81	4.04	8000	13497
	-	0.00	0.00	8000	36		50.00	13.81	4.04	8000	13251
	-	0.26	0.14	8000	2114		75.00	13.81	4.05	8000	13106
	-	0.52	0.25	8000	3917		100.00	13.82	4.06	8000	13005
	-	0.72	0.34	8000	5091		250.00	13.82	4.08	8000	12661
	-	1.20	0.55	8000	7156		500.00	13.83	4.10	8000	12335
	-	1.99	0.83	8000	9301		750.00	13.81	4.11	8000	11072
	-	2.13	0.89	8000	9593		1000.0	13.81	4.11	8000	11024
	-	2.58	1.05	8000	10329		1307.0	13.81	4.11	8000	10928
	-	3.02	1.17	8000	10925		1440.0	13.81	4.12	8000	10913
	-	3.47	1.32	8000	11419		2013.0	13.81	4.15	8000	10845
	-	4.14	1.50	8000	11996						
	-	4.59	1.66	8000	12323						
	-	5.05	1.77	8000	12601						
	-	5.51	1.91	8000	12845						
	-	5.97	2.01	8000	13057						

Test:

R6

Initial Height [mm] 107.44
Initial Area [mm²] 1055.8
Mass [gr] 196.5
Back Pressure [kPa] 200.0

Void ratio 0.530
Saturation Index, B 0.949
Shearing Rate [%/min] 0.0416
Confining Pressure [kPa] 8000

	Time [min]	ϵ_1 [%]	ϵ_v [%]	σ'_3 [kPa]	σ'_d [kPa]		Time [min]	ϵ_1 [%]	ϵ_v [%]	σ'_3 [kPa]	σ'_d [kPa]
Isotropic Compression	-	0.00	0.00	100	-	Triaxial Compression	-	3.61	1.41	8000	12097
	-	0.02	0.37	300	-		-	4.20	1.58	8000	12557
	-	0.08	0.79	800	-		-	4.61	1.71	8000	12833
	-	0.13	1.03	1300	-		-	5.01	1.83	8000	13087
	-	0.17	1.23	1800	-		-	5.62	2.02	8000	13423
	-	0.20	1.36	2300	-		-	6.46	2.27	8000	13810
	-	0.23	1.52	2800	-		-	7.31	2.50	8000	14105
	-	0.26	1.62	3300	-		-	8.36	2.79	8000	14436
	-	0.28	1.73	3800	-		-	9.40	3.05	8000	14696
	-	0.32	1.84	4300	-		-	10.22	3.27	8000	14904
	-	0.35	1.93	4800	-		-	11.59	3.61	8000	15188
	-	0.37	2.02	5300	-		-	12.52	3.81	8000	15343
	-	0.40	2.10	5800	-	Ending Relaxation	0.01	13.84	4.26	8000	15343
	-	0.43	2.17	6300	-		0.10	13.84	4.26	8000	15260
	-	0.46	2.26	6800	-		0.25	13.84	4.26	8000	15098
	-	0.48	2.32	7300	-		0.50	13.84	4.26	8000	14815
	-	0.50	2.40	7800	-		0.75	13.84	4.26	8000	14544
	-	0.52	2.43	8000	-		1.00	13.84	4.26	8000	14332
	-	0.52	2.45	8000	-		2.50	13.84	4.26	8000	14220
Triaxial Compression	-	0.00	0.00	8000	0		5.00	13.84	4.26	8000	14159
	-	0.05	0.03	8000	574		7.50	13.84	4.27	8000	14117
	-	0.14	0.06	8000	1295		10.00	13.84	4.27	8000	13632
	-	0.25	0.10	8000	2310		25.00	13.84	4.27	8000	13555
	-	0.31	0.12	8000	2884		50.00	13.84	4.30	8000	13392
	-	0.55	0.28	8000	4638		75.00	13.84	4.31	8000	13251
	-	0.82	0.42	8000	6200		100.00	13.84	4.32	8000	13146
	-	1.02	0.50	8000	7122		250.00	13.85	4.33	8000	12795
	-	1.25	0.60	8000	8042		500.00	13.86	4.35	8000	12524
	-	1.49	0.69	8000	8819		750.00	13.84	4.36	8000	10837
	-	1.77	0.80	8000	9560		1000.0	13.84	4.36	8000	10857
	-	2.19	0.95	8000	10401		1440.0	13.84	4.36	8000	10814
	-	2.66	1.12	8000	11152						
	-	2.75	1.13	8000	11188						
	-	2.83	1.18	8000	11289						
	-	3.13	1.25	8000	11639						

Test:

Multiple 1-Day Stress Relaxation

Initial Height [mm]	107.44	Void ratio	0.532
Initial Area [mm ²]	1058.9	Saturation Index, B	0.904
Mass [gr]	196.8	Shearing Rate [%/min]	0.416
Back Pressure [kPa]	200.0	Confining Pressure [kPa]	8000

	Time [min]	ϵ_1 [%]	ϵ_v [%]	σ'_3 [kPa]	σ'_d [kPa]		Time [min]	ϵ_1 [%]	ϵ_v [%]	σ'_3 [kPa]	σ'_d [kPa]
Isotropic Compression	-	0.00	0.00	100	-	First Relaxation	0.01	1.01	0.48	8000	6617
	-	0.03	0.38	300	-		0.10	1.02	0.48	8000	6575
	-	0.08	0.81	868	-		0.25	1.01	0.48	8000	6485
	-	0.12	1.00	1300	-		0.50	1.01	0.49	8000	6451
	-	0.16	1.17	1800	-		0.75	1.01	0.49	8000	6415
	-	0.19	1.32	2300	-		1.00	1.02	0.49	8000	6383
	-	0.22	1.46	2800	-		2.50	1.02	0.49	8000	6269
	-	0.25	1.57	3300	-		5.00	1.01	0.49	8000	6057
	-	0.29	1.67	3800	-		7.50	1.01	0.49	8000	6023
	-	0.32	1.77	4300	-		10.00	1.01	0.51	8000	5885
	-	0.35	1.87	4800	-		25.00	1.01	0.53	8000	5739
	-	0.37	1.95	5300	-		50.00	1.02	0.53	8000	5641
	-	0.41	2.06	5800	-		75.00	1.02	0.53	8000	5553
	-	0.43	2.14	6300	-		100.00	1.02	0.53	8000	5500
	-	0.46	2.23	6800	-		250.00	1.02	0.54	8000	5381
	-	0.48	2.32	7300	-		500.00	1.02	0.54	8000	5283
	-	0.51	2.41	7800	-		750.00	1.02	0.54	8000	5199
	-	0.52	2.47	8000	-		1000.0	1.01	0.54	8000	4810
	-	0.52	2.67	8000	-		1410.0	1.01	0.54	8000	4799
Triaxial Compression	-	0.00	0.00	8000	0	Triaxial Compression	-	1.01	0.54	8000	4799
	-	0.04	0.02	8000	442		-	1.04	0.54	8000	5366
	-	0.12	0.06	8000	1067		-	1.07	0.54	8000	5960
	-	0.21	0.10	8000	1904		-	1.10	0.55	8000	6424
	-	0.30	0.16	8000	2672		-	1.11	0.55	8000	6615
	-	0.55	0.27	8000	4356		-	1.13	0.56	8000	6775
	-	0.77	0.37	8000	5546		-	1.14	0.57	8000	6829
	-	0.92	0.44	8000	6236		-	1.18	0.57	8000	7081
	-	0.99	0.47	8000	6524		-	1.21	0.59	8000	7286
	-	1.01	0.48	8000	6617		-	1.25	0.60	8000	7458
							-	1.29	0.61	8000	7623
							-	1.31	0.62	8000	7691
							-	1.33	0.62	8000	7758
							-	1.39	0.64	8000	7952
							-	1.47	0.67	8000	8201
							-	1.71	0.75	8000	8842

Test:

Multiple 1-Day Stress Relaxation (continued)

Initial Height [mm]	107.44	Void ratio	0.532
Initial Area [mm ²]	1058.9	Saturation Index, B	0.904
Mass [gr]	196.8	Shearing Rate [%/min]	0.416
Back Pressure [kPa]	200.0	Confining Pressure [kPa]	8000

	Time [min]	ϵ_1 [%]	ϵ_v [%]	σ'_3 [kPa]	σ'_d [kPa]		Time [min]	ϵ_1 [%]	ϵ_v [%]	σ'_3 [kPa]	σ'_d [kPa]
Triaxial Compression	-	2.04	0.88	8000	9563	Triaxial Compression	-	3.47	1.35	8000	11550
	-	2.20	0.93	8000	9873		-	3.50	1.35	8000	11583
	-	2.44	1.02	8000	10282		-	3.56	1.37	8000	11655
	-	2.62	1.08	8000	10539		-	3.62	1.38	8000	11708
	-	2.89	1.15	8000	10910		-	3.86	1.45	8000	11929
	-	3.11	1.22	8000	11176		-	3.94	1.47	8000	11994
Second Relaxation	0.01	3.11	1.22	8000	11176	Triaxial Compression	-	4.19	1.54	8000	12198
	0.10	3.11	1.22	8000	11112		-	4.28	1.58	8000	12260
	0.25	3.11	1.22	8000	11021		-	4.44	1.62	8000	12371
	0.50	3.11	1.22	8000	10925		-	4.61	1.69	8000	12496
	0.75	3.11	1.22	8000	10865		-	5.08	1.80	8000	12774
	1.00	3.11	1.22	8000	10817		-	5.58	1.97	8000	13047
	2.50	3.11	1.22	8000	10529		-	6.01	2.06	8000	13249
	5.00	3.11	1.22	8000	10296		-	6.48	2.17	8000	13427
	7.50	3.11	1.22	8000	10243		-	6.85	2.27	8000	13582
	10.00	3.11	1.22	8000	10032		-	6.95	2.30	8000	13616
	25.00	3.11	1.23	8000	9741	Third Relaxation	0.01	6.95	2.30	8000	13616
	50.00	3.11	1.23	8000	9486		0.10	6.95	2.30	8000	13542
	75.00	3.11	1.24	8000	9430		0.25	6.95	2.30	8000	13420
	100.00	3.11	1.24	8000	9370		0.50	6.95	2.30	8000	13327
	250.00	3.12	1.24	8000	9123		0.75	6.95	2.30	8000	13182
	500.00	3.12	1.24	8000	8911		1.00	6.95	2.30	8000	13154
	750.00	3.12	1.24	8000	8790		2.50	6.95	2.30	8000	12847
	1000.0	3.11	1.24	8000	8258		5.00	6.95	2.30	8000	12589
	1440.0	3.11	1.24	8000	8238		7.50	6.95	2.30	8000	12520
Triaxial Compression	-	3.11	1.24	8000	8238		10.00	6.95	2.31	8000	12322
	-	3.14	1.25	8000	9294		25.00	6.95	2.31	8000	12064
	-	3.21	1.26	8000	10545		50.00	6.95	2.33	8000	11737
	-	3.24	1.27	8000	10807		75.00	6.95	2.33	8000	11591
	-	3.27	1.27	8000	11005		100.00	6.95	2.33	8000	11493
	-	3.30	1.29	8000	11150		250.00	6.96	2.34	8000	11178
	-	3.32	1.29	8000	11257		500.00	6.96	2.35	8000	10910
	-	3.38	1.31	8000	11402		750.00	6.95	2.35	8000	10071
	-	3.41	1.32	8000	11457		1000.0	6.94	2.35	8000	9985
	-	3.44	1.33	8000	11507		1304.0	6.94	2.35	8000	9900

Test:

Multiple 1-Day Stress Relaxation (continued)

Initial Height [mm]	107.44	Void ratio	0.532
Initial Area [mm ²]	1058.9	Saturation Index, B	0.904
Mass [gr]	196.8	Shearing Rate [%/min]	0.416
Back Pressure [kPa]	200.0	Confining Pressure [kPa]	8000

	Time	ε_1 [%]	ε_v [%]	σ'_3	σ'_d		Time	ε_1 [%]	ε_v [%]	σ'_3	σ'_d
	[min]			[kPa]	[kPa]		[min]			[kPa]	[kPa]
Triaxial Compression	-	6.94	2.35	8000	9900	Ending Relaxation	0.01	13.88	4.05	8000	15303
	-	7.04	2.35	8000	12390		0.10	13.88	4.05	8000	15226
	-	6.91	2.28	8000	13602		0.25	13.88	4.05	8000	15102
	-	6.95	2.30	8000	13616		0.50	13.88	4.05	8000	14968
	-	6.94	2.35	8000	9900		0.75	13.88	4.05	8000	14893
	-	7.04	2.35	8000	12390		1.00	13.88	4.05	8000	14824
	-	7.09	2.37	8000	13090		2.50	13.88	4.05	8000	14517
	-	7.18	2.37	8000	13651		5.00	13.88	4.06	8000	14104
	-	7.20	2.38	8000	13711		7.50	13.88	4.07	8000	14041
	-	7.26	2.37	8000	13817		10.00	13.88	4.08	8000	13801
	-	7.32	2.39	8000	13883		25.00	13.88	4.10	8000	13629
	-	7.39	2.41	8000	13917		50.00	13.89	4.10	8000	13375
	-	7.61	2.45	8000	13994		75.00	13.89	4.11	8000	13218
	-	7.79	2.50	8000	14063		100.00	13.89	4.12	8000	13107
	-	8.27	2.63	8000	14187		190.00	13.90	4.14	8000	12825
	-	8.76	2.75	8000	14330		500.00	13.91	4.17	8000	12357
	-	9.26	2.88	8000	14453		750.00	13.91	4.17	8000	12147
	-	9.67	2.99	8000	14548		1000.0	13.91	4.17	8000	11943
	-	10.18	3.13	8000	14665		1320.0	13.88	4.17	8000	10768
	-	10.60	3.24	8000	14747						
	-	11.10	3.36	8000	14840						
	-	11.53	3.45	8000	14915						
	-	12.02	3.61	8000	15013						
	-	12.52	3.70	8000	15087						
	-	12.93	3.82	8000	15154						
	-	13.42	3.96	8000	15242						
	-	13.88	4.05	8000	15303						

Test:

2-Month Stress Relaxation

Initial Height [mm]	107.95	Void ratio	0.530
Initial Area [mm ²]	1051.4	Saturation Index, B	0.950
Mass [gr]	196.6	Shearing Rate [%/min]	0.0416
Back Pressure [kPa]	200.0	Confining Pressure [kPa]	8000

	Time [min]	ε_1 [%]	ε_v [%]	σ'_3 [kPa]	σ'_d [kPa]		Time [min]	ε_1 [%]	ε_v [%]	σ'_3 [kPa]	σ'_d [kPa]
Isotropic Compression	-	0.00	0.00	100	-	Relaxation	0.01	3.16	1.29	8000	11237
	-	0.04	0.37	300	-		0.10	3.16	1.29	8000	11170
	-	0.13	0.71	800	-		0.25	3.16	1.29	8000	11086
	-	0.18	0.91	1300	-		0.50	3.16	1.28	8000	11002
	-	0.21	1.12	1800	-		0.75	3.16	1.28	8000	10946
	-	0.25	1.26	2300	-		1.00	3.16	1.29	8000	10806
	-	0.28	1.40	2800	-		2.50	3.16	1.29	8000	10676
	-	0.32	1.52	3300	-		5.00	3.16	1.30	8000	10454
	-	0.35	1.64	3800	-		7.50	3.16	1.30	8000	10372
	-	0.38	1.75	4300	-		10.00	3.16	1.30	8000	10158
	-	0.41	1.85	4800	-		25.00	3.16	1.31	8000	9821
	-	0.44	1.94	5300	-		50.00	3.16	1.34	8000	9763
	-	0.47	2.00	5800	-		75.00	3.16	1.38	8000	9559
	-	0.50	2.09	6300	-		100.00	3.16	1.40	8000	9526
	-	0.53	2.16	6800	-		250.00	3.16	1.40	8000	9258
	-	0.55	2.24	7300	-		500.00	3.16	1.40	8000	8935
	-	0.58	2.33	7800	-		750.00	3.16	1.40	8000	8838
	-	0.59	2.37	8000	-		1000.0	3.16	1.40	8000	8501
	-	0.59	2.47	8000	-		2500.0	3.16	1.40	8000	8335
Triaxial Compression	-	0.00	0.00	8000	0		5000.0	3.16	1.40	8000	8200
	-	0.08	0.04	8000	725		7500.0	3.16	1.40	8000	8065
	-	0.21	0.12	8000	1789		10000	3.16	1.40	8000	7704
	-	0.29	0.15	8000	2337		25000	3.16	1.40	8000	7491
	-	0.50	0.25	8000	3736		49750	3.16	1.40	8000	7281
	-	0.73	0.37	8000	5062		75000	3.16	1.40	8000	7196
	-	0.97	0.47	8000	6166		87360	3.16	1.48	8000	7216
	-	1.20	0.58	8000	7104						
	-	1.67	0.76	8000	8588						
	-	2.13	0.95	8000	9684						
	-	2.60	1.12	8000	10493						
	-	2.81	1.18	8000	10800						
	-	3.06	1.27	8000	11128						
	-	3.11	1.29	8000	11181						
	-	3.16	1.29	8000	11237						

Tests Presented in Chapter 7

Test: 3 Hours Creep-1 Week Stress Relaxation

Initial Height [mm]	108.46	Void ratio	0.533
Initial Area [mm ²]	1050.1	Saturation Index, B	0.975
Mass [gr]	196.9	Shearing Rate [%/min]	0.0416
Back Pressure [kPa]	200.0	Confining Pressure [kPa]	8000

	Time [min]	ϵ_1 [%]	ϵ_v [%]	σ'_3 [kPa]	σ'_d [kPa]		Time [min]	ϵ_1 [%]	ϵ_v [%]	σ'_3 [kPa]	σ'_d [kPa]
Isotropic Compression	-	0.00	0.00	100	-	Creep	0.01	3.11	1.22	8000	11523
	-	0.02	0.30	300	-		0.10	3.13	1.22	8000	11890
	-	0.07	0.68	800	-		0.25	3.15	1.22	8000	11679
	-	0.12	0.92	1300	-		0.50	3.15	1.22	8000	11510
	-	0.15	1.12	1800	-		0.75	3.16	1.22	8000	11537
	-	0.18	1.25	2300	-		1.00	3.16	1.22	8000	11529
	-	0.21	1.37	2800	-		2.50	3.20	1.23	8000	11528
	-	0.24	1.49	3300	-		5.00	3.26	1.26	8000	11520
	-	0.27	1.59	3800	-		7.50	3.31	1.28	8000	11515
	-	0.30	1.69	4300	-		10.00	3.34	1.30	8000	11516
	-	0.33	1.78	4800	-		25.00	3.48	1.33	8000	11497
	-	0.35	1.87	5300	-		50.00	3.60	1.36	8000	11521
	-	0.38	1.95	5800	-		75.00	3.68	1.39	8000	11528
	-	0.40	2.03	6300	-		100.00	3.73	1.44	8000	11524
	-	0.43	2.11	6800	-		180.00	3.86	1.47	8000	11529
	-	0.45	2.18	7300	-						
	-	0.47	2.26	7800	-						
	-	0.48	2.29	8000	-						
	-	0.48	2.30	8000	-						
Triaxial Compression	-	0.00	0.00	8000	0						
	-	0.04	0.02	8000	492						
	-	0.10	0.05	8000	1106						
	-	0.25	0.13	8000	2567						
	-	0.30	0.16	8000	2962						
	-	0.52	0.26	8000	4634						
	-	0.76	0.37	8000	6101						
	-	0.98	0.46	8000	7122						
	-	1.31	0.59	8000	8263						
	-	1.68	0.71	8000	9262						
	-	2.14	0.88	8000	10184						
	-	2.60	1.04	8000	10900						
	-	3.03	1.18	8000	11431						
	-	3.11	1.22	8000	11523						

Test: 3 Hours Creep-1 Week Stress Relaxation (continued)

Initial Height [mm]	108.46	Void ratio	0.533
Initial Area [mm ²]	1050.1	Saturation Index, B	0.975
Mass [gr]	196.9	Shearing Rate [%/min]	0.0416
Back Pressure [kPa]	200.0	Confining Pressure [kPa]	8000

	Time	ϵ_1	ϵ_v [%]	σ'_3	σ'_d		Time	ϵ_1	ϵ_v [%]	σ'_3	σ'_d
	[min]	[%]		[kPa]	[kPa]		[min]	[%]		[kPa]	[kPa]
Relaxation	0.01	3.86	1.47	8000	11529						
	0.10	3.86	1.47	8000	11516						
	0.25	3.86	1.47	8000	11510						
	0.50	3.86	1.47	8000	11496						
	0.75	3.86	1.47	8000	11461						
	1.00	3.86	1.47	8000	11424						
	2.50	3.86	1.47	8000	11396						
	5.00	3.86	1.47	8000	11356						
	7.50	3.86	1.47	8000	11323						
	10.00	3.86	1.47	8000	11295						
	25.00	3.86	1.47	8000	11108						
	50.00	3.86	1.47	8000	10982						
	75.00	3.86	1.48	8000	10889						
	100.00	3.86	1.48	8000	10815						
	250.00	3.87	1.51	8000	10554						
	500.00	3.87	1.52	8000	10335						
	750.00	3.88	1.55	8000	10199						
	1000.0	3.86	1.55	8000	9403						
	1500.0	3.86	1.55	8000	9366						
	2500.0	3.85	1.55	8000	9157						
	5000.0	3.85	1.51	8000	8981						
	7500.0	3.86	1.47	8000	8783						
	10050	3.86	1.47	8000	8629						

Test:

1 Day Creep-1 Week Stress Relaxation

Initial Height [mm]	107.70	Void ratio	0.530
Initial Area [mm ²]	1054.2	Saturation Index, B	0.929
Mass [gr]	196.7	Shearing Rate [%/min]	0.0416
Back Pressure [kPa]	200.0	Confining Pressure [kPa]	8000

	Time [min]	ϵ_1 [%]	ϵ_v [%]	σ'_3 [kPa]	σ'_d [kPa]		Time [min]	ϵ_1 [%]	ϵ_v [%]	σ'_3 [kPa]	σ'_d [kPa]
Isotropic Compression	-	0.00	0.00	100	-	Creep	0.01	3.15	1.29	8000	11047
	-	0.04	0.30	300	-		0.10	3.18	1.29	8000	11392
	-	0.10	0.66	800	-		0.25	3.19	1.29	8000	11220
	-	0.15	0.90	1300	-		0.50	3.20	1.29	8000	11070
	-	0.18	1.07	1800	-		0.75	3.21	1.30	8000	11052
	-	0.22	1.22	2300	-		1.00	3.21	1.30	8000	11064
	-	0.26	1.35	2800	-		2.50	3.26	1.30	8000	11092
	-	0.29	1.45	3300	-		5.00	3.33	1.34	8000	11079
	-	0.32	1.58	3800	-		7.50	3.35	1.36	8000	11073
	-	0.35	1.68	4300	-		10.00	3.41	1.37	8000	11059
	-	0.38	1.77	4800	-		25.00	3.55	1.42	8000	11051
	-	0.40	1.85	5300	-		50.00	3.67	1.47	8000	11029
	-	0.43	1.95	5800	-		75.00	3.76	1.52	8000	11168
	-	0.46	2.02	6300	-		100.00	3.83	1.54	8000	11142
	-	0.48	2.10	6800	-		250.00	4.04	1.65	8000	11082
	-	0.51	2.16	7300	-		500.00	4.20	1.72	8000	11034
	-	0.53	2.25	7800	-		750.00	4.28	1.78	8000	11003
	-	0.55	2.28	8000	-		1000.0	4.35	1.80	8000	10980
	-	0.55	2.31	8000	-		1550.0	4.48	1.85	8000	11001
Triaxial Compression	-	0.00	0.00	8000	0						
	-	0.08	0.04	8000	687						
	-	0.17	0.07	8000	1403						
	-	0.24	0.11	8000	1964						
	-	0.48	0.23	8000	3656						
	-	0.72	0.33	8000	4995						
	-	0.97	0.44	8000	6212						
	-	1.18	0.53	8000	7055						
	-	1.65	0.73	8000	8516						
	-	2.12	0.91	8000	9546						
	-	2.59	1.08	8000	10327						
	-	2.83	1.16	8000	10663						
	-	3.06	1.24	8000	10943						
	-	3.11	1.26	8000	10995						
	-	3.15	1.29	8000	11047						

Test: 1 Day Creep-1 Week Stress Relaxation (continued)

Initial Height [mm]	107.70	Void ratio	0.530
Initial Area [mm ²]	1054.2	Saturation Index, B	0.929
Mass [gr]	196.7	Shearing Rate [%/min]	0.0416
Back Pressure [kPa]	200.0	Confining Pressure [kPa]	8000

	Time [min]	ϵ_1 [%]	ϵ_v [%]	σ'_3 [kPa]	σ'_d [kPa]		Time [min]	ϵ_1 [%]	ϵ_v [%]	σ'_3 [kPa]	σ'_d [kPa]
Relaxation	0.01	4.48	1.85	8000	11001						
	0.10	4.48	1.85	8000	10997						
	0.25	4.48	1.85	8000	10988						
	0.50	4.48	1.85	8000	10980						
	0.75	4.48	1.85	8000	10975						
	1.00	4.48	1.85	8000	10969						
	2.50	4.48	1.85	8000	10947						
	5.00	4.48	1.85	8000	10923						
	7.50	4.48	1.85	8000	10903						
	10.00	4.48	1.85	8000	10890						
	25.00	4.48	1.85	8000	10829						
	50.00	4.48	1.85	8000	10766						
	75.00	4.48	1.85	8000	10718						
	100.00	4.48	1.85	8000	10681						
	250.00	4.48	1.86	8000	10527						
	500.00	4.49	1.87	8000	10368						
	750.00	4.49	1.88	8000	10260						
	1000.00	4.49	1.88	8000	10174						
	1500.00	4.48	1.88	8000	9763						
	2500.00	4.48	1.89	8000	9509						
	5000.00	4.48	1.89	8000	9339						
	7500.00	4.49	1.90	8000	9275						
	10000.0	4.48	1.89	8000	9041						

Test:

1 Week Creep-1 Week Stress Relaxation

Initial Height [mm]	108.20	Void ratio	0.533
Initial Area [mm ²]	1050.6	Saturation Index, B	0.949
Mass [gr]	196.5	Shearing Rate [%/min]	0.416
Back Pressure [kPa]	200.0	Confining Pressure [kPa]	8000

	Time [min]	ϵ_1 [%]	ϵ_v [%]	σ'_3 [kPa]	σ'_d [kPa]		Time [min]	ϵ_1 [%]	ϵ_v [%]	σ'_3 [kPa]	σ'_d [kPa]
Isotropic Compression	-	0.00	0.00	100	-	Creep	0.01	3.17	1.24	8000	11195
	-	0.02	0.30	300	-		0.10	3.20	1.24	8000	11509
	-	0.09	0.69	800	-		0.25	3.23	1.24	8000	11350
	-	0.14	0.93	1300	-		0.50	3.23	1.24	8000	11169
	-	0.17	1.12	1800	-		0.75	3.24	1.24	8000	11166
	-	0.21	1.30	2300	-		1.00	3.25	1.28	8000	11185
	-	0.24	1.43	2800	-		2.50	3.29	1.32	8000	11189
	-	0.26	1.55	3300	-		5.00	3.37	1.32	8000	11204
	-	0.29	1.67	3800	-		7.50	3.43	1.32	8000	11187
	-	0.32	1.77	4300	-		10.00	3.47	1.34	8000	11191
	-	0.35	1.88	4800	-		25.00	3.62	1.40	8000	11200
	-	0.38	1.99	5300	-		50.00	3.76	1.44	8000	11199
	-	0.41	2.08	5800	-		75.00	3.84	1.46	8000	11215
	-	0.43	2.15	6300	-		100.00	3.90	1.50	8000	11207
	-	0.46	2.25	6800	-		250.00	4.08	1.57	8000	11264
	-	0.48	2.33	7300	-		500.00	4.35	1.68	8000	11231
	-	0.50	2.43	7800	-		750.00	4.46	1.68	8000	11208
	-	0.51	2.46	8000	-		1000.0	4.55	1.72	8000	11196
	-	0.51	2.50	8000	-		1500.0	4.68	1.76	8000	11202
Triaxial Compression	-	0.00	0.00	8000	0		2500.0	4.84	1.81	8000	11178
	-	0.09	0.07	8000	895		5000.0	5.04	1.92	8000	11169
	-	0.20	0.13	8000	1903		7500.0	5.17	1.93	8000	11185
	-	0.27	0.13	8000	2477		10000	5.28	1.98	8000	11186
	-	0.49	0.26	8000	4063						
	-	0.78	0.39	8000	5730						
	-	0.97	0.49	8000	6591						
	-	1.24	0.59	8000	7625						
	-	1.66	0.77	8000	8812						
	-	2.15	0.94	8000	9808						
	-	2.59	1.08	8000	10492						
	-	2.82	1.15	8000	10793						
	-	3.08	1.22	8000	11094						
	-	3.13	1.23	8000	11138						
	-	3.17	1.24	8000	11195						

Test: 1 Week Creep-1 Week Stress Relaxation (continued)

Initial Height [mm]	108.20	Void ratio	0.533
Initial Area [mm ²]	1050.6	Saturation Index, B	0.949
Mass [gr]	196.5	Shearing Rate [%/min]	0.416
Back Pressure [kPa]	200.0	Confining Pressure [kPa]	8000

	Time	ϵ_1	ϵ_v [%]	σ'_3	σ'_d		Time	ϵ_1	ϵ_v [%]	σ'_3	σ'_d
	[min]	[%]		[kPa]	[kPa]		[min]	[%]		[kPa]	[kPa]
Relaxation	0.01	5.28	1.98	8000	12347						
	0.10	5.28	1.98	8000	12336						
	0.25	5.28	1.98	8000	12320						
	0.50	5.28	1.98	8000	12303						
	0.75	5.28	1.98	8000	12288						
	1.00	5.28	1.98	8000	12277						
	2.50	5.28	1.98	8000	12160						
	5.00	5.28	1.98	8000	12134						
	7.50	5.28	1.98	8000	12103						
	10.00	5.28	1.98	8000	12077						
	25.00	5.28	1.98	8000	11973						
	50.00	5.28	1.98	8000	11872						
	75.00	5.29	1.97	8000	11784						
	100.00	5.29	1.97	8000	11701						
	250.00	5.28	1.97	8000	11219						
	500.00	5.28	1.97	8000	11091						
	750.00	5.28	1.97	8000	10988						
	1000.00	5.29	1.98	8000	10907						
	1500.00	5.28	1.98	8000	10612						
	2500.00	5.28	1.98	8000	10429						
	5000.00	5.28	1.97	8000	10168						
	7500.00	5.29	1.96	8000	9990						
	10100.00	5.28	1.95	8000	9797						

Test:

3 Hours Stress Relaxation-1 Week Creep

Initial Height [mm]	108.46	Void ratio	0.534
Initial Area [mm ²]	1046.5	Saturation Index, B	0.927
Mass [gr]	196.1	Shearing Rate [%/min]	0.0416
Back Pressure [kPa]	200.0	Confining Pressure [kPa]	8000

	Time [min]	ϵ_1 [%]	ϵ_v [%]	σ'_3 [kPa]	σ'_d [kPa]		Time [min]	ϵ_1 [%]	ϵ_v [%]	σ'_3 [kPa]	σ'_d [kPa]
Isotropic Compression	-	0.00	0.00	100	-	Relaxation	0.01	3.18	1.34	8000	10760
	-	0.04	0.39	300	-		0.10	3.18	1.34	8000	10691
	-	0.10	0.81	800	-		0.25	3.18	1.34	8000	10627
	-	0.14	1.05	1300	-		0.50	3.18	1.35	8000	10548
	-	0.18	1.26	1800	-		0.75	3.18	1.35	8000	10313
	-	0.21	1.42	2300	-		1.00	3.18	1.35	8000	10219
	-	0.25	1.55	2800	-		2.50	3.18	1.36	8000	10198
	-	0.28	1.69	3300	-		5.00	3.18	1.37	8000	10052
	-	0.31	1.80	3800	-		7.50	3.18	1.37	8000	9861
	-	0.34	1.92	4300	-		10.00	3.18	1.37	8000	9814
	-	0.37	2.02	4800	-		25.00	3.18	1.38	8000	9604
	-	0.40	2.11	5300	-		50.00	3.19	1.39	8000	9417
	-	0.42	2.21	5800	-		75.00	3.19	1.40	8000	9305
	-	0.45	2.29	6300	-		100.00	3.19	1.40	8000	9222
	-	0.48	2.37	6800	-		125.00	3.19	1.40	8000	9160
	-	0.50	2.45	7300	-		150.00	3.18	1.40	8000	8756
	-	0.53	2.54	7800	-		180.00	3.18	1.40	8000	8751
	-	0.54	2.60	8000	-						
	-	0.54	2.63	8000	-						
Triaxial Compression	-	0.00	0.00	8000	0						
	-	0.04	0.02	8000	369						
	-	0.12	0.06	8000	975						
	-	0.22	0.10	8000	1666						
	-	0.45	0.23	8000	3258						
	-	0.71	0.35	8000	4737						
	-	0.99	0.48	8000	6035						
	-	1.14	0.55	8000	6611						
	-	1.70	0.79	8000	8284						
	-	2.06	0.92	8000	9070						
	-	2.55	1.12	8000	9921						
	-	3.00	1.27	8000	10540						
	-	3.09	1.31	8000	10651						
	-	3.14	1.32	8000	10706						
	-	3.18	1.34	8000	10760						

Test: 3 Hours Stress Relaxation-1 Week Creep (continued)

Initial Height [mm]	108.46	Void ratio	0.534
Initial Area [mm ²]	1046.5	Saturation Index, B	0.927
Mass [gr]	196.1	Shearing Rate [%/min]	0.0416
Back Pressure [kPa]	200.0	Confining Pressure [kPa]	8000

	Time	ϵ_1	ϵ_v [%]	σ'_3	σ'_d		Time	ϵ_1	ϵ_v [%]	σ'_3	σ'_d
	[min]	[%]		[kPa]	[kPa]		[min]	[%]		[kPa]	[kPa]
Creep	0.01	3.18	1.40	8000	8751						
	0.10	3.18	1.40	8000	8749						
	0.25	3.18	1.40	8000	8747						
	0.50	3.18	1.40	8000	8744						
	0.75	3.18	1.40	8000	8744						
	1.00	3.18	1.40	8000	8744						
	2.50	3.18	1.40	8000	8742						
	5.00	3.18	1.40	8000	8742						
	7.50	3.18	1.40	8000	8742						
	10.00	3.18	1.40	8000	8742						
	25.00	3.18	1.40	8000	8740						
	50.00	3.18	1.40	8000	8738						
	75.00	3.18	1.40	8000	8744						
	100.00	3.18	1.40	8000	8726						
	250.00	3.19	1.40	8000	8633						
	500.00	3.19	1.41	8000	8504						
	750.00	3.19	1.41	8000	8411						
	1000.00	3.19	1.41	8000	8344						
	1500.00	3.20	1.41	8000	8740						
	2500.00	3.22	1.43	8000	8574						
	5000.00	3.27	1.43	8000	8716						
	7500.00	3.31	1.44	8000	8830						
	10000.00	3.35	1.43	8000	8792						

Test:

1 Day Stress Relaxation-1 Week Creep

Initial Height [mm]	107.95	Void ratio	0.532
Initial Area [mm ²]	1050.2	Saturation Index, B	0.909
Mass [gr]	196.1	Shearing Rate [%/min]	0.0416
Back Pressure [kPa]	200.0	Confining Pressure [kPa]	8000

	Time [min]	ϵ_1 [%]	ϵ_v [%]	σ'_3 [kPa]	σ'_d [kPa]		Time [min]	ϵ_1 [%]	ϵ_v [%]	σ'_3 [kPa]	σ'_d [kPa]
Isotropic Compression	-	0.00	0.00	100	-	Relaxation	0.01	3.17	1.33	8000	11285
	-	0.04	0.34	300	-		0.10	3.17	1.32	8000	11211
	-	0.10	0.74	800	-		0.25	3.17	1.32	8000	11131
	-	0.14	0.96	1300	-		0.50	3.17	1.32	8000	11050
	-	0.18	1.13	1800	-		0.75	3.17	1.32	8000	10939
	-	0.21	1.28	2300	-		1.00	3.17	1.32	8000	10905
	-	0.24	1.41	2800	-		2.50	3.17	1.32	8000	10672
	-	0.28	1.52	3300	-		5.00	3.17	1.31	8000	10343
	-	0.31	1.64	3800	-		7.50	3.17	1.35	8000	10306
	-	0.35	1.80	4300	-		10.00	3.17	1.38	8000	10269
	-	0.38	1.88	4800	-		25.00	3.17	1.39	8000	10011
	-	0.41	1.96	5300	-		50.00	3.17	1.40	8000	9737
	-	0.44	2.06	5800	-		75.00	3.17	1.40	8000	9655
	-	0.47	2.13	6300	-		100.00	3.17	1.41	8000	9582
	-	0.49	2.21	6800	-		250.00	3.18	1.48	8000	9325
	-	0.52	2.30	7300	-		500.00	3.18	1.52	8000	9111
	-	0.55	2.38	7800	-		750.00	3.18	1.56	8000	8977
	-	0.56	2.43	8000	-		1000.0	3.19	1.57	8000	8875
	-	0.57	2.81	8000	-		1440.0	3.17	1.57	8000	8206
Triaxial Compression	-	0.00	0.00	8000	0						
	-	0.00	0.00	8000	46						
	-	0.09	0.05	8000	703						
	-	0.18	0.09	8000	1515						
	-	0.28	0.16	8000	2356						
	-	0.54	0.27	8000	4115						
	-	0.76	0.39	8000	5365						
	-	0.99	0.50	8000	6427						
	-	1.23	0.61	8000	7340						
	-	1.71	0.80	8000	8792						
	-	2.21	1.00	8000	9860						
	-	2.60	1.13	8000	10520						
	-	2.84	1.22	8000	10858						
	-	3.08	1.30	8000	11176						
	-	3.12	1.32	8000	11227						
	-	3.17	1.33	8000	11285						

Test:

1 Day Stress Relaxation-1 Week Creep (continued)

Initial Height [mm]	107.95	Void ratio	0.532
Initial Area [mm ²]	1050.2	Saturation Index, B	0.909
Mass [gr]	196.1	Shearing Rate [%/min]	0.0416
Back Pressure [kPa]	200.0	Confining Pressure [kPa]	8000

	Time	ε_1	ε_v [%]	σ'_3	σ'_d		Time	ε_1	ε_v [%]	σ'_3	σ'_d
	[min]	[%]		[kPa]	[kPa]		[min]	[%]		[kPa]	[kPa]
Creep	0.01	3.17	1.57	8000	8206						
	0.10	3.18	1.57	8000	8950						
	0.25	3.17	1.57	8000	8599						
	0.50	3.16	1.57	8000	8353						
	0.75	3.16	1.57	8000	8302						
	1.00	3.15	1.57	8000	8226						
	2.50	3.15	1.57	8000	8222						
	5.00	3.15	1.57	8000	8217						
	7.50	3.15	1.57	8000	8215						
	10.00	3.15	1.57	8000	8213						
	25.00	3.15	1.57	8000	8213						
	50.00	3.15	1.57	8000	8224						
	75.00	3.15	1.57	8000	8215						
	100.00	3.15	1.57	8000	8221						
	250.00	3.16	1.57	8000	8244						
	500.00	3.16	1.57	8000	8239						
	750.00	3.16	1.57	8000	8226						
	1000.0	3.16	1.55	8000	8157						
	1500.0	3.16	1.57	8000	8116						
	2500.0	3.16	1.58	8000	8201						
	5000.0	3.17	1.58	8000	8167						
	7500.0	3.17	1.58	8000	8201						
	10000	3.18	1.58	8000	8174						
	12000	3.18	1.59	8000	8101						

Test:

1 Week Stress Relaxation-1 Week Creep

Initial Height [mm]	108.20	Void ratio	0.529
Initial Area [mm ²]	1046.2	Saturation Index, B	0.929
Mass [gr]	196.2	Shearing Rate [%/min]	0.0416
Back Pressure [kPa]	200.0	Confining Pressure [kPa]	8000

	Time [min]	ϵ_1 [%]	ϵ_v [%]	σ'_3 [kPa]	σ'_d [kPa]		Time [min]	ϵ_1 [%]	ϵ_v [%]	σ'_3 [kPa]	σ'_d [kPa]
Isotropic Compression	-	0.00	0.00	100	-	Relaxation	0.01	3.18	1.28	8000	11255
	-	0.02	0.27	300	-		0.10	3.18	1.27	8000	11141
	-	0.07	0.64	800	-		0.25	3.18	1.27	8000	10950
	-	0.13	0.88	1300	-		0.50	3.18	1.27	8000	10826
	-	0.17	1.06	1800	-		0.75	3.18	1.27	8000	10806
	-	0.20	1.20	2300	-		1.00	3.18	1.27	8000	10789
	-	0.23	1.32	2800	-		2.50	3.18	1.28	8000	10480
	-	0.26	1.43	3300	-		5.00	3.18	1.28	8000	10423
	-	0.28	1.53	3800	-		7.50	3.18	1.28	8000	10354
	-	0.31	1.64	4300	-		10.00	3.18	1.28	8000	10298
	-	0.34	1.72	4800	-		25.00	3.18	1.29	8000	9981
	-	0.37	1.81	5300	-		50.00	3.18	1.29	8000	9677
	-	0.39	1.89	5800	-		75.00	3.18	1.30	8000	9619
	-	0.42	1.98	6300	-		100.00	3.18	1.30	8000	9552
	-	0.45	2.06	6800	-		250.00	3.19	1.32	8000	9313
	-	0.47	2.14	7300	-		500.00	3.19	1.33	8000	9123
	-	0.50	2.22	7800	-		750.00	3.19	1.34	8000	9006
	-	0.51	2.26	8000	-		1000.0	3.20	1.34	8000	8922
	-	0.52	2.36	8000	-		1440.0	3.18	1.33	8000	8209
	-	0.00	0.00	8000	0		2500.0	3.18	1.28	8000	8201
Triaxial Compression	-	0.00	0.00	8000	32		5000.0	3.18	1.32	8000	7856
	-	0.10	0.06	8000	966		7500.0	3.18	1.29	8000	7796
	-	0.19	0.11	8000	1791		10000	3.18	1.29	8000	7720
	-	0.28	0.15	8000	2542						
	-	0.51	0.26	8000	4123						
	-	0.75	0.37	8000	5563						
	-	0.94	0.46	8000	6306						
	-	1.25	0.59	8000	7498						
	-	1.73	0.78	8000	8863						
	-	2.22	0.95	8000	9886						
	-	2.62	1.08	8000	10535						
	-	3.09	1.23	8000	11137						
	-	3.13	1.25	8000	11190						
	-	3.18	1.28	8000	11255						

Test: 1 Week Stress Relaxation-1 Week Creep (continued)

Initial Height [mm]	108.20	Void ratio	0.529
Initial Area [mm ²]	1046.2	Saturation Index, B	0.929
Mass [gr]	196.2	Shearing Rate [%/min]	0.0416
Back Pressure [kPa]	200.0	Confining Pressure [kPa]	8000

	Time	ε_1	ε_v [%]	σ'_3	σ'_d		Time	ε_1	ε_v [%]	σ'_3	σ'_d
	[min]	[%]		[kPa]	[kPa]		[min]	[%]		[kPa]	[kPa]
Creep	0.01	3.18	1.29	8000	7720						
	0.10	3.19	1.29	8000	8015						
	0.25	3.19	1.28	8000	7860						
	0.50	3.19	1.28	8000	7803						
	0.75	3.19	1.28	8000	7787						
	1.00	3.19	1.28	8000	7781						
	2.50	3.18	1.28	8000	7767						
	5.00	3.18	1.28	8000	7767						
	7.50	3.18	1.28	8000	7767						
	10.00	3.18	1.28	8000	7767						
	25.00	3.18	1.28	8000	7770						
	50.00	3.18	1.28	8000	7770						
	75.00	3.18	1.28	8000	7772						
	100.00	3.18	1.28	8000	7772						
	250.00	3.18	1.28	8000	7776						
	500.00	3.18	1.28	8000	7778						
	750.00	3.18	1.28	8000	7776						
	1000.00	3.18	1.28	8000	7776						
	1500.00	3.18	1.28	8000	7765						
	2500.00	3.18	1.28	8000	7734						
	5000.00	3.18	1.24	8000	7735						
	7500.00	3.19	1.24	8000	7712						
	10090.0	3.19	1.24	8000	7705						

Test:

Multiple 1-Day Creep-Stress Relaxation

Initial Height [mm]	107.95	Void ratio	0.534
Initial Area [mm ²]	1053.6	Saturation Index, B	0.950
Mass [gr]	196.5	Shearing Rate [%/min]	0.0416
Back Pressure [kPa]	200.0	Confining Pressure [kPa]	8000

	Time [min]	ϵ_1 [%]	ϵ_v [%]	σ'_3 [kPa]	σ'_d [kPa]		Time [min]	ϵ_1 [%]	ϵ_v [%]	σ'_3 [kPa]	σ'_d [kPa]
Isotropic Compression	-	0.00	0.00	100	-	First Creep	0.01	1.04	0.53	8000	6547
	-	0.02	0.28	300	-		0.10	1.06	0.54	8000	6463
	-	0.08	0.66	800	-		0.25	1.07	0.55	8000	6385
	-	0.13	0.89	1300	-		0.50	1.08	0.55	8000	6308
	-	0.17	1.09	1800	-		0.75	1.09	0.57	8000	6330
	-	0.21	1.24	2300	-		1.00	1.10	0.57	8000	6334
	-	0.24	1.38	2800	-		2.50	1.13	0.58	8000	6341
	-	0.27	1.50	3300	-		5.00	1.16	0.58	8000	6336
	-	0.30	1.62	3800	-		7.50	1.17	0.59	8000	6334
	-	0.33	1.73	4300	-		10.00	1.19	0.60	8000	6332
	-	0.36	1.82	4800	-		25.00	1.27	0.64	8000	6561
	-	0.39	1.90	5300	-		50.00	1.31	0.65	8000	6552
	-	0.41	2.00	5800	-		75.00	1.34	0.65	8000	6544
	-	0.44	2.09	6300	-		100.00	1.36	0.66	8000	6560
	-	0.47	2.16	6800	-		266.00	1.41	0.68	8000	6545
	-	0.49	2.24	7300	-		516.00	1.44	0.69	8000	6534
	-	0.52	2.34	7800	-		750.00	1.47	0.69	8000	6529
	-	0.53	2.37	8000	-		1000.0	1.48	0.69	8000	6526
	-	0.53	2.39	8000	-		1450.0	1.51	0.69	8000	6546
Triaxial Compression	-	0.00	0.00	8000	0	Triaxial Compression	-	1.51	0.69	8000	6546
	-	0.01	0.01	8000	147		-	1.53	0.69	8000	7349
	-	0.11	0.06	8000	1040		-	1.56	0.69	8000	7779
	-	0.20	0.11	8000	1970		-	1.60	0.69	8000	8174
	-	0.29	0.18	8000	2596		-	1.65	0.70	8000	8482
	-	0.52	0.31	8000	4104		-	1.69	0.72	8000	8663
	-	0.76	0.42	8000	5356		-	1.74	0.76	8000	8836
	-	0.90	0.46	8000	5951		-	1.79	0.80	8000	9003
	-	1.04	0.53	8000	6547		-	1.85	0.81	8000	9160
							-	1.92	0.82	8000	9339
							-	1.99	0.83	8000	9479
							-	2.06	0.86	8000	9647
							-	2.16	0.91	8000	9841
							-	2.62	1.07	8000	10624
							-	3.09	1.27	8000	11246
							-	3.18	1.29	8000	11346

Test:

Multiple 1-Day Creep-Stress Relaxation (continued)

Initial Height [mm]	107.95	Void ratio	0.534
Initial Area [mm ²]	1053.6	Saturation Index, B	0.950
Mass [gr]	196.5	Shearing Rate [%/min]	0.0416
Back Pressure [kPa]	200.0	Confining Pressure [kPa]	8000

	Time [min]	ε_1 [%]	ε_v [%]	σ'_3 [kPa]	σ'_d [kPa]		Time [min]	ε_1 [%]	ε_v [%]	σ'_3 [kPa]	σ'_d [kPa]
First Relaxation	0.01	3.18	1.29	8000	11346	Tri. Comp.	-	5.42	1.90	8000	13061
	0.10	3.18	1.29	8000	10738		-	5.88	2.03	8000	13280
	0.25	3.18	1.29	8000	10475		-	6.34	2.17	8000	13496
	0.50	3.18	1.29	8000	10413		-	6.81	2.29	8000	13703
	0.75	3.18	1.29	8000	10342		-	7.11	2.36	8000	13813
	1.00	3.18	1.29	8000	10157	Second Creep	0.01	7.11	2.36	8000	13813
	2.50	3.18	1.29	8000	9816		0.10	7.25	2.38	8000	13689
	5.00	3.18	1.29	8000	9743		0.25	7.32	2.40	8000	13772
	7.50	3.18	1.29	8000	9677		0.50	7.43	2.44	8000	13768
	10.00	3.18	1.29	8000	9611		0.75	7.51	2.47	8000	13764
	25.00	3.18	1.29	8000	9069		1.00	7.58	2.49	8000	13754
	50.00	3.18	1.29	8000	8681		2.50	7.84	2.58	8000	13719
	75.00	3.18	1.29	8000	8659		5.00	8.07	2.63	8000	13690
	100.00	3.18	1.29	8000	8634		7.50	8.22	2.69	8000	13660
	250.00	3.18	1.29	8000	8513		10.0	8.32	2.72	8000	13644
	500.00	3.19	1.29	8000	8362		25.0	8.75	2.84	8000	13773
	750.00	3.19	1.29	8000	8263		50.0	9.24	2.98	8000	13781
	1000.0	3.18	1.29	8000	7495		75.0	9.47	3.09	8000	13745
	1410.0	3.18	1.28	8000	7763		100.0	9.62	3.11	8000	13711
Triaxial Compression	-	3.18	1.28	8000	7763		250.0	10.07	3.28	8000	13650
	-	3.24	1.31	8000	9361		500.0	10.38	3.39	8000	13597
	-	3.27	1.32	8000	10087		750.0	10.58	3.46	8000	13567
	-	3.32	1.33	8000	10721		1000	10.71	3.51	8000	13552
	-	3.38	1.34	8000	11348		1350	10.91	3.57	8000	13722
	-	3.46	1.37	8000	11525						
	-	3.53	1.38	8000	11684						
	-	3.60	1.39	8000	11805						
	-	3.66	1.41	8000	11888						
	-	3.74	1.43	8000	11964						
	-	3.81	1.46	8000	12049						
	-	3.88	1.47	8000	12095						
	-	4.02	1.51	8000	12204						
	-	4.25	1.58	8000	12389						
	-	4.48	1.66	8000	12548						
	-	4.95	1.78	8000	12835						

Test: Multiple 1-Day Creep-Stress Relaxation (continued)

Initial Height [mm]	107.95	Void ratio	0.534
Initial Area [mm ²]	1053.6	Saturation Index, B	0.950
Mass [gr]	196.5	Shearing Rate [%/min]	0.0416
Back Pressure [kPa]	200.0	Confining Pressure [kPa]	8000

	Time [min]	ε_1 [%]	ε_v [%]	σ'_3 [kPa]	σ'_d [kPa]		Time [min]	ε_1 [%]	ε_v [%]	σ'_3 [kPa]	σ'_d [kPa]
Triaxial Compression	-	10.91	3.57	8000	13722						
	-	10.94	3.58	8000	15304						
	-	10.97	3.58	8000	15436						
	-	11.00	3.58	8000	15559						
	-	11.07	3.58	8000	15612						
	-	11.14	3.58	8000	15590						
	-	11.19	3.58	8000	15567						
	-	11.28	3.59	8000	15523						
	-	11.47	3.64	8000	15460						
	-	11.70	3.70	8000	15420						
	-	11.93	3.73	8000	15386						
	-	12.86	3.92	8000	15401						
	-	13.79	4.12	8000	15444						
Ending Relaxation	0.01	13.79	4.12	8000	15444						
	0.10	13.79	4.12	8000	14519						
	0.25	13.79	4.09	8000	14366						
	0.50	13.79	4.10	8000	13891						
	0.75	13.79	4.12	8000	13862						
	1.00	13.79	4.12	8000	13838						
	2.50	13.79	4.13	8000	13354						
	5.00	13.79	4.14	8000	13298						
	7.50	13.79	4.14	8000	12992						
	10.00	13.79	4.15	8000	12960						
	25.00	13.79	4.16	8000	12538						
	50.00	13.79	4.18	8000	12449						
	75.00	13.80	4.19	8000	12339						
	100.00	13.80	4.19	8000	12250						
	250.00	13.79	4.19	8000	11517						
	500.00	13.80	4.20	8000	11383						
	750.00	13.80	4.22	8000	11261						
	1000.00	13.80	4.22	8000	11156						
	1450.00	13.81	4.24	8000	10999						
	2675.00	13.80	4.24	8000	9842						

Test:

100% Stress Relaxation

Initial Height [mm]	108.20	Void ratio	0.529
Initial Area [mm ²]	1046.2	Saturation Index, B	0.929
Mass [gr]	196.2	Shearing Rate [%/min]	0.0416
Back Pressure [kPa]	200.0	Confining Pressure [kPa]	8000

	Time [min]	ε_1 [%]	ε_v [%]	σ'_3 [kPa]	σ'_d [kPa]		Time [min]	ε_1 [%]	ε_v [%]	σ'_3 [kPa]	σ'_d [kPa]
Isotropic Compression	-	0.00	0.00	100	-	Relaxation	0.01	3.18	1.28	8000	11255
	-	0.02	0.27	300	-		0.10	3.18	1.27	8000	11141
	-	0.07	0.64	800	-		0.25	3.18	1.27	8000	10950
	-	0.13	0.88	1300	-		0.50	3.18	1.27	8000	10826
	-	0.17	1.06	1800	-		0.75	3.18	1.27	8000	10806
	-	0.20	1.20	2300	-		1.00	3.18	1.27	8000	10789
	-	0.23	1.32	2800	-		2.50	3.18	1.28	8000	10480
	-	0.26	1.43	3300	-		5.00	3.18	1.28	8000	10423
	-	0.28	1.53	3800	-		7.50	3.18	1.28	8000	10354
	-	0.31	1.64	4300	-		10.00	3.18	1.28	8000	10298
	-	0.34	1.72	4800	-		25.00	3.18	1.29	8000	9981
	-	0.37	1.81	5300	-		50.00	3.18	1.29	8000	9677
	-	0.39	1.89	5800	-		75.00	3.18	1.30	8000	9619
	-	0.42	1.98	6300	-		100.00	3.18	1.30	8000	9552
	-	0.45	2.06	6800	-		250.00	3.19	1.32	8000	9313
	-	0.47	2.14	7300	-		500.00	3.19	1.33	8000	9123
	-	0.50	2.22	7800	-		750.00	3.19	1.34	8000	9006
	-	0.51	2.26	8000	-		1000.0	3.20	1.34	8000	8922
	-	0.52	2.36	8000	-		1440.0	3.18	1.33	8000	8209
Triaxial Compression	-	0.00	0.00	8000	0		2500.0	3.18	1.28	8000	8201
	-	0.00	0.00	8000	32		5000.0	3.18	1.32	8000	7856
	-	0.10	0.06	8000	966		7500.0	3.18	1.29	8000	7796
	-	0.19	0.11	8000	1791		10000	3.18	1.29	8000	7720
	-	0.28	0.15	8000	2542						
	-	0.51	0.26	8000	4123						
	-	0.75	0.37	8000	5563						
	-	0.94	0.46	8000	6306						
	-	1.25	0.59	8000	7498						
	-	1.73	0.78	8000	8863						
	-	2.22	0.95	8000	9886						
	-	2.62	1.08	8000	10535						
	-	3.09	1.23	8000	11137						
	-	3.13	1.25	8000	11190						
	-	3.18	1.28	8000	11255						

Test:

Creep-Stress Relaxation 3

Initial Height [mm]	107.70	Void ratio	0.533
Initial Area [mm ²]	1053.0	Saturation Index, B	0.947
Mass [gr]	196.8	Shearing Rate [%/min]	0.0416
Back Pressure [kPa]	200.0	Confining Pressure [kPa]	8000

	Time [min]	ϵ_1 [%]	ϵ_v [%]	σ'_3 [kPa]	σ'_d [kPa]		Time [min]	ϵ_1 [%]	ϵ_v [%]	σ'_3 [kPa]	σ'_d [kPa]
Isotropic Compression	-	0.00	0.00	100	-	Creep and Relaxation	0.01	3.17	1.33	8000	11280
	-	0.01	0.31	300	-		0.10	3.17	1.33	8000	11251
	-	0.06	0.78	800	-		0.25	3.17	1.33	8000	11222
	-	0.09	1.08	1300	-		0.50	3.18	1.34	8000	11179
	-	0.13	1.30	1800	-		0.75	3.18	1.34	8000	11150
	-	0.16	1.48	2300	-		1.00	3.18	1.34	8000	11114
	-	0.18	1.66	2800	-		2.50	3.19	1.34	8000	10982
	-	0.21	1.80	3300	-		5.00	3.20	1.35	8000	10811
	-	0.24	1.95	3800	-		7.50	3.21	1.35	8000	10737
	-	0.27	2.08	4300	-		10.00	3.22	1.36	8000	10681
	-	0.29	2.18	4800	-		25.00	3.23	1.38	8000	10481
	-	0.32	2.29	5300	-		50.00	3.25	1.39	8000	10303
	-	0.35	2.40	5800	-		75.00	3.26	1.40	8000	10195
	-	0.37	2.49	6300	-		100.00	3.26	1.41	8000	10116
	-	0.40	2.60	6800	-		250.00	3.28	1.44	8000	9857
	-	0.42	2.68	7300	-		500.00	3.30	1.45	8000	9659
	-	0.44	2.78	7800	-		750.00	3.31	1.46	8000	9543
	-	0.45	2.81	8000	-		1000.0	3.32	1.49	8000	9463
	-	0.45	2.88	8000	-		1500.0	3.33	1.50	8000	9355
Triaxial Compression	-	0.00	0.00	8000	0		2500.0	3.34	1.53	8000	9196
	-	0.02	0.01	8000	199		5000.0	3.36	1.53	8000	8981
	-	0.12	0.07	8000	1299		7500.0	3.37	1.55	8000	8859
	-	0.18	0.12	8000	2037		10200	3.37	1.53	8000	8772
	-	0.30	0.18	8000	3045						
	-	0.52	0.29	8000	4568						
	-	0.77	0.41	8000	5887						
	-	0.98	0.50	8000	6793						
	-	1.25	0.62	8000	7775						
	-	1.71	0.81	8000	9047						
	-	2.15	0.96	8000	9920						
	-	2.62	1.12	8000	10613						
	-	2.85	1.21	8000	10900						
	-	3.08	1.30	8000	11170						
	-	3.12	1.32	8000	11216						
	-	3.17	1.33	8000	11280						

Test:

Creep-Stress Relaxation 2

Initial Height [mm]	107.95	Void ratio	0.540
Initial Area [mm ²]	1062.9	Saturation Index, B	0.962
Mass [gr]	197.4	Shearing Rate [%/min]	0.0416
Back Pressure [kPa]	200.0	Confining Pressure [kPa]	8000

	Time [min]	ϵ_1 [%]	ϵ_v [%]	σ'_3 [kPa]	σ'_d [kPa]		Time [min]	ϵ_1 [%]	ϵ_v [%]	σ'_3 [kPa]	σ'_d [kPa]
Isotropic Compression	-	0.00	0.00	100	-	Creep and Relaxation	0.01	3.00	1.27	8000	11383
	-	0.03	0.38	300	-		0.10	3.00	1.27	8000	11374
	-	0.08	0.80	800	-		0.25	3.01	1.27	8000	11361
	-	0.13	1.03	1300	-		0.50	3.02	1.27	8000	11340
	-	0.17	1.24	1800	-		0.75	3.02	1.28	8000	11326
	-	0.20	1.41	2300	-		1.00	3.03	1.28	8000	11307
	-	0.23	1.54	2800	-		2.50	3.05	1.29	8000	11233
	-	0.26	1.66	3300	-		5.00	3.08	1.32	8000	11152
	-	0.29	1.79	3800	-		7.50	3.10	1.33	8000	11098
	-	0.32	1.90	4300	-		10.00	3.11	1.34	8000	11054
	-	0.34	1.99	4800	-		25.00	3.16	1.35	8000	10898
	-	0.37	2.09	5300	-		50.00	3.20	1.38	8000	10775
	-	0.40	2.19	5800	-		75.00	3.23	1.39	8000	10699
	-	0.43	2.29	6300	-		100.00	3.25	1.39	8000	10644
	-	0.45	2.36	6800	-		250.00	3.31	1.44	8000	10467
	-	0.47	2.45	7300	-		500.00	3.35	1.46	8000	10329
	-	0.49	2.52	7800	-		750.00	3.38	1.47	8000	10246
	-	0.50	2.57	8000	-		1000.0	3.40	1.49	8000	10192
	-	0.50	2.60	8000	-		1500.0	3.43	1.50	8000	10100
Triaxial Compression	-	0.00	0.00	8000	0		2500.0	3.46	1.49	8000	9998
	-	0.03	0.02	8000	376		5000.0	3.51	1.49	8000	9841
	-	0.12	0.08	8000	1485		7500.0	3.54	1.47	8000	9746
	-	0.23	0.14	8000	2597		10000	3.57	1.46	8000	9676
	-	0.31	0.20	8000	3300						
	-	0.53	0.31	8000	4877						
	-	0.82	0.45	8000	6732						
	-	1.05	0.57	8000	7691						
	-	1.24	0.64	8000	8304						
	-	1.49	0.73	8000	8998						
	-	1.76	0.85	8000	9630						
	-	2.14	0.98	8000	10310						
	-	2.63	1.15	8000	10991						
	-	2.86	1.22	8000	11230						
	-	2.96	1.26	8000	11335						
	-	3.00	1.27	8000	11383						

Test:

Creep-Stress Relaxation 1

Initial Height [mm]	108.20	Void ratio	0.533
Initial Area [mm ²]	1058.5	Saturation Index, B	0.951
Mass [gr]	198.0	Shearing Rate [%/min]	0.0416
Back Pressure [kPa]	200.0	Confining Pressure [kPa]	8000

	Time [min]	ϵ_1 [%]	ϵ_v [%]	σ'_3 [kPa]	σ'_d [kPa]		Time [min]	ϵ_1 [%]	ϵ_v [%]	σ'_3 [kPa]	σ'_d [kPa]
Isotropic Compression	-	0.00	0.00	100	-	Creep and Relaxation	0.01	3.16	1.28	8000	11396
	-	0.02	0.36	300	-		0.10	3.19	1.28	8000	11910
	-	0.09	0.80	800	-		0.25	3.19	1.28	8000	11246
	-	0.14	1.03	1300	-		0.50	3.19	1.28	8000	11216
	-	0.18	1.22	1800	-		0.75	3.19	1.29	8000	11228
	-	0.21	1.39	2300	-		1.00	3.19	1.29	8000	11186
	-	0.24	1.53	2800	-		2.50	3.23	1.30	8000	11303
	-	0.28	1.64	3300	-		5.00	3.27	1.31	8000	11283
	-	0.31	1.75	3800	-		7.50	3.30	1.31	8000	11275
	-	0.34	1.86	4300	-		10.00	3.33	1.31	8000	11242
	-	0.90	1.95	4800	-		25.00	3.42	1.37	8000	11168
	-	0.40	2.03	5300	-		50.00	3.49	1.40	8000	11123
	-	0.43	2.11	5800	-		75.00	3.53	1.41	8000	11085
	-	0.45	2.21	6300	-		100.00	3.57	1.42	8000	11056
	-	0.48	2.29	6800	-		250.00	3.68	1.46	8000	10965
	-	0.50	2.36	7300	-		500.00	3.76	1.51	8000	10833
	-	0.53	2.43	7800	-		750.00	3.81	1.53	8000	10814
	-	0.54	2.49	8000	-		1000.0	3.85	1.54	8000	10801
Triaxial Compression	-	0.54	2.60	8000	-		1500.0	3.91	1.57	8000	10757
	-	0.00	0.00	8000	0		2500.0	3.98	1.59	8000	10722
	-	0.09	0.06	8000	865		5000.0	4.07	1.60	8000	10683
	-	0.18	0.11	8000	1674		7500.0	4.12	1.61	8000	10613
	-	0.28	0.16	8000	2452		10100	4.16	1.61	8000	10579
	-	0.51	0.28	8000	4012						
	-	0.76	0.38	8000	5412						
	-	0.98	0.49	8000	6407						
	-	1.21	0.59	8000	7305						
	-	1.44	0.69	8000	8074						
	-	1.68	0.78	8000	8737						
	-	2.14	0.94	8000	9781						
	-	2.60	1.10	8000	10619						
	-	2.85	1.18	8000	11012						
	-	3.07	1.25	8000	11291						
	-	3.11	1.26	8000	11339						
	-	3.16	1.28	8000	11396						

Test:

100% Creep

Initial Height [mm]	108.20	Void ratio	0.533
Initial Area [mm ²]	1050.6	Saturation Index, B	0.949
Mass [gr]	196.5	Shearing Rate [%/min]	0.416
Back Pressure [kPa]	200.0	Confining Pressure [kPa]	8000

	Time [min]	ε_1 [%]	ε_v [%]	σ'_3 [kPa]	σ'_d [kPa]		Time [min]	ε_1 [%]	ε_v [%]	σ'_3 [kPa]	σ'_d [kPa]
Isotropic Compression	-	0.00	0.00	100	-	Creep	0.01	3.17	1.24	8000	11195
	-	0.02	0.30	300	-		0.10	3.20	1.24	8000	11509
	-	0.09	0.69	800	-		0.25	3.23	1.24	8000	11350
	-	0.14	0.93	1300	-		0.50	3.23	1.24	8000	11169
	-	0.17	1.12	1800	-		0.75	3.24	1.24	8000	11166
	-	0.21	1.30	2300	-		1.00	3.25	1.28	8000	11185
	-	0.24	1.43	2800	-		2.50	3.29	1.32	8000	11189
	-	0.26	1.55	3300	-		5.00	3.37	1.32	8000	11204
	-	0.29	1.67	3800	-		7.50	3.43	1.32	8000	11187
	-	0.32	1.77	4300	-		10.00	3.47	1.34	8000	11191
	-	0.35	1.88	4800	-		25.00	3.62	1.40	8000	11200
	-	0.38	1.99	5300	-		50.00	3.76	1.44	8000	11199
	-	0.41	2.08	5800	-		75.00	3.84	1.46	8000	11215
	-	0.43	2.15	6300	-		100.00	3.90	1.50	8000	11207
	-	0.46	2.25	6800	-		250.00	4.08	1.57	8000	11264
	-	0.48	2.33	7300	-		500.00	4.35	1.68	8000	11231
	-	0.50	2.43	7800	-		750.00	4.46	1.68	8000	11208
	-	0.51	2.46	8000	-		1000.0	4.55	1.72	8000	11196
	-	0.51	2.50	8000	-		1500.0	4.68	1.76	8000	11202
Triaxial Compression	-	0.00	0.00	8000	0		2500.0	4.84	1.81	8000	11178
	-	0.09	0.07	8000	895		5000.0	5.04	1.92	8000	11169
	-	0.20	0.13	8000	1903		7500.0	5.17	1.93	8000	11185
	-	0.27	0.13	8000	2477		10000	5.28	1.98	8000	11186
	-	0.49	0.26	8000	4063						
	-	0.78	0.39	8000	5730						
	-	0.97	0.49	8000	6591						
	-	1.24	0.59	8000	7625						
	-	1.66	0.77	8000	8812						
	-	2.15	0.94	8000	9808						
	-	2.59	1.08	8000	10492						
	-	2.82	1.15	8000	10793						
	-	3.08	1.22	8000	11094						
	-	3.13	1.23	8000	11138						
	-	3.17	1.24	8000	11195						

Tests Presented in Chapter 8

Test:

Multiple 0 kPa Stress Drop-Creep

Initial Height [mm]	107.44	Void ratio	0.530
Initial Area [mm ²]	1055.8	Saturation Index, B	0.949
Mass [gr]	196.5	Shearing Rate [%/min]	0.416
Back Pressure [kPa]	200.0	Confining Pressure [kPa]	8000

	Time [min]	ε_1 [%]	ε_v [%]	σ'_3 [kPa]	σ'_d [kPa]		Time [min]	ε_1 [%]	ε_v [%]	σ'_3 [kPa]	σ'_d [kPa]
Isotropic Compression	-	0.00	0.00	100	-	First Creep	0.01	1.01	0.52	8000	6213
	-	0.02	0.37	300	-		0.10	1.02	0.52	8000	6384
	-	0.08	0.79	800	-		0.25	1.03	0.53	8000	6378
	-	0.13	1.03	1300	-		0.50	1.04	0.53	8000	6312
	-	0.17	1.23	1800	-		0.75	1.04	0.54	8000	6273
	-	0.20	1.36	2300	-		1.00	1.05	0.54	8000	6239
	-	0.23	1.52	2800	-		2.50	1.07	0.54	8000	6244
	-	0.26	1.62	3300	-		5.00	1.09	0.55	8000	6243
	-	0.28	1.73	3800	-		7.50	1.10	0.56	8000	6241
	-	0.32	1.84	4300	-		10.00	1.11	0.58	8000	6243
	-	0.35	1.93	4800	-		25.00	1.14	0.60	8000	6247
	-	0.37	2.02	5300	-		50.00	1.17	0.61	8000	6254
	-	0.40	2.10	5800	-		75.00	1.21	0.64	8000	6359
	-	0.43	2.17	6300	-		100.00	1.22	0.65	8000	6356
	-	0.46	2.26	6800	-		250.00	1.27	0.66	8000	6344
	-	0.48	2.32	7300	-		500.00	1.31	0.69	8000	6336
	-	0.50	2.40	7800	-		750.00	1.33	0.69	8000	6245
	-	0.52	2.43	8000	-		1000.0	1.33	0.67	8000	6239
	-	0.52	2.45	8000	-		1440.0	1.35	0.66	8000	6270
Triaxial Compression	-	0.00	0.00	8000	0	Triaxial Compression	-	1.35	0.66	8000	6270
	-	0.08	0.05	8000	774		-	1.37	0.67	8000	6792
	-	0.18	0.09	8000	1611		-	1.43	0.69	8000	7405
	-	0.28	0.18	8000	2353		-	1.49	0.71	8000	7792
	-	0.52	0.30	8000	3873		-	1.53	0.75	8000	7964
	-	0.74	0.41	8000	5029		-	1.56	0.76	8000	8093
	-	0.79	0.42	8000	5240		-	1.58	0.77	8000	8161
	-	0.83	0.43	8000	5460		-	1.67	0.78	8000	8435
	-	0.88	0.47	8000	5665		-	1.79	0.81	8000	8738
	-	0.93	0.49	8000	5875		-	1.91	0.86	8000	8990
	-	1.01	0.52	8000	6213		-	2.16	0.94	8000	9475
							-	2.41	1.03	8000	9907

Test:

Multiple 0 kPa Stress Drop-Creep (continued)

Initial Height [mm]	107.44	Void ratio	0.530
Initial Area [mm ²]	1055.8	Saturation Index, B	0.949
Mass [gr]	196.5	Shearing Rate [%/min]	0.416
Back Pressure [kPa]	200.0	Confining Pressure [kPa]	8000

	Time [min]	ε_1 [%]	ε_v [%]	σ'_3 [kPa]	σ'_d [kPa]		Time [min]	ε_1 [%]	ε_v [%]	σ'_3 [kPa]	σ'_d [kPa]
Triaxial Comp.	-	2.61	1.09	8000	10231	Triaxial Compression	-	5.05	1.87	8000	12695
	-	2.89	1.17	8000	10617		-	5.08	1.88	8000	12706
	-	3.13	1.27	8000	10937		-	5.13	1.89	8000	12733
	-	3.31	1.33	8000	11142		-	5.29	1.94	8000	12816
Second Creep	0.01	3.31	1.33	8000	11142	Triaxial Compression	-	5.42	1.97	8000	12867
	0.10	3.33	1.33	8000	11481		-	5.67	2.02	8000	13004
	0.25	3.34	1.37	8000	11306		-	5.91	2.12	8000	13126
	0.50	3.34	1.37	8000	11164		-	6.15	2.17	8000	13248
	0.75	3.35	1.37	8000	11083		-	6.40	2.24	8000	13356
	1.00	3.35	1.37	8000	11045		-	6.65	2.33	8000	13462
	2.50	3.39	1.38	8000	11161		-	6.77	2.36	8000	13512
	5.00	3.46	1.39	8000	11161		-	6.84	2.36	8000	13534
	7.50	3.50	1.39	8000	11152		-	6.91	2.38	8000	13573
	10.00	3.54	1.40	8000	11166	Third Creep	0.01	6.91	2.38	8000	13573
	25.00	3.69	1.46	8000	11151		0.10	6.93	2.38	8000	13739
	50.00	3.82	1.51	8000	11233		0.25	6.93	2.38	8000	13619
	75.00	3.92	1.55	8000	11218		0.50	6.94	2.39	8000	13494
	100.00	3.99	1.59	8000	11209		0.75	6.94	2.40	8000	13417
	250.00	4.21	1.65	8000	11175		1.00	6.95	2.41	8000	13419
	500.00	4.38	1.71	8000	11151		2.50	7.01	2.42	8000	13556
	750.00	4.48	1.76	8000	11170		5.00	7.09	2.46	8000	13552
	1000.0	4.55	1.77	8000	11159		7.50	7.16	2.47	8000	13541
	1440.0	4.65	1.78	8000	11166		10.00	7.22	2.49	8000	13543
Triaxial Compression	-	4.65	1.78	8000	11166		25.00	7.49	2.58	8000	13544
	-	4.66	1.78	8000	11430		50.00	7.81	2.70	8000	13573
	-	4.67	1.78	8000	11743		75.00	8.00	2.78	8000	13552
	-	4.72	1.79	8000	12285		100.00	8.13	2.83	8000	13537
	-	4.77	1.80	8000	12481		250.00	8.56	2.97	8000	13476
	-	4.81	1.80	8000	12553		500.00	8.88	3.07	8000	13427
	-	4.87	1.82	8000	12611		750.00	9.14	3.17	8000	13604
	-	4.89	1.82	8000	12626		1000.0	9.36	3.23	8000	13571
	-	4.92	1.83	8000	12636		1252.0	9.53	3.29	8000	13598
	-	4.96	1.84	8000	12653						
	-	4.99	1.85	8000	12668						
	-	5.02	1.85	8000	12685						

Test:

Multiple 0 kPa Stress Drop-Creep (continued)

Initial Height [mm]	107.44	Void ratio	0.530
Initial Area [mm ²]	1055.8	Saturation Index, B	0.949
Mass [gr]	196.5	Shearing Rate [%/min]	0.416
Back Pressure [kPa]	200.0	Confining Pressure [kPa]	8000

	Time	ε_1 [%]	ε_v [%]	σ'_3	σ'_d		Time	ε_1 [%]	ε_v [%]	σ'_3	σ'_d
	[min]			[kPa]	[kPa]		[min]			[kPa]	[kPa]
Triaxial Compression	-	9.53	3.29	8000	13598	Ending Relaxation	0.01	13.84	4.26	8000	15343
	-	9.53	3.29	8000	13879		0.10	13.84	4.26	8000	15260
	-	9.55	3.29	8000	14144		0.25	13.84	4.26	8000	15098
	-	9.56	3.29	8000	14375		0.50	13.84	4.26	8000	14815
	-	9.58	3.29	8000	14557		0.75	13.84	4.26	8000	14544
	-	9.60	3.29	8000	14684		1.00	13.84	4.26	8000	14332
	-	9.63	3.29	8000	14761		2.50	13.84	4.26	8000	14220
	-	9.65	3.29	8000	14801		5.00	13.84	4.26	8000	14159
	-	9.68	3.30	8000	14828		7.50	13.84	4.27	8000	14117
	-	9.79	3.31	8000	14838		10.00	13.84	4.27	8000	13632
	-	9.81	3.31	8000	14831		25.00	13.84	4.27	8000	13555
	-	9.84	3.31	8000	14825		50.00	13.84	4.30	8000	13392
	-	9.88	3.32	8000	14819		75.00	13.84	4.31	8000	13251
	-	9.90	3.32	8000	14819		100.00	13.84	4.32	8000	13146
	-	9.91	3.34	8000	14822		250.00	13.85	4.33	8000	12795
	-	9.95	3.35	8000	14824		500.00	13.86	4.35	8000	12524
	-	10.00	3.36	8000	14822		750.00	13.84	4.36	8000	10837
	-	10.06	3.37	8000	14823		1000.0	13.84	4.36	8000	10857
	-	10.10	3.38	8000	14823		1440.0	13.84	4.36	8000	10814
	-	10.34	3.43	8000	14832						
	-	10.56	3.48	8000	14854						
	-	10.80	3.53	8000	14875						
	-	11.03	3.59	8000	14907						
	-	11.26	3.65	8000	14938						
	-	11.52	3.71	8000	14992						
	-	11.76	3.77	8000	15027						
	-	11.97	3.82	8000	15057						
	-	12.23	3.88	8000	15093						
	-	12.43	3.92	8000	15124						
	-	12.90	4.04	8000	15201						
	-	13.37	4.15	8000	15278						
	-	13.60	4.21	8000	15306						
	-	13.84	4.26	8000	15343						

Test:

Multiple 2500 kPa Stress Drop-Creep

Initial Height [mm]	107.70	Void ratio	0.530
Initial Area [mm ²]	1051.8	Saturation Index, B	0.952
Mass [gr]	196.2	Shearing Rate [%/min]	0.416
Back Pressure [kPa]	200.0	Confining Pressure [kPa]	8000

	Time [min]	ε_1 [%]	ε_v [%]	σ'_3 [kPa]	σ'_d [kPa]		Time [min]	ε_1 [%]	ε_v [%]	σ'_3 [kPa]	σ'_d [kPa]
Isotropic Compression	-	0.00	0.00	100	-	First Creep	0.01	0.85	0.40	8000	3253
	-	0.03	0.33	300	-		0.10	0.88	0.40	8000	3655
	-	0.10	0.76	868	-		0.25	0.89	0.40	8000	3583
	-	0.14	0.96	1300	-		0.50	0.88	0.40	8000	3434
	-	0.17	1.13	1800	-		0.75	0.88	0.40	8000	3380
	-	0.21	1.28	2300	-		1.00	0.88	0.40	8000	3405
	-	0.24	1.41	2800	-		2.50	0.88	0.40	8000	3500
	-	0.26	1.53	3300	-		5.00	0.90	0.40	8000	3498
	-	0.29	1.63	3800	-		7.50	0.90	0.40	8000	3498
	-	0.31	1.73	4300	-		10.00	0.90	0.40	8000	3512
	-	0.34	1.83	4800	-		25.00	0.91	0.40	8000	3507
	-	0.37	1.90	5300	-		50.00	0.92	0.41	8000	3598
	-	0.40	1.99	5800	-		75.00	0.92	0.41	8000	3593
	-	0.42	2.07	6300	-		100.00	0.92	0.41	8000	3591
	-	0.45	2.15	6800	-		250.00	0.92	0.41	8000	3584
	-	0.47	2.22	7300	-		500.00	0.92	0.39	8000	3580
	-	0.49	2.29	7800	-		750.00	0.92	0.39	8000	3582
	-	0.50	2.33	8000	-		1000.0	0.93	0.37	8000	3579
	-	0.50	2.34	8000	-		1413.0	0.93	0.37	8000	3590
Triaxial Compression	-	0.00	0.00	8000	0	Triaxial Compression	-	0.93	0.40	8000	3592
	-	0.07	0.03	8000	606		-	0.99	0.45	8000	5179
	-	0.17	0.08	8000	1443		-	1.02	0.46	8000	5594
	-	0.27	0.13	8000	2233		-	1.04	0.46	8000	5852
	-	0.49	0.24	8000	3665		-	1.08	0.47	8000	6136
	-	0.71	0.34	8000	4818		-	1.14	0.48	8000	6460
	-	0.80	0.37	8000	5271		-	1.17	0.50	8000	6641
	-	0.89	0.42	8000	5649		-	1.21	0.50	8000	6801
	-	0.93	0.45	8000	5847		-	1.27	0.56	8000	7030
	-	0.98	0.47	8000	6050		-	1.31	0.57	8000	7269
	-	0.85	0.40	8000	3253		-	1.35	0.58	8000	7313
							-	1.39	0.58	8000	7448
							-	1.43	0.59	8000	7577
							-	1.49	0.61	8000	7760
							-	1.55	0.63	8000	7940
							-	1.64	0.68	8000	8212

Test:

Multiple 2500 kPa Stress Drop-Creep (continued)

Initial Height [mm]	107.70	Void ratio	0.530
Initial Area [mm ²]	1051.8	Saturation Index, B	0.952
Mass [gr]	196.2	Shearing Rate [%/min]	0.416
Back Pressure [kPa]	200.0	Confining Pressure [kPa]	8000

	Time [min]	ε_1 [%]	ε_v [%]	σ'_3 [kPa]	σ'_d [kPa]		Time [min]	ε_1 [%]	ε_v [%]	σ'_3 [kPa]	σ'_d [kPa]
Triaxial Compression	-	1.88	0.79	8000	8854	Triaxial Compression	-	3.57	1.35	8000	11553
	-	2.12	0.86	8000	9419		-	3.63	1.37	8000	11643
	-	2.35	0.95	8000	9866		-	3.69	1.38	8000	11721
	-	2.57	1.02	8000	10260		-	3.75	1.42	8000	11798
	-	2.85	1.09	8000	10685		-	3.84	1.43	8000	11870
	-	3.04	1.19	8000	10964		-	3.92	1.44	8000	11950
	-	3.23	1.21	8000	11199		-	4.08	1.51	8000	12097
	-	3.27	1.24	8000	11262		-	4.50	1.63	8000	12417
	-	3.32	1.26	8000	11314		-	4.91	1.74	8000	12685
	-	3.23	1.24	8000	8624		-	5.37	1.88	8000	12953
Second Creep	0.01	3.23	1.24	8000	8624	Triaxial Compression	-	5.84	2.03	8000	13198
	0.10	3.27	1.23	8000	9543		-	6.31	2.16	8000	13408
	0.25	3.27	1.23	8000	9558		-	6.79	2.28	8000	13612
	0.50	3.27	1.23	8000	9481		-	6.83	2.28	8000	13623
	0.75	3.27	1.23	8000	9402		-	6.88	2.30	8000	13635
	1.00	3.27	1.23	8000	9343		-	6.80	2.30	8000	10681
	2.50	3.25	1.23	8000	8922	Third Creep	0.01	6.80	2.30	8000	10681
	5.00	3.24	1.23	8000	8716		0.10	6.85	2.30	8000	11729
	7.50	3.24	1.23	8000	8859		0.25	6.85	2.30	8000	11369
	10.00	3.24	1.23	8000	8853		0.50	6.83	2.30	8000	10926
	25.00	3.24	1.24	8000	8847		0.75	6.82	2.30	8000	10713
	50.00	3.24	1.25	8000	8798		1.00	6.82	2.30	8000	10560
	75.00	3.24	1.25	8000	8762		2.50	6.85	2.30	8000	11204
	100.0	3.24	1.25	8000	8734		5.00	6.86	2.30	8000	11254
	250.0	3.25	1.25	8000	8617		7.50	6.86	2.30	8000	11243
	500.0	3.25	1.26	8000	8507		10.00	6.86	2.30	8000	11219
Triaxial Compression	760.0	3.26	1.29	8000	8637		25.00	6.87	2.30	8000	11318
	910.0	3.26	1.29	8000	8581		50.00	6.88	2.30	8000	11394
	1410.0	3.27	1.29	8000	8640		75.00	6.88	2.32	8000	11307
	-	3.27	1.29	8000	8640		100.00	6.89	2.32	8000	11300
	-	3.31	1.30	8000	9660		250.00	6.91	2.34	8000	11290
	-	3.35	1.31	8000	10399		500.00	6.93	2.36	8000	11276
	-	3.40	1.31	8000	10925		750.00	6.94	2.36	8000	11268
Triaxial Compression	-	3.46	1.32	8000	11248		1000.0	6.95	2.36	8000	11268
	-	3.52	1.33	8000	11430		1300.0	6.97	2.36	8000	11259

Test:

Multiple 2500 kPa Stress Drop-Creep (continued)

Initial Height [mm]	107.70	Void ratio	0.530
Initial Area [mm ²]	1051.8	Saturation Index, B	0.952
Mass [gr]	196.2	Shearing Rate [%/min]	0.416
Back Pressure [kPa]	200.0	Confining Pressure [kPa]	8000

	Time	ε_1 [%]	ε_v [%]	σ'_3	σ'_d		Time	ε_1 [%]	ε_v [%]	σ'_3	σ'_d
	[min]			[kPa]	[kPa]		[min]			[kPa]	[kPa]
Triaxial Compression	-	6.97	2.36	8000	11259	Ending Relaxation	0.01	13.77	4.06	8000	15435
	-	7.02	2.39	8000	12949		0.10	13.77	4.06	8000	15317
	-	6.88	2.30	8000	13635		0.25	13.78	4.06	8000	15177
	-	6.80	2.30	8000	10681		0.50	13.78	4.07	8000	14878
	-	6.97	2.36	8000	11259		0.75	13.77	4.07	8000	14644
	-	7.02	2.39	8000	12949		1.00	13.77	4.07	8000	14624
	-	7.08	2.40	8000	13426		2.50	13.77	4.08	8000	14480
	-	7.13	2.40	8000	13688		5.00	13.77	4.08	8000	14186
	-	7.19	2.42	8000	13833		7.50	13.77	4.08	8000	14086
	-	7.25	2.42	8000	13910		10.00	13.77	4.09	8000	14021
	-	7.31	2.44	8000	13967		25.00	13.78	4.09	8000	13718
	-	7.47	2.47	8000	14035		50.00	13.79	4.11	8000	13466
	-	7.72	2.53	8000	14106		75.00	13.79	4.11	8000	13309
	-	8.21	2.65	8000	14241		100.00	13.79	4.11	8000	13198
	-	8.70	2.77	8000	14375		188.00	13.80	4.13	8000	12935
	-	9.12	2.90	8000	14466		500.00	13.81	4.16	8000	12506
	-	9.63	3.02	8000	14604		750.00	13.81	4.16	8000	12301
	-	10.06	3.13	8000	14701		1000.0	14.18	4.13	8000	12106
	-	10.57	3.26	8000	14815		1320.0	13.77	4.17	8000	10519
	-	10.98	3.38	8000	14880						
	-	11.48	3.51	8000	14967						
	-	11.91	3.62	8000	15030						
	-	12.37	3.73	8000	15100						
	-	12.84	3.85	8000	15186						
	-	13.31	3.96	8000	15383						
	-	13.77	4.06	8000	15435						

Test:

Multiple 5000 kPa Stress Drop-Creep

Initial Height [mm]	107.70	Void ratio	0.530
Initial Area [mm ²]	1056.3	Saturation Index, B	0.955
Mass [gr]	197.0	Shearing Rate [%/min]	0.416
Back Pressure [kPa]	200.0	Confining Pressure [kPa]	8000

	Time [min]	ε_1 [%]	ε_v [%]	σ'_3 [kPa]	σ'_d [kPa]		Time [min]	ε_1 [%]	ε_v [%]	σ'_3 [kPa]	σ'_d [kPa]
Isotropic Compression	-	0.00	0.00	100	-	First Creep	0.01	0.77	0.43	8000	1585
	-	0.02	0.25	300	-		0.10	0.77	0.43	8000	1632
	-	0.08	0.65	800	-		0.25	0.77	0.43	8000	1634
	-	0.12	0.85	1300	-		0.50	0.77	0.43	8000	1636
	-	0.16	1.03	1800	-		0.75	0.77	0.43	8000	1636
	-	0.19	1.17	2300	-		1.00	0.77	0.43	8000	1638
	-	0.22	1.29	2800	-		2.50	0.77	0.43	8000	1618
	-	0.25	1.40	3300	-		5.00	0.77	0.43	8000	1625
	-	0.28	1.49	3800	-		7.50	0.77	0.43	8000	1621
	-	0.30	1.58	4300	-		10.00	0.77	0.43	8000	1618
	-	0.33	1.67	4800	-		25.00	0.77	0.43	8000	1623
	-	0.36	1.76	5300	-		50.00	0.77	0.43	8000	1623
	-	0.39	1.84	5800	-		75.00	0.77	0.43	8000	1605
	-	0.42	1.93	6300	-		100.0	0.77	0.43	8000	1598
	-	0.44	2.01	6800	-		250.0	0.77	0.43	8000	1623
	-	0.47	2.10	7300	-		500.0	0.77	0.43	8000	1652
	-	0.49	2.18	7800	-		750.0	0.77	0.43	8000	1656
	-	0.50	2.21	8000	-		1000.0	0.77	0.43	8000	1658
	-	0.50	2.26	8000	-		1450.0	0.77	0.40	8000	1608
	-	0.00	0.00	8000	0		1600.0	0.77	0.37	8000	1603
Triaxial Compression	-	0.10	0.07	8000	939	Triaxial Comp.	-	0.77	0.37	8000	1603
	-	0.18	0.11	8000	1580		-	0.80	0.40	8000	2388
	-	0.27	0.17	8000	2360		-	0.84	0.40	8000	3226
	-	0.50	0.28	8000	3932		-	0.89	0.43	8000	3455
	-	0.74	0.39	8000	5240		-	0.94	0.45	8000	4885
	-	0.83	0.43	8000	5692		-	0.98	0.46	8000	5639
	-	0.88	0.45	8000	5906		-	1.03	0.47	8000	6228
	-	0.92	0.46	8000	6111		-	1.09	0.50	8000	6634
	-	0.97	0.48	8000	6309		-	1.14	0.52	8000	6946
	-	0.77	0.43	8000	1585		-	1.20	0.56	8000	7205
							-	1.26	0.57	8000	7436
							-	1.32	0.58	8000	7652
							-	1.44	0.64	8000	8056
							-	1.70	0.75	8000	8792
							-	2.10	0.89	8000	9703

Test:

Multiple 5000 kPa Stress Drop-Creep (continued)

Initial Height [mm]	107.70	Void ratio	0.530
Initial Area [mm ²]	1056.3	Saturation Index, B	0.955
Mass [gr]	197.0	Shearing Rate [%/min]	0.416
Back Pressure [kPa]	200.0	Confining Pressure [kPa]	8000

	Time [min]	ε_1 [%]	ε_v [%]	σ'_3 [kPa]	σ'_d [kPa]		Time [min]	ε_1 [%]	ε_v [%]	σ'_3 [kPa]	σ'_d [kPa]
Triaxial Comp.	-	2.60	1.04	8000	10592	Triaxial Compression	-	3.78	1.47	8000	12092
	-	3.07	1.18	8000	11228		-	4.01	1.54	8000	12296
	-	3.12	1.21	8000	11292		-	4.50	1.67	8000	12668
	-	3.16	1.24	8000	11344		-	4.93	1.78	8000	12916
	-	2.97	1.22	8000	6419		-	5.47	1.92	8000	13205
Second Creep	0.01	2.97	1.22	8000	6419	Triaxial Compression	-	5.87	2.04	8000	13383
	0.10	2.98	1.20	8000	6678		-	6.33	2.14	8000	13571
	0.25	2.98	1.20	8000	6559		-	6.80	2.26	8000	13754
	0.50	2.98	1.20	8000	6460		-	6.85	2.27	8000	13773
	0.75	2.97	1.20	8000	6405		-	6.89	2.29	8000	13788
	1.00	2.97	1.20	8000	6399		-	6.94	2.30	8000	13812
	2.50	2.97	1.20	8000	6399		-	6.77	2.24	8000	8863
	5.00	2.97	1.20	8000	6403	Third Creep	0.01	6.77	2.24	8000	8863
	7.50	2.97	1.20	8000	6405		0.10	6.78	2.24	8000	9208
	10.00	2.97	1.20	8000	6408		0.25	6.78	2.25	8000	9192
	25.00	2.97	1.20	8000	6403		0.50	6.78	2.25	8000	9026
	50.00	2.97	1.17	8000	6412		0.75	6.78	2.26	8000	8993
	75.00	2.97	1.17	8000	6412		1.00	6.78	2.26	8000	8950
	100.0	2.97	1.17	8000	6410		2.50	6.78	2.26	8000	8938
	250.0	2.97	1.18	8000	6402		5.00	6.78	2.26	8000	8944
	500.0	2.97	1.18	8000	6391		7.50	6.78	2.26	8000	8944
	750.0	2.97	1.17	8000	6379		10.00	6.78	2.26	8000	8946
	1000.0	2.97	1.17	8000	6366		25.00	6.78	2.27	8000	8943
	1350.0	2.98	1.17	8000	6387		50.00	6.78	2.27	8000	8941
Triaxial Compression	-	2.98	1.17	8000	6387		75.00	6.78	2.27	8000	8935
	-	3.00	1.20	8000	6924		100.00	6.78	2.27	8000	8929
	-	3.02	1.21	8000	7574		250.00	6.78	2.27	8000	8894
	-	3.05	1.21	8000	8273		500.00	6.78	2.27	8000	8856
	-	3.09	1.22	8000	9177		750.00	6.78	2.29	8000	8821
	-	3.14	1.24	8000	10022		1000.0	6.78	2.29	8000	8789
	-	3.19	1.27	8000	10700		1300.0	6.78	2.29	8000	8921
	-	3.26	1.29	8000	11237						
	-	3.36	1.34	8000	11562						
	-	3.45	1.38	8000	11735						
	-	3.55	1.41	8000	11867						

Test: Multiple 5000 kPa Stress Drop-Creep (continued)

Initial Height [mm]	107.70	Void ratio	0.530
Initial Area [mm ²]	1056.3	Saturation Index, B	0.955
Mass [gr]	197.0	Shearing Rate [%/min]	0.416
Back Pressure [kPa]	200.0	Confining Pressure [kPa]	8000

	Time	ε_1 [%]	ε_V [%]	σ'_3	σ'_d		Time	ε_1 [%]	ε_V [%]	σ'_3	σ'_d
	[min]			[kPa]	[kPa]		[min]			[kPa]	[kPa]
Triaxial Compression	-	6.78	2.29	8000	8921	Ending Relaxation	0.01	13.80	4.01	8000	15396
	-	6.89	2.29	8000	13788		0.10	13.80	4.03	8000	15303
	-	6.94	2.30	8000	13812		0.25	13.80	4.03	8000	15139
	-	6.91	2.30	8000	12011		0.50	13.80	4.03	8000	14969
	-	6.78	2.29	8000	8921		0.75	13.80	4.03	8000	14934
	-	6.82	2.29	8000	10068		1.00	13.80	4.03	8000	14888
	-	7.08	2.35	8000	13617		2.50	13.80	4.03	8000	14448
	-	6.91	2.30	8000	12011		5.00	13.80	4.04	8000	14367
	-	6.96	2.32	8000	12800		7.50	13.80	4.05	8000	14279
	-	7.03	2.33	8000	13369		10.00	13.80	4.05	8000	14186
	-	7.08	2.35	8000	13617		25.00	13.81	4.06	8000	13898
	-	7.14	2.37	8000	13755		50.00	13.81	4.08	8000	13637
	-	7.21	2.38	8000	13837		75.00	13.82	4.08	8000	13472
	-	7.29	2.38	8000	13903		100.00	13.82	4.08	8000	13352
	-	7.52	2.44	8000	14008		250.00	13.83	4.09	8000	12952
	-	7.73	2.50	8000	14079		500.00	13.83	4.11	8000	12645
	-	8.20	2.61	8000	14197		750.00	13.84	4.12	8000	12444
	-	8.67	2.74	8000	14328		1000.0	13.84	4.12	8000	12309
	-	9.18	2.87	8000	14445		1320.0	13.80	4.12	8000	10833
	-	10.07	3.11	8000	14659						
	-	11.00	3.35	8000	14860						
	-	11.96	3.57	8000	15038						
	-	12.89	3.80	8000	15219						
	-	13.80	4.01	8000	15396						

Test:

0 kPa Stress Drop-1 Week Creep

Initial Height [mm]	108.20	Void ratio	0.533
Initial Area [mm ²]	1050.6	Saturation Index, B	0.949
Mass [gr]	196.5	Shearing Rate [%/min]	0.416
Back Pressure [kPa]	200.0	Confining Pressure [kPa]	8000

	Time [min]	ε_1 [%]	ε_v [%]	σ'_3 [kPa]	σ'_d [kPa]		Time [min]	ε_1 [%]	ε_v [%]	σ'_3 [kPa]	σ'_d [kPa]
Isotropic Compression	-	0.00	0.00	100	-	Creep	0.01	3.17	1.24	8000	11195
	-	0.02	0.30	300	-		0.10	3.20	1.24	8000	11509
	-	0.09	0.69	800	-		0.25	3.23	1.24	8000	11350
	-	0.14	0.93	1300	-		0.50	3.23	1.24	8000	11169
	-	0.17	1.12	1800	-		0.75	3.24	1.24	8000	11166
	-	0.21	1.30	2300	-		1.00	3.25	1.28	8000	11185
	-	0.24	1.43	2800	-		2.50	3.29	1.32	8000	11189
	-	0.26	1.55	3300	-		5.00	3.37	1.32	8000	11204
	-	0.29	1.67	3800	-		7.50	3.43	1.32	8000	11187
	-	0.32	1.77	4300	-		10.00	3.47	1.34	8000	11191
	-	0.35	1.88	4800	-		25.00	3.62	1.40	8000	11200
	-	0.38	1.99	5300	-		50.00	3.76	1.44	8000	11199
	-	0.41	2.08	5800	-		75.00	3.84	1.46	8000	11215
	-	0.43	2.15	6300	-		100.00	3.90	1.50	8000	11207
	-	0.46	2.25	6800	-		250.00	4.08	1.57	8000	11264
	-	0.48	2.33	7300	-		500.00	4.35	1.68	8000	11231
	-	0.50	2.43	7800	-		750.00	4.46	1.68	8000	11208
	-	0.51	2.46	8000	-		1000.0	4.55	1.72	8000	11196
	-	0.51	2.50	8000	-		1500.0	4.68	1.76	8000	11202
	-	0.00	0.00	8000	0		2500.0	4.84	1.81	8000	11178
Triaxial Compression	-	0.09	0.07	8000	895		5000.0	5.04	1.92	8000	11169
	-	0.20	0.13	8000	1903		7500.0	5.17	1.93	8000	11185
	-	0.27	0.13	8000	2477		10000	5.28	1.98	8000	11186
	-	0.49	0.26	8000	4063						
	-	0.78	0.39	8000	5730						
	-	0.97	0.49	8000	6591						
	-	1.24	0.59	8000	7625						
	-	1.66	0.77	8000	8812						
	-	2.15	0.94	8000	9808						
	-	2.59	1.08	8000	10492						
	-	2.82	1.15	8000	10793						
	-	3.08	1.22	8000	11094						
	-	3.13	1.23	8000	11138						
	-	3.17	1.24	8000	11195						

Test:

2500 kPa Stress Drop-1 Week Creep

Initial Height [mm]	108.20	Void ratio	0.535
Initial Area [mm ²]	1053.1	Saturation Index, B	0.975
Mass [gr]	196.7	Shearing Rate [%/min]	0.416
Back Pressure [kPa]	200.0	Confining Pressure [kPa]	8000

	Time [min]	ϵ_1 [%]	ϵ_v [%]	σ'_3 [kPa]	σ'_d [kPa]		Time [min]	ϵ_1 [%]	ϵ_v [%]	σ'_3 [kPa]	σ'_d [kPa]
Isotropic Compression	-	0.00	0.00	100	-	Creep	0.01	3.13	1.26	8000	8708
	-	0.02	0.31	300	-		0.10	3.13	1.26	8000	8869
	-	0.09	0.70	800	-		0.25	3.13	1.26	8000	8809
	-	0.14	0.94	1300	-		0.50	3.13	1.26	8000	8752
	-	0.19	1.14	1800	-		0.75	3.13	1.26	8000	8727
	-	0.23	1.31	2300	-		1.00	3.13	1.26	8000	8725
	-	0.26	1.44	2800	-		2.50	3.12	1.26	8000	8721
	-	0.29	1.57	3300	-		5.00	3.12	1.26	8000	8721
	-	0.32	1.69	3800	-		7.50	3.12	1.26	8000	8716
	-	0.35	1.81	4300	-		10.00	3.12	1.27	8000	8716
	-	0.38	1.90	4800	-		25.00	3.12	1.27	8000	8700
	-	0.41	1.99	5300	-		50.00	3.12	1.27	8000	8729
	-	0.44	2.08	5800	-		75.00	3.13	1.29	8000	8721
	-	0.47	2.16	6300	-		100.00	3.13	1.29	8000	8712
	-	0.49	2.23	6800	-		250.00	3.13	1.30	8000	8669
	-	0.51	2.30	7300	-		500.00	3.14	1.30	8000	8545
	-	0.54	2.37	7800	-		750.00	3.14	1.31	8000	8466
	-	0.55	2.41	8000	-		1000.0	3.14	1.32	8000	8403
	-	0.55	2.42	8000	-		1500.0	3.16	1.34	8000	8743
Triaxial Compression	-	0.00	0.00	8000	0		2500.0	3.17	1.35	8000	8736
	-	0.01	0.00	8000	140		5000.0	3.20	1.38	8000	8735
	-	0.10	0.08	8000	1057		7500.0	3.23	1.40	8000	8742
	-	0.20	0.11	8000	1886		10000	3.25	1.41	8000	8752
	-	0.29	0.17	8000	2637		11240	3.26	1.41	8000	8755
	-	0.52	0.31	8000	4198						
	-	0.75	0.40	8000	5477						
	-	0.99	0.50	8000	6509						
	-	1.22	0.61	8000	7373						
	-	1.69	0.79	8000	8724						
	-	2.15	0.95	8000	9723						
	-	2.63	1.11	8000	10515						
	-	2.86	1.18	8000	10829						
	-	3.08	1.24	8000	11100						
	-	3.19	1.29	8000	11222						
	-	3.13	1.26	8000	8708						

Test:

5000 kPa Stress Drop-1 Week Creep

Initial Height [mm]	108.46	Void ratio	0.533
Initial Area [mm ²]	1049.4	Saturation Index, B	0.953
Mass [gr]	196.7	Shearing Rate [%/min]	0.416
Back Pressure [kPa]	200.0	Confining Pressure [kPa]	8000

	Time [min]	ϵ_1 [%]	ϵ_v [%]	σ'_3 [kPa]	σ'_d [kPa]		Time [min]	ϵ_1 [%]	ϵ_v [%]	σ'_3 [kPa]	σ'_d [kPa]
Isotropic Compression	-	0.00	0.00	100	-	First Creep	0.01	2.82	1.12	8000	6270
	-	0.02	0.33	300	-		0.10	2.82	1.12	8000	6268
	-	0.07	0.71	800	-		0.25	2.82	1.13	8000	6271
	-	0.11	0.92	1300	-		0.50	2.82	1.14	8000	6270
	-	0.14	1.11	1800	-		0.75	2.82	1.14	8000	6268
	-	0.17	1.25	2300	-		1.00	2.82	1.14	8000	6266
	-	0.20	1.39	2800	-		2.50	2.82	1.14	8000	6270
	-	0.23	1.50	3300	-		5.00	2.82	1.14	8000	6275
	-	0.26	1.60	3800	-		7.50	2.82	1.14	8000	6277
	-	0.28	1.70	4300	-		10.00	2.82	1.14	8000	6279
	-	0.31	1.80	4800	-		25.00	2.82	1.14	8000	6288
	-	0.34	1.88	5300	-		50.00	2.82	1.16	8000	6291
	-	0.36	1.97	5800	-		75.00	2.82	1.17	8000	6274
	-	0.39	2.06	6300	-		100.00	2.82	1.18	8000	6278
	-	0.41	2.13	6800	-		250.00	2.82	1.19	8000	6270
	-	0.43	2.20	7300	-		500.00	2.82	1.22	8000	6278
	-	0.45	2.27	7800	-		750.00	2.82	1.23	8000	6266
Triaxial Compression	-	0.46	2.32	8000	-		1000.0	2.82	1.23	8000	6257
	-	0.46	2.34	8000	-		1500.0	2.82	1.23	8000	6235
	-	0.00	0.00	8000	0		2500.0	2.82	1.23	8000	6188
	-	0.01	0.01	8000	140		5000.0	2.83	1.24	8000	6266
	-	0.12	0.06	8000	1244		7500.0	2.84	1.24	8000	6275
	-	0.19	0.10	8000	1916		10175	2.84	1.24	8000	6248
	-	0.29	0.14	8000	2801						
	-	0.49	0.25	8000	4368						
	-	0.71	0.36	8000	5687						
	-	0.93	0.44	8000	6787						
	-	1.21	0.55	8000	7853						
	-	1.69	0.76	8000	9236						
	-	2.13	0.90	8000	10130						
	-	2.60	1.06	8000	10836						
	-	2.83	1.14	8000	11130						
	-	2.97	1.18	8000	11291						
	-	3.01	1.19	8000	11354						
	-	2.82	1.12	8000	6270						

Test:

Multiple 0 kPa Stress Drop-Stress Relaxation

Initial Height [mm]	107.44	Void ratio	0.532
Initial Area [mm ²]	1058.9	Saturation Index, B	0.904
Mass [gr]	196.8	Shearing Rate [%/min]	0.416
Back Pressure [kPa]	200.0	Confining Pressure [kPa]	8000

	Time [min]	ε_1 [%]	ε_v [%]	σ'_3 [kPa]	σ'_d [kPa]		Time [min]	ε_1 [%]	ε_v [%]	σ'_3 [kPa]	σ'_d [kPa]
Isotropic Compression	-	0.00	0.00	100	-	First Relaxation	0.01	1.01	0.48	8000	6617
	-	0.03	0.38	300	-		0.10	1.02	0.48	8000	6575
	-	0.08	0.81	868	-		0.25	1.01	0.48	8000	6485
	-	0.12	1.00	1300	-		0.50	1.01	0.49	8000	6451
	-	0.16	1.17	1800	-		0.75	1.01	0.49	8000	6415
	-	0.19	1.32	2300	-		1.00	1.02	0.49	8000	6383
	-	0.22	1.46	2800	-		2.50	1.02	0.49	8000	6269
	-	0.25	1.57	3300	-		5.00	1.01	0.49	8000	6057
	-	0.29	1.67	3800	-		7.50	1.01	0.49	8000	6023
	-	0.32	1.77	4300	-		10.00	1.01	0.51	8000	5885
	-	0.35	1.87	4800	-		25.00	1.01	0.53	8000	5739
	-	0.37	1.95	5300	-		50.00	1.02	0.53	8000	5641
	-	0.41	2.06	5800	-		75.00	1.02	0.53	8000	5553
	-	0.43	2.14	6300	-		100.00	1.02	0.53	8000	5500
	-	0.46	2.23	6800	-		250.00	1.02	0.54	8000	5381
	-	0.48	2.32	7300	-		500.00	1.02	0.54	8000	5283
	-	0.51	2.41	7800	-		750.00	1.02	0.54	8000	5199
Triaxial Compression	-	0.52	2.47	8000	-	Triaxial Compression	1000.0	1.01	0.54	8000	4810
	-	0.52	2.67	8000	-		1410.0	1.01	0.54	8000	4799
	-	0.00	0.00	8000	0		-	1.01	0.54	8000	4799
	-	0.04	0.02	8000	442		-	1.04	0.54	8000	5366
	-	0.12	0.06	8000	1067		-	1.07	0.54	8000	5960
	-	0.21	0.10	8000	1904		-	1.10	0.55	8000	6424
	-	0.30	0.16	8000	2672		-	1.11	0.55	8000	6615
	-	0.55	0.27	8000	4356		-	1.13	0.56	8000	6775
	-	0.77	0.37	8000	5546		-	1.14	0.57	8000	6829
	-	0.92	0.44	8000	6236		-	1.18	0.57	8000	7081
	-	0.99	0.47	8000	6524		-	1.21	0.59	8000	7286
	-	1.01	0.48	8000	6617		-	1.25	0.60	8000	7458
							-	1.29	0.61	8000	7623
							-	1.31	0.62	8000	7691
							-	1.33	0.62	8000	7758
							-	1.39	0.64	8000	7952
							-	1.47	0.67	8000	8201
							-	1.71	0.75	8000	8842

Test: Multiple 0 kPa Stress Drop-Stress Relaxation (continued)

Initial Height [mm]	107.44	Void ratio	0.532
Initial Area [mm ²]	1058.9	Saturation Index, B	0.904
Mass [gr]	196.8	Shearing Rate [%/min]	0.416
Back Pressure [kPa]	200.0	Confining Pressure [kPa]	8000

	Time [min]	ε_1 [%]	ε_v [%]	σ'_3 [kPa]	σ'_d [kPa]		Time [min]	ε_1 [%]	ε_v [%]	σ'_3 [kPa]	σ'_d [kPa]
Triaxial Compression	-	2.04	0.88	8000	9563	Triaxial Compression	-	3.47	1.35	8000	11550
	-	2.20	0.93	8000	9873		-	3.50	1.35	8000	11583
	-	2.44	1.02	8000	10282		-	3.56	1.37	8000	11655
	-	2.62	1.08	8000	10539		-	3.62	1.38	8000	11708
	-	2.89	1.15	8000	10910		-	3.86	1.45	8000	11929
	-	3.11	1.22	8000	11176		-	3.94	1.47	8000	11994
Second Relaxation	0.01	3.11	1.22	8000	11176	Triaxial Compression	-	4.19	1.54	8000	12198
	0.10	3.11	1.22	8000	11112		-	4.28	1.58	8000	12260
	0.25	3.11	1.22	8000	11021		-	4.44	1.62	8000	12371
	0.50	3.11	1.22	8000	10925		-	4.61	1.69	8000	12496
	0.75	3.11	1.22	8000	10865		-	5.08	1.80	8000	12774
	1.00	3.11	1.22	8000	10817		-	5.58	1.97	8000	13047
	2.50	3.11	1.22	8000	10529		-	6.01	2.06	8000	13249
	5.00	3.11	1.22	8000	10296		-	6.48	2.17	8000	13427
	7.50	3.11	1.22	8000	10243		-	6.85	2.27	8000	13582
	10.00	3.11	1.22	8000	10032		-	6.95	2.30	8000	13616
	25.00	3.11	1.23	8000	9741	Third Relaxation	0.01	6.95	2.30	8000	13616
	50.00	3.11	1.23	8000	9486		0.10	6.95	2.30	8000	13542
	75.00	3.11	1.24	8000	9430		0.25	6.95	2.30	8000	13420
	100.00	3.11	1.24	8000	9370		0.50	6.95	2.30	8000	13327
	250.00	3.12	1.24	8000	9123		0.75	6.95	2.30	8000	13182
	500.00	3.12	1.24	8000	8911		1.00	6.95	2.30	8000	13154
	750.00	3.12	1.24	8000	8790		2.50	6.95	2.30	8000	12847
	1000.0	3.11	1.24	8000	8258		5.00	6.95	2.30	8000	12589
	1440.0	3.11	1.24	8000	8238		7.50	6.95	2.30	8000	12520
Triaxial Compression	-	3.11	1.24	8000	8238		10.00	6.95	2.31	8000	12322
	-	3.14	1.25	8000	9294		25.00	6.95	2.31	8000	12064
	-	3.21	1.26	8000	10545		50.00	6.95	2.33	8000	11737
	-	3.24	1.27	8000	10807		75.00	6.95	2.33	8000	11591
	-	3.27	1.27	8000	11005		100.00	6.95	2.33	8000	11493
	-	3.30	1.29	8000	11150		250.00	6.96	2.34	8000	11178
	-	3.32	1.29	8000	11257		500.00	6.96	2.35	8000	10910
	-	3.38	1.31	8000	11402		750.00	6.95	2.35	8000	10071
	-	3.41	1.32	8000	11457		1000.0	6.94	2.35	8000	9985
	-	3.44	1.33	8000	11507		1304.0	6.94	2.35	8000	9900

Test: Multiple 0 kPa Stress Drop-Stress Relaxation (continued)

Initial Height [mm]	107.44	Void ratio	0.532
Initial Area [mm ²]	1058.9	Saturation Index, B	0.904
Mass [gr]	196.8	Shearing Rate [%/min]	0.416
Back Pressure [kPa]	200.0	Confining Pressure [kPa]	8000

	Time	ε_1 [%]	ε_v [%]	σ'_3	σ'_d		Time	ε_1 [%]	ε_v [%]	σ'_3	σ'_d
	[min]			[kPa]	[kPa]		[min]			[kPa]	[kPa]
Triaxial Compression	-	6.94	2.35	8000	9900	Ending Relaxation	0.01	13.88	4.05	8000	15303
	-	7.04	2.35	8000	12390		0.10	13.88	4.05	8000	15226
	-	6.91	2.28	8000	13602		0.25	13.88	4.05	8000	15102
	-	6.95	2.30	8000	13616		0.50	13.88	4.05	8000	14968
	-	6.94	2.35	8000	9900		0.75	13.88	4.05	8000	14893
	-	7.04	2.35	8000	12390		1.00	13.88	4.05	8000	14824
	-	7.09	2.37	8000	13090		2.50	13.88	4.05	8000	14517
	-	7.18	2.37	8000	13651		5.00	13.88	4.06	8000	14104
	-	7.20	2.38	8000	13711		7.50	13.88	4.07	8000	14041
	-	7.26	2.37	8000	13817		10.00	13.88	4.08	8000	13801
	-	7.32	2.39	8000	13883		25.00	13.88	4.10	8000	13629
	-	7.39	2.41	8000	13917		50.00	13.89	4.10	8000	13375
	-	7.61	2.45	8000	13994		75.00	13.89	4.11	8000	13218
	-	7.79	2.50	8000	14063		100.00	13.89	4.12	8000	13107
	-	8.27	2.63	8000	14187		190.00	13.90	4.14	8000	12825
	-	8.76	2.75	8000	14330		500.00	13.91	4.17	8000	12357
	-	9.26	2.88	8000	14453		750.00	13.91	4.17	8000	12147
	-	9.67	2.99	8000	14548		1000.0	13.91	4.17	8000	11943
	-	10.18	3.13	8000	14665		1320.0	13.88	4.17	8000	10768
	-	10.60	3.24	8000	14747						
	-	11.10	3.36	8000	14840						
	-	11.53	3.45	8000	14915						
	-	12.02	3.61	8000	15013						
	-	12.52	3.70	8000	15087						
	-	12.93	3.82	8000	15154						
	-	13.42	3.96	8000	15242						
	-	13.88	4.05	8000	15303						

Test:

Multiple 2500 kPa Stress Drop-Stress Relaxation

Initial Height [mm]	107.70	Void ratio	0.536
Initial Area [mm ²]	1055.7	Saturation Index, B	0.947
Mass [gr]	196.5	Shearing Rate [%/min]	0.416
Back Pressure [kPa]	200.0	Confining Pressure [kPa]	8000

	Time [min]	ε_1 [%]	ε_v [%]	σ'_3 [kPa]	σ'_d [kPa]		Time [min]	ε_1 [%]	ε_v [%]	σ'_3 [kPa]	σ'_d [kPa]
Isotropic Compression	-	0.00	0.00	100	-	First Relaxation	0.01	0.90	0.43	8000	3888
	-	0.03	0.35	300	-		0.10	0.90	0.45	8000	3896
	-	0.10	0.65	800	-		0.25	0.90	0.45	8000	3898
	-	0.15	0.90	1300	-		0.50	0.90	0.45	8000	3900
	-	0.19	1.09	1800	-		0.75	0.90	0.45	8000	3900
	-	0.23	1.24	2300	-		1.00	0.90	0.45	8000	3902
	-	0.26	1.38	2800	-		2.50	0.90	0.45	8000	3907
	-	0.29	1.51	3300	-		5.00	0.90	0.45	8000	3902
	-	0.32	1.62	3800	-		7.50	0.90	0.45	8000	3902
	-	0.34	1.73	4300	-		10.00	0.90	0.45	8000	3900
	-	0.37	1.82	4800	-		25.00	0.90	0.45	8000	3891
	-	0.40	1.90	5300	-		60.00	0.90	0.45	8000	3871
	-	0.43	1.99	5800	-		75.00	0.90	0.45	8000	3873
	-	0.45	2.07	6300	-		100.00	0.90	0.45	8000	3840
	-	0.48	2.15	6800	-		250.00	0.90	0.45	8000	3720
	-	0.51	2.22	7300	-		500.00	0.90	0.43	8000	3690
	-	0.53	2.28	7800	-		750.00	0.90	0.41	8000	3687
	-	0.54	2.32	8000	-		1000.0	0.90	0.40	8000	3697
	-	0.54	2.35	8000	-		1440.0	0.90	0.37	8000	3714
Triaxial Compression	-	0.00	0.00	8000	0	Triaxial Compression	-	0.90	0.37	8000	3714
	-	0.09	0.06	8000	838		-	0.93	0.37	8000	4574
	-	0.18	0.09	8000	1632		-	0.96	0.37	8000	5142
	-	0.30	0.14	8000	2520		-	0.98	0.40	8000	5655
	-	0.50	0.25	8000	3906		-	1.02	0.41	8000	6092
	-	0.79	0.38	8000	5506		-	1.05	0.42	8000	6415
	-	0.88	0.43	8000	5933		-	1.08	0.43	8000	6674
	-	0.93	0.46	8000	6157		-	1.12	0.46	8000	6870
	-	0.98	0.49	8000	6375		-	1.16	0.48	8000	7052
	-	0.90	0.43	8000	3888		-	1.22	0.49	8000	7286
							-	1.32	0.52	8000	7669
							-	1.47	0.59	8000	8152
							-	1.68	0.65	8000	8704
							-	2.19	0.86	8000	9804
							-	2.61	0.98	8000	10480
							-	2.84	1.08	8000	10801

Test: Multiple 2500 kPa Stress Drop-Stress Relaxation (continued)

Initial Height [mm]	107.70	Void ratio	0.536
Initial Area [mm ²]	1055.7	Saturation Index, B	0.947
Mass [gr]	196.5	Shearing Rate [%/min]	0.416
Back Pressure [kPa]	200.0	Confining Pressure [kPa]	8000

	Time [min]	ε_1 [%]	ε_v [%]	σ'_3 [kPa]	σ'_d [kPa]		Time [min]	ε_1 [%]	ε_v [%]	σ'_3 [kPa]	σ'_d [kPa]
Triaxial Comp.	-	3.08	1.12	8000	11072	Triaxial Compression	-	3.66	1.23	8000	11678
	-	3.12	1.15	8000	11132		-	3.78	1.27	8000	11788
	-	3.17	1.17	8000	11193		-	4.02	1.34	8000	11969
	-	3.11	1.15	8000	8666		-	4.48	1.48	8000	12266
Second Relaxation	0.01	3.11	1.15	8000	8666	Triaxial Compression	-	5.01	1.62	8000	12563
	0.10	3.11	1.15	8000	8671		-	5.42	1.74	8000	12771
	0.25	3.11	1.15	8000	8673		-	5.92	1.89	8000	13022
	0.50	3.11	1.15	8000	8675		-	6.42	2.03	8000	13232
	0.75	3.11	1.15	8000	8677		-	6.67	2.09	8000	13338
	1.00	3.11	1.15	8000	8680		-	6.81	2.12	8000	13395
	2.50	3.11	1.15	8000	8680		-	6.88	2.14	8000	13408
	5.00	3.11	1.16	8000	8679		-	6.90	2.17	8000	13412
	7.50	3.11	1.16	8000	8677		-	6.93	2.18	8000	13432
	10.00	3.11	1.15	8000	8673		-	6.96	2.18	8000	13442
	25.00	3.10	1.14	8000	8657		-	6.90	2.17	8000	10925
	50.00	3.11	1.14	8000	8632		0.01	6.90	2.17	8000	10925
	75.00	3.11	1.15	8000	8611		0.10	6.90	2.17	8000	10929
	100.0	3.11	1.15	8000	8594		0.25	6.90	2.17	8000	10931
	250.0	3.11	1.14	8000	8487		0.50	6.90	2.17	8000	10933
	500.0	3.11	1.14	8000	8161		0.75	6.90	2.17	8000	10935
	750.0	3.11	1.12	8000	8114		1.00	6.90	2.17	8000	10935
	1000.0	3.11	1.11	8000	8073	Third Relaxation	2.50	6.90	2.17	8000	10935
	1440.0	3.11	1.10	8000	7724		5.00	6.90	2.17	8000	10927
Triaxial Compression	-	3.11	1.10	8000	7724		7.50	6.90	2.17	8000	10920
	-	3.13	1.10	8000	8753		10.00	6.90	2.17	8000	10910
	-	3.16	1.10	8000	9406		25.00	6.90	2.17	8000	10861
	-	3.18	1.10	8000	9982		50.00	6.90	2.17	8000	10748
	-	3.21	1.11	8000	10427		75.00	6.90	2.17	8000	10627
	-	3.25	1.11	8000	10762		100.0	6.90	2.17	8000	10588
	-	3.28	1.12	8000	10998		250.0	6.90	2.17	8000	10411
	-	3.32	1.15	8000	11160		500.0	6.91	2.17	8000	10244
	-	3.35	1.16	8000	11270		750.0	6.91	2.17	8000	10137
	-	3.39	1.17	8000	11354		1000.0	6.91	2.15	8000	10052
	-	3.45	1.17	8000	11451		1320.0	6.90	2.15	8000	9477
	-	3.51	1.21	8000	11528						

Test: Multiple 2500 kPa Stress Drop-Stress Relaxation (continued)

Initial Height [mm]	107.70	Void ratio	0.536
Initial Area [mm ²]	1055.7	Saturation Index, B	0.947
Mass [gr]	196.5	Shearing Rate [%/min]	0.416
Back Pressure [kPa]	200.0	Confining Pressure [kPa]	8000

	Time	ε_1 [%]	ε_v [%]	σ'_3	σ'_d		Time	ε_1 [%]	ε_v [%]	σ'_3	σ'_d
	[min]			[kPa]	[kPa]		[min]			[kPa]	[kPa]
Triaxial Compression	-	6.90	2.15	8000	9477	Ending Relaxation	0.01	13.81	3.90	8000	14913
	-	6.92	2.17	8000	10514		0.10	13.82	3.90	8000	14823
	-	6.96	2.18	8000	11502		0.25	13.82	3.90	8000	14639
	-	7.00	2.18	8000	12318		0.50	13.82	3.90	8000	14326
	-	7.05	2.20	8000	12906		0.75	13.81	3.90	8000	14118
	-	7.10	2.23	8000	13253		1.00	13.81	3.90	8000	14079
	-	7.16	2.24	8000	13448		2.50	13.81	3.90	8000	14013
	-	7.22	2.24	8000	13548		5.00	13.81	3.90	8000	13649
	-	7.31	2.26	8000	13623		7.50	13.81	3.91	8000	13613
	-	7.41	2.27	8000	13672		10.00	13.81	3.91	8000	13565
	-	7.57	2.32	8000	13727		25.00	13.81	3.91	8000	13155
	-	7.80	2.37	8000	13801		50.00	13.82	3.91	8000	12981
	-	8.21	2.49	8000	13909		75.00	13.82	3.91	8000	12848
	-	8.71	2.61	8000	14034		100.00	13.82	3.92	8000	12750
	-	9.15	2.72	8000	14136		250.00	13.83	3.93	8000	12396
	-	10.10	2.97	8000	14313		500.00	13.84	3.93	8000	12108
	-	11.01	3.20	8000	14480		750.00	13.84	3.93	8000	11919
	-	12.01	3.44	8000	14628		1000.0	13.84	3.93	8000	11805
	-	12.88	3.67	8000	14788		1450.0	13.81	3.93	8000	10383
	-	13.81	3.90	8000	14913						

Test:

Multiple 5000 kPa Stress Drop-Stress Relaxation

Initial Height [mm]	107.70	Void ratio	0.532
Initial Area [mm ²]	1057.7	Saturation Index, B	0.917
Mass [gr]	197.0	Shearing Rate [%/min]	0.416
Back Pressure [kPa]	200.0	Confining Pressure [kPa]	8000

	Time [min]	ϵ_1 [%]	ϵ_v [%]	σ'_3 [kPa]	σ'_d [kPa]		Time [min]	ϵ_1 [%]	ϵ_v [%]	σ'_3 [kPa]	σ'_d [kPa]
Isotropic Compression	-	0.00	0.00	100	-	First Relaxation	0.01	0.76	0.40	8000	1449
	-	0.04	0.24	300	-		0.10	0.76	0.40	8000	1458
	-	0.12	0.64	800	-		0.25	0.76	0.40	8000	1461
	-	0.17	0.84	1300	-		0.50	0.76	0.40	8000	1470
	-	0.21	1.02	1800	-		0.75	0.76	0.40	8000	1472
	-	0.24	1.15	2300	-		1.00	0.76	0.40	8000	1472
	-	0.28	1.28	2800	-		2.50	0.76	0.40	8000	1479
	-	0.31	1.39	3300	-		5.00	0.76	0.40	8000	1481
	-	0.34	1.50	3800	-		7.50	0.76	0.40	8000	1485
	-	0.38	1.59	4300	-		10.00	0.76	0.40	8000	1485
	-	0.41	1.67	4800	-		25.00	0.76	0.40	8000	1494
	-	0.44	1.77	5300	-		50.00	0.76	0.40	8000	1506
	-	0.46	1.83	5800	-		75.00	0.76	0.40	8000	1517
	-	0.50	1.91	6300	-		100.0	0.76	0.41	8000	1526
	-	0.52	1.99	6800	-		250.0	0.76	0.42	8000	1533
	-	0.55	2.05	7300	-		500.0	0.76	0.45	8000	1519
	-	0.58	2.11	7800	-		750.0	0.76	0.46	8000	1530
	-	0.59	2.16	8000	-		1000.0	0.76	0.46	8000	1555
	-	0.59	2.17	8000	-		1450.0	0.76	0.46	8000	1564
	-	0.59	2.17	8000	-		1625.0	0.76	0.46	8000	1564
Triaxial Compression	-	0.00	0.00	8000	0	Triaxial Compression	-	0.76	0.46	8000	1564
	-	0.09	0.05	8000	813		-	0.80	0.47	8000	2536
	-	0.18	0.11	8000	1613		-	0.85	0.48	8000	3443
	-	0.27	0.15	8000	2354		-	0.89	0.49	8000	4331
	-	0.51	0.26	8000	3977		-	0.94	0.53	8000	5184
	-	0.74	0.38	8000	5317		-	0.98	0.55	8000	5508
	-	0.87	0.44	8000	6001		-	1.04	0.56	8000	6418
	-	0.93	0.47	8000	6203		-	1.09	0.58	8000	6773
	-	0.98	0.49	8000	6405		-	1.15	0.62	8000	7050
	-	0.76	0.40	8000	1449		-	1.23	0.64	8000	7373
	-	0.76	0.40	8000	1449		-	1.30	0.66	8000	7661
							-	1.46	0.72	8000	8186
							-	1.62	0.81	8000	8639
							-	2.14	0.99	8000	9790
							-	2.61	1.15	8000	10552

Test: Multiple 5000 kPa Stress Drop-Stress Relaxation (continued)

Initial Height [mm]	107.70	Void ratio	0.532
Initial Area [mm ²]	1057.7	Saturation Index, B	0.917
Mass [gr]	197.0	Shearing Rate [%/min]	0.416
Back Pressure [kPa]	200.0	Confining Pressure [kPa]	8000

	Time [min]	ε_1 [%]	ε_v [%]	σ'_3 [kPa]	σ'_d [kPa]		Time [min]	ε_1 [%]	ε_v [%]	σ'_3 [kPa]	σ'_d [kPa]
Triaxial Comp.	-	3.09	1.30	8000	11151	Triaxial Compression	-	4.48	1.76	8000	12395
	-	3.14	1.33	8000	11219		-	4.98	1.89	8000	12697
	-	3.17	1.36	8000	11255		-	5.41	2.01	8000	12918
	-	3.02	1.30	8000	6294		-	5.93	2.18	8000	13161
Second Relaxation	0.01	3.02	1.30	8000	6294	Triaxial Compression	-	6.35	2.29	8000	13327
	0.10	3.02	1.30	8000	6299		-	6.81	2.42	8000	13491
	0.25	3.02	1.30	8000	6301		-	6.86	2.43	8000	13510
	0.50	3.02	1.30	8000	6308		-	6.91	2.44	8000	13535
	0.75	3.02	1.30	8000	6310		-	6.95	2.45	8000	13540
	1.00	3.02	1.30	8000	6312		-	6.81	2.43	8000	8573
	2.50	3.02	1.30	8000	6339	Third Relaxation	0.01	6.81	2.43	8000	8573
	5.00	3.02	1.30	8000	6343		0.10	6.81	2.43	8000	8581
	7.50	3.02	1.30	8000	6345		0.25	6.81	2.43	8000	8586
	10.00	3.02	1.30	8000	6347		0.50	6.81	2.43	8000	8592
	25.00	3.02	1.31	8000	6355		0.75	6.81	2.43	8000	8596
	50.00	3.02	1.31	8000	6361		1.00	6.81	2.43	8000	8601
	75.00	3.02	1.32	8000	6369		2.50	6.81	2.43	8000	8609
	100.0	3.02	1.32	8000	6373		5.00	6.81	2.43	8000	8616
	250.0	3.02	1.32	8000	6377		7.50	6.81	2.43	8000	8618
	500.0	3.02	1.32	8000	6344		10.00	6.81	2.43	8000	8620
	750.0	3.02	1.32	8000	6325		25.00	6.81	2.44	8000	8627
	1000.0	3.02	1.32	8000	6311		50.00	6.81	2.44	8000	8625
	1450.0	3.02	1.32	8000	6250		75.00	6.81	2.44	8000	8623
Triaxial Compression	-	3.02	1.32	8000	6250		100.00	6.81	2.44	8000	8629
	-	3.04	1.33	8000	6967		250.00	6.81	2.43	8000	8566
	-	3.08	1.34	8000	8091		500.00	6.81	2.41	8000	8533
	-	3.14	1.36	8000	9501		750.00	6.81	2.41	8000	8487
	-	3.19	1.40	8000	10328		1000.0	6.81	2.39	8000	8448
	-	3.26	1.41	8000	10986		1350.0	6.81	2.37	8000	8197
	-	3.34	1.42	8000	11300						
	-	3.42	1.45	8000	11476						
	-	3.50	1.47	8000	11590						
	-	3.59	1.50	8000	11682						
	-	3.78	1.56	8000	11878						
	-	4.03	1.64	8000	12075						

Test: Multiple 5000 kPa Stress Drop-Stress Relaxation (continued)

Initial Height [mm]	107.70	Void ratio	0.532
Initial Area [mm ²]	1057.7	Saturation Index, B	0.917
Mass [gr]	197.0	Shearing Rate [%/min]	0.416
Back Pressure [kPa]	200.0	Confining Pressure [kPa]	8000

	Time	ε_1 [%]	ε_V [%]	σ'_3	σ'_d		Time	ε_1 [%]	ε_V [%]	σ'_3	σ'_d
	[min]			[kPa]	[kPa]		[min]			[kPa]	[kPa]
Triaxial Compression	-	6.81	2.37	8000	8197	Ending Relaxation	0.01	13.82	4.11	8000	15136
	-	6.85	2.37	8000	9785		0.10	13.82	4.11	8000	15037
	-	6.92	2.41	8000	11592		0.25	13.82	4.11	8000	14915
	-	7.00	2.43	8000	12811		0.50	13.82	4.11	8000	14709
	-	7.10	2.45	8000	13353		0.75	13.82	4.11	8000	14675
	-	7.20	2.47	8000	13553		1.00	13.82	4.11	8000	14616
	-	7.28	2.49	8000	13648		2.50	13.82	4.12	8000	14338
	-	7.38	2.52	8000	13689		5.00	13.82	4.12	8000	14006
	-	7.52	2.54	8000	13745		7.50	13.82	4.13	8000	13841
	-	7.75	2.62	8000	13830		10.00	13.82	4.14	8000	13719
	-	8.22	2.72	8000	13973		25.00	13.82	4.14	8000	13492
	-	8.74	2.88	8000	14130		50.00	13.83	4.16	8000	13252
	-	9.15	2.98	8000	14235		75.00	13.83	4.17	8000	13099
	-	10.08	3.23	8000	14437		100.00	13.83	4.17	8000	12985
	-	11.10	3.47	8000	14637		250.00	13.84	4.18	8000	12590
	-	12.01	3.73	8000	14813		500.00	13.85	4.20	8000	12257
	-	12.88	3.93	8000	14968		750.00	13.85	4.21	8000	12055
	-	13.70	4.07	8000	15118		1000.0	13.82	4.21	8000	10594
	-	13.82	4.11	8000	15136		1400.0	13.82	4.20	8000	10546

Test:

0 kPa Stress Drop-1 Week Stress Relaxation

Initial Height [mm]	108.20	Void ratio	0.529
Initial Area [mm ²]	1046.2	Saturation Index, B	0.929
Mass [gr]	196.2	Shearing Rate [%/min]	0.416
Back Pressure [kPa]	200.0	Confining Pressure [kPa]	8000

	Time [min]	ϵ_1 [%]	ϵ_v [%]	σ'_3 [kPa]	σ'_d [kPa]		Time [min]	ϵ_1 [%]	ϵ_v [%]	σ'_3 [kPa]	σ'_d [kPa]
Isotropic Compression	-	0.00	0.00	100	-	Relaxation	0.01	3.18	1.28	8000	11255
	-	0.02	0.27	300	-		0.10	3.18	1.27	8000	11141
	-	0.07	0.64	800	-		0.25	3.18	1.27	8000	10950
	-	0.13	0.88	1300	-		0.50	3.18	1.27	8000	10826
	-	0.17	1.06	1800	-		0.75	3.18	1.27	8000	10806
	-	0.20	1.20	2300	-		1.00	3.18	1.27	8000	10789
	-	0.23	1.32	2800	-		2.50	3.18	1.28	8000	10480
	-	0.26	1.43	3300	-		5.00	3.18	1.28	8000	10423
	-	0.28	1.53	3800	-		7.50	3.18	1.28	8000	10354
	-	0.31	1.64	4300	-		10.00	3.18	1.28	8000	10298
	-	0.34	1.72	4800	-		25.00	3.18	1.29	8000	9981
	-	0.37	1.81	5300	-		50.00	3.18	1.29	8000	9677
	-	0.39	1.89	5800	-		75.00	3.18	1.30	8000	9619
	-	0.42	1.98	6300	-		100.00	3.18	1.30	8000	9552
	-	0.45	2.06	6800	-		250.00	3.19	1.32	8000	9313
	-	0.47	2.14	7300	-		500.00	3.19	1.33	8000	9123
	-	0.50	2.22	7800	-		750.00	3.19	1.34	8000	9006
	-	0.51	2.26	8000	-		1000.0	3.20	1.34	8000	8922
	-	0.52	2.36	8000	-		1440.0	3.18	1.33	8000	8209
Triaxial Compression	-	0.00	0.00	8000	0		2500.0	3.18	1.28	8000	8201
	-	0.00	0.00	8000	32		5000.0	3.18	1.32	8000	7856
	-	0.10	0.06	8000	966		7500.0	3.18	1.29	8000	7796
	-	0.19	0.11	8000	1791		10000	3.18	1.29	8000	7720
	-	0.28	0.15	8000	2542						
	-	0.51	0.26	8000	4123						
	-	0.75	0.37	8000	5563						
	-	0.94	0.46	8000	6306						
	-	1.25	0.59	8000	7498						
	-	1.73	0.78	8000	8863						
	-	2.22	0.95	8000	9886						
	-	2.62	1.08	8000	10535						
	-	3.09	1.23	8000	11137						
	-	3.13	1.25	8000	11190						
	-	3.18	1.28	8000	11255						

Test:

2500 kPa Stress Drop-1 Week Stress Relaxation

Initial Height [mm]	107.70	Void ratio	0.529
Initial Area [mm ²]	1053.8	Saturation Index, B	0.951
Mass [gr]	196.7	Shearing Rate [%/min]	0.416
Back Pressure [kPa]	200.0	Confining Pressure [kPa]	8000

	Time [min]	ε_1 [%]	ε_v [%]	σ'_3 [kPa]	σ'_d [kPa]		Time [min]	ε_1 [%]	ε_v [%]	σ'_3 [kPa]	σ'_d [kPa]
Isotropic Compression	-	0.00	0.00	100	-	Relaxation	0.01	3.14	1.27	8000	8776
	-	0.04	0.30	300	-		0.10	3.14	1.27	8000	8780
	-	0.11	0.72	800	-		0.25	3.14	1.27	8000	8782
	-	0.17	0.97	1300	-		0.50	3.14	1.27	8000	8785
	-	0.21	1.15	1800	-		0.75	3.14	1.27	8000	8785
	-	0.25	1.28	2300	-		1.00	3.14	1.27	8000	8787
	-	0.29	1.40	2800	-		2.50	3.14	1.27	8000	8785
	-	0.33	1.52	3300	-		5.00	3.14	1.27	8000	8813
	-	0.36	1.63	3800	-		7.50	3.14	1.27	8000	8818
	-	0.40	1.74	4300	-		10.00	3.14	1.27	8000	8804
	-	0.42	1.82	4800	-		25.00	3.14	1.27	8000	8765
	-	0.45	1.91	5300	-		50.00	3.14	1.27	8000	8747
	-	0.48	1.99	5800	-		75.00	3.14	1.28	8000	8724
	-	0.51	2.07	6300	-		100.00	3.14	1.28	8000	8669
	-	0.53	2.16	6800	-		250.00	3.14	1.28	8000	8574
	-	0.56	2.22	7300	-		500.00	3.14	1.28	8000	8451
	-	0.58	2.30	7800	-		750.00	3.14	1.29	8000	8383
	-	0.60	2.33	8000	-		1000.0	3.14	1.29	8000	8301
	-	0.60	2.37	8000	-		1500.0	3.14	1.29	8000	7945
Triaxial Compression	-	0.00	0.00	8000	0		2500.0	3.14	1.30	8000	7884
	-	0.07	0.02	8000	648		5000.0	3.14	1.33	8000	7672
	-	0.17	0.08	8000	1415		7500.0	3.14	1.33	8000	7549
	-	0.26	0.14	8000	2151		10000	3.14	1.33	8000	7403
	-	0.49	0.25	8000	3731		11220	3.14	1.33	8000	7249
	-	0.73	0.36	8000	5048						
	-	0.96	0.46	8000	6130						
	-	1.20	0.55	8000	7049						
	-	1.67	0.74	8000	8499						
	-	2.13	0.91	8000	9551						
	-	2.60	1.06	8000	10370						
	-	2.83	1.12	8000	10694						
	-	3.07	1.21	8000	11069						
	-	3.12	1.23	8000	11137						
	-	3.17	1.20	8000	11198						
	-	3.21	1.28	8000	11259						
	-	3.14	1.27	8000	8776						

Test:

5000 kPa Stress Drop-1 Week Stress Relaxation

Initial Height [mm]	107.19	Void ratio	0.532
Initial Area [mm ²]	1066.2	Saturation Index, B	0.949
Mass [gr]	197.7	Shearing Rate [%/min]	0.416
Back Pressure [kPa]	200.0	Confining Pressure [kPa]	8000

	Time [min]	ε_1 [%]	ε_v [%]	σ'_3 [kPa]	σ'_d [kPa]		Time [min]	ε_1 [%]	ε_v [%]	σ'_3 [kPa]	σ'_d [kPa]
Isotropic Compression	-	0.00	0.00	100	-	Relaxation	0.01	3.12	1.27	8000	6278
	-	0.04	0.39	300	-		0.10	3.12	1.27	8000	6284
	-	0.09	0.84	800	-		0.25	3.12	1.27	8000	6288
	-	0.13	1.11	1300	-		0.50	3.12	1.27	8000	6295
	-	0.17	1.33	1800	-		0.75	3.12	1.27	8000	6297
	-	0.20	1.48	2300	-		1.00	3.12	1.27	8000	6299
	-	0.23	1.62	2800	-		2.50	3.12	1.27	8000	6313
	-	0.26	1.75	3300	-		5.00	3.12	1.27	8000	6319
	-	0.29	1.86	3800	-		7.50	3.12	1.27	8000	6324
	-	0.32	1.97	4300	-		10.00	3.12	1.27	8000	6323
	-	0.35	2.07	4800	-		25.00	3.12	1.28	8000	6311
	-	0.37	2.16	5300	-		50.00	3.12	1.29	8000	6305
	-	0.40	2.26	5800	-		75.00	3.12	1.29	8000	6305
	-	0.42	2.33	6300	-		100.00	3.12	1.29	8000	6304
	-	0.45	2.42	6800	-		250.00	3.12	1.31	8000	6290
	-	0.48	2.50	7300	-		500.00	3.12	1.35	8000	6234
	-	0.50	2.58	7800	-		750.00	3.12	1.37	8000	6220
	-	0.51	2.62	8000	-		1000.0	3.12	1.39	8000	6211
	-	0.51	2.66	8000	-		1450.0	3.12	1.39	8000	6196
Triaxial Compression	-	0.00	0.00	8000	0		2500.0	3.12	1.39	8000	6128
	-	0.09	0.07	8000	759		5000.0	3.12	1.39	8000	6112
	-	0.19	0.10	8000	1600		7500.0	3.12	1.39	8000	6036
	-	0.30	0.16	8000	2420		10050	3.12	1.39	8000	6003
	-	0.51	0.25	8000	3920						
	-	0.74	0.35	8000	5172						
	-	0.97	0.45	8000	6255						
	-	1.21	0.56	8000	7189						
	-	1.34	0.60	8000	7652						
	-	1.68	0.75	8000	8657						
	-	2.17	0.93	8000	9720						
	-	2.67	1.09	8000	10502						
	-	3.07	1.22	8000	11022						
	-	3.17	1.25	8000	11136						
	-	3.31	1.30	8000	11281						
	-	3.12	1.27	8000	6278						

Appendix B: Sieving Data for Tests Presented

Tests Presented in Chapter 4

Sieve No.	Sieve Opening Size [mm]	Finer Than [%]			
		Test			
		Confining Pressure=25 kPa	Confining Pressure=50 kPa	Confining Pressure=250 kPa	Confining Pressure=500 kPa
20	0.850	100.00	100.00	100.00	100.00
40	0.425	1.21	1.54	0.86	1.82
60	0.250	0.28	0.33	0.24	0.66
80	0.180	0.17	0.19	0.16	0.43
100	0.150	0.09	0.11	0.13	0.34
200	0.075	0.00	0.01	0.06	0.15
Pan	-----	0.00	0.00	0.00	0.00

Sieve No.	Sieve Opening Size [mm]	Finer Than [%]			
		Test			
		Confining Pressure=1000 kPa	Confining Pressure=2000 kPa	Confining Pressure=4000 kPa	Confining Pressure=8000 kPa
20	0.850	100.00	100.00	100.00	100.00
40	0.425	5.46	15.59	24.45	45.87
60	0.250	2.28	7.03	11.64	25.55
80	0.180	1.50	4.65	7.92	18.38
100	0.150	1.21	3.88	6.64	15.37
200	0.075	0.52	1.79	3.25	7.17
Pan	-----	0.00	0.00	0.00	0.00

Sieve No.	Sieve Opening [mm]	Finer Than [%]			
		Test			
		Confining Pressure=12000 kPa	Confining Pressure=14000 kPa	Strain Rate=0.00260 %/min, $\sigma'_3=250$ kPa	Strain Rate=0.0416 %/min, $\sigma'_3=250$ kPa
20	0.850	100.00	100.00	100.00	100.00
40	0.425	53.57	59.62	0.94	0.86
60	0.250	33.66	37.79	0.27	0.24
80	0.180	24.02	28.40	0.18	0.16
100	0.150	20.93	25.18	0.15	0.13
200	0.075	10.07	14.06	0.07	0.06
Pan	-----	0.00	0.00	0.00	0.00

Sieve No.	Sieve Opening [mm]	Finer Than [%]			
		Test			
		Strain Rate=0.666 %/min, $\sigma'_3=250$ kPa	Strain Rate=0.00260 %/min, $\sigma'_3=8000$ kPa	Strain Rate=0.0416 %/min, $\sigma'_3=8000$ kPa	Strain Rate=0.666 %/min, $\sigma'_3=8000$ kPa
20	0.850	100.00	100.00	100.00	100.00
40	0.425	1.87	46.40	45.87	43.96
60	0.250	0.53	26.04	25.55	24.03
80	0.180	0.31	18.92	18.38	16.97
100	0.150	0.20	15.83	15.37	14.39
200	0.075	0.03	7.87	7.17	6.66
Pan	-----	0.00	0.00	0.00	0.00

Sieve No.	Sieve Opening [mm]	Finer Than [%]			
		Test			
		Isotropically Aged for 0 Minutes	Isotropically Aged for 45 Minutes	Isotropically Aged for 1440 Minutes	Isotropically Aged for 10080 Minutes
20	0.850	100.00	100.00	100.00	100.00
40	0.425	47.14	45.87	44.95	44.79
60	0.250	26.73	25.55	25.62	25.51
80	0.180	19.26	18.38	18.35	18.38
100	0.150	16.80	15.37	16.11	16.02
200	0.075	8.21	7.17	7.80	7.85
Pan	-----	0.00	0.00	0.00	0.00

Sieve No.	Sieve Opening [mm]	Finer Than [%]			
		Test			
		K_0 Condition-Aged for 0 Minutes	K_0 Condition-Aged for 45 Minutes	K_0 Condition-Aged for 1440 Minutes	K_0 Condition-Aged for 10080 Minutes
20	0.850	100.00	100.00	100.00	100.00
40	0.425	41.96	46.52	44.19	46.48
60	0.250	24.26	26.95	25.73	27.20
80	0.180	17.49	19.34	18.50	19.68
100	0.150	15.55	17.15	16.28	17.46
200	0.075	7.78	8.48	8.02	8.65
Pan	-----	0.00	0.00	0.00	0.00

Tests Presented in Chapter 5

Sieve No.	Sieve Opening [mm]	Finer Than [%]			
		Test			
		[^] Strain Rate=0.00260 %/min- σ'_3 =8000 kPa	[^] Strain Rate=0.0416 %/min- σ'_3 =8000 kPa	[^] Strain Rate=0.666 %/min- σ'_3 =8000 kPa	[^] Strain Rate=0.00260 %/min- σ'_3 =250 kPa
20	0.850	100.00	100.00	100.00	100.00
40	0.425	16.84	20.95	25.36	0.39
60	0.250	6.15	8.22	10.82	0.10
80	0.180	3.62	4.93	6.73	0.07
100	0.150	2.87	3.95	5.49	0.04
200	0.075	1.11	1.55	2.35	0.01
Pan	-----	0.00	0.00	0.00	0.00

Sieve No.	Sieve Opening [mm]	Finer Than [%]			
		Test			
		[^] Strain Rate=0.0416 %/min- σ'_3 =250 kPa	[^] Strain Rate=0.666 %/min- σ'_3 =250 kPa	Type I	Type II
20	0.850	100.00	100.00	100.00	100.00
40	0.425	0.82	0.35	3.49	37.49
60	0.250	0.06	0.04	1.15	18.04
80	0.180	0.04	0.01	0.64	11.04
100	0.150	0.03	0.01	0.48	8.41
200	0.075	0.02	0.01	0.17	3.24
Pan	-----	0.00	0.00	0.00	0.00

Sieve No.	Sieve Opening [mm]	Finer Than [%]			
		Test			
		Type III	Type IV	Type V	Type VI
20	0.850	100.00	100.00	100.00	100.00
40	0.425	61.04	75.43	81.89	86.40
60	0.250	41.69	60.27	69.60	77.21
80	0.180	32.42	52.20	62.73	71.87
100	0.150	28.78	48.92	60.00	69.72
200	0.075	17.05	34.72	47.22	62.92
Pan	-----	0.00	0.00	0.00	0.00

Sieve No.	Sieve Opening [mm]	Finer Than [%]			
		Test			
		C1	C2	C3	C4
20	0.850	100.00	100.00	100.00	100.00
40	0.425	1.22	3.49	8.26	11.19
60	0.250	0.38	1.15	2.91	4.13
80	0.180	0.22	0.64	1.66	2.36
100	0.150	0.16	0.48	1.27	1.80
200	0.075	0.06	0.17	0.46	0.69
Pan	-----	0.00	0.00	0.00	0.00

Sieve No.	Sieve Opening [mm]	Finer Than [%]			
		Test			
		C5	C6	C7	Multiple 1-Day Creep
20	0.850	100.00	100.00	100.00	100.00
40	0.425	16.00	28.88	31.97	37.68
60	0.250	6.10	12.94	15.05	18.88
80	0.180	3.59	8.32	10.05	12.81
100	0.150	2.86	6.81	8.33	10.62
200	0.075	1.10	3.01	3.72	5.07
Pan	-----	0.00	0.00	0.00	0.00

Sieve No.	Sieve Opening [mm]	Finer Than [%]			
		Test			
		2-Month Creep			
20	0.850	100.00			
40	0.425	31.11			
60	0.250	14.45			
80	0.180	9.15			
100	0.150	7.45			
200	0.075	3.10			
Pan	-----	0.00			

Tests Presented in Chapter 6

Sieve No.	Sieve Opening [mm]	Finer Than [%]			
		Test			
		Strain Rate=0.00260 %/min-Without Correction	Strain Rate=0.0416 %/min-Without Correction	Strain Rate=0.666 %/min-Without Correction	Strain Rate=0.00260 %/min-With Correction
20	0.850	100.00	100.00	100.00	100.00
40	0.425	11.13	9.69	11.04	10.71
60	0.250	3.73	3.26	3.57	3.67
80	0.180	2.12	1.87	1.99	2.06
100	0.150	1.67	1.45	1.55	1.59
200	0.075	0.59	0.54	0.54	0.60
Pan	-----	0.00	0.00	0.00	0.00

Sieve No.	Sieve Opening [mm]	Finer Than [%]			
		Test			
		Strain Rate=0.0416 %/min-With Correction	Strain Rate=0.666 %/min-With Correction	Strain Rate=0.00260 %/min-Undrained With Correction	Strain Rate=0.0416 %/min-Undrained With Correction
20	0.850	100.00	100.00	100.00	100.00
40	0.425	10.33	9.89	11.82	10.04
60	0.250	3.48	3.37	4.54	3.73
80	0.180	1.94	1.90	2.53	1.98
100	0.150	1.51	1.48	1.96	1.47
200	0.075	0.59	0.57	0.70	0.40
Pan	-----	0.00	0.00	0.00	0.00

Sieve No.	Sieve Opening [mm]	Finer Than [%]			
		Test			
		Strain Rate=0.666 %/min-Undrained With Correction	Strain Rate=0.00260 %/min- $\sigma'_3=250$ kPa	Strain Rate=0.0416 %/min- $\sigma'_3=250$ kPa	Strain Rate=0.666 %/min- $\sigma'_3=250$ kPa
20	0.850	100.00	100.00	100.00	100.00
40	0.425	9.57	0.48	0.26	0.47
60	0.250	3.60	0.06	0.06	0.05
80	0.180	1.97	0.04	0.04	0.03
100	0.150	1.59	0.03	0.03	0.02
200	0.075	0.54	0.02	0.03	0.00
Pan	-----	0.00	0.00	0.00	0.00

Sieve No.	Sieve Opening [mm]	Finer Than [%]			
		Test			
		R1	R2	R3	R4
20	0.850	100.00	100.00	100.00	100.00
40	0.425	1.26	2.68	10.33	24.00
60	0.250	0.34	0.83	3.48	10.83
80	0.180	0.20	0.45	1.94	6.49
100	0.150	0.15	0.34	1.51	5.37
200	0.075	0.06	0.12	0.59	2.30
Pan	-----	0.00	0.00	0.00	0.00

Sieve No.	Sieve Opening [mm]	Finer Than [%]			
		Test			
		R5	R6	Multiple 1-Day Stress Relaxation	2-Month Stress Relaxation
20	0.850	100.00	100.00	100.00	100.00
40	0.425	37.06	37.68	37.74	20.11
60	0.250	18.53	18.88	18.85	7.77
80	0.180	12.78	12.81	12.60	4.62
100	0.150	10.77	10.62	10.47	3.63
200	0.075	5.04	5.07	5.05	1.35
Pan	-----	0.00	0.00	0.00	0.00

Tests Presented in Chapter 7

Sieve No.	Sieve Opening [mm]	Finer Than [%]			
		Test			
		3 Hours Creep-1 Week Stress Relaxation	1 Day Creep-1 Week Stress Relaxation	1 Week Creep-1 Week Stress Relaxation	3 Hours Stress Relaxation-1 Week Creep
20	0.850	100.00	100.00	100.00	100.00
40	0.425	13.61	16.00	19.33	11.41
60	0.250	5.00	6.10	7.58	4.02
80	0.180	2.79	3.59	4.57	2.25
100	0.150	2.16	2.86	3.68	1.76
200	0.075	0.81	1.10	1.47	0.68
Pan	-----	0.00	0.00	0.00	0.00

Sieve No.	Sieve Opening [mm]	Finer Than [%]			
		Test			
		1 Day Stress Relaxation-1 Week Creep	1 Week Stress Relaxation-1 Week Creep	Multiple 1-Day Creep-Stress Relaxation	^100% Creep
20	0.850	100.00	100.00	100.00	100.00
40	0.425	11.22	11.07	35.30	19.33
60	0.250	3.92	3.95	17.55	7.58
80	0.180	2.20	2.23	11.75	4.57
100	0.150	1.73	1.72	9.79	3.68
200	0.075	0.66	0.66	4.66	1.47
Pan	-----	0.00	0.00	0.00	0.00

Sieve No.	Sieve Opening [mm]	Finer Than [%]			
		Test			
		Creep-Stress Relaxation 1	Creep-Stress Relaxation 2	Creep-Stress Relaxation 3	100% Stress Relaxation
20	0.850	100.00	100.00	100.00	100.00
40	0.425	13.23	12.12	11.08	11.07
60	0.250	5.21	4.63	4.20	3.95
80	0.180	2.93	2.56	2.26	2.23
100	0.150	2.40	2.04	1.71	1.72
200	0.075	0.85	0.67	0.54	0.66
Pan	-----	0.00	0.00	0.00	0.00

Tests Presented in Chapter 8

Sieve No.	Sieve Opening [mm]	Finer Than [%]			
		Test			
		Multiple 0 kPa Stress Drop-Creep	Multiple 2500 kPa Stress Drop-Creep	Multiple 5000 kPa Stress Drop-Creep	0 kPa Stress Drop-1 Week Creep
20	0.850	100.00	100.00	100.00	100.00
40	0.425	37.68	37.33	38.16	19.33
60	0.250	18.88	18.54	18.89	7.58
80	0.180	12.81	12.41	12.53	4.57
100	0.150	10.62	10.32	10.48	3.68
200	0.075	5.07	4.96	5.04	1.47
Pan	-----	0.00	0.00	0.00	0.00

Sieve No.	Sieve Opening [mm]	Finer Than [%]			
		Test			
		2500 kPa Stress Drop-1 Week Creep	5000 kPa Stress Drop-1 Week Creep	Multiple 0 kPa Stress Drop-Stress Relaxation	Multiple 2500 kPa Stress Drop-Stress Relaxation
20	0.850	100.00	100.00	100.00	100.00
40	0.425	10.76	9.88	37.74	37.33
60	0.250	3.82	3.46	18.85	18.49
80	0.180	2.10	1.91	12.60	12.33
100	0.150	1.63	1.50	10.47	10.30
200	0.075	0.60	0.50	5.05	4.91
Pan	-----	0.00	0.00	0.00	0.00

Sieve No.	Sieve Opening [mm]	Finer Than [%]			
		Test			
		Multiple 5000 kPa Stress Drop-Stress Relaxation	0 kPa Stress Drop-1 Week Stress Relaxation	2500 kPa Stress Drop-1 Week Stress Relaxation	5000 kPa Stress Drop-1 Week Stress Relaxation
20	0.850	100.00	100.00	100.00	100.00
40	0.425	37.51	11.07	10.20	9.74
60	0.250	18.66	3.95	3.61	3.31
80	0.180	12.39	2.23	2.01	1.75
100	0.150	10.35	1.72	1.54	1.35
200	0.075	4.97	0.66	0.56	0.36
Pan	-----	0.00	0.00	0.00	0.00

Bibliography

- Abrantes, A.E., and Yamamuro, J.A. (2002): Experimental and data analysis techniques used for high strain rate tests on cohesionless soil, *Geotechnical Testing Journal*, 25(2), 128-141.
- Adachi, T., and Okano, M. (1974): A constitutive equation for normally consolidated clay, *Soils and Foundations*, 14(4), 55-73.
- Adachi, T., and Oka, F. (1982a): Constitutive equations for normally consolidated clay based on elasto-viscoplasticity, *Soils and Foundations*, 22(4), 57-70.
- Adachi, T., and Oka, F. (1982b): Constitutive equations for normally consolidated clays and assigned works for clay, *Results of the International Workshop on Constitutive Relations for Soils*, Grenoble, G. Gudehus et al., eds., 123-140.
- Adachi, T., Oka, F., and Mimura, M. (1987): Mathematical structure of an overstress elasto-viscoplastic model for clay, *Soils and Foundations*, 27(3), 31-42.
- Adachi, T., Oka, F., and Mimura, M. (1996): State of the art: Modeling aspects associated with time dependent behavior of soils, *Measuring and modeling time dependent soil behavior*, Geotechnical Special Publication No. 61, T.C. Sheahan and V.N. Kaliakin, eds. ASCE, New York, 61-95.
- Akai, K., Adachi, T., and Nishi, K. (1977): Mechanical properties of soft rocks, *Proceedings, 9th International Conference, Soil Mechanics and Foundation Engineering*, Tokyo, 1, 7-10.

- Al-Sanad, H.A. and Ismael, N.F. (1996): Effects of Aging on Freshly Deposited or Densified Calcareous Sands, Transportation Research Record 1547, 76-81.
- Allen, W.A., Mayfield, E.B., and Morrison, H.L. (1957): Dynamics of a projectile penetrating sand, Journal of Applied Physics, 28(3), 370-376.
- Anh Dan, L. Tatsuoka, F., and Koseki, J. (2006): Viscous effects on the stress-strain behavior of gravelly soil in drained triaxial compression, Geotechnical Testing Journal, 29(4), 330-340.
- Ashby, M.F. and Jones, D.R.H. (1986): Engineering materials 2, an introduction to microstructures, processing and design, Oxford: Pergamon.
- Augustesen, A., Liingaard, M. and Lade, P.V. (2004): Evaluation of time dependent behavior of soils, International Journal of Geomechanics, ASCE, 4(3), 137-156.
- Baker, T.C. and Preston, F.W. (1946a): Fatigue of glass under static loads, Journal of Applied Physics, 17, 170-178.
- Baker, T.C. and Preston, F.W. (1946b): The effect of water on the strength of glass, Journal of Applied Physics, 17, 179-188.
- Bishop, A.W., and Eldin, A.K.G. (1953): The effect of stress history on the relation between ϕ and porosity in sand, Proceedings, 3rd International Conference on Soil Mechanics and Foundation Engineering, Zurich, 1, 100-105.
- Baxter, C. D. P, and Mitchell, J. K. (2004): Experimental study on the aging of sands, Journal of Geotechnical Engineering, 130(10), 1051-1062.
- Been, K. and Jefferies, M.G. (1985): A state parameter for sands, Géotechnique 35(2), 99-112.

- Bishop, A.W. (1954): Correspondence on shear characteristics of a saturated silt measured in triaxial compression, *Géotechnique*, 4, 43-45.
- Bjerrum, L. (1967): Engineering geology of Norwegian normally consolidated marine clays as related to the settlements of buildings, *Géotechnique*, 17(2), 83-119.
- Bjerrum, L. (1973): Problems of soil mechanics and construction on soft clays and structurally unstable soils, *Proceedings, 8th International Conference, Soil Mechanics and Foundation Engineering, Moscow*, 13, 111-159.
- Blackwelder, E. (1923): The origin of central Kansas oil domes, *Bulletin, American Association of Petroleum Geologists*, 4, 89-94.
- Bolton, M. D., Nakata, Y., and Cheng, Y. P. (2008): Micro- and macromechanical behaviour of DEM crushable materials, *Géotechnique*, 58(6), 471-480.
- Borm, G., and Haupt, M. (1988): Constitutive behavior of rock salt: Power-law or hyperbolic sine creep?, *6th International Conference on Numerical Methods in Geomechanics*, G. Swoboda, ed., Balkema, Rotterdam, The Netherlands, 1883-1893.
- Botset, H.G., and Reed, B.W. (1935): Experiment on compressibility of sand, *Bull. Am. Soc. Pet. Geol.*, 19, 1053-1061.
- Bowman, E.T. (2002): The ageing and creep of dense granular materials, *Ph.D. Thesis*, University of Cambridge, Cambridge, UK.
- Bowman, E. T. and Soga, K. (2003): Creep, ageing and microstructural change in dense granular materials, *Soils and Foundations*, 43(4), 107-117.
- Bowman, E.T. and Soga, K. (2005): Mechanisms of setup of displacement piles in sand, laboratory creep tests, *Canadian Geotechnical Journal*, 42(5), 1391-1407.

- Buisman, A.S. (1936): Results of long duration settlement tests, Proceedings, 1st International Conference on Soil Mechanics and Foundation Engineering, Cambridge, Mass., 1, 103-107.
- Callister, W.D., Jr. (2005): Materials Science and Engineering, Wiley.
- Casagrande, A. and Shannon, W.L. (1948): Strength of soils under dynamic loads, Proceedings, ASCE, 74(4), 591-632.
- Caudle, W.N., Pope, A.Y., McNeill, R.L., and Margason, B.E. (1967): The feasibility of rapid soil investigations using high-speed, earth-penetrating projectiles, Proceedings, International Symposium on Wave Propagation and Dynamic Properties of Earth Materials, University of New Mexico Press, Albuquerque, N.M., 945-955.
- Charles, R.J. (1958a): Static fatigue of glass: I, Journal of Applied Physics, 29, 1549-1553.
- Charles, R.J. (1958b): Static fatigue of glass: II, Journal of Applied Physics, 29, 1554-1560.
- Charles R. J. (1959): The strength of the silicate glasses and some crystalline oxides, Proceedings, International Conference on Fracture, 225-249.
- Charles, R.J. (1961): In progress in Ceramic Science, Edited by J. E. Burke. Pergamon Press, New York, 1, 1-38.
- Charlie, W.A., Rwebyogo, M.F. and Doehring, D.O. (1992): Time-dependent cone penetration resistance due to blasting, Journal of Geotechnical Engineering, ASCE, 118(8), 1200-1215.

- Chow, F.C., Jardine, R.J., Brucy, F. and Nauroy, J.F. (1997): Time related increases the shaft capacities of driven piles in sand, *Géotechnique*, 47(2), 353-361.
- Chow, F.C., Jardine, R.J., Brucy, F., and Nauroy, J.F. (1998): Effects of time on capacity of pipe piles in dense marine sand, *Journal of Geotechnical and Geoenvironmental Engineering*, ASCE, 124(3), 254-264.
- Colliat-Dangus, J.L., Desrues, J. and Foray, P. (1988): Triaxial testing of granular soil under elevated cell pressure, *Advanced triaxial testing of soil and rock*, ASTM, edited by Donaghe et al., Philadelphia, 290-310.
- Coop, M.R., Sorensen, K.K., Bodas Freitas, T. and Georgoutsos, G. (2004): Particle Breakage during Shearing of a Carbonate Sand, *Géotechnique* 54(3), 157-163.
- Coop, M.R. and Lee, I.K. (1993): The behaviour of granular soils at elevated stresses, In *Predictive soil mechanics*, Proceedings of the C.P. Wroth Memorial Symposium, 186-198. London, Thomas Telford.
- Crawford, C. B; Morrison, K I. (1996): Case histories illustrate the importance of secondary-type consolidation settlements in the Fraser River delta, *Canadian Geotechnical Journal*, 33(6), 866-878.
- Cruden, D.M. (1974): The static fatigue of brittle rock under uniaxial compression, *International Journal of Rock Mechanics and Mining Sciences and Geomechanics Abstracts*, Pergamon Press, 11, 67-73.
- Dafalias, Y.F. (1986): Bounding surface plasticity. I: Mathematical foundation and hypoplasticity, *Journal of Engineering Mechanics*, ASCE, 112(9), 966-987.

- Daouadji, A. and Hicher, P.Y. (2010): An enhanced constitutive model for crushable granular materials, *International Journal of Numerical and Analytical Methods in Geomechanics*, 34, 555-580.
- Daramola, O. (1980): Effect of consolidation age on stiffness of sand, *Géotechnique*, 30(20), 213-216.
- de Souza, J.M. (1958): Compressibility of sand at high pressure, MS thesis, Massachusetts Institute of Technology, Cambridge, Mass., 63-64.
- DeBeer, E. E. (1963): The scale effect in the transposition of the results of deep sounding tests on the ultimate bearing capacity of piles and caisson foundations, *Géotechnique*, London, England, 13(1), 39-75.
- Denisov, N.Y. and Reltov, B.Y. (1961): The influence of certain processes on the strength of soils, *Proceedings, International Conference, Soil Mechanics and Foundation Engineering*, Paris, 1, 75-78.
- Desai, C.S., and Zhang, D. (1987): Viscoplastic model for geological materials with generalized flow rule, *International Journal of Numerical and Analytical Methods in Geomechanics*, 11, 603-620.
- di Benedetto, H., Tatsuoka, F., Lo Presti, D., Sauzéat, C. and Geoffroy, H. (2005): Time effects on the behaviour of geomaterials, Keynote Lecture, *Proceedings 3rd International Symposium on Deformation Characteristics of Geomaterials*, IS Lyon (Di Benedetto et al. eds), Balkema, September, 2003, 2, 59-123.
- di Prisco, C., and Imposimato, S. (1996): Time dependent mechanical behaviour of loose sands, *Mechanics of Cohesive-Frictional Materials*, 1(1), 45-73.

- di Prisco, C., Imposimato, S., and Vardoulakis, I. (2000): Mechanical modelling of drained creep triaxial tests on loose sand, *Géotechnique*, 50(1), 73-82.
- Dowding, C.H., and Hryciw, R.D. (1986): A laboratory study of blast densification of saturated sand, *Journal of Geotechnical Engineering, ASCE*, 112(2), 187-199.
- Dragon, A., and Mroz, Z. (1979): A model for plastic creep of rock-like materials accounting for the kinetics of fracture. *International Journal of Rock Mechanics and Mining Sciences and Geomechanics Abstracts*, 16, 253-259.
- Drescher, A., and De Josselin De Jong, G. (1972): Photoelastic verification of a mechanical model for the flow of a granular material, *Journal of the Mechanics and Physics of Solids*, 20, 337-351.
- Enomoto, T., Tatsuoka, F., Shishime, M., Kawabe, S. and Di Benedetto, H. (2007a): Viscous property of granular material in drained triaxial compression, *Soil Stress-Strain Behavior: Measurement, Modeling and Analysis, Proceedings, Geotechnical Symposium in March 16-17, 2006 (Ling et al, eds)*, 383-397.
- Enomoto, T., Kawabe, S. and Tatsuoka, F. (2007b): Viscosity of round granular materials in drained triaxial compression, *Proceedings of 13th Asian Regional Conference on Geotechnical Engineering and Soil Mechanics, Kolkata*, 19-22.
- Evans, A.G. and Johnson, H. (1975): The fracture and its dependence on slow crack growth, *Journal of Materials Science*, 10, 214-222.
- Feda, J. (1992): *Creep of soils and related phenomena, Developments in Geotechnical Engineering*, Elsevier Science, North-Holland, Amsterdam, The Netherlands, 68.

- Fischer-Cripps, A.C. (1997): Predicting Hertzian fracture, *Journal of material science*, 32, 1277-1285.
- Fukumoto, T. (1992): Particle breakage characteristics of granular soils, *Soils and Foundations*, 32(1), 26-40.
- Fuller, W and Thompson, S. E, (1907): The laws of proportioning concrete, *Transactions of the ASCE*. Paper no 1053, 67-143.
- Garlanger, J. E. (1972): The consolidation of soils exhibiting creep under constant effective stress, *Géotechnique*, 22(1), 71-78.
- Glathart, J.L. and Preston, F.W. (1946): The fatigue modulus of glass, *Journal of Applied Physics*, 17, 189-195.
- Gong, J. and Du, C. (2000): Environmental effects on the room-temperature static fatigue behavior of polycrystalline mullite, *Material Science and Engineering*, A283, 76-81.
- Griffith, A. A. (1924): Theory of rupture, 1st International Congress of Applied Mechanics, Delft, 55-63.
- Griggs, D.T., Turner, F.J., and Heard H.C. (1960): Deformation of rocks at 500° to 800°C, *Geology Society of America Memoir*, 79, 39-104.
- Gurney, C. and Pearson, S. (1949): The effect of the surrounding atmosphere on the delayed fracture of glass, *Proceedings of the Physical Society-Section B*, 62 469-476.
- Hagerty, M.M., Hite, D.R., Ullrich, C.R. and Hagerty, D.J. (1993): One-dimensional compression of granular media, *Journal of Geotechnical Engineering*, 119(1), 1-18.

- Hall, E.B., and Gordon, B.B. (1963): Triaxial testing with large-scale high pressure equipment, laboratory shear testing of soils, Special Tech. Publication No. 361, ASTM, Philadelphia, Pa. 315-328.
- Ham, T.G., Nakata, Orense, R., Hyodo, M. (2010): Influence of water on the compression behavior of decomposed granite soil, *Journal of Geotechnical and Geoenvironmental Engineering*, 136(5), 697-705.
- Hammond, M.L. and Ravits, S.F. (1963): Influence of environment on brittle fracture of silica, *Journal of the American Ceramic Society*, 46(7), 329-332.
- Hannink, G. (1994): Settlement of high-rise buildings in Rotterdam, *Proceedings, 13th International Conference on Soil Mechanics and Foundation Engineering*, New Delhi, 2, 44 1-444.
- Hardin, B.O. (1985): Crushing of soil particles, *Journal of Geotechnical Engineering*, ASCE, 111(10), 1177-1192.
- Harremoes, P. (1959): Compressibility of ground sand at high pressures, MS thesis, Massachusetts Institute of Technology, Cambridge, Mass.
- Hayano, K., Matsumoto, M., Tatsuoka, F. and Koseki, J. (2001): Evaluation of time-dependent deformation property of sedimentary soft rock and its constitutive modelling, *Soils and Foundations*, 41(2), 21-38.
- Hazen, A. (1911): Discussion of dams on sand foundations, by A. C. Koenig, *Trans.*, ASCE, New York, N.Y., 73.
- Hendron, A. J. (1963): The behavior of sand in one-dimensional compression, PhD Thesis, University of Illinois, Urbana, Ill.

- Henrych, J. (1979): The dynamics of explosion and its use, Elsevier, Amsterdam, The Netherlands, 205.
- Holestol, K., Kjaernsli, B. and Torblaa, I. (1965): Compression of tunnel spoil at Venemo Dam, Proceedings, 6th international Conference on Soil Mechanics and Foundation Engrg., Montreal, Canada, 2, 490-494.
- Huneault, P.A. (1992): Strain-hardening relaxation. Journal of Applied Mechanics, 59, 217-219.
- Hunsche, U. (1988): Measurements of creep in rock salt at small strain rates, The Mechanical Behavior of Salt, Proceedings, 2nd Conference, E. R. Hardy Jr. and M. Langer, eds., Trans Tech Publications, Clausthal- Zellerfeld, Germany, 187–196.
- Jaeger, J.C. and Cook, N.G.W. (1969): Fundamentals of rock mechanics, Methuen and Co. Ltd., London.
- Joshi, R.C., Achari, A., Kaniraj, SR., and Wijeweera, H. (1995): Effect of aging on the penetration resistance of sands, Canadian Geotechnical Journal, 32(5), 767-782.
- Katona, M.G. (1984): Evaluation of viscoplastic cap model, Journal of Geotechnical Engineering, 110(8), 1106-1125.
- Katona, M.G., and Mulert, M.A. (1984): A viscoplastic cap model for soils and rock. Mechanics of engineering materials, C.S. Desai and R.H. Gallagher, eds., Wiley, New York, 335-350.
- Kavazanjian, E., and Mitchell, J.K. (1977): A general stress-strain-time formulation for soils, Proceedings, 9th International Conference of Soil Mechanics and Foundation Engineering, 113-120.

- Kikumoto, M., Wood, D.M. and Russell, A. (2010): Particle crushing and deformation behaviour, *Soils and Foundations*, 50(4), 547-563.
- Kiyota, T. and Tatsuoka, F. (2006): Viscous property of loose sand in triaxial compression, extension and cyclic loading, *Soils and Foundations*, 46(5), 665-684.
- Kjaernsli, B., and Sande, A. (1963): Compressibility of some coarse-grained materials, *Proceedings of European Conference on Soil Mechanics and Foundation Engineering.*, Weisbaden, Germany, 245-251.
- Komornik. A., Wiseman, G., and Zeitlen, J.G. (1972): Building settlement on end-bearing driven piles, *Proceedings, American Society of Civil Engineering Specialty Conference on Performance of Earth and Earth-supported Structures*, Lafayette, Ind., 1(2), 1135-1153.
- Kongsukprasert, L. and Tatsuoka, F. (2005): Ageing and viscous effects on the deformation and strength characteristics of cement-mixed gravely soil in triaxial compression, *Soils and Foundations*, 45(6), 55-74.
- Kou, S. Q., Liu, H. Y., Lindqvist, P.-A., Tang, C. A., and Xu, X. H. (2001): Numerical investigation of particle breakage as applied to mechanical crushing. Part II: Interparticle breakage, *International Journal of Rock Mechanics and Mining Sciences*, 38, 1163-1172.
- Kropschot, R.H. and Mikesell, R.P., (1957): Strength and fatigue of glass at very low temperatures, *Journal of Applied Physics*, 28(5), 610-614.
- Kuhn, M.R. (1987): Micromechanical aspects of soil creep, PhD dissertation, University of California at Berkeley, Berkeley, Calif.

- Kuhn, M.R. and Mitchell, J.K. (1993): New perspectives on soil creep, *Journal of Geotechnical Engineering*, 119(3), 507-524.
- Kuwano, R., and Jardine, R. (2002): On measuring creep behaviour in granular materials through triaxial testing, *Canadian Geotechnical Journal*, 39(5), 1061-1074.
- Lacerda, W.A., and Houston, W.N. (1973): Stress relaxation in soils, *Proceedings, 8th International Conference, Soil Mechanics and Foundation Engineering*, 1, 221-227.
- Ladanyi, B., and Melouki, M. (1993): Determination of creep properties of frozen soils by means of borehole stress relaxation tests, *Canadian Geotechnical Journal*, 30, 170-186.
- Ladanyi, B., and Benyamina, M.B. (1995): Triaxial relaxation testing of a frozen sand. *Canadian Geotechnical Journal*, 32, 496-511.
- Lade, P.V. (1994): Creep effects on static and cyclic instability of granular soils, *Journal of Geotechnical Engineering*, 120(2), 404-419.
- Lade, P.V. (2007): Experimental study and analysis of creep and stress relaxation in granular materials. *Proceedings, Geo-Denver (CD-ROM)*, Denver.
- Lade, P.V., and Duncan, J. M. (1973): Cubical triaxial tests on cohesionless soil, *J. Soil Mech. and Found. Div.*, 99(SM10), 793-812.
- Lade, P.V., Liggio, Jr., C.D. and Nam, J. (2009): Strain rate, creep, and stress drop-creep experiments on crushed coral sand, *J. Geotechnical and Geoenvironmental Engineering, ASCE*, 135(7), 941-953.

- Lade, P.V., Liggio, Jr., C.D., and Yamamuro, J.A. (1998): Effects of non-plastic fines on minimum and maximum void ratios of sand, *Geotechnical Testing Journal*, ASTM, GTJODJ, 21(4), 336-347.
- Lade, P.V. and Liu, C.T. (1998): Experimental study of drained creep behavior of sand, *J. Engr. Mech. ASCE*, 124(8), 912-920.
- Lade, P.V., Nam, J. and Liggio, Jr., C.D. (2010): Effects of particle crushing in stress drop-relaxation experiments on crushed coral sand, *J. Geotechnical and Geoenvironmental Engineering*, ASCE, 136(3), 500-509.
- Lade, P.V., Yamamuro, J.A., and Bopp, P.A. (1996): Significance of particle crushing in granular materials, *Journal of Geotechnical Engineering*, ASCE, 122(4), 309-316.
- Lagioia, R., (1998): Creep and apparent preconsolidation in carbonate soils. *The geotechnics of hard soil-soft rocks*, edited by Evangelista, A. and Picarelli, L., Balkema, Rotterdam, The Netherlands.
- Lawn, B. (1993): *Fracture of brittle solids*, 2nd edition, Cambridge University Press.
- le Roux, H. (1965): The strength of fused quartz in water vapor, *Proceedings, Royal Society, London, Section A*, 286, 390-401.
- Lee, K.L. (1977): Adhesion bonds in sands at high pressures, *Journal of the Geotechnical Engineering Division, Proceedings of the ASCE*, 103(GT8), 908-913.
- Lee, K.L. and Farhoomand, I. (1967): Compressibility and crushing of granular soils in anisotropic triaxial compression, *Canadian Geotechnical Journal*; 4, 68-86.

- Lee, K.L. and Seed, H.B. (1967): Drained Strength Characteristics of Sands, Journal of the Soil Mechanics and Foundations Division, ASCE 93(SM6), 117-141.
- Lee, K.L, Seed, H.B., and Dunlop, P. (1967): Effect of moisture on the strength of a clean sand, Journal of the Geotechnical Engineering Division, Proceedings of the ASCE, 93(SM6), 17-40.
- Lee, K.L, Seed, H.B., and Dunlop, P. (1969): Effect of transient loading on the strength of sand, Proceedings, 7th International Conference on Soil mechanics and Foundation Engineering, Mexico, 1, 239-247.
- Lemaitre, J. and Chaboche, J.L. (1994): Mechanics of solid materials, Cambridge University Press.
- Leslie, D.D. (1963): Large Scale Triaxial Tests on Gravelly Soils, Proceedings, 2nd Pan-American Conference on Soil Mechanics and Foundation Engineering, Sao Paulo. Brazil, 1, 183-202.
- Leung, C.F., Lee, F.H. and Yet, N.S. (1996): The role of particle breakage in pile creep in sand, Canadian Geotechnical Journal, 33(6), 888-898.
- Leroueil, S., Kabbaj, M., Tavenas, F., and Bouchard, R. (1985): Stress-strain-strain rate relation for the compressibility of sensitive natural clays, Géotechnique, 35(2), 159-180.
- Leroueil, S. and Marques, M.E.S. (1996): State of the Art: Importance of train rate and temperature effects in geotechnical engineering, Measuring and Modeling Time Dependent Soil Behavior, Geotech. Spec. Publ. No. 61, Sheahan, T.C., and Kaliakin, V.N., eds, ASCE, Reston, VA, 1-60.

- Liingaard, M., Augustesen, A. and Lade, P.V. (2004): Characterization of models for time-dependent behavior of soils, *International Journal of Geomechanics*, ASCE, 4(3), 157-177.
- LO, X.1. (1959) po presur — Strain R2lation — zbip of Nor11y CorRsolidated Urd±sturbed C1€ys - Part 11”: E:cperirtal In’nstigaior. and Practi1 Appiicac. Cad±a C.cthnic.al Journal, v2.. 6 c 4, pp. 395—412.
- Lo, K.Y. (1969): The pore pressure-strain relationship of normally consolidated undisturbed clays-part II: experimental investigation and practical applications, *Canadian Geotechnical Journal*, 6(4), 395-412.
- Ludwick, P. (1922): Uber den Einfluss der Deformationsgeschwindigkeit bei bleibenden Deformationen mit besonderer Berucksichtigung der Nachwirkungserscheinungen, *Phys. Z.*, 10(12), 411-417.
- Marsal, R.J. (1967): Large scale testing of rockfill materials, *Journal of the Soil Mechanics and Foundations Division*, 93(3M2), 27-43.
- Matsui, T., and Abe, N. (1985a): Elasto-viscoplastic constitutive equation of normally consolidated clays based on flow surface theory, 5th International Conference on Numerical Methods in Geomechanics, Nagoya, Japan, 407-413.
- Matsui, T., and Abe, N. (1985b): Undrained creep characteristics of normally consolidated clay based on the flow surface model, *Proceedings, 11th International Conference, Soil Mechanics and Foundation Engineering*, 140-143.
- Matsushita, M., Tatsuoka, F. Koseki, J., Cazaciu, B., Benedetto, H. and Yasin, S.J.M. (1999): Time effects on the pre-peak deformation properties of sands, *Pre-failure*

- Deformation Characteristics of Geomaterials, Jamiolkowski, Lancelotta, and Lo Presti, eds., Balkema, Rotterdam, 681-689.
- McDowell, G.R. and Bolton, M.D. (1998): On the micro mechanics of crushable aggregates, *Géotechnique* 48(5), 667-679.
- Mejia, C.A., Vaid, Y.P., and Negussey, D. (1988): Time dependent behaviour of sand, International Conference on Rheology and Soil Mechanics, Coventry, England.
- Meschyan, S.R. (1995): Experimental rheology of clayey soils, *geotechnika* 13 (selected translation of Russian geotechnical literature), A. A. Balkema, Rotterdam/Brookfield.
- Mesri, G. (1973): Coefficient of secondary compression, *Journal of the Soil Mechanics and Foundations Division*, 99(1), 123-137.
- Mesri, G., Feng, T. W., and Benak, J. M. (1990): Postdensification penetration resistance of clean sands, *Journal of Geotechnical Engineering*, 116(7), 1095-1115.
- Mesri, G., and Godlewski, P.M. (1977): Time and stress compressibility interrelationship, *Journal of Geotechnical Engineering*, 103(5), 417-430.
- Michalske, T.A. and Freiman, S.W. (1981): A molecular interpretation of stress corrosion in silica, *Nature*, 295, 511.
- Michalske, T.A. and Freiman, S.W. (1983): A molecular mechanism for stress corrosion in vitreous silica, *Journal of American Ceramics Society*, 66, 284-288.
- Mitchell, J.K. (2008): Aging in Sand- A Continuing Enigma?, 6th International Conference on Case Histories in Geotechnical Engineering, Arlington, Virginia, 1-21.
- Mitchell, J.K. (1993): Fundamentals of soil behavior, 2nd Ed., Wiley, New York.

- Mitchell, J.K. and Solymar, Z.V. (1984): Time dependent strength gain in freshly deposited or densified sand, *Journal of Geotechnical Engineering, ASCE*, 110(11), 1559-1576.
- Miura, N. and O-Hara, S. (1979): Particle-crushing of a decomposed granite soil under shear stresses, *Soils and Foundations*, 19(3), 1-14.
- Miura, N. and Yamanouchi, T. (1973): Compressibility and drained shear characteristics of a sand under high confining pressures, *Tech. Reps of the Yamaguchi University*, 1(2), 271-290.
- Miura, N., and Yamanouchi, T. (1975): Effect of water on the behavior of a quartz-rich sand under high stresses, *Soils and Foundations*, 15(4), 23-34.
- Miura, N. and Yamanouchi, T. (1977): Effect of particle-crushing on the shear characteristics of a sand, *Proceedings of the JSCE*, No. 260, 109-418 (in Japanese).
- Mould, R.E. and Southwick, R.D. (1959): Strength and static fatigue of abraded glass under controlled ambient conditions: II, *Journal of American Ceramics Society*, 42, 582-592.
- Mould, R.E. (1961): Strength and static fatigue of abraded glass under controlled ambient conditions: IV, Effect of surrounding medium, *Journal of American Ceramics Society*, 44, 481-491.
- Murayama, S. (1983): Formulation of stress-strain-time behavior of soils under deviatoric stress condition, *Soils and Foundations*, 23(2), 43-57.
- Murayama, S., Michihiro, K., and Sakagami, T. (1984): Creep characteristics of sands, *Soils and Foundations*, 24(2), 1-15.

- Murayama, S. and Shibata, T. (1961): Rheological Properties of Clays, Proceedings, 5th International Congress on Soil Mechanics and Foundations, Paris, 269-273.
- Nakata, Y., Hyde, A.F.L., Hyodo, M., and Murata H. (1999): A probabilistic to sand particle crushing in triaxial test, *Géotechnique*, 49(5), 567-583.
- Nakata, Y., Hyodo, M., Hyde, A.F.L., Kato, Y., and Murata, H. (2001a): Microscopic particle crushing of sand subjected to high pressure and one-dimensional compression, *Soils and Foundations*, 41(1), 69-82.
- Nakata, Y., Kato, Y., Hyodo, M., Hyde, A.F.L., and Murata, H. (2001b): One-dimensional compression behaviour of uniformly graded sand related to single particle crushing strength, *Soils and Foundations*, 41(2), 39-51.
- Nash N. L. (1953): The shearing resistance of a fine closely graded sand, Proceedings, 3rd International Conference on Soil Mechanics and Foundation Engrg., Zurich, 1, 160-164.
- Nash. K.L. and Dixon R.K. (1961): The measurement of pore pressure in sand under rapid triaxial tests, Proceedings of Conference on the Pore Pressure and Suction in Soils, Butterworths, London, 21-25.
- Nova, R. (1982): A viscoplastic constitutive model for normally consolidated clay, International Union of Theoretical and Applied Mechanics Conference on Deformation and Failure of Granular Materials, Delft, The Netherlands, 287-295.
- Obert, L. and Duvall, W. (1942): Use of subaudible noise for prediction of rockbursts, U.S. Bur. Mines Rept. Invest. 3634, 1-13.

- Oka, F., Adachi, T. and Mimura, M. (1988): Elasto-viscoplastic constitutive models for clays, Proceedings, International Conference Rheology and Soil Mechanics, Elsevier, Science, New York, 12-28.
- Olszak, W., and Perzyna, P. (1966): On elastic-viscoplastic soils, rheology and soil mechanics, International Union of Theoretical and Applied Mechanics Symposium, Grenoble, Springer, Berlin.
- Olszak, W., and Perzyna, P. (1970): Stationary and nonstationary viscoplasticity, McGraw-Hill, New York [Kanninen, F. (1969): Inelastic behavior of solids. Battelle Institute Materials of Science Colloquia, Columbus and Atwood Lake, Ohio, 53-75].
- Oldecop, L.A. and Alonso, E.E. (2007): Theoretical investigation of time-dependent behaviour of rockfill, *Géotechnique*, 57(3), 289-301.
- Orowan, E. (1944): The fatigue of glass under stress, *Nature*, 154, 341-343.
- Orowan, E. (1955): Energy criteria of fracture, *Welding Journal Research Supplement*, 34(3), 1575-1605.
- Perzyna, P. (1963a): The constitutive equations for work-hardening and rate sensitive plastic materials, *Proceedings of Vibration Problems*, 3(4), 281-290.
- Perzyna, P. (1963b): The constitutive equations for rate sensitive plastic materials, *Quarterly of Applied Mathematics*, 20(4), 321-332.
- Perzyna, P. (1963c): The study of the dynamical behaviour of rate sensitive plastic materials, *Archives of Mechanics Stos.*, 1(15), 113-130.
- Perzyna, P. (1966): Fundamental problems in viscoplasticity, *Advances in Applied Mechanics*, 9, 244-377.

- Prevost, J.H. (1976): Undrained stress-strain-time behavior of clays, *Journal of Geotechnical Engineering*, 102(12), 1245-1259.
- Rabotnov, Y.N. (1969): Creep problems in structural members, North-Holland, Amsterdam, The Netherlands.
- Ramamurthy, T. (1969): Crushing phenomena in granular soils, *Journal of the Indian National Society of Soil Mechanics and Foundation Engineering*, 8, 67-86.
- Roberts, J. (1964): Sand compressibility as a factor in oil field subsidence, D.Sc. Thesis, Massachusetts Institute of Technology, Cambridge, Mass.
- Roberts, J.E. and de Souza, J. M. (1958): The compressibility of sands, *Proceedings of ASTM*, 58, 1269-1277.
- Rowe, P.W. (1962): The Stress dilatancy relations for static equilibrium of an assembly of particles in contact, *Proceedings, Royal Society, London, Series A*, 269, 500-527.
- Russell, A.R. and Khalili, N. (2004): A bounding surface plasticity model for sands exhibiting particle crushing, *Canadian Geotechnical Journal*, 41, 1179-1192.
- Rutledge, P.C., (1947): Cooperative triaxial shear research program of the Corps of Engineers, Progress Report, Waterways Experiment Station, Vicksburg, Miss.
- Rüsch, H. (1960): Researches toward a general flexural theory for structural concrete, *Journal of the American Concrete Institute*, 57(1), 1-28.
- Saada, A.S. (1962): A rheological analysis of shear and consolidation of saturated clays, *HRB Bulletin* 342, 52-75.

- Salim W, Indraratna B.A. (2004): New elastoplastic constitutive model for coarse granular aggregates incorporating particle breakage, *Canadian Geotechnical Journal*, 657-671.
- Santamarina, J. C. (2003): Soil behavior at the microscale: Particle forces, *Proceedings, Soil Behavior and Soft Ground Construction*, GSP No. 119, ASCE, Reston, Va., 25-56.
- Santucci de Magistris, F., and Tatsuoka, F. (1999): Time effects on the stress-strain behaviour of Metramo silty sand, Prefailure deformation characteristics of geomaterials. M. Jamiolkowski, R. Lancelotta, and D. LoPresti, eds. Balkema, Rotterdam, The Netherlands, 681-689.
- Schmertmann, J. H. (1987): Discussion of "Time-dependent strength in freshly deposited or densified sand, by J. K. Mitchell and Z. V. Solymar. *Journal of Geotechnical Engineering*, ASCE, 113(2), 173-175.
- Schmertmann, J. H. (1991): The mechanical aging of soils, *Journal of Geotechnical Engineering*, ASCE, 117(9), 1288–1330.
- Schmitz, G.K. and Metcalfe, A.G. (1966): Stress Corrosion of E-glass Fibers, *Industrial and Engineering Chemistry, Research and Development*, 5(1), 1-8.
- Schoening, F.R.L. (1960): On the strength of glass in water vapor, *Journal of Applied Physics*, S1, 1779-1784.
- Scholz, C.H. (1968a): Microfracturing and the inelastic deformation of rock in compression, *Journal of Geophysical Research*, 73(4), 1417-1432.
- Scholz, C.H. (1968b): Mechanism of Creep in Brittle Rock, *Journal of Geophysical Research*, 73(10), 3295-3302.

- Scholz, C.H. (1968c): Microfractures, aftershocks, and seismicity, *Bulletin of the Seismological Society of America*, 68, 1117-1130.
- Scholz, C.H. (1972): Static fatigue of quartz, *Journal of Geophysical research*, 77(11), 2104-2114.
- Schurkow, S. (1932): The influence of adsorbed layers on the strength of quartz fibers, *Phys., Z. der Sowjetunion*, 1, 123-131.
- Seed, H.B. (1976): Some aspects of sand liquefaction under cyclic loadings, *Proceedings, behaviour of off-shore Structures, Norway*, 374-391.
- Seed, H.B. and Lee, K.L. (1967): Undrained strength characteristics of cohesionless soils, *Journal of Soil Mechanics and Foundations Division, ASCE*, 93(SM6), 333-360.
- Seed, H.B. and Lundgren, R. (1954): Investigation of the effect of transient loading on the strength and deformation characteristics of saturated sands, *Proceedings of ASTM*, 54, 1288-1306.
- Sekiguchi, H., and Ohta, H. (1977): Induced anisotropy and time dependency in clays, *Proceedings, 9th International Conference of Soil Mechanics and Foundation Engineering, Tokyo*, 229-238.
- Sekiguchi, H. (1984): Theory of undrained creep rupture of normally consolidated clay based on elasto-viscoplasticity, *Soils and Foundations*, 24(1), 129-147.
- Sekiguchi, H. (1985): Macrometric approaches-static-intrinsically time dependent constitutive laws of soils, *Rep., ISSMFE Subcommittee on Constitutive Laws of Soils and Proceedings of Discussion Session 1A, International Society of Soil Mechanics*

- and Foundation Engineering, Subcommittee on Constitutive Laws of Soils, 11th ICFMFE, San Francisco, 66-98.
- Sheahan, T.C. and Kaliakin, V.N. (1999): Microstructural considerations and validity of the correspondence principle for cohesive soils, Engineering Mechanics, Proceedings of the 13th Conference, N. Jones and R. Ghanem, eds., ASCE publ., Baltimore, MD, USA.
- Silvestri, V., Soulie', M., Touchan, Z., and Fay, B. (1988): Triaxial relaxation tests on a soft clay, Advanced triaxial testing of soil and rock, ASTM, Philadelphia, 321-337.
- Singh, A., and Mitchell, J.K. (1968): General stress-strain-time function for soils, Journal of the Soil Mechanics and Foundations Division, 94(1), 21-46.
- Skempton, A. W. (1954): The pore pressure coefficients A and B, Géotechnique, 4, 143–147.
- Skrzypek, J.J. (1993): Plasticity and creep-Theory, examples, and problems (English edition), B. H., Richard, ed., CRC Press, London.
- Sorensen, K.K., Baudet, B.A. and Simpson, B. (2007): Influence of structure on the time-dependent behaviour of a stiff sedimentary clay, Géotechnique, 57(1), 113-124.
- Sowers, G.F., Williams, R.C., and Wallace, T.S. (1965): Compressibility of Broken Rock and the Settlement of Rockfills, Proceedings of the 6th International Conference on Soil Mechanics and Foundations Engineering, Montreal, Canada, II, 561-565.
- Suklje, L. (1957): The analysis of the consolidation process by the isotaches method, Proceedings, 4th International Conference, Soil Mechanics and Foundation Engineering, 1, 200-206.

- Suresh, S. (1998): Fatigue of Materials, 2nd edition, Cambridge University Press.
- Sweeney, M., and Lambson, M.D. (1991): Long term settlement of storage tanks on sand, Proceedings, 10th European Conference on Soil Mechanics and Foundation Engineering, Florence, 2, 587-591.
- Tang, C. A., Xu, X. H., Kou, S. Q., Lindqvist, P.-A., and Liu, H. Y. (2001): Numerical investigation of particle breakage as applied to mechanical crushing, Part I: Single-particle breakage, International Journal of Rock Mechanics and Mining Sciences, 38, 1147-1162.
- Tatsuoka, F. (2007): Inelastic deformation characteristics of geomaterial, Special Lecture, Soil Stress-Strain Behavior: Measurement, Modeling and Analysis, Proceedings of Geotechnical Symposium in Roma, March 16-17, 2006 (Ling et al., eds.), 1-108.
- Tatsuoka, F., di Benedetto, H., Enomoto, T., Kawabe, S. and Kongkitkul, W. (2008): Various viscosity types of geomaterials in shear and their mathematical expression, Soils and Foundations, 48(1), 41-60.
- Tatsuoka, F., Enomoto, T., and Kiyota, T. (2006): Viscous property of geomaterial in drained shear, Geomechanics II–Testing, Modeling and Simulation, Proceedings of 2nd Japan-U.S. Workshop, Kyoto, ASCE Geotechnical Special Publication, No. 156, Lade and Nakai, eds., 285-312.
- Tatsuoka, F., Santucci de Magistris, F., Hayano, K., Momoya, Y., and Koseki, J. (2000): Some new aspects of time effects on the stress-strain behaviour of stiff geomaterials, The Geotechnics of Hard Soils-Soft Rocks, 1998, R. Evangelista and L. Picarelli, eds., Balkema, Rotterdam, The Netherlands, 2, 1285-1371.

- Tatsuoka, F., Shihara, M., di Benedetto, H., and Kuwano, R. (2002): Time-dependent shear deformation characteristics of geomaterials and their simulation, *Soils and Foundations*, 42(2), 103-129.
- Tavenas, F., Leroueil, S., La Rochelle, P., and Roy, M. (1978): Creep behavior of an undisturbed lightly overconsolidated clay, *Canadian Geotechnical Journal*, 15(3), 402-423.
- Taylor, D.W. (1942): Research on consolidation of clays. Serial 85, Massachusetts Institute of Technology, Department of Civil and Sanitary Engineering, Cambridge, Mass.
- Taylor, D.W. (1948): Fundamentals of soil mechanics, John Wiley & Sons, Inc., New York, N.Y.
- Terzaghi, K. (1925): Elastic behavior of sand and clay, *Engineering News Record.*, 95 (Dec), 987.
- Terzaghi, K. (1960): Discussion on settlement of salt springs and lower Bear River concrete face dams, *Trans. ASCE*, 125(2), 139-148.
- Terzaghi, K., and Peck, R.B. (1948): Soil mechanics in engineering practice, 1st Ed., John Wiley & Sons, Inc., New York, N.Y., 61.
- Thomann, T.G. and Hryciw, R.D. (1992): Stiffness and strength changes in cohesionless soils due to disturbance, *Canadian Geotechnical Journal*, 29(5), 853-861.
- Valdes, J.R. and Caban, B. (2006): Monitoring the hydraulic conductivity of crushing sands, *Geotechnical Testing Journal*, 29(14), 322-329.

- Van Mier, J.G.M. (2009): Mode II fracture localization in concrete loaded in compression, *Journal of Engineering Mechanics*, ASCE, 135(1), 1-8.
- Vesic, A., and Clough, G.W. (1968): Behavior of granular materials under high stresses, *Journal of the Soil Mechanics and Foundation Engineering Division*, ASCE, 94(3), 661-668.
- Vialov, S., and Skibitsky, A.: Problems of the rheology of soils, *Proceedings*, 5th International Congress on Soil Mechanics and Foundations, Paris, 387-392.
- Weibull, W. (1939): A statistical theory of the strength of materials, *Proceedings of Royal Swedish Academy of Engineering Science*, 151, Stockholm, Sweden.
- Weibull, W. (1951): A statistical distribution function of wide applicability, *Journal of Applied Mechanics*, 18, 293-297.
- Whitman. R.V. and Healy. K.A, (1962): Shear strength of sands during rapid loadings, *Journal of the Soil Mechanics and Foundation Division*, ASCE, 88(SM 2), 99-132.
- Wiederhorn, S.M. (1975): Crack growth as an interpretation of static fatigue, *J. Non-Crystalline Solids*, 19, 169-181.
- Wiederhorn, S.M. and Bolz, L.H. (1970): Stress corrosion and static fatigue of glass, *Journal of American Ceramics Society*, 53, 543-548.
- Wiederhorn, S.M. and Johnson, H. (1973): Effect of electrolyte pH on crack propagation in glass, *Journal of American Ceramics Society*, 56, 192-197.
- Wijk, G. (1978): Some new theoretical aspects of indirect measurements of the tensile strength of rocks, *International Journal of Rock Mechanics and Mining Sciences and Geomechanics Abstracts*, 15, 149-160.

- Wood, D.M. (2007): The magic of sands- the 20th Bjerrum lecture presented in Oslo, 25 November 2005, *Canadian Geotechnical Journal*, 44(11), 1329-1350.
- Yamamuro, J.A. and Lade, P.V. (1993): Effects of strain rate on instability of granular soils, *Geotechnical Testing Journal*, 16(3), 304-313.
- Yamamuro, J.A., Bopp, P.A., and Lade, P.V., (1996): One-dimensional compression of sands at high pressures, *Journal of Geotechnical Engineering, ASCE*, 122(2), 147-154.
- Yao, Y.P., Yamamoto, H., Wang, N.D., (2008): Constitutive model considering sand crushing, *Soils and Foundations*, 48(4), 603-608.
- Yin, J.H. (1999): Nonlinear creep of soils in oedometer tests, *Géotechnique*, 49(2), 699-707.
- Yin, J.H., and Graham, J. (1989a): Viscous-elastic-plastic modeling of one-dimensional time-dependent behaviour of clays, *Canadian Geotechnical Journal*, 26, 199-209.
- Yin, J.H., and Graham, J. (1989b): General elastic viscous plastic constitutive relationships for 1D straining in clays, *Proceedings, 3rd International Symposium Numerical Models in Geomechanics*, 108-117.
- Yin, J.H., and Graham, J. (1994): Equivalent times and one-dimensional elastic viscoplastic modelling of time-dependent stress-strain behaviour of clays, *Canadian Geotechnical Journal*, 31, 45-52.
- Yin, J.H., and Graham, J. (1996): Elastic visco-plastic modelling of one-dimensional consolidation, *Géotechnique*, 46(3), 515-527.
- York, D.L., Brusey, W.G., Clemente, F.M., and Law, S.K. (1994): Setup and relaxation in glacial sand, *Journal of Geotechnical Engineering, ASCE*, 120(9), 1498-1513.

- Zeller, J., and Wullimann, R. (1957): The shear strength of the shell materials for the Goschenalp Dam, Switzerland, Proceedings, 4th International Conference on Soil Mechanics and Foundation Engineering, London, 2, 399-404.
- Zienkiewicz, O.C., and Corneau, I.C. (1974): Visco-plasticity-plasticity and creep in elastic solids-A unified numerical solution approach, International Journal for Numerical Methods in Engineering , 8, 821-845.
- Zienkiewicz, O.C., Humpheson, C., and Lewis, R.W. (1975): Associated and nonassociated viscoplasticity and plasticity in soil mechanics, Géotechnique, 25(4), 671-689.